The Hydrodynamic Effects of Long-line Mussel Farms

A thesis
submitted in partial fulfilment
of the requirements for the Degree
of
Doctor of Philosophy in Civil Engineering
at the
University of Canterbury
by
David Russell Plew

University of Canterbury
Christchurch, New Zealand
2005

ABSTRACT

The hydrodynamic effects of long-line mussel farms are studied through a two-pronged approach. Large-scale hydrodynamic effects are investigated through the use of field measurements, primarily at a large mussel farm in Golden Bay, New Zealand (230 long-lines, covering an area of 2.45 km by 0.65 km). The research focuses on three areas: the effect of the farm on currents, mixing and stratification, and the dissipation of wave energy. Measurements are also made of the forces on long-line anchor ropes, and a limited investigation is made of phytoplankton depletion. The second approach is the use of laboratory drag measurements and Particle Tracking Velocimetry (PTV) to study the effect of mussel dropper (vertical lengths of mussel-encrusted crop rope) roughness and spacing on flow at small scales. These experiments provide data on very rough cylinders, and on cylinder arrays.

The field measurements show that the local effects of mussel farms on currents are significant, but that magnitudes of the effects depend on dropper density, mussel sizes, orientation of the long-lines to the flow, and other parameters that are necessary to characterise the complex interactions between a farm and the flow. The drag on the submerged structures reduces water velocities within the Golden Bay farm by between 47% and 67%. Mussel farms present a porous obstacle to the flow, and flow that does not pass through the farm must be directed around or beneath it. The field measurements indicate that at the study site, most of the flow is diverted around the farm despite its large horizontal dimensions. The droppers at the study site extend over most of the water column (average dropper length ~ 8 m, average water depth ~ 11 m), providing a restriction to the flow beneath the farm. The strength of the density stratification may also favour a horizontal diversion. The flow around the farm is essentially two-dimensional. This suggests that two-dimensional numerical models should be sufficient to obtain reasonable predictions of the velocity drop within, and the diversion around, mussel farms. A simple two-dimensional pipe-network model gives reasonable estimates of the velocity within the farm, demonstrating that the drag of the farm may be adequately parameterised through local increases of bed friction. A wake in the form of reduced velocities extends downstream of the farm, and a mixing layer analogy suggests that this wake spreads slowly. The downstream extent of the wake cannot be determined, although it is likely to be limited by the tidal excursion.

The degree of vertical mixing caused by the flow through a mussel farm cannot be quantified, although there are clear interactions between the stratification and the farm. Two mixing mechanisms are considered. A shear layer is generated beneath the farm due to the difference in velocities between the retarded flow within the farm and the flow beneath. Shear layers beneath mussel farms are likely to be weak unless the ambient currents are strong. It will be necessary for stratification to be weak or non-existent for this mechanism to generate significant mixing. The second mechanism is smaller-scale turbulence generated by the mussel droppers. Although the efficiency of this form of mixing is likely to

be low, the large number of mussel droppers suggests that there will be some enhancement of vertical mixing.

Frequency-dependent wave attenuation is recorded, and is predicted with some success by an analytical model. Both the model and the field data show that wave dissipation increases as the wave period decreases. Wave energy dissipation at the study site averages approximately 10%, although the measurements are made during a period of low wave heights (H_s < 0.25 m). Measurements of long-line anchor rope tension at two study sites indicate that the loadings are induced by the tide, currents, and waves. Dynamic wave loadings may be significant, and higher wave forces are measured at the offshore end of a long-line.

The issue of seston or phytoplankton depletion is considered briefly through the examination of fluorescence, turbidity, and acoustic backscatter data. Although the results are consistent with a reduction of seston within the farm, differences between the inside and outside of the farm are not statistically significant.

Mussel droppers resemble extremely rough circular cylinders, with the mussel shells forming the surface roughness elements. Drag measurements and PTV flow visualisation are used to investigate the importance of the large surface roughness, and the influence of dropper spacing and long-line orientation on flow. Drag measurements conducted with smooth and rough cylinders show that high surface roughness (k_s/D ~ 0.092) has little effect on the drag coefficient of single cylinders in the range 4,000 < Re < 13,000, yet increases the drag coefficient of a row of cylinders normal to the flow. High surface roughness on single cylinders has the effect of shortening the near-wake region, increasing the peak turbulent kinetic energy (TKE) behind the cylinder, and decreasing the Strouhal number (S_t = 0.21, 0.19, 0.17 for k_s/D = 0, 0.048, and 0.094 respectively). Arrays of rough cylinders (k_s/D = 0.094) demonstrate similar flow characteristics to those of smooth cylinders. At cylinder spacings of S/D < 2.2, the surface roughness acts to favour the formation of a particular metastable wake pattern, whereas different metastable wake patterns are formed each run behind the smooth cylinders. The experiments show that the drag on single row arrays of cylinders are related to the cylinder spacing (increasing drag with decreasing spacing), and the drag also varies with the sine of the angle to the flow, except where the array is at low angles to the flow. The PTV measurements provide new data regarding the two-dimensional distributions of velocity, TKE, and turbulence statistics behind the cylinder arrays.

ACKNOWLEDGEMENTS

Support for this research was provided by the New Zealand Foundation for Research Science and Technology (FRST) through a Top Achiever Doctoral Scholarship. The National Institute of Water and Atmospheric Research New Zealand (NIWA) also provided support through the Centre of Excellence in Aquaculture and Marine Ecology (CEAME) in the form of funding, equipment, and personnel for field trips.

I would like to thank my three supervisors, Dr Bob Spigel, Dr Roger Nokes, and Dr Mark Davidson, for their invaluable support, advice, guidance, attention to detail, and good humour. I have enjoyed working with you all, and appreciate the many significant contributions you have made, both to this project and to my education. This project turned out to be larger and more complex than any of us expected, and I am particularly thankful for your ability to see the larger picture and to steer me in the right direction.

Thanks to the technical staff of the Department of Civil Engineering, University of Canterbury, Ian Sheppard, Kevin Wines, Richard Newton, Michael Weavers and Colin Bliss, without whose creativeness and skills the laboratory work would not have been possible.

Many NIWA staff members assisted me in this research. I particularly thank Dr Craig Stevens who provided considerable advice and guidance. Thanks also to Dr Barb Hayden for frequently supplying information and to John Fenwick, Ralph Dickson, and Warren Thompson for their assistance with field work.

The field work was also supported by OCEL, particularly Gary Teear who willing shared his experience and knowledge of the engineering aspects of mussel farming. Thanks also to Pigeon Bay Aquaculture who helped install instrumentation on their mussel long-lines.

Saving the best until last, a big thank-you to my wife Elizabeth; without your love, patience, understanding, and encouragement, I may not have made it through at all.

TABLE OF CONTENTS

LIST OF FIGURES

LIST OF TABLES

LIST OF SYMBOLS AND NOTATION

The notation and symbols used in this thesis are defined within each chapter where they are introduced. Due to the large number of parameters that must be described, some notation or symbols may have alternative meanings in different chapters. The notation and symbols used in each chapter are listed here.

Notation for Chapter 3

C_{bed}	Friction coefficient for bed
C_D	Drag coefficient
C_f	Friction Coefficient
C_{farm}	Friction coefficient for mussel farm
D	Diameter
f	Pipe friction factor
g	Gravitational acceleration
H	Pressure (m)
h	Water depth
K	Kinetic energy
L	Conduit length
L_d	Dropper length
n	Dropper density (number per unit area)
R	Hydraulic radius
Re	Reynolds Number
S	Bed friction number
S_c	Critical bed friction number
S_z	Velocity shear gradient
U	Velocity
u, u_1, u_2	Velocity in mixing layer
U_0	Upstream or free-stream velocity
Vn, Ve	North and East Velocity Components
w	Conduit width
x, y	Horizontal direction
z	Vertical direction (positive upwards)
α	Mixing layer growth parameter
α_0	Deep-water mixing layer growth parameter
β	Bearing (clockwise from North) of long-line
γ	Angle between long-line and current
δ	Mixing layer width
ε	Roughness element size
θ	Bearing (clockwise from North) of current
λ	Characteristic mixing layer parameter
ν	Kinematic viscosity
ρ	Fluid density
τ	Shear stress

Notation for Chapter 4

ψ	Background potential energy flux parameter
ΔE	PE_{mix} - PE
E_b	Background potential energy
g	Gravitational acceleration
g'	$g\Delta\rho/\rho$
h	Height of gravity current
H_f	Obstacle Height
K_z	Diffusivity
l_m	Mixing length scale
N	Buoyancy frequency
$\hat{n}$	Unit vector normal to a surface
PE	Potential energy of water column
PE_{mix}	Potential energy of a fully mixed water column
Ri	Gradient Richardson number
Ri_b	Bulk Richardson number
Ri_b'	Modified bulk Richardson number
S_z	Velocity shear gradient
S_z	Velocity shear gradient
U	Velocity
$\mathbf{u}$	Water velocity vector
U_0	Upstream or free-stream velocity
W	Work
z	Vertical direction
α	Velocity reduction factor
κ	Molecular diffusivity
ρ	Fluid density
ρ'	ρ- ρ_0
ρ_0	Reference density
σ_t	Density Anomaly
Φ_d	Diapycnal mixing rate

Notation for Chapter 5

ζ_b	Water particle excursion at the bed
ϕ	Cylinder or dropper diameter
β	A wave parameter (see equation 5.4)
α	RMS correction factor
β_{dw}	Value of β in deep water
a	Wave dissipation parameter (see equation 5.9)
a_{rms}	Root-mean-squared acceleration
A_{rms}	Root-mean-squared acceleration averaged over a dropper length
C_d	Wave drag coefficient
C_D	Wind drag coefficient
C_g	Group velocity
C_m	Wave added mass (inertial) coefficient
d	Water depth
D	Wave dissipation parameter (see equation 5.9)
d_{90}	90^{th} percentile of bed particle size distribution
E	Wave energy (per unit area of ocean)
F	Force

f	Wave frequency
F_a	Inertial (accelerative) wave force
f_b	Kamphuis bed friction factor
F_d	Drag wave force
H	Wave height
$\dot{h}$	Rate of change of wave height
H_0	Initial wave height
H_{m0}	Predicted wave height generated by wind
Hs	Significant wave height
k	Wave number
K	Keulegan-Carpenter number
k_e	Equivalent sand grain size
k_s	Surface roughness size
K_s	Shoaling coefficient
L_d	Dropper length
n	Dropper density (number of droppers per unit area)
T	Wave period
t	Time
T_b	Burst duration (when measuring waves)
T_p	Predicted wave period
u	Velocity at the dropper
u_*	Friction velocity for wind
U_{10}	Wind speed at 10 m above surface
u_m	Maximum horizontal water particle velocity in a wave cycle
u_{rms}	Root-mean-squared velocity
U_{rms}	Root-mean-squared velocity averaged over a dropper length
W	Work
X	Fetch length
z	Vertical position (zero at surface, positive upwards)
λ	Wave length
ρ	Water density

Notation for Chapter 8

ν	Kinematic viscosity
ρ	Water density
C_d	Drag coefficient
C_L	Transverse or lift coefficient
D	Diameter
f	Frequency
F_D	Drag force
F_L	Transverse or lift force
k_s	Size of surface roughness
L	Cylinder Length
Re	Reynolds number
S	Centre to centre spacing of cylinders in a row
S_t	Strouhal number
U_0	Free-stream (or tow) velocity

Notation for Chapter 9

C_{12}	Non-dimensional particle matching cost
P1	Particle in frame 1
P2	Particle in frame 2
$\mathbf{r}_1$	Position vector of particle in frame 1 (*P1*)
$\mathbf{r}_2$	Position vector of particle in frame 2 (*P2*)
$\mathbf{r}_{pred}$	Predicted position of particle *P1* in frame 2
sw_x, sw_y	Width and height of PTV analysis search window

Notation for Chapters 10, 11 and 12

ν	Kinematic viscosity
ρ	Water density
ε	Dissipation
ν_t	Turbulent eddy viscosity
$< >$	Time-averaged variable
C_D	Drag coefficient
C_L	Transverse or lift coefficient
C_u	Constant in k-ε models
D	Diameter
E	Power spectral density for velocity fluctuations
f	Frequency
f	Frequency
f_0	Eddy shedding frequency ($f_0 = S_t U_0/D$)
F_D	Drag force
F_L	Transverse or lift force
F_r	Froude number
H	Water depth
k	Turbulent kinetic energy
k_p	Particle loss coefficient
k_s	Size of surface roughness
L	Cylinder Length
n_p	Number of particles
n_{p0}	Initial number of particles
P	Turbulent production
R	Spacing between rows of cylinders (measured from centre to centre)
Re	Reynolds number
S	Centre to centre spacing of cylinders in a row
S_{ij}	Mean strain rate
s_{ij}	Fluctuating strain rate
S_t	Strouhal number
S_t	Strouhal number
T_*	Time-scale for eddy shedding
TKE	Turbulent kinetic energy (from horizontal velocity components u and v only)
U	Time-averaged velocity in the x direction
u	Turbulent fluctuation in the x direction
U_0	Free-stream (or tow) velocity
V	Time-averaged velocity in the y direction
v	Turbulent fluctuation in the y direction
x	In the downstream direction
x_0	Length of recirculating region behind cylinder
y	Perpendicular to the direction of mean flow

CHAPTER 1 INTRODUCTION AND BACKGROUND

1.1 Introduction

The rapid growth of the mussel farming industry in New Zealand has accentuated the need to consider the sustainability and potential environmental impacts of large scale mussel aquaculture. While a number of previous studies have considered biological issues such as nutrient demand, bio-deposition, and spat (juvenile mussel) recruitment, there has been no concerted assessment of the hydrodynamic effects of mussel farms. An understanding of the hydrodynamic impacts on currents, waves, and mixing is essential for predicting the extent of a farm's influence, and has significant feedback to the biological processes that govern the growth of the mussels (e.g. water velocities, nutrient supply rates, wave exposure). The purpose of this thesis is to develop an understanding of the effects of long-line mussel farms on water currents, waves, and mixing through field and laboratory based studies.

In the following sections of this introductory chapter, relevant history and issues relating to mussel farming in New Zealand are described. This is followed by a description of current mussel farming practices. Finally, the approach used in this thesis to study the hydrodynamics of mussel farming is outlined.

1.2 Background

Aquaculture (farming of marine organisms) is a rapidly growing industry in New Zealand. Currently mussels, salmon, and paua and scallops are farmed commercially along the New Zealand coastline. Of these, mussel farming is the most popular and fastest growing aquaculture activity. The species commercially grown in New Zealand is *Perna canaliculus* (Gmelin), commonly known as green or green-lipped mussels, and marketed as Greenshell^{TM} mussels. *Perna canaliculus* is the largest of the 12 mussel species found in New Zealand waters, and is native to New Zealand. As of 2001, there were more than 600 mussel farms in New Zealand, with the industry employing over 2000 people, exporting mussels to 64 countries (Ross and Hooker, 2001). Internationally, New Zealand was the 6th largest producer of mussels in 2002, with an annual production of 79,725 metric tons (t) (unprocessed weight), behind China 663,866 t, Spain 201,102 t, Italy 138,249 t, Thailand 112,482 t, and Denmark 110,873 t (FAOSTAT, 2004). Most of the New Zealand production is exported. In terms of New Zealand seafood export monetary value, mussels are second only to Hoki, averaging NZ $150 million annually from 2001 to 2003.

The collapse of the dredge fishery prompted the development of mussel farming in New Zealand, and the first commercial mussel rafts were established in the late 1960s. The first attempt at commercial farming

was in the Hauraki Gulf on the North Island of New Zealand, near where the dredge fishery had existed (Hickman, 1989), but the main focus for mussel farming shifted to the Marlborough Sounds at the top of the South Island. Initially, Spanish style raft cultivation was used; however, experimentation led to the development of a long-line system better suited to New Zealand conditions. The early growth of the mussel farming industry was hampered by concern over the social and economic acceptability of the use of coastal waters to which New Zealanders had a strong tradition of free and ready access (Hickman, 1989, 1991). The mussel farming industry grew rapidly in the early 1990s due to improvements to the long-line farming system, and a concerted international marketing effort.

In July 1996, a moratorium was imposed under Section 152 of the Resource Management Act 1991 prohibiting local bodies (councils) from granting coastal permits required for activities such as marine farming. The subsequent lifting of the moratorium on marine farming in July 1999 lead to a surge in resource applications to construct mussel farms both in small embayments (such as within the Marlborough Sounds and Banks Peninsula) and further offshore (such as Golden Bay and Clifford Bay). Some of these applications were for large farms occupying several hundred hectares. There was (in essence) a gold rush for space, with applicants applying for large areas partly so as not to miss out, and partly to prevent other parties from having exclusive rights to farm particular areas. Without an effective coastal management plan addressing marine farming, there was no framework in place requiring applicants to consider the environmental aspects of their proposed marine farming activity. At the same time, public concern regarding the potential environmental impact of large-scale intensive marine farming was increasing. As a result, a second moratorium preventing new applications was imposed from the 25 March 2002 to allow the New Zealand Government to make legislative provisions for aquaculture in the form of an amendment to the Resource Management Act. The moratorium was lifted when the Aquaculture Reform Act 2004 came into effect on the 1st January 2005. The moratorium also allowed Regional Councils time to develop appropriate Coastal Management Plans that included aquaculture, and scientists further opportunity to conduct research into the likely impacts of aquaculture.

With the growth in the size and number of mussel farms, increased emphasis has been placed on assessing the potential environmental impacts of intensive and large scale aquaculture. In particular, there is concern that the increased number and size of mussel farms may not be sustainable due to the availability of nutrients, and that there may be adverse environmental impacts including phytoplankton depletion, bio-deposition, reduced biodiversity through mono-culture, and habitat modification. This has prompted a range of research activities, of which this thesis forms part.

1.3 Mussel Farming Practices

Commercial farming of *Perna canaliculus* in New Zealand uses the continuous long-line system. Long-line structures are approximately 100-120 m in length and consist of two parallel backbone ropes supported by buoys placed a few metres apart (Figure 1.1). The buoys are typically cylindrical (with rounded ends) with approximate dimensions of 1.2 m length, 0.7 m diameter, and are made from black polyethylene. Spat-laden culture rope is looped continuously from the backbones, and can total 5 km or more in length depending on the water depth. The culture rope hangs vertically in loops. In this thesis, the term *dropper* is used to define a vertical segment of crop rope. Each loop therefore forms two droppers. This terminology extends from earlier farming methods where individual lengths of crop rope were used rather than the continuous rope used currently (Hayden, 1995).

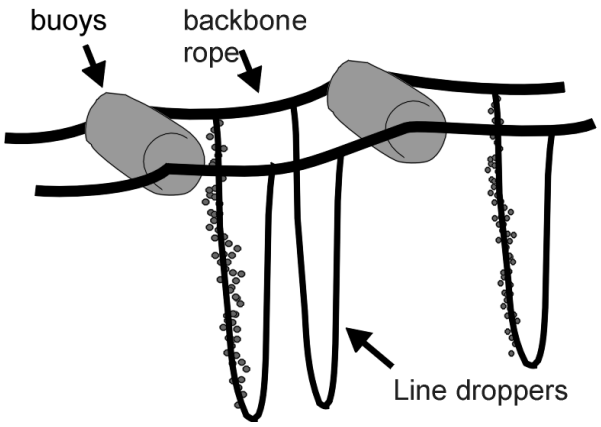

Figure 1.1 Details of a New Zealand mussel long-line.

In the early years of mussel farming, mussel droppers were short in length, extending approximately 6 m or less below the surface. In more recent years, in an effort to maximise production, the droppers extend to the full depth (35 m in parts of Pelorus Sound) with a small gap beneath to prevent the droppers dragging at low tide.

The long-lines are moored, typically with single lines (warps or anchor ropes) running to anchor blocks or screw anchors on the sea bed (Figure 1.2). The number and spacing of buoys is altered as the crop matures to support the increasing mass.

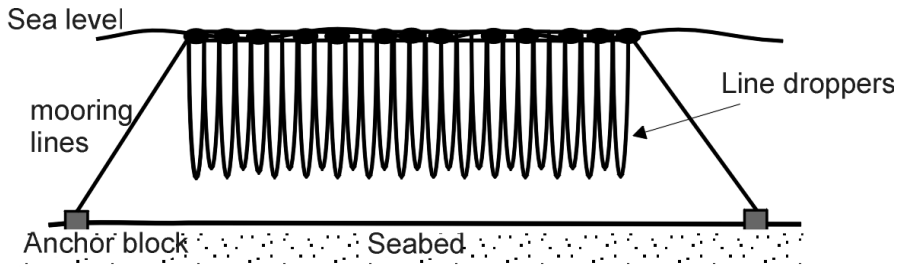

Figure 1.2 Elevation sketch of a long-line.

The majority of the farms currently operating in New Zealand are small in size, and are located near to the shore in sheltered areas. A typical unit consists of 8 to 10 parallel long-lines, occupying an area of 3 hectares. Long-lines are generally oriented parallel to the shore, and are spaced 15 – 25 m apart (Figure 1.3).

Figure 1.3 Photograph of a mussel farm at Pigeon Bay, Banks Peninsula, New Zealand.

Larger farms typically consist of blocks of smaller units in close proximity. Presently, large areas of the Marlborough Sounds are extensively farmed, and to a lesser extent Golden Bay, and the Coromandel. In Figure 1.4, an aerial photograph of Crail Bay, Pelorus Sound, shows several small mussel farms clustered along the coastline. The practice of locating several small mussel farms along the coastline is often referred to as ribbon farming.

Figure 1.4 Aerial photograph of several small mussel farms, which appear as small dark squares near the shore line, Crail Bay, Pelorus Sound, New Zealand (from Philips *et al.*, 2003).

The main source of spat, or juvenile mussels, is from seaweed irregularly deposited on 90 mile beach, near Kaitaia in the north of New Zealand. A smaller amount is also caught on "Christmas tree" rope, a black polypropylene rope incorporating sacking off-cuts to increase its surface area, hung from long-lines in the Marlborough Sounds or the Wainui Inlet, Golden Bay (Hickman, 1989, 1991). Spat is attached to crop ropes using a tubular knitted cotton stocking that holds the mussels against the crop rope. The mussels quickly (within 2-3 days) attach themselves to the crop rope, a fibrous black polypropylene rope, and the cotton stocking rots away within 2 – 3 weeks (Hayden, 1995). Generally the crop ropes are stripped and thinned part way through the growing process. Early practice targeted mussel culture densities of 300-350 mussels per metre of rope (Hickman, 1989), but current farms use a lower mussel density of 120 to 180 mussels per metre. While they can grow to a length of 250 mm, green-lipped mussels are typically harvested at a shell size of anywhere between 80 and 150 mm. Harvest size can be reached in as little as 18 months, depending on site conditions and desired crop size.

Many of the recently submitted resource applications are for either an intensification of farming (more farms in the same area) or for construction of very large farms, some over 100 hectares in size. Due to space limitations and the difficulty of acquiring permits in the near shore region due to concerns regarding potential environmental impact, conflicts of use, aesthetic considerations, and sustainability, likely industry expansion will be offshore. The offshore expansion has started to a degree in areas such as Golden Bay, where a large farm of over 160 hectares is currently in operation. Although close to shore (~ 2.5 km), the Collingwood, Golden Bay farm (Figure 1.5) is in an exposed area in comparison to the small

farms in inlets within the Marlborough Sounds (e.g. Figure 1.4). The Collingwood farm was the primary study site used for the field experiments presented in this thesis.

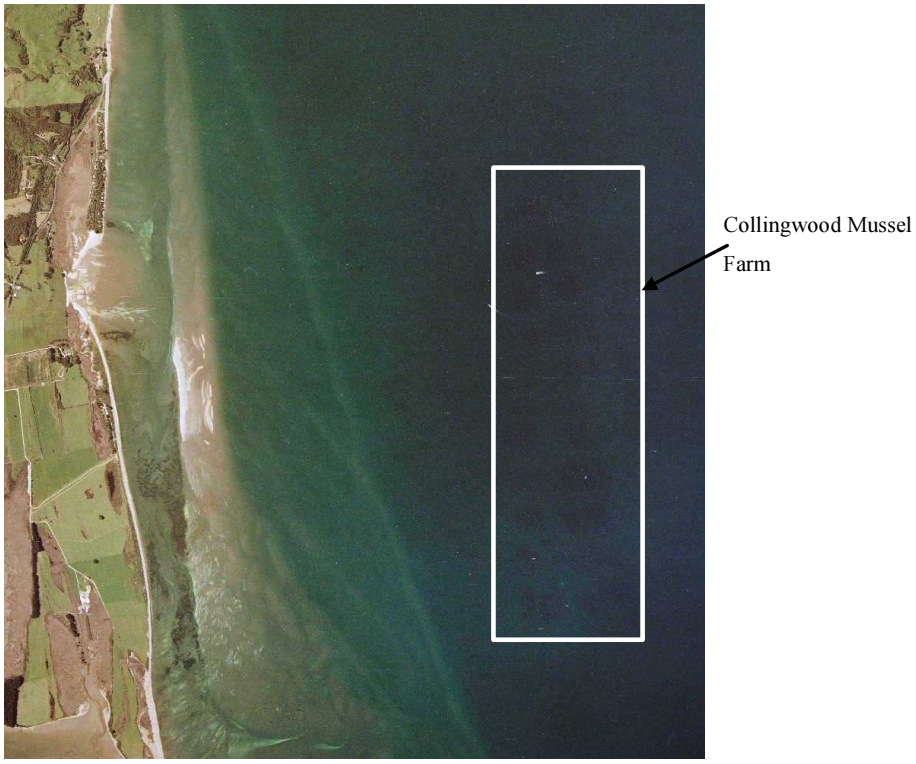

Figure 1.5 Large offshore mussel farm near Collingwood, Golden Bay. The farm consists of 230 long-lines, arranged in 20 blocks of 10-12. The farm measures 2.5 x 0.65 km, and is approximately 2.5 km from the shore (photograph provided by NIWA).

1.4 Thesis Outline

The focus of this thesis is an assessment of the hydrodynamic effects of mussel farming. Field and laboratory measurements are used to understand and quantify the effect of mussel farm structures on currents, waves, and mixing. The motivation for this research arises from the need to incorporate hydrodynamics into environmental studies due to both the direct significance of habitat alteration through the potential for reduced water velocities and wave energy, and the role of hydrodynamics in the transport and dispersion of nutrients and wastes. For example, assessments of phytoplankton depletion should include the effect of reduced water velocities from the drag on the submerged long-line elements.

Studying the hydrodynamic effects of mussel farms was a much more complex undertaking than originally imagined. The term 'hydrodynamic effect' encompasses a broad range of possible fluid dynamic behaviours. There are many different physical scales to consider, from very large (kilometres) to very small (millimetres). There is also great variability between different mussel farm configurations and

the location of farms. Farms vary in size from a few long-lines to several hundred. Some farm sites are shallow, others are in deep water. Some sites may have strong density stratification, while others are well mixed. Conditions may vary from a sheltered embayment to offshore with significant wave action and strong currents. There was relatively little previous research to guide this study. As a result, this project is to some degree a pilot study, identifying major issues and problems relating to the hydrodynamic effects of mussel farms. This thesis is therefore broad in scope and exploratory in nature.

A two-pronged approach is used in this thesis to investigate the effects of mussel long-lines on hydrodynamics: field studies, and laboratory studies. Because of the two approaches, this thesis is essentially presented in two parts, with the field studies in chapters 2 to 7, and laboratory studies in chapters 8 to 12. An overall summary and conclusions chapter (chapter 13) connects the two and places each in context.

Due to the exploratory nature of this research, the structure of the thesis does not follow the conventional pattern. Rather than the traditional format of the development of a theoretical or semi-empirical model, followed by supporting laboratory experiments, and perhaps comparison with field studies, this thesis follows a topical approach. In the field studies section, each chapter addresses a different aspect of the hydrodynamic effects of mussel farms (although these aspects may interlink). Relevant sections of theory or scaling are embedded within each chapter. This provides a more logical progression, with each chapter being mostly self-contained. The field studies primarily consider large scale hydrodynamic effects; that is to say effects that have scales of the order of the farm. The original intention of the laboratory experiments was to study the farm scale effects in a controlled environment. However, it soon became apparent that large scale flow effects were strongly influenced by small scale parameters such as the spacing and configuration of mussel droppers. A decision was therefore made to use the laboratory study to focus on the dropper scale, and to progressively build up an understanding of the larger farm scale features. Unfortunately, as the mussel droppers have diameters of 0.1 to 0.2 m, and the farm may have dimensions in excess of a kilometre, there was a large gap between these scales that could not be bridged within the scope of this thesis.

The field studies commence with a review of literature where the effects of aquaculture on hydrodynamics have been considered, along with a description of the study sites and instrumentation used for the field measurements (Chapter 2). The following chapters each consider a particular effect of long-line aquaculture, with results and discussions regarding water currents (Chapter 3), stratification (Chapter 4), and waves (Chapter 5). Additional chapters consider the structural loadings on a long-line (Chapter 6), and a brief consideration of depletion of seston (phytoplankton, and inorganic or organic particles in suspension), (Chapter 7).

The second approach is the use of laboratory-based tow tests and Particle Tracking Velocimetry imaging to gain an understanding of the factors affecting energy dissipation through drag, and an insight into the small scale flow features around individual mussel droppers (chapters 8 to 12). These small scale flow features are of particular interest due to the role they play in phytoplankton uptake by the mussels, and because the large scale effects on currents result from the cumulative effect of flow around hundreds (or even thousands) of mussel droppers. The approach followed in the laboratory experiments is to model the mussel long-lines as arrays of very rough circular cylinders. This section commences with a review of the literature on the flow around cylinders and cylinder arrays (Chapter 8). The following chapter describes the methodology used in the laboratory experiments (Chapter 9). Results for single cylinders are presented in Chapter 10, single rows of cylinders in Chapter 11, and other cylinder array configurations in Chapter 12.

CHAPTER 2 INTRODUCTION TO FIELD WORK

2.1 Introduction

A mussel long-line consists of many submerged or partly submerged items that will induce drag when moving relative to the water. These items include the mussel droppers, the buoys, and the anchor ropes. In terms of surface area, the mussel droppers are the most significant. The drag forces on the structure will consist of a quasi-steady component caused by currents, and a fluctuating component due to wave motion. A large mussel farm may consist of several hundred long-lines, and it is possible that the combined drag is sufficient to significantly affect water currents, and dissipate wave energy. Reduction of water currents within a mussel farm would lead to reduced nutrient fluxes through the farm, which in turn may lead to greater nutrient or phytoplankton depletion, and reduced mussel growth. Dissipation of wave energy may cause effects inshore from the farm such as changes in sediment transport, erosion, and possibly even changing the habitat of the affected area for different aquatic plant or animal species. Additionally, turbulence generated by the farm may result in mixing and changes in the density stratification of the water column.

In the following chapters of this thesis, field measurements are used to elucidate the effects a mussel farm may have on currents (Chapter 3), mixing/stratification (Chapter 4), and waves (Chapter 5). Additionally, a brief analysis of the measured wave loadings on the anchor ropes of a mussel long-line is presented in Chapter 6. Finally, in Chapter 7, measurements of fluorescence, turbidity, and acoustic backscatter obtained during the measurements of currents and water salinity/temperature presented in other chapters are analysed to gain insight into the potential for depletion of seston (all particulate matter, biotic and abiotic, in the water column) by a large mussel farm.

The present chapter serves as an introduction to the field work. Presented in the following sections of this chapter are a literature review of previous studies relating to the effect of aquaculture structures, or other comparable obstacles (e.g. kelp beds), on currents, mixing, and waves; an outline of the methodology used in field studies presented in this thesis; and a description of the two field sites where measurements were made.

2.2 Literature Review

2.2.1 Effect of Aquaculture on Currents

Studies of mussel farming in New Zealand have focused mainly on phytoplankton abundance and seasonality (Bradford *et al.*, 1987; Gibbs *et al.*, 1992; Gibbs and Vant, 1997; Ross *et al.*, 1998; Ogilvie *et*

al., 2000), as well as nutrient change, benthic communities, hydrodynamic and water column properties (Kaspar *et al.*, 1985; Gibbs *et al.*, 1991). Internationally, studies have had a similar focus (Gray and Farrukh, 1979; Dahlback and Gunnarsson, 1981; Hatcher *et al.*, 1994; Grant *et al.*, 1995; Haamer, 1996; Mirto *et al.*, 2000; Pilditch *et al.*, 2001).

Early studies of mussel long-line farms identified that current speed has an influence on mussel growth, but did not show that the physical structure of mussel farms restricted flow (Rosenberg and Loo, 1983). The first known studies showing that mussel long-lines cause a reduction of water velocities were carried out in Pelorus Sound, New Zealand, 1984 (Waite, 1989; Gibbs *et al.*, 1991).

Waite (1989) and Gibbs *et al.* (1991) took measurements around small mussel farms (8 to 10 long-lines) in sheltered embayments within Pelorus Sound, New Zealand. The data presented by these authors were from the same study (Gibbs, 2004, *pers. com.*), although there are some variations in the results presented.

Waite and Gibbs *et al.* found that water movement through a mussel farm was attenuated to about 30% of the velocity of the water approaching the farm, with the remainder being forced below or around the farm. Water velocity profiles were measured over 12 m of the water column at 1 m intervals both inside a long-line (between backbones) and in the 20 m channel between two long-lines. Droppers on the long-lines extended to a depth of 6 m. Inside the long-line, no movement of water could be detected in the upper 5 m, but velocities increased rapidly to 0.2 m s^{-1} below the long-line. Large fluctuations in velocity were measured at 8 m (2 m below the droppers). Mean velocities increased almost linearly with depth from 5 to 10 m. Waite suggested that the large fluctuations in velocity at 8 m depth (0.15 ± 0.10 m s^{-1}) indicate unstable boundary layers between the slow moving water in the upper layers and the fast moving water under the farm. Between long-lines, the velocity profile showed a slow moving upper layer (approximately 0.07 m s^{-1} in the upper 5 m), and a fast moving lower layer (~0.22 m s^{-1} below 10 m depth). The large fluctuations of velocity seen at 8 m depth beneath the droppers were not seen in the open space between the long-lines.

Current meters deployed in and around a farm for 2 months showed that velocities inside the farm (3 m depth) were lower than beneath the farm (10 m depth). The velocity decreases were 44% adjacent to a long-line with 55 mm mussels, and 66% next to 100 mm mussels. Velocities offshore from the farm were similar in magnitude to velocities beneath the farm (0.066 ± 0.005 m s^{-1} offshore, 0.058 ± 0.004 m s^{-1} below farm). Flow through the mussel farm was strongly aligned with the direction of the long-lines, in contrast to flow under the long-lines. Waite suggests that the long-line structures were relatively

impermeable to currents, preventing transverse flow through the long-lines. Instead flow was directed parallel to long-lines.

Water currents were strongly directional with few deviations or reverse flows, particularly within the farms. The farms at these sites were close to shore, and general farming practice is to orient long-lines parallel to the coast. Certainly the close proximity of the coastline would cause flow to follow a single axis, however the long-lines may also have acted to channel flow parallel to the coastline.

Gibbs *et al.* found that the mussel farms appeared to have little effect on water movement beyond the immediate area of the farm. The most significant effect was the 70% reduction of water velocity through the farm. At the time of their study, mussel farms in Pelorus sound were small, typically 8-10 long-lines each, and relatively shallow (5 m dropper length, compared to the 10 to 15 m dropper length of later farms). These farms were also in low velocity areas. It is possible that larger farms, particularly those where droppers extend over more of the water depth, would have an effect that extends a considerable distance from the farm (in the form of a downstream wake).

In many other countries mussels are grown on ropes suspended from rafts. The rafts are generally rectangular in shape, with regularly spaced dropper ropes. These rafts form a three-dimensional porous blockage, as compared to the two-dimensional porous fence-like structure a long-line structure presents.

Reduced water velocities have been measured within mussel rafts in the Ría de Arousa, Spain (Blanco *et al.*, 1996). These rafts were restrained by an anchored chain attached to the middle of one side of the raft. Rafts were therefore expected to align with the ambient current. It was found that water velocities were generally higher on the downstream end of the farm than in the centre, which Blanco *et al.* suggests as indicating that flow must enter from more than one side of the raft. It is likely that wind stresses on the parts of the raft above the water surface, and possibly an uneven distribution of dropper ropes, caused a rotation of the rafts to the flow. As no measurement of the depth of droppers was given, it is difficult to interpret their vertical velocity profiles.

Observations of water currents in and around mussel rafts have also been made in Saldanha Bay, South Africa (Boyd and Heasman, 1998). Two sizes of mussel raft were used at this site. Small rafts measured 11 m x 14 m, and large rafts 11 m x 22 m. All rafts had dropper lengths of 6 m. Dropper spacing in the long axis was 0.6 m. Across the rafts, droppers were spaced at either 0.6 m or 0.9 m, giving raft dropper densities of 3.0 droppers m^{-2} and 2.0 droppers m^{-2} respectively. Velocities within rafts were measured by tracking small drogues at 2 m depth. The drogues showed water currents within the raft were aligned along one of the major axes (either along or across the raft, seldom diagonally). In-raft velocities were

found to be influenced by crop maturity (the fastest in-raft velocities were measured through rafts with immature mussels) and dropper spacing. For mature crops, mean water velocities within rafts as a percentage of ambient velocities were 13% for 3.0 dropper m^{-2} rafts, and 25% for 2.0 dropper m^{-2} rafts. The relationship between ambient velocities and in-raft velocities appeared linear over the range measured. Little or no velocity retardation was detected under rafts. Drogue tracking also showed that flow was diverted around rafts.

Numerical modelling of the hydrodynamic effects of aquaculture structures includes studies of the distribution of wastes from fish cages in the Gulf of Maine (Panchang *et al.*, 1997), and a model of the effect of kelp and scallop culture on tidal current speed and flow patterns in Sungo Bay, China (Grant and Bacher, 2001). Panchang *et al* used a 2-D finite-difference model to calculate wind and tidally generated currents, which were then used to predict transport of excess fish food and fecal pellets. Panchang *et al* did not attempt to include any farm-induced drag in the model. They did however vary the bed friction over the model domain to obtain reasonably good simulations of observed data. The bed friction factors were related to depth, not farm location.

The study of Grant and Bacher (2001) of the effects of kelp and scallop farms is related more closely to mussel farming. Kelp and scallops at their study site were grown on suspended long-lines. Scallops were contained either in lantern nets or by ear-hanging, and kelps tied freely to ropes. A 2-D numerical model was used to estimate the effect of the kelp and scallop culture on currents. Drag from the suspended aquaculture was parameterised by local non-directional increases in bottom friction. Comparisons were made using model output with, and without, farms present. They predicted a 20% decrease in current speed within the main navigation channel, and 54% within culture areas.

The studies summarised here show that the effects of aquaculture structures on currents can be significant. There are some important issues that still need to be addressed. No measurements of velocities have been presented for large long-line mussel farms consisting of several hundred long-lines. While evidence suggests flow is diverted under or around individual long-lines in small farms, does a large farm cause similar re-direction on a large scale? Further research is required to identify the relationship between mussel diameter and velocity reduction, along with the effect of density of long-lines. The drag on mussel long-lines will be a function of the angle of incidence to the on-coming flow, an issue not addressed in previous studies. Although the small farms studied by Gibbs *et al.* (1991) did not appear to have an effect on water movement away from the immediate vicinity of the farm, this may not be the case for much larger farms. There is also a need for a relatively easy to use model that could predict the likely effects of a mussel farm on water velocities. These are areas that are investigated in this thesis.

2.2.2 Effect of Aquaculture on Mixing

There is reasonable evidence in the literature to suggest that the drag from a mussel farm may result in some degree of modification to water currents. Turbulence will be generated as the water flows past the rough mussel droppers, ropes and buoys. This turbulence has the potential to enhance mixing, both laterally and vertically. Few published studies consider or discuss the possible interaction between mussel farms and physical water column properties. Waite (1989) noted that large fluctuations in velocity were measured at a depth 2 m beneath mussel droppers, and suggested a mixing layer may have formed between the retarded flow near the surface and the faster flow beneath the long-line. Such a mixing layer would enhance vertical mixing processes.

Gibbs *et al.* (1991) measured a number of water column properties around small mussel farms (6 to 10 long-lines) in Pelorus Sound, New Zealand. They found no obvious difference between dissolved oxygen (DO) profiles measured within farms and in the open bay. While no salinity or temperature profiles within the farm were presented, profiles of DO, temperature and salinity measured away from the farm show some association of higher DO with less dense, colder fresh water (particularly in Crail Bay). The DO profiles therefore give an indication of the stratification in the water column. That DO profiles did not obviously differ inside and outside the farm suggests that little vertical mixing was induced by the farm. Strong vertical mixing would homogenise the water column, causing a more uniform DO profile. It should be noted that the farms studied were small, with short dropper lengths, and in a low velocity environment (mean velocities near the farm were < 0.05 m s^{-1}).

2.2.3 Effect of Aquaculture on Waves

The response of individual mussel long-lines to waves has been treated in detail numerically and observationally (Paul and Grosenbaugh, 2000; Grosenbaugh *et al.*, 2002; Raman-Nair and Colbourne, 2003); however, the long-lines in these studies were of a different configuration than those commonly used in New Zealand. The long-lines were located in deeper water, with fewer buoyancy elements, and were completely submerged rather than at the surface. These studies focused on the effect of the waves on the long-lines, in terms of loads on the long-line components and anchors. In the investigation presented here, the primary focus is the effect of the long-line on waves. Very little research has been published regarding the effect of long-line aquaculture on waves. Grant and Bacher (2001), in their study of flow through scallop and kelp culture in Sungo Bay, China, note that ocean swells travelled throughout the bay, but rarely were there whitecaps within the culture areas. This gives little information other than implying that long-wave length (low frequency) waves were not greatly attenuated by the aquaculture structures. Anecdotally, the pilot of the boat chartered for the Golden Bay field experiments presented in

this thesis described how in rough conditions, he would alter his course to pass inshore of the mussel farm. His experience was that wave conditions were typically calmer inshore of the farm than offshore.

Some kelp beds have dimensions and plant densities similar to the size and dropper density of mussel farms. Although much of the mass is near the surface, some kelp species have an understory consisting of trunks which extend from the hold-fast (attached to the seabed) to the canopy. These flexible trunks may have similar effects on waves to mussel droppers. The effect of kelp beds on waves has been studied numerically by Dalrymple *et al.* (1984), and analytically by Kobayashi *et al.* (1993) who compare their solution with laboratory experiments by Asano *et al*. (1988). The general approach of these authors is to estimate wave energy dissipation from the work done by drag on submerged kelp. However, in field measurements, Elwany *et al.* (1995) found that a 350 m wide bed of giant kelp off Calsbad, California, had no significant effect on transitional and shallow water waves. It should be noted that kelp plants are essentially isolated from one another, and likely to be more flexible than the mussel long-line. The elements of a long-line are connected, thus movement of the long-line will be partially restrained. This is likely to increase the dissipation of wave energy.

Other structures that may be comparable are breakwaters. Breakwaters are designed to reduce the transmission of wave energy through reflection and dissipation. For immobile porous breakwaters (e.g. rubble barriers), reflection normally accounts for the majority of the reduction in wave transmission (Massel, 1976; Yu, 1995). This appears to be true for some types of floating cage breakwaters (Murali and Mani, 1997). However, other forms of breakwater offer far greater dissipation with very little reflection. These are generally buoyant breakwaters where motion is allowed (Williams and McDougal, 1996). In particular, tethered float breakwaters, which consist of dense arrays of surface floats individually tethered, cause considerable reduction in wave transmission through drag-induced energy loss, particularly at higher frequencies (Seymour and Hanes, 1979).

Mussel long-lines are more porous than most breakwaters, and although partially restrained through connection at the surface, the mussel droppers are flexible, suggesting that reductions in transmitted energy may be primarily through dissipation rather than reflection. Breakwaters are generally linear (fence-like) structures aligned perpendicular to the wave motion, whereas kelp beds can occupy large areas. Large mussel farms consist of a number of linear objects, at what could be a random orientation to waves, spread over a large area. For the purpose of estimating the effect of large mussel farms on waves, the approach used in this thesis is to consider the farm as a spatially distributed source of wave energy dissipation similar to the treatment of kelp beds.

2.3 Description of Field Work

2.3.1 Field Sites

Field work was conducted at two study sites, both located on the South Island of New Zealand (Figure 2.1). The first site is a large mussel farm located in Golden Bay, a large bay at the north of the South Island. The second site was located in Pigeon Bay, a smaller bay on Banks Peninsula, on the East coast of the South Island.

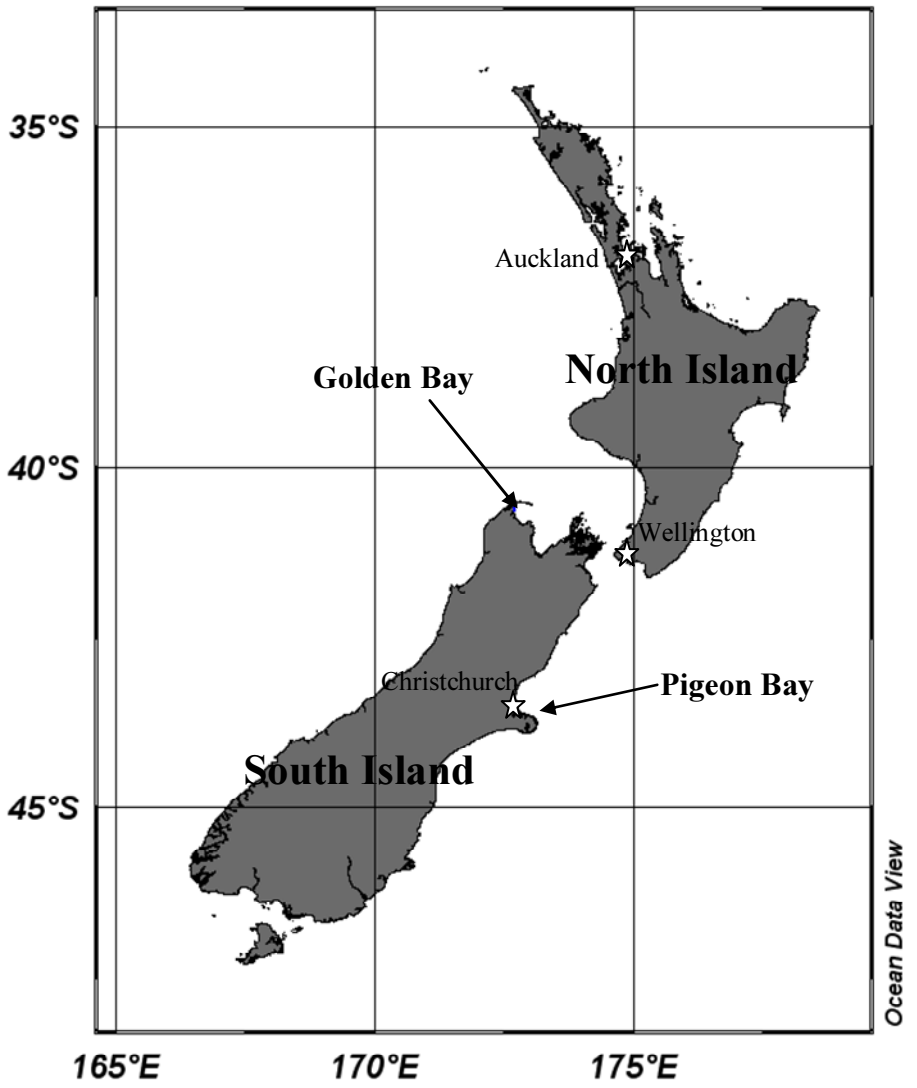

Figure 2.1 Location of Field Sites

The Golden Bay study site was selected as it contains one of the largest mussel farms currently in operation in New Zealand, is located some distance off-shore, and is in a semi-exposed environment due to the large size of Golden Bay. The Pigeon Bay site is more representative of a typical New Zealand mussel farm as it is small in size and located near to shore in a relatively sheltered environment (although this particular farm is subject to significant wave action).

2.3.1.1 Golden Bay

The majority of the results presented in this thesis are from two sets of data taken at the Golden Bay site, near the township of Collingwood (Figure 2.2). This site has strong tidally driven currents, is moderately exposed to waves, and is some distance from shore. The bathymetry around the farm is uniform, slightly sloping upwards towards the shore.

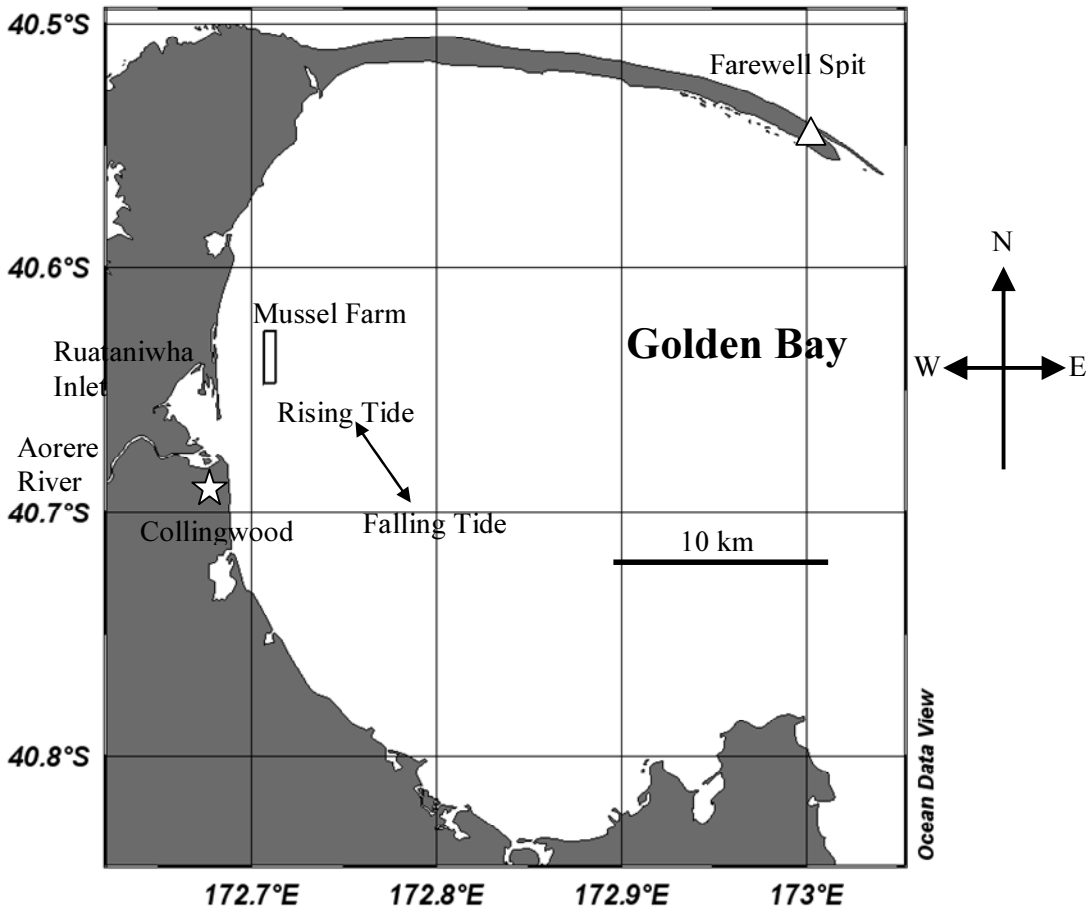

Figure 2.2 Map of Golden Bay.

The mussel farm is situated approximately 2.5 km offshore, and has dimensions of 2450 m by 650 m in plan with the long axis in a northerly direction parallel to the coast. Mean (mid-tide) water depth at the site varies from 9 to 12 m, with a maximum tidal range of 4.2 m. Predominant tidal flow directions are north-west/south-east on rising/falling tides respectively, with currents at mid-tide around 0.15 m s^{-1}. The farm consists of 230 long-lines arranged in 20 blocks. The blocks form two columns of 10 blocks each, with approximately 100 to 200 m between blocks. Long-lines within each block are parallel to each other, but the orientation of long-lines varies from block to block. The location and orientations of long-lines are shown in Figure 2.3. The long-lines are shown by dark lines drawn onto the photograph. Not all long-

lines are shown as the dark buoys were difficult to distinguish from the background. The average long-line length is 120 m, supporting 4 km of dropper rope per long-line. Dropper length varies depending on local water depth but averages 8 m. Dropper density *n* averaged over the entire farm is estimated to be between 0.06 and 0.07 droppers m^{-2}.

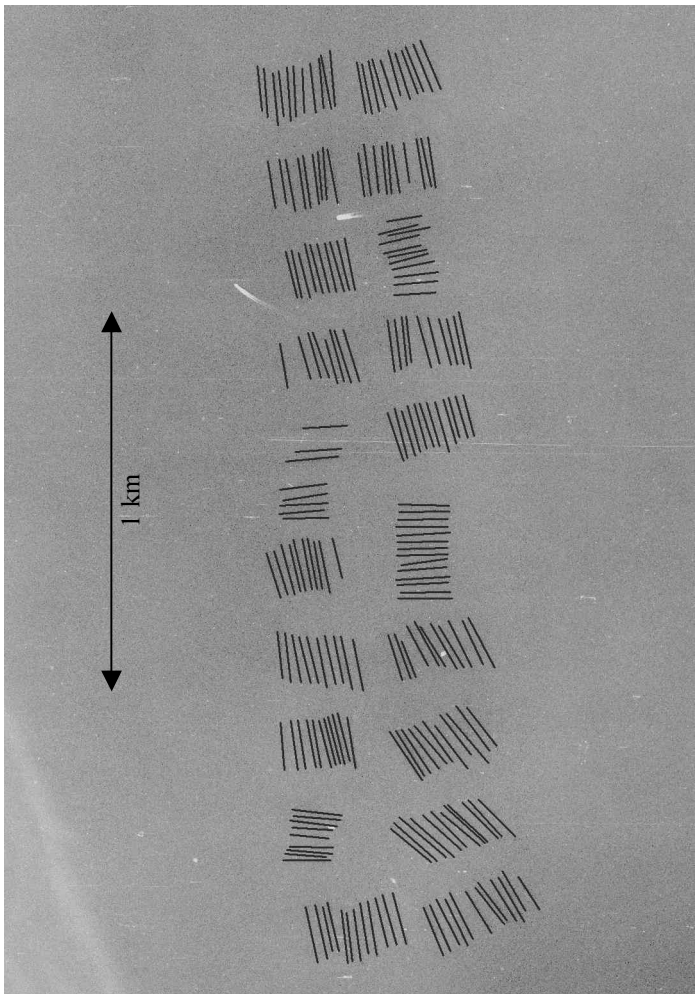

Figure 2.3 Aerial photograph of Collingwood mussel farm showing location and orientation of long-lines.

The Aorere River enters the bay to the south of the farm via the Ruataniwha Inlet. This river, with a mean flow of around 20 m^3 s^{-1}, provides the largest source of freshwater to the bay in the vicinity of the farm. During the winter months when measurements were taken, the water temperature in the river was lower than that in the bay. A permanent meteorological station is sited at the lighthouse near the end of Farewell Spit, indicated by the triangle in Figure 2.2.

2.3.1.2 Pigeon Bay

As indicated, other measurements were taken at a mussel farm in Pigeon Bay. Pigeon Bay is approximately 30 km from the city of Christchurch, and may be reached either by road or sea (from Lyttelton Harbour), Figure 2.4.

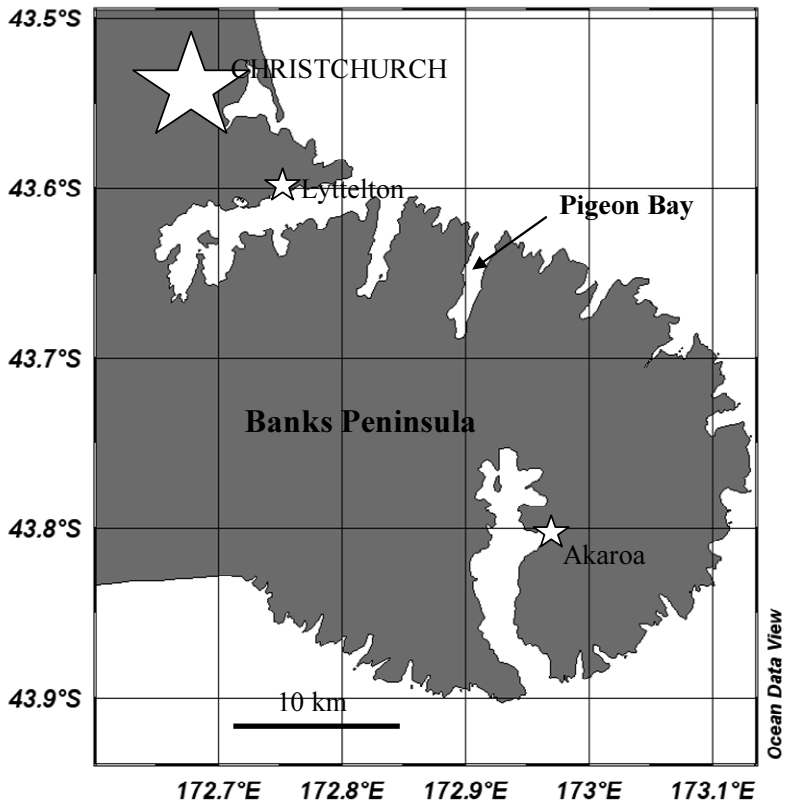

Figure 2.4 Location of Pigeon Bay on Banks Peninsula.

The farm is small in size, consisting of 6 blocks of 8 long-lines each. The entire farm is within 200 m of the shore, with long-lines oriented parallel to the shoreline. Pigeon Bay has approximate dimensions of 7 km length, and 1.2 km width, with the long-axis of the bay opening to the NNE (Figure 2.5). Mean water depth at the study site averages 10 m, with a maximum tidal range of 2.5 m.

Little reliable data regarding the effect of the farm was obtained from this site partly because of the small size of the farm (6 blocks of 8 long-lines, of which only 3 blocks were stocked with mussels during the 2001-2002 experiments), proximity to the coast (the entire farm was within 200 m of the shore), and several instrumentation faults. However, load-cells were installed on the anchor ropes of a long-line at this site allowing measurement of the forces on the long-line (presented in chapter 6).

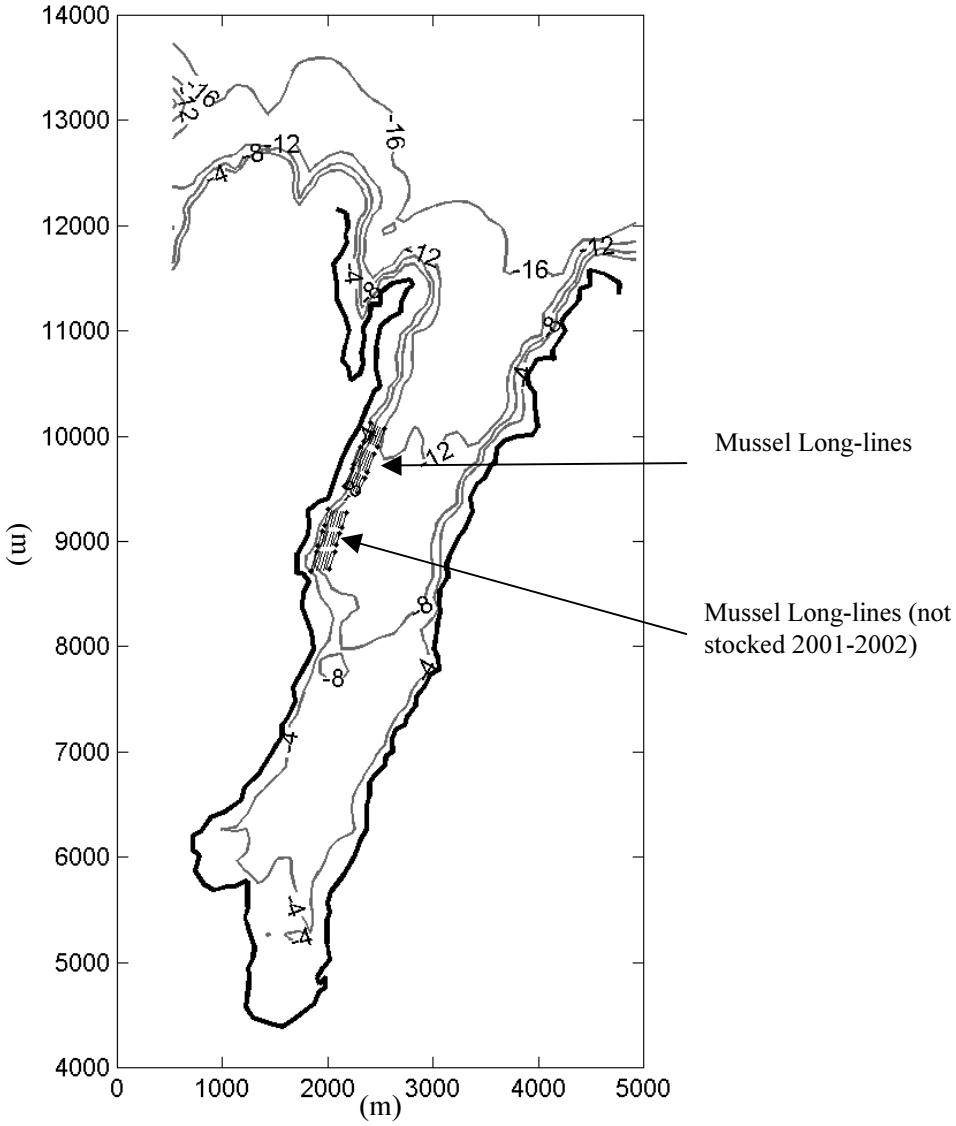

Figure 2.5 Pigeon Bay bathymetry (depth in m) and farm layout.

2.3.2 Instrumentation

2.3.2.1 ADP/ADCP

Acoustic Doppler Profilers (ADP) and Acoustic Doppler Current Profilers (ADCP) were used to measure water velocities. These instruments are essentially the same, but from different manufacturers. The instruments consist of three or four acoustic transducers attached to a body containing the electronics. The basic principle of operation is that sound waves are emitted by each transducer along a narrow axis. The transducers then record sound waves reflected from suspended particles in the water column. Motion of the suspended particles relative to the transducer alters the frequency of the reflected signal depending on

the relative velocity and direction (the Doppler effect). The transducers are oriented in different directions so that by comparing the reflected signal at each transducer, the water velocity can be resolved in 3 dimensions. The delay between sending and receiving the reflected signal allows the distance from the instrument of a velocity measurement to be obtained. Velocities can be measured in a user-specified number of depth-cells, thereby providing a vertical profile of water velocities. The range and resolution of the instrument depends on the frequency of the emitted signal, with higher resolution but less distance range obtained for higher signal frequencies.

An ADP/ADCP can be either moored on the sea floor (looking upwards) to provide a time series of velocity profiles at a location, or mounted on a boat facing downwards to obtain cross-sections or transects of velocity. Instruments with a bottom tracking facility measure the motion of the instrument relative to the sea-bed, allowing velocities to be referenced to the seabed rather than the moving instrument. The instruments contain internal compasses and tilt sensors to allow velocities to be resolved as north, east, and vertical components.

Three types of acoustic Doppler instruments were used during the field experiments. Sontek Acoustic Doppler Profilers (ADP) were used as moored instruments to provide velocity time series. A Sontek ADP was tested as a boat-mounted instrument but was found to give low data quality. A Sontek Pulse Coherent Acoustic Doppler Profiler (PCADP) was also tested as a boat-mounted instrument, but suffered similar data quality issues. The PCADP is capable of higher resolution velocity measurements than the standard ADP. Both the Sontek ADP and PCADP had only 3 transducers. This meant that if a poor signal was received on one transducer, no velocity measurement was obtained. As a result, a large proportion of velocity samples from boat mounted measurements had to be discarded. The Sontek instruments worked well as moored instruments (Figure 2.6).

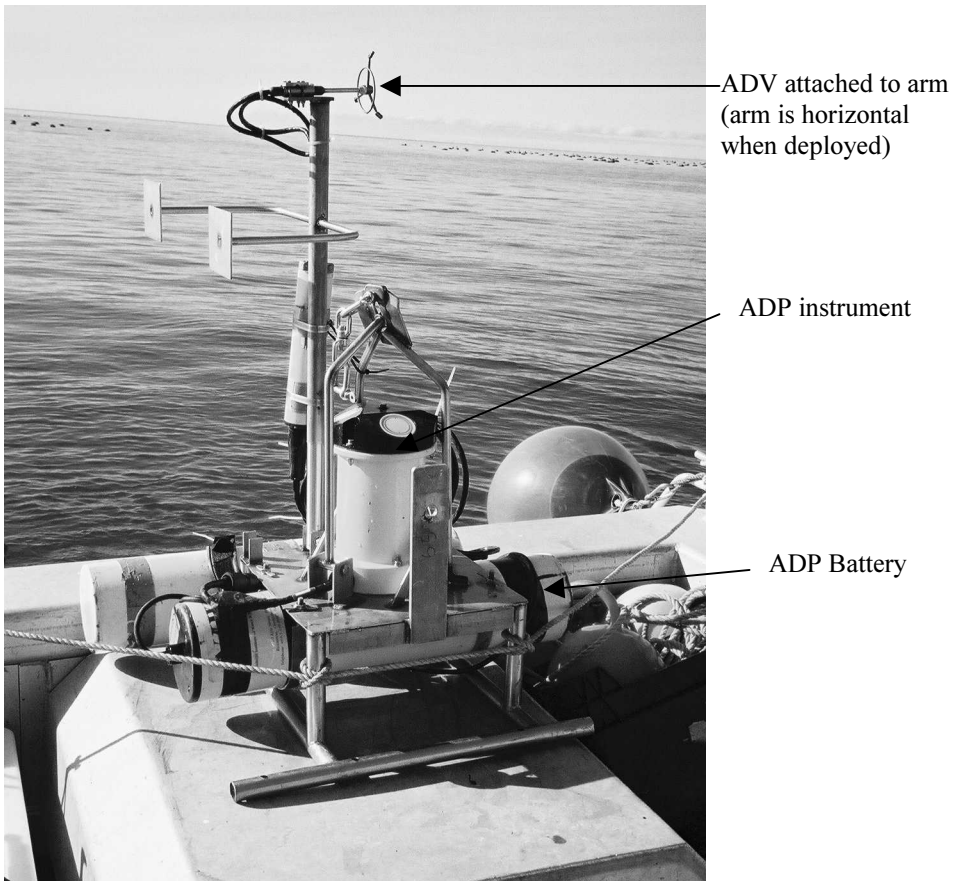

Figure 2.6 Sontek ADP mooring. The vertical arm has an Acoustic Doppler Velocimeter (ADV) attached. This arm was lowered to a horizontal position before deployment.

The third instrument used was a RD Instruments Acoustic Doppler Current Profiler Workhorse (RDI ADCP). This instrument has 4 acoustic transducers (Figure 2.7), and was found to give more reliable velocity measurements when used as a boat-mounted instrument. An RDI ADCP was also moored to provide a velocity profile time series at the Collingwood site.

Additional information on these instruments may be found at the websites of the respective manufacturers (www.sontek.com and www.rdinstruments.com).

Figure 2.7 RDI ADCP workhorse being prepared for deployment.

2.3.2.2 CTD

Measurements of conductivity, temperature, fluorescence and turbidity were made using a variety of CTD (conductivity, temperature, depth) instruments. The two instruments used for the data presented in this thesis were a RBR XR-420-CTD Marine (10th and 17th April 2002), and a Seabird SBE19 CTD (15th to 17th May 2003). Values of salinity and density were calculated from the measured conductivity and temperature by software provided with the instruments. The manufacturer's specifications for the sensors on the two instruments are given in Table 2.1.

Instrument	Sensor	Accuracy	Resolution
RBR XR-420 CTD Marine	Conductivity (inductive cell)	± 0.003 mS/cm	
	Temperature (platinum resistance)	± 0.005 ^{o}C	± 0.00005 ^{o}C
	Pressure (Sensym piezo-resistive strain-gauge)	± 0.075 m	± 0.0015 m
Seabird SBE19 CTD	Conductivity	± 0.0005 mS/cm	± 0.00005 mS/cm
	Temperature	± 0.005 ^{o}C	± 0.0002 ^{o}C
	Pressure (Druck silicon strain-gauge)	± 0.1 m	± 0.002 m

Table 2.1 Specifications of CTD sensors.

Both the RBR and Seabird instruments logged at a frequency of 4 Hz. Full details of these instruments can be found at the website of each manufacturer (www.rbr-global.com and www.seabird.com). The Seabird SBE19 CTD is shown as it is about to be deployed in Figure 2.8.

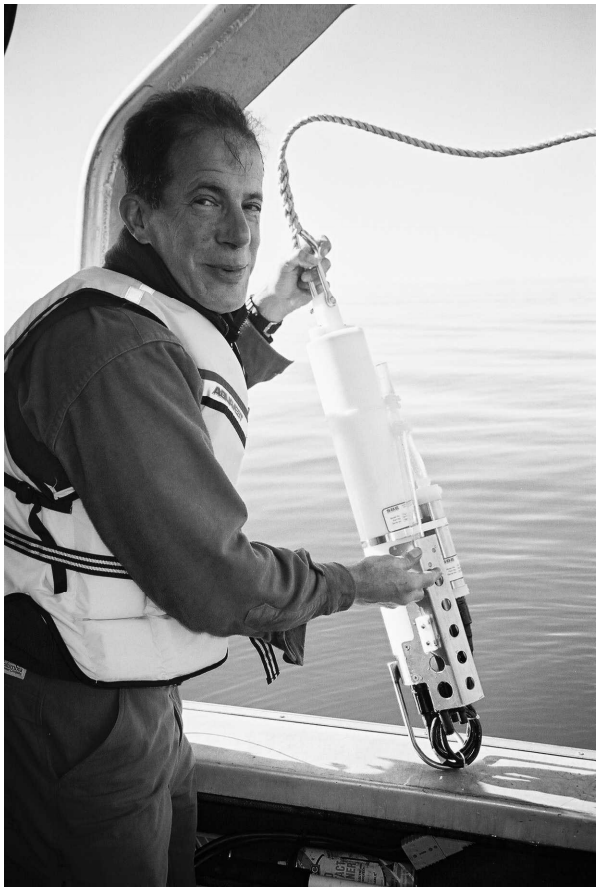

Figure 2.8 Seabird SBE19 CTD held by Dr. Bob Spigel.

2.3.2.3 BIOFISH

Measurements of water properties were also measured using a BIOFISH. This is a variant of a CTD that is towed through the water rather than lowered at one location. The BIOFISH consists of a body to which sensors and a data logger are mounted, a towing bridle, and motorised wings. The angles of the wings are altered as the instrument is towed so that the instrument oscillates vertically through the water. A diagram of the BIOFISH is shown in Figure 2.9.

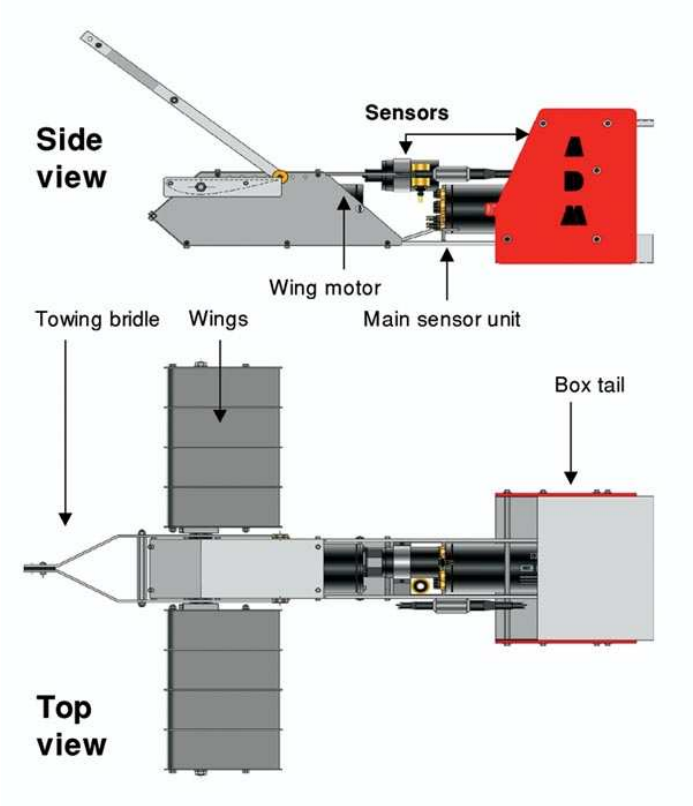

Figure 2.9 Diagram of BIOFISH

The BIOFISH samples at 4 Hz. Seven sensors were installed at the time of operation (2^{nd} – 9^{th} August 2003): depth, temperature, conductivity, oxygen, chlorophyll *a* fluorescence, light transmission (water clarity) and ambient light levels. Three additional sensors were mounted on the boat: GPS for position, echo-sounder for bottom depth, and a surface light sensor to correct for ambient light level fluctuations.

2.3.2.4 DOBIE Wave Gauge

Wave measurements were obtained using DOBIE wave gauges. The DOBIE wave gauge, manufactured by NIWA Instrument Systems, consists of a pressure transducer and a logger (Figure 2.10). DOBIEs were typically programmed to record in bursts of 2048 samples at 5 Hz. Wave spectra were obtained from pressure spectra by adjusting for the frequency-dependent attenuation of pressure with depth. DOBIEs were deployed on the sea floor. A limitation of using a bed-mounted pressure recorder such as a DOBIE is that deep water waves, which do not penetrate to the bottom, can not be detected. The pressure sensor on the DOBIE wave gauge is rated to 100 psi (690 kPa or approximately 69 m), with accuracy ~ 0.005% of full scale (0.035 kPa or 0.003 m).

Full details of the DOBIE wave gauge can be found at the NIWA Instruments Systems website (www.niwa.co.nz/rc/instrumentsystems/dobie).

Figure 2.10 DOBIE wave gauge.

CHAPTER 3 EFFECT OF MUSSEL FARMS ON CURRENTS

3.1 Introduction

The studies summarised in chapter 2 indicate that the effects of aquaculture structures on currents may be significant. There remain a number of important issues to address. In particular, studies of long-line mussel farms of the form used in New Zealand have focused on small farms, typically located in low velocity environments close to the shore. Large farms, both existing and proposed, consist of several hundred long-lines in exposed areas where currents may be significantly higher. While evidence suggests that flow is diverted under, or around, individual long-lines in small farms, the combined effect of many long-lines is not clear. Although the small farms studied by Gibbs *et al.* (1991) did not appear to have an effect on water movement away from the immediate vicinity of the farm, this may not be the case for much larger farms. There are a number of factors requiring further research that may influence the drag of long-lines on the water. For example, mussel dropper diameter, long-line density, long-line orientation, and the length of the mussel droppers relative to the water depth may all influence drag and the resulting velocity attenuation. There is also a need for a relatively easy to use model that could predict the likely effects of a mussel farm on water velocities.

The focus of this chapter is to assess the degree of water velocity reduction within a large mussel farm. Also, the issue of flow diversion around the farm will be studied, and an assessment made of the extent over which drag-induced velocity reductions will occur.

A description of the methodology used to conduct field measurements of drag-induced velocity modification by a large mussel farm is given in section 3.2. Measurements from ADCP transects and moorings are presented in section 3.3. Two simple models for velocity attenuation from drag on the mussel droppers are developed in section 3.4. The measurements and model predictions are interpreted and discussed in section 3.5, and the key findings summarised in section 3.6.

3.2 Field Observations

3.2.1 Study Site

Measurements of water velocities were made at the Collingwood mussel farm in Golden Bay. This site is described in detail in Chapter 2. Water velocities were recorded within and around the farm using both moored and boat-mounted Acoustic Doppler Current Profilers.

3.2.2 ADP/ADCP moorings

Acoustic Doppler Profiler (ADP) moorings were used to obtain continuous time-series of velocity over several tidal cycles at selected points inside and outside the farm. Instruments were moored on the sea bed, and their locations determined by GPS.

3.2.2.1 Field Trip 1: 10-17 April 2002

A Sontek 1000 kHz Acoustic Doppler Profiler (ADP) was moored on the bed within a block of long-lines near the southern end of the farm (Figure 3.1). This instrument recorded velocity profile ensembles (time averages) at 30 second intervals and 1 m vertical resolution during a 1 week deployment. A second instrument was deployed north of the farm to provide data on flow outside the farm. Unfortunately, this second instrument failed and no data was retrieved.

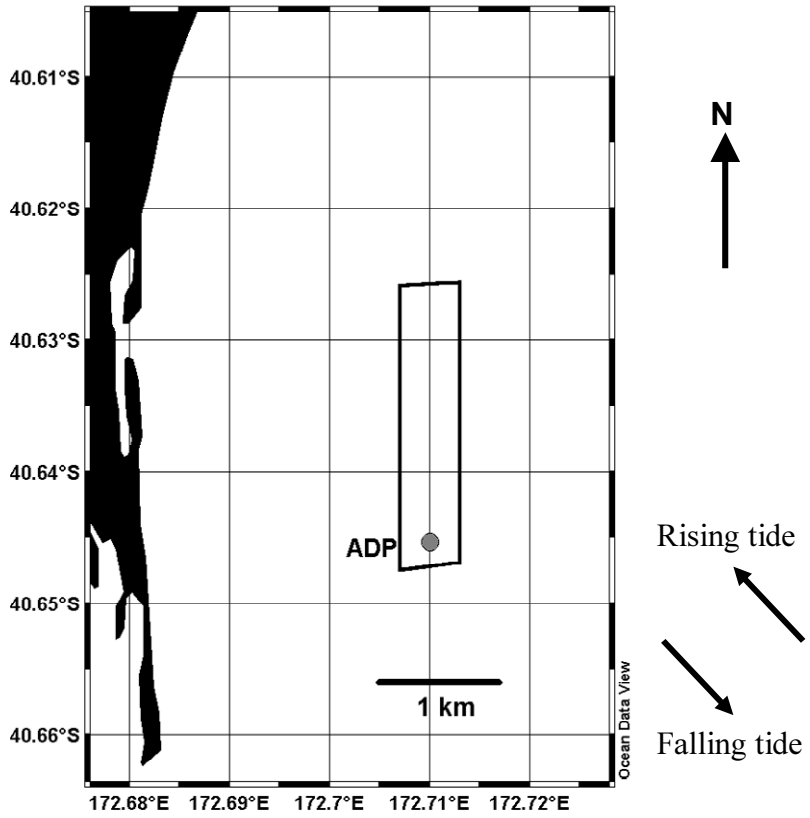

Figure 3.1 Location of ADP mooring 10-17 April 2002. Directions of mean tidal currents are indicated by the arrows to the lower right of the drawing.

3.2.2.2 Field Trip 2: 15-17 May 2003

During a second field experiment 13 months later, three ADP/ADCP instruments were deployed for a duration of approximately 2.5 days as follows:

- ADP 1, a Sontek 500 kHz ADP (instrument 4111) was deployed 1.2 km north of the farm. This instrument recorded 3 minute velocity profile ensembles at 1 m vertical resolution.

- ADP 2, a Sontek 1000 kHz ADP (instrument C283) was deployed inside the farm towards the southern end. This instrument was located between long-line blocks, and near the farm centre-line. This instrument also recorded 3 min velocity profile ensembles at 1 m resolution.
- ADP 3, an RD Instruments Acoustic Doppler Current Profiler (RDI ADCP), was deployed a short (~100 m) distance inshore (west) of the farm. This instrument recorded 15 min velocity profile ensembles at 0.5 m vertical resolution.

The mooring locations for these instruments are shown in Figure 3.2.

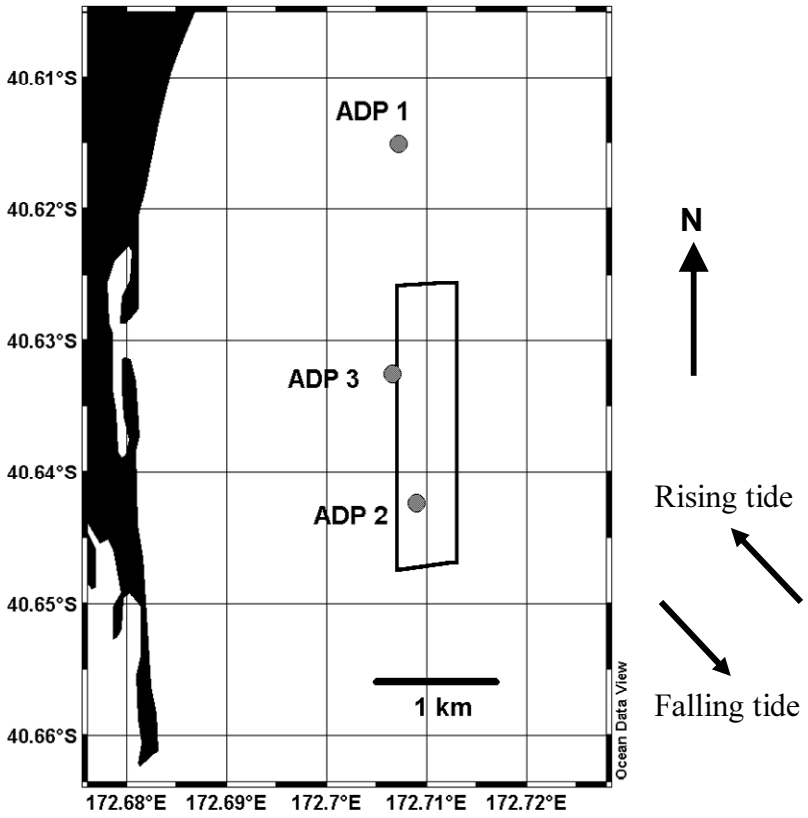

Figure 3.2 Locations of ADP moorings for 15-17 May 2003. Directions of mean tidal currents are indicated by the arrows to the lower right of the drawing.

Data from both of the SonTek ADP instruments (2003 deployment) required a compass correction due to significant magnetic interference, probably from the battery located beneath each instrument. This resulted in an error in the direction of measured water velocities. The error was –127^{o} for ADP 1, and +74^{o} at ADP 2. The procedure by which the corrections were obtained is described in Appendix A. The RDI ADCP instrument (ADP 3) had a smaller internal battery, and did not appear to suffer from this problem. Data were also adjusted from magnetic north to true north (21.15^{o} counter clockwise from magnetic north at this site).

3.2.3 ADCP Velocity Transects

Velocity transects were recorded using boat mounted ADP instruments during both field trips. A Sontek PCADP (Pulse-coherent Acoustic Doppler Profiler) was used during the 2002 study, while a 1200 kHz RDI ADCP was used to obtain the 2003 data. Velocity data were recorded at 0.25 m vertical resolution, and ensemble averages recorded every 2 seconds. Both the PCADP and RDI ADCP were operated in bottom track mode, where the instrument records the motion of the bed relative to the instrument, computing water velocities with respect to the bed. Position coordinates for each velocity ensemble were obtained from differential GPS. The RDI ADCP was the superior instrument for this application, giving higher quality data (less noise, and a lower percentage of missed velocity measurements).

3.3 Results

The results from field measurements are grouped according to particular effects of interest. In the following sections, data are presented illustrating the reduction in water velocities within the farm, the diversion of flow around the farm, the velocity shear generated by faster flow under the farm, and measurements in the wake of the farm.

3.3.1 Reduction of Water Velocities within the Mussel Farm

Water velocities within the farm were clearly reduced in comparison to those outside the farm. This was demonstrated by both ADCP velocity transects through the farm, and from the ADP mooring data.

3.3.1.1 ADP Moorings

Data from the ADP moorings from May 2003 (Figure 3.2) allowed comparison of velocities inside and outside the Collingwood mussel farm. ADP 1 was assumed to record water velocities not affected by the farm. Depth-averaged water velocity profiles recorded by this instrument show that currents were strongly tidal, with maximum velocities occurring near mid-tide and lowest velocities at high and low tides (Figure 3.3).

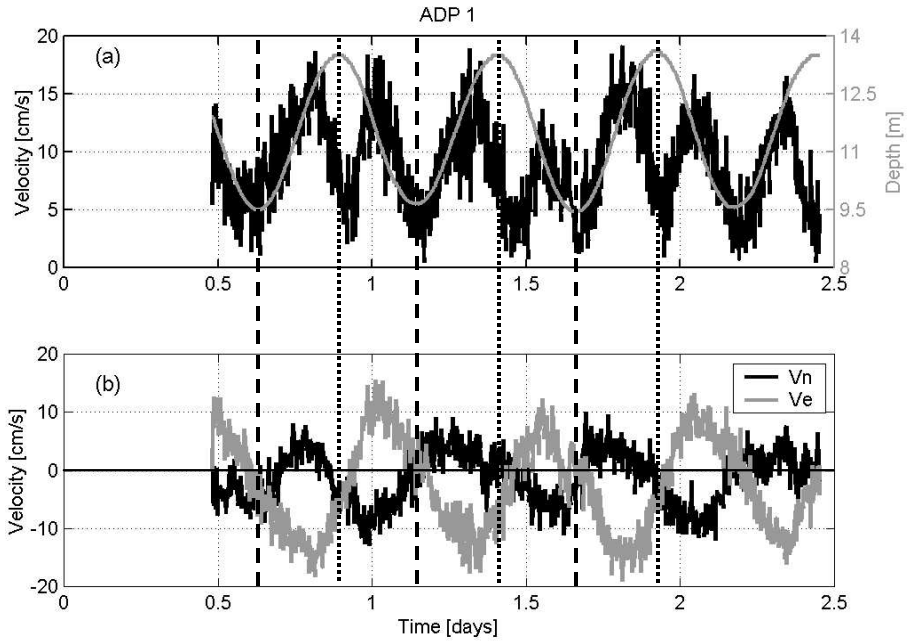

Figure 3.3 (a) Depth-averaged velocity magnitude (black line, scale on left axis) and tidal water depth (grey line, scale on right axis), and (b) depth-averaged North and East velocity components at ADP 1 (2003). Dashed lines indicate low tide, and dotted lines high tide.

Velocity attenuation by the farm was most easily detected at or near mid-tide when velocities were highest. Depth-averaged velocities were averaged over a 2 hour period at mid-tide from the lower 9 m of the water column. Data from greater than 9 m above the bed was not included in the averaging due to higher signal noise near the surface. The mid-tide velocities at ADP 1 were 12.2 cm/s and 9.8 cm/s on rising and falling tides respectively.

Velocities recorded by the instrument located within the farm, ADP 2, were lower than at ADP 1 (north of the farm). ADP 2 was located in a central navigation channel that runs north/south through the farm (see Figure 2.3), and approximately 500 m from the south end of the farm. Velocities were strongly tidal, and were north-east/south-west on rising/falling tides (Figure 3.4). Peak depth-averaged velocities occurred at or slightly before mid-tide on rising tides (particularly the North velocity component). Velocity magnitudes at mid-tide were higher on the rising tide than the falling tide. This was also seen outside the farm at ADP 1. Velocity magnitudes, averaged over the bottom 9 m, were 9.1 cm/s and 7.6 cm/s on rising/falling tides respectively. The in-farm velocities (ADP 2) were 75% and 78% of those at ADP 1 on rising and falling tides respectively. These ratios are sufficiently close to indicate the reduction in velocities inside the farm is the same (i.e. 24%) on rising and falling tides. Although Figure 3.2 indicates that ADP 2 was moored west of the farm centreline, the flow would have passed through a similar number of long-lines to reach ADP 2 on both rising and falling tides.

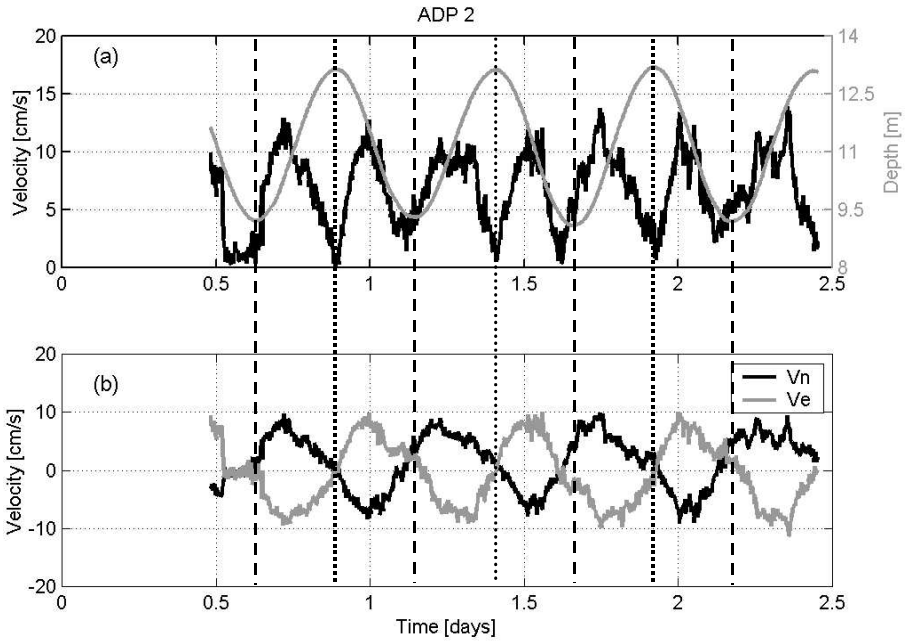

Figure 3.4 (a) Depth-averaged velocity magnitude and tidal depth, and (b) depth-averaged North and East velocity components at ADP 2. Dashed lines indicate low tide, and dotted lines high tide.

Significant differences between velocities on rising and falling tides were recorded at the western edge of the farm by ADP 3 (Figure 3.5). Velocity magnitudes were lower on rising tides when the instrument was downstream of the farm. Depth-averaged velocities were 7.6 cm/s on rising tides, and 12.9 cm/s on falling tides.

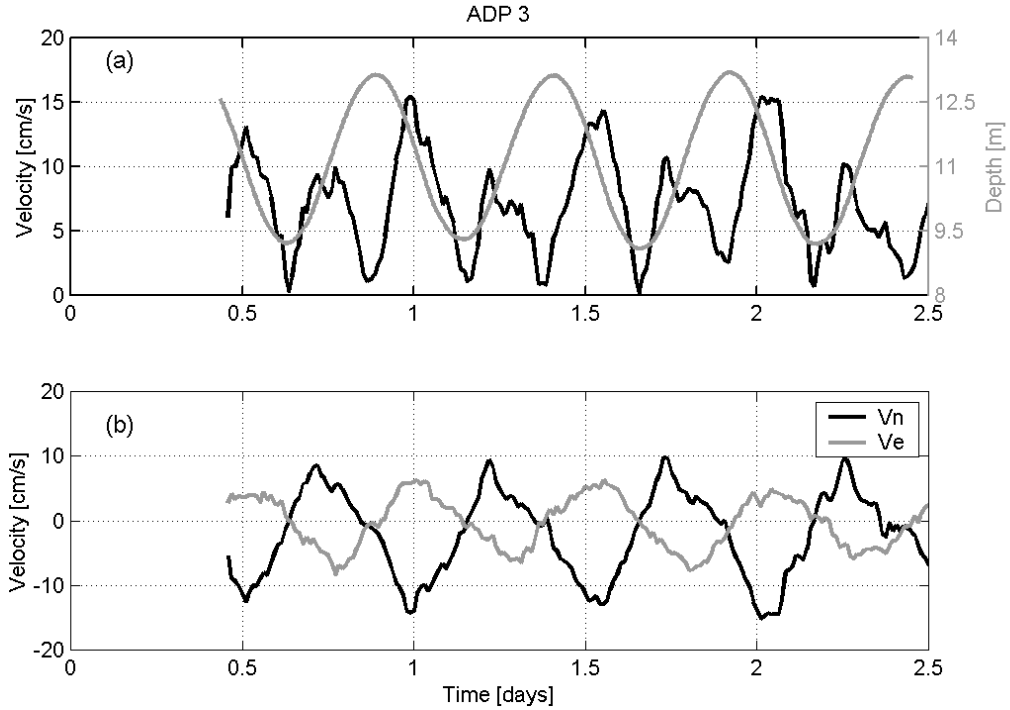

Figure 3.5 (a) Depth-averaged velocity magnitude and tidal water depth, (b) depth-averaged North and East velocity components recorded at ADP 3.

The depth-averaged mid-tide velocities on the west edge of the farm (ADP 3) were 62% of the velocities north of the farm (ADP 1) on the rising tide, and 132% on the falling tide. The greater reduction of velocities on rising tides at ADP 3 (38%) in comparison to that at ADP 2 (24%) is reflective of the greater distance through the farm water has travelled to reach this instrument.

Depth-averaged velocities from 2 hours at mid-tide for rising and falling tides are summarised in Table 3.1, and by the compass plot in Figure 3.6.

	North of Farm ADP 1	In Farm ADP 2	West edge of farm ADP 3
Rising Tide	12.2 cm/s @ 286^{o}	9.2 cm/s @ 311^{o}	7.6 cm/s @ 303^{o}
Falling Tide	9.8 cm/s @ 130^{o}	7.6 cm/s @ 125^{o}	12.9 cm/s @ 154^{o}

Table 3.1 Depth-averaged velocities and directions averaged from 2hrs at mid-tide at moored ADP instruments.

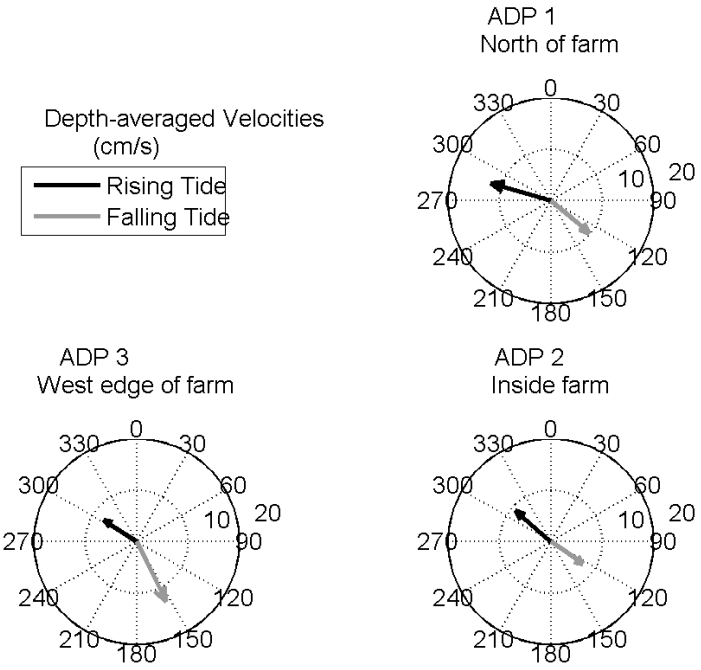

Figure 3.6 Depth-averaged velocity vectors on rising and falling tides, Collingwood mussel farm, 15-17 May 2003.

The depth-averaged velocities calculated above include flow beneath the farm as the droppers did not extend the full water depth. The reduction of velocities over the depth of the droppers will be higher. The in-farm velocity reduction can be obtained from velocity measurements near the mid-height of the mussel droppers. The length of mussel droppers averaged approximately 8 m. The change in water depth due to

the tide over the 2 hour mid-tide averaging period is approximately 2 m. As the mussel droppers are supported from the surface, the proximity of the mussel dropper to the bed changes with the tide. A representative height above the bed for the mid-height of the droppers is 8 m at ADP 1 and ADP 3, and 7.5 m at APD 2. Mid-tide water velocity magnitudes at these depths (from 1 m velocity bins) are summarised in Table 3.2 and Figure 3.7.

	ADP 1 (8m)	ADP 2 (7.5m)	ADP 3 (8m)
Rising	12.2 cm/s@ 290 ^{o}	11.3 cm/s @ 315 ^{o}	4.2 cm/s @ 317 ^{o}
Falling	10.4 cm/s @ 136 ^{o}	5.5 cm/s @ 140 ^{o}	11.5 @150 ^{o}

Table 3.2 Mid-tide velocity magnitudes and directions at mid-dropper depth from ADP moorings, 15-17 May 2003.

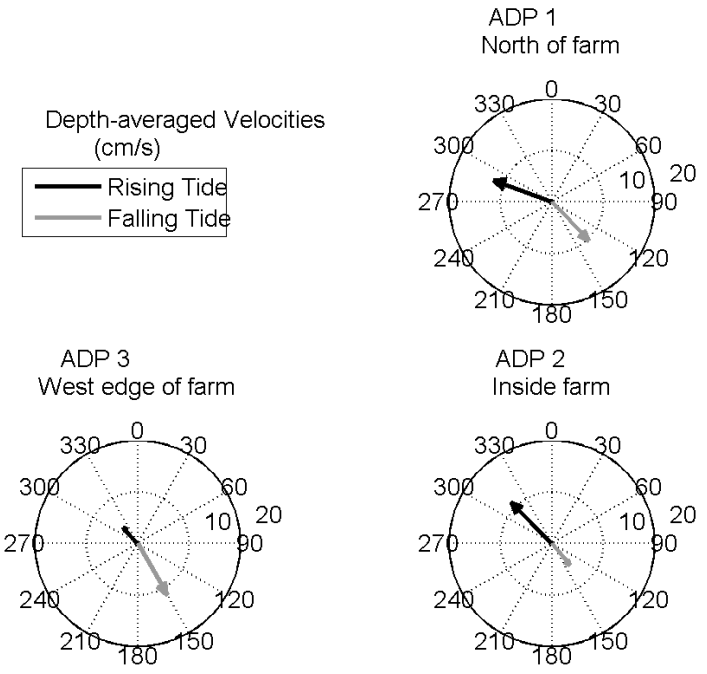

Figure 3.7 Mid-tide velocity vectors at mid-dropper depth, Collingwood mussel farm, 15-17 May 2003.

On falling tides, mid-dropper water velocities at ADP 2 were 47% lower than at ADP 1. On rising tides, the decrease in velocity was smaller at 8%. Also, on rising tides, the velocity at mid-dropper depth was higher than the depth-averaged velocity, indicating that velocities decreased with depth (i.e. no undercurrent, see Figure 3.14). There are a number of possible explanations for the difference between profiles on rising and falling tides. The long-lines to the south-east of ADP 2 (upstream on rising tides) were nearly in-line with the mean tidal currents. In contrast, long-lines to the north-west (upstream on falling tides) were at a greater angle to the flow. It is likely that on rising tides, the upstream long-lines had less affect on flow due to their orientation. This is discussed further in section 3.3.2. A further possibility is the location of the ADP 2 within the central navigation channel between long-line blocks.

On rising tides, water may have been directed along this channel by the blocks of long-lines each side. A transect recorded on the rising tide (Figure 3.11) offers some support to this, particularly in the upper water column, however the velocity direction recorded by ADP 2 is north-west, rather than north along the farm axis. With an average depth at ADP 2 of approximately 11 m, the velocities in Figure 3.7 are at similar depths to the water velocity vectors in Figure 3.8(a) and Figure 3.11(a). A third possibility is that mussels on the long-lines south-east of ADP 2 were immature (small in size). The drag on these long-lines would therefore have been smaller, resulting in less modification to vertical velocity profiles.

On the western edge of the farm, at ADP 3, downstream velocities (rising tide) were 66% lower than at ADP 1. The difference in velocities at the farm edge for upstream and downstream conditions (falling and rising tides) is clear in Figure 3.7. In summary, ADP mooring data indicate a reduction of velocities within the farm of up to 66%.

3.3.1.2 Velocity Transects

Due to the poor quality of data obtained using the Sontek PCADP for measuring velocity transects during the 2002 experiments, only the data obtained over the period 15-17 May 2003 are presented. A number of velocity transects were recorded through the farm using a boat-mounted ADCP (RDI Instruments). Conditions during this period were calm with little wind. The selected transects shown here are typical of those recorded over this period.

A number of north-south transects recorded during a falling tide on the afternoon of 16 May 2003 are plotted in Figure 3.8. Measurements of the first transect (1 in Figure 3.8) commenced at 13:31, and the final transect (6) was completed at 15:31, with low tide at 15:50. All transects, with the exception of transect 3, were measured from north to south. While the horizontal distance between velocity ensembles depended on boat speed (with multiple ensembles recorded at the same location if the boat was stationary), velocity ensembles were averaged over 4 m depths (16 depth bins) and 200 m length intervals in Figure 3.8.

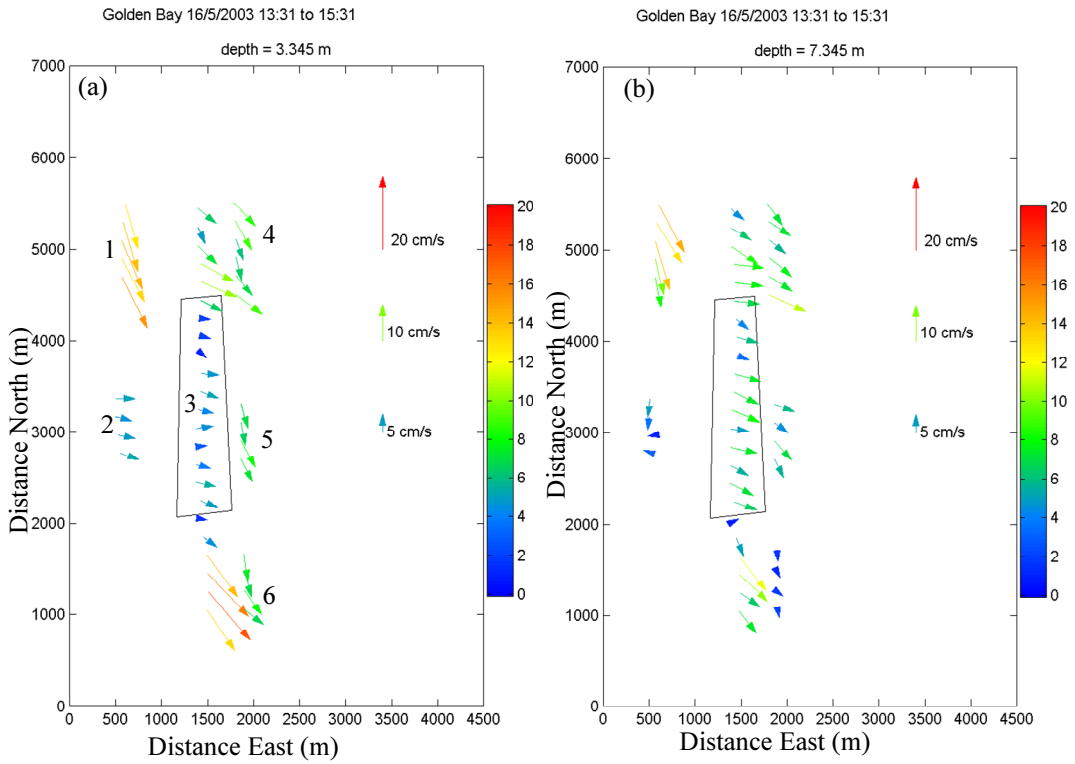

Figure 3.8 Velocity vectors averaged over 4 m depths centred at (a) 3.3 m and (b) 7.7 m, 16 May 2003 on the falling tide.

In Transect 3, substantially decreased velocities were recorded near the surface within the farm (Figure 3.8(a)). Within the farm, velocities were predominantly easterly, with a small southerly component. The higher velocities at the south of transect 4 may indicate an acceleration around the farm. The low velocities in transect 6 probably result from this transect being recorded close to low tide.

More detail of the flow structure through the farm can be seen in vertical profiles of velocity from the central transect (transect 3) (Figure 3.9). Velocities are averaged over a horizontal distance of 500 m, and plotted as north and east velocity components. A strong decrease in the north velocity component occurred inside the farm. Immediately upstream of the farm the east velocity component increased slightly, indicating a diversion of water around the farm. Velocities south (downstream) of the farm recovered rapidly.

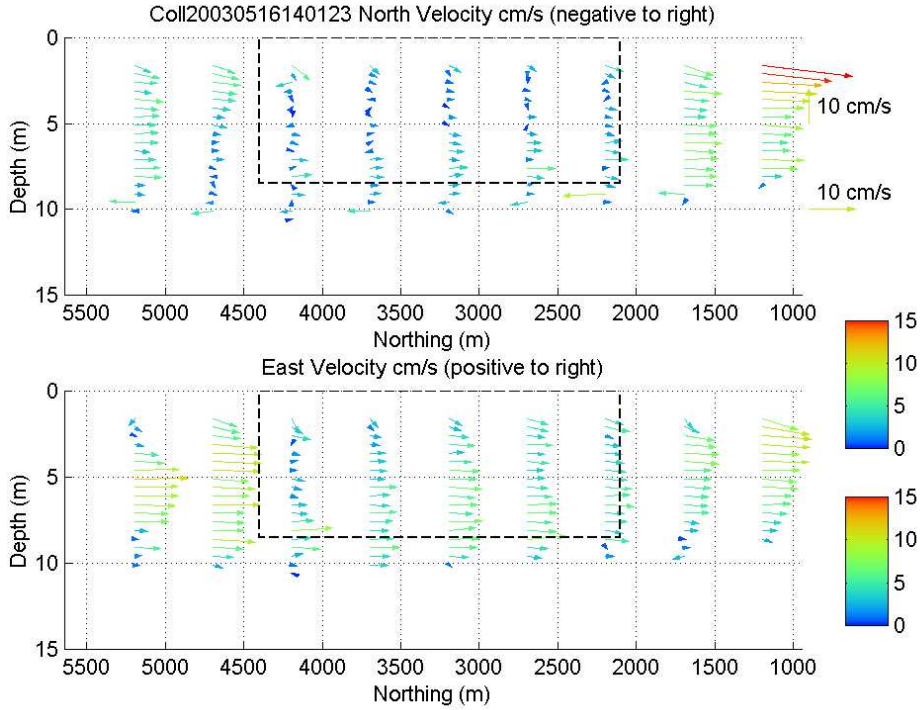

Figure 3.9 Profiles of velocity components from transect through mussel farm, 16 May 2003 14:01 to 14:48, falling tide. Farm location indicated by box. Transect shown from north (left) to south (right).

As this transect was recorded towards the end of the falling tide, tidal variations in water velocity are expected. This transect was measured from south to north, so velocities to the north may appear lower due to the tide. A tidal velocity correction procedure, based on velocities recorded at ADP 1, is described in Appendix B. This correction procedure compensates for the reduction in velocities due to the changing tide so that the effect of the farm is more clearly seen. Tidally corrected velocities within, and beneath, the farm are plotted in Figure 3.10.

After applying the tidal correction, velocities within the farm were approximately 50% of those upstream (north) of the farm. Velocities north of the farm are still less than south of the farm, even after applying the tidal correction. Velocities beneath the farm may have increased slightly, but any increase is insufficient to compensate for the decrease seen within the farm.

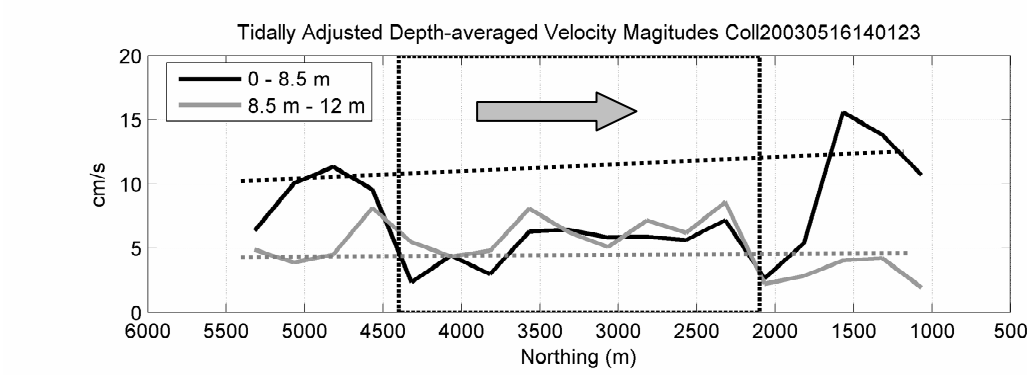

Figure 3.10 Velocity magnitudes from transect 3, 16 May 2003, with a tidal correction applied. Dotted lines indicate the likely velocity in absence of farm.

Velocities measured through the farm on a rising tide are plotted in Figure 3.11. This transect was recorded from south to north, from 9:02 to 10:04, 17 May 2003 (high tide was at 10:31). Significant reductions in velocity were again seen in the upper water column (Figure 3.11(a)), accompanied by a directional change. On this transect, velocities in the upper water column within the farm were in a northerly direction along the farm axis, unlike velocities on the falling tide which were easterly across the farm (Figure 3.9). Wind speed was low (<1 m/s) and unlikely to have generated significant surface currents during either transect.

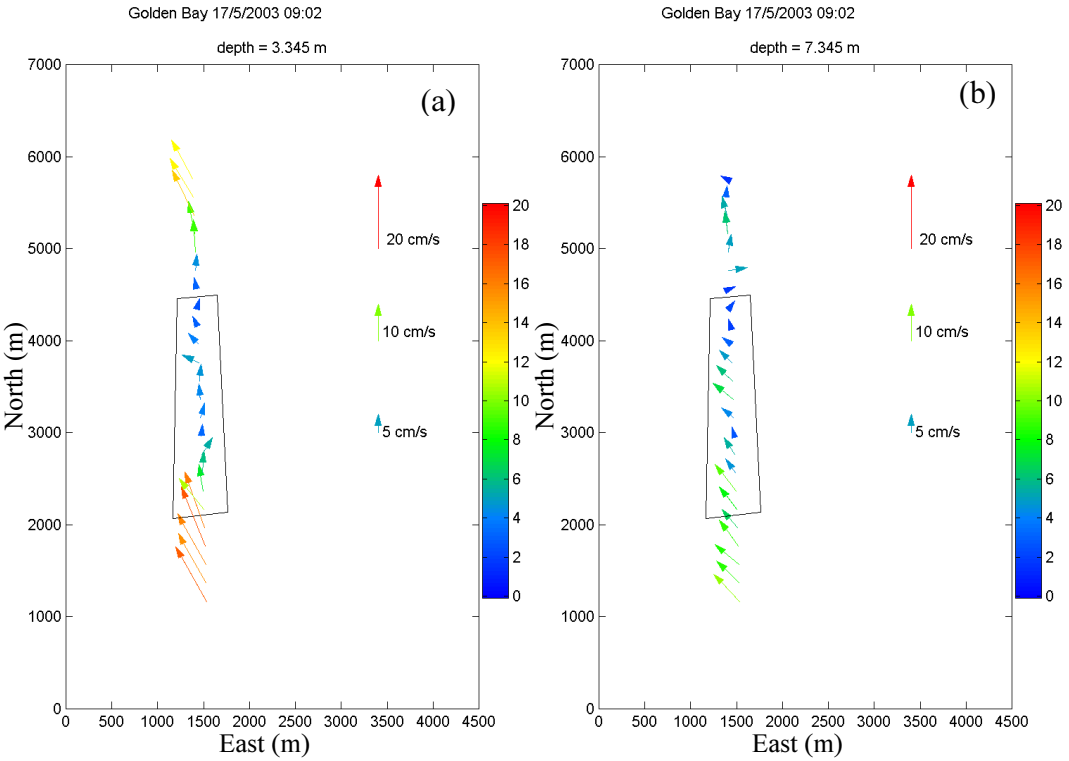

Figure 3.11 Velocity transects on rising tide, 17 May 2003. Velocities averaged over 200 m lengths and 4 m depths centred on (a) 3.3 m and (b) 7.3 m.

The tidally corrected velocity magnitudes plotted in Figure 3.12 (see Appendix B for the correction procedure) indicate the reduction of velocities within the farm (0 - 8.5 m depth), and the recovery of velocities downstream of the farm. Velocities within the farm decrease from approximately 15 cm s^{-1} to 5 cm s^{-1}, a 67% decrease. There is some increase of velocity beneath the farm, but the trend is not as clear as the decrease in the upper water column.

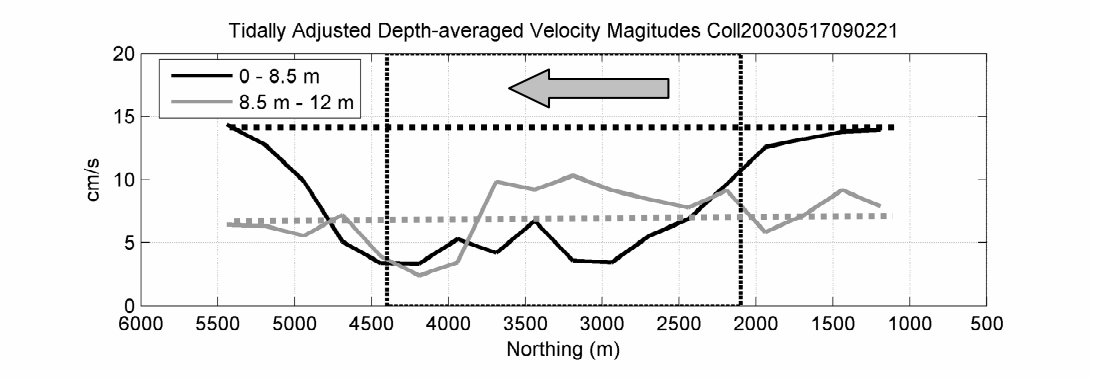

Figure 3.12 Velocity magnitudes from transect through farm, 17 May 2002 with tidal correction applied. Dotted lines indicate the likely velocity in absence of farm.

3.3.2 Velocity Shear beneath the Farm

It has been shown that velocities within the Collingwood mussel farm were reduced due to the farm drag. To maintain continuity, the decreased velocity within the farm must result in a diversion of fluid either under, or around, the farm. This diversion should be detected by higher velocities under, or around the perimeter of, the farm.

Velocity data recorded by the ADP moored within, and on the edge of, the farm revealed higher velocities at depths below the mussel droppers. At the ADP moored within the farm from 10-17 April 2002, velocities averaged over a 2 hr period at mid-tide over 12 tidal cycles show a distinct underflow beneath the farm (Figure 3.13). This underflow and the associated vertical velocity shear ($S_z = dU/dz$) were strongest on the falling tide. The location of the instrument within the farm (Figure 3.1) required water on the falling tide to pass a greater distance through the farm before reaching the instrument, accentuating the influence of the farm drag. As ensembles were collected every 3 minutes, each rising and falling tide provided 40 mid-tide data points. The standard deviations indicated in Figure 3.13 are calculated from all data points (360 in total) at each depth. Velocity shears reached values of around $S_z = 0.020$ s^{-1}, and were centred on a depth comparable to the bottom of the dropper lines (3.5 m above the bed). On the falling tide, where the effects of the farm were most apparent, velocities averaged 0.046 m s^{-1} inside the farm, and 0.087 m s^{-1} beneath the farm (90% greater).

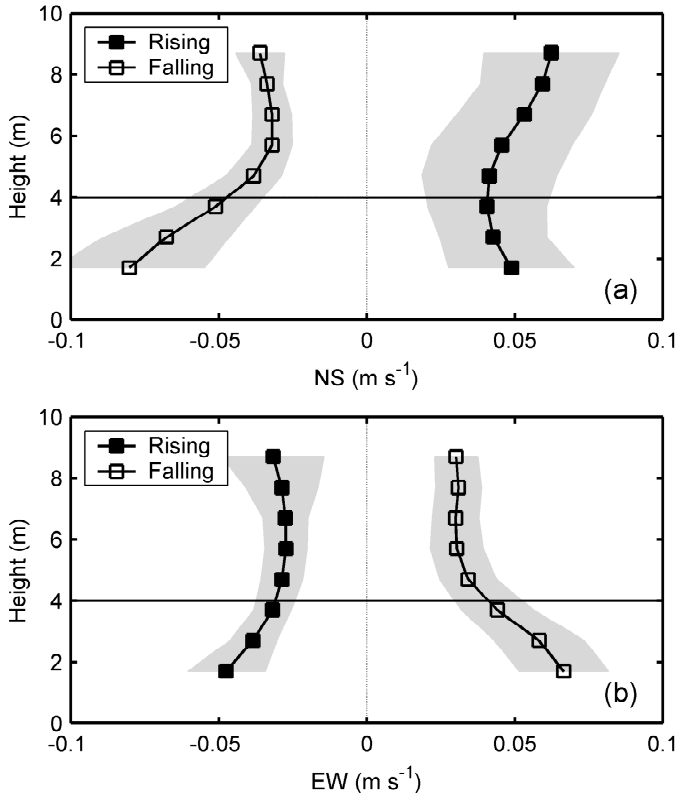

Figure 3.13 ADP results from the south end of the Collingwood farm 10-17April 2002. (a) North (positive)-South and (b) East (positive) -West velocities. Solid symbols show data averages from the peak 2 hours from 12 rising tides, while empty circles show averages for falling tides. The grey region represents +/- one standard deviation, and the horizontal line shows the approximate base of the mussel dropper lines. The free surface (not shown) varies between 10 and 12 m.

Similar underflows beneath the farm were recorded within the farm during the second deployment (15-17 May 2003, ADP 2) on falling tides. The highest velocity shear gradients recorded on the falling tide were 0.014 s^{-1} at 5 m above the bed. This was a weaker shear than that measured during the 2002 deployment, probably as ADP 2 was deployed within the central navigation channel approximately 100 m from the nearest long-line, while the ADP in the 2002 deployment was located within 15 m of long-lines, and inside a long-line block.

The underflow was not seen on the rising tides. As described in section 3.3.1.1, upstream long-lines on the rising tide were nearly in-line with the rising tide. As this provides less blockage to the approaching flow, there is likely to be less reduction of velocities within the depth of the farm. The rising tide profiles in Figure 3.14 appear to indicate that there was no significant diversion beneath the farm. Data at ADP 2 (2003) were recorded over 4 tidal cycles, providing 160 mid-tide data points.

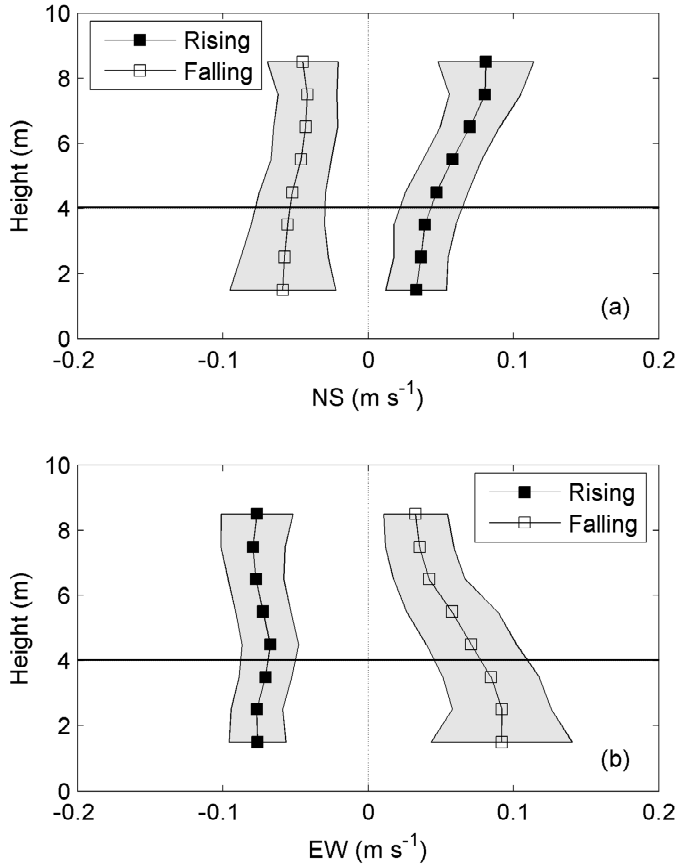

Figure 3.14 (a) North (positive) - South, and (b) East (positive) - West velocities averaged from 2 hours at mid-tide inside Collingwood mussel farm (ADP 2), 15-17 May 2003. Shaded area is ± 1 standard deviation, and horizontal line indicates approximate bottom of mussel farm. Water surface varies between 10 and 12 m.

The effect of the farm is most clearly demonstrated in the velocity profiles recorded by ADP 3 on the western edge of the farm (Figure 3.15). Mid-tide velocities at this location were calculated from 15 minute ensembles rather than from the 3 minute ensembles recorded at ADP 2. The water currents recorded by ADP 3 were clearly higher on falling tides, which is when the instrument is upstream of the farm. On the rising tide (when the instrument was downstream of the farm), north velocity components were small, with westerly currents increasing towards the bed with a maximum at 2 m. The highest velocity shear on rising tides was $S_z = 0.015$ s^{-1} at 3.75 m above the bed.

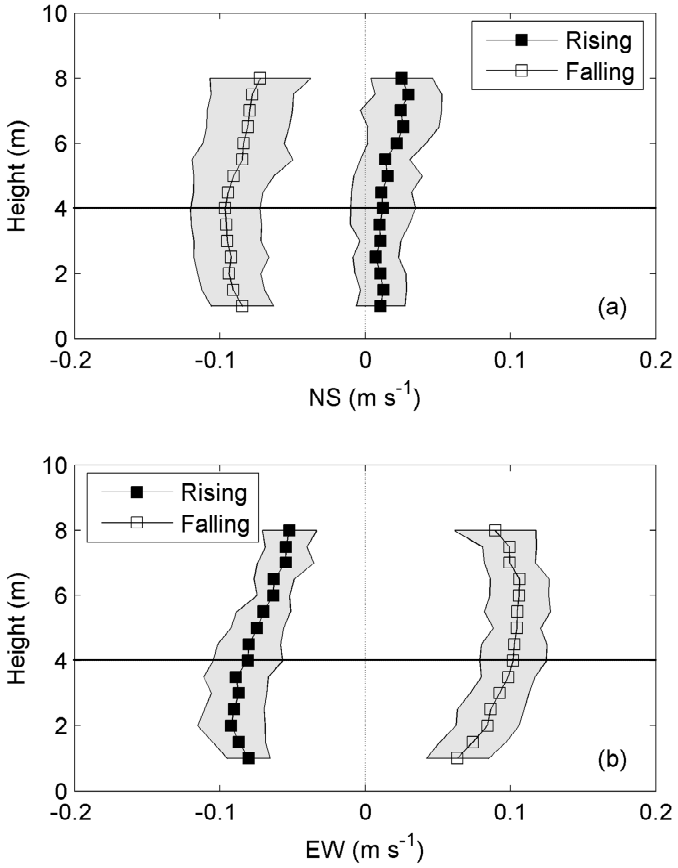

Figure 3.15 (a) North (positive) - South, and (b) East (positive) - West velocities averaged from 2 hours at mid-tide west edge of Collingwood mussel farm (ADP 3), 15-17 May 2003. Shaded area is ± 1 standard deviation, and horizontal line indicates approximate bottom of mussel farm. Water surface varies between 10 and 12 m.

There appears to be a link between the height of the peak velocity shear above the bed, the strength of the velocity shear, and the distance of the instrument from long-lines. Stronger velocity shears were recorded close to the long-lines. During the 2002 experiment, the ADP was moored within a block of long-lines, where the effect of flow underneath long-lines would be strongest (maximum velocity shear 0.020 s^{-1}at 3.5 m above the bed). In 2003, ADP 2 was moored within the farm but at least 100 m from the nearest long-line (S_z = 0.014 s^{-1} at 5 m above the bed). ADP 3 moored on the west of the farm was located closer to long-lines than ADP 2 (S_z = 0.015 s^{-1} at 3.75 m above the bed). The distance above the bed where the maximum shear gradient occurs also increases with distance from the long-lines. This is perhaps indicative of bottom friction, which would slow velocities near the bed through drag, decreasing the shear gradient as momentum is transferred up through the water column with the reestablishment of a logarithmic velocity profile (in the absence of significant wind shear on the free-surface).

Although measurements from moored ADP and ADCP transects within the farm boundary showed that velocities below the farm were greater than within the farm, velocities in the undercurrent did not increase significantly above those recorded away from the farm. There did not appear to be a substantial diversion

of flow beneath the farm. The proximity of the mussel droppers to the bed should be noted. At extreme low tide, some mussel droppers were observed (via underwater video) to touch the bottom. At mid-tide, the gap between bed and droppers would be in the range 2 to 4 m (depending on dropper length and location within the farm). Thus the gap beneath the farm is relatively small, restricting the ability of fluid to pass beneath the farm. Instead, flow must be diverted horizontally around the farm. This should be detectable by higher velocities near the farm perimeter, and by diversion of streamlines around the farm.

3.3.3 Flow Diversion around the Mussel Farm

A significant reduction of velocity within the Collingwood mussel farm has been shown, and consequently an accompanying diversion of flow around the farm is expected. The evidence for diversion around the farm in the ADCP transects was rather weak. For example, an increase in velocities and easterly shift at the upstream (northern) end of the farm on falling tides can be detected in transect 3, see Figure 3.8(a) and (b). Transect 4, located north east of the farm also showed higher velocities with a strong easterly component, consistent with a diversion of flow around the north of the farm. More convincing evidence of flow diversion is seen in the comparison of mid-tide average velocities at ADP 1 and ADP 3. As the farm is rectangular, with the long axis lying north-south, the falling tide flows diagonally across the farm in a south-east direction. This placed ADP 3 mid-way along one of the upstream edges of the farm. As the farm partially blocked the tidal flow, acceleration is expected in a southerly direction along the western edge of the farm. Depth-averaged velocities at ADP 3 were 32% higher than at ADP 1 on falling tides (Figure 3.6), supporting the theory of an acceleration around the farm.

Given the vertical and horizontal dimensions of both the farm and mussel long-lines, it might be expected that water would be more easily diverted under long-lines than around the farm. However, the shallow nature of the study site coupled with the high dropper length/water depth ratio would limit flow underneath the farm. At a deeper site with a larger gap beneath long-lines, it is likely that more flow would be diverted underneath the farm, as opposed to around the sides. Strong density stratification is another factor that would inhibit diversion beneath the farm. The role of stratification will be discussed in Chapter 4.

3.3.4 Extent of the Farm Wake

The momentum deficit from the reduction of velocities within the farm will persist downstream from the farm as a wake. The size and strength of this wake is an important issue in considering environmental impacts of the farm, and for the positioning of future farms in relation to the present farm. The wake of the farm consists of the interaction of the individual wakes from the thousands of mussel droppers. However, it is convenient to consider the farm as a single large porous body. The farm wake will spread

laterally, but velocities will recover as the wake spreads. Near the farm, the wake may have a nearly constant velocity across its width, but as the wake spreads downstream, it will develop a Gaussian profile typical of the far wakes of bluff bodies. The wake from the farm in this study could be seen in transects taken on the falling tide, 15 May 2003, Figure 3.16. At the closest point, transect 5 was 500 m from the south-east corner of the farm. Reductions in water velocities can be seen at mid-depth over a length of 1500 m along the southern-most transect. Measured in a south-east direction, the furthest point of the wake (as detectable in the velocity transect south of the farm) is approximately 2.3 km from the farm boundary. This is similar to the tidal excursion which, calculated from ADP 1 north of the farm, was 2.4 km. The southern-most transect shown in Figure 3.16 was measured near low tide, when the motion of water would be close to the full tidal excursion. Unfortunately, no transects were taken further from the farm to confirm the length of the wake. As the velocities plotted in Figure 3.16 have not been corrected for the tidally-induced reduction in velocities, the transects can not be compared directly. However, velocities along a transect may be compared, indicating the relative reduction within, and in the wake of, the farm.

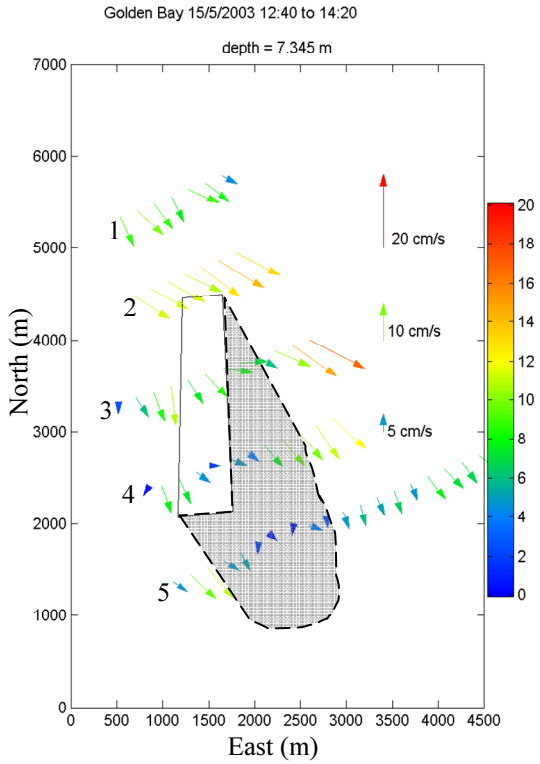

Figure 3.16 Mid-water depth velocities from 15 May 2003. Shaded area indicates the probable extent of the wake. Velocities have not been corrected for tidal variation.

3.4 Velocity Attenuation Models

The field measurements indicated the size and extent of the effect of the Collingwood mussel farm on water currents. In order to assess the likely effect at other sites, there is a need for predictive models. These models should ideally account for effects such as dropper diameter, dropper density, and long-line

orientation. In this section, two relatively simple predictive models are developed to assess the impact of the farm on water velocities. The first model is an analytical solution based on kinetic energy losses. The second model is based on a pipe-network analogy to simulate the likely diversion of fluid around the farm.

3.4.1 Analytical Energy Loss Model

The most significant source of drag from a mussel long-line are the crop ropes. A typical mussel long-line, with a length of 120 m, may have 3 to 5 km of crop rope hanging in loops (droppers). With a typical diameter of order 0.1 m, the combined projected area (not accounting for any sheltering of droppers behind other droppers) is ~ 500 m^2. In comparison, the same long-line may have up to 20 buoys, which are cylindrical with diameter ~ 1 m and length ~ 1.2 m. If completely submerged, (a rare and undesirable occurrence), the combined projected area of the buoys (end on) will be ~ 15 m^2, less than 3% of the total submerged area. Drag on the buoys will therefore be considered negligible, and is not considered further.

Explicit determination of the flow development through, and around, a mussel farm requires solving the conservation of momentum equation in two (and potentially three) dimensions. This requires knowledge of the flow in the farm region as well as the local bathymetry, distribution of long-lines, dropper density, and spatial variations of crop maturity (which determine dropper diameter). Wakes from upstream long-lines will result in lower velocities, and therefore lower drag on downstream long-lines. The orientation of long-lines to the flow will also have an influence on drag, with long-lines in-line with the flow presenting less frontal area. A further complication is that some of the flow approaching the farm will be diverted around or under the farm. The analytical model developed here does not attempt to include all these factors. Instead, bulk estimates of energy lost will be made from a relatively simple kinetic energy loss analysis. The intention is to provide rough estimates of velocity reduction that can indicate trends, and highlight the influence of dropper density on drag.

As a first approximation, all mussel droppers are assumed to act independently. Only flow within the mussel farm is considered, and flows under or around the farm neglected. The energy lost from the mean flow due to farm drag can be estimated from the rate at which work is done by the farm on the fluid. The boundary condition upstream of the farm is a velocity U_0, giving a kinetic energy per unit volume of $\frac{1}{2}\rho U_0^2$. The rate of energy lost to drag on a single dropper is calculated from the rate of work done $F_d U$, where F_d, the drag force, is calculated from

$$F_d = C_D \rho D L_d \frac{U^2}{2}, \tag{3.1}$$

where C_D is a drag coefficient for a single dropper, D the dropper diameter, L_d the dropper length, and U the water velocity at the dropper.

The rate of work done per unit area (m^2) of farm is nF_dU, where n is the number of droppers per square metre (m^2). Most of this energy is lost to the turbulent wake (there may also be small losses to the elasticity of the long-lines and moorings). Assuming that only kinetic energy losses occur, the rate of change of kinetic energy per unit area of farm (dK/dt) equals the work done on fluid so that

$$\frac{dK}{dt} = \frac{d\left(\frac{1}{2}\rho L_d U^2\right)}{dt} = -\frac{1}{2} n \rho C_D D L_d U^3 . \qquad (3.2)$$

The velocity can be determined as a function of x, the distance travelled through the farm (in the direction of flow), by using $dU/dx = 1/U\, dU/dt$. Integrating with respect to x yields

$$\frac{U}{U_0} = \exp\left(-\frac{nC_D D x}{2}\right). \qquad (3.3)$$

The horizontal velocity decreases through the farm as kinetic energy is lost to turbulence. To maintain continuity, there must be leakage of fluid through the sides, or base, of the farm. This method only considers kinetic energy. In reality there will be an exchange between kinetic and potential energy through changes in the free-surface elevation. In particular, a backwater curve will form upstream of the farm, resulting in a partial diversion of flow around the farm. The velocity at the upstream end of the farm will therefore be less than the free-stream velocity.

3.4.2 Analytical Model Results

The analytical expression for predicting the reduction of velocity within the farm (equation 3.3) requires a parameterisation of the dropper diameter, drag coefficient, and dropper density. The diameter of a mussel dropper is not easy to define given the highly irregular shape. Noting that the product of the drag coefficient and diameter $C_D D$ determines dropper drag, the choice of dropper diameter is somewhat arbitrary provided that the drag coefficient is based on the same definition. Later in this thesis (Chapter 10), the drag coefficient for a dropper with mussels at harvest size is measured by towing a short length of a dropper. The measured $C_D D$ was 0.18 m. The remaining parameter to specify is the dropper density n, which is estimated as 0.06 droppers m^{-2} for the Collingwood site.

Using the laboratory measured value for $C_D D$ in raw form results in a prediction of far greater velocity attenuation within the farm than was measured in the field. For example, in Figure 3.12, the velocity measured at 800 m into the farm was approximately $U/U_0 = 0.3$. The model predicts $U/U_0 = 0.01$ at $x =$ 800 m. In the development of the model, each dropper was assumed to be independent with no interaction. In reality, the droppers are arranged in rows (long-lines). There will be a degree of sheltering due to the orientation of the long-lines to the flow. Significantly improved estimates of velocity reduction can be obtained by modifying the drag coefficient to account for long-line orientation. The long-lines in

the Collingwood farm are at a range of angles to the tidal currents. At the north and south ends of the farm, 15° to 25° is a representative value. Standard design procedure for calculating wind loadings on porous fences is to modify the drag coefficient by the sine of the angle of the fence to the flow (Cook, 1985). As an approximation, the drag coefficient of the mussel dropper is modified by the long-line orientation to give $C_D D = 0.18 \sin(20^o) = 0.062$ m. The modified drag coefficient produces an improved estimate of $U/U_0 = 0.23$ at $x = 800$ m.

A factor not considered is the spatial and temporal variation of dropper diameters over the farm. As the farm is harvested and re-seeded on a rotational basis, the actual dropper diameter will differ both in time and space as the mussels grow. While the size distribution of dropper diameters will be similar, the spatial distribution will vary over time. Using the diameter for a dropper with mature mussels will lead to a conservative estimate of the velocity attenuation.

The effect of dropper density is illustrated in Figure 3.17, with higher dropper densities increasing the reduction of velocities within the farm. The model predicts that velocities within the farm drop in an exponential fashion. There is some evidence of this seen in the field measurements at the upstream end of the farm (particularly Figure 3.12).

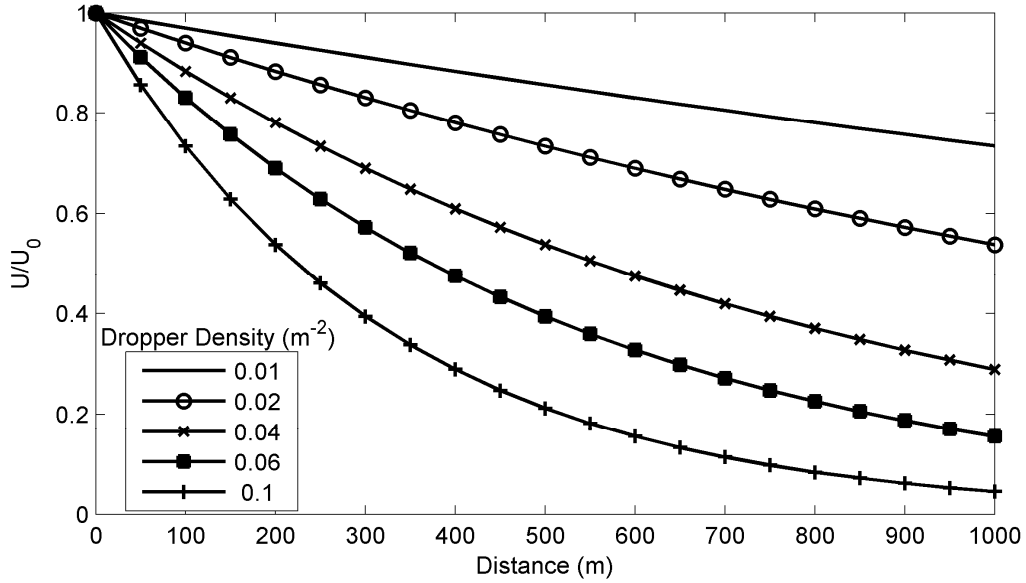

Figure 3.17 Analytical prediction for velocity decay through farm. A range of mussel dropper densities (droppers per m^2) are shown, with the solid boxes (0.06) comparable to the Collingwood mussel farm. A modified drag coefficient of $C_D D = 0.18 \sin(20^o) = 0.062$ is used.

3.4.3 Pipe-Network Model

The analytical model developed above only considered losses in kinetic energy in a 1-dimensional fashion, and did not account for any potential energy changes, or maintain continuity of mass other than

assuming that flow was diverted outward through the side of the farm as the velocity decreased. In reality, the tidal flow through the farm is driven by pressure differences. Energy losses due to the work done against the farm will result in changes of both kinetic energy (velocity), and potential energy (free-surface elevation). Small changes in free-surface elevation cause significant pressure differentials, and should be considered in order to gain a more complete understanding of the behaviour of the flow through and around the mussel farm. Most importantly, the formation of a backwater curve will result in a horizontal diversion upstream of the farm. To address some of the factors neglected in the analytical model (free-surface elevation, potential energy, two-dimensional flow, continuity of mass/volume), a pipe-network model is used as a more complex analysis tool.

The pipe-network model developed here is a simple, quasi two-dimensional, pressure driven, discrete model. The model is not strictly two-dimensional as the momentum equations are reduced to a one-dimensional form. The flow is also confined to particular directions because of the layout of the pipes. A full description and development of the pipe-network model is given in Appendix C, with a brief summary provided here. The equations for pipe friction have been modified to take the form of an open channel flow. This allows the use of a bed friction coefficient for determining energy losses.

Nodes are regularly spaced to form a rectangular grid (Figure 3.18). Each node is connected to the nearest neighbouring nodes by conduits. The friction from the bed and the mussel droppers is parameterised by the coefficient C_f, such that the shear stress on the fluid is

$$\tau = \frac{1}{2}\rho C_f U|U|. \tag{3.4}$$

The drag from the farm is represented by increased frictional losses; conduits in the area representing the farm have a higher friction coefficient than conduits outside the farm. The friction coefficient within the farm represents both the bottom friction and the farm drag.

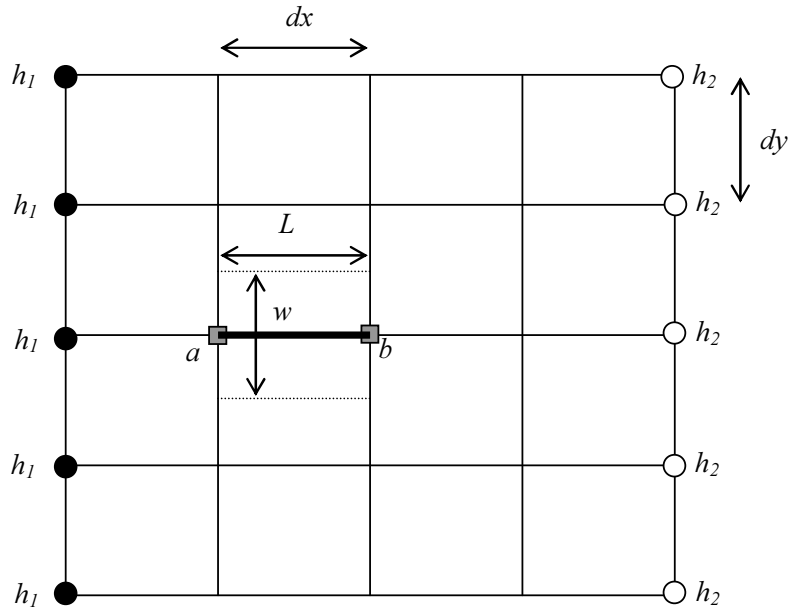

Figure 3.18 Example of grid for pipe-network model. Nodes are spaced at *dx* and *dy* in the *x* and *y* directions. Pressures are specified at inlet nodes (h_1) and outlet nodes (h_2). The conduit connecting nodes *a* and *b* (marked by the thick line) has a length *L* = *dx*, and width *w* = *dy*.

Frictional losses through each conduit are a function of the conduit length L (determined by the node spacing), hydraulic radius R (the water depth), and friction coefficient C_f. The energy or pressure change through a conduit is a function of the velocity U,

$$\Delta H = -\frac{C_f L}{R}\frac{U|U|}{2g}. \qquad (3.5)$$

The conduit width must be specified if the grid spacings vary in the x and y directions. Otherwise, if conduit widths are assumed to be the same, the capacity of the network to transport fluid will be reduced in one direction (less total area of pipes in one direction) resulting in higher velocities (and therefore higher frictional losses) in that direction to maintain continuity. To account for differences in grid spacing, the conduit width is specified as the spacing between the grid points. Conduits oriented in the y direction have a width $w = dx$, and conduits in the x direction have a width $w = dy$ (see Figure 3.18). As velocities are of more interest than conduit flows, the actual values of conduit width are less important than the ratio of conduit widths. If an equal grid spacing is used in both directions, the widths cancel. As the pressure variations over the site are likely to be small (a few mm) compared to the water depth (~10 m), variations in water depth between conduits can be assumed to be due only to the shape of the bed, and variations in the free-surface ignored. For simplicity, a flat bed is assumed. In terms of the pipe-network analogy, this is equivalent to specifying that all pipes have equal diameter (or equal hydraulic radius for the conduits).

The pressure at each node point in the grid is calculated iteratively so that continuity at each node is satisfied. Continuity is calculated by summing the inflows and outflows from the pipes connected to the node. The flow in each conduit, Q_j, is the velocity multiplied by the cross-sectional area Rw. A Gauss-Seidel type iterative procedure is used to calculate the pressure at each node (see Appendix C for details).

The choice of friction factor is the key factor determining the pressure losses. The pressure at the inlet and outlet nodes will determine the velocities within the grid. However, as pressure scales with the square of velocity, the velocities at the grid points can be non-dimensionalised (by an upstream velocity) so that inlet and outlet node pressures are arbitrary. Similarly, in terms of assessing the likely diversion of flow around the farm, the absolute values of friction factor are less important than the ratio of bed-friction to farm friction. These points will be illustrated in the example in the next section.

The pipe-network model only calculates a pressure driven flow, and does not account for turbulent momentum diffusion. This is particularly important in the wake region downstream of the farm. Also, the pipe-network model only provides a steady-state solution, and can not be used to simulate time-varying flows over a tidal cycle. As a quasi two-dimensional model, the farm is assumed to extend to the bed, and any influence of density stratification on flow is not resolved.

3.4.4 Pipe-Network Model Results

To parameterise the farm drag in the pipe-network model, a friction coefficient for the farm can be derived by expressing the drag on the droppers as a force per unit area (refer to equation (C.13) in Appendix C for more detail).

$$C_{farm} = nC_D DL_d \,. \tag{3.6}$$

The friction inside the farm is the sum of both the dropper drag and the bed friction. For conduits within the farm, the friction coefficient is $C_{bed} + C_{farm}$. Using the unmodified value of $C_D D = 0.18$, dropper density 0.06, and dropper length 8.5 m, the farm friction factor is $C_{farm} = 0.092$.

The bed-friction coefficient is obtained from pipe friction data. An estimate of friction coefficient for the rough bed can be obtained from pipe friction data. The bed friction coefficient for a channel C_f can be related to the pipe friction factor f by

$$C_f = f\frac{R}{D}. \tag{3.7}$$

The ratio of hydraulic radius to diameter for a pipe is $R = D/4$, giving $C_f = f/4$. Bed friction can then be calculated from the Moody diagram, or from the following approximation (Swamee and Jain, 1976)

$$f = \frac{1.325}{\left[\ln\left(\frac{\varepsilon}{3.75D} + \frac{5.74}{\mathrm{Re}^{0.9}}\right)\right]^2}. \qquad (3.8)$$

The Reynolds number in equation (3.8) is calculated from the pipe diameter, $Re = UD/v = 4UR/v$. The seabed at the Collingwood farm is mostly sand, although detritus from the farm (shells) probably presents additional roughness. A roughness element size of ε = 2 mm is assumed. Based on an assumed depth of 10 m, and average velocities of 0.10 m s^{-1}, the bed friction coefficient is estimated from equations (3.7) and (3.8) as C_f = 0.0027 (~ 0.003).

The drag coefficient in the analytical model was adjusted for the orientation of the flow relative to the long-line. A similar adjustment can be incorporated into the pipe-network model. To determine the adjustment to the farm drag coefficient, first consider the drag on a long-line. The drag on a long-line is a function of the angle of incidence, ($\gamma = \theta - \beta$), of the approaching flow (see Figure 3.19), and is assumed to be determined by

$$F_D = \tfrac{1}{2}\rho A C_D U^2 \sin\gamma . \qquad (3.9)$$

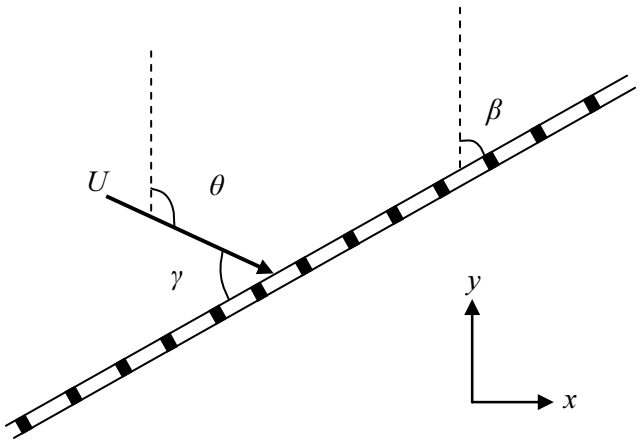

Figure 3.19 Definition diagram (looking downward) for the angle of the approaching flow relative to the long-line angle.

There may also be a lift force perpendicular to the drag force, but this will be assumed to be negligible. As the flow in the pipe-network model is confined to the x or y directions, the drag force is also resolved into x and y components,

$$\begin{aligned} F_x &= \tfrac{1}{2}\rho A C_D U^2 \sin\gamma \sin\theta \\ F_y &= \tfrac{1}{2}\rho A C_D U^2 \sin\gamma \cos\theta \end{aligned} . \qquad (3.10)$$

The velocity U at a node is calculated from the velocities in the x and y directions, so the drag components can be calculated as

$$\begin{aligned} F_x &= \tfrac{1}{2}\rho A C_D U_x^{\,2} \frac{\sin\gamma}{\sin\theta} \\ F_y &= \tfrac{1}{2}\rho A C_D U_y^{\,2} \frac{\sin\gamma}{\cos\theta} \end{aligned} \quad . \tag{3.11}$$

The farm friction coefficient can therefore be modified in the x and y directions based on the direction of the flow at the nodes, and the orientation of the long-lines. The modified farm drag coefficients for pipes in the x and y direction (C_{fx} and C_{fy}) are

$$\begin{aligned} C_{fx} &= C_{farm} \frac{\sin\gamma}{\sin\theta} \\ C_{fy} &= C_{farm} \frac{\sin\gamma}{\cos\theta} \end{aligned} \quad . \tag{3.12}$$

In practice, the farm friction coefficient for each pipe is obtained by averaging the value of θ at the nodes at either end.

By specifying a pressure gradient along the boundary nodes, a flow diagonally across the farm can be induced. In Figure 3.20, the flow is generated by specifying boundary pressures of H = 1.0 m at the upper left corner, H = 0 m at the lower right corner, and H = 0.5 m at the other two boundary corner nodes. The pressures at the other boundary nodes are obtained by linearly interpolating from the corner nodes. The pressure-driven flow can be seen to diverge around the farm. The plot on the left of Figure 3.20 uses a constant friction coefficient within the farm of C_{farm}/C_{bed} = 30, while the friction coefficient in the plot on the right of Figure 3.20 is modified using equation (3.12) for a long-line angle of $\beta = -15^{o}$.

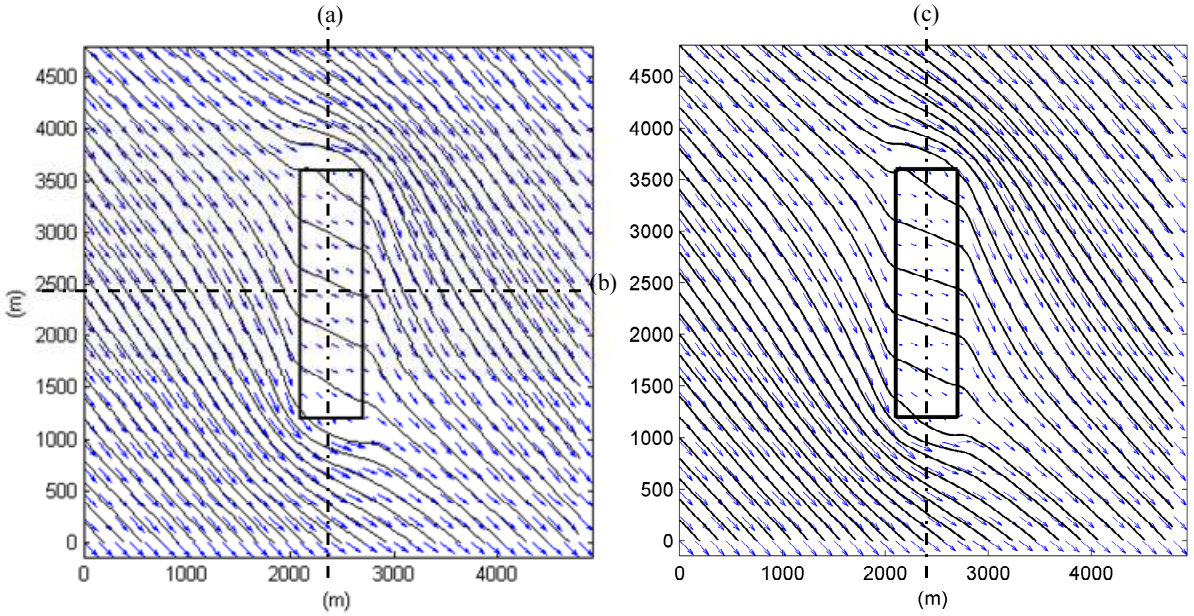

Figure 3.20 Pipe-network model simulation with non-directional drag coefficient (left), and directional with long-lines oriented at -15°. The pressure gradient is diagonally across farm, with a 150 m x 240 m grid. Cross-section (a) and (b) are shown in Figure 3.21; cross-section (c) is shown in Figure 3.22. C_{farm}/C_{bed} = 30.

Cross-sections of velocity magnitude through the centre of the farm in both the x and y direction are plotted in Figure 3.21. Velocities are non-dimensionalised by the velocity at the upper left-hand corner node (U_0). Calculated velocities within the farm using a non-directional farm friction of C_{farm}/C_{bed} = 30 are U/U_0 = 0.32, which is in agreement with the field measurements. High velocity shear is seen at the farm boundaries. Velocities at the domain boundaries are not uniform, as can be seen at the edges of Figure 3.20 and Figure 3.21. This is a result of the diversion of flow caused by the farm, and from imposing a linear pressure gradient along the boundary.

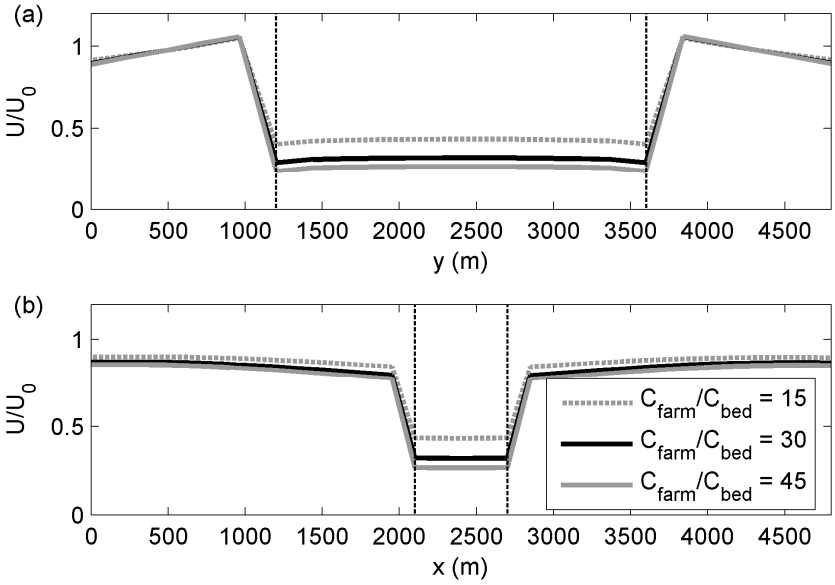

Figure 3.21 Cross-sections of velocity magnitude through farm from pipe-network model for three values of non-directional farm friction ratio (a) south to north, and (b) west to east. The edges of the farm are indicated by the vertical lines.

Typical long-line orientations at the Collingwood site were $\beta \sim -15^{o}$, where β is positive clockwise from north. Cross-sections of velocity calculated for $\beta = -30^{o}$, -15^{o}, and 0^{o} are plotted in Figure 3.22. For comparison, field data from the transect shown in Figure 3.12 are also plotted (open circles).

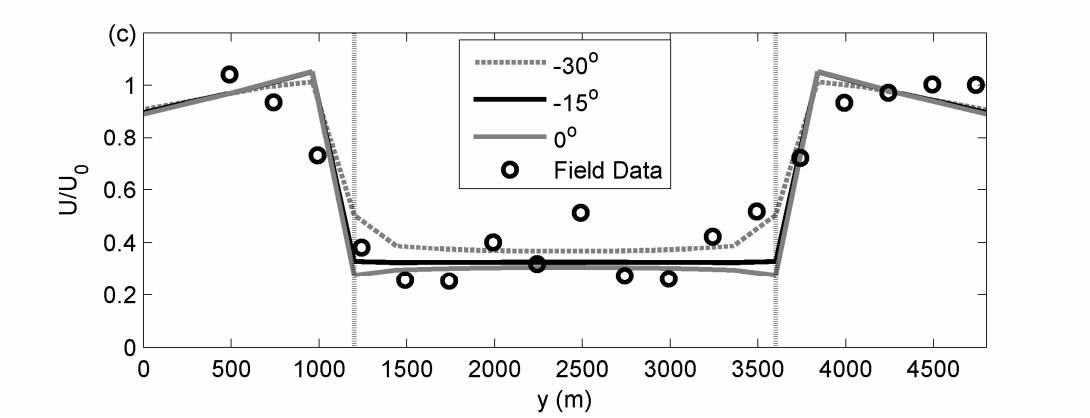

Figure 3.22 Cross-sections of velocity magnitude sections through mussel farm from pipe-network model at long-line orientations of -30°, -15° (typical of farm) and 0°. The edges of the farm are indicated by vertical lines. $C_{farm}/C_{bed} = 30$.

With $\beta = -15^{o}$, the pipe-network model predicts velocities within the farm of $U/U_0 = 0.33$. This is only slightly higher than the previous value calculated without accounting for long-line orientation ($U/U_0 = 0.32$). Simulations with a long-line orientation of $\beta = +45^{o}$ (approximately normal to the approaching flow) gave in-farm velocities of $U/U_0 = 0.29$, and at $\beta = -60^{o}$, $U/U_0 = 0.72$. This last value simulates flow where long-lines are nearly in-line with the flow through the farm.

The pipe network model appears to give reasonable estimates of velocities within the farm using a friction coefficient derived assuming drag on non-interacting cylinders. The friction coefficient can be modified to account for long-line orientation; however, the effect on in-farm velocities is small unless the angle between the long-lines and in-farm flow is small. The pipe network model is still relatively simplistic, and is not likely to be accurate in the wake region where turbulent momentum transport will control the rate of wake spread.

3.5 Discussion

3.5.1 Reduction of Velocities within the Farm

The measured reduction in velocity within the large farm in this study (a reduction of 47% to 67%) is similar to the measurements of Waite (1989) and Gibbs *et al.* (1991) (70% within a small farm of 8-10 long-lines), and the numerical predictions of Grant and Bacher (2001) (54% decrease in velocity with areas of scallop and kelp aquaculture). This is somewhat surprising given the differences in size and configuration of the farms in these studies. As in Waite (1989) and Gibbs *et al.* (1991), higher velocities were recorded underneath long-lines, with significant velocity shears generated between the undercurrent and in-farm flow. Where this present study differs is in the area where modification to currents and velocity profiles can be detected. Gibbs *et al.* found that the mussel farms appeared to have little effect on water movement beyond the immediate area of the farm. Measurements only 25 m away from long-lines did not appear to be influenced by the presence of the farm. However, the Collingwood mussel farm is essentially a collection of smaller farms in close proximity, with blocks of long-lines 100 to 200 m apart. The ADP mooring on the west edge of the farm (ADP 3) showed significant changes in velocity profile and current speeds at a distance of 100 m from the nearest long-line. More significantly, a distinct wake was detected downstream of the farm, indicating that effects of large farms are not confined to the immediate area of the farm.

The analytical and pipe-network models both gave reasonably accurate estimates of velocity reduction within the farm, although the drag-coefficient in the analytical model needed to be reduced to account for long-line orientation to the flow. A similar modification in the pipe-network model had little effect unless the angle between the flow within the farm and the long-lines was small. A 67% reduction of velocities was predicted for flow diagonally across the farm, in good agreement with the field data.

Large offshore mussel farms have similarities with kelp beds in that both cover large areas, and present a significant, but porous, obstacle to flow. Reduction of long-shore currents by large beds of giant kelp, *Macrocystis pyrifera*, at Pt. Loma, California was measured by Jackson and Winant (1983) and Jackson (1998). The kelp bed in these studies had dimensions of 7 km long by 1.5 km wide, and depths varied

over the site from 6 to 30 m. Jackson and Winant described the kelp plants as being attached to a hard bed by a hold-fast, from which multiple fronds grow. Each frond consisted of a rope-like stipe, with a diameter of ~ 1 cm. Small air bladders (pnematocyts) provided buoyancy causing the fronds to float. An individual plant typically had 40 fronds, which intertwined to form a hard column between the bottom and the surface. The column of fronds had a diameter of 10 to 20 cm, similar to the diameter of a mussel dropper. The fronds diverge at the surface forming a canopy. While the canopy of fronds form a dense mat which can completely cover the surface (Jackson, 1998), the drag over much of the depth is caused by the columns of fronds. Plant densities at the Pt. Loma bed are reported as in the range 0.01 to 0.1 plants m^{-2}. This is similar to the density of mussel droppers at the Collingwood mussel farm studied here (0.06 droppers m^{-2}). Jackson and Winant found that root-mean-squared velocities (over several tidal cycles, representing average currents rather than accounting for short period fluctuations such as from waves) within the kelp bed were between 0.43 and 0.54 in the long-shore direction, and between 0.30 and 0.44 in the cross-shore direction of velocities at a control site outside the bed. This is very similar to the velocity reduction detected inside the Collingwood mussel farm, where velocities are between 0.33 and 0.53 of velocities outside the farm.

3.5.2 Diversion of Flow Around and Under the Farm

Consistent with the reduction of velocity within the mussel farm was an accompanying diversion of flow around the farm. Measurements from ADP and ADCP within the farm showed velocities near the bed were higher than over the depth of the mussel droppers. The velocities in the undercurrent were similar, or slightly higher, in magnitude to those recorded away from the farm. However, the small increase was insufficient to compensate for the reduction of velocities within the farm. It is likely that the close proximity of the mussel droppers to the bed prevented significant diversion beneath the farm. The modification to the vertical water velocity profiles is significant, and the difference in velocity between the in-farm and beneath farm currents generates a velocity shear that could have significant influence on mixing processes. The shear gradient may form a mixing layer similar to those created above submerged vegetation (Ghisalberti and Nepf, 2002), and plant canopies (Cionco, 1965; Finnigan, 2000). Depending on the degree of density stratification, Kelvin-Helmholtz instabilities, growing to roller-type vortices, may form at the interface between the slower in-farm velocities and the faster undercurrent. These vortices would enhance and dominate mass and momentum transfer through the mixing layer. This effect, and the controlling influence of stratification, will be discussed in more detail in Chapter 4.

3.5.3 Area Influenced by the Farm

The momentum deficit within the farm will persist downstream of the farm as a spreading wake. This wake will spread laterally, but velocities will recover as the wake spreads. If a farm were placed in a uniform current, then the wake would persist for a large distance downstream. However, the currents at

the study site were predominantly tidal, reversing in direction from rising to falling tide. This effect can be understood more clearly by imagining the farm moving back and forth over a tidal cycle through stationary water, rather than the water flowing past a stationary farm. The area immediately affected by the wake will be limited by the tidal excursion. However, turbulent momentum transfer will spread the effect of the wake some distance further. At ADP 1, north of the farm, depth-averaged velocities over the tidal cycle vary from 0.05 to 0.15 m s^{-1}. Integrating the velocities at this location over half the tidal period (one rising or falling tide) gives a tidal excursion of approximately 2.5 km, similar to the length of the farm. At sites where there is a net residual current over many tidal cycles, this residual could be reduced or altered by the momentum loss generated by the farm.

While the region of low velocities downstream of the farm has been referred to as a wake, it is more appropriate to consider the farm wake as two mixing layers (about a vertical plane) separated by the width of the farm. Unlike the wake of a solid body, there is no stagnation point (point of zero velocity) on the downstream end of the farm, and no evidence of any recirculation zone. Instead, there is a region of low velocity bounded either side by faster moving fluid. The mixing layers that form between the farm-retarded flow and the faster moving surrounding flow will grow independently until they eventually merge some distance downstream. Therefore, first estimates of the spread of the farm wake can be made using a mixing layer analogy.

Recent research has shown that wakes and mixing layers in flows that are shallow compared to the horizontal dimensions exhibit different behaviour from those in deep water. For example, high Reynolds number flows around cylinders where the flow depth is small compared to the cylinder diameter have wakes that resemble that of low Reynolds number flows around cylinders where the depth is much greater than the cylinder diameter. The shallow flow and the bottom friction act to restrict the ability of large scale turbulent structures to decay three-dimensionally (Chen and Jirka, 1995). The flow downstream of a mussel farm may resemble a shallow water mixing layer as the farm width (~ 650 m) is much larger than the flow depth (~ 10 m). Therefore, it is necessary to calculate whether the mixing layer growth behind a mussel farm will be influenced by the water depth.

3.5.3.1 Deep Water Mixing Layers

A mixing layer develops along the boundary of two flows with different velocities. Mixing layers play an important role in the transport of mass and momentum between the two flows. A plane mixing layer occurs where the mean flow is two-dimensional. A deep water mixing layer is a special case of the plane mixing layer where the boundary between the two flows is vertical. The deep water mixing layer has attracted considerable research, particularly as the instabilities that develop within the mixing layer result in the formation of eddy structures. Due to the flow geometry, the eddy structures are at first two-

dimensional. Larger structures are formed via the vortex pairing mechanism (Moser and Rogers, 1993). Further downstream the two-dimensional structures become unstable and disintegrate into three-dimensional turbulence.

Analytically, it can be shown that the width of the deep-water mixing layer grows at a constant rate downstream. This has also been confirmed in many experiments. Following Uijttewaal and Booij (2000), the width δ of a two-dimensional plane mixing layer is defined as the maximum slope thickness:

$$\delta = \frac{u_1 - u_2}{\left(\partial u/\partial y\right)_{\max}}. \tag{3.13}$$

For most experimental configurations, the growth rate is proportional to the characteristic mixing layer parameter $\lambda = (u_1 - u_2)/(u_1 + u_2)$, where u_1 and u_2 are the undisturbed streamwise velocities. The growth rate of the mixing layer is expressed as

$$\frac{d\delta}{dx} = \alpha_0 2\lambda. \tag{3.14}$$

In deep water, the constant of proportionality α_0 has an empirically determined value of 0.09 (Uijttewaal and Booij, 2000).

3.5.3.2 Shallow Water Mixing Layers

Uijttewaal and Booij (2000) describe two factors that have a significant influence on the development and growth of the mixing layer in shallow flow. Firstly, when the flow depth is small, large eddies in the mixing layer are restricted to two-dimensional motion, and are unable to disintegrate into smaller three-dimensional turbulence. The large eddies can then only be broken down by the action of vertical velocity gradients, and small scale three-dimensional turbulence. The dissipation of energy from the large scale eddies will be slower than if these eddies were able to disintegrate three-dimensionally. Secondly, bed friction restricts the growth of the mixing layer.

The effects of bed friction and shallowness on mixing layer growth can be expressed by a single parameter, the wake stability or bed friction number S (Chu *et al.*, 1991)

$$S = \frac{C_f}{4\lambda}\frac{\delta}{h}, \tag{3.15}$$

where h is the water depth, and C_f the bed friction coefficient ($C_f = 2\tau/\rho U^2$). There is a critical value for the wake stability number S_c above which bottom friction prevents the growth of the mixing layer (Chu *et*

al., 1983; Chen and Jirka, 1997). The critical wake stability number for a mixing layer lies within the range 0.06 to 0.12. The value for S_c of 0.08 found by Uijttewaal and Booij is used here.

The bottom friction modifies the constant of proportionality in the expression for mixing layer growth rate (equation (3.14)) so that, from Chu and Babarutis (1988)

$$\alpha = \alpha_0 \left(1 - \frac{S}{S_c} \right), \qquad S \le S_c . \tag{3.16}$$

The value of α will vary with distance x

$$\frac{d\alpha}{dx} = \frac{d}{dx}\left[\alpha_0 \left(1 - \frac{C_f}{4\lambda S_c} \frac{\delta}{h} \right) \right], \quad S < S_c \tag{3.17}$$

$$= 0, \qquad S \ge S_c .$$

To balance the bottom friction, a streamwise pressure gradient must occur. This pressure gradient, in the form of a free surface slope, results in a decrease in depth and an increase in velocity downstream. In laboratory experiments (Chu and Babarutis, 1988; Uijttewaal and Booij, 2000) the free surface slope is measurable. However, Froude numbers in the field are an order of magnitude lower than for the laboratory experiments ($Fr_{\text{field}} \sim 0.015$, $Fr_{\text{lab}} \sim 0.28$), so free surface slopes are also smaller. For simplification, the change in depth will be ignored. Equation (3.17) can be re-written as

$$\frac{d\alpha}{dx} = -\frac{\alpha_0 C_f}{4\lambda h S_c} \frac{d\delta}{dx}, \qquad S \le S_c . \tag{3.18}$$

Solving equations (3.14) (with α_0 replaced by α) simultaneously with equation (3.18) allows an expression to be derived for the mixing layer width as a function of distance:

$$\alpha = \alpha_0 \exp\left[-\frac{\alpha_0 C_f}{2S_c} \frac{x}{h} \right], \qquad S \le S_c . \tag{3.19}$$

$$\delta = \frac{4\lambda S_c h}{C_f} \left(1 - \exp\left[-\frac{\alpha_0 C_f}{2S_c} \frac{x}{h} \right] \right), \qquad S \le S_c . \tag{3.20}$$

The maximum thickness of the mixing layer is limited by the bottom friction, and has the value

$$\delta_{\max} = \frac{4\lambda S_c h}{C_f} . \tag{3.21}$$

3.5.3.3 Application of mixing layer analogy

These equations may be used to estimate the rate of growth of the two mixing layers generated by the farm. To estimate the spread of the mixing layers, the following parameters have been chosen as representative of the farm: h = 10 m and bed friction C_f = 0.003. The ratio of velocities behind the farm to the surrounding flow were in the range u_2/u_1 = 0.5 and u_2/u_1 = 0.33. The growth of the mixing layer is calculated using these two values as limits (λ = 0.33 and 0.5 respectively).

The maximum possible thickness of the mixing layer predicted by equation 3.21 is 356 m (λ = 0.33) or 533 m (λ = 0.5). The growth of the mixing layer is slow, with a mixing layer thickness at the tidal excursion of 2500 m estimated as between 143 m (λ = 0.33) and 215 m (λ = 0.33), Figure 3.23(a). The effect of the shallowness is small, as deep-water mixing layers would have spread to between 150 m (λ = 0.33) and 225 m (λ = 0.33). For comparison, the farm width is 650 m from east to west, and as the flow crosses the farm at an angle, the effective width is greater. At the end of the tidal excursion, the two mixing layers from either side of the farm would not have spread sufficiently to merge. The influence of bed coefficient on the mixing layer width, bed friction number and growth rate constant can be seen in Figure 3.23. Higher bed roughness decreases the mixing layer growth rate, while a higher velocity difference (higher λ) increases the spread of the mixing layer, Figure 3.23(a) and (b). The bed friction number or wake stability factor and growth rate coefficient, Figure 3.23(c) and (d), are not dependent on λ, but are influenced by the choice of bed friction coefficient.

The slow growth of the mixing layer indicates that lateral turbulent momentum diffusion is also slow. The mixing layer formulation does not account for transverse pressure gradients. An area of lower pressure is likely to form downstream of the farm as predicted by the pipe-network model. This pressure gradient would cause the flow around the farm to converge downstream, reducing the width of the wake. However the growth of the mixing layer would counteract this convergence to a degree by reducing pressure gradients through transverse momentum transport.

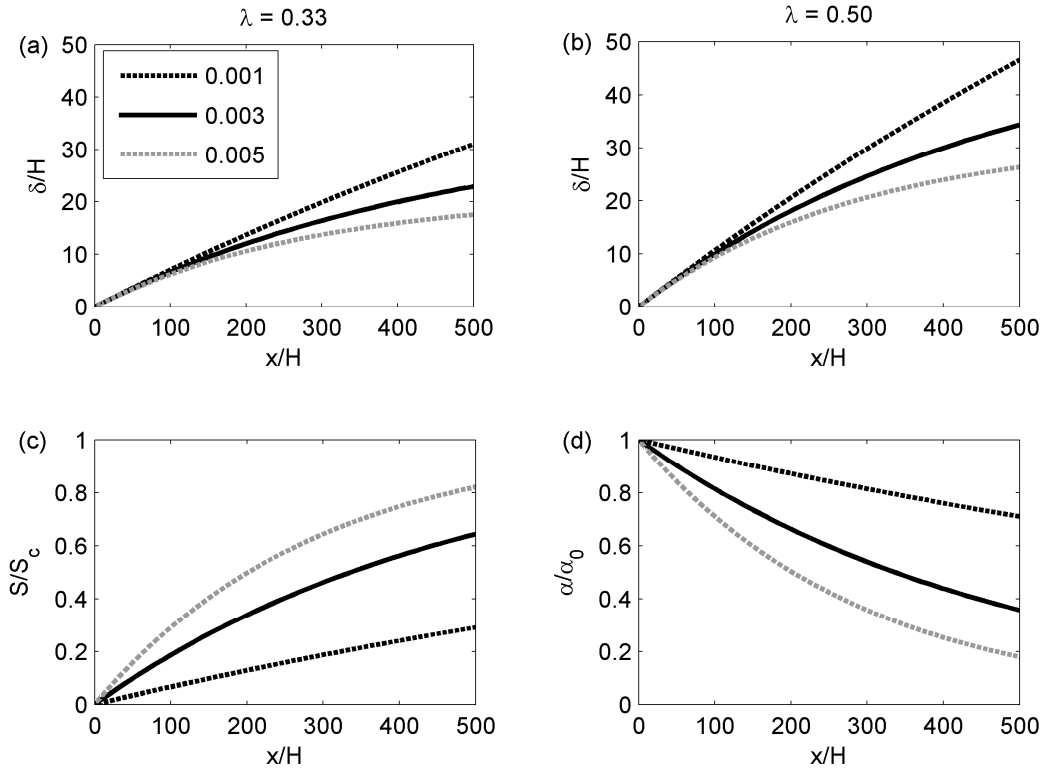

Figure 3.23 (a) mixing layer thickness for λ = 0.33, (b) mixing layer thickness for λ = 0.50, (c) wake stability or bed friction number, and (d) growth rate coefficient for three values of bed friction coefficient (refer to the legend), α_0 = 0.09, S_c = 0.08.

3.6 Summary

Mussel farms are capable of having large local effects on water currents. Reductions of velocity of between 47 and 67% were measured at the Collingwood mussel farm. Velocities were decreased within the farm, but flow was able to pass beneath the long-lines. Significant velocity shears ($dU/dz \sim 0.2$ s^{-1}) developed between the slower moving fluid within the farm and the faster undercurrent. The mixing layer formed in this region may influence vertical mixing processes, depending on how much stability is induced by density stratification (see Chapter 4).

Velocities beneath the mussel farm were similar to, or only slightly higher than, those recorded outside the farm, indicating that flow was diverted around rather than under the farm. Higher velocities were recorded along one boundary where the direction of currents indicates that flow was diverted by the farm. Downstream of the farm, a momentum deficit (wake) was present which was detected at a distance up to 2.3 km in a downstream direction from the farm boundary. It is likely that the size of the wake would be limited by the tidal excursion. However, it is possible that larger areas could be affected by alteration of net residual currents over several tidal cycles.

The reduction of velocities within the farm is similar to that reported for large kelp beds where the densities of kelp plants, and the diameter of the kelp column, are similar to the mussel droppers.

A simple analytical model based on kinetic energy losses indicates the importance of dropper density on velocity reduction. However this model requires modification to the dropper drag coefficient to obtain results resembling the field data. A quasi-two dimensional model based on a pipe-network analogy gives a good prediction of velocities within the farm using a parameterisation of the dropper drag on a unit area basis. The drag in the pipe-network model could be modified to account for long-line orientation. The success of this simple model suggests that two-dimensional models using an increased bed-friction in the farm are likely to give reasonable results, particularly where farms have large horizontal dimensions compared to the depth, or where the water column is strongly stratified, so that diversion is primarily around the farm rather than beneath it.

CHAPTER 4 EFFECT OF MUSSEL FARMS ON MIXING AND STRATIFICATION

4.1 Introduction

In the previous chapter on the effect of mussel farms on currents, it was shown that significant energy loss occurs in the form of a reduction in water velocities. This energy loss is caused by the drag on the submerged mussel droppers. The velocity shears and turbulence generated as a result of this drag have the potential to enhance mixing, both vertically and horizontally. In this chapter, the effect of a mussel farm on density stratification is examined through field observations. A number of cross-sections of density through the farm are examined to qualitatively assess the impact of the farm. The experimental methods are described in section 4.2, the results in section 4.3, and a discussion of these results in section 4.4. The chapter concludes with a summary in section 4.5.

4.2 Experimental Methods

4.2.1 Study Site

Measurements of water column properties were made at the Collingwood, Golden Bay, mussel farm on the 10th and 17th April 2002, 15th to 17th May 2003, and 2nd to 9th August 2003. The last data set was recorded by NIWA personnel as part of a separate study, and is used here by permission.

4.2.2 Measurement of Water Column Properties

Interaction between fluid stratification and the mussel farm was investigated by conducting surveys of water column properties (mostly temperature and conductivity, and occasionally fluorescence and turbidity) using Conductivity, Temperature, Depth probes (CTD), combined with measurements of water velocity profiles from boat-mounted Acoustic Doppler Current Profilers (ADCP) and moored Acoustic Doppler Profilers (ADP). Salinity and density were calculated from the conductivity and temperature data. Values of salinity are reported in practical salinity units (PSU), which approximate closely to grams per kilogram. Surveys consisted of transects through or adjacent to the mussel farm.

A different survey strategy was employed during the 2nd to 9th August 2003 measurements. For these data, the measurements consisted of measuring velocities, chlorophyll *a* fluorescence, salinity, and temperature around the perimeter of the farm. This was to enable a control-volume method to be used by NIWA in an attempt to estimate phytoplankton depletion rates within the farm. I was given permission to use the velocity, temperature, and salinity data to estimate diapycnal (across density contours) mixing rates inside the farm. A total of 12 of these surveys were recorded, providing a data set of salinity, temperature, and velocity profiles at 0.5 m vertical resolution and at an average horizontal spacing of 70 m.

4.2.3 Instrumentation

CTD instruments were provided by NIWA. The instruments used for each study are listed in Table 4.1.

Survey No.	Site	Date	Instrument
1	Collingwood	10 and 17 April 2002	RBR XR-420-CTD
2	Collingwood	15-17 May 2003	Seabird SBE19 CTD
3	Collingwood	2-9 August 2003	BIOFISH

Table 4.1 CTD instruments used for field measurements.

Some of the instruments used had additional sensors measuring properties such as fluorescence (13th to 15th Nov 2001, 8th Feb 2002, 10th and 17th Apr 2002), and turbidity (10th and 17th Apr 2002).

CTD profiles were taken by gently lowering the instrument, attached by rope, from the side of a small (6-7 m) boat. Locations of profiles were recorded using GPS. Surveys with the BIOFISH were taken by towing the instrument behind the boat at an average speed of 9 km/hr. The BIOFISH is described in Chapter 2.

4.3 Results

A large number of measurements were taken during the various field surveys. For clarity, a selection of the measurements, indicating key features, are presented in this chapter. Other measurements are presented in Appendix D. Transect numbers and locations are also explained in Appendix D.

4.3.1 Site Properties

Surveys of water properties at the Collingwood, Golden Bay mussel farm were taken on 5 days: 10th April 2002, 17th April 2002, and 15th to 17th May 2003. These surveys can be grouped into two sets, April 2002 and May 2003, based on water conditions at the time of the surveys. Both sets of surveys (April 2002 and May 2003) were taken in late autumn/early winter during cool, calm conditions.

A common feature from all surveys at the Collingwood site was a stratification dominated by salinity, with a cool, fresher fluid above warmer, saline fluid. Also seen in both survey sets is that water north of the farm was consistently cooler and fresher than that south of the farm. As the salinity difference between these areas (typically ~ 0.3 PSU) had a larger influence on the density than the temperature difference (typically ~ 0.9^{o}C), the warm salty fluid would intrude underneath the cool fresher layer. This structure had the appearance of a gravity current or front. An example of the front is seen beneath the farm in Figure 4.1(a). This structure is present in all transects measured through the farm, but is also

present in parallel transects offshore from the farm, e.g. Figure 4.1(b). The water velocities recorded in conjunction with these measurements are plotted in Figure 3.9.

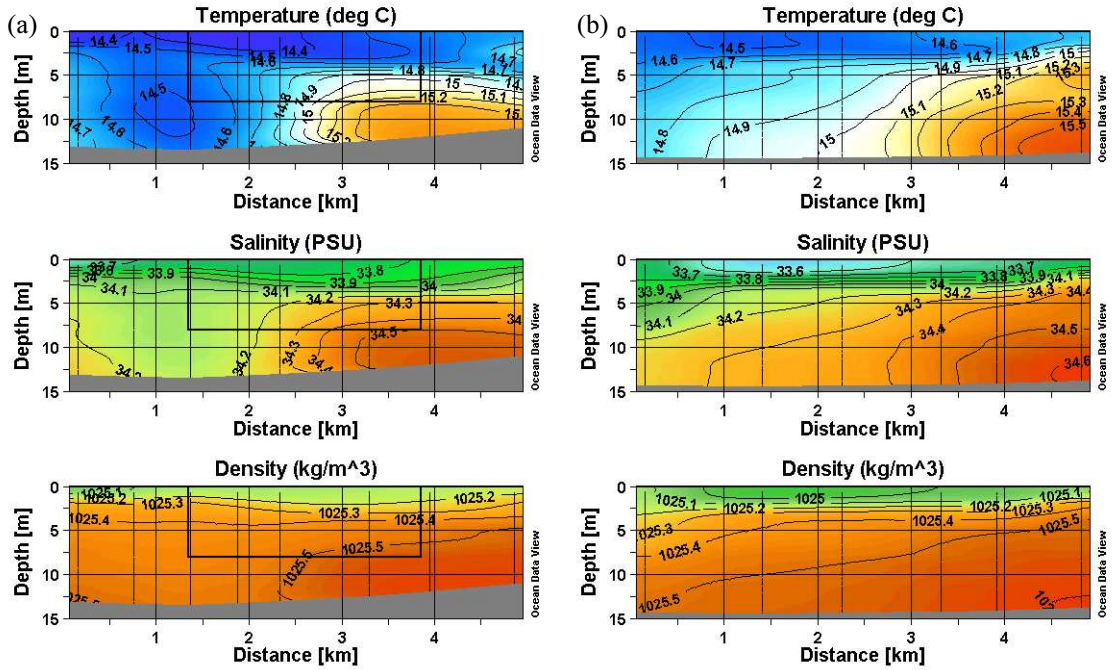

Figure 4.1 Parallel transects of temperature, salinity, and density (a) through farm (left panel, 160503-2) and (b) offshore of farm (right panel, 160503-3). Both transects are north (left) – south (right), and the farm location is indicated by the rectangle in the left panel. Tidal currents were from left (north) to right (south) and into the page (see Figure 3.9).

The density front indicated in Figure 4.1 has the potential to drive a gravity current from right to left as plotted. The speed of the current can be estimated from the density difference between the fluid within the front and that to the left of the front (~ 0.1 kg/m^3), and from the height of the current (~ 5 m). Using these values, a gravity current velocity of $U \sim \sqrt{h g \Delta\rho / \rho}$ = 0.07 m s^{-1} is estimated. This is a significant current considering that velocities upstream of the farm were around 0.10 m s^{-1}. The density front does not have a sharp edge, rather the density varies horizontally over a distance of around 1.5 km (based on the temperature and salinity plots), so is likely to travel slower than predicted. The density gradient in Figure 4.1 is attempting to drive a current against the tide. However, the measured water velocities (see Figures 3.8, 3.9 and 3.10) do not indicate a strong influence from the density gradient. It is possible that the density gradient prevented higher velocities occurring beneath the farm.

The transects of temperature and salinity are consistent with a source of cool, fresh water mixing with water in the bay. The most significant source of fresh water to Golden Bay in the vicinity of the mussel farm is the Aorere River, mean flow ~ 20 m^3 s^{-1}, which drains into Golden Bay via the Ruataniwha Inlet approximately 3 km south-west of the farm. It is not clear why salinity and temperature are low north of

the farm when the river plume can be detected at the surface south of the farm in many transects (see Appendix D).

Water properties were measured in the Aorere River, and 11 km offshore near the middle of Golden Bay on the 16 May 2003. The flow in the Aorere River on the 16 May 2003 was 14 m^3 s^{-1}. Temperature, salinity, and density profiles for the two sites are plotted in Figure 4.2. The profile in the river was taken as far upstream as could be safely reached by boat (approximately 1.5 km upstream from the mouth of the Ruataniwha Inlet). The profile in the river shows strong density stratification due to a salt wedge intrusion. The upper layer (approximately 1.2 m deep) had a temperature of 9.5^{o}C and salinity of 2.6 PSU. The lower layer has a higher temperature of 13.1^{o}C and salinity of 33.4 PSU. The upper layer represents the freshwater input into the bay, while the lower layer is a mix of the bay water and fresh water.

At the offshore location, three distinct layers could be detected, increasing in temperature and salinity deeper into the water column. The density increases at an almost linear rate, with small steps detected at the interfaces between the three layers. The upper layer (0-6 m) has a temperature and salinity of 15.5^{o}C and 34.63 PSU, although temperature increased slightly with depth. This may be an indication of surface cooling, with air temperatures on the 16th May 2003 varying from a low of 2^{o}C to a maximum of 14^{o}C. The air temperature at the time of measuring the profile was not recorded, but is estimated to be in the range 8 to 10^{o}C. The increasing density indicates that the upper layer was not completely mixed. This is consistent with the observation of no wind and little wave action. The middle layer (6 – 15 m) has a constant salinity (34.69 PSU) with temperature decreasing with depth. The bottom layer shows both salinity and temperature increasing with depth. These profiles are likely to have been generated by a series of discharge events of cool fresh water into the bay, with the uppermost layer the most recent.

The fluid in the area around the farm had temperature and salinity less than that measured at the offshore site. The temperature-salinity plot, Figure 4.3, with contours of density anomaly $\sigma_t = (\rho - 1000)$, indicates the variation of salinity and temperature in the area around the farm on the afternoon of 16 May 2003. The values for salinity around the farm are centred on a value of 34.1 PSU, whereas the offshore site has an average salinity of 34.7 PSU. Assuming that salinity is conservative, the water around the farm consists of approximately (34.7-34.1)/34.7 = 1.7% fresh water.

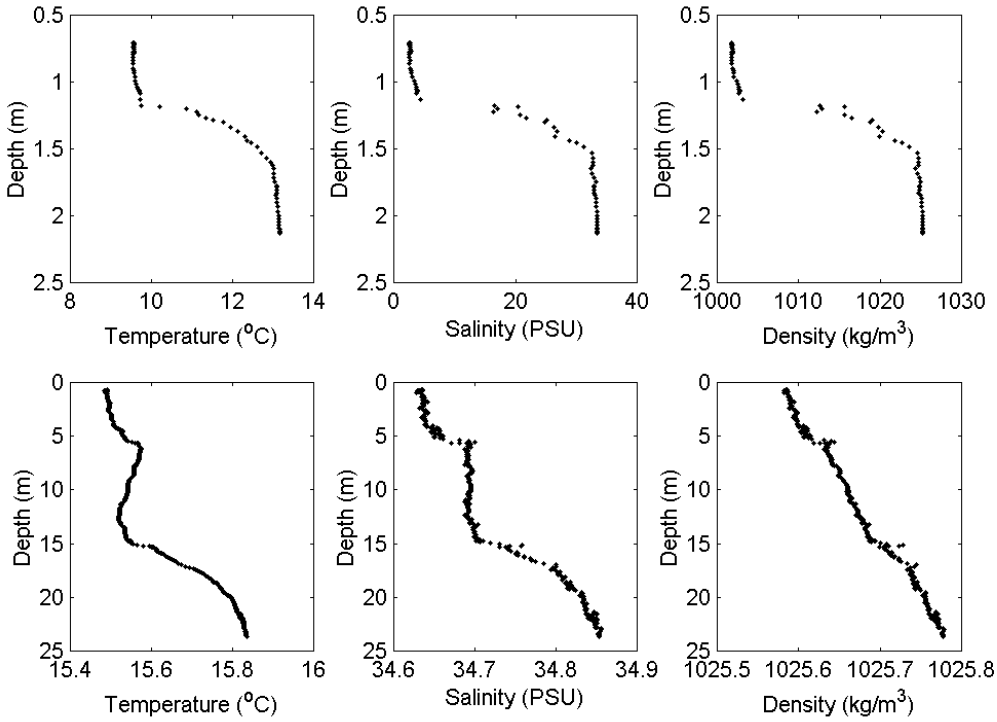

Figure 4.2 Profiles of temperature, salinity and density in Aorere River at Bridge (top) and 11 km offshore in Golden Bay (bottom).

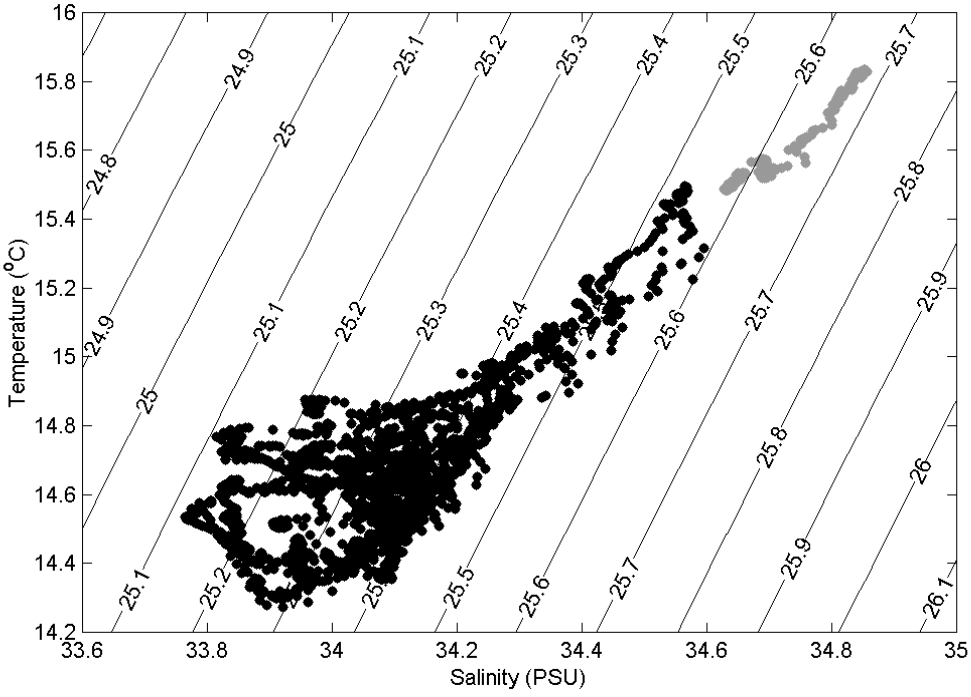

Figure 4.3 Temperature salinity diagram from profiles in and near farm (black dots), and 11 km offshore (grey dots) with contours of density anomaly.

4.3.2 Observations of Interactions between the Stratification and the Mussel Farm

The front of warm saline fluid beneath the cool fresher water can be seen to interact with the farm. As described in the previous chapter, water velocities within the farm are reduced by the drag from the mussel farm, resulting in an undercurrent beneath the farm that is faster than flow within the farm. Two transects through the long axis of the farm, Figure 4.4 and Figure 4.5, show the density front distorted by the velocity gradients. The first transect (Figure 4.4) was taken towards the end of the rising tide. Profiles of velocity taken in conjunction with the CTD measurements (see Figures 3.11 and 3.12) showed that water currents were from right to left, relative to Figure 4.4, with a component out of the page. The density front can be seen in all three plots of temperature, salinity, and density, but is most visible in the temperature plot, Figure 4.4(a). The density front appears to have been blocked by the upstream (right) end of the farm at x = 3.8 km, as indicated by the slope of the isotherms. However, it is able to flow under the farm, forming a large toe extending to approximately x = 2 km. At the upstream end of the farm (right as plotted), strong density gradients occur as the flow is blocked by the farm. In this example, the horizontal density gradients act in the same direction as the tidal flow. Velocities were slightly higher beneath the farm.

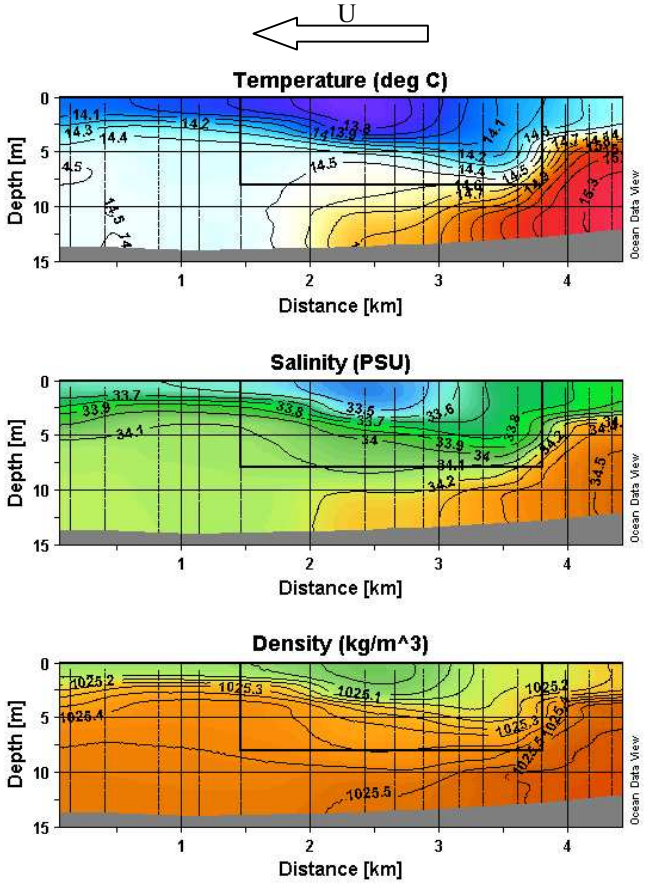

Figure 4.4 Transect through farm (indicated by rectangle) near high tide with flow from right to left. Transect 170503-1A.

The divergence of the isopycnals within the farm may indicate that vertical mixing is occurring, leading to a reduction in density stratification. However, there is insufficient information in this transect alone to determine if mixing has occurred, particularly as this transect represents an “instantaneous” picture of the density distribution.

A second transect, shown in Figure 4.5, was taken approximately 6 hours later on the falling tide when water currents were from left to right as plotted, with a component into the page. The density front has been carried south (right) by the currents. The main body of the front is no longer within the transect, but the toe, previously underneath the farm, is still visible. The strong density gradients seen south (right) of the farm in Figure 4.4 are now much weaker, which is possibly another indication of vertical mixing. The change in depth between Figure 4.4 and Figure 4.5 of approximately 3.5 m is due to the tide. As the mussel long-lines are suspended from the surface, the gap between the bottom of the droppers and the seabed is reduced as the tide falls.

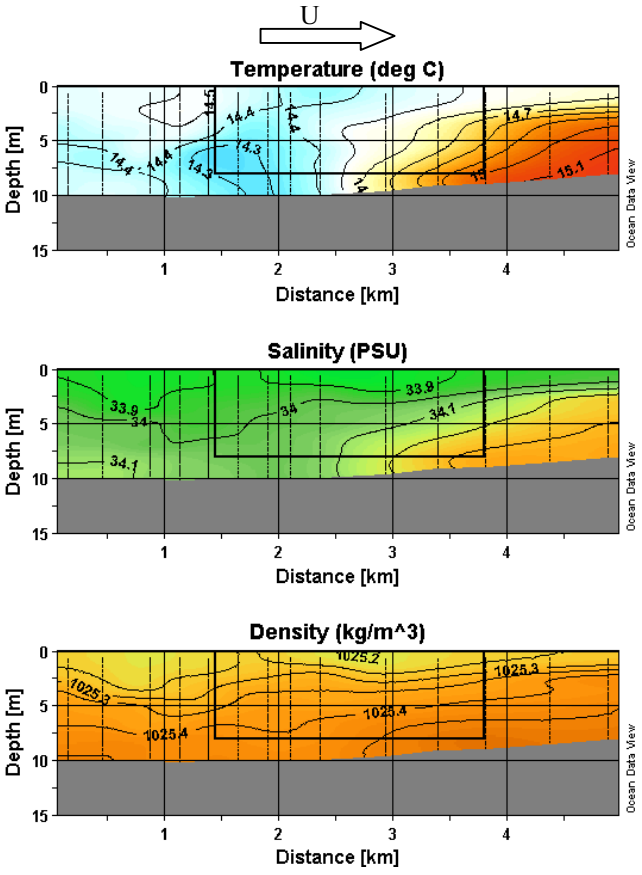

Figure 4.5 Transect through farm (indicated by rectangle) near low tide with flow from left to right. Transect 170503-4A.

A deepening of isopycnals at the upstream end of the farm was seen in some transects. An example of this can be seen in Figure 4.6, a transect through the long axis (north-south) of the farm on 17 April 2002. This transect was recorded on the falling tide, with water currents from left to right as plotted (with a

component into the page). There is little variation in the water temperature through this transect apart from at the southern (right) end where warmer temperatures were measured where the depth decreases to 5 m. The density is dominated by salinity. The density contours dip down significantly at the upstream (left) end of the farm, the lowest point occurring near the farm boundary at x = 2.8 km. The depression of the isopycnals upstream of the farm is thought to be related to the deceleration of the fluid, and a transfer from kinetic energy to potential energy as work is done against the density gradient. This is discussed further in section 4.4.1.

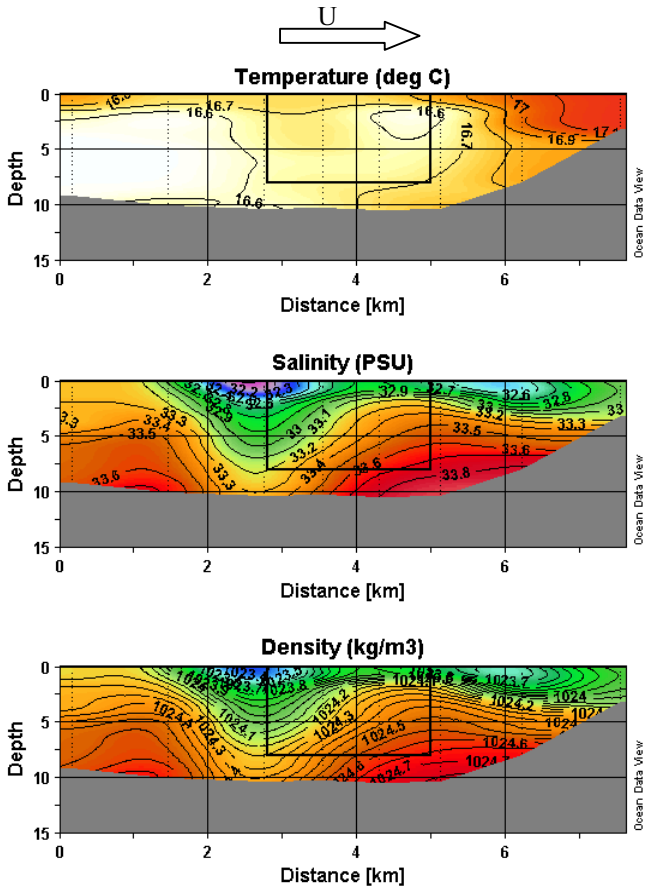

Figure 4.6 Transect through Collingwood mussel farm on falling tide, currents left to right. Transect 170402-6.

A similar, but smaller, deepening of isopycnals was seen in a parallel transect taken 0.8 km offshore from that plotted in Figure 4.6. Due to the easterly component of the falling tide, the part of the transect in Figure 4.7 from approximately 3.2 km to 5.6 km is in the wake of the farm. The density contours dip to a minimum at about 3.2 km. The lowest point in the density contours in this transect through the farm occurred at 2.8 km. The southward shift of the dip in the density contours between the two transects is consistent with the observed flow directions on falling tides. The dip in density contours was not seen in a parallel transect inshore of the farm (see Transect 170402-5 in Appendix D).

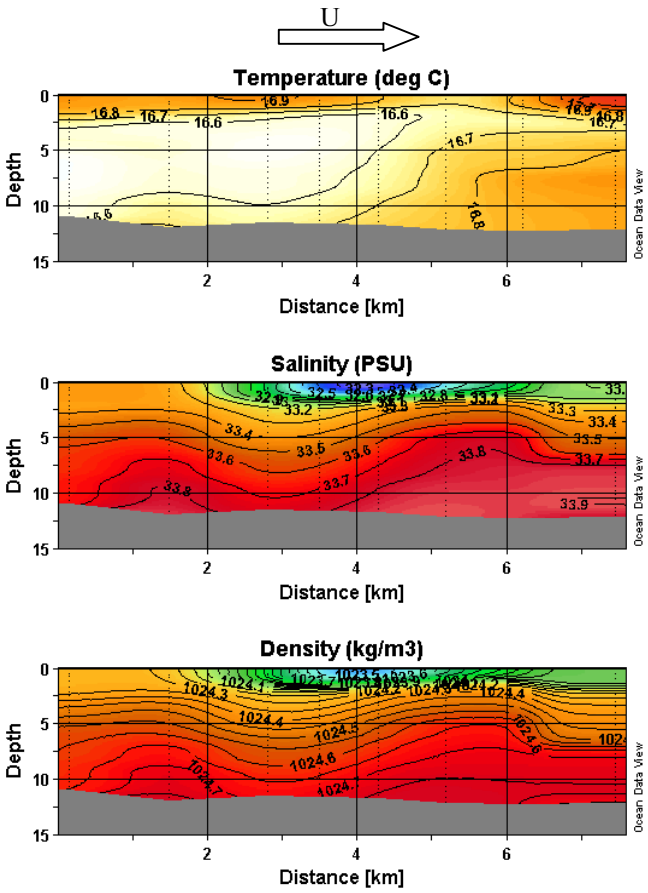

Figure 4.7 Transect taken offshore (west) of Collingwood mussel farm on falling tide, currents from left to right. Transect 170402-7.

The strong vertical density gradients seen in most profiles through the farm are likely to have prevented flow being diverted underneath the farm. During a period of comparatively weak stratification at the upstream end of the farm, advection of fluid beneath the farm could be seen in a sequence of transects taken through the upstream (north) end of the farm on a falling tide. Temperature, salinity, and density along transects 170503-2A, 170503-3A, and 170503-4A are plotted in Appendix D. Inspection of these transects shows that isopycnals were widely spaced. The variations in temperature had only a small effect on density, but visually aid in tracking the motion of bodies of water. Temperature profiles along the three transects, recorded at intervals of approximately 2 hours, are plotted in Figure 4.8.

Two particular bodies of water can be identified from the isotherms in Figure 4.8(a). The first is a small area of warmer water enclosed by the 14.5°C contour at approximately 0.3 km, 6 m depth. The second is a larger mass of cooler water enclosed by the 14.3°C contour mid-depth from 0.6 to 1.5 km. In the second transect, Figure 4.8(b), the smaller warm mass (14.5°C) has been advected south (right) towards the farm, but is now deeper at 8 m. It appears that this fluid should pass under the farm, but it is not detected in the third transect. This warm mass is small in size (length of 0.25 km). It would be difficult to accurately track the movement of a body of fluid that has dimensions similar to or smaller than the spacing between

CTD profiles (200 m to 300 m). Also, the contouring algorithm of Ocean Data View (Schlitzer, 2004), used to plot the cross-sections in this chapter, may obscure small spatial variations in water properties.

The cooler mass (14.3°C) seen in Figure 4.8(a) is distorted in the subsequent transects by the velocity shear. In particular, in Figure 4.8(b) and (c), the lower part of this body of fluid is stretched in the downstream direction in comparison to the fluid in the farm by the undercurrent.

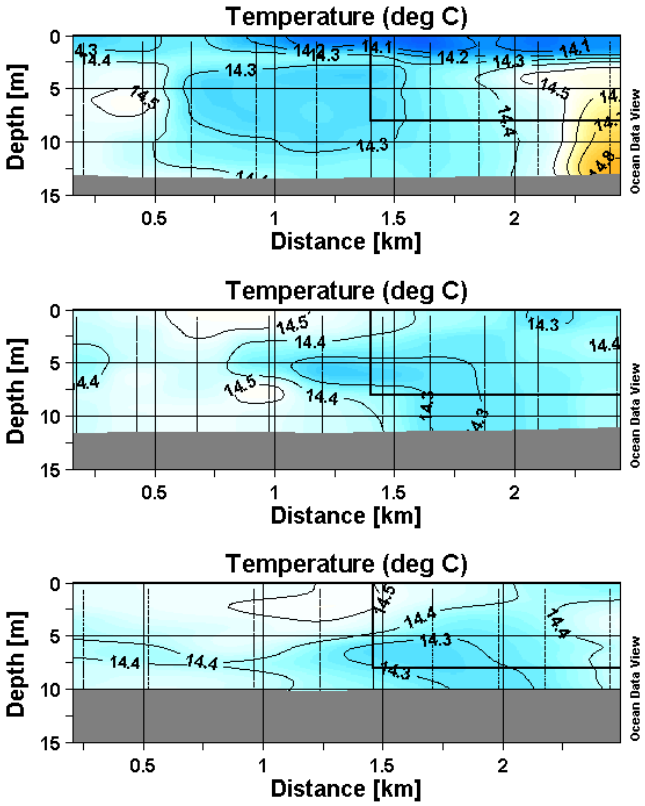

Figure 4.8 Series of temperature transects at 2 hour intervals through upstream end of farm. Flow is from left to right.

ADCP measurements of velocity, made in conjunction with the CTD surveys plotted above, indicate that velocities within the farm were at an angle to the farm axis varying between 10° and 30°. This means that fluid was advected across the plotted transects (into the page as plotted in Figure 4.8). Given that velocities within the farm peaked around ~ 0.07 m s^{-1} on falling tides, the cross-farm motion between transects would be less than 0.07 m s^{-1} x 7200 s x sin(30°) = 250 m. From tracking the centre of the mass enclosed by the 14.3°C isotherms, a southward movement between transects of ~ 400 m can be estimated. This gives a velocity of approximately 0.06 m s^{-1} which is consistent with the ADCP measurements.

Some of the apparent distortion of the cooler mass seen in Figure 4.8 may be due to taking slices through different parts of the fluid mass as it is translated sideways through the farm. Cross-farm (east-west) transects were recorded that intersect the above transects at x = 2.3 km. These transects were too far south

to detect the cooler 14.3°C mass, but show that similar patches of cooler water are wide, comparable with the farm width (~ 650 m). Therefore, it is likely that the distortion of the cooler fluid body underneath the farm is primarily due to the velocity shear between the slower velocities inside the farm and the faster current beneath.

4.3.3 Estimates of Mixing from a Control Volume Analysis

An unsuccessful attempt was made to estimate the rate of mixing caused by the farm by using a control volume approach. A methodology for estimating the rate of diapycnal mixing within a control volume is described in Appendix E. This method is an expansion of the approach used by Winters *et al.* (1995), with modifications to include the flux of material through the boundaries of the control volume. The approach is to consider the flux and changes of background potential energy E_b. The background potential energy is the minimum possible potential energy that can be obtained by a re-arrangement of the fluid. For example, a stratified fluid will have minimum potential energy when the isopycnals are horizontal. Mixing (in a closed system) results in a non-reversible increase of background potential energy.

In an open system, the rate of mixing Φ_d (units of W) can be calculated using a control volume approach from the rate of change in E_b, and from the flux of background potential energy through the control volume boundary. An additional term is required to account for the rate of change of the mass within the control volume. In control volume form, the rate of diapycnal mixing can be calculated from equation (4.1) (refer to Appendix E for the derivation of this equation).

$$\Phi_d = \frac{d}{dt}E_b \underbrace{+g\oint \psi \mathbf{u}\cdot\hat{n}dS}_{advection} \underbrace{-\kappa g\oint z_* \nabla\rho\cdot\hat{n}dS}_{diffusion} \underbrace{-g\int_V \rho\frac{\partial z_*}{\partial t}dV}_{changing\ mass}. \qquad (4.1)$$

The terms in equation 4.1 are the gravitation acceleration g, $\mathbf{u}$ the water velocity vector, $\hat{n}$ an outward-pointing unit vector normal to the surface S, κ the molecular diffusivity, ρ density. The reference depth z_* is the depth inside the control volume at which a fluid of density ρ would be located if the fluid with the control volume was arranged to give the minimum potential energy. Thus

$$E_B = \int_V \rho g z_* dV\ . \qquad (4.2)$$

The flux of background potential energy through the surface of the control volume surface is determined by the advection term in equation (4.1), where

$$\psi = \int^{\rho} z_*(\hat{\rho})d\hat{\rho}\ . \qquad (4.3)$$

In order to evaluate equation (4.1), a control volume was constructed around the Collingwood mussel farm by measuring profiles of water velocity around the farm perimeter with a boat-mounted ADCP.

Simultaneously, profiles of salinity and temperature (giving water density) were measured using the BIOFISH. Due to the size of the farm, each circuit of the farm took approximately 40 minutes. At the start and end of each circuit, water column properties were measured at 9 locations within the farm in order to determine the rate of change in E_b, and to evaluate the changing mass term in equation (4.1). The diffusion term was neglected (see Appendix E for an assessment of the size of this term). A total of 12 circuits were measured over the period 2 to 9 August 2003.

The control volume approach was not successful. Estimates of diapycnal mixing rates were around 2.7 W/m^3, which were 3 to 4 orders of magnitude higher than the amount of energy available through drag on the farm. A number of factors are considered responsible. Firstly, the control volume approach essentially requires estimating small differences between large values. The effect of error in any of the integral terms in equation (4.1) is compounded as the rate of mixing is a second order effect in comparison to the flux and storage of background potential energy. The control volume approach requires instantaneous velocities and densities at all points around and within the control volume. It was not possible to measure at all points around the control volume at the same instant, so it was assumed that average velocities could be used. Neither was it possible to accurately determine the rate of change of E_b and z_* within the control volume as this required measurement of density everywhere within the control volume. Nine profiles were insufficient to represent the density distributions within the control volumes, which covered an area of ~ 1.6 x 10^6 m^2. Over the time taken to circuit the farm, tidal induced depth changes of up to 1.2 m (with mean water depth of 12 m) occurred, as well as tidally induced changes in velocity. A correction for the effect of the tide was made (see Appendix E), but there were still discrepancies between the flux of mass through, and storage of mass within, the control volume. Without satisfying continuity of mass, it is little surprise that background potential energy calculations were unsuccessful.

4.4 Discussion

4.4.1 Interactions with the Farm - Energy considerations

There were clear interactions between the mussel farm and the density stratification at the Collingwood mussel farm. One of the most dramatic was the depression of the isopycnals at the upstream end of the farm (e.g. Figure 4.6). This is considered to be due to a transfer of energy from kinetic energy (as the fluid decelerates) into potential energy as work is done against the density gradient by depressing the isopycnals. The amount that the isopycnals deepen would be a function of the density gradient and the velocity, with larger depressions at high velocities, and smaller depressions with high density differences.

The horizontal dimensions (width ~ 650 m) compared to the depth (~ 10 m) of the farm suggests that flow would be more readily diverted under the farm than around. However, the small increase in velocity beneath the farm suggests that most of the fluid is instead diverted horizontally around the farm. If the

fluid is stratified, less dense fluid near the surface would need to move against the density gradient in order to pass beneath the farm. The density stratification would impose a buoyancy force opposing this. A sufficiently strong vertical density gradient would prevent the less dense fluid near the surface from flowing beneath the farm, instead forcing a horizontal diversion.

For fluid to flow beneath the farm, the isopycnal of that density must be depressed below the bottom of the farm. The density gradient will therefore play an important role in whether fluid is diverted under or around the farm. A consideration of energetics can be made to determine how far the isopycnals are depressed, and if the less dense fluid near the surface is therefore able to pass beneath the farm.

Kinetic energy from the upstream flow will be converted to potential energy as the fluid slows. Some of this potential energy will produce a small rise in the free-surface elevation, but work will also be done against the vertical density gradient by forcing the less dense fluid deeper. For less dense fluid to pass beneath the farm, work must be done against the density gradient. The work required (per unit volume) is

$$W = \int_{z_1}^{z_2} \left(\rho(z) - \rho_1 \right) g dz \,, \tag{4.4}$$

where ρ_1 is the density of the fluid attempting to pass beneath the farm, and $\rho(z)$ is the density at a depth of z. The available energy to do the work may be estimated from the change in kinetic energy as the fluid slows upstream of the farm. The fluid approaching the farm will have a kinetic energy of $\frac{1}{2}\rho U^2$ per unit volume.

Considering initially a non-porous stationary obstacle in a linearly stratified flow, with an upstream velocity of U_0, obstacle height of H_f, and density gradient of $\partial\rho/\partial z$ (Figure 4.9), for fluid at the surface to pass beneath the farm, there must be sufficient kinetic energy to overcome the density gradient. Expressed as a ratio of work that must be done against the density gradient to the available kinetic energy:

$$\frac{\int_0^{H_f} \frac{\partial \rho}{\partial z} g dz}{\frac{1}{2}\rho U_0^{\,2}} < 1 \tag{4.5}$$

Equation (4.5) is a bulk Richardson number (e.g. Turner, 1973) as can be seen by evaluating the integral and dividing through by the density

$$Ri_b = \frac{H_f g'}{U_0^{\,2}}, \tag{4.6}$$

where $g' = g\,\Delta\rho/\rho$, and $\Delta\rho$ is the change in density between the surface and H_f.

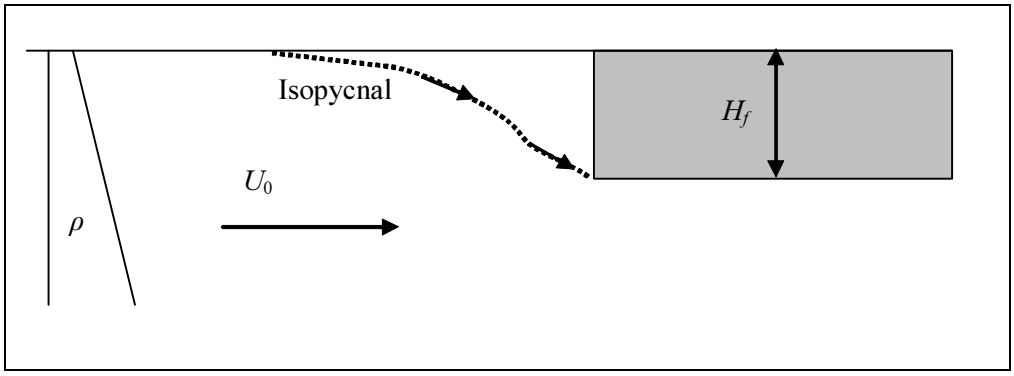

Figure 4.9 Linearly stratified flow passing beneath an obstacle.

As the farm is porous, some of the flow will pass through the farm. Therefore, not all of the kinetic energy is available to do work in deepening the isopyncals. The change in kinetic energy can be evaluated from the difference in velocities far upstream and at the farm boundary. In the previous chapter, the pipe-network model and the field measurements indicate that velocities within the farm are essentially uniform. If the velocity inside the farm is αU_0, then the modified bulk Richardson number is

$$Ri_b' = \frac{H_f g'}{U_0^2 \left(1-\alpha^2\right)}. \qquad (4.7)$$

Significant flow underneath the farm is expected if $Ri_b' < 1$. For example, in Figure 4.1(a), the density difference between the surface and at 8 m depth (upstream of the farm) is ~ 0.35 kg m^{-3}, and velocities were around 0.1 m s^{-1}. The field data indicates that a velocity reduction of ~ 50 to 67% may occur. Assuming a reduction of 50% (α = 0.5), the modified bulk Richardson number for this flow is 3.6. This indicates that most of the flow will be diverted around the farm rather than beneath.

4.4.2 Mixing Considerations through Changes in Potential Energy

A measure of the strength of stratification is the energy that would be required to fully mix the water column so that the density is uniform. Mixing a stabily stratified fluid to create a uniform density would raise the centre of mass, increasing the potential energy. In order to compare potential energy along a transect, it is convenient to subtract a global minimum density ρ_0 and calculate potential energy using the modified density $\rho' = \rho - \rho_0$. Modified potential energy per unit area is therefore calculated as

$$PE' = \int_0^H \rho' g z dz, \qquad (4.8)$$

where H is the water depth. The potential energy per unit area of the same fluid if it were fully mixed (constant density) can be calculated as

$$PE_{mix}' = \frac{gH\int_0^H \rho' dz}{2}. \qquad (4.9)$$

The actual potential energy values can be obtained by adding $\frac{1}{2}\rho_0 g H^2$. If a fluid is being mixed, the potential energy (*PE*) will increase. There should also be a decrease in the difference between the actual potential energy and the potential energy if fully mixed:

$$\Delta E = PE_{mix} - PE \ . \qquad (4.10)$$

ΔE represents the energy per unit area required to completely mix the water column. This method is only useful if the same body of fluid can be tracked over time, or if the fluid was uniformly stratified before mixing. In and around the Collingwood farm, there were two interacting bodies of fluid, with a cooler fresh source of water interacting with the warmer saline water of the bay. The different average density between these two masses resulted in a difference in calculated potential energy. This difference dominated variations in potential energy along transects, and may have disguised changes caused by vertical mixing. For example, a strong interaction between the Collingwood farm and the stratified fluid could be seen in Figure 4.4. This transect was recorded on a rising tide when water velocities were north-east, or from right to left in Figure 4.4. This transect is re-plotted in Figure 4.10 with the *x* axis reversed so that the currents are from left (south) to right (north). As variations in water depth change potential energy, PE_{mix} and ΔE were calculated from the upper 12 m for this transect, and are plotted in Figure 4.11. By doing this, it is assumed that the fluid below 12 m does not interact with that above, which is not a particularly reliable assumption. Note, however that density differences below 12 m were small. The high *PE* and PE_{mix} upstream (left) of the farm are due to the higher average density resulting from the blocked warm, salty fluid situated there. Moving downstream through the farm, both *PE* and PE_{mix} decrease as the average density is reduced by the cooler fresh water near the surface. Both measures of potential energy increase over the second half of the farm. The variation of PE_{mix} reveals the variability in average density, caused by the changes in temperature and salinity along this transect. This variation in average density is responsible for much of the change in *PE*, obscuring any changes in *PE* caused by vertical mixing. The difference, ΔE, which is an indication of the degree of stratification, decreases immediately inside the farm (2200 m in Figure 4.11(b)), and also decreases at the downstream end of the farm. While these are areas where mixing might be expected, the increase in ΔE inside the farm from 2200 m to 3500 m is not consistent with mixing.

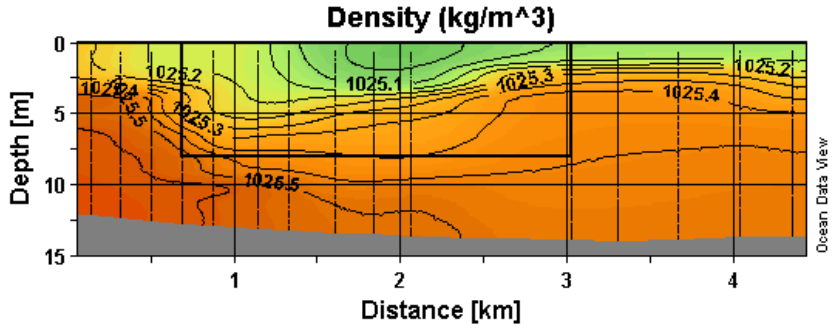

Figure 4.10 Transect 170503-1A through farm, with *x* axis reversed. Tidal flow from left (south) to right (north). Position of farm indicated by the rectangle.

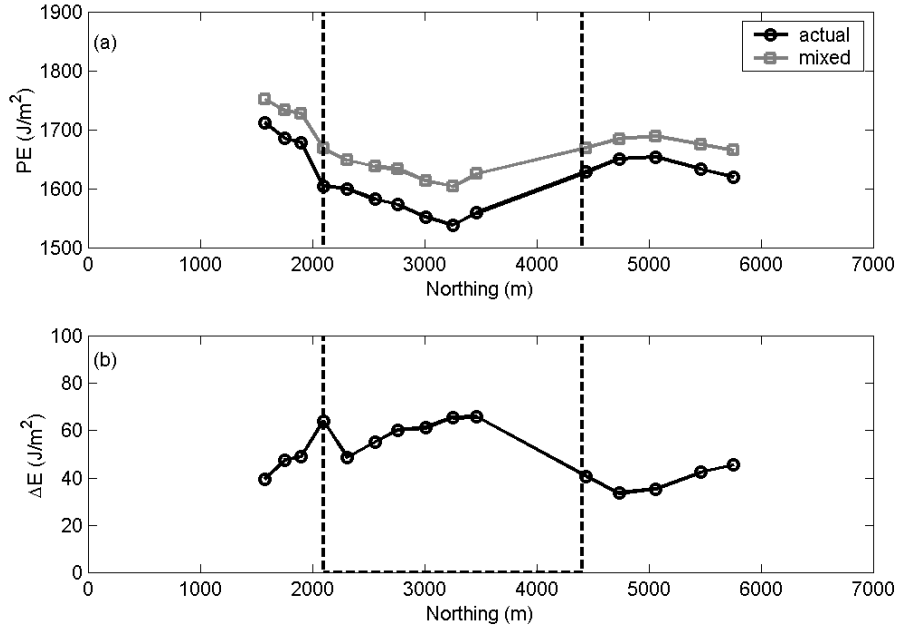

Figure 4.11 (a) potential energy and potential energy if fully mixed, (b) energy input required to mix water column for transect 170503-1A. Flow is from left to right, and the farm boundaries are indicated by the dashed vertical lines.

4.4.3 Mixing and Stability

The velocity shear gradients at the bottom of the farm, caused by the faster velocities beneath the farm, have the potential to enhance vertical mixing by creating a mixing layer. Large instabilities from the mixing layer at the bottom of the farm would result in exchange between fluid in the farm and that beneath. However, density stratification would limit the effectiveness of this mixing layer.

The gradient Richardson number R_i indicates the stability of a stratified shear flow:

$$R_i = N^2 / S_z^2 \qquad (4.11)$$

The gradient Richardson number is the ratio of the strength of the density gradient (resisting mixing) to the strength of the velocity shear driving the mixing. The density gradient is represented by N, the buoyancy frequency in rad s^{-1}

$$N^2 = -\frac{g}{\rho_0}\frac{\partial \rho}{\partial z} \tag{4.12}$$

and S_z, the velocity shear

$$S_z = \frac{\partial U}{\partial z} \tag{4.13}$$

At high values of R_i, the stabilising effect of the density gradient dampens turbulence, restricting vertical mixing. Stratified shear flows are stable if $R_i > 0.25$ everywhere in the flow (Miles, 1961).

From the moored ADP data at the Collingwood site, velocity shears of $dU/dz \sim 0.01$ to 0.02 s^{-1} were measured at a depth level with the bottom of the droppers. Density gradients, and therefore N^2, are highly variable. In Figure 4.4, vertical density gradients vary between $d\rho/dz = 0.1/1.6 = 0.0625$ kg m^{-3}/m at the upstream end of the farm (0.6 km in Figure 4.4), and $0.05/5 = 0.01$ kg m^{-3}/m at the downstream end of the farm (3.0 km in Figure 4.4). Thus buoyancy frequencies will be in the range $N^2 = 1.0 \times 10^{-4}$ to 6.0×10^{-4} (rad s^{-1})^2. This gives estimates for R_i between 0.25 and 6. While it is possible that there are areas in the flow where a strong velocity shear coincides with a weak density gradient (leading to a locally low R_i), it appears that at the Collingwood site, the density stratification should be sufficiently strong to dampen instabilities in the mixing layer at the base of the farm.

Inspection of velocity profiles from the moored ADP (Figure 3.18) show that the thickness of the mixing layer at the bottom of the farm is around 4 m. A common formulation for the diffusivity of a mixing layer is $K_z = l_m^2\, dU/dz$ where l_m is the mixing length scale. For this situation, the dominant length scale for mixing is the mixing layer thickness, giving $K_z \sim 4^2 \times 0.015 = 0.24$ m^2 s^{-1}. This is a very large diffusivity that would suggest high vertical exchanges of momentum. However, this formulation does not account for the effects of the density gradient, which inhibits the vertical mixing. In contrast, empirical relationships, based on field measurements between Richardson number and diffusivity (Stevens, 2003) suggest that K_z will be of the order 10^{-6} to 10^{-4} m^2 s^{-1}.

The turbulence generated by the drag on the droppers is a second mechanism that may produce mixing. The turbulence generated by the arrays of mussel droppers may resemble the turbulence generated by the grids used in mixing experiments. Efficiencies of mixing by grids are low, with typically less than 6% of the work done used for mixing (Rehmann and Koseff, 2004). The efficiency is also a function of the density stratification. The work by the flow against the droppers, assuming a velocity within the farm of

0.075 m s^{-1}, was estimated to be ~ 0.002 W m^{-3}. At an efficiency of 6%, the change of potential energy would be approximately 1.2 x 10^{-4} W m^{-3}. With a farm volume of ~ 3 x 10^{7} m^{3}, the rate of change of potential energy expected inside the farm due to dropper turbulence would be 3600 J s^{-1}. A first assessment of the effect this rate of mixing might have on vertical density distributions can be made noting that the total energy required to mix the water columns is typically 40 J m^{-2} (Figure 4.11), or 3.4 J m^{-3} assuming 12 m water depth. Flows were typically diagonally across the farm. Assuming a flow direction 45^{o} across the farm, a farm width of 650 m, and a velocity within the farm of ~ 0.075 m s^{-1}; the residence time within the farm will be ~ 650 / cos(45^{o}) / 0.075 = 12,300 s (3.4 hours). The increase in potential energy during this time would be 1.2 x 10^{-4} x 1.23 x 10^{4} = 1.5 J m^{-3}. This is around 45% of the energy required to completely mix the water column, so some amount of de-stratification is likely.

4.5 Summary

There are clear indications of an interaction between the mussel farm and the stratified fluid. The mussel farm, by presenting a porous blockage to the flow, causes an upstream depression of the isopycnals. If the isopycnals are depressed sufficiently, then a considerable proportion of the approaching flow may be diverted under the farm. At this site, the stratification was sufficiently strong to prevent this from occurring, and the flow was instead diverted around the farm. A modified bulk Richardson number can be used to estimate whether a stratified fluid would be diverted around or beneath the farm.

It was not possible to determine if significant vertical mixing was caused by the mussel farm. Two mechanisms for mixing were considered. The first mechanism is a mixing layer generated by the velocity shear between the farm and the undercurrent. The gradient Richardson number, estimated to be in the range 0.25 to 6, suggests that the strength of stratification was likely to be sufficient to have prevented the shear layer from generating significant mixing. The second mechanism is the turbulence generated by the flow around the mussel droppers. Analogy with grid turbulence studies suggests that some degree of mixing may be produced by the dropper turbulence.

A control volume approach was used to attempt to quantify the degree of mixing caused by the farm. However, the inability to measure density distributions within the farm to sufficient resolution, coupled with the size of the farm, and the variability in water velocities and water depth caused by the tide contributed to this approach being unsuccessful.

CHAPTER 5 WAVE DISSIPATION BY MUSSEL FARMS

5.1 Introduction

Waves play an important role in coastal processes. They play a significant role in erosion and sediment transport. Waves also play a part in biological diversity as certain species may adapt to a particular wave environment. Mussel farms may act as a source of wave dissipation as energy may be lost through drag on the submerged structures. If a mussel farm has a significant effect on wave energy, there may be implications for the environment down-wave of the farm. As discussed in Chapter 2 (section 2.2.3) there does not appear to have been any research on the dissipation of wave energy by large mussel farms. There is potential for some degree of wave dissipation based on visual observations in kelp and scallop culture areas (Grant and Bacher, 2001), and anecdotal evidence from boat skippers who frequent the area of the Golden Bay study site. Analogy was made with kelp beds, where no significant wave dissipation was measured (Elwany *et al.*, 1995), and with breakwaters which are intentionally designed for the purpose of wave energy dissipation. Mussel long-lines are likely to lie between these two situations, having a higher porosity and flexibility than breakwaters, but lower flexibility and higher connectivity than the plants within a kelp bed.

In this chapter, the effects of a long-line mussel farm on wave energy are investigated through the development of an analytical model, and from comparison of wave records inshore and offshore of the large Collingwood mussel farm (Golden Bay, New Zealand).

5.2 Analytical Model

5.2.1 Model Development

Wave attenuation is considered using an analytical energy dissipation model similar to the method used for estimating the energy lost from currents in Chapter 3. The analytical model developed here is also presented in Plew *et al*. (2005). Energy is transferred from the wave field to turbulence as the waves propagate through the farm. In this approach, reflection of wave energy is not considered. This follows the approach used in estimating wave energy loss through vegetation (Dalrymple *et al.*, 1984; Kobayashi *et al.*, 1993).

The development of this analytical model requires two approximations. First, the choice of an appropriate velocity scale, and second, the parameterisation of acceleration-related forces. As a starting point, the structure is assumed to be fixed (inflexible and immobile), and the root-mean-squared wave velocity u_{rms} is used as the velocity scale to determine the drag. In reality wave-driven flexible structures move and flex (Seymour and Hanes, 1979; Falnes, 2002; Grosenbaugh *et al.*, 2002) and the actual drag is a function

of the relative velocity of the structure to the fluid. The existence of a net current in addition to wave orbital velocities further complicates the response (Stevens *et al.*, 2001), as does the interaction between floats (Stevens *et al.*, 2003). These factors are neglected in the development of this model for simplification, and because these effects are secondary to energy dissipation due to drag.

The force from a non-breaking wave on a stationary object includes a drag force F_d and an accelerative force F_a, and can be calculated from the widely used Morison equation (Morison *et al.*, 1950)

$$\begin{aligned} F &= F_d + F_a \\ &= \tfrac{1}{2} C_d \rho \phi L_d u^2 + C_m \rho \pi \frac{\phi^2}{4} L_d \frac{\partial u}{\partial t}. \end{aligned} \tag{5.1}$$

The velocity at the dropper u is calculated using linear wave theory, with C_d the drag coefficient, C_m an added mass coefficient, ϕ representing the dropper diameter, L_d the average dropper length, and ρ the water density. The rate of work done on a dropper is obtained from

$$\frac{dW}{dt} = Fu \tag{5.2}$$

Because the Morison equation is derived from potential flow where dissipation is ignored, the accelerative term is eliminated if the work done on the mussel dropper is calculated by integrating equation (5.2) over a wave period. While it is possible that the drag and accelerative forces oppose and cancel out for some of a wave cycle, it is likely, given the continuous wave spectrum, the high Reynolds number and the inherent response of the mooring itself, that the accelerative component is significant. Therefore we use root-mean-square (RMS) values for velocity and acceleration in estimates of wave energy attenuation. Only horizontal velocities are considered, as it is assumed that the droppers are able to move vertically in response to the waves, minimising the vertical velocities relative to the mussel droppers. This may lead to underestimating the dissipation.

Linear wave theory for surface waves gives water velocity and acceleration as a function of water depth d, position z (zero at surface, positive upwards), wave number $k = 2\pi/\lambda$ where λ is the wave length, wave period T, and wave height H. The RMS velocity u_{rms} and acceleration a_{rms} derived from linear wave theory for transitional waves are given in equations (5.3).

$$\begin{aligned} u_{rms} &= \frac{1}{\sqrt{2}} \frac{H}{2} \frac{gTk}{2\pi} \frac{\cosh\left[k\left(z+d\right)\right]}{\cosh\left[kd\right]}, \\ a_{rms} &= \frac{2\pi}{T} u_{rms}. \end{aligned} \tag{5.3}$$

As the mussel droppers generally only extend over the upper part of the water column, u_{rms} is averaged over the length of the dropper. The average RMS velocity U_{rms} is calculated by integrating from the bottom of the dropper ($z = -L_d$) to the surface ($z = 0$),

$$\begin{aligned} U_{rms} &= \frac{1}{L_d}\int_{z=-L_d}^{z=0} u_{rms}\,dz \\ &= \frac{1}{\sqrt{2}}\frac{1}{L_d}\frac{gT}{2\pi}\frac{\sinh\left[kd\right]-\sinh\left[k\left(d-L_d\right)\right]}{\cosh\left[kd\right]}\frac{H}{2} \\ &= \beta\frac{H}{2} \end{aligned} \tag{5.4}$$

where $\beta = \frac{1}{\sqrt{2}}\frac{1}{L_d}\frac{gT}{2\pi}\frac{\sinh\left[kd\right]-\sinh\left[k\left(d-L_d\right)\right]}{\cosh\left[kd\right]}$.

The RMS acceleration is similarly derived:

$$A_{rms} = \frac{2\pi}{T}U_{rms}\,. \tag{5.5}$$

From (5.1) and (5.2), it can be deduced that the rate of work done is proportional to u^3 from the drag term, and $udu/dt = ½\, du^2/dt$ in the accelerative term. As RMS velocities are used, a coefficient α is required in the drag term such that $\frac{1}{T}\int_0^T \left|U^3\right| dt = \alpha U_{RMS}{}^3$. In linear wave theory, velocities at any fixed point are assumed to be sinusoidal in time, giving $\alpha = 1.20$. The work done on mussel droppers per unit area (m^2) of ocean depends on the dropper density n (droppers m^{-2}).

$$\begin{aligned} \frac{dW}{dt} &= n\left[\alpha\,\tfrac{1}{2}C_d\rho\phi L_d U_{rms}{}^2 + C_m\rho\pi\frac{\phi^2}{4}L_d A_{rms}\right]U_{rms} \\ &= \frac{1}{2}n\rho\phi L_d\left[\alpha C_d\left(\frac{H}{2}\right)^3 + C_m\frac{\phi\pi^2}{T\beta}\left(\frac{H}{2}\right)^2\right]\beta^3 \end{aligned}\,. \tag{5.6}$$

The wave energy per unit area of ocean is related to the square of the wave height,

$$E = \frac{\rho g H^2}{8}\,. \tag{5.7}$$

Assuming that the rate of work done on the droppers equals the rate of loss in wave energy, and that energy loss due to bottom friction is negligible (see discussion), then the change of wave energy is given by

$$\frac{\partial E}{\partial t} = 2H\frac{\partial H}{\partial t}\frac{\rho g}{8} = -\frac{1}{2}n\rho\phi L_d\left[\alpha C_d\left(\frac{H}{2}\right)^3 + C_m\frac{\phi\pi^2}{T\beta}\left(\frac{H}{2}\right)^2\right]\beta^3\,. \tag{5.8}$$

By separation of variables and integrating, the wave height can be determined as a function of time t and initial wave height H_0 so that

$$\frac{H}{H_0} = \frac{aD(t)}{a + H_0 - H_0 D(t)}, \tag{5.9}$$

where $a = 2\frac{C_m}{\alpha C_d}\frac{\phi\pi^2}{T\beta}$, and $D(t) = \exp\left[-\frac{an\phi L_d \alpha C_d}{4g}\beta^3 t\right]$.

As wave energy travels at the group velocity C_g, the wave height at a distance through the farm can be determined by substituting $t = x/C_g$ where

$$C_g = \frac{1}{2}\left[1 + \frac{2kd}{\sinh(2kd)}\right]\frac{gT}{2\pi}\tanh(kd), \tag{5.10}$$

and

$$\frac{H(x)}{H_0} = \frac{aD(x)}{a + H_0 - H_0 D(x)}$$
$$D(x) = \exp\left[-\frac{an\phi L_d \alpha C_d}{4g}\beta^3 \frac{x}{C_g}\right]. \tag{5.11}$$

The wave energy scales with the square of the wave height, so $E/E_0 = (H/H_0)^2$. If a wave spectrum is available, then this analysis could be repeated using the appropriate wave height for each wave period to obtain an attenuation spectrum.

An assumption implicit in this formulation is that there are no sheltering effects between the mussel droppers. Seymour and Hanes (1979) obtained excellent predictions of energy attenuation through tethered float breakwaters by making the same assumption, and the floats in their experiments were more closely spaced than the mussel droppers here.

5.2.2 Wave Force Coefficients

The energy loss scaling requires suitable values for the coefficients for wave drag C_d and inertia C_m. Drag and added mass coefficients for both rough and smooth cylinders have been found to vary significantly with Keulegan-Carpenter number $K=(u_m/T\phi)$ where u_m is maximum horizontal water particle velocity in a wave cycle, T wave period, and ϕ the cylinder diameter (Nath, 1987; Sarpkaya, 1987; Sarpkaya, 1990; Wolfram and Naghipour, 1999). Consequently, it is not appropriate to use the drag coefficient for a mussel dropper obtained in laboratory tow tests at constant velocities (refer Chapter 10) for wave force calculations. Instead, wave force coefficients (C_d and C_m) are estimated from published data for rough cylinders.

Experimental evidence has shown that the drop in cylinder drag coefficient (in steady flow) caused by the boundary layer becoming turbulent (critical flow) occurs at lower Reynolds numbers as the surface roughness is increased (Fage and Warsap, 1929; Achenbach and Heinecke, 1981). For progressively rougher cylinders, the drop in drag coefficient at critical flow is smaller, and the post-critical drag coefficient is higher. It appears that if roughness was increased sufficiently, the drop in C_d at critical flow may disappear totally, resulting in a near independence of C_d from Reynolds number, similar to that seen for sharp cornered bluff bodies such as square or triangular cylinders (Lindsey, 1938). Cylinders with surface roughness/diameter ratios of order $k_s/\phi > 0.01$ have critical and post-critical C_d (in steady flow) of approximately 0.85 and 1.0 respectively (Niemann and Hölscher 1990, reproduced in Zdravkovich 2003). The mussel dropper, resembling a very rough cylinder, has a similar steady flow drag coefficient of 0.89, obtained from laboratory drag tests, see Chapter 10. Therefore, in the absence of direct measurements of the wave coefficients C_d and C_m for a mussel dropper, it is assumed that as the mussel dropper has a similar steady flow drag co-efficient to a rough circular cylinder, the wave force coefficients will also be similar. Values for wave force coefficients of $C_d = 1.7$ and $C_m = 2.0$ are suggested for heavily roughened piles in the absence of a current (Wolfram and Naghipour, 1999). The effect of a current is to reduce both coefficients, a complication that is neglected here for the purpose of simplicity. As a result, this method may over-estimate wave dissipation.

5.2.3 Application of Wave Dissipation Model

The energy loss scaling developed here shows a number of trends. The energy dissipation increases with distance through the farm, and also with dropper density. Figure 5.1 shows the increasing wave energy dissipation with distance through the farm at different values of dropper density. Values for the wave force coefficients are $C_d = 1.7$ and $C_m = 2.0$. Other parameters have been chosen to be representative of the Collingwood field site where the field experiments (which are presented below) were conducted. Values used were dropper length $L_d = 8.0$ m, depth $d = 12.0$ m, density $\rho = 1024$ kg m^{-3}, dropper diameter $\phi = 0.14$ m. The initial wave height is assumed to be 0.5 m, and dissipation is calculated for a wave frequency of 0.1 Hz.

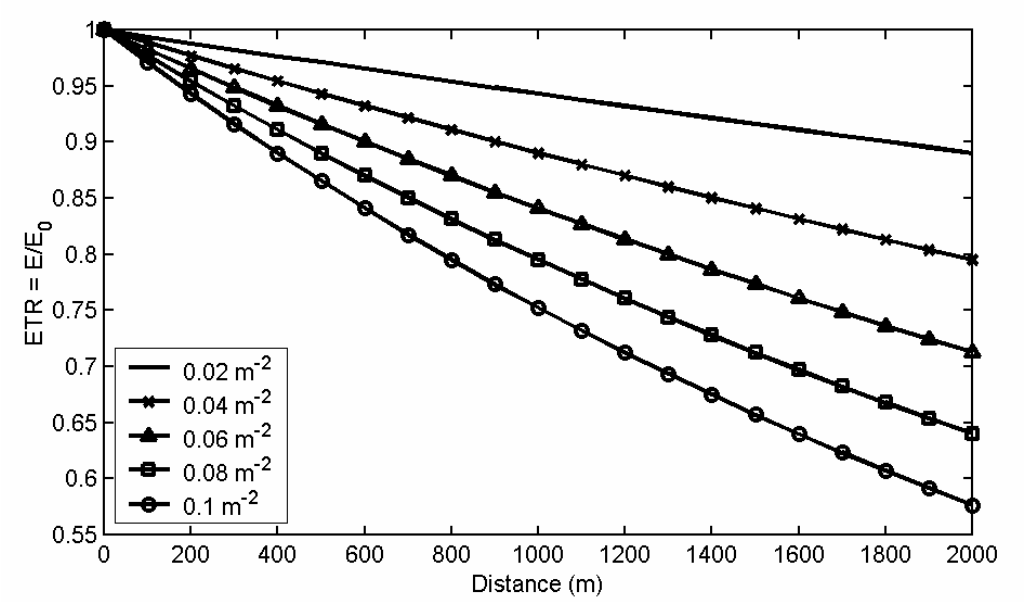

Figure 5.1 Energy Transmission Ratio (ETR) as a function of distance and dropper density (values given in legend).

The energy loss predicted by the model is frequency dependent, with dissipation increasing with frequency (Figure 5.2). The model results plotted in Figure 5.2 indicate that at high frequencies, the Energy Transmission Ratio (ETR = $E_{inshore}/E_{offshore}$) values begin to converge. In fact, if the calculation is continued to higher frequencies than plotted, the ETR converges to a single value independent of both frequency and initial wave height. As frequency increases, the model predicts that deep-water waves (high frequency) are attenuated at the same rate independently of both frequency and initial wave height. This can be verified using the linear wave equations for deep-water waves rather than for transition waves when deriving equations (5.3) and (5.10). The subsequent equations remain unchanged, except that the deep-water value for β is

$$\beta_{dw} = \frac{1}{\sqrt{2}} \frac{gT}{2\pi L_d} \left[1 - \exp\left(-\frac{4\pi^2 L_d}{gT^2} \right) \right] \tag{5.12}$$

and by using the expression for deep water group velocity

$$C_g = \frac{gT}{4\pi}, \tag{5.13}$$

the term $D(x)$ in (5.11) becomes

$$\begin{aligned} D(x) &= \exp\left(-\frac{an\phi L_d \alpha C_d}{4g} \beta_{dw}^3 \frac{4\pi}{gT} x \right) \\ &= \exp\left(-\frac{nC_m \phi^2 \pi}{4L_d} x \left[1 - \exp\left(-\frac{4\pi^2 L_d}{gT^2} \right) \right]^2 \right). \end{aligned} \tag{5.14}$$

By using algebraic manipulation, it can be deduced that as frequency is increased so that $T \to 0$, the term $D(x)$ from equation (5.11) approaches a constant value, while a, defined in equation (5.9), becomes very large. Therefore,

$$\begin{aligned} &T \to 0 \\ &D(x) \to \exp\left(-\frac{nC_m \phi^2 \pi}{4L_d} x \right). \\ &\frac{H(x)}{H_0} \to D(x) \end{aligned} \tag{5.15}$$

The energy transmission ratio is calculated as $\left(H/H_0\right)^2$, therefore the ETR for high frequency waves is independent of both initial wave height and frequency. The high frequency asymptote for the parameters used in plotting Figure 5.2 can be calculated as 0.7407.

The behaviour of the model at high frequency (in predicting a constant ETR) results from the inclusion of the inertial force in the energy loss calculation. For very high frequency waves, the wave forces on the cylinder are primarily due to the acceleration of the fluid. Fluid displacements and velocities are small, so the drag force disappears. Generally the waves of interest in terms of environmental effects are transitional or shallow water waves.

Predicted dissipation is also a function of the initial wave height, with dissipation increasing for waves of larger amplitude (Figure 5.2).

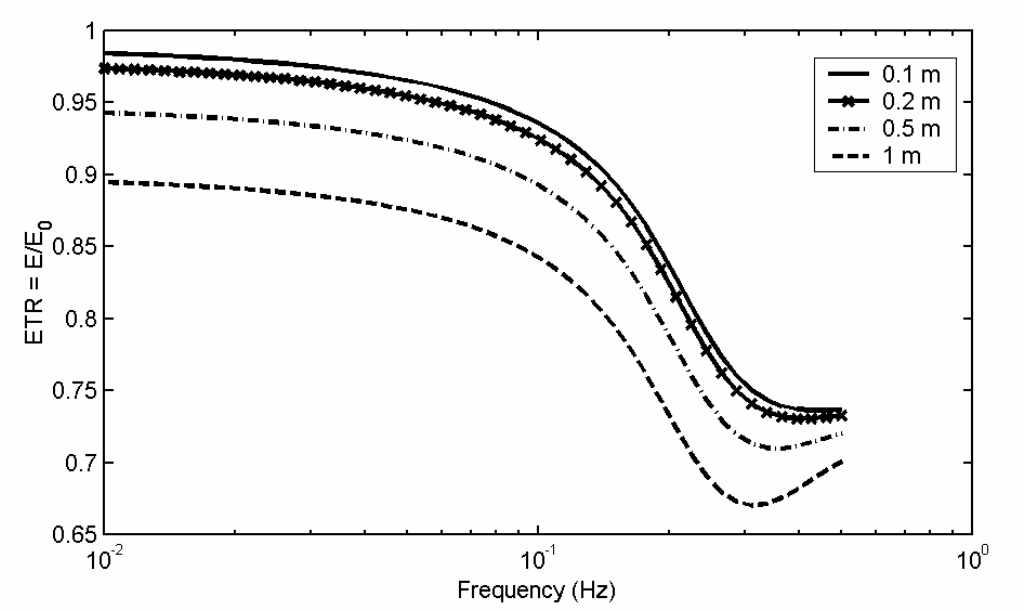

Figure 5.2 Energy transmission ratio (ETR) from wave model as function of initial wave height (in legend). Dropper length L_d = 8.0 m, depth d = 12.0 m, density ρ = 1024 kg m^{-3}, dropper diameter ϕ = 0.14 m, distance x = 650 m, dropper density n = 0.06, C_d = 1.7, C_m = 2.0.

The sensitivity of predicted ETR to the wave force coefficients is indicated in Figure 5.3. Varying the drag coefficient C_d by 10% has little effect on ETR (Figure 5.3(a)). However ETR at high frequencies is sensitive to the inertial coefficient C_m, with a 10% variation in C_m causing a 3% variation in ETR at 0.5 Hz (Figure 5.3(b)). The small effect of C_d can be seen by inspection of the term $D(x)$ in equation (5.11), and by inserting the expression for a from equation (5.9). By doing this, it can be seen that $D(x)$ is a function of C_m, as C_d cancels out. As H is related more strongly to $D(x)$ than a, H is more strongly dependant on C_m than C_d.

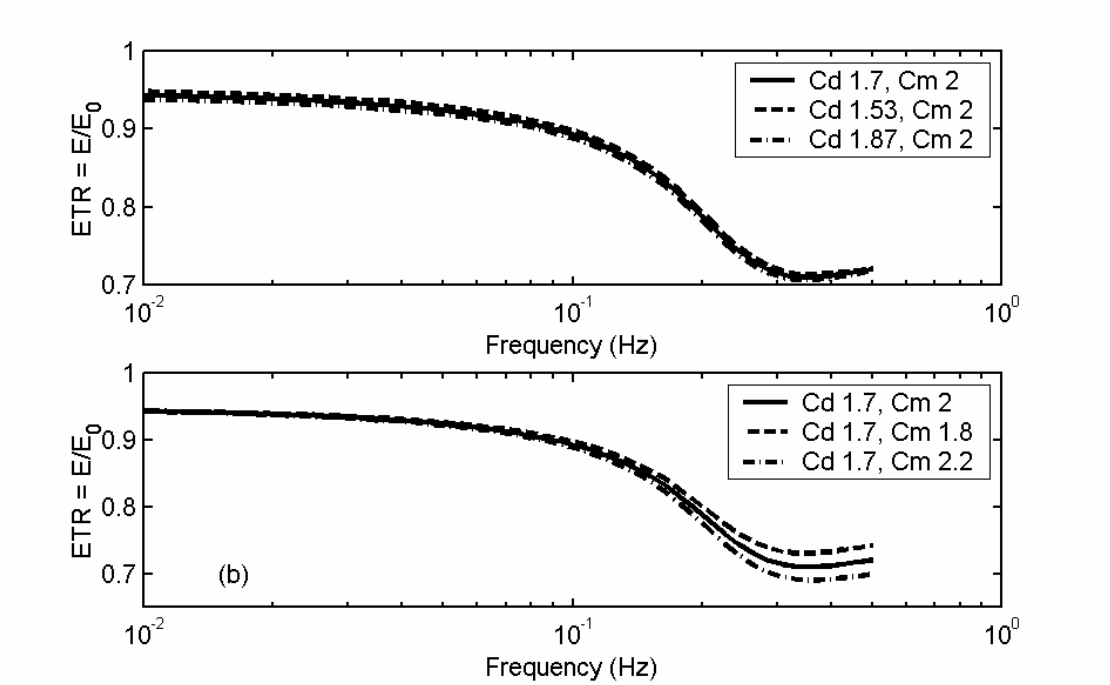

Figure 5.3 Influence of wave force coefficients on ETR from wave model for a (a) 10% variation in C_d, (b) 10% variation in C_m. Initial wave height is, 0.5 m, dropper length L_d = 8.0 m, depth d = 12.0 m, density ρ = 1024 kg m^{-3}, dropper diameter ϕ = 0.14 m, distance x = 650 m, dropper density n = 0.06.

The method developed in this thesis includes both the inertia and drag force terms in estimating the energy loss. In their estimation of wave attenuation caused by vegetation, Dalrymple *et al*. (1984) and Kobayashi *et al*. (1993) only used the drag term. Both analyses were based on linear wave theory, and as discussed above, the accelerative (or inertial) term in (8.2) cancels out when integrated over a wave period. In contrast, Massel (1976) derives the forces on an array of cylinders for the case when the inertial term dominates. Seymour and Hanes (1979) show both inertial and drag terms in their spectral derivation of the energy transmission ratio through a tethered float breakwater. The relative importance of these terms depends on the size of the accelerations in comparison to orbital velocities (a function of wave number, and wave amplitude) and the cylinder diameter. From equation (5.1), the relative magnitudes of the drag and inertial force components can be compared. Using RMS values for velocity and acceleration, the ratio of these forces is

$$\frac{F_d}{F_m} \propto \frac{C_d}{C_m}\frac{u_{rms}T}{\pi^2\phi} \tag{5.16}$$

As the wave force coefficients are essentially constants, equation (5.16) represents the ratio of the excursion of a wave orbit to the diameter of the cylinder. Essentially, we could expect that the inertia term will dominate when the cylinder is large relative to the distance a particle travels in a wave period. Massel's analysis was intended for calculating the forces on large piles, whereas the derivations of Dalrymple *et al.* and Kobayashi *et al.* consider the wave motion to be large relative to the diameter of the cylinder (vegetation).

The ratio of the dissipation caused by the drag and inertial terms in the method in this thesis equates to *H/a*. This ratio is plotted in Figure 5.4, using the same parameters used in Figure 5.2.

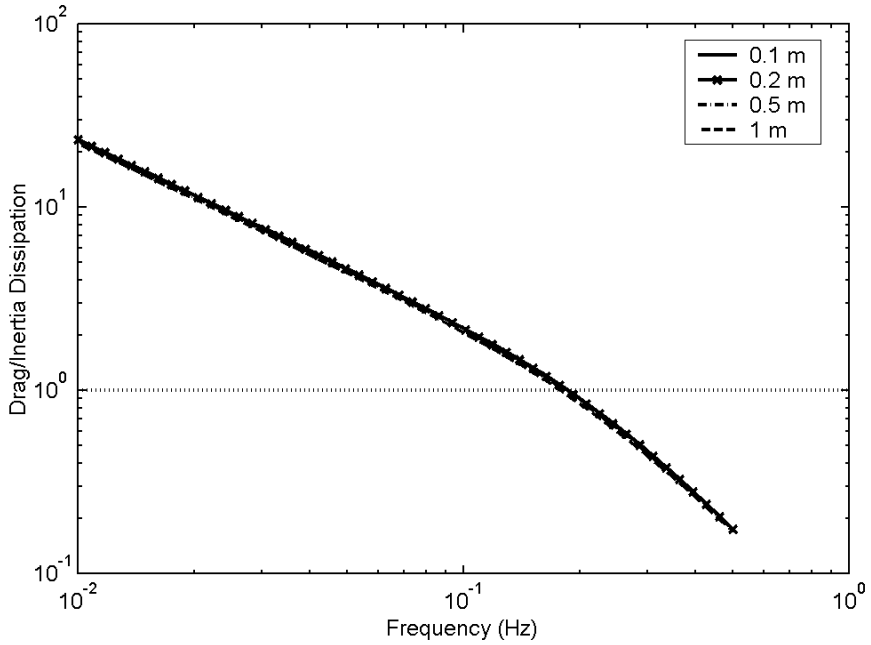

Figure 5.4 Ratio of predicted dissipation from drag and inertia terms versus frequency. L_d = 8.0 m, depth d = 12.0 m, density ρ = 1024 kg m^{-3}, dropper diameter ϕ = 0.14 m, distance x = 650 m, dropper density n = 0.06 m^{-2}, C_d = 1.7, C_m = 2.0.

Figure 5.4 shows that dissipation from the drag term is larger than dissipation from the inertial term at frequencies lower than 0.18 Hz. Initial wave height does not have any significant effect on the ratio of dissipation from the drag and inertial terms.

5.3 Field Study - Methodology

5.3.1 Study Site

Measurements of wave energy were taken at the large offshore farm near the township of Collingwood in Golden Bay. The study site was described in detail in Chapter 2. Key parameters relevant to this investigation are: dimensions of 2450 m by 650 m in plan with the long axis parallel to the coast, mean water depth varying from 9 m (inshore) to 12 m (offshore), and a maximum tidal range of 4.2 m. The dominant tidal flow directions are north-west/south-east on rising/falling tides respectively, with currents at mid-tide around 0.15 m s^{-1}. Dropper length varies depending on local water depth, but averages 8 m. Dropper density n averaged over the farm is estimated to be between 0.06 and 0.07 droppers m^{-2}.

5.3.2 Instrumentation

Wave spectra inshore and offshore of the farm were obtained during two deployments, 10-17 April 2002, and 15-17 May 2003, using DOBIE wave gauges (NIWA Instrument Systems). The long-lines between dobies during both deployments were oriented north-south, with 23 long-lines between the offshore and inshore dobie during the 2002 deployment, and 22 long-lines during the 2003 deployment. The size of mussels on these long-lines was not recorded.

During each deployment two DOBIE pressure wave gauges (NIWA Instrument Systems) were used, one offshore, and the other inshore of the farm (see Figure 5.5). DOBIEs were placed on the seabed, with the sensor approximately 0.2 m above the seabed. The instruments recorded bursts of 2048 samples at 5 Hz every 15 minutes. Pressure spectra were calculated for each burst using overlapping Hanning windows of 256 samples. Wave spectra were derived from the pressure spectra by adjusting for the frequency-dependent attenuation of pressure fluctuations with depth, e.g. Young (1999).

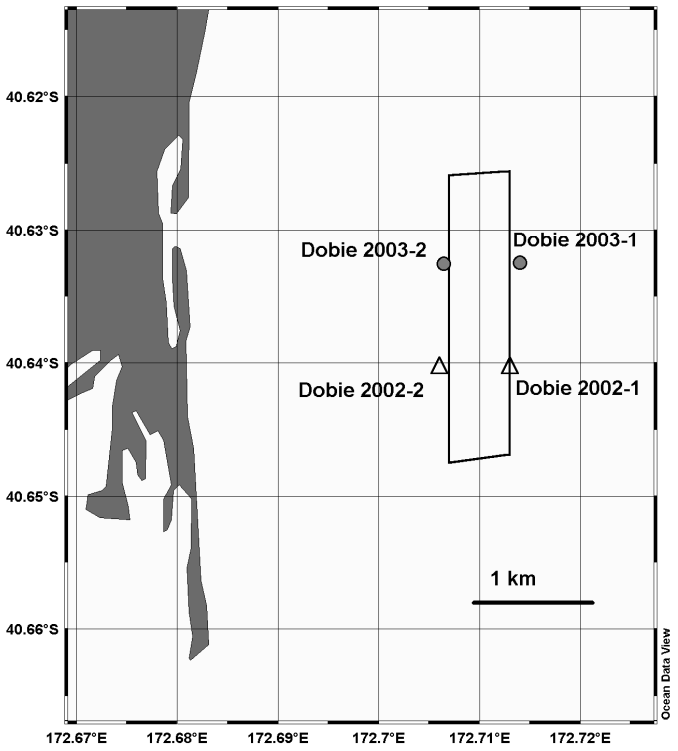

Figure 5.5 Location of Dobie wave gauges for 2002 (triangles) and 2003 (circles).

Wave data were recorded from 14:00 10 April 2002 to 15:00 17 April 2002 during the first deployment. During the second deployment, wave data were recorded from 11:15 15 May 2003 to 12:15 17 May 2003.

5.4 Results

5.4.1 Wave Data

As bottom-mounted pressure recorders were used, only shallow (long wavelength/low frequency) and transitional waves could be detected. Pressure variations due to deep-water waves, defined as having a wavelength less than twice the depth do not penetrate to the bed and so could not be measured. Using this definition, waves with frequencies in excess of 0.27 Hz could not be accurately measured.

Wave heights during both deployments were small. Significant wave height *Hs* is defined as 4 times the standard deviation of the water surface. Significant wave heights were calculated using the procedure described in the Dobie documentation (NIWA, 1998). A summary of this procedure is given in Appendix F. Only the part of the energy spectra with frequencies less than 0.27 Hz (corresponding with the cut-off frequency) was used to calculate *Hs*. During the 10-17 April 2002 deployment, significant wave heights at the inshore and offshore wave gauges were nearly identical, averaging 0.063 m offshore and 0.063 m inshore; reaching peak values of 0.257 m offshore, and 0.264 m inshore. As significant wave heights are nearly identical, only the offshore significant wave heights are shown in Figure 5.6.

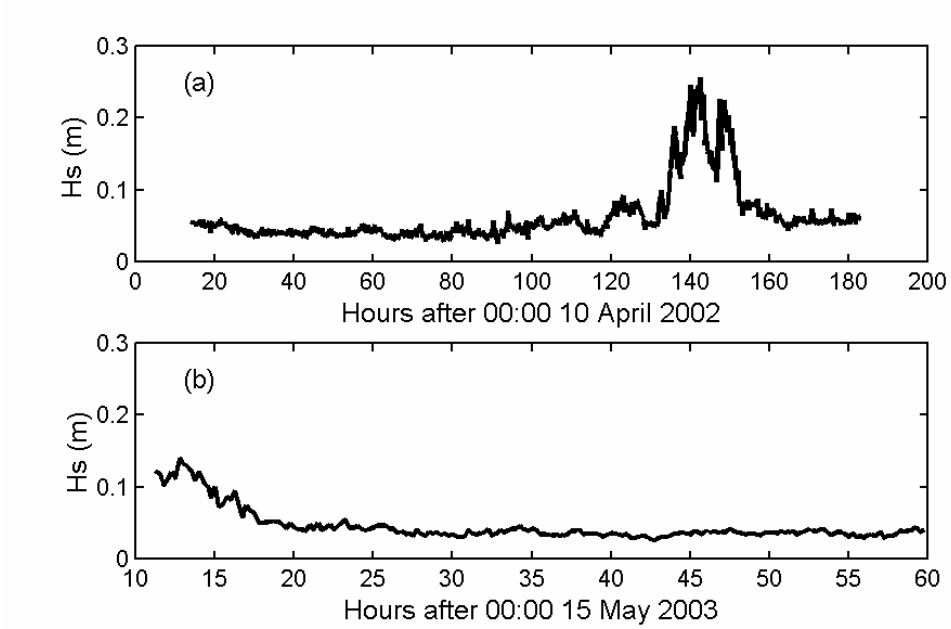

Figure 5.6 Calculated significant wave heights (Hs) at Collingwood mussel farm offshore wave gauges for (a) 10-17 April 2002, and (b) 15-17 May 2003.

Wave spectra at the inshore and offshore sites were similar (Figure 5.7(a)). Wave energy is highest for short period (high frequency) waves, increasing up to the cut-off frequency. A peak in energy in the middle of the wave spectrum occurs around 0.08 Hz (wave period of 12.5 seconds).

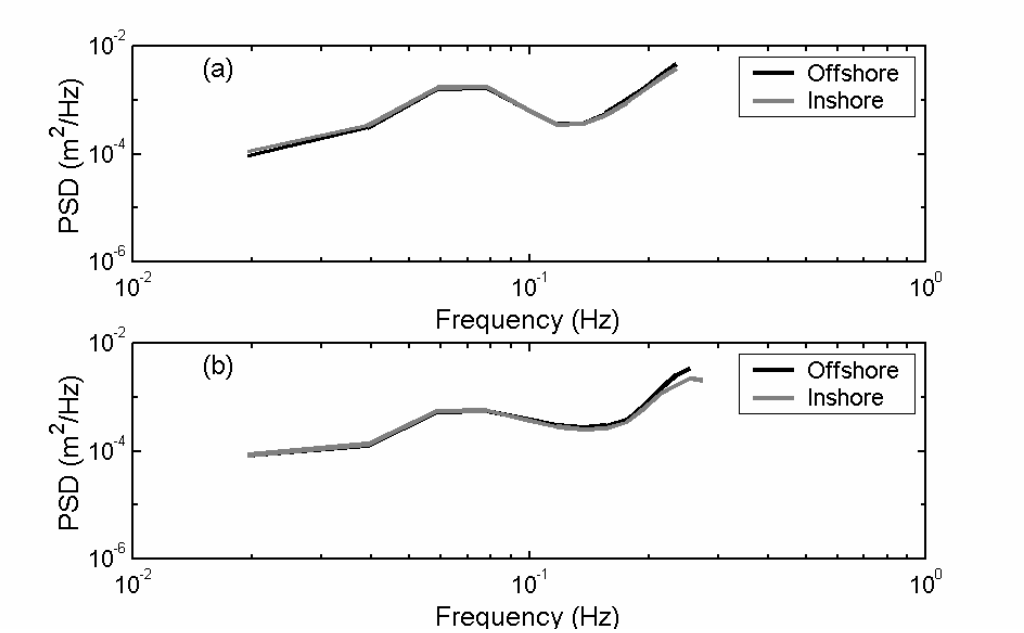

Figure 5.7 Wave power spectral density (PSD) at Collingwood mussel farm (a) 10-17 April 2002, (b) 15-17 May 2003.

Significant wave heights during the 15-17 May 2003 deployment averaged 0.046 m offshore, 0.045 inshore; peaking at 0.140 m offshore, and 0.137 inshore (Fig. 5.6(b)). Wave spectra for the offshore and inshore sites are shown in Figure 5.7(b). Wave spectra were similar to those recorded in the 2002 deployment, showing increased energy at short wave periods, but with a mid-spectral peak around 0.08 Hz.

It is unfortunate that wave energy increases with frequency up to the cut-off frequency, without showing signs of a roll-off in energy with frequency. As such, it is possible that significant wave energy was present in short wavelengths, and that this energy was not detected using the instruments deployed. Certainly the maximum wave energy at higher frequencies would be limited by maximum wave steepness for deep water waves of $H/\lambda < 0.142$ (Michell, 1893). We can deduce from this that for deep water waves, maximal wave energy is proportional to f^{-4}, where $f = 1/T$ is the wave frequency. Similarly, maximum possible wave height H is proportional to f^{-2}. The maximum possible wave height for a wave of frequency 1 Hz is 0.22 m. At 0.27 Hz (the cut-off frequency), maximum possible wave height is 1.62 m, far greater than any waves observed during the deployment. The only (and somewhat vague) indication that the wave energy at higher frequencies was not significant is from visual observation of low wave heights, dominated by long swell. Analysis of the effect of the farm on wave energy will be confined to frequencies below the threshold for deepwater waves.

5.4.2 Wave Direction and Wind Generated Waves

In comparing the offshore and inshore wave data, waves are assumed to propagate from east (offshore) to west across the farm. Therefore, the wave dissipation calculated from the field measurements will be in error if the direction of wave propagation is other than from east to west. The DOBIE wave gauge is non-directional, therefore no information regarding the direction of wave propagation can be obtained directly. From inspection of a map of the Golden Bay area, it is clear that long wavelength ocean swell can only enter from the east. Shorter period waves could be generated more locally (within Golden Bay) due to wind, and these wind waves could come from a variety of directions. To determine if wind generated waves, moving in directions other than from east to west, were significant, simple wave models can be used to estimate the likely size and period of wind generated waves.

Wind data was obtained from a permanent meteorological station at Farewell Spit, approximately 30 km north-west of the mussel farm. This site is sufficiently exposed that wind speeds and directions should have been similar to those at the mussel farm. Additionally, the spit on which the meteorological station was sited is sufficiently slender that the atmospheric boundary layer should be similar to that over the open bay. The air speed data should therefore not require correction. The wind sensor was mounted at 10 m above the ground.

The wind data (hourly averages) over the 10-17 April 2002 deployment show that wind directions were predominantly either from the west or the east, Figure 5.8(a). During the 15-17 May 2003 deployment, winds were almost always from the west, with winds from between 260^{o} and 280^{o} occurring for 46% of the deployment, Figure 5.8(b). Winds from the east will generate waves travelling in a westerly direction, that is, directly across the farm. This is consistent with the assumption of offshore to inshore wave motion made in analysing the wave data. However, wind from the west would generate waves travelling in the opposite direction (from inshore to offshore). If these waves were significant and detectable (i.e. at a frequency below the deep water cut-off frequency), they may result in an incorrect calculation of wave energy dissipation.

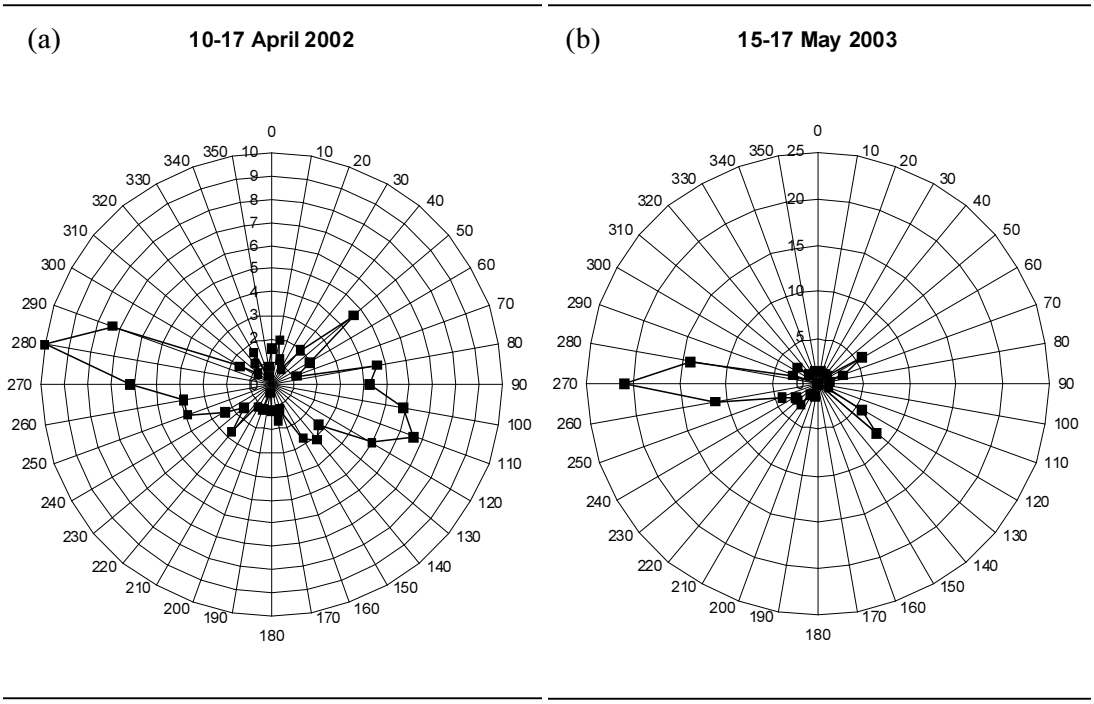

Figure 5.8 Wind direction frequency (as %) at Farewell Spit (a) 10-17 April 2002 and (b) 15-17 May 2003.

Westerly winds averaged ~ 6 m s^{-1}, with the highest hourly averaged wind speed from the west of 11.3 m s^{-1} (Figure 5.9). As the fetch over which the westerly wind can generate waves is limited by the distance between the farm and the coast (2.5 km), it is appropriate to use the highest hourly averaged wind speed to estimate the largest wind-generated waves.

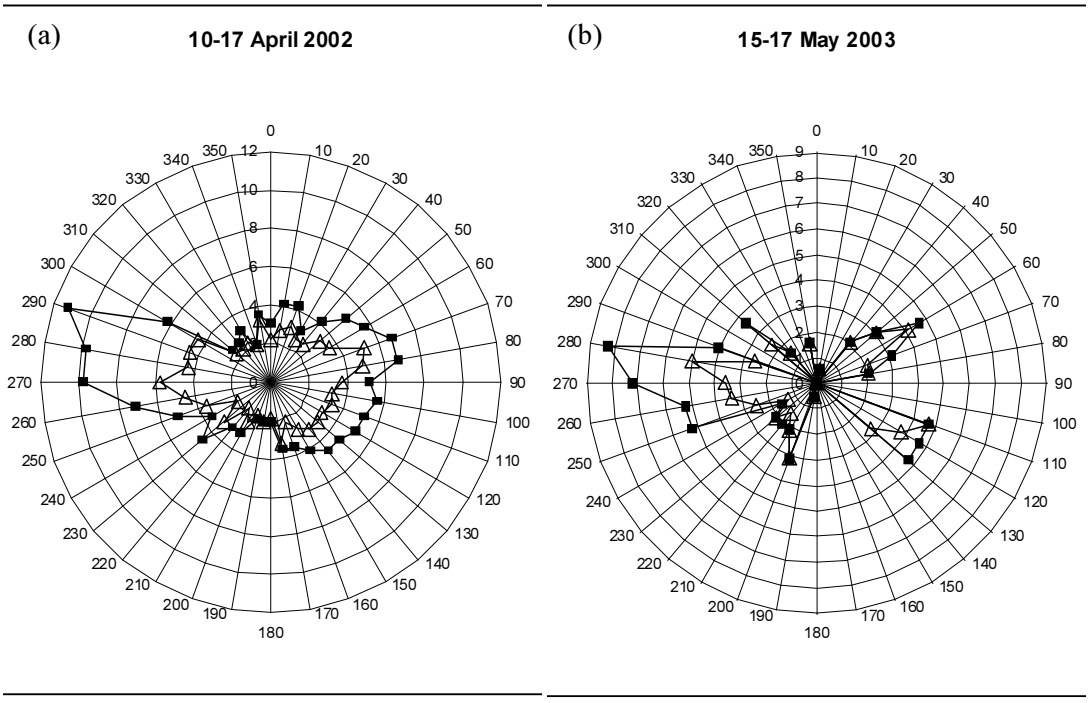

Figure 5.9 Average (open triangles) and maximum (solid squares) wind speeds in m/s at Farewell Spit (a) 10-17 April 2002 and (b) 15-17 May 2003.

Equations II-2-36 in the U.S. Army Corps of Engineers Ocean Engineering Manual (USACE, 2003) give a method of estimating the wave height H_{m0} of a wave generated by wind blowing over a fetch of length X

$$\frac{gH_{m0}}{u_*^2} = 0.0413\left(\frac{gX}{u_*^2}\right)^{\frac{1}{2}}, \tag{5.17}$$

where the friction velocity u_* is related to the wind speed at a height of 10 m above the water surface U_{10} by

$$C_D = \frac{u_*^2}{U_{10}^2}. \tag{5.18}$$

The wind drag coefficient C_D is a function of the wind speed,

$$C_D = 0.001\left(1.1 + 0.035U_{10}\right). \tag{5.19}$$

Here the maximum measured wind speed of U_{10} = 11.3 m s^{-1} will be used, as lower wind speeds will result in smaller wave heights and higher wave frequencies (see equation (5.20)). If the wave frequency calculated from the maximum wind speed is higher than the deep water cut-off frequency, lower wind speeds need not be considered. Using U_{10} = 11.3 m s^{-1} for the wind speed, the wind drag coefficient is C_D = 0.0015. This gives a friction velocity u_* = 0.437 m s^{-1}. The available fetch for winds from the west is X = 2500 m. The predicted wave height for the maximum wind speed of 11.3 m s^{-1} is obtained from (5.17), giving H_{m0} = 0.29 m.

The predicted wave period T_p for the wind generated waves is determined by

$$\frac{gT_P}{u_*} = 0.651\left(\frac{gX}{u_*^2}\right)^{\frac{1}{3}} \tag{5.20}$$

The predicted wave period for waves generated by the maximum westerly wind is therefore T_p = 1.46 s, or a wave frequency of 0.68 Hz. As this is above the cut-off frequency for deep water waves, these wind generated waves will not be detected by the DOBIE wave gauges. The equations (5.17) and (5.20) apply only to deep water waves, and modification would be required for transitional or shallow waves. As noted above, the wave frequency predicted for the wind-generated waves is above the cut-off for deep water waves, therefore the use of these equations is appropriate. Thus, in determining wave dissipation from the wave data, we can safely assume that waves within the frequency range recorded were travelling from east to west directly across the mussel farm.

5.4.3 Wave Shoaling

As the mean water depth varies across the Collingwood mussel farm, a correction is required to account for the effect of wave shoaling. As waves propagate from deeper to shallower water, they increase in height as they slow and as their wave length is reduced (the wave period remains the same). As wave spectra are calculated from the wave heights, shoaling would result in a higher wave energy being measured at the shallower, inshore, site. Therefore, the inshore wave spectra require correction for the increased wave height caused by shoaling.

The shoaling coefficient K_s is calculated using equation (5.21) (e.g. Dean and Dalrymple, 1991), where H_1 and H_2 are the wave heights at the offshore and inshore site, k_1 and k_2 the wave number at each site (a function of both depth and wave frequency), and d_1 and d_2 the depths.

$$K_s = \frac{H_2}{H_1} = \frac{\tanh\left[k_1 d_1\right]}{\tanh\left[k_2 d_2\right]} \frac{\left[1 + 2k_1 d_1 \Big/ \sinh\left(2k_1 d_1\right)\right]}{\left[1 + 2k_2 d_2 \Big/ \sinh\left(2k_2 d_2\right)\right]} \tag{5.21}$$

As wave spectral energy is proportional to the square of the wave height, the wave energy at the inshore site is corrected by dividing by K_s^2. This correction factor is a function of frequency.

The average depth at the offshore site (in the 2002 deployment) is 12.8 m, compared to 11.5 at the inshore site. During the 2003 deployment, averaged depths were 13.3 m and 11.4 m at the offshore and inshore sites respectively.

As an example of the effect of wave shoaling, the shoaling coefficient for a wave with frequency 0.08 Hz is 1.018, which would cause a 4% increase in the wave spectral energy recorded at the inshore site (using d_1 = 12.8 m and d_2 = 11.5 m).

5.4.4 Calculation of Dissipation

To determine if dissipation of wave energy by the mussel farm could be detected, wave spectral energy was compared at each frequency. As bursts were recorded simultaneously offshore and inshore of the farm, each burst provides an offshore/inshore data pair of wave energy over a range of frequencies.

Energy dissipation for each frequency has been obtained by plotting the inshore wave energy (corrected for shoaling) against the offshore wave energy for all bursts (see example in Figure 5.10). The slope of the regression line for each wave frequency gives the ratio of energy transmitted through the farm. A linear regression is used, and forced through the origin as zero wave transmission is expected if no wave energy is present. Waves are assumed to propagate from offshore to inshore.

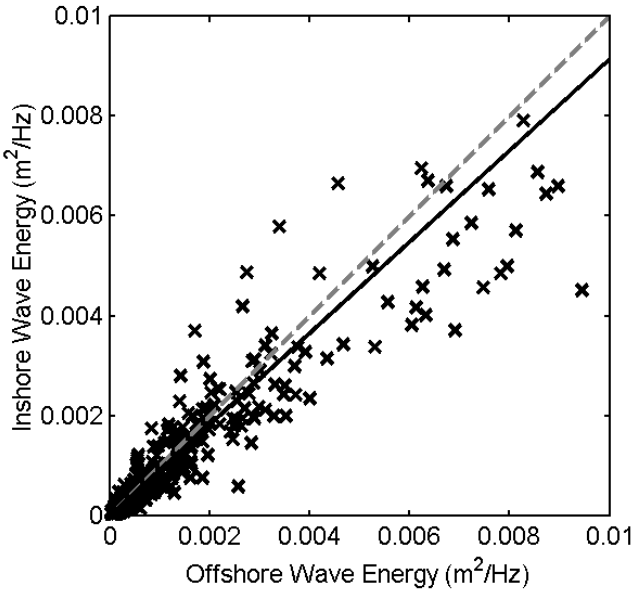

Figure 5.10 Offshore versus inshore wave energy at 0.195 Hz, 10-17 April 2002. The slope of the linear regression (solid black line) indicates the ratio of energy transmitted to the inshore site. The dashed grey line indicates 100% transmission.

The energy transmission ratios (ETR) for each deployment are plotted in Figure 5.11 as a 95% confidence interval for the regression coefficient (slope). Also plotted in Figure 5.11 is the predicted ETR from the wave dissipation model developed above. The parameters used for the wave model were dropper length L_d = 8.0 m, depth d = 12.0 m, density ρ = 1024 kg m^{-3}, dropper diameter ϕ = 0.14 m. This dropper diameter is an assumed value, and is representative of mussel droppers where the mussels are near harvest size. Wave dissipation was calculated assuming an initial wave height H_0 = 0.2 m at a distance x = 650 m (the farm width).

The ETR decreased with frequency, indicating that wave energy dissipation increased with increasing wave frequency. The measured wave dissipation varied between the two deployments. This may be due to a combination of the different location of the wave gauges and differences in crop density, crop maturity, and orientation of long-lines between the instruments. Wave dissipation was higher at most frequencies during the second deployment (2003), apart from near 0.2 Hz, where the ETR (2003) was approximately 1, indicating no dissipation. This compares with an ETR of 0.95 during 2002. The confidence interval is wider for the 2003 ETR values, which reflects the fewer samples recorded.

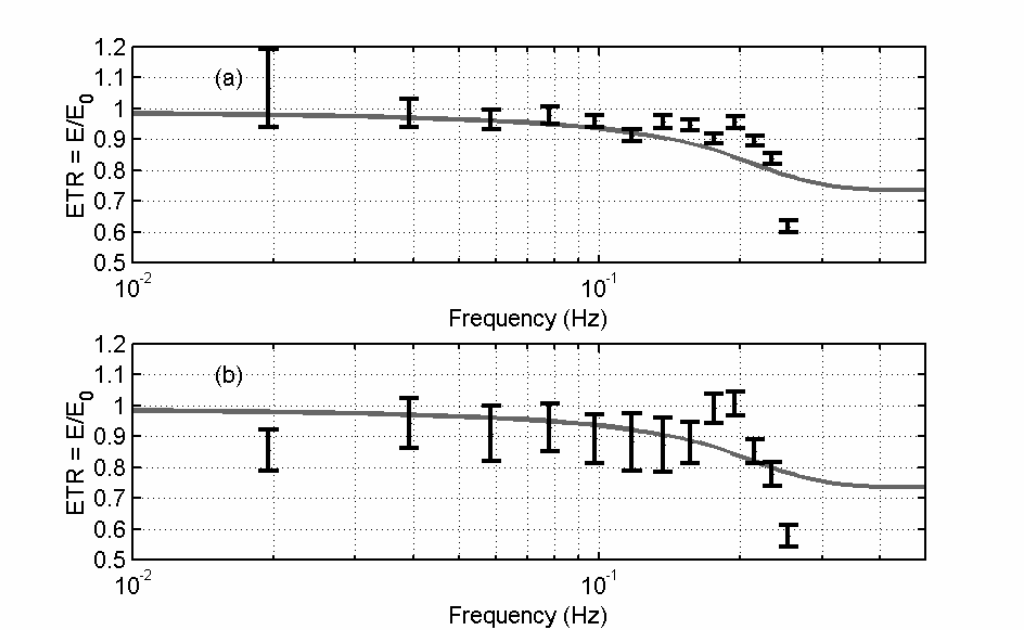

Figure 5.11 ETR corrected for effects of wave shoaling for (a) 10-17 April 2002, and (b) 15-17 May 2003. Solid line shows predicted dissipation from wave model.

During the 2002 deployment, little or no dissipation was seen at frequencies less than 0.1 Hz, but increased (decreasing ETR) as frequency increased (Fig. 5.11(a)). Dissipation was around 5% (± 2%) at 0.15 Hz, 10% (± 2%) at 0.2 Hz, and 39% (± 2%) at 0.25 Hz.

During the 2003 deployment, at frequencies below 0.15 Hz, dissipation was nearly constant at approximately 10 %, although the confidence interval is wide at ± 8%. At 0.2 Hz, dissipation was 5% (± 4%), increasing to 42% (± 4%) at 0.25 Hz.

5.4.5 Effect of Instrument Spacing

As a distance of 700 m separated the wave recorders, there was a delay between the time energy from a wave group would be detected by the offshore and inshore instruments. This delay can be calculated from the group velocity C_g, which varies between $\sqrt{gd}$ for shallow water (low frequency) waves, and $(gT)/(4\pi)$ for deep-water (high frequency) waves. The highest wave frequency that could be detected was 0.27 Hz, therefore the wave group velocities were within the range 10.8 m.s^{-1} and 2.89 m.s^{-1}. The travel time between the two instruments for a wave group was in the range 65 to 242 seconds, with the higher value for the highest wave frequencies detected (at the cut-off frequency). This travel time introduces the possibility that if wave conditions are changing over time, the lag between wave conditions offshore and inshore may have introduced an error in the dissipation calculations. This error will be a function of the wave frequency, and the rate at which average wave heights are changing. The largest error will occur for high frequency waves (which have the slowest travel times), and when the wave heights change rapidly in proportion to the initial wave heights.

The error in wave energies between the offshore and inshore sites due to rapid changes in wave conditions can be estimated by assuming that average wave heights increase or decrease at a constant rate $\dot{h}$ (m.s^{-1}). Wave height at the offshore site, assuming a linear rate of change, is

$$H_{offshore} = H_0 + \dot{h}t \tag{5.22}$$

where H_0 is the initial wave height (m) at the offshore site, and t is time (seconds). At the inshore site, wave heights will lag by the frequency-dependent wave energy travel time Δt:

$$H_{inshore} = H_0 + \left[t - \Delta t\right]\dot{h} \tag{5.23}$$

Wave energy is proportional to the square of wave height (see equation (5.7)). Wave spectral energy densities represent the wave energy averaged over the burst duration T_b, so wave energy can be calculated by integrating (5.22) and (5.23);

$$\begin{aligned} \bar{E}_{offshore} &= \frac{1}{T_b}\int_0^{T_b} H_0^{\,2} + 2H_0\dot{h}t + \dot{h}^2t^2 dt \\ &= H_0^{\,2}\left[1 + \frac{\dot{h}}{H_0}T_b + \frac{1}{3}\left(\frac{\dot{h}}{H_0}\right)^2 T_b^{\,2}\right] \end{aligned} \tag{5.24}$$

and

$$\begin{aligned} \bar{E}_{inshore} &= \frac{1}{T_b}\int_0^{T_b} H_0^2 + 2H_0\dot{h}\left[t - \Delta t\right] + \left[t - \Delta t\right]^2\dot{h}^2 dt \\ &= H_0^2 - 2H_0\dot{h}\Delta t + H_0\dot{h}T_b + \dot{h}^2\left(\frac{1}{3}T_b^{\,2} - \Delta t T_b + \Delta t^2\right) \\ &= H_0^2\left[1 + \frac{\dot{h}}{H_0}\left(T_b - 2\Delta t\right) + \left(\frac{\dot{h}}{H_0}\right)^2\left(\frac{1}{3}T_b^{\,2} - \Delta t T_b + \Delta t^2\right)\right] \end{aligned} \tag{5.25}$$

The ratio of the inshore and offshore wave energies gives the error induced by a linear increase of wave height with time.

$$error = 1 - \frac{\bar{E}_{inshore}}{\bar{E}_{offshore}} \tag{5.26}$$

where a positive value of *error* indicates that the inshore energy is lower than offshore, and

$$\frac{\bar{E}_{inshore}}{\bar{E}_{offshore}} = 1 - \frac{\Delta t\left[2\frac{\dot{h}}{H_0} + \left(\frac{\dot{h}}{H_0}\right)^2\left(T_b - \Delta t\right)\right]}{1 + \frac{\dot{h}}{H_0}T_b + \frac{1}{3}\left(\frac{\dot{h}}{H_0}\right)^2 T_b^{\,2}} \tag{5.27}$$

Although the calculations above were for average wave heights, significant wave heights may also be used as the ratio of energies are compared. The wave records indicate that the maximum rate of change of significant wave heights (Figure 5.6) was an increase of approximately 0.1 m over 3 hours, from an initial wave height of ~ 0.1 m. The rate of change of wave height is 9.26 x 10^{-5} s^{-1}, or 0.333 hr^{-1}. The travel time for wave energy between the offshore and inshore sites as a function of wave frequency is plotted in Figure 5.12(a), and the expected error in energy ratios due to a rapid increase in wave heights is plotted for two wave height increase rates in Figure 5.12(b).

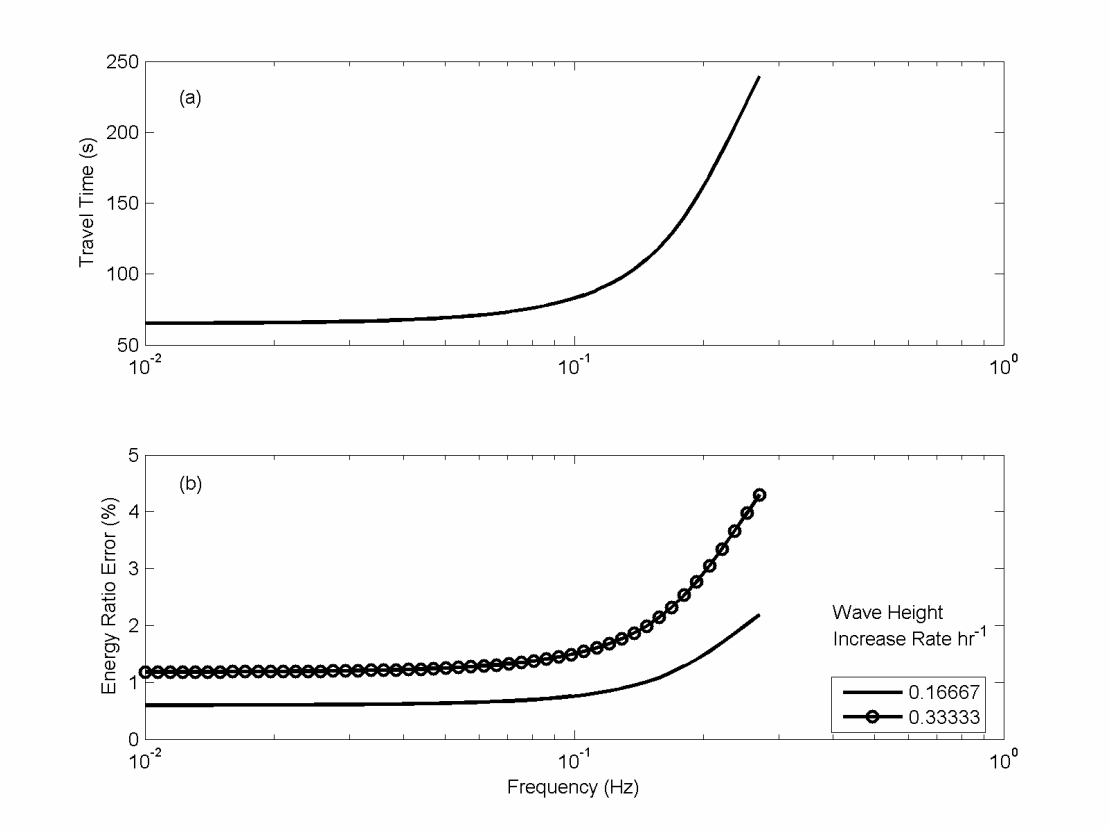

Figure 5.12 (a) Time taken for wave energy to travel 700 m in 11.8 m depth, (b) % difference between wave gauges at 700 m due to rapid increase of wave heights (increase rates in legend).

The energy ratio errors plotted in Figure 5.12(b) are for wave heights increasing over time. When wave heights are decreasing, the errors will be negative, indicating higher energy at the inshore site. The energy ratio errors represent the likely error for a single burst. As Figure 5.6(b) indicates, wave heights changed slowly during the 2003 experiment, therefore the errors will be small, and are not considered to have significantly influenced the results. During the 2002 experiment, wave height changes were much more rapid; however, increases and decreases in wave heights appear to have occurred at similar rates (Figure 5.6(a)). Therefore the travel-time induced errors, which are only significant for less than 10% of the wave record, would cancel out to some degree. While no attempt has been made to correct the data for any wave travel time induced error due to the complicated and time-consuming nature of the procedure required, it is likely that the error in ETR resulting from wave travel time is less than 0.5%.

5.5 Discussion

The model presented here provides a first order estimate of wave energy dissipation through a mussel farm. A number of assumptions were made in order to obtain a relatively simple model. The farm was modelled as a field of immobile, rough cylinders (representing the droppers) with sufficient separation so that interaction between cylinders did not occur. Clearly there will be interaction between the droppers due to their close spacing (as seen in the laboratory drag experiments), nor are the droppers immobile. Instead they are flexible, and can move and sway in response to wave forces. The droppers are also structurally connected, with the long-line forming a flexible chain of buoyancy (floats) and drag elements (droppers) anchored at either end. This connectivity raises the possibility of structural resonance, and of increased dissipation at particular frequencies. Related to the issue of dropper spacing is that of long-line orientation. The laboratory measurements and current model both indicate the importance of the orientation of long-lines to currents for drag. Similarly, the orientation of long-lines to wave direction may also have important implications for wave drag. In particular, if a long-line is oriented in the direction of wave propagation, the ratio of wavelength to long-line length may be an important parameter, as at shorter wavelengths, forces on different parts of a long-line may be in different directions. In the field data presented here, wave dissipation was measured across the mussel farm where long-lines were oriented perpendicular to the direction of wave propagation. Due to the direction of prevailing winds, the geometry of Golden Bay, and the limitation imposed by using bed-mounted pressure transducers, field data were obtained only for waves travelling from offshore to onshore (east to west) across the farm. Finally, interaction between currents and waves can have significant effects on the drag on circular piles. Wolfram and Naghipour (1999) found that the presence of a current reduced the drag coefficients C_d and C_m. This phenomenon may also occur for mussel droppers. These are all factors requiring further research in order to improve models of wave energy dissipation by mussel farms.

Despite the deficiencies described above, the model presented here does give reasonable estimates of wave energy dissipation when compared with the measured values. The model agrees with the field measured ETR for frequencies < 0.12 Hz. The model does not predict the increase in ETR at frequencies near 0.2 Hz, and dissipation at higher frequencies is under-predicted (ETR overestimated). As observed wave energy was low, with significant wave heights peaking at 0.25 m during the first deployment (2002), and 0.14 m during the second (2003), the accuracy of the model for more exposed sites cannot be tested. It is likely that the motion of the long-line and droppers will become more significant as wave heights increase, making the assumption of immobile rough cylinders invalid.

The peak in ETR around 0.2 Hz is particularly interesting, indicating that the mussel farm is particularly porous to wave energy around this frequency. As the long-line consists of a series of interconnected drag (the droppers) and buoyancy (the floats) elements, a range of dynamic responses to wave forcing is possible. These responses may include structural resonance, motion of the long-line or long-line elements, and possibly transfer and release of energy at different frequencies. Analysis of the dynamic behaviour of a long-line is beyond the scope of this thesis, however as part of the field experiments presented here, other investigators from NIWA (C.L. Stevens and M. Smith) deployed accelerometers on long-lines. Their data may help address some of these issues, and may be published shortly.

The effect of bottom friction was not considered in the analysis of the results. Bottom friction would have a stronger effect at low frequencies where the wave penetration to the bed is high, decaying to no effect for high frequency (deep-water) waves. Using a deep-water wave definition of wavelength less than twice the depth, bed friction would approach zero at a wave frequency of between 0.26 Hz and 0.28 Hz (the variation is due to the tidal depth variation). Bottom friction is negligible at this site, as can be determined following the methodology outlined in Dean and Dalrymple (1991). This method proceeds as follows. Firstly, making the assumption that the boundary layer is turbulent, the bed roughness is characterised by an equivalent sand grain size k_e such that

$$k_e = 2d_{90} \tag{5.28}$$

where d_{90} is the particle diameter that 90% of bed particles are smaller than. Next, the water particle excursion at the bed ζ_b (calculated assuming no boundary layer) is obtained from linear wave theory:

$$\zeta_b = \frac{H}{2}\frac{1}{\sinh(kd)} \tag{5.29}$$

A bed friction factor f_b proposed by Kamphuis (1975) is based on the ratio of k_e/ζ_b such that

$$f_b = 0.1\left(\frac{k_e}{\zeta_b}\right)^{3/4} \text{ for } \frac{k_e}{\zeta_b} > 0.02\,, \tag{5.30}$$

or

$$\frac{1}{2\sqrt{f_b}} + \ln\left(\frac{1}{2\sqrt{f_b}}\right) = -0.35 - \frac{4}{3}\ln\left(\frac{k_e}{\zeta_b}\right) \text{ for } \frac{k_e}{\zeta_b} < 0.02\,. \tag{5.31}$$

The wave amplitude at a distance x can then be calculated from:

$$\frac{H(x)}{H_0} = \frac{1}{1 + \dfrac{2f_b}{3\pi}\dfrac{\frac{1}{2}H_0 x k^2}{\left[2kd + \sinh(2kd)\right]\sinh(kd)}} \tag{5.32}$$

The two DOBIE wave recorders in both experiments were separated by a distance of approximately 700 m. Assuming a bed sediment size of d_{90} = 0.5 mm, water depth of 11.8 m and wave amplitude of 0.5 m, a wave with frequency 0.08 Hz (the dominant wave frequency during the 2002 experiment) will decrease in amplitude by approximately 0.03%, equating to an energy loss of less than 0.1% ($E_2/E_1 = \left(H_2/H_1\right)^2$). This is far less than the observed losses of ~ 5%. Bed friction can be safely neglected from the analysis of these results.

In comparison with kelp beds, where Elwany *et al.* (1995) found no significant loss of wave energy, dissipation through the mussel farm was around 5-20%, with the higher dissipation at high frequencies. As identified by Seymour (1996), the ability of the kelp to move with the waves would reduce the drag on the plants, and therefore minimise dissipation of wave energy. The mussel droppers are also able to move with the waves, but their motion is constrained as they are interconnected at the surface to the back-bone ropes and the floats.

As discussed briefly in the introduction, breakwaters provide protection from waves through a combination of wave reflection and dissipation. The energy transmission ratios for breakwaters are low by design. Suspended pipe breakwaters, which resemble a rigid mussel long-line, can have values of ETR in the range 0.4 to 0.8 depending on the spacing of the pipes and the wave parameters (Mani and Jayakumar, 1995). As this is for a single array of cylinders, the effect on the wave energy is far greater than that of the mussel long-line, noting that ETR measured in the field represents the effect of waves passing through in excess of 20 long-lines. It is likely that for the suspended pipe breakwater, much of the incoming wave energy was reflected rather than dissipated, although this was not measured. This is certainly the assumption used in most theoretical analyses of wave transmission through arrays of cylinders (e.g. Massel, 1976). Other floating breakwaters give values of ETR considerably lower than that measured for the mussel farm. Some examples of these are given in Table 5.1. In comparison with these structures, the effect of the mussel farm on wave energy is small.

Type of Breakwater	Reported ETR
Mussel Farm	0.8-0.95
Suspended Pipe (Mani and Jayakumar, 1995)	0.4-0.8
Cage Floating (Murali and Mani, 1997)	< 0.5
Tethered Float (Seymour and Hanes, 1979)	~ 0.2
Submerged/semi-submerged dynamic breakwater (Williams and McDougal, 1996)	0.6-0.95

Table 5.1 Energy transmission values for breakwaters.

5.6 Summary

Field measurements of shallow water (low frequency) and transitional (moderate frequency) waves at the mussel farm near Collingwood, Golden Bay indicated wave dissipation of around 5-20%. This dissipation is a function of frequency, with dissipation generally increasing at higher frequencies. This dissipation is particular to the characteristics of this site, and the size, density and orientation of the long-lines, and the relatively shallow depth should be considered if future comparison is to be made with other locations. Also, measurements were made during a period of low wave energy, with significant wave heights < 0.25 m. In more severe conditions, the motion of the long-line in response to wave action may have an important influence on wave dissipation. An analytical model, using root-mean-squared (RMS) velocities to parameterise the contribution of drag and inertial forces, predicts the degree of wave dissipation with reasonable success.

CHAPTER 6 FORCES ON LONG-LINE ANCHOR ROPES

6.1 Introduction

The effect of mussel farms on wave energy has been investigated in the previous chapter. Wave energy is lost through the drag on the submerged structure of the long-lines. These forces will result in a structural response of the long-line. The dynamic response of a submerged mussel long-line to waves and currents has been treated analytically by Raman-Nair and Colbourne (2003). The long-lines currently used in New Zealand differ from those modelled by Raman-Nair and Colbourne in that they are suspended at the surface. As a result, they will be more susceptible to the influence of waves, particularly of higher frequencies, as wave motion attenuates with depth at a faster rate for higher frequency waves. Modelling the motion of, and forces in, a mussel long-line is a complex issue and beyond the scope of this thesis. Instead, measurements of the tension in a mooring rope in response to the combined action of waves, tide, and currents are presented here as a guide for further research, and as a comparison with the wave energy dissipation presented in the preceding chapter. The data presented here is essentially data of opportunity, in that the load-cells used were primarily intended to allow direct measurement of mussel long-line drag, and instead were found to be more suited to measuring the static and dynamic loadings on the moorings.

In the following sections of this chapter, the study sites, equipment, installation methods and data recording periods are described in section 6.2, the results for two study sites are presented and analysed in sections 6.3 (Collingwood) and 6.4 (Pigeon Bay), and the sites are compared and results discussed in section 6.5, with a summary in section 6.6.

As the configuration of the long-lines on which load-cells were installed at the two sites differ in the orientation to the wave field, the results for the two sites are presented separately.

6.2 Methodology

6.2.1 Study Sites

Load-cells were installed on the anchor ropes of a mussel long-line during two separate deployments. The first deployment coincided with measurements of wave dissipation at the Collingwood mussel farm, Golden Bay, 15-17 May 2003. A load-cell was installed on a single anchor rope of a long-line oriented nearly perpendicular to the direction of wave propagation. Conditions were calm over the duration of the deployment. Mussel sizes on the selected long-line were 40-50 mm, and mussels were clumped rather than being evenly distributed over the length of the dropper ropes. The location of the long-line where the load-cell was installed, in relation to the farm, is indicated in Figure 6.1. The long-line was oriented north-south, and the load-cell installed on the anchor rope at the north end of the long-line.

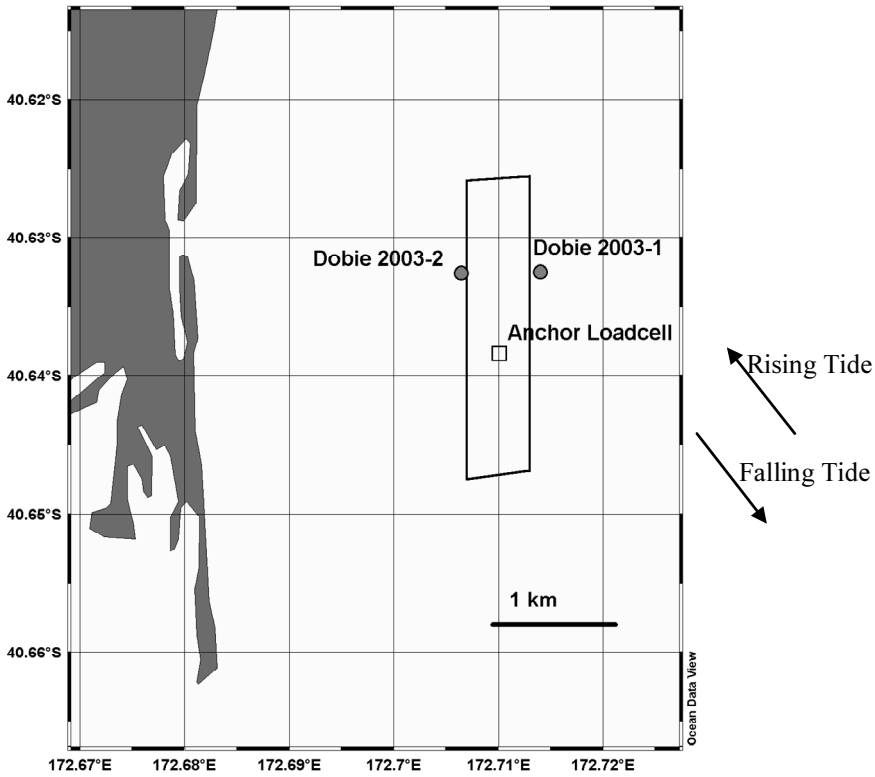

Figure 6.1 Location of load-cell at Collingwood mussel farm, 15-17 May 2003. The load-cell was installed on the anchor rope at the north end of a long-line.

The second deployment was at Pigeon Bay, Banks Peninsula (Figure 6.2). This load-cell deployment was part of a collaborative study on the motion of, and forces on, mussel long-lines by NIWA and OCEL (an ocean engineering consultancy). The wave data presented here are used with their permission. Two load-cells were deployed, one on each anchor rope at either end of a long-line. The long-line selected had mature mussels (80-90 mm shell length), and was orientated NE/SW, parallel to the long axis of the bay. Due to the orientation of the long-line and the bay, waves travelled along the length of the long-line, as opposed to across the long-line as at Golden Bay. The long-line was the most seaward long-line at the Pigeon Bay site. The load-cells were deployed from 23rd June to 5th July 2004. Wave data from DOBIE wave gauges moored near the site were obtained from 15:30 17th June to 16:00 24 June 2004, and 14:30 29 June to 16:30 5 July 2004.

This site is exposed to ocean swell from the north-east. The position of the monitored long-line in relation to the mussel farm and the bay is indicated in Figure 6.2. The average (mid-tide) water depth in the vicinity of the instrumented long-line was 13 m.

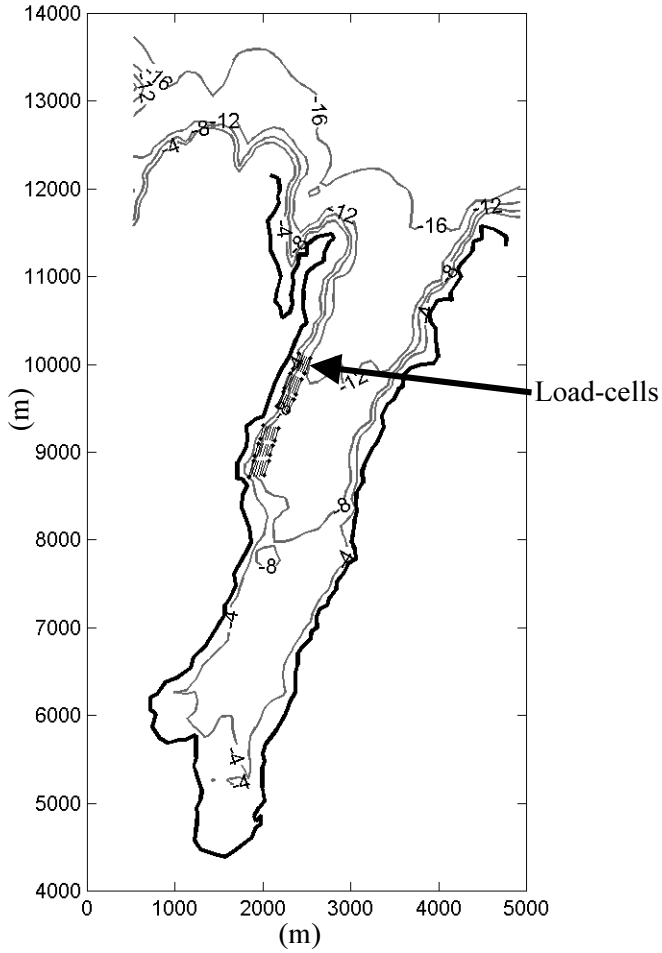

Figure 6.2 Bathymetry of Pigeon Bay. Farm is located mid-way along bay on west side. Load-cells were deployed on most seaward long-line July 2004 (see arrow). Co-ordinates and depths (with respect to MLW) are (m).

6.2.2 Description of Load-cells

Submersible tension load-cells (Figure 6.3) were fabricated for these experiments by technicians in the Department of Civil Engineering, University of Canterbury. Two load-cells were manufactured from stainless steel bolts, with the central portion milled to a square cross-section. Eight strain-gauges were attached to this central section in a full-bridge arrangement (to allow self-compensation for temperature fluctuation). The load-cells were waterproofed using a combination of epoxy and rubber tape. The load cells were calibrated to 25 kN, and were accurate to 2% within this range. Data were recorded on a custom built logger. The logger was battery powered, and used removable flash cards for data storage. Tension was recorded at 10 Hz for bursts of approximately 7 minutes, with bursts sampled every 15 minutes at Golden Bay, and 30 minutes at Pigeon Bay. An anti-aliasing filter (low pass filter) was incorporated into the logger to remove high frequency components above 10 Hz (the logger sampled at a higher frequency, but only recorded at 10 Hz). Long cables connected the load-cells to the logger. The design allowed a load-cell to be attached at either end of the long-line, and for loads to be recorded

simultaneously. This required approximately 200 m of cable (75 m on one load-cell, and 125 m on the other). The cables were at risk of breakage and tangled easily. A suggestion for future research is to construct separate data loggers for each load-cell, allowing shorter cable lengths to be used. If synchronous logging of the load-cells is desired, a radio link between the two (or more) data loggers could be considered as a means of starting logging simultaneously.

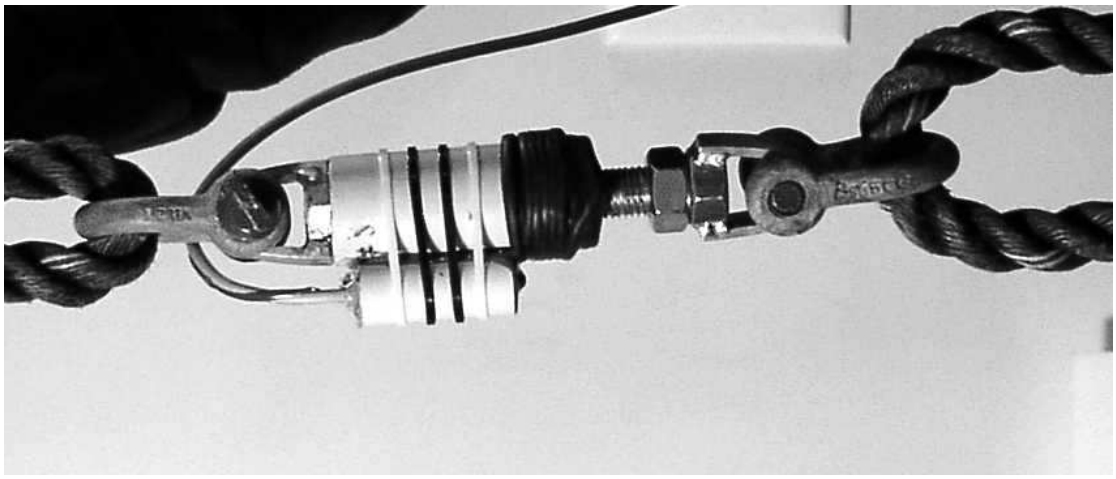

Figure 6.3 Load cell constructed from stainless steel bolt.

6.2.3 Load-Cell Installation

At the Golden Bay site, a boat used for harvesting the mussels was used to lift part of the anchor rope (warp) out of the water, and hydraulic rams used to take tension out of the anchor rope. The load-cell was installed using two short lengths of 24 mm 3 strand (twisted) polypropylene rope shackled one each end of the load-cell. One length of rope was spliced into the anchor rope (32 mm polypropylene 3 strand), and the other end tied to a bridle at the end of the long-line. This procedure short-circuited the anchor rope so that the load-cell took the full tension. The anchor rope remained attached as a precaution in the event of failure of the load-cell or attachments, and allowed retrieval of the load-cell (by cutting the short connecting lengths of 24 mm rope) without assistance from the mussel boat. The original plan was to install the load-cells on a long-line with mature mussels. However, the hydraulic ram system on the mussel boat struggled to raise and sufficiently slacken the anchor rope to allow safe installation of the load-cell. A second and successful attempt was made on a long-line with less mature crop (mussel shell length 40-50 mm).

At Pigeon Bay (2004), a second warp, with the load-cell attached, was connected to a long-line and the sea-floor anchor by a diver. A mussel barge was used to tension this warp so that the original anchor rope became slack. The original anchor rope was left in place, but took no load. This installation was performed by the farm owners (Pigeon Bay Aquaculture) and OCEL.

6.2.4 Data Records

6.2.4.1 Golden Bay

The duration of the wave data and load-cell data are given in Table 6.1. A total of 137 simultaneous wave/load sample bursts were obtained.

Wave Data	Start	Finish	Number of records
Dobie 2003-1 and Dobie 2003-2	11:15 15 May 2003	12:15 17 May 2003	153 at 15 min
Load-Cell Data	14:00 15 May 2003	1:30 17 May 2003	143 at 15 min

Table 6.1 Wave gauge and load-cell deployment times for Golden Bay 2003.

6.2.4.2 Pigeon Bay

The periods during which wave data from Dobie wave gauges and load data from the load-cells were obtained are listed in Table 6.2. Due to difficulty in installing the load-cells at the time of deploying the first wave gauge, the load data starts 6 days after the first wave record. Unfortunately, the wave gauge recorded for less time than anticipated due to an instrument malfunction. There is therefore a gap in the wave data before the wave record from the second wave gauge commences.

Wave Data	From	To	Number of records
Deployment 1	15:30 17 June 2004	16:00 24 June 2004	339 at 30 min
Deployment 2	19:30 29 June 2004	3:00 7 July 2004	118 at 1hr30min
Load-Cell Data			
Deployment 1	14:00 23 June 2004	12:30 29 June 2004	286 at 30 min
Deployment 2	16:00 29 June 2004	16:30 5 July 2004	290 at 30 min

Table 6.2 Wave gauge and load-cell deployment times for Pigeon Bay 2004.

Two sets of overlapping wave/data records were obtained:

- 14:00 23 June 2004 to 16:00 24 June 2004 at 30 minute intervals (53 records),
- 17:30 29 June 2004 to 1:00 4 July 2004 at 1hr30 intervals (70 records).

6.3 Results from Golden Bay 2003

6.3.1 Wave Data

Wave data from the Golden Bay study site for the period of 15-17 May 2003 were presented in the previous chapter. Significant wave heights were small, averaging 0.046 m, and peaking at 0.14 m (see Figure 5.6(b)).

6.3.2 Static Loads

Static loads on anchor ropes were obtained by averaging over each 5 minute burst. Static loads from an anchor rope at the Collingwood mussel farm site from 15-17 May 2003 were strongly related to the tide, as indicated in Figure 6.4. The dominant static load on the anchors was due to tidal depth variation rather than currents. The load increase with tide suggests that the buoys nearest the anchor became partially submerged.

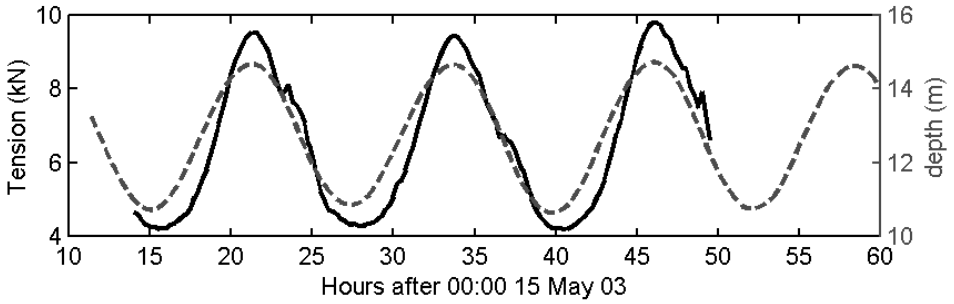

Figure 6.4 Anchor rope tension (solid line) 15-17 May 2003, Collingwood (force on left axis). Water depth at the offshore wave gauge is shown as a dashed line (depth on right axis).

Static loads were highest at high tide (9.8 kN) and lowest slightly after low tide (4.2 kN). On rising tides, immediately after low tide, the tension lagged behind the change in depth. This lag is probably indicative of the current-induced drag forces, which would increase the load on the upstream anchor rope, while reducing the load on the downstream anchor rope. The load-cell was at the upstream end of the long-line on falling tides, and the downstream end on rising tides. This may also explain why tension was lowest after low tide.

The difference in anchor rope tension on rising and falling tides is readily discernible by plotting the tension against water depth (Figure 6.5). At the same water depth, tension on the falling tide was approximately 2 kN higher than on rising tides. As discussed above, on falling tides the currents were in a south-easterly direction, dragging the long-line away from the northern anchor where the load-cell was installed.

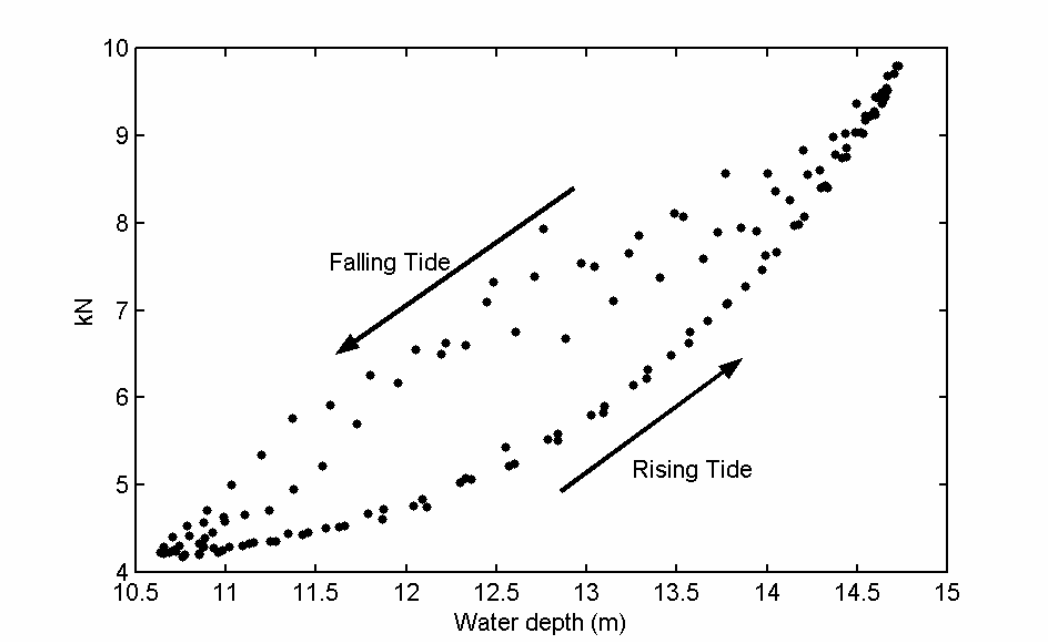

Figure 6.5 Anchor rope tension versus tide, showing higher tension on falling tides.

Over all three falling tides during which tension was recorded, a small temporary increase in load can be seen approximately 2 to 3 hours after high tide. The cause of this is unknown, but it may relate to motion of the long-line. On the rising tide, the long-line would be pushed by the tidal currents towards the load-cell. On falling tides, the currents would move the long-line in the opposite direction. The small load peak may indicate the point where this motion is arrested by the tension in the northern anchor rope.

6.3.3 Dynamic Loads

As current strength varies slowly over the tidal cycle, the largest dynamic load is from waves. During the Collingwood 2003 deployment, wave amplitudes were small, but some influence of the waves on load was detected. Figure 6.6 shows the variation in maximum and minimum loads during each burst over the deployment duration. The variation between peak and minimum loads was small, suggesting wave forces were small during the deployment. This is consistent with the small wave amplitudes recorded over this period.

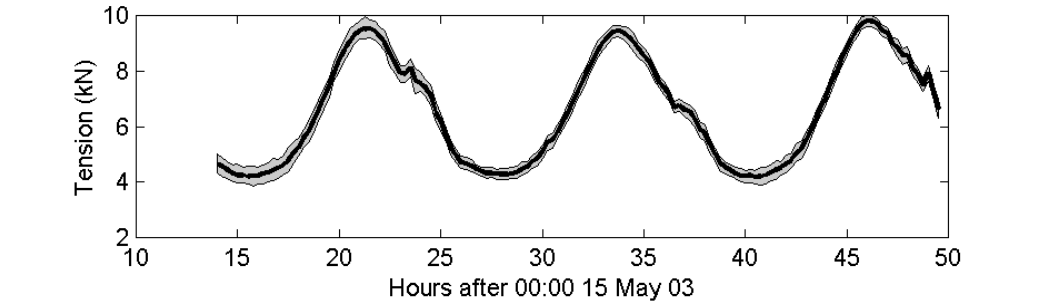

Figure 6.6 Average anchor rope tension, with minimum and maximum loads (shaded region).

The minimum and maximum recorded loads were 3.8 and 10.0 kN. The largest variation between maximum and minimum load during a burst was 0.95 kN, with a mean variation (average of the variation from each burst) of 0.56 kN.

Load spectra are similar in frequency response to the wave field recorded at the offshore DOBIE wave gauge (Figure 6.7). Load spectra were calculated using Hanning windows of 1024 samples, overlapping by 512 samples.

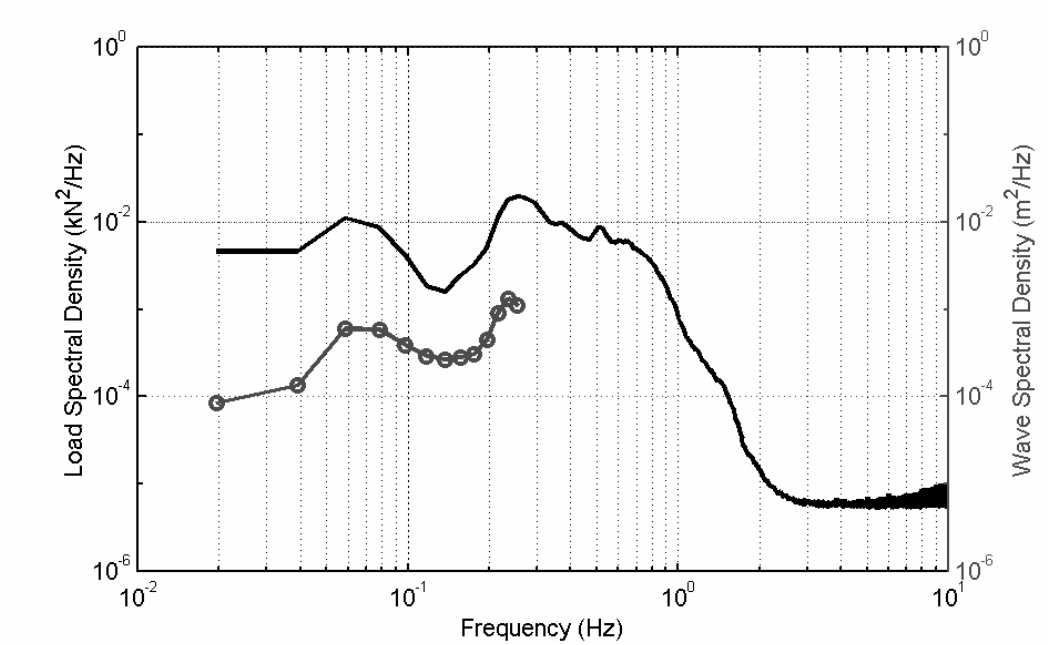

Figure 6.7 Anchor rope average load spectra (black line, left axis), and average wave spectral density (grey line with open circles, right axis) for Collingwood, 15-17 May 2003.

In order to determine the spectral response of the anchor rope tension to the applied wave field, wave spectra and load spectra were matched for each burst, giving a time-series of paired wave and load power spectral densities (PSD) at a range of frequencies. By plotting, for each frequency, the PSD for load and wave against each other, a linear regression could be fit to the data, e.g. Figure 6.8(a), indicating the dependence of the anchor rope tension to the wave energy as a function of frequency (Figure 6.8(b)). The strength of the regressions was not high, as indicated by the low R^2 values in Figure 6.8(c). This may be due to both the scatter in the PSD values, and the small range of wave heights during the experiment. A larger range of wave sizes is likely to allow better regression analysis.

The regression coefficients indicate the strength of the response of the anchor rope tension to the wave energy, so may be considered as response coefficients. As the coefficients vary with frequency, they describe a frequency response function. These coefficients show that load response is strongest for low frequency waves, and decreases with increasing frequency. There is, however, a peak in the response at

about 0.18 Hz, which coincides with lower wave dissipation recorded at similar frequencies (see Figure 5.11(b)).

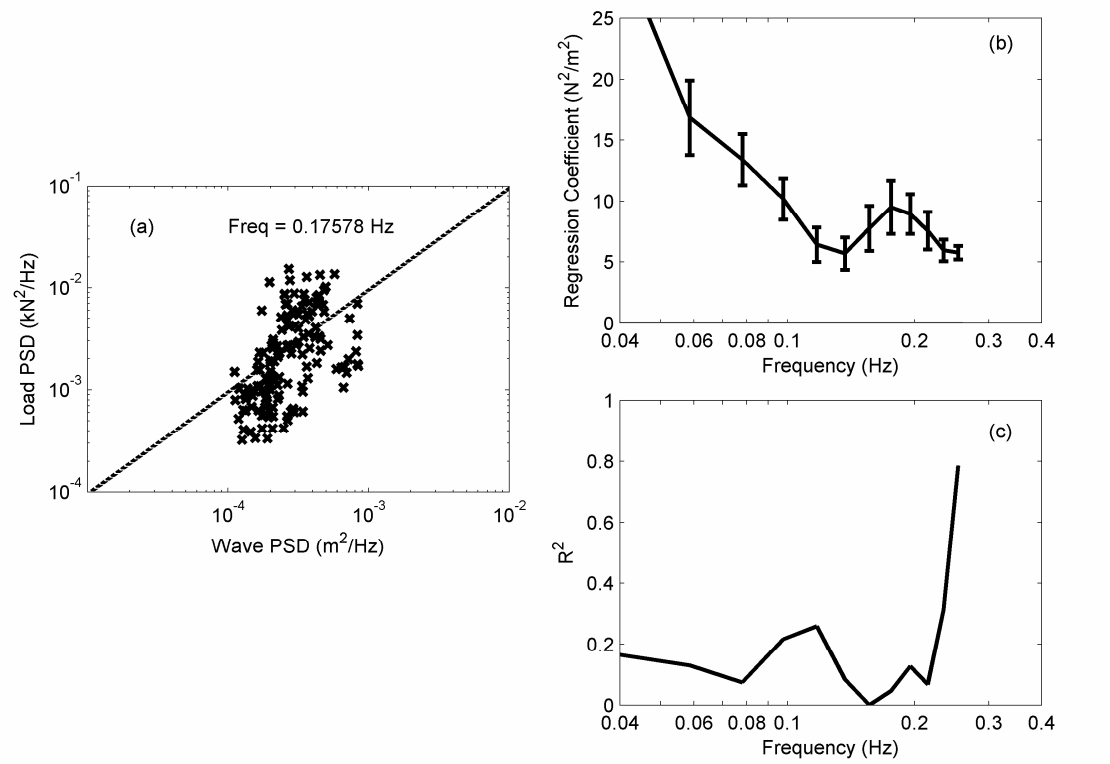

Figure 6.8 (a) Load PSD vs wave PSD for load-cell at 0.176 Hz with dashed line indicating linear regression, (b) slope of this regression as a function of frequency with 95% error bars (frequency response function), and (c) R^2 value for the regression for Collingwood 15-17 May 2003.

The relationship between wave spectra and load spectra was assumed to be linear when the response coefficients were calculated. To validate this assumption, the regressions were repeated, fitting a least-squares exponential of the form $y = Ax^b$. The exponent b was found to be close to one, indicating a linear relationship, although there was an increase in exponent with increasing frequency. The R^2 values for the exponential regressions were similar or lower than those for the linear regressions, indicating that no advantage is gained by using an exponential relationship; particularly as the range of wave heights over the deployment were small.

6.4 Results from Pigeon Bay 2004

6.4.1 Wave Data

Significant wave heights and mean wave periods calculated from the wave gauge data are plotted in Figure 6.9. The gap in the middle of the wave record is the period between the first wave gauge terminating logging, and the deployment of the second wave gauge. Unfortunately this coincided with the period of maximum observed anchor rope load fluctuations on the night of the 27th June 2004 (see Figure

6.10). Significant wave heights peaked late in the evening in the 18th June (*Hs* ~ 2.5 m), which is before the deployment of the load-cells. Wave heights were generally small over the deployment (*Hs* ~ 0.3 m).

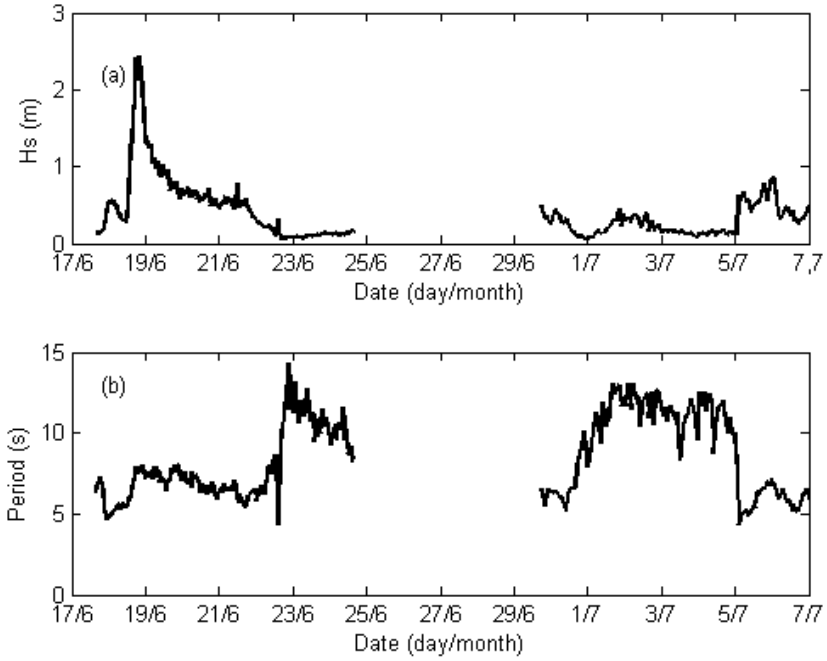

Figure 6.9 (a) Significant wave heights and (b) mean wave period at Pigeon Bay from 17 June to 7 July 2004.

6.4.2 Static Loads

Anchor rope tensions were dominated by tidal water variations (Figure 6.10 and Figure 6.11), with similar average loads seen at both ends of the long-line. The variability in load was greatest at the offshore end of the long-line, with peak loads occurring late on the 27 June 2004. No wave data was recorded at this time. The inshore load-cell suffered a fault (due to water entering a damaged cable) just before 02:00 4 July 2004, and no further data was obtained from the inshore load-cell after this time.

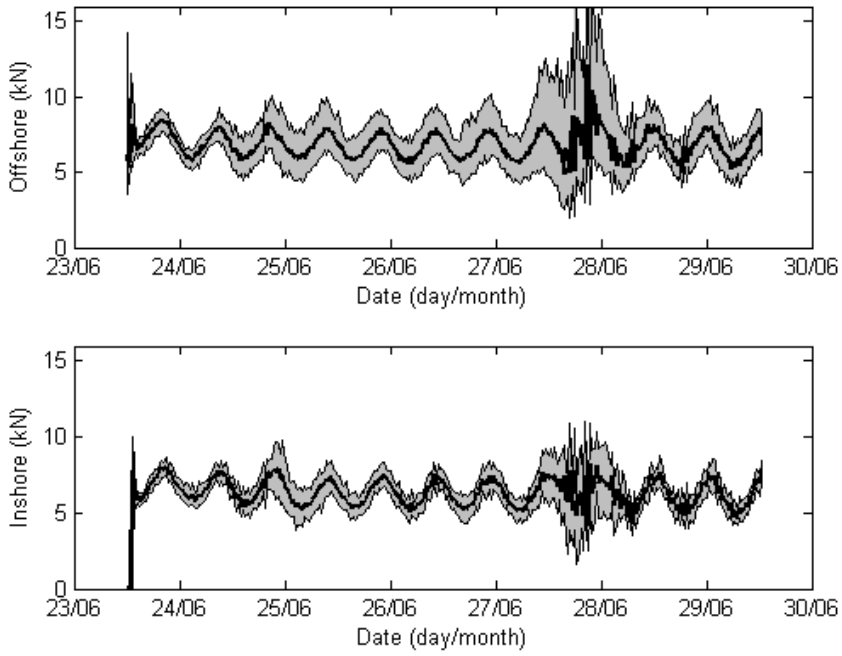

Figure 6.10 Long-line anchor rope tension Pigeon Bay 23 - 29 June 2004. Shaded area indicates maximum and minimum loads.

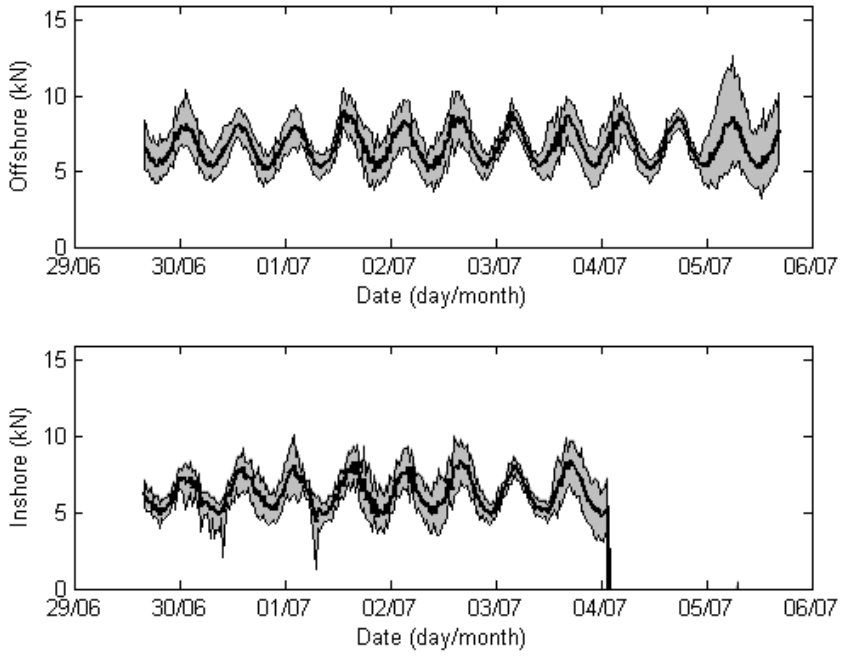

Figure 6.11 Long-line anchor rope tension Pigeon Bay 29 June 5 - July 2004.

Burst-averaged loads were dominated by the tidal water level variation, with the highest average loads at both ends of the long-line coinciding with high tide (Figure 6.12).

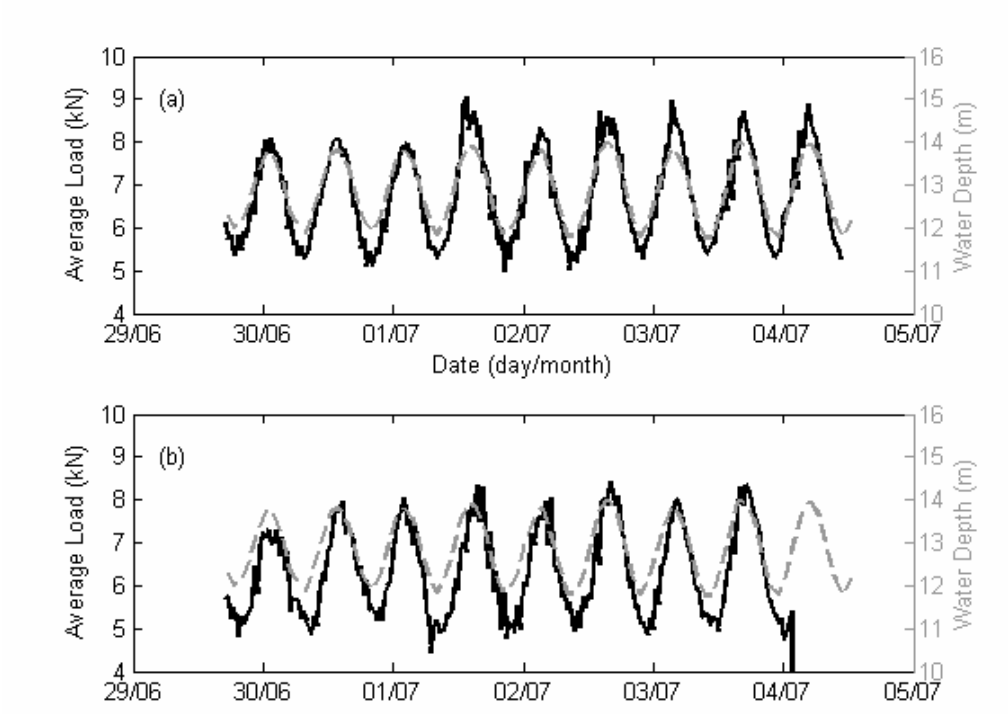

Figure 6.12 Burst averaged anchor rope tension at (a) offshore and (b) inshore anchor rope load-cells. Tidal water depth shown as dashed grey line.

Unlike at Golden Bay, tidal currents did not appear to cause a large difference between anchor rope tensions on rising and falling tides. A small load increase, of ~ 0.5 kN, was seen at the offshore anchor rope on rising tides as compared to falling tides, Figure 6.13(a), but no difference can be discerned for the inshore anchor rope, Figure 6.13(b). On rising tides, the offshore anchor rope was at the upstream end of the long-line, consistent with an increase in tension caused by the tidal current. Any difference in load between rising and falling tides was small (~ 0.5 kN) compared to the variation in load caused by the changing water depth (~ 4 kN).

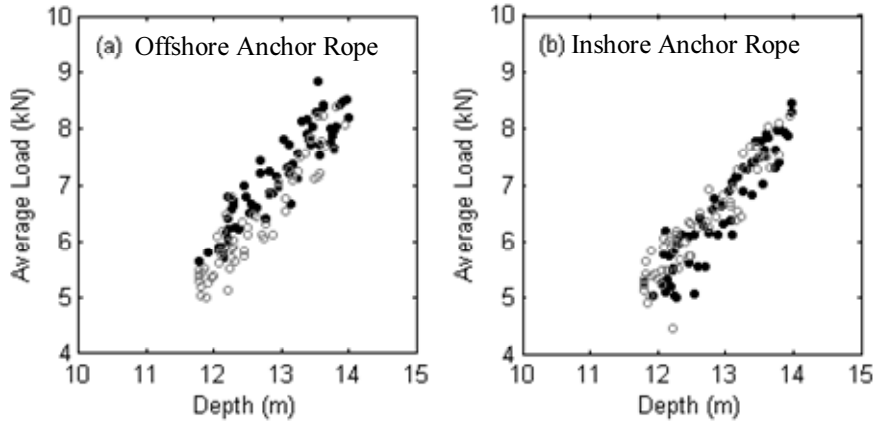

Figure 6.13 Burst-averaged load plotted against water depth on rising (solid black circles) and falling (open grey circles) tides for (a) offshore anchor rope, and (b) inshore anchor rope.

The smaller changes in load due to water currents at this site in comparison to Golden Bay may be attributed to differences in long-line configuration and orientation, as well as the speed of the water currents. These are considered in more depth in section 6.5.1.

6.4.3 Dynamic Loads

An example of the wave and load time series data is plotted in Figure 6.14. Larger load variability can be seen at the offshore anchor rope compared to the inshore anchor rope. The wave data and load data were not synchronised, and the wave data were recorded approximately 50 m away from the farm. Therefore, the wave and load time-series can not be directly compared at any instant. The pressure data indicate maximum water level fluctuations of ~ 0.3 m, with maximum load variations of ± 2 kN and ± 1 kN at the offshore and inshore anchor ropes respectively.

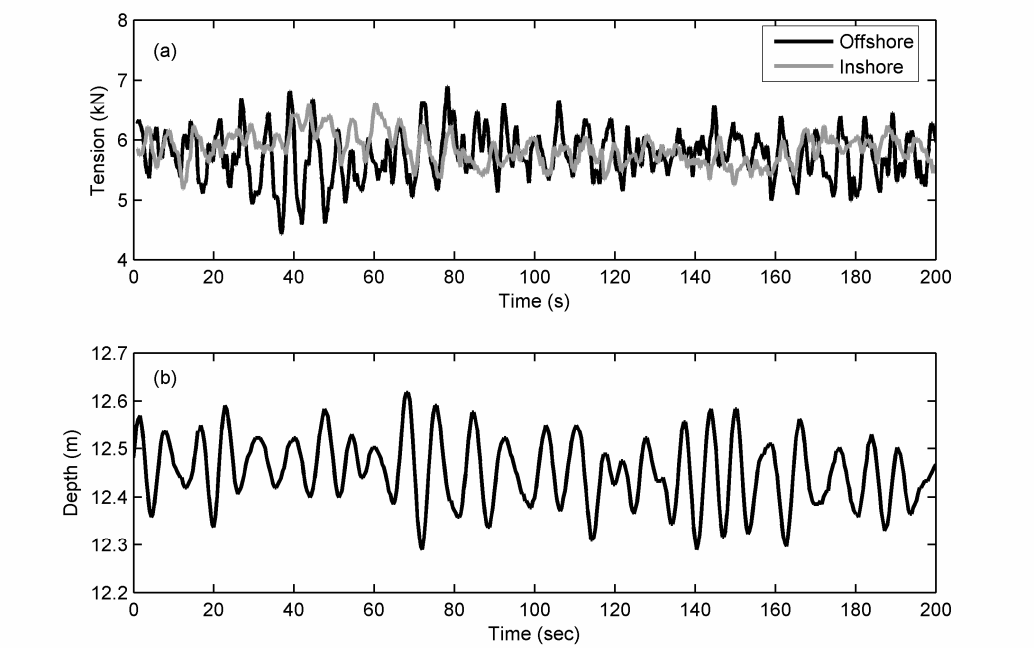

Figure 6.14 Time-series of (a) anchor rope tension and (b) pressure at 17:30 29 June 2004. Note that the wave data are not synchronised with the load-cell data – there is a small, but unknown time offset between them.

While the load and wave time-series cannot be compared on a wave by wave basis due to the small, but unknown, time offset, spectra may be compared as bursts were recorded at a similar time (within 1 minute of each other). Spectra averaged over the periods when both wave and load records were obtained are plotted in Figure 6.15. The load spectra tend to follow the trends seen in the wave spectra, except at low frequencies where the load spectra are high. This low frequency behaviour may be due to a sieching-type motion of the long-line, which will be discussed in more detail below. Both load-cells show spectral peaks at about 0.08 Hz, corresponding with the peak wave energy. In the mid-frequency range (0.11 to 0.30 Hz), a stronger response was seen at the offshore load-cell. The lower energy in the inshore load spectra in this range is consistent with the observation of lower load variability at the inshore end of the long-line (Figure 6.14). Both load-cells show high PSD (power spectral densities) at frequencies above

that of the deep-water wave cut-off frequency (0.245 Hz). In particular, a PSD peak is seen at 0.39 Hz for both load-cells. Wave spectra give an indication of increasing wave energy towards the deep-water cut-off frequency, but the cut-off is too low to determine if the high load PSD at high frequency is due to high wave energy.

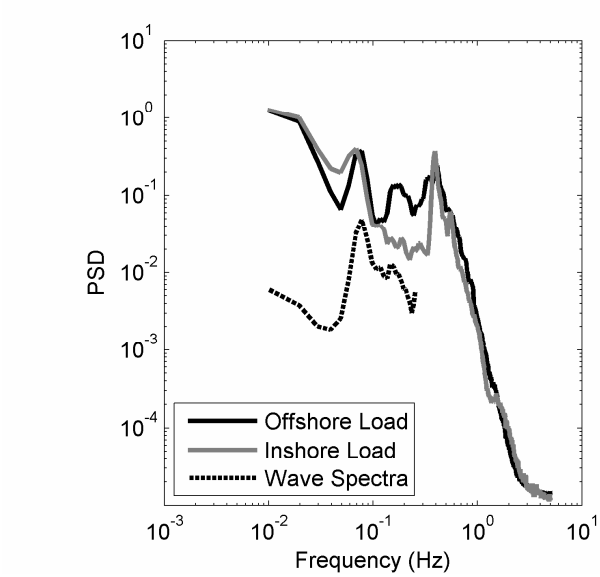

Figure 6.15 Average spectra for anchor rope tension (kN^2/Hz) and wave field (m^2/Hz) from 14:00 23 June 2004 to 16:00 24 June 2004 and 17:30 29 June 2004 to 01:00 4 July 2004.

In general, the phase of tide had no significant effect on the average load spectra, with similar average spectra seen on rising and falling tides (Figure 6.16).

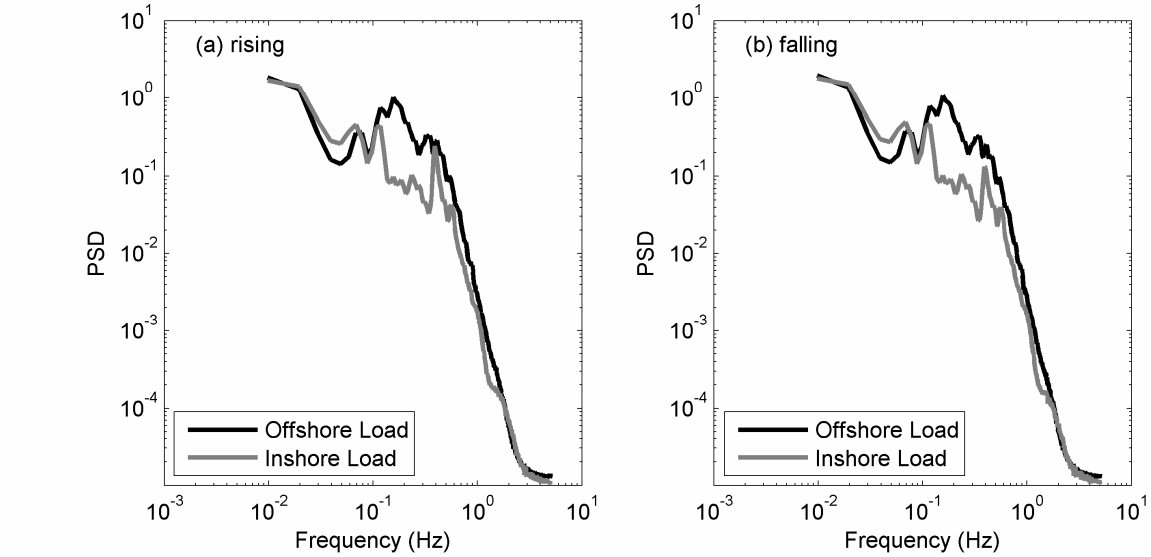

Figure 6.16 Average load spectra on (a) rising and (b) falling tides, Pigeon Bay 14:00 23 June to 01:00 4 July 2004.

Peak loads were obtained shortly after 21:00 on the 27th June 2004. As no wave records were obtained at this time, the size of the waves that resulted in the highest loads is unknown. As indicated in the plot of the load record, Figure 6.17(a), high loads with large variability occurred on the offshore anchor, while loads were significantly smaller and more uniform on the inshore anchor rope. A maximum load of 17.7 kN was recorded on the offshore anchor rope, with variations of up to 8 kN during a single wave. The load spectra, plotted in Figure 6.17(b), has peaks at ~ 0.11 Hz (period of 9 s), with a smaller peak at 0.25 Hz (period of 4 s). The tide was rising at this point, and the tidally induced currents would tend to pull the farm away from the offshore anchor rope towards the inshore one, thereby increasing the mean loads on the offshore anchor rope, and reducing those on the inshore anchor rope.

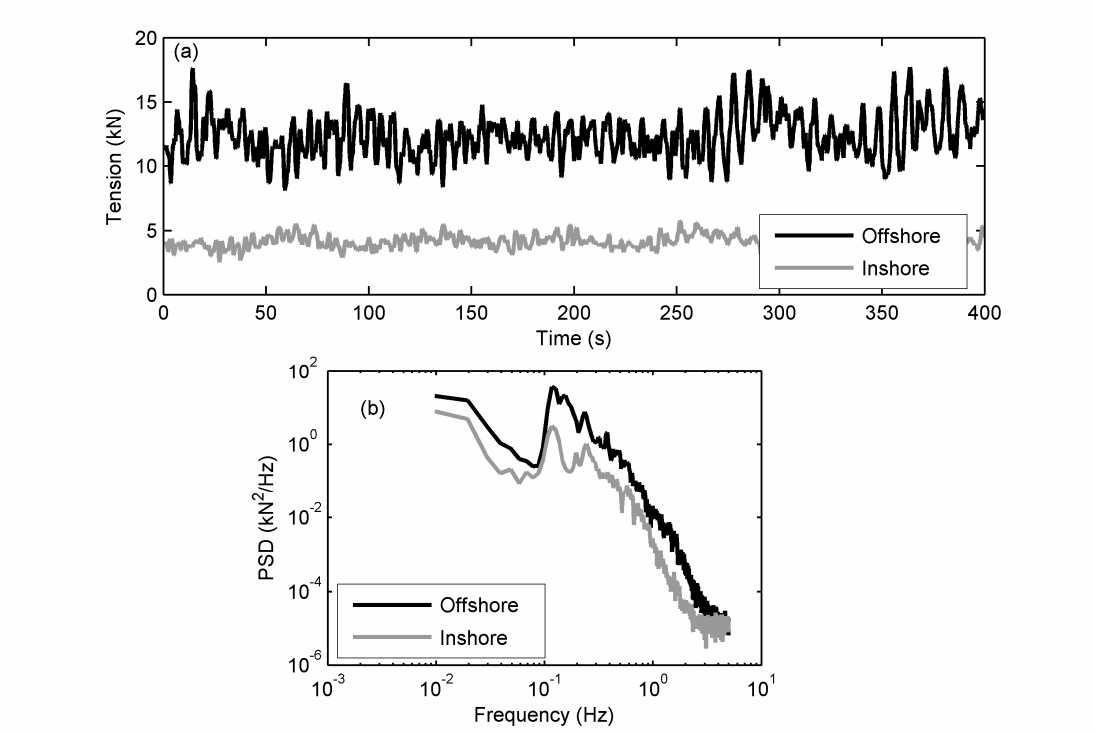

Figure 6.17 (a) Load record and (b) load spectra from 21:00 27/6/2004 (rising tide).

The low dynamic loading recorded by the inshore load-cell may be related to the low mean tension. The anchor ropes would hang in a catenary under low loads. At high loads, they would be taut. Thus with low anchor rope tensions, a greater movement of the long-line may occur with less change in tension. A taut anchor rope allows less movement, and will experience greater changes in load. Such a low value of mean tension was only detected over a short period during the deployment. The difference in tension between the inshore and offshore anchor rope was unusually large, and suggests that either currents were particularly strong during this period, or the wave field acted in conjunction with the tidal currents to push the long-line in the inshore direction.

The period of high wave activity continued into the morning of the 28th June 2004. The load fluctuations on the inshore anchor rope increased as the tide changed, with the current pulling the long-line in the offshore direction. An example of the load record during strong waves on the falling tide is plotted in Figure 6.18. In this sample, the average load on the inshore load-cell was greater than that of the offshore load-cell. While the size of load fluctuation at the inshore load-cell was greater than that in Figure 6.17, the load fluctuations, and load spectra, were still greater at the offshore load-cell. It appears that high wave energy, with the waves acting in the direction of the current, produce the greatest loadings on the offshore anchor rope.

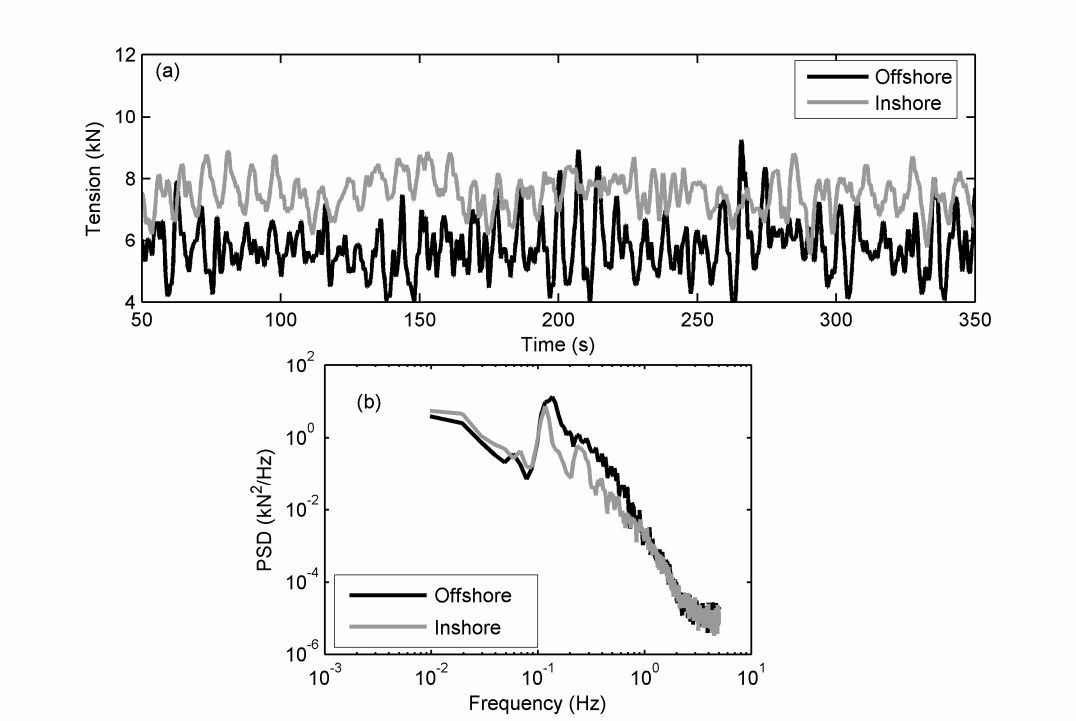

Figure 6.18 (a) Load record and (b) load spectra from 02:30 28/6/2004 (falling tide).

On occasions, the load records indicate a low frequency oscillation of the long-line, with loads alternatively increasing and decreasing either end as the structure moves. As shown in Figure 6.19(a), this can cause load variations of the order of 3 kN. The data plotted were recorded on the falling tide during a period of low wave energy. Inspection of the load time-series indicates that the period of oscillation was approximately 120 s. This corresponds with high energy spectral density seen at low frequencies of around 0.01 Hz. It is not clear what causes this behaviour. It may be due to the elasticity of the structure and the mooring ropes, with the structure oscillating at a low frequency.

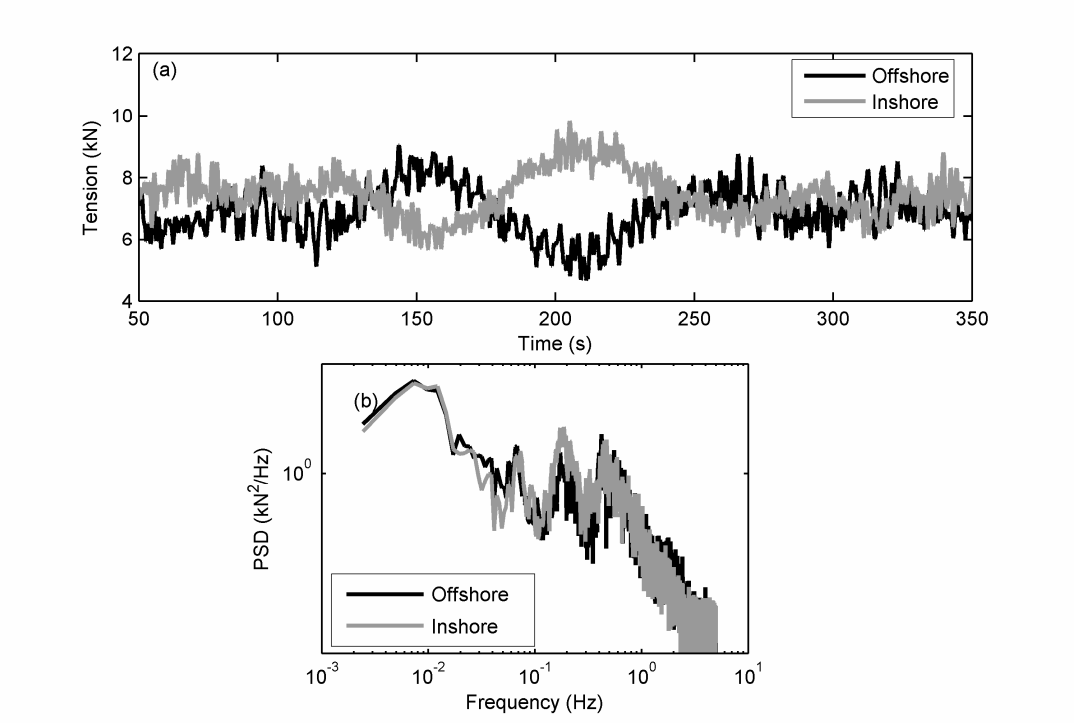

Figure 6.19 (a) Load record and (b) load spectra from 23:30 24/6/2004.

Following the method used with the Collingwood data, an indication of the dependence of load on the applied wave field can be obtained by constructing a regression of load PSD against the wave PSD at each frequency (e.g. Figure 6.20(a)). A linear regression is used, and forced through a y intercept of zero as no fluctuating load is expected if there is no wave energy. In support of this assumption, regression coefficients calculated with no restriction on the y-intercept gave very similar results for frequencies above 0.05 Hz. As we are primarily interested in frequencies within the range of ocean swell, the ratios of load spectra to wave spectra were calculated for frequencies in the range 0.05 Hz to 0.234 Hz (wave periods between 20 seconds and 4.3 seconds. The results are plotted in Figure 6.20(b), and the R^2 value for the regressions shown in Figure 6.20(c). The regression slope indicates the relative response in anchor rope tension to wave energy (frequency response function).

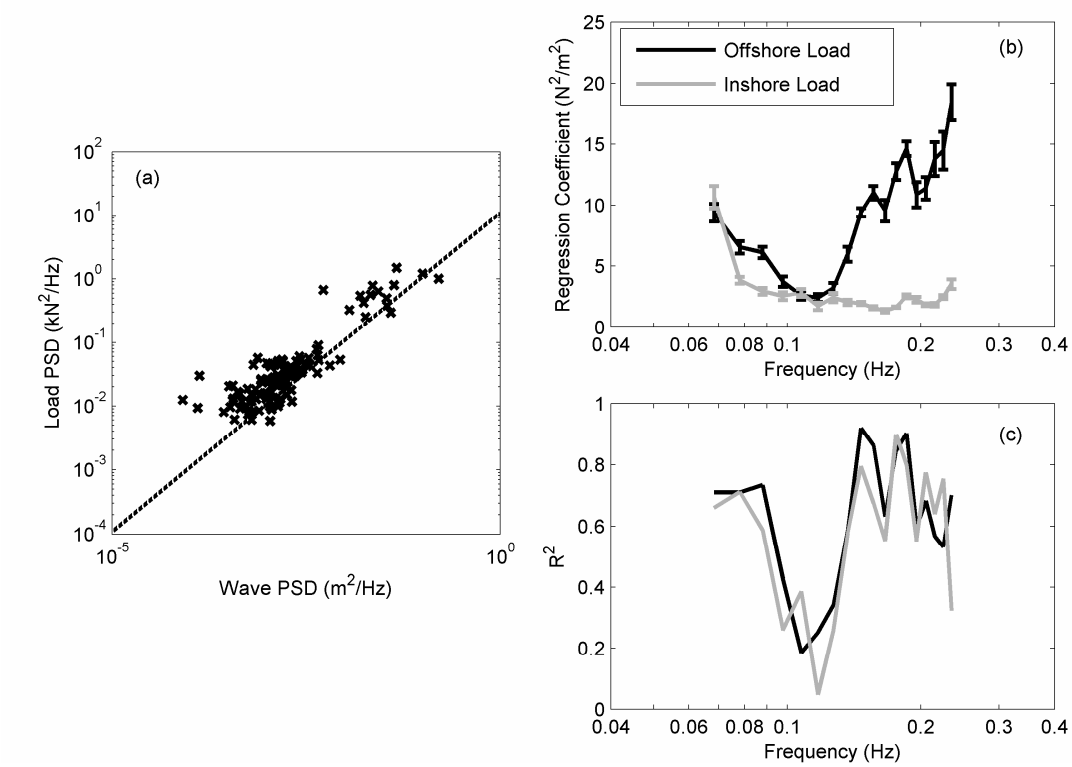

Figure 6.20 (a) Load PSD vs wave PSD for offshore load-cell at 0.195 Hz with dashed line indicating linear regression, (b) slope of this regression as a function of frequency with 95% error bars, and (c) R^2 value for the regression.

To determine the appropriateness of assuming a linear relationship between wave PSD and load PSD, an exponential function of the form $y = Ax^b$ was also fit by regression. While the regression exponent b was found to fall within the range 0.64 and 0.96 for the offshore load-cell, and between 0.59 and 0.88 for the inshore load-cell, the R^2 values for the exponential regression were no better than for the linear regression (Figure 6.21). Therefore, the assumption of a linear wave to load PSD relationship is considered to give a sufficient estimate of the frequency response function.

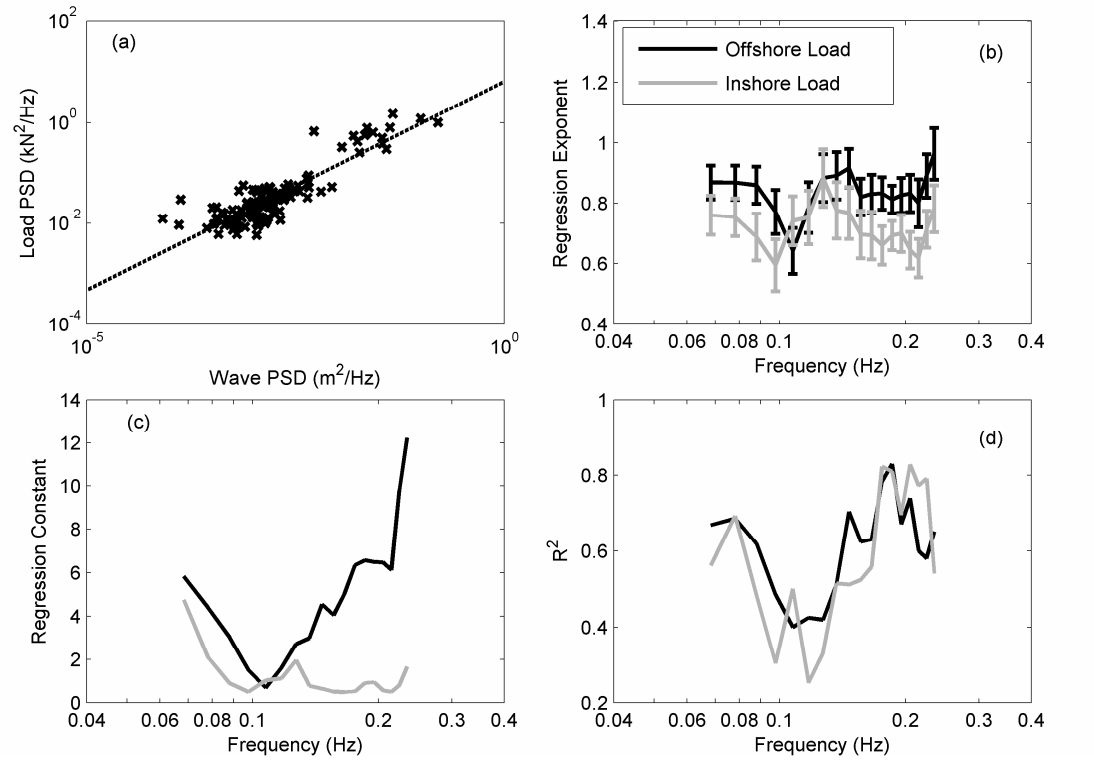

Figure 6.21 (a) Load PSD vs wave PSD for offshore load-cell at 0.195 Hz with dashed line indicating exponential regression, (b) exponent *b* from regression $y = Ax^b$ as a function of frequency with 95% error bars, (c) constant *A* for regression, and (d) R^2 value for the exponential regression.

6.5 Discussion

6.5.1 Static Loads

The anchor rope tension at both sites was dominated by tidal water depth variations, with high loads at high tide, and low loads at low tide. The tidal depth variation of 4.15 m at Golden Bay resulted in a change in static load (or dead-load, caused by the buoyancy of the floats) of 5.7 kN, while at Pigeon Bay, the tidal variation of 2.7 m resulted in dead-load changes of 4.0 kN. Superimposed on the tidal load was the effect of currents, causing variations of approximately 2 kN between rising and falling tides at Golden Bay, and ~ 0.5 kN at Pigeon Bay, and waves. Mussel long-lines are generally constructed so that the maximum slope of the anchor ropes is 2:1, or 26.6° from horizontal. At mid-tide, when currents were strongest, the slope of the anchor ropes would be approximately 23° at Golden Bay, and 24.5° at Pigeon Bay. The horizontal component of the change in anchor rope tension indicates the size of the drag on the long-line. Current drag was therefore approximately 1.8 kN at Golden Bay, and 0.4 kN at Pigeon Bay.

The difference between the two sites in the tension variation attributed to drag can be explained by the geometry and site characteristics. At Golden Bay, currents approached ~ 0.1 m/s, the long-line was orientated at an angle to the flow of 30°, and the droppers had an average length of ~ 8 m. At Pigeon Bay, the currents were lower (~ 0.05 m/s based on field measurements), the long-line was inline with the tidal

currents, the droppers were shorter with a length ~ 4 m, and droppers were more widely spaced. These factors would result in reduced drag forces from tidal currents at the Pigeon Bay site relative to the Golden Bay site. The larger mussels on the long-line at Pigeon Bay would have increased the drag, but it is likely this effect was small in comparison to that of orientation and current strength.

6.5.2 Wave Forces

The anchor rope forces at both sites were observed during periods of small wave heights, with the exception of a short period at Pigeon Bay where large fluctuations in load were recorded, but no wave record was obtained at that time. This assessment of the wave-induced loadings on mussel farm anchor lines therefore relates only to relatively mild wave conditions where significant wave heights are less than 0.5 m.

The measurements of anchor rope tension show that wave action can cause significant load variation. The spectral response indicates that the anchor rope loads are strongly linked with the wave spectra, with load spectra closely following the wave spectra for long-lines orientated both across, and in-line with, the waves. The spectral response of the anchor loads with respect to the wave field was a function of frequency. At the Golden Bay field site, where the long-line was oriented across the wave field, the strongest response was seen at low frequencies, with the response coefficients (derived from a linear regression) decreasing with frequency. It is not immediately clear what happens at frequencies above the deep-water cut-off (0.27 Hz) as waves with frequencies above this point could not be recorded using a pressure sensor on the seabed. A similar behaviour was seen for the inshore load-cell at Pigeon Bay. However the spectra here show a peak in load fluctuations at frequencies above the deep-water cut-off, indicating a high sensitivity to high frequency waves. The anchor rope tensions are produced by a combination of wave drag against the structure, and perhaps more importantly, the buoyancy of the floats. As a wave passes, the buoyancy of the floats causes them to rise and fall with the wave. At very low wave frequencies, a strong response might be expected as the whole long-line is raised and lowered by the passing wave. In the extreme case, the tidal fluctuations produced large variations in anchor rope tension. As the wave frequency increases, the wave length decreases. Different parts of the long-line may be at different parts of a wave cycle, generating opposing loads along the length of the structure which could cancel to some degree. This would reduce the loadings on the anchor ropes. This effect would increase with increasing wave frequency as the wave length decreases. For example, at Pigeon Bay, waves with a frequency above ~ 0.08 Hz would have a wave-length shorter than the length of the long-line, and the response coefficients for the inshore load-cell were low. However, at high wave frequencies, where the water surface movements are rapid, the mass of the droppers may prevent the floats from accelerating in response to the waves. As the floats are submerged, the buoyant force will increase rapidly. The high

sensitivity of the anchor ropes to high frequency waves is likely due to the inertia of the buoys and mussel droppers near the anchor rope.

For the long-line oriented inline with the wave motion (Pigeon Bay), larger wave load variability was seen at the offshore anchor rope. In contrast to the inshore load-cell, the offshore load-cell shows a strong increase of the response coefficient (frequency response function) at frequencies greater than 0.14 Hz. Without direct measurements of the long-line motion, we can only speculate as to why the spectral response at the offshore load-cell was so much stronger than at the inshore load-cell at high frequencies. It is possible that there is some degree of wave energy dissipation, particularly at higher wave frequencies, along the length of the long-line. The up-wave (or offshore) buoys and droppers may provide a degree of shelter to those further along the long-line. Wave attenuation measured across the Golden Bay farm was found to be small (previous chapter); however, waves travelled across rather than along the long-lines. With waves travelling along a long-line, it is possible that locally there is considerable wave energy lost to drag on the droppers and buoys. The reason for the peak in load spectra at the inshore load-cell at ~ 0.4 Hz is not clear, although the high frequency suggests that the waves may have been generated locally, and so did not travel from offshore to inshore.

The observation of a higher response coefficient at frequencies around 0.18 Hz at the Golden Bay farm coincides with a decrease in wave energy dissipation detected at similar frequencies. In the previous chapter, wave dissipation was assumed to be caused by drag on the submerged elements of the long-lines. The higher load response coupled with the lower dissipation may indicate that some form of structural response occurs at these frequencies. It is possible that parts of the long-line, such as the droppers, respond readily at these frequencies, and so move with the waves. The reduced velocity of the water relative to the dropper would result in less drag, and may be the source of the reduced dissipation. This relationship between the greater response of the anchor rope tensions to waves forces, and the reduced wave dissipation at 0.18 Hz is worthy of further study.

6.5.3 Response to Large Waves

No wave record was obtained during the period of highest anchor rope loads recorded at the Pigeon Bay site. An estimate of the likely wave heights can be made using the regression-calculated response coefficients. Noting that the exponential regressions indicate that the relationship between the wave PSD and load PSD were slightly non-linear, the coefficients plotted in Figure 6.21(b) and (c) are used to estimate the wave spectra corresponding to the offshore load spectra during peak loads, e.g. Figure 6.17(b). This method gives an estimate for significant wave heights of 1.9 ± 0.1 m. The regression constants for the inshore load-cell give a similar estimate for significant wave height of 1.85 ± 0.05 m. It should be noted that at no point during the deployment did tension on any of the monitored anchor ropes

decrease to zero. This means that the anchor ropes were not slack at any time. This is worthy of consideration as it is likely that snatch loads could be high if a slack anchor rope allows part of the long-line to build momentum.

6.6 Summary

The tension in the anchor ropes of mussel long-lines was measured for a long-line in Golden Bay oriented perpendicular to the direction of wave propagation, and for a long-line at Pigeon Bay oriented in-line with the direction of wave propagation. At both sites, the tension in the anchor ropes was primarily controlled by the tide, with highest loads at high tides. Superimposed on the tidal signal was the effect of currents, with drag forces from currents contributing approximately 2 kN to the tension on the mussel long-line in Golden Bay, and ~ 0.5 kN at Pigeon Bay.

Even though wave energy was generally low at both sites, the anchor rope tension at both sites showed a strong response to the waves with load spectra following the shape of wave spectra. For the mussel long-line at Pigeon Bay, oriented in-line with the wave direction, the highest peak loads and largest load variations were recorded on the up-wave anchor rope. The up-wave or offshore anchor rope also responded more strongly to mid-frequency waves than the inshore anchor rope. This response was particularly evident for waves with wave-lengths less than half the long-line length. The inshore anchor rope of the long-line aligned with the waves (Pigeon Bay) showed a similar frequency dependent response to wave spectra as the anchor rope of the long-line across the waves (Golden Bay). Both anchor ropes at the Pigeon Bay site showed a load spectra peak at ~ 0.4 Hz, which may be due to locally generated waves travelling at directions other than from offshore to inshore.

Some interesting behaviours were observed at Pigeon Bay. During a period of low wave energy while the tide was falling, a low frequency (period 120 s) oscillation of loads between the inshore and offshore anchor tension could be seen. This suggests that the long-line was moving back and forth as a coherent body. During the period when the largest wave loadings were recorded, the offshore anchor rope showed large tension fluctuations of up to 8 kN, while the inshore anchor rope had both a lower mean tension (thought to be due to the combined action of waves and tidal flow) and fluctuations of less than 1 kN. The data suggests that higher loads occur at the offshore anchor rope, and that waves acting in the direction of the current cause the highest wave loads for the offshore anchor rope. This indicates that the offshore anchor rope is the most critical for the purpose of structural design.

CHAPTER 7 EFFECT OF MUSSEL FARMS ON SESTON DEPLETION

7.1 Introduction

An important issue with large scale aquaculture is the depletion of seston (Hawkins *et al.*, 1999; Pilditch *et al.*, 2001). Seston consists of photosynthetic algae (phytoplankton), and inorganic or organic particles (other than algae) in suspension. Large concentrations of filter-feeders such as mussels may be able to consume seston at a rate significantly higher than re-growth or production can occur. The action of currents may result in any region of depletion extending over an area larger than the farm, thereby reducing food supply to other organisms in the vicinity of the farm. A key aspect of assessing the impact of aquaculture is the determination of the magnitude and extent of any seston depletion.

While this thesis is primarily concerned with physical as opposed to biological effects, measurements of fluorescence and turbidity obtained during CTD casts (used to assess mixing and stratification), along with acoustic backscatter from ADCP transects provide potentially useful information on the degree of phytoplankton depletion caused by the Collingwood mussel farm. In this chapter, a brief description of how the data were obtained is given in section 7.2, and observations of fluorescence, turbidity and backscatter are reported in section 7.3. These observations, and estimates of mussel feeding rates, are used to consider the likely scale and magnitude of seston depletion in section 7.4, and a summary presented in section 7.5.

7.2 Experimental Methods

7.2.1 Study Site

Measurements reported in this chapter were made in the vicinity of the mussel farm at Collingwood, Golden Bay on the 10th and 17th April. This site was described in detail in section 2.3.1.1.

7.2.2 Measurement of Water Column Properties

The measurements of fluorescence and turbidity were obtained from CTD casts measuring conductivity and temperature in order to assess the effect of the farm on mixing and stratification (Chapter 4). Backscatter data has been extracted from the ADCP transects of water velocities presented in Chapter 3. Surveys consisted of transects through or adjacent to the mussel farm.

7.2.3 Instrumentation

A RBR XR-420-CTD was used at the Collingwood site on the 10th and 17th April 2002. This instrument had additional sensors for fluorescence (wave length 450-500 nm) and turbidity. CTD profiles or casts were taken by gently lowering the instrument by hand from the side of a small (6-7 m length) boat.

Locations of profiles were recorded using GPS. Backscatter data was extracted from velocity transects measured with a 1200 kHz RDI ADCP Workhorse.

7.3 Results

7.3.1 Site Properties

A detailed description of water conditions at the study site is given in section 4.3.1. In summary, density at the site was primarily controlled by salinity differences, with cool fresher water overlying warmer saline water, particularly at the northern end of the farm.

7.3.2 Chlorophyll *a* Depletion

Chlorophyll fluorescence (wave length 450-500 nm) is a widely used method of measuring chlorophyll *a* concentrations, which in turn can be used for estimating phytoplankton concentration (Lorenzen, 1966). Chlorophyll *a* concentration can only be used in estimating the concentration of phytoplankton, as organisms that do not photosynthesise, such as zooplankters, do not have chlorophyll. In these experiments, fluorescence was measured using a CTD equipped with a fluorometer. However, the conversion from fluorometer output to phytoplankton biomass is not straightforward, as the ratios of fluorescence to chlorophyll *a*, and of chlorophyll *a* to phytoplankton biomass are highly variable. A number of the factors that influence these ratios are summarised by Cullen (1982), and include variations in fluorescence to chlorophyll *a* ratios due to nutrient starvation, variability among taxa, and photo-inhibition due to strong light. The ratio of chlorophyll *a* to phytoplankton biomass also varies due to factors such as nitrogen limitation, irradiance, temperature, and species composition. It is therefore not sufficient to apply a general conversion factor to obtain chlorophyll *a* or phytoplankton concentrations from measured fluorescence. As a minimum, fluorometer data requires calibration against extracted chlorophyll *a* concentration from samples collected on site. As this calibration was not done, the fluorescence data collected at Pigeon Bay and at the Collingwood field site on the 10th and 17th April 2002 can only give qualitative indications of changes in chlorophyll *a* concentration, and therefore phytoplankton levels. The factors influencing the ratios of fluorescence to chlorophyll *a*, and of chlorophyll *a* to phytoplankton biomass are unlikely to vary over the study site to the extent that significant increases in biomass are accompanied by a decrease in fluorescence. Therefore, fluorescence is reported as the fluorometer output voltage, with higher voltage, indicating higher fluorescence, interpreted as indicating higher concentrations of chlorophyll *a* and phytoplankton.

At the Collingwood (Golden Bay) study site, there was little evidence of reduced fluorescence within the farm. Two surveys were taken of water properties in and around the farm on 17th April 2002, the first in the morning on a rising tide, and the second in the afternoon on a falling tide. Profiles have been grouped inside and outside of the farm. Profiles taken on the edge or within 100 m of the farm were grouped with

those inside the farm if they were immediately downstream of the farm. As the two surveys were taken at different times, the data are plotted separately in Figure 7.1. There is considerable variation in fluorescence outside the farm in both surveys, particularly from 4 to 10 m depth. Profiles of fluorescence within the farm taken in the morning, Figure 7.1(a) solid circles, show fluorescence grouped at the lower end of the range of fluorescence observed outside the farm (open circles). In the afternoon, Figure 7.1(b), fluorescence within the farm lies in the middle of the fluorescence range measured outside the farm. Fluorescence decreased towards the surface during both surveys, which may be due to photo-inhibition as described above.

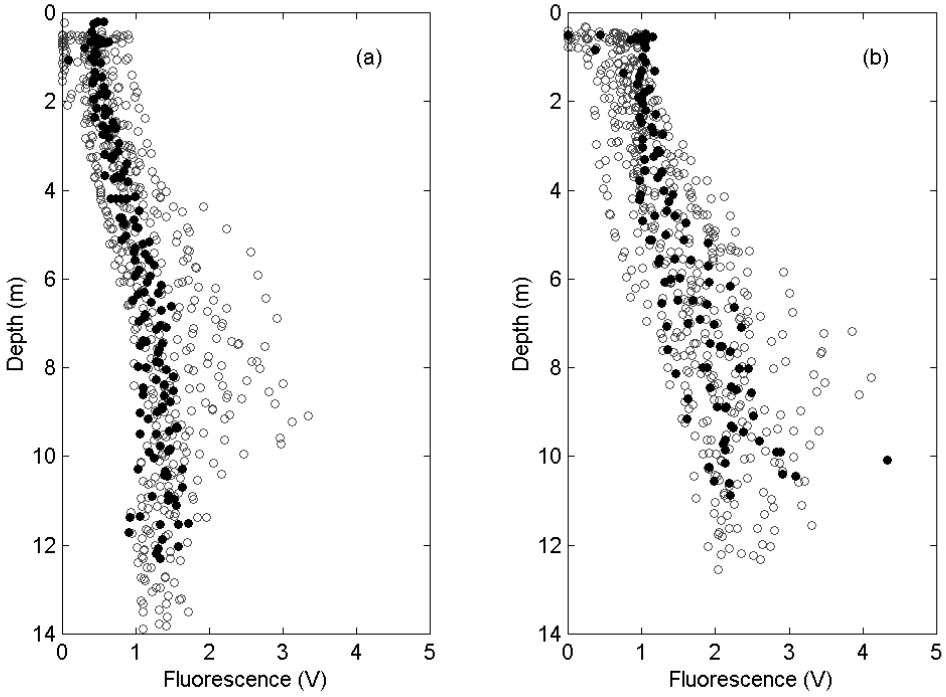

Figure 7.1 Fluorescence versus depth for (a) 17 April 2002 am, and (b) 17 April 2002 pm. Solid black circles are profiles within the farm, grey open circles are profiles outside the farm.

Fluorescence was higher in the second survey (taken in the afternoon), particularly deeper in the water column. Inside the farm, there was an increase in both the average and the variability of fluorescence compared to the data from the morning survey.

If fluorescence gives an indication of the concentration of phytoplankton, then it might be expected that depletion within the farm would be highest in the morning. The phytoplankton concentration is a balance between consumption (by the mussels) and production (growth). As phytoplankton production requires light, production rates would be lower during the night. Assuming a constant consumption rate by the mussels, phytoplankton consumption is more likely to exceed production during the night, leading to a reduction in observed fluorescence. During the day, with higher production rates, the phytoplankton

levels may recover. As both surveys were taken during daylight, the fluorescence to chlorophyll ratios should be similar as photo-inhibition induced changes in fluorescence occur rapidly with changes in light intensity (Vincent, 1979). This supports the interpretation of the data that the phytoplankton concentrations increase between the two surveys. The body of water sampled is not necessarily the same in both surveys, as the tidal excursion (measured inside the farm at the moored ADP) is of order 1.5 km. However, as surveys were made near the middle of the rising and falling tides during the same tidal cycle, fluid is likely to be in a similar position.

Statistically, there is no significant difference between the fluorescence levels inside and outside the farm. Fluorescence data has been grouped into 2 m depth bins, and the average and standard deviations calculated for each bin. These values are plotted as a profile in Figure 7.2. Considering the data from the morning survey, when phytoplankton depletion might be expected to be greater, the data shows that variability in fluorescence (standard deviation) was higher outside the farm (Figure 7.2(a)). While the average values of fluorescence inside the farm were lower than outside, particularly between depths of 5 and 9 m, they were within one standard deviation.

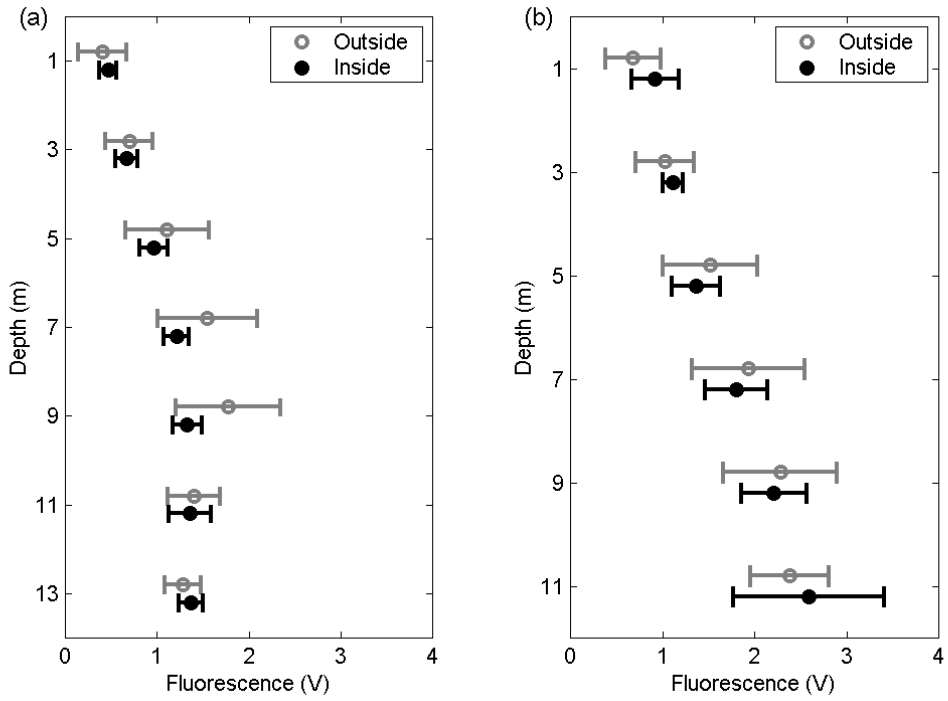

Figure 7.2 Fluorescence averaged into 2 m depth bins inside and outside Collingwood mussel farm, (a) 17 April 2002 am, (b) 17 April 2002 pm. The error bars show ± 1 standard deviation.

7.3.3 Turbidity and ADCP backscatter

At the Collingwood, Golden Bay, study site, turbidity was measured in conjunction with CTD/fluorescence on the 10th and 17th April 2002. Areas of low turbidity appeared to occur within the

farm. Turbidity data is plotted against depth in Figure 7.3(a), while Figure 7.3(b) shows turbidity data averaged into 2 m depth bins. As with the fluorescence data, the average values of turbidity were lower inside the farm, as was the variability indicated by the standard deviation shown in Figure 7.3(b). However the lower turbidity within the farm is not statistically significant, lying within one standard deviation of the turbidity outside the farm.

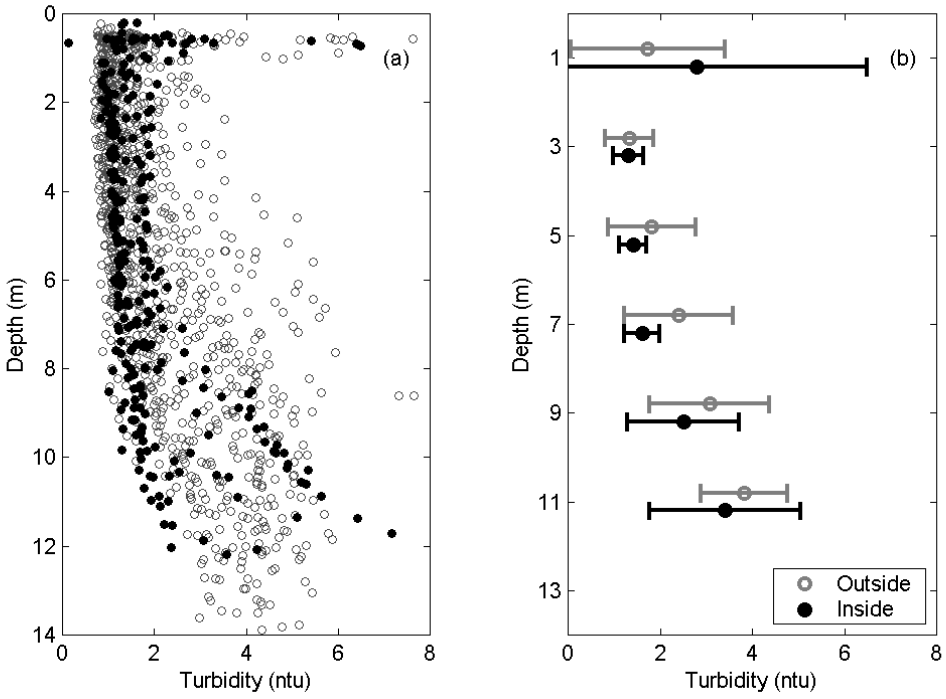

Figure 7.3 (a) measurements of turbidity inside (solid dots) and outside (open grey circles) Collingwood mussel farm, and (b) turbidity averaged into 2 m depth bins inside and outside farm, error bars show ± 1 standard deviation.

Consistent with the observation of reduced turbidity was a small decrease in ADCP backscatter data inside the farm. An ADCP operates by measuring the Doppler frequency shift in sound waves reflected from suspended material (both organic and inorganic) in the water column. One useful parameter obtained from ADCP measurements is the strength of the reflected signal, or backscatter. Backscatter has been used to estimate suspended sediment concentrations (Miller *et al.*, 1999), and detect plumes of suspended sediment (Trump *et al.*, 2000) or detritus (Massa and Bosma, 2000). It has also been related to density and type of zooplankton, (Flagg and Smith, 1989; Roe *et al.*, 1996; Stanton *et al.*, 1996).

The reduction in backscatter is small, ~ 2 to 3 dB, as shown in the cross-section plotted in Figure 7.4, taken on the morning of 17 May 2003.

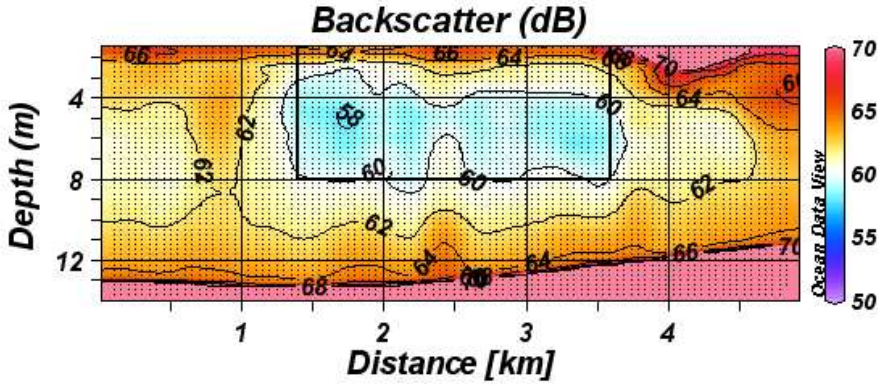

Figure 7.4 Cross-section through farm (rectangle from ~ 1.4 to 3.6 km) showing back-scatter intensity. Tidal currents were from right to left.

Back-scatter shows a minimum at a depth of 4 to 6 m in most transects, including those taken outside the farm. However the lowest backscatter occurs in or near the farm. Low back-scatter can also be seen downstream of the farm, in a region consistent with a wake In Figure 7.5, a cross-section west to east through the farm is plotted. Given that the tidal currents during this transect were in a south-east direction, the low backscatter to the right of the farm (>1.7 km on the *x* axis) is in the farm wake.

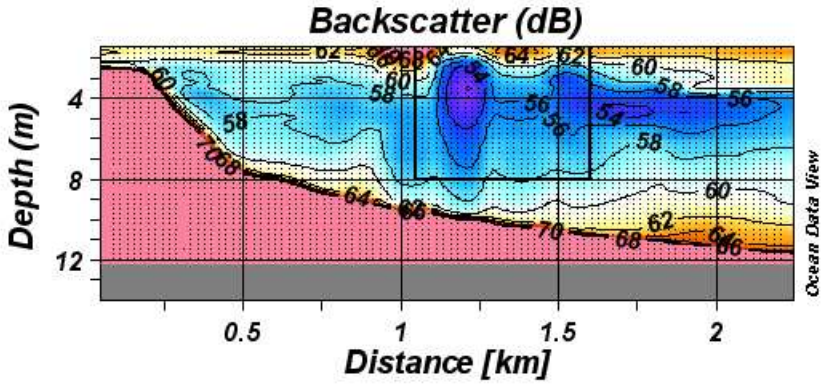

Figure 7.5 Cross-section of back-scatter intensity west (left) to east (right) through Collingwood mussel farm (rectangle from ~ 1.05 to 1.6 km). Tidal currents are from left to right.

Changes in the amount of backscatter indicate that there is a change in either the density or type of scattering material in the water column. The factor responsible for the change can not be identified as water samples were not analysed for suspended sediment concentrations or plankton species.

7.4 Discussion

The slight reductions of fluorescence, turbidity and backscatter within the Collingwood mussel farm are consistent with seston depletion (Ogilvie, 2000; Pilditch *et al.*, 2001). The reduction detected was not

statistically significant, due in part to the high variability in both fluorescence and turbidity outside the farm. A reduction in fluorescence would indicate that phytoplankton is depleted. Turbidity reduction may result from the mussels filtering out suspended solids, and rejecting these in the form of pseudofaeces (particles bound in mucous). Psuedofaeces are relatively large in size compared to suspended sediment. Although the suspended sediment is still present, it is bound up into larger masses, and turbidity would be decreased. The psuedofaeces settle slowly, so remain suspended in the water column for some time. The effect on backscatter is less clear, as there is no information regarding the acoustic properties of pseudofaeces. However a net reduction in particulates, both organic and inorganic, would be expected to cause a reduction in backscatter.

Whether significant depletion should be expected can be estimated using mussel feeding rates. Clearance rates for *P. canaliculus* are related to both the size of the mussel and food availability (Waite, 1989; Hawkins *et al.*, 1999). Typical clearance rates, as litres of water filtered by a mussel per hour, obtained from NIWA (unpublished) are used in Table 7.1. Except for at very high seston concentrations, the clearance rate expresses the volume of water from which mussels effectively remove all organic particulates. Measurements of mussel size distributions at the Collingwood mussel farm were made by NIWA staff in early 2002 (unpublished data). From these, the total clearance rate for the farm can be estimated.

Mussel size (mm)	Clearance Rate (litres hr^{-1} per mussel)	Number of mussels	Combined clearance rate (m^3 hr^{-1})
35-60	1.3	22,468,000	29,208
60-85	4	44,242,000	176,968
85-100	8	35,046,000	280,368
Total			486,544

Table 7.1 Clearance rates for *P. canaliculus* by size range (Hatton 2004, unpublished data), mussel size distribution for Collingwood farm (NIWA 2002, unpublished data), and total clearance rate.

Using the farm dimensions of 2450 m by 650 m, and an average dropper length of 8 m, the volume of the farm is 12,740,000 m^3. Therefore, the mussels will require 26 hours to clear an equivalent volume. However, the water in the farm is not stationary; rather it is carried through the farm by the tide. It is more informative to compare the total clearance rate against the volume flux through the farm. From the ADP mooring within the farm (ADP2 15th to 17th May 2003), average mid-tide velocities within the upper 8 m of the farm are 5.47 cm s^{-1}. As the current enters the farm at an angle of 55^o to the long-axis of the farm, the net flow rate into the farm is 0.0547 x 8 x (2450 x sin(55^o) + 650 x cos(55^o)) = 1041 m^3 s^{-1} or 3,750,000 m^3 hr^{-1}. The mussel clearance rate is approximately 13% of the flow rate through the farm.

Based on this calculation, it is not surprising that observed changes in fluorescence, turbidity and acoustic backscatter are small.

It is possible that depletion of seston greater than the 13% estimate could occur as patches of water may pass through the site several times due to the oscillatory tidal flow. The same water would then be re-filtered several times. This suggests that residual tidal velocities (the net displacement over several tidal cycles) could be used in depletion estimates. For example, if the tide carried water 2.5 km to the north on one phase of the tide, but only 2.3 km south on the opposite phase, the net tidal displacement would be 0.2 km. If the farm were 2.4 km long, a particle would be within the farm for a total of 2.4/0.2 = 12 tidal cycles or ~ 6 days. A major problem with this method is the neglect of the horizontal turbulent diffusion that would occur over several tidal cycles. This diffusion would reduce the net residence time within the farm. The longest record of velocities within in the farm obtained in this study was 1 week (10-17th April 2002), insufficient to accurately estimate residual velocities. Also, the growth rates of the different organisms that make up seston would need to be considered, as production may offset depletion to some degree. These factors could be addressed by a coupled biological/hydrodynamic model, such as that of Pilditch *et al*. (2001). Such a model should ideally be two- or three- dimensional, rather than the one-dimensional model of Pilditch *et al.*, to account for lateral diffusion. As Pilditch *et al*. identify, such models would be limited without more exact measurements of the dispersion coefficients.

7.5 Summary

While small decreases of fluorescence, turbidity, and acoustic backscatter (from ADCP measurements) were seen inside the farm, these decreases were not significant, partly because of the high variability in these properties outside the farm. Estimates using mussel clearance rates indicate that the mussel crop is able to filter approximately 13% of the flow through the farm.

CHAPTER 8 INTRODUCTION TO LABORATORY EXPERIMENTS

8.1 Introduction

Physical large-scale effects of mussel long-line structures have been described in the preceding chapters. In particular, analytical predictions and field measurements were used to quantify changes in water currents (chapter 3), mixing (chapter 4) and wave energy (chapter 5). The key factor responsible for the effects of the mussel farm was the drag on the submerged structures, particularly the mussel droppers that constitute the bulk of the farm. The reduced velocities within and downstream of the farm, the energy dissipated through turbulence, and the mechanical stirring causing diapycnal mixing all result from the combined interactions of the fluid with thousands of mussel droppers. The large-scale hydrodynamic effects of the farm are therefore determined by small-scale flow interactions with individual mussel droppers, and even individual mussels. Because of this connection between the large and small scale hydrodynamics, the field-based study presented in the earlier chapters is complemented in this and subsequent chapters by an investigation of flow features on the scale of the mussel droppers. As well as the hydrodynamic implications (e.g. drag, energy dissipation, turbulence), these small-scale flow features have important biological implications. Mussels are filter feeders and rely on fluid transport for supply and removal of nutrients and waste. Understanding how various configurations of mussel long-lines affect this transport will aid in improved design of these structures.

The approach followed in the following chapters is to consider a mussel long-line as an array of very rough circular cylinders. The basis for this approach is geometric. The mussel crop rope hangs in vertical loops. Except at the bottom of the loops, each loop resembles two vertical lines (droppers). The droppers resemble very rough circular cylinders in cross-section (Figure 8.1), with lengths around 2 orders of magnitude greater than their diameter. The roughness elements of the mussel droppers are the protruding mussel shells. From this viewpoint, some insight into the small-scale flow features may be gained from existing knowledge on cylinder flows.

There has been an almost overwhelming amount of research on flow around circular cylinders, inspired by the wide range of behaviours exhibited by what is conceptually a simple system. However, there are a number of areas relevant to the flow around mussel droppers where the knowledge is incomplete. These areas will be identified in the literature review that follows, and summarised in section 8.3. In particular, the areas where there are gaps in the literature include the effect of large surface roughnesses, and of the interactions between smooth and rough cylinders in arrays.

Figure 8.1 Close-up view of mussel dropper.

Two approaches are used in the experiments presented in the thesis: drag measurements, and Particle Tracking Velocimetry (PTV). These two methods provide different but complementary data. Drag is a fundamental parameter as the drag on mussel droppers determines the structural loads, and the effect on the flow through energy dissipation. PTV is a quantitative flow visualisation technique that provides information on the flow patterns and distributions of turbulence caused by an obstacle. The two-dimensional flow fields that can be captured using PTV allow insight into the mechanisms and interactions that influence drag, flow modification, turbulence, and energy dissipation. These two methods are described in detail in Chapter 9.

In the following sections of this chapter, literature on the flow around circular cylinders and cylinder arrays are reviewed to establish a knowledge base that may be applied to the flow around mussel droppers (section 8.2). This is followed by an outline of the areas of research investigated in the thesis. In following chapters, results from a range of experiments are presented which were designed to investigate particular effects relevant to configurations used in mussel aquaculture. Chapter 9 describes the methodology, equipment and techniques for experiments using particle tracking velocimetry (PTV) and drag measurement. Chapter 10 presents experimental results for single cylinders, focusing on the effect of extreme surface roughness. Chapter 11 presents results from experiments on single rows of smooth and rough cylinders normal to the flow. In Chapter 12, other cylinder configurations are examined, including double rows of cylinders normal to the flow, and single rows at an angle to the flow.

8.2 Literature Review

8.2.1 Definition of Key Parameters

Before reviewing the literature, the key parameters and dimensionless groups for cylinder flow will be defined. Firstly, the two fundamental scales for flow around a cylinder are the diameter D, and the undisturbed fluid velocity U_0. The most significant factor in cylinder flow is the importance of viscosity. These three parameters form the Reynolds number, using the kinematic viscosity ν,

$$Re = \frac{U_0 D}{\nu}. \tag{8.1}$$

Surface roughness may have an effect on the flow, and is expressed as the ratio of the size of the roughness k_s to the cylinder diameter,

$$\frac{k_s}{D}. \tag{8.2}$$

While the mean flow around long cylinders is essentially two-dimensional, three-dimensional effects become important for shorter cylinders. The effect of cylinder length L is non-dimensionalised as an aspect ratio,

$$\frac{L}{D}. \tag{8.3}$$

In an array of regularly spaced cylinders, another governing parameter is the centre to centre spacing of the cylinders S. Spacing is also non-dimensionalised by cylinder diameter,

$$\frac{S}{D}. \tag{8.4}$$

The forces F (units of N) on the cylinder are non-dimensionalised as a drag coefficient in the direction of flow,

$$C_D = \frac{2F_D}{\rho D L U_0^{\,2}}, \tag{8.5}$$

where ρ is the fluid density; and a lift coefficient for forces perpendicular to the mean flow,

$$C_L = \frac{2F_L}{\rho D L U_0^{\,2}}. \tag{8.6}$$

Finally, a characteristic of cylinder flow is the regular shedding of eddies. The frequency f of eddy shedding is expressed in non-dimensional form by the Strouhal number,

$$S_t = f\frac{D}{U_0}. \tag{8.7}$$

8.2.2 Flow Around Single Smooth Cylinders

The flow around a cylinder passes through a range of different regimes as the flow transitions from fully laminar to fully turbulent. Fully laminar flow occurs at very low Reynolds numbers, and is not relevant to the present study. The transition from a laminar to turbulent condition does not occur at all regions in the flow simultaneously, rather a succession of transitions occur (Roshko and Fiszdon, 1969). These transition states can be classified by the region of flow in which the transition from laminar to turbulent flow occurs.

The transition states for smooth circular cylinders are primarily governed by Reynolds number. However, transition states are sensitive to small disturbances such as free-stream turbulence or surface roughness. These disturbances can initiate transitions at lower Reynolds numbers, or inhibit the occurrence of some flow structures. This review will begin with disturbance-free flow around a single smooth cylinder, and the effect of a disturbance such as surface roughness will be discussed latter.

As indicated above, a succession of turbulent transitions occurs at different regions in the flow. Zdravkovich (1997) presents a thorough review of these transition states, and provides much of the information summarised below. Before describing this progression, the key regions in the flow where these transitions occur are identified in Figure 8.2. Upstream of the cylinder is the uniform turbulence-free flow with velocity U_0. Behind the cylinder is the wake, where velocities are reduced with respect to the mean flow. A free shear layer is formed between the wake and surrounding flow. Two separation points occur where the wake detaches from the cylinder. A boundary layer occurs along the surface of the cylinder upstream of the separation points.

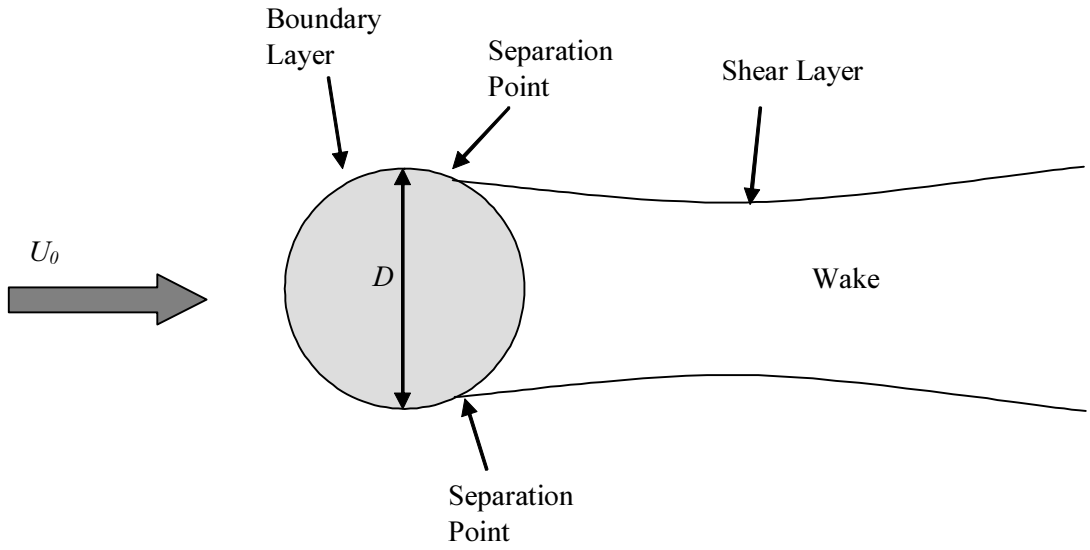

Figure 8.2 Regions of flow around a circular cylinder.

Progressing from a low to very high Reynolds number, turbulence in the flow around the cylinder occurs first in the wake, where laminar vortices become turbulent as they are distorted three-dimensionally downstream. The turbulence spreads upstream with increasing Reynolds number, but the free-shear layers surrounding the wake remain laminar.

The second region of the flow to become turbulent is that of the free-shear layers. The transition point moves upstream with increasing Reynolds number.

The third and final region to become turbulent is the cylinder boundary layer. Turbulence first occurs at the separation points, and spreads upstream around the cylinder with increasing Reynolds number until the entire boundary layer is turbulent. Zdravkovich (1990) describes a transition state before the boundary layer transition where transition to turbulence occurs around the separation point. However, he suggests that these two states can be treated as one, and in a latter publication (Zdravkovich, 1997) transition at the separation points is not treated separately from boundary layer transition.

A notation for these flow states, based on the region where the transition to turbulence is occurring (Zdravkovich, 1997), is given in Table 8.1. The Reynolds number boundaries for each flow state are not sharp due to variation in experiments, and as very small disturbances can trigger transition at a lower Reynolds numbers.

State	Description	*Re* Range
L	Laminar	0 to 180-200
TrW	Transition in wake, laminar elsewhere	180-200 to 350-400
TrSL	Transition in shear layers, turbulent wake	350-400 to 10^5 - $2x10^5$
TrBL	Transition in boundary layers	10^5-$2x10^5$ to $6x10^6$-$8x10^6$
T	Fully turbulent flow	$>8x10^6$

Table 8.1 Flow states for single smooth cylinder in undisturbed flow, from Zdravkovich (1997).

Each of these states may be sub-divided into regimes based on identifiable flow structures. In relation to the experiments presented in following chapters where Reynolds numbers are in the range 1,000 – 6,000, the relevant flow states are TrSL, and, due to the influence of surface roughness (discussed in 8.2.3), the TrBL state. More detailed division of these two states follow.

In the transition-in-shear-layers (TrSL) state, turbulence develops in the free-shear layers between the cylinder wake and the surrounding flow, while the cylinder boundary layers remain laminar. In many fluid dynamics text books and early literature, this state is referred to as subcritical flow, based on the

laminar flow in the boundary layer (Wieselsberger, 1921). This implies that there is some critical point where the boundary layer becomes turbulent. As will be described later, turbulence develops gradually in the boundary layer. The terms subcritical, critical, and supercritical have been superseded by the more precise flow states given in Table 8.1.

The transition to turbulence in the shear layers progresses through three stages with increasing Reynolds numbers. The three stages are:

- TrSL1: development of transition waves (350-400) < *Re* < (1,000-2,000)
- TrSL2: formation of transition eddies (1,000-2,000) < *Re* < (20,000-40,000)
- TrSL3: sudden turbulent bursts (20,000-40,000) < *Re* < (100,000-200,000)

In the first stage (TrSL1), waves develop along the shear layer. At higher Reynolds numbers (TrSL2) the transition waves roll up into discrete two-dimensional eddies along the shear layer before becoming turbulent. With further increases in Reynolds number (TrSL3), turbulence occurs directly in the shear layers (without the formation of the two-dimensional eddies) a short distance downstream of the cylinder. Zdravkovich (1997) describes this as a sudden burst to turbulence.

The Strouhal number, which is based on the frequency of eddy shedding (or the frequency of the transition waves in the TrSL1 regime), increases with *Re* in the TrSL1 regime, reaching a constant value of ~ 0.21 in the TrSL2 and TrSL3 regimes (Figure 8.3).

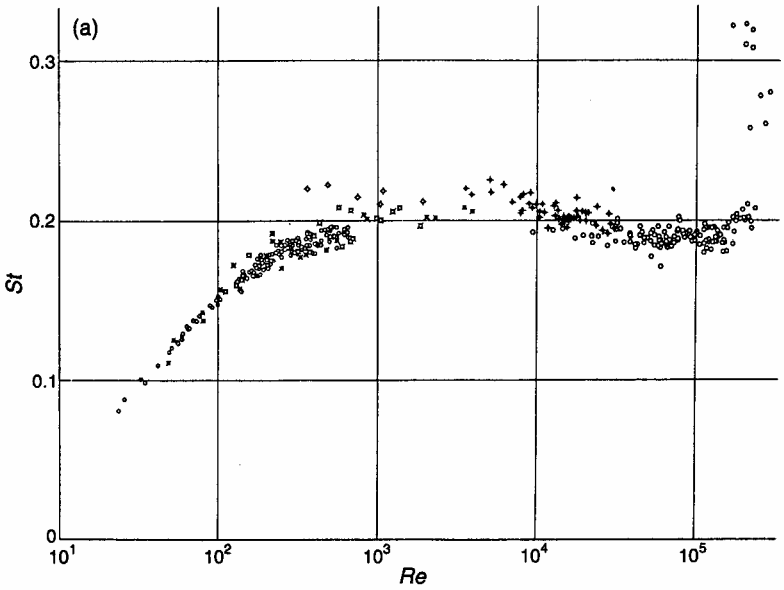

Figure 8.3 Compilation of Strouhal number versus Reynolds number, from Zdravkovich (1997).

There are 5 identified steps in the transition to turbulence in the cylinder boundary layer. In order of increasing Reynolds number, they are:

- TrBL0: precritical regime $(1.0\text{x}10^5 – 2.0\text{x}10^5) < Re < (3.0\text{x}10^5 – 3.4\text{x}10^5)$
- TrBL1: one-bubble regime $(3.0\text{x}10^5 – 3.4\text{x}10^5) < Re < (3.8\text{x}10^5 – 4.0\text{x}10^5)$
- TrBL2: two-bubble regime $(3.8\text{x}10^5 – 4.0\text{x}10^5) < Re < (5.0\text{x}10^5 – 1.0\text{x}10^6)$
- TrBL3: super-critical regime $(5.0\text{x}10^5 – 1.0\text{x}10^6) < Re < (3.4\text{x}10^6 – 6.0\text{x}10^6)$
- TrBL4: post-critical regime $(3.4\text{x}10^6 – 6.0\text{x}10^6) < Re <$ unknown

In the precritical (TrBL0) regime, turbulence occurs in the free-shear layers progressively closer to the separation points. The separation points slowly move downstream with increasing Re, resulting in a gradual decrease in drag coefficient (C_D). As *Re* increases, the separated shear layers become sufficiently turbulent to reattach to the cylinder (Bearman, 1969), first on one side (TrBL1), and then both sides (TrBL2) forming separation bubbles. The asymmetry of the single separation bubble results in a lift (cross-stream) force on the cylinder. There is a sudden drop in drag-coefficient as this occurs. A further increase in Reynolds number results in two separation bubbles forming symmetrically either side of the cylinder. The transition from one to two bubbles occurs suddenly, and the symmetry removes the mean lift force. The drag coefficient is constant in the TrBL2 regime ($C_D \sim 0.35$). In the TrBL1 and TrBL2 regimes, the boundary layers are laminar before initial separation. The separated shear layer becomes turbulent, and then reattaches to the cylinder. The shear layer is turbulent where it finally separates from the cylinder.

In the TrBL3 regime, the transition to turbulence in the separated shear layer shifts upstream towards the laminar separation point, which in turn disrupts and fragments the separation bubbles along the cylinder. Periodic eddy shedding is prevented by the irregular series of separation bubbles along the cylinder; however, semi-regular flow fluctuations have been reported, with Stouhal numbers in the range 0.46-0.50 (Achenbach and Heinecke, 1981). The drag coefficient fluctuates between 0.3 and 0.7 with the irregular formation of separation bubbles, but there is a general increase in drag coefficient with increasing Re.

Finally, turbulence develops upstream of initial separation (TrBL4). As the Reynolds number increases, the transition in the boundary layer moves further forward towards the front of the cylinder. Regular eddy shedding reappears in this regime with a Strouhal number of 0.27 (Roshko, 1961). The drag coefficient is constant at approximately 0.7.

The variations in drag coefficient as a function of Reynolds number are shown in Figure 8.4, reproduced from Zdravkovich (1997).

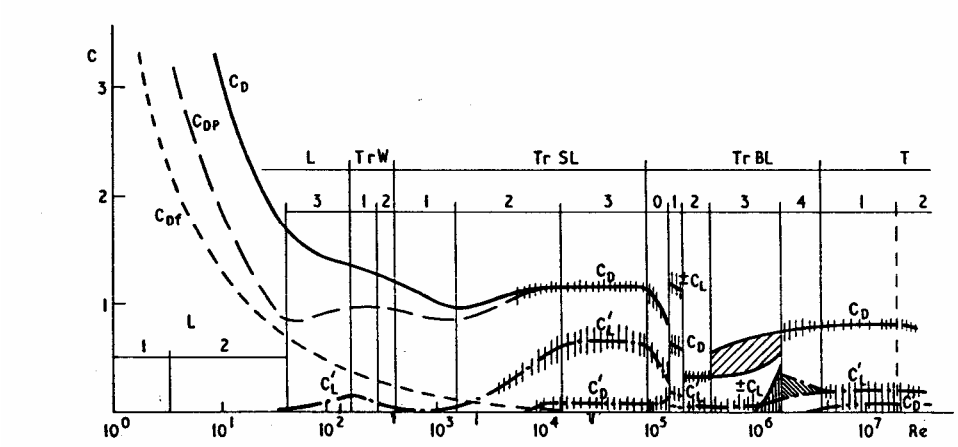

Figure 8.4 Drag coefficient for a smooth cylinder as function of Reynolds number in undisturbed flow, from Zdravkovich (1997). C_{Df} is the viscous drag, C_{DP} the pressure drag, and C_D the total drag. Coefficients for the fluctuations in drag and lift forces are C'_D and C'_L respectively.

For visualisations of flow around smooth cylinders in many of the flow regimes described above, the review by Coutanceau and Defaye (1991) is recommended. In particular, visualisation of flow around smooth cylinders at Reynolds numbers in the range used in experiments in this thesis (1,000 – 10,000) can be found in their Figures 14, 15, 20-23; and the transition from TrBL0 to TrBL2 can be seen in the sequence in Figure 24.

8.2.3 Surface Roughness

While the governing parameter for the state of flow for smooth cylinders is the Reynolds number, surface roughness can lower the Reynolds number at which transition occurs, and in some cases govern the state of flow.

Before considering roughness, the concept of a smooth cylinder warrants some discussion. It is clear that no real object can be perfectly smooth. While a surface may visually appear smooth, or feel smooth to the touch, surface irregularities will become apparent under sufficient magnification. The definition of smoothness should therefore be when the surface irregularities and imperfections are sufficiently small that they have no effect on the flow. In the words of Prandtl (1961) (English translation from Zdravkovich, 2003):

> *Slightly rough surfaces may be regarded as effectively smooth when the irregularities are completely imbedded in the laminar boundary. At high Re, when the laminar boundary layer becomes thinner, such roughness may become effective in causing an increase in drag.*

At low Reynolds numbers, when the laminar boundary layers are thick, surface roughness should have little effect. Conversely, the flow should be sensitive to surface roughness at high Reynolds numbers.

This is supported by experimental data, where at low Reynolds numbers, drag coefficients are independent of surface roughness.

Surface roughness is defined as the mean size of surface excrescences. Many of the rough cylinders used in previous experiments were fabricated by fixing sand to the surface, either with a glue or epoxy, or by wrapping the cylinder with sand paper. It is therefore not surprising that the size of cylinder surface roughness is commonly expressed as an equivalent sand grain diameter k_s. A further factor that becomes more important as the roughness increases is the change in diameter resulting from the added material on the cylinder surface. An effective diameter can be estimated by adding the roughness height to the smooth cylinder diameter, as demonstrated in Figure 8.5.

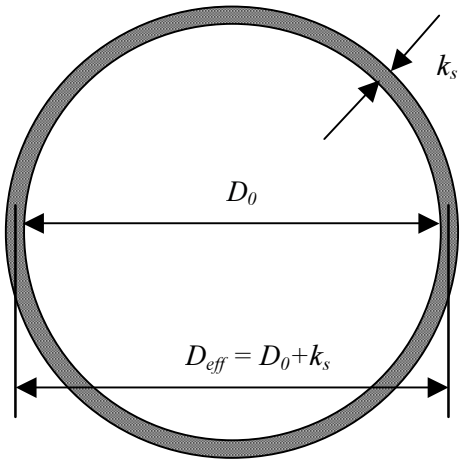

Figure 8.5 Definition of effective diameter and surface roughness. D_0 is the diameter of the cylinder, and k_s the size of the surface roughness. The cylinder diameter is increased by 2 x k_s/2, giving $D_{eff} = D_0 + k_s$.

The most dramatic and widely known influence of surface roughness is the promotion of the transition to turbulent boundary layer state at lower Reynolds numbers. The drop in drag coefficient associated with this transition is observed to occur at lower Reynolds numbers even for very small surface roughness ratios (Fage and Warsap, 1929; Achenbach, 1971; Güven *et al.*, 1980). Increasing the surface roughness ratio causes the drop in drag coefficient to occur at lower Reynolds numbers, however the minimum drag coefficient is also higher. It appears that if the roughness was increased sufficiently, the fall in drag coefficient would disappear.

The relationship between roughness and drag minimum C_{Dmin}, and the Reynolds numbers at which the drag minimum occurs Re_{min} can be estimated from the graph of drag data compiled by Güven *et al.* (1980), reproduced in Figure 8.6.

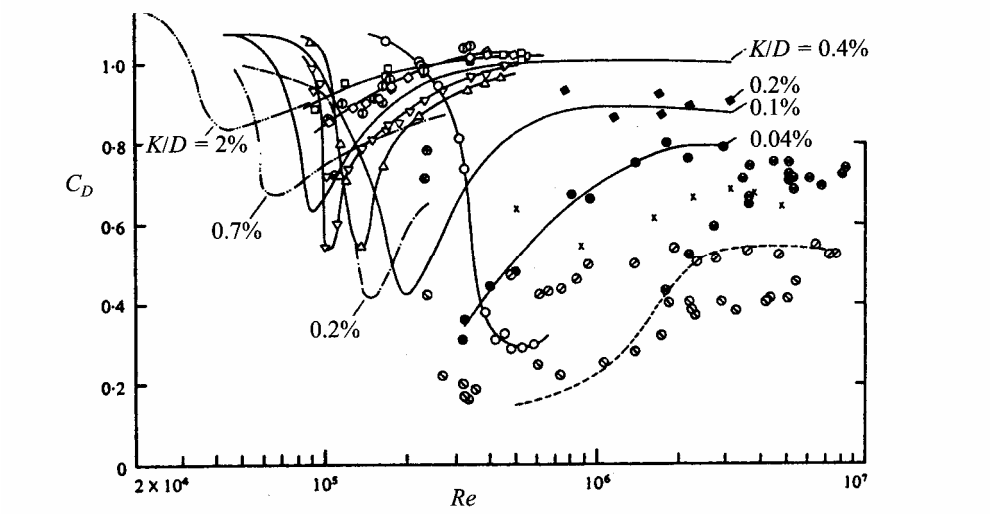

Figure 8.6 Drag coefficients for rough circular cylinders, from Güven *et al.* (1980)

The values of drag minimum and the Reynolds number where these occur are plotted as functions of surface roughness in Figure 8.7.

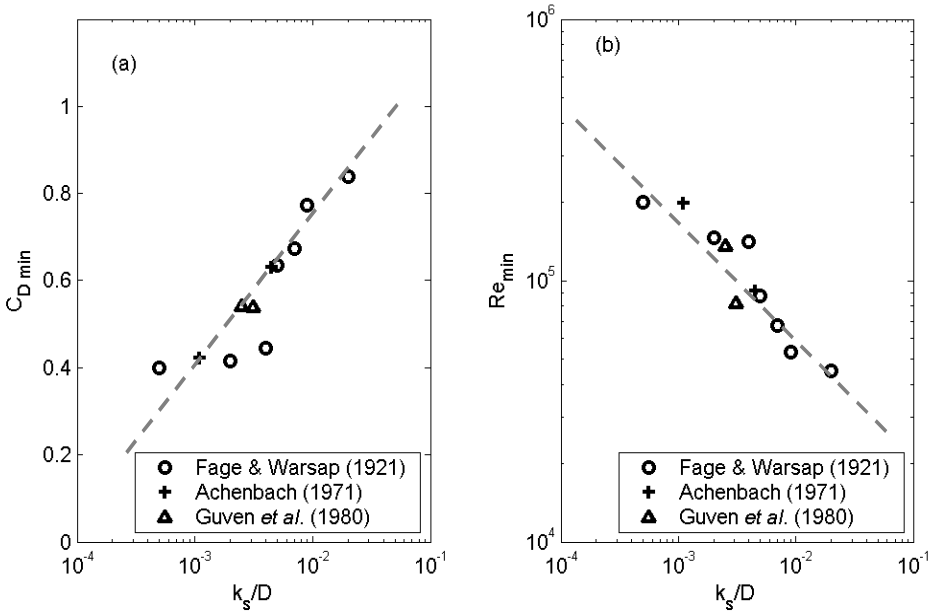

Figure 8.7 (a) Minimum drag coefficients, and (b) Reynolds number at minimum drag, adapted from Güven et al. (1980).

No data have been found showing drag coefficients for cylinders with roughness greater than $k_s/D = 0.02$. Published data shows that the drag coefficient at Reynolds numbers below where the drop in C_D occurs is 1.18 for all rough cylinders with $k_s/D < 0.02$. By plotting C_{Dmin} versus Re_{min} for the rough cylinder data and extrapolating back to a C_{Dmin} of 1.18 (Figure 8.8), an estimate can be made of the roughness where no drag decrease occurs. From Figure 8.8, the C_D drop is predicted to disappear at $Re \sim 17{,}000$. From Figure 8.7(b), a maximum effective roughness of $k_s/D \sim 0.2$ is estimated.

Clearly this prediction makes the tenuous assumption that the drag behaviour of very rough cylinders follows the trend of less rough cylinders. Secondly, it is assumed that such large roughness does not protrude through the laminar boundary layer and so alter the pre-transition drag coefficient from C_D = 1.18.

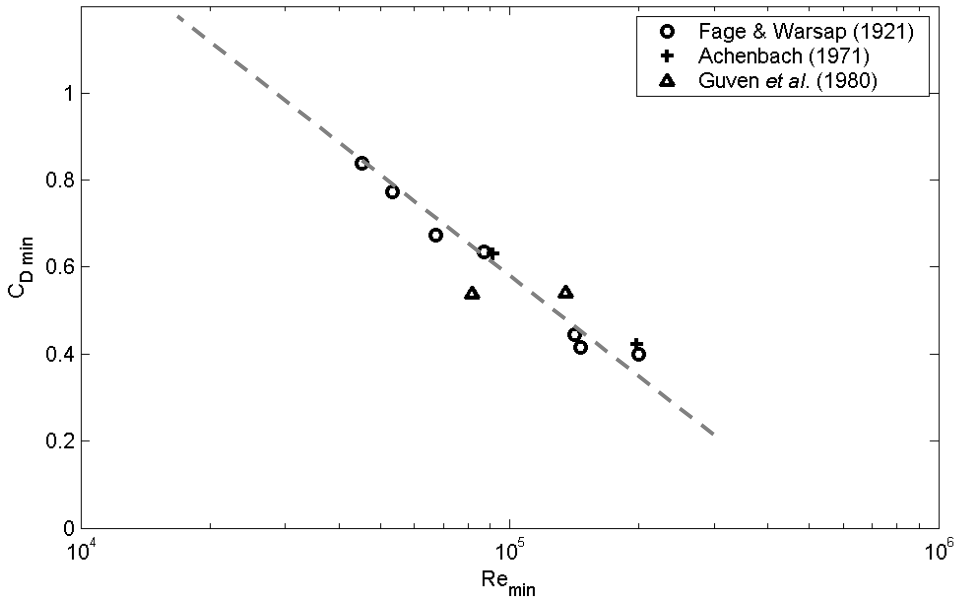

Figure 8.8 Minimum drag coefficients plotted against Reynolds number.

At Reynolds numbers beyond the point of drag minimum, C_D recovers to higher values as surface roughness increases. This relationship appears asymptotic in that the increase is largest for low roughness, but collapses to $C_D \sim 1.0$ at roughness $k_s/D > 0.0045$ (Güven *et al.*, 1980).

While a progression of transition regimes for the TrBL state was described for smooth cylinders, the TrBL1, TrBL2 and TrBL3 regimes are disturbed by small k_s/D, and obliterated by large k_s/D. For high roughness, the TrBL0 regime is followed directly by the TrBL4 regime. A consequence of this is that with higher surface roughness, the eddy shedding does not cease as it does for smooth cylinders in the TrBL3 regime (Achenbach and Heinecke, 1981; Buresti, 1981).

8.2.4 Free-Stream Turbulence

Free-stream turbulence has a similar effect to surface roughness in lowering the Reynolds numbers at which some transition states occur. Free-stream turbulence is defined by turbulence intensity, T_i, and a turbulence length scale, T_s. Turbulence intensity is the ratio of the root-mean-squared velocity fluctuation (in the streamwise direction) and the time-averaged velocity. The turbulence length scale is an estimate of the size of the dominant eddies, and is calculated from a spatial correlation function of the velocities in

the streamwise direction. Of the two, turbulence intensity appears to have the greatest effect on cylinder flow (Bearman and Morel, 1983; Zdravkovich, 1990).

The effect of free-stream turbulence on the TrSL1 state (laminar transition waves along the free-shear layers) is almost undetectable. Norberg (1986) conducted experiments at turbulence intensities of 0.1% and 1.4% and found no effect on Strouhal number over the range $40 < Re < 2000$. The TrSL2 regime (formation of eddies in the free-shear layers) is sensitive to even small free-stream turbulence (Gerrard, 1965; Norberg, 1986). Free-stream turbulence disrupts the transition eddies and promotes turbulence along the free-shear layers. This results in an upstream shift of peaks in the streamwise velocity fluctuations (u') behind the cylinder.

In the TrSL3 regime, where there is an abrupt transition to turbulence in the free-shear layers, the effect of free-stream turbulence is confined to the short section of laminar flow in the shear layer (upstream of where the transition to turbulence occurs). This short length scale means that the turbulence length scale T_s must be small for free-stream turbulence to have an effect (Surry, 1972).

In the TrBL (transition in boundary layer) state, the effect of free-stream turbulence is similar to that of surface roughness in causing the TrBL1 and TrBL2 regimes to be initiated at lower Reynolds numbers.

8.2.5 Porous Cylinders

From visual inspection of a mussel dropper (Figure 8.1), the extreme size of the roughness elements (mussel shells) in comparison to the diameter suggests that some fluid may flow between the shells, making the object somewhat porous. There is limited published data on porous cylinders, but Alridge *et al.* (1978) reported a 20% increase in drag coefficient (in comparison to a solid cylinder) for a hollow perforated cylinder with 60% open area at Re 10^4 to 2.6×10^5. Downstream of the cylinder along the edge of the wake, eddies developed that were small in scale and independent of each other, unlike the large, strongly correlated eddies behind a smooth cylinder. At higher porosities, the drag coefficient will drop as at 100% porosity, the drag must be zero.

8.2.6 Flow Around Other Bluff Bodies

The roughness elements on a mussel dropper are the mussel shells. At harvest, the mussel shells measure ~ 100 mm in length. The rope to which the mussels attach has a thickness of around 25 mm. Before calculating a roughness ratio, there is first the difficulty in defining the diameter of a body with such large roughness elements. The definition for cylinder roughness allows an estimate of diameter by adding the roughness size to the diameter of the smooth cylinder. While these are suitable for cylinders with a relatively small surface roughness, it is not a suitable method for defining the diameter of a mussel

dropper as it does not account for the dense packing of the mussel shells, with interweaved basal threads and other marine growth. A number of alternative approaches are available, including using a cylinder diameter based on equivalent volume, projected area, or the simplest method of using twice the average mussel size. These different definitions are discussed further in Chapter 10. However, any of the proposed methods suggest the ratio of shell length to cylinder (or dropper) diameter approaches values of the order 0.5. This raises the issue of whether a cylinder is a suitable object to use to model a mussel dropper.

Drag coefficients for a range of bluff bodies can be found in most fluid text books. Most of these values date back to the work of Lindsey (1938). Lindsey measured drag on circular, semi tubular (semicircular), elliptical, square, and triangular cylinders in a wind tunnel. A trend for sharp edge bodies (square and triangular cylinders) was the near constant drag coefficient over a wide range of Reynolds number (Figure 8.9). Sharp edges promote separation at low Reynolds numbers, whereas for the circular and elliptical cylinders, the flow remains attached to the surface for longer. The shape and irregular edges of the mussel droppers may promote a similar low-Reynolds number separation.

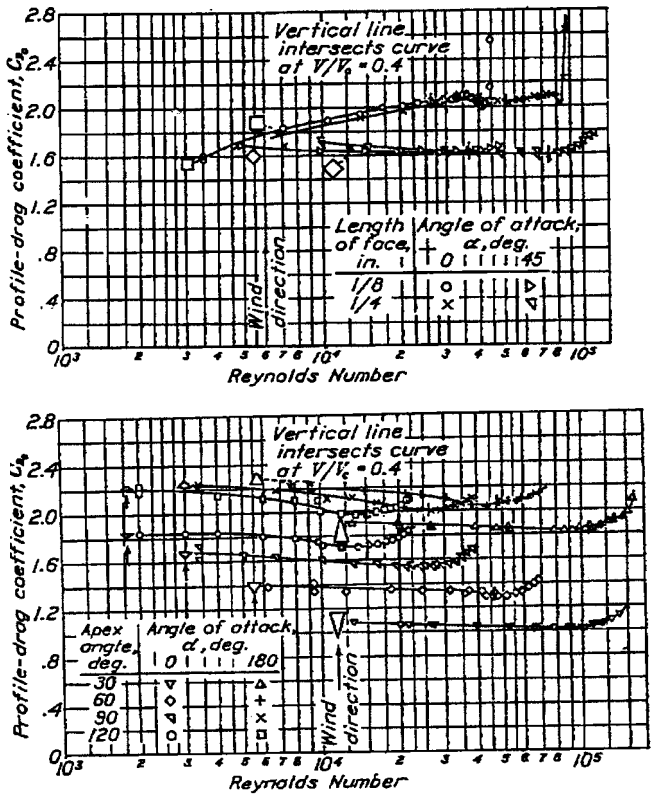

Figure 8.9 Drag coefficients for sharp-edged cylinders, from Lindsey (1938).

Based on the comparison with sharp-edged bluff bodies, it is likely that mussel droppers will show a near constant drag coefficient over a wide range of Reynolds numbers, and separation is likely to occur at low Reynolds numbers. While the comparison with circular cylinders is still valid, a mussel dropper likely

falls somewhere on the continuum from a smooth cylinder to sharp-edged bluff body such as a square cylinder.

8.2.7 Cylinder Arrays

Where cylinders are widely spaced, they essentially behave independently, and can be considered as single cylinders. If cylinders are closely spaced, various interactions can occur between the cylinders depending on the orientation, spacing, and number of cylinders. There are a wealth of published data for the double cylinder configuration, and a thorough summary can be found in Chapter 26 of Zdravkovich's review of circular cylinders (Zdravkovich, 2003). In this thesis, the focus is on arrays of several cylinders, so a full treatment of the double-cylinder configuration is not appropriate. However a brief summary of the double-cylinder configuration provides a useful guide to the behaviour of cylinder arrays.

For the side-by-side double cylinder configuration, a spacing of 1.1-1.2 < S/D < 2-2.2 has been found to cause biased wakes. A narrow wake forms behind one cylinder, while a wide wake forms behind the other. The biased flow is bistable (has two stable configurations), and may switch intermittently. At a narrower spacing, 1 < S/D < 1.1-1.2, a single eddy street forms behind both cylinders, which act as a single bluff body with a weak flow between them. At wider spacing of 2-2.2 < S/D < 4-5, the wakes are equal and synchronised in phase (the eddy streets mirror each other). At S/D > 4 –5, the cylinders behave independently.

A similar wake bias has been found for arrays of closely spaced cylinders normal to the flow. Several researchers have noted that the gap-flow jets passing between the cylinders pair, forming a non-uniform distribution of wake sizes across the array (Morgan, 1960; Bradshaw, 1965; Moretti and Cheng, 1987; Zdravkovich and Stonebanks, 1990; Zdravkovich, 1993).

A clear demonstration of this behaviour is seen in a photograph by Bradshaw (1965) of smoke through a single row of cylinders at S/D = 1.5, Re = 1500 (reproduced in Figure 8.10). The purpose of Bradshaw's research was to discover the cause of uneven velocity and shear stress downstream of wind-tunnel damping screens. However, the same phenomenon has been studied in heat-exchangers.

Cowdrey (1968) noted that the non-uniform flow behind an array of closely spaced cylinders would change intermittently. Zdravkovich and Stonebanks (1990) use the term "metastable flow" to describe these flow patterns that remain stable for a period of time, but change seemingly at random. Zdravkovich and Stonebanks suggest that the spatial non-uniformity is caused by irregular coalescence of gap-flows downstream of the array, and that the intermittent change between metastable states is due to a re-pairing of jets in different combinations.

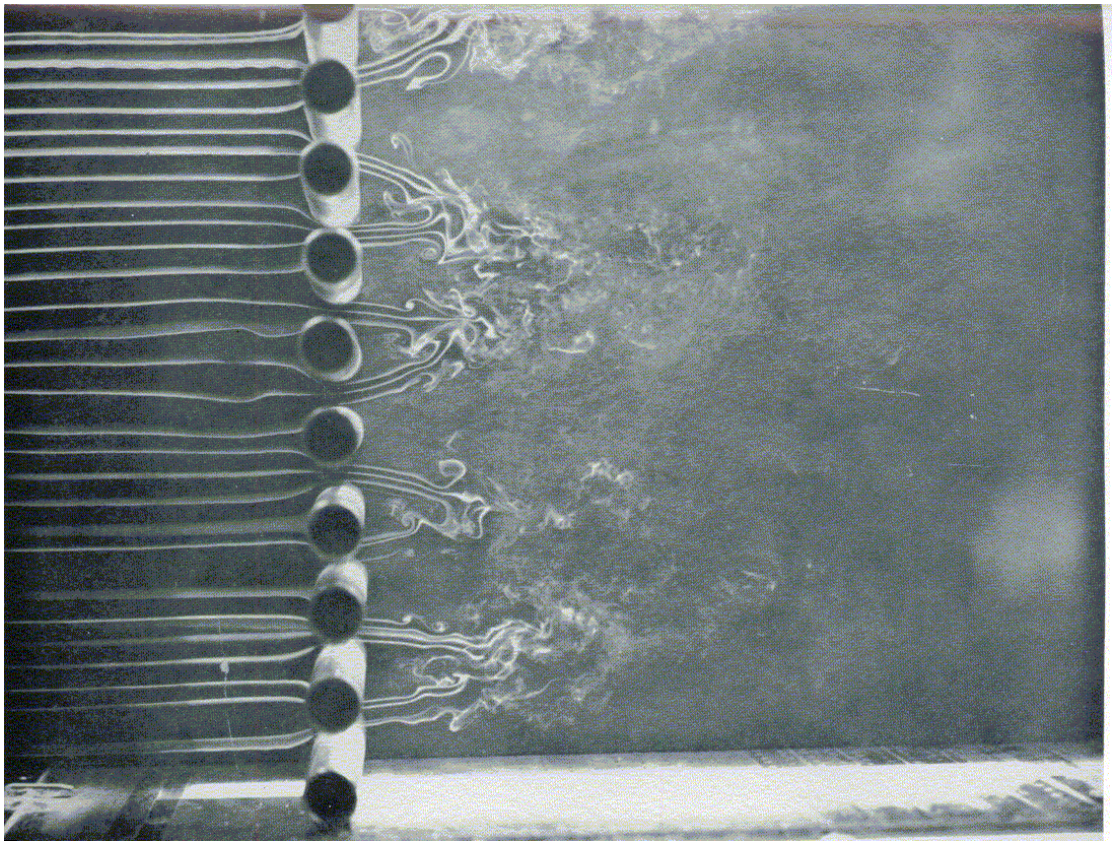

Figure 8.10 Flow through a single row of cylinder at *S/D* = 1.5, *Re* = 1500, from Bradshaw (1965).

There is some variation in the literature regarding the spacing required for the metastable flow patterns to occur; however, the generally agreed range is for $S/D < 2.0$ to 2.2 (Zdravkovich, 2003), which is in agreement with the double-cylinder configuration. Slightly higher values have been suggested for porous screens, commonly an open area ratio of 0.57, which equates to a cylinder spacing $S/D = 2.3$ (Morgan, 1960; Bradshaw, 1965).

For two closely spaced bluff bodies where the flow is biased, forming a wide wake behind one body and a narrow wake behind the other, there are two Strouhal numbers (for eddy shedding), one for each wake. For a closely spaced row of cylinders, there may be several Strouhal numbers due to variation in wake sizes. Moretti and Cheng (1987) suggest that at cylinder spacing of $1.5 < S/D < 2.2$, they expect jets to join in pairs, and for there to be two eddy shedding frequencies due to formation of two different sized wake regions. At closer cylinder spacing ($S/D < 1.5$), they argue that a wider range of wake sizes will occur across the array as the jets cluster in groups of three, four or more. However the compilation by Zdravkovich and Stonebanks (1990) of Strouhal number versus cylinder spacing data shows that at $S/D < 2.2$, a wide range of eddy shedding frequencies can be expected. The wide range is due in part to the interchange between various metastable flow patterns. This does not necessarily contradict Moretti and Cheng's theory as there may be only two eddy shedding frequencies for a single metastable flow pattern when $1.5 < S/D < 2.2$.

The non-uniform wake sizes also occur within and behind multiple rows of cylinders, for both staggered and non-staggered rows (Zdravkovich and Stonebanks, 1990; Price *et al.*, 1995; Umeda and Yang, 1999; Zdravkovich, 2003).

Considerable interaction also occurs when cylinders are in-line with the flow. The interaction depends greatly on the cylinder spacing. At close cylinder spacing, several cylinders may be contained within the free-shear layers shed from the upstream cylinder. The eddy shedding is also suppressed at close spacing. As the spacing is increased, there may be intermittent reattachment of free-shear layers from upstream cylinders, and eddy shedding commences behind downstream cylinders. Visualisation of flow past an in-line array of 3 cylinders was done by Igarashi and Suzuki (1984), and 4 cylinders by Igarashi (1986), reproduced in Figures 27.4 and 27.27 in Zdravkovich (2003). These flow patterns depend both on S/D and Re. The variation in drag coefficients and Strouhal numbers with spacing are complex due to the reattachment and the interference with eddy shedding. In general, both drag coefficients and Strouhal numbers decrease as the gap between cylinders is reduced.

No data have been found for closely spaced single cylinder rows at an angle to the flow. At small angles (nearly in-line), similar wake interactions may be expected as those that occur for the in-line array, however the offset of the downstream cylinders may interfere with reattachment of shear layers. Likewise, at angles approaching 90^o to the flow, the flow patterns may resemble those behind arrays normal to the flow. However, the downstream-offset of neighbouring cylinders may have an influence on the biasing of the gap-flow jets, and this could either prevent the occurrence of non-uniform wakes sizes or, alternatively, favour a particular non-uniform wake-size distribution to the extent that the intermittent change between metastable states does not occur. Clearly more research is required to address these issues.

8.3 Motivation for Laboratory Experiments

It is clear from the literature review that there is a wealth of published research on the flow around cylinders, particularly for smooth circular cylinders. The effect of surface roughness on cylinders has received some attention; however, there has been little, if any, investigation of surface roughness ratios greater than $k_s/D \sim 0.02$. Arrays of cylinders, in particular single rows normal to the flow and in-line with the flow, have also been studied, and the conditions required for metastable pairing of gap-flow jets are well known ($S/D < 2.2$). A mechanism responsible for this pairing has been suggested but not yet conclusively proven. The visualisation and measurement of flow properties behind these arrays have been restricted to point measurements of velocities or pressure, and photography of dye/smoke streaks.

In order to better understand small-scale flow properties of particular relevance to mussel aquaculture, there are a number of issues requiring further research. In particular, the effect of mussel dropper roughness and irregularity on drag and flow needs to be investigated. While it is convenient, for the purpose of assessing likely hydrodynamic effects, to assume that the mussel droppers resemble cylinders, this assumption requires validation. There are also several areas of interest relating to cylinder arrays that are worthy of further research. In particular, a better understanding of the effect of cylinder spacing and orientation will aid in assessing energy dissipation and transport of nutrients around the mussel droppers. The effect of high cylinder surface roughness in arrays of cylinders is another area that has received little attention. Recent advances in quantitative flow visualisation, such as PTV and PIV may allow better understanding of the interaction between the fluid and structures by providing detailed flow fields of velocity and turbulence characteristics, as opposed to the point-measurements and qualitative visualisation techniques employed in the past.

With these factors in mind, the following experimental programme was developed:

- Tow tests were performed on smooth and rough cylinders, and on arrays of cylinders to measure the effect of surface roughness and cylinder spacing on drag. Most tests of cylinder arrays were for single rows of cylinders orientated normal to the flow. However, in some experiments, double rows and rows angled to the flow were tested. The drag on a length of mussel dropper was also measured as comparison
- Particle Tracking Velocimetry (PTV) was used to measure velocity fields around a mussel dropper, and around cylinders and arrays of cylinders to investigate the effect of roughness, spacing, and orientation on mean flow patterns, turbulence, and transport.

The primary purpose of these experiments was to provide data that will aid in understanding the small scale hydrodynamic processes around mussel droppers. Additionally, the use of PTV provides new data sets that we hope will be of value for future research into both aquaculture and cylinder array flow, particularly for the calibration and evaluation of numerical models. It is impossible to study every conceivable cylinder array configuration. Therefore, a number of key configurations are selected, chosen for their applicability to the mussel farming application. A detailed description of the experiments, methods, and results follow in Chapters 9 to 12.

CHAPTER 9 LABORATORY METHODOLOGY

9.1 Introduction

Two types of laboratory experiments are presented in this thesis: drag force measurements, and flow visualisation using Particle Tracking Velocimetry (PTV). The PTV system is the key component of the flow visualisation experiments. The particular system used in these experiments, Streamline (Nokes, 2004a), is not yet widely used outside of the University of Canterbury. Therefore, this chapter begins with a detailed description of the Streamline PTV system. The theory behind the PTV system, a description of the steps and processes required to obtain velocity data from an image sequence, and an assessment of the accuracy of the system are presented in section 9.2. In section 9.3, the methodology and equipment used in the flow visualisation experiments are described. Finally, the methodology and equipment for the drag measurements are described in section 9.4.

9.2 Particle Tracking Velocimetry

9.2.1 General Description of Particle Tracking Velocimetry

A Particle Tracking Velocimetry (PTV) system, Streamline 5.0, (Nokes, 2004a) was used to measure velocity fields around cylinders and cylinder arrays. PTV is a method of obtaining two-dimensional velocity fields using digital video photography to track the motion of particles suspended in a flow. PTV is a quantitative flow visualisation technique, similar in some aspects to the more widely used Particle Image Velocimetry (PIV). To explain the reasons for choosing a PTV system, it is helpful to first briefly describe the basis of the system.

The principle behind a PTV system is relatively simple. The fluid flow to be studied is seeded with fine particles, and illuminated with a thin sheet of light. The motions of particles within the light sheet are recorded using a high speed digital video camera orthogonal to the light sheet. The particles are tracked from frame to frame using a range of possible algorithms. Velocities are calculated for particles from their displacement between images, and the time interval between image capture. Velocities are interpolated onto a rectangular grid, providing a time series of two-dimensional velocity fields.

The similarity between PTV and the more widely used Particle Image Velocity (PIV method) is that both provide time-series of velocity fields from digital images of flows seeded with particles. In PIV systems, the images of the flow are analysed in pairs by calculating cross-correlations of intensity fields in the two frames. The cross-correlations are carried out using small sub-windows, typically 32x32 pixels in size. A maximum in the cross-correlation provides an estimate of the velocity for the flow in the region of the

sub-window. By dividing the image into a number of sub-windows (which may overlap) an instantaneous two-dimensional velocity field is calculated.

The primary difference between PIV and PTV is that PIV calculates velocities for regions of flow based on image intensities (Figure 9.1), while PTV calculates velocities for individual particles (Figure 9.2). The major advantage of a PTV system is that velocities in areas of high shear may be more accurately resolved, as the sub-windows required for the cross-correlation in the PIV system mean that some degree of spatial averaging is inevitable (Mauti *et al.*, 2000). A caveat for the PTV system is that velocities are obtained at random locations within the flow based on the location of particles at any particular instant rather than on a rectangular grid. Velocities at grid points are calculated by interpolating from the velocities of the particles. Particles must be closely spaced for the interpolation process to accurately resolve velocities in areas where there are strong variations in shear or rotation.

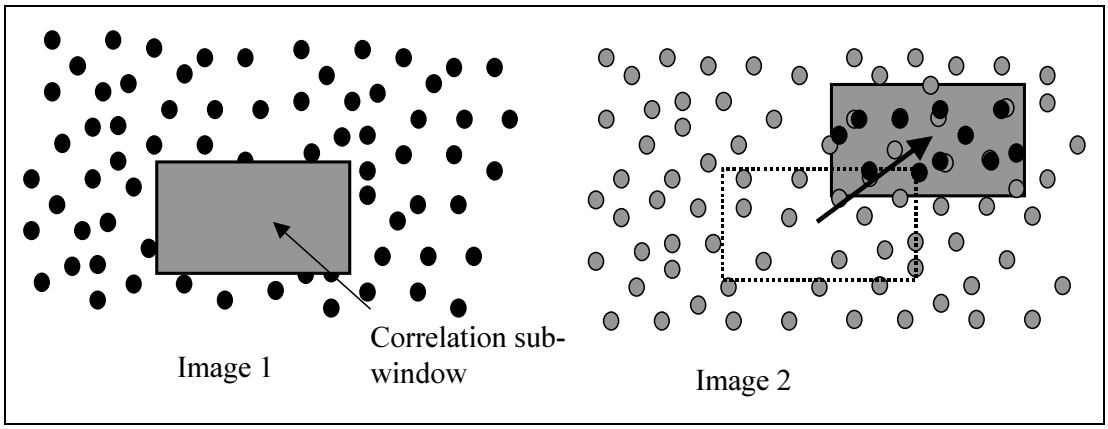

Figure 9.1 PIV system. Cross-correlations of image intensities are calculated to determine the movement of a sub-window between images.

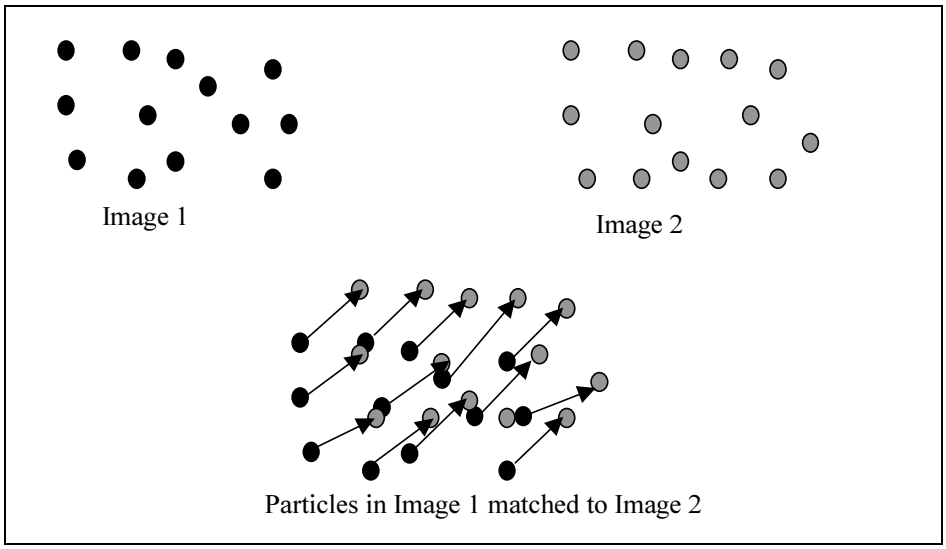

Figure 9.2 PTV system. Individual particles are tracked from one frame to the next.

Although the concept of PTV is simpler than PIV, it is a complicated procedure in practice. The greatest challenge occurs in accurately tracking particles between frames, particularly if the movement of the particles is large relative to the spacing between particles. A number of algorithms can be used to track the particles, and the methods used in analysing data here are described in detail later in this chapter.

A particle tracking system was selected for this research for two main reasons. Firstly, it allows rapid measurement of high resolution two-dimensional velocity fields that cannot be obtained practically using point velocity instruments such as Acoustic Doppler Velocimeters (ADV), Laser Doppler Anemometers (LDA), hot-wire anemometers or pressure probe techniques. Secondly, the nature of the flow around cylinders means that there are areas of strong shear, particularly along wake boundaries. Some of the fluid structures are likely to be small in scale, particularly in the wake regions. Due to the spatial averaging inherent in PIV, a PTV system was more likely to accurately resolve flow details in these areas of high shear and small spatial scales.

The particular PTV system used, Streamline version 5.0, is a proprietary software package used in the Department of Civil Engineering, University of Canterbury. The software uses a three-step process to produce velocity data. The three steps are particle identification, particle matching, and velocity field calculation. Descriptions of each process relevant to the experiments presented here are given below. The Streamline software also has a number of additional features and options not described here. A more complete description of Streamline can be found in the Streamline Operation Manual (Nokes, 2004b), and Nokes *et al.* (submitted to Experiments in Fluids).

9.2.2 Particle Identification Process

In the particle identification process, the location and size of particles are determined based on light intensities in each individual image (refer to section 9.3.3 for details of the particles used). Images are converted to a two-dimensional array of pixel colour values. Each pixel has three colour values, one each for blue, red and green, ranging from a minimum intensity of 0 to a maximum of 255. Any of the three colours, or an average of the three (as was used in experiments presented in this thesis) may be used as an intensity field. Images acquired from monochrome cameras still use three colour values per pixel, however all three colour values are the same intensity (grey scale). The location and size of particles in the image are obtained using three parameters: *threshold*, *maximum threshold,* and *minimum diameter*. A Gaussian image algorithm is used to determine the location of particles. This algorithm first looks for a pixel that has a local intensity maximum that exceeds the *maximum threshold* intensity. Adjacent pixels that have intensity above the *threshold* intensity are considered to be part of the same particle unless another local intensity maximum occurs, in which case a second particle is identified. A Gaussian distribution of intensity is assumed for each particle, and is fit in both the x and y directions through the

pixels with intensities higher than the *threshold*. This provides sub-pixel accuracy for the particle position (the location of the peak in the Gaussian distribution). The particle radius is determined by the number of pixels with intensities greater than the *threshold* either side of the particle with maximum intensity. The diameter of the particle must exceed the *minimum diameter* to be recorded.

The sketch in Figure 9.3 demonstrates this procedure. Four local intensity maximums occur, however the maximum threshold is exceeded only at (b) and (c). The number of neighbouring pixels that exceed the threshold define the particle diameter. The diameter of particle (c) is less than the minimum diameter, so it is rejected.

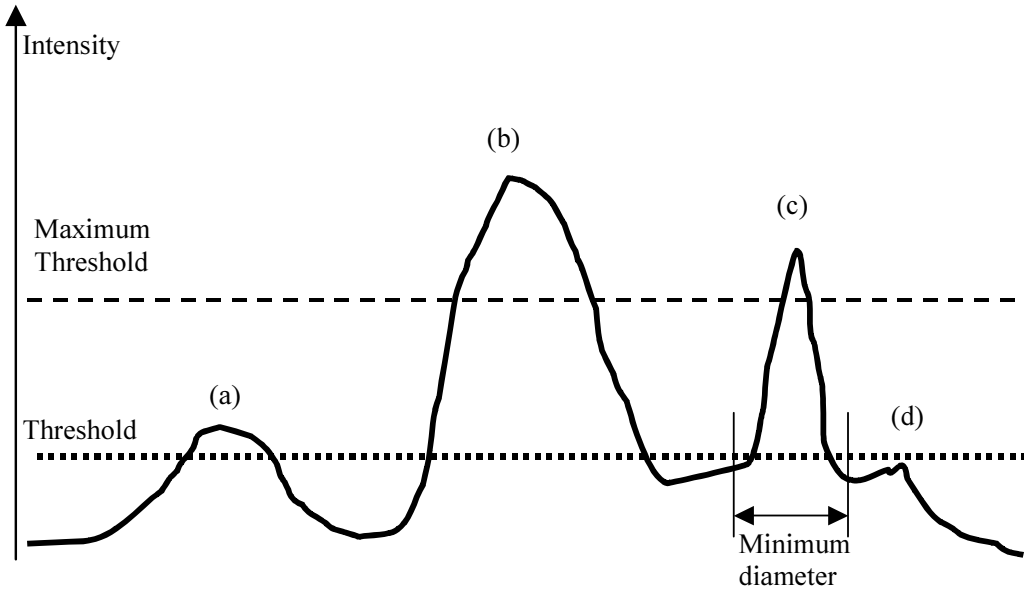

Figure 9.3 Particle identification. Local intensity maximum occur at (a) – (d), however only (b) meets all the criteria for particle identification.

The accuracy of using a Gaussian distribution to locate the centre of the particle depends on the number of pixels involved. If particles are small, measuring 1 or 2 pixels in size, then the particle location can not be estimated to better than ¼ pixel accuracy (typically ± 0.075 mm).

9.2.3 Particle Matching Process

In the particle matching process, the software attempts to match particles from frame to frame. There are a number of methods available in Streamline to find and optimise particle matches, and those used in these experiments will be described in detail below. In essence, for a particle in one frame, each method calculates the desirability of matching that particle to particles in the next frame. A particle may have several possible or candidate matches in the subsequent frame. The desirability of each candidate match is determined by a cost, so that the most favourable match has the lowest cost.

An optimisation algorithm (the auction algorithm) is employed to determine the particle matches that lead to the lowest overall cost (for all particles in the frame to be matched). This means that an individual particle may not necessarily be matched to the candidate particle with lowest cost, and it is also possible that some particles may not be matched at all. However, by minimising the total cost, an optimal solution for all particles is obtained.

Particle matching costs are calculated using a variety of costing strategies. Each costing strategy calculates a cost indicating the desirability of a candidate particle match. The different costing strategies may be used separately, in combination simultaneously with a weighting applied to each strategy, or sequentially, so that matches generated by previous costing strategies are used to find more or improved matches. As particles are expected to move a limited distance in the time interval between frames, a rectangular *search window* is specified indicating the region (relative to the particle) in which to search for potential matches. Careful choice of the search window size can greatly improve the speed of the matching process by reducing the number of candidate matches to be analysed.

To limit the generation of poor or undesirable matches, a *maximum matching cost* (MMC) is specified for the matching analysis. Any match with a cost that exceeds the MMC is eliminated. The selection of an appropriate value of the MMC is crucial to a successful analysis. If the MMC is set too low, then correct matches will be excluded. Conversely if the MMC is too high, then computation time will be increased as spurious candidate matches are included in the optimisation process, or incorrect matches may be made for particles that have no correct match in the subsequent frame.

Combinations of 4 different costing strategies were used to obtain particle matches in the experiments presented here. Each costing strategy calculates a non-dimensional cost for the match between *P1*, a particle in the first frame, and *P2*, a particle in the second frame.

The simplest strategy used was *distance costing*. *Distance costing* determines the cost for a match based on the proximity of a particle to the position of the particle in the previous frame. The cost is proportional to the distance between the particles. This costing strategy is particularly useful where particle displacements between frames are small compared to the spacing between particles (particle density). The non-dimensional cost for a potential match is calculated by dividing the distance between particle locations by the size of the search window. The cost is

$$C_{12} = \frac{\left|\mathbf{r_1} - \mathbf{r_2}\right|}{\frac{1}{2}\sqrt{sw_x^{\,2} + sw_y^{\,2}}} \tag{9.1}$$

where $\mathbf{r_1}$ and $\mathbf{r_2}$ are the position vectors of the two particles, while sw_x and sw_y are the width and height of the PTV analysis search window.

A more complicated but more powerful strategy is *correlation costing*. *Correlation costing* is based on a cross-correlation of the intensity fields of sub-windows in the two frames being matched. A rectangle of specified dimensions centred on a particle in the first frame (*P1*) is overlaid on a rectangle of identical size centred on a particle in the second frame (*P2*). Each rectangle is a pixel array with the intensities representing particles within the rectangle specified by a Gaussian distribution. The strength of the cross-correlation between the intensities determines the cost, with a high cross-correlation (indicating a strong match) giving a low cost. This procedure is repeated for all particles in frame 2 within the specified search window. A number of parameters can be adjusted to improve the performance of the correlation costing. The dimensions of the correlation window can be altered to increase the number of particles that are overlaid in the correlation calculation, or reduced to minimise the effects of shear or rotation. The particles can also be inflated to increase the overlap between particles (Figure 9.4), which can improve costing performance particularly in areas of strong velocity gradients.

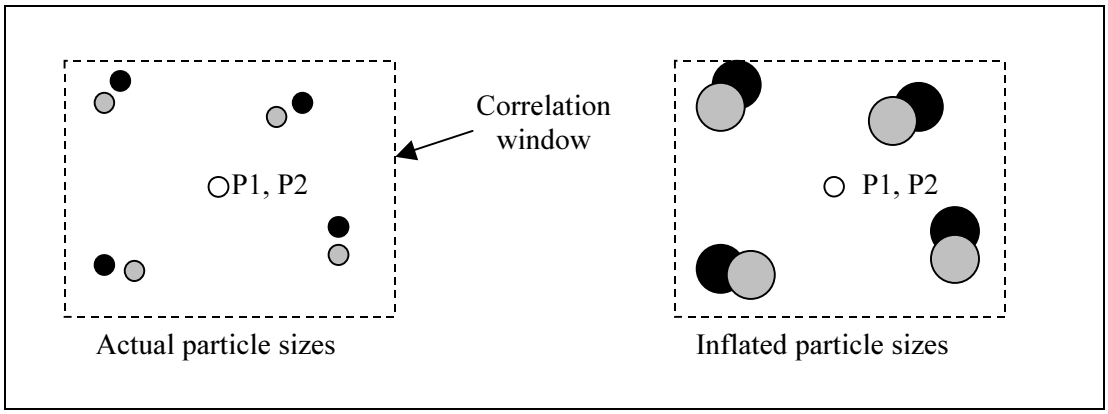

Figure 9.4 Correlation costing is calculated by cross-correlating the intensities of particles in a rectangle around P1 in 1st frame (black circles) overlaid on particles in rectangle about P2 in frame 2 (grey circles). The particles P1 and P2 (white circles) are excluded from the correlation. Inflating the particle sizes to increase overlap gives a higher correlation.

The *correlation costing* strategy is a very effective particle matching method for densely seeded flows. This strategy is less effective if particle densities are low, or if there is significant velocity shear or vorticity in the flow. The non-dimensional cost is calculated by

$$C_{12} = 1 - \frac{cross\ correlation_{12}}{\sqrt{auto_1 auto_2}}, \qquad (9.2)$$

where $cross\ correlation_{12}$ is the cross-correlation of the intensities in the rectangles excluding particles *P1* and *P2*, and $auto_1$ and $auto_2$ are the auto-correlations of each rectangle excluding particles *P1* and *P2*.

Correlation costing has much in common with the correlation used in a PIV (particle image velocimetry) system. In PIV, a frame is divided into a number of sub-windows, and correlations calculated to determine the most favourable location in the next frame for each sub-window. The key difference

between the correlations in the PTV and PIV systems is that in PTV, the correlations are used to match individual particles, while PIV calculates an average velocity for each sub-window.

For all of the experiments presented here, a combination of the *distance* and *correlation* costing strategies was used as the first process for matching particles. In calculating matching costs, a weighted average of the two costing strategies gave the net cost for a particle match. Distance costs were weighted by 0.2, and correlation costs by 0.8. Particle diameters were increased by a factor of three to improve the correlation matching, and a default cost of 0.6 was used for correlation costing if the costing could not be calculated due to an absence of particles in the correlation window. A MMC of 0.6 for the combined weighted cost was used to limit poor matches.

To improve on the particle matches obtained from the combined *distance* and *correlation* costing strategies, two further strategies were employed. These strategies, *polynomial velocity costing*, and *space average velocity costing* use existing matches to find more matches, and to remove or correct bad matches.

Polynomial velocity costing constructs a particle path by fitting a polynomial through the path of all particles matched to *P1* in previous frames, and to *P2* in subsequent frames. Polynomials are fit using least-squares regression to the *x* and *y* coordinates of particles in the path. The path length (number of frames in which matches have been made) determines the order of polynomial employed according to the following formula,

$$order = \frac{path\ length}{2}. \tag{9.3}$$

Non-integral values for the polynomial order are rounded down. The non-dimensional matching cost for the polynomial velocity costing is calculated by

$$C_{12} = \frac{fit\ error}{average\ displacement} \tag{9.4}$$

where *fit error* is calculated from the distance between the actual position and their position in the polynomial fit for particles *P1* and *P2*. In the Streamline software, this is the *local error* option. A *total error* can also be calculated where the positions of all particles in the path are compared with their position predicted by the polynomial fit. The *average displacement* is simply the average displacement between frames of particles in the path. If the average displacement is less than a default normalisation length (1 mm was used for analysing the laboratory data), the default normalisation length is substituted.

The maximum number of past or future particle matches to be used in calculating the least-squares polynomial can also be specified (a maximum of 5 matches in either direction were permitted when analysing the laboratory data).

Space average velocity costing predicts the position of a particle in the next frame from the spatial average of velocities of particles surrounding the particle (*P1*) in the present frame. An averaging window with user-specified dimensions (typically 20 mm by 20 mm) is used to calculate a weighted average velocity. Velocities of particles within the window surrounding *P1* are inversely weighted by their distance from *P1*. The matching cost for a particle in the next frame (*P2*) is determined by how close that particle is to the predicted position. The non-dimensional cost is calculated from

$$C_{12} = \frac{\left|\mathbf{r}_{pred} - \mathbf{r}_2\right|}{\left|\mathbf{r}_{pred} - \mathbf{r}_1\right|} \tag{9.5}$$

where $\mathbf{r}_{pred}$ is the predicted position of *P1* in frame 2 using the space average velocity estimate, $\mathbf{r}_1$ the location of particle *P1*, and $\mathbf{r}_2$ the location of particle *P2*.

In the analysis of the laboratory data, the *polynomial velocity costing* and *space average velocity costing* strategies were used simultaneously after executing the combined *distance* and *correlation* costing strategies described previously. The combined *polynominal velocity* and *space average* costing strategy was repeated 3 times. On the first and third iterations, the analysis proceeded from the first to last frame, however the direction was reversed on the second iteration so that analysis went from the last frame to the first. The weighting for polynomial velocity costing was 0.6, with a default costing of 0.5 (before weighting) used if there were no matched particles to create a particle path. The space average velocity costing was weighted by 0.4, with a default costing of 0.8. The MMC for the combined costing was set at 0.4.

9.2.4 Velocity Field Calculation Process

In the final process, velocity fields are calculated from the particle matches obtained in the particle matching process. Velocities can be calculated for particles that have matches in the next or previous frame based on their displacement and the time interval between the frames. Velocities can be calculated as a single estimate using a match to the previous or subsequent frame, or as a double estimate using matches in both directions. Estimates of velocity based on matches in both directions are likely to be more accurate, however information from particles matched in only one direction will then be discarded.

As particles are randomly distributed within frames, an interpolation process is used to calculate velocities at regularly spaced grid points. Streamline uses the method of Cline and Renka (1984) to construct Delaunay or Thiessen triangulation as a basis for interpolation. Essentially, triangles are formed

using particles with velocity estimates as vertices. The Thiessen triangulation means that the minimum interior angle in two adjacent triangles is maximised, which prevents triangulations from being overly long and thin, and ensures that interpolations are based on particles that are close together.

To calculate the velocity at a grid point, Streamline determines which triangle includes that grid point, and interpolates from the velocities at the triangle vertices onto the grid point (Figure 9.5). The maximum acceptable size for the triangle can be specified so that if the triangle containing a grid point exceeds this size, the velocity is left undefined. This prevents interpolating velocities from particles that are far from the grid point.

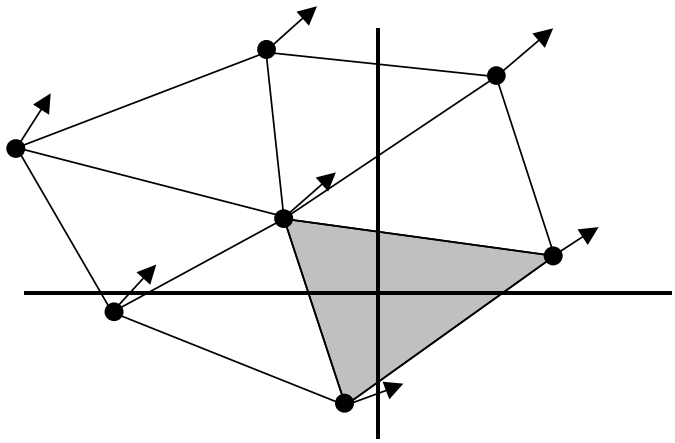

Figure 9.5 Interpolation triangulations are formed from the particles (black dots) with velocity estimates (arrows). The velocity at the grid point (intersection of the solid horizontal and vertical lines) is calculated by interpolation from the velocity at the three vertices of the triangle containing the grid point (shaded triangle).

A second option employed for velocity interpolation is a binning process based on Cowen and Monismith (1997). In the binned interpolation, velocities within a specified area around each grid point are averaged to provide a velocity estimate at that grid point (Figure 9.6). In the experiments presented here, binned velocity estimates were used at grid points where interpolation triangles exceeded an acceptable maximum size. Consequently, triangulations containing a grid point that were overly large would be rejected, while particles very close to the grid point provided an accurate estimate of velocity at the grid point. In regions of low particle density, this increased the likelihood of an accurate velocity estimate at the grid points.

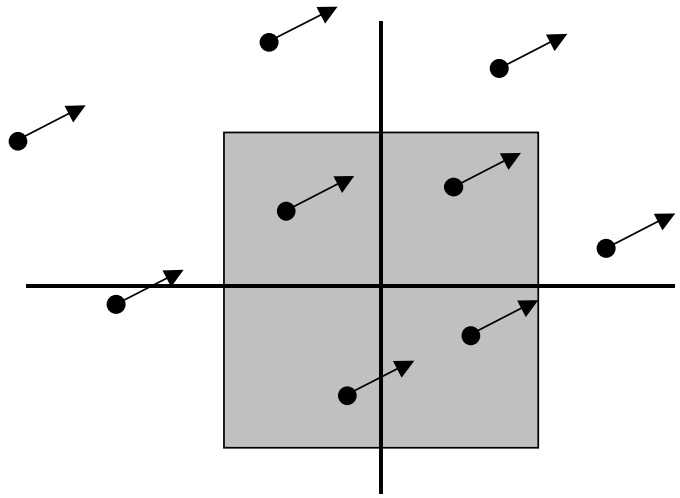

Figure 9.6 Velocity field calculation by binning. The velocity at the grid point (intersection of horizontal and vertical lines) is calculated by averaging the velocities of the four particles within the specified binning area (shaded rectangle).

Once velocity fields are calculated at each time step, other flow field characteristics can be calculated, including turbulent kinetic energy, turbulent velocity fluctuations, and vorticity.

9.2.5 Data Quality

There are a number of potential error sources in the PTV process, ranging from incorrect particle identification through to interpolation errors.

9.2.5.1 Camera Vibration

Camera vibration will result in velocity fluctuations additional to those due to turbulence. Any quantity calculated from instantaneous velocity values would then contain error. Mean flow quantities are not affected by the camera vibration as the vibration is removed by averaging. Ideally, secure mounting can prevent camera vibration. To assess the effect of camera vibration on these experiments, analysis of calibration runs (with no cylinders in the flow) were made to determine the effect of camera vibration on velocity spectra. The calibration runs analysed here were selected due to a relatively insecure camera mounting, and represent a worst-case situation for vibration.

The velocity fluctuations caused by the camera vibration will be essentially the same over the entire field of view, whereas true turbulent fluctuations vary over the flow field. From the calibration runs, velocity fluctuations resulting from camera vibration were estimated by averaging velocities over the entire frame. The assumption made was that in the calibration runs where ambient turbulence was low, a spatial average over a sufficiently large area provided a mean flow velocity. Fluctuations in this spatial average

are the result of synchronous fluctuations occurring throughout the flow field due to the motion of the camera. This provided a method for removing the effect of camera vibration for these runs. Firstly, the PTV analysis was conducted to calculate velocity fields. Then, at each time step (or camera frame), the entire flow field was spatially averaged, to provide a spatially averaged velocity $\langle u(t) \rangle$. The fluctuations (in time) of the spatially averaged velocity represented the error induced by camera vibration. By subtracting this error, calculated as $u_e(t) = \langle u(t) \rangle - |u|$ where $|u|$ was the time average of $\langle u(t) \rangle$, from the velocities measured everywhere in the flow, the error induced by camera vibration could be reduced.

In Figure 9.7(a), a velocity record is plotted from an experiment where the camera was towed over a tank with no cylinders placed in the flow. The signal shows a regular high frequency oscillation, with RMS (root-mean-squared) variation of 1.69 mm/s. By subtracting the fluctuation of the spatial average over the entire field of view (Figure 9.7(b)), much of the velocity variation is removed from the signal (Figure 9.7(c)). The RMS fluctuation of the corrected signal is 0.91 mm/s.

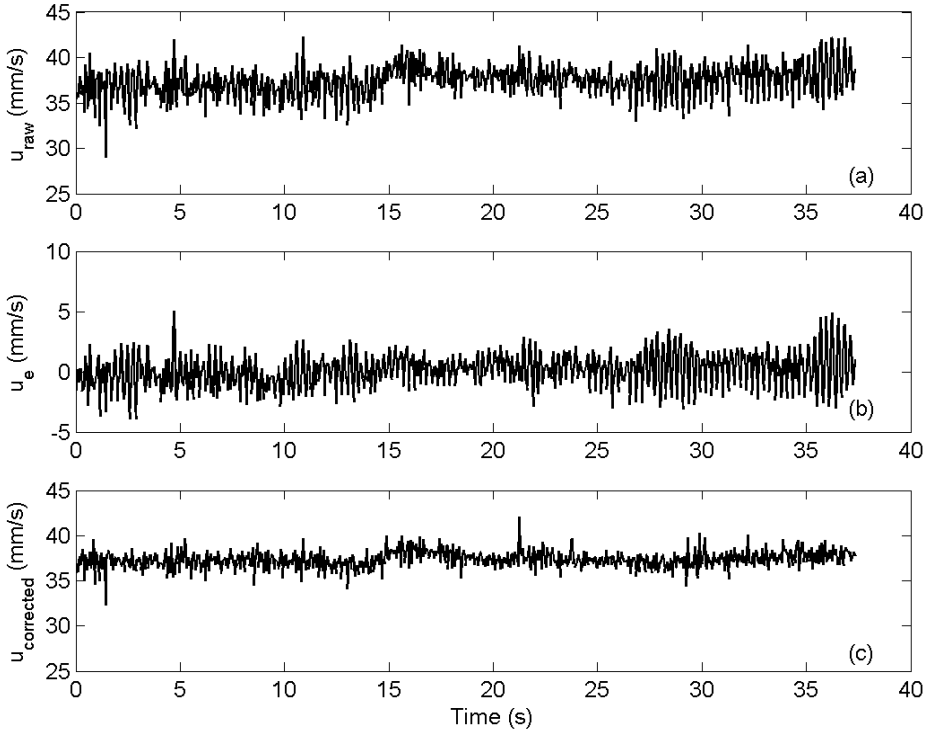

Figure 9.7 (a) raw u velocity at a point in the flow, (b) velocity correction calculated from spatial average, (c) corrected u velocity at point in flow.

A comparison of velocity spectra shows that vibration induced peaks at 0.35 Hz and 0.7 Hz were removed from the corrected velocity signal (Figure 9.8)

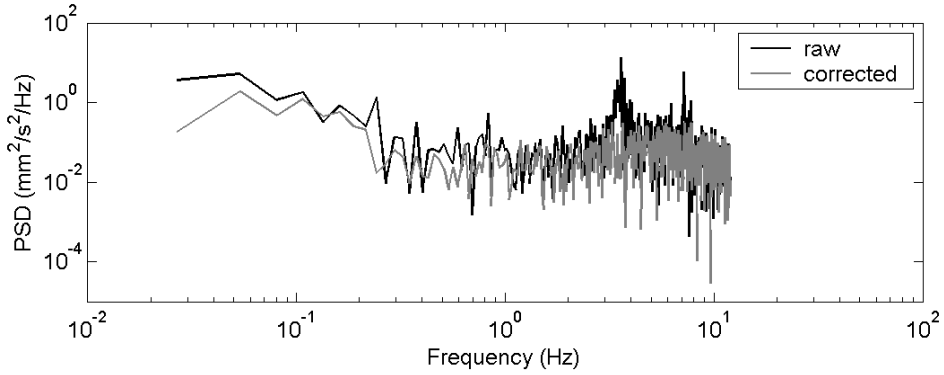

Figure 9.8 velocity spectra from calibration run before and after vibration filtering.

Despite the reduction in signal variation, applying this technique for vibration filtering generally had an insignificant effect on any of the calculated flow fields around cylinders and arrays of cylinders (for example a reduction in TKE of less than 2%). This correction was therefore not applied to any of the data presented in this thesis.

9.2.5.2 Particle Identification Process

Errors can be introduced in the particle identification process by either incorrect specification of camera pixel length scales (mm/pixel) or inter-frame time intervals, and through failing to identify particles correctly.

Length scales (mm/pixel) were calculated by placing a ruler in the field of view positioned at the same height as the light sheet. The length scale was calculated by dividing the length on the ruler by the length in pixels in the image. This procedure was repeated whenever the camera was moved. Typical distances measured to calculate length scales were 200 mm (± 2 mm). The pixel displacements equating to this distance depended on the camera elevation above the light-sheet, but typical values were around 670 ± 1 pixels. Length scales for most experiments were around 0.3 mm/pixel. Based on the error estimates for length and pixel displacements, the error in length scale was of order 1%.

Time intervals between frames were measured by recording elapsed time on a digital clock for a large number (1500) of frames. Thus the time step between frames was calculated with a high level of accuracy (error ± 6.7 x 10^{-6} sec/frame). In Streamline, the time interval between frames could be specified to 0.00001 sec. The majority of the images were captured at frame rates of either 24 or 43.55 Hz (Δt = 0.04167 and 0.02296 seconds), giving time step errors of 0.01% and 0.02% respectively.

Additional errors can be caused by lens distortion. Lens distortion results in a rectangle appearing either compressed or stretched at the edges, as indicated in Figure 9.9.

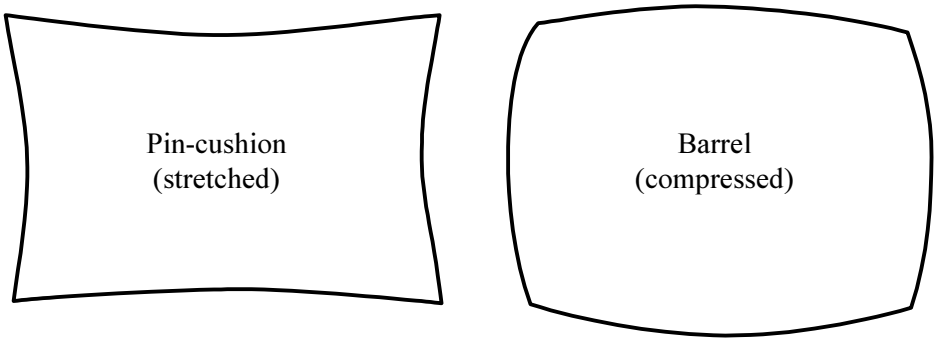

Figure 9.9 Pin-cushion and Barrel lens distortion modes.

Lens distortion is greatest for wide-angle lenses. A 25 mm focal length lens was used to give a desirable balance between field of view and minimal distortion. This lens gave a slight barrel distortion, leading to a small underestimate of velocities at the edges of the image. Compression at the edges of the image was 0.3% in comparison to the centre of the image.

Errors in identifying particles may arise if the intensity of the particle image is not Gaussian in nature, if particles are sufficiently close that they overlap, or if the illumination of particles is so low that there is little variation between particle intensities and the background. Also, if particles are small, measuring 1 or 2 pixels in size, the particle location can be estimated to no better than ¼ pixel accuracy. It is also possible for a single particle to have multiple intensity peaks due to shape, shadowing, orientation, and multiple light sources. Differences in light sensitivity for pixels of different colours can also have an effect. The JAI Bayer filter colour camera used in the experiments (described in section 9.3.5) had significantly higher light sensitivity at green pixels than at blue or red. As a result, the images needed to be converted to true colour before storing in a compressed format (JPEG). File compression was used to reduce disk space, as typical raw images were 1298 KB (TIFF format), with a single experimental run generating up to 1200 frames.

Errors in particle positions, length scales, and time steps will result in similar errors in the derived velocity fields. The errors generated by lens distortion (0.3% at edges), and precision of length (1%) and time scales (< 0.02%) are systematic errors that are constant in time. Their combined effect is small, and not considered to be of significance in comparison to other sources of error. Errors induced from locating particles (previous paragraph) are random in nature. It is expected that average velocity fields will be unaffected as time averaging will compensate for random errors. Instantaneous particle velocities will be affected to a degree, with a ± ¼ pixel accuracy for particle location corresponding to an instantaneous

velocity error of ~ ± 1.8 mm s^{-1} at a camera speed of 24 Hz, or 3.3 mm s^{-1} at a camera speed of 43.55 Hz. Due to the interpolation process, velocities from 3 particles are used to estimate velocity at grid points; therefore, there will be some degree of averaging, which should reduce the instantaneous velocity error. The particle location error is also smaller if the particles are sufficiently large that Gaussian profiles can be used to determine the particle centre. Based on typical towing velocities, the maximum instantaneous velocity error will be $u/U_0 \sim 0.05$. In summary, the errors from the particle identification process depend on particle size and how accurately the particle location can be determined. For the range of velocities used in these experiments, the maximum error in instantaneous velocity due to uncertainty in particle location will be around 5%.

9.2.5.3 Particle Matching Process

Errors may be generated during the particle matching process through incorrect particle matches, or missing correct particle matches. As identified in the particle matching process description (section 9.2.3), the accuracy of matching particles depends on several factors including: particle seeding density, particle displacement between frames (a function of the flow speed and camera frame capture rate), the rate of particles entering and leaving the light sheet, the degree of shear and rotation in the flow, as well as the costing strategies used. A large number of matches are considered desirable as this leads to a reduction in the size of the interpolation triangles when generating velocity fields. A high particle seeding density may result in an increased number of matches. Both correlation and space average velocity costing strategies work well with higher particle densities; however, they have difficulty in areas of high shear or rotation. The effect of shear and rotation may be reduced by limiting the inter-frame particle displacements through using either high frame-capture rates or low flow velocities.

The JAI camera used in the experiments had two frame-capture rates, 24 Hz (1292 x 1028 pixels) and 43.55 Hz (1292 x 512 pixels). The lower rate was found to allow successful matching of 70-80% of particles for tow velocities of < 80 mm/s. At higher tow velocities the faster camera frame capture rate was used. Bad particle matches could only be detected by visual inspection. The Streamline software allowed the particle matches and particles in a number of frames to be displayed as an image sequence or movie. Bad matches could be detected if they differ from surrounding matches, or did not appear to follow a consistent path. Bad matches were best avoided through careful selection of the matching algorithms and the values of the algorithm parameters.

9.2.5.4 Velocity Field Calculation Process

The most significant source of potential error in the velocity field calculation process arises from the interpolation process. The interpolation of velocities from randomly spaced matched particles onto a

regular grid will be most accurate if the particles are closely spaced. Where matched particles are widely spaced, they may be in quite separate regions of the flow, and therefore the interpolation from these velocities may not give a true representation of velocity at the grid point. Low densities of matched particles may occur in particular parts of the flow through difficulty in matching in regions of high shear or rotation, or if shadows cast by the cylinder array reduce the illumination of particles.

The interpolation process leads to a smoothing of gradients in velocity, and may reduce the magnitude of local peak or minimum velocities. Restricting the permitted size of the triangulation or velocity bins when interpolating on to a grid point can be used to reduce these errors.

A second source of error arises when calculating time-averaged quantities from the velocity time series at each grid point. If velocity estimates at a grid point are obtained for only a small number of frames, then the average of these values may not be a true measure of the actual mean (under-sampling). A measure of the number of velocity estimates obtained at each grid point is the *coverage* parameter. The coverage parameter is the ratio of the number of frames in which velocity estimates were obtained, to the total number of frames analysed. The coverage parameter can be improved by either increasing the density of matched particles (through denser particle seeding, lower particle identification thresholds, or improved particle matching), or by increasing the maximum acceptable size of interpolation triangles or bins. This second method must be balanced against the need to prevent over-large interpolations as described in the previous paragraph. A third option is to repeat the same experiment a number of times, and to average the data from all runs.

The effect of varying the size limits for the interpolation triangles is demonstrated with a profile of velocities on the centreline behind a single, smooth cylinder (Figure 9.10). The velocities and coverage factors in Figure 9.10 were calculated from a sequence of 750 frames, with an average of 1045 matched particles per frame. The images covered an area 406 x 323 mm, with an average matched particle density of 0.008 particles/mm^2. The cylinder diameter was 39.65 mm.

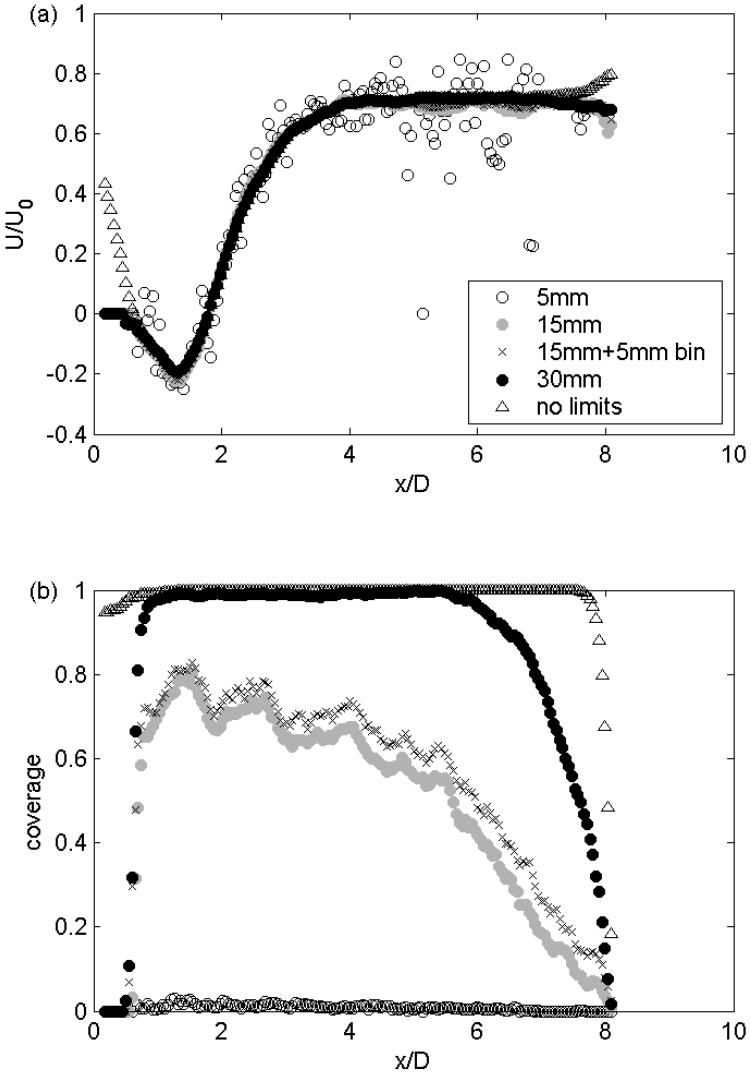

Figure 9.10 (a) Time-averaged streamwise velocities behind single cylinder, and (b) coverage factor at different interpolation triangulation limits.

At the smallest triangle limit of 5 mm, the number of frames contributing to each velocity estimate (coverage) was low, and the centreline velocity profile showed considerable variation with a number of missing or bad data points. With interpolation triangle limits of 15 mm or greater, velocity profiles were smoother and coverage improved. The slight variations in centreline velocities at $x/D > 5$ with an interpolation limit of 15 mm were reduced if multiple runs were averaged together. Also, by allowing the PTV system to use a 5 mm bin where interpolation triangles exceeded 15 mm, coverage was increased and the velocity profile smoothed. However, by permitting overly coarse interpolations, such as an interpolation limit of 30 mm or no limit on interpolation, there was a small reduction in the magnitude of the minimum velocity (local minimum) at $x/D \sim 1.5$. A small amount of detail regarding peak values was lost by allowing the interpolation to be overly coarse. For this data at least, the effect of changing interpolation limits was slight (with the exception of the lowest limits of 5 mm), which may be attributed to the high density of matched particles.

Centreline profiles presented in this thesis have been calculated using 15 mm triangle limits, with 5 mm bin limits imposed if the triangle limits were exceeded. These profiles were typically calculated at a grid spacing of 2 mm. The two-dimensional velocity fields were calculated using 25 mm interpolation limits (with 5 mm bins), to provide greater coverage, and therefore smoother average fields. These fields were calculated at a grid spacing of 5 mm. Finally, velocity spectra required continuous time series. Consequently spectra were calculated from velocity fields where no interpolation limits were applied. This may have resulted in a suppression of velocity fluctuations in regions where particle densities were low.

9.2.5.5 Performance of Streamline in Other Studies

Mean velocities are relatively simple to measure, and a high accuracy can be expected as many of the errors described above can be removed or reduced through averaging. Turbulent statistics, which are calculated from velocity fluctuations, are more challenging to measure accurately. The Streamline PTV system has been used in other studies where it has been found to give reliable and accurate results. The PTV system used in these experiments was used by Dark (2003) to study double-diffusive turbulent jets. Dark's profiles of both time-averaged and RMS axial velocities across a jet show excellent agreement with the LDV (laser-Doppler velocimeter) measurements of Papanicolau and List (1988). This indicates that the Streamline system is capable of measuring turbulent velocity fluctuations with a high degree of accuracy.

9.3 Methodology for Flow Visualisation

9.3.1 Towing Tank and Trolley

All of the laboratory experiments were conducted in a glass walled tank of length 6.0 m, width 1.5 m, and depth 1.0 m (Figure 9.11). Fresh water was used in all experiments (temperature 12-18 ^{o}C). Test specimens were towed beneath a trolley running on rails along the length of the tank. The trolley was driven by a 3-phase electric motor, with trolley speed controlled by a variable speed drive. The trolley and trailer ran on rubber wheels and was driven by rack and pinion.

The trolley speed was measured using a digital clock triggered by micro-switches attached to the rails. The speed was calculated by dividing the measured distance between the micro-switches by the elapsed time. The distance between the two micro-switches was 1797 ± 1 mm, and the elapsed time measured to 1/100th of a second.

Figure 9.11 Towing tank and trolley used for flow visualisation experiments. Light boxes can be seen to the left of the tank, and a large Perspex boat to which cylinders were attached is suspended from the trolley.

9.3.2 Test Specimens

For the flow visualisation experiments, test cylinders were constructed from PVC tubing or wood, with sand or fine gravel providing surface roughness. Cylinders were spray painted black with a mat acrylic paint to reduce illumination of the cylinders in the light sheet. While the surface roughness of the painted PVC cylinders was not quantified, the roughness is very low in comparison to the other test cylinders. Providing that the surface roughness does not protrude through the laminar boundary on the cylinder surface, the cylinder will be hydraulically smooth. As experiments were conducted at Reynolds numbers of less than 10^4, Figure 8.7 indicates that the PVC cylinder will behave as if it were hydraulically smooth. For the remainder of this thesis, these cylinders are described by the term "smooth", acknowledging that the surface has a very low roughness rather than being perfectly smooth. The PVC cylinders had an outer diameter of 42.2 mm.

Cylinders with a surface roughness ratio of 0.045 were produced by coating PVC cylinders with sand grains sieved to a uniform size of 2 mm. The sand covering was applied using a rapid setting two-pot epoxy resin (Selleys Araldite 5 minute Everyday) on the cylinder surface, and immersing the cylinder in a tube filled with the sand. As a result of coating the cylinder, the mean diameter was increased by 2 mm, giving an effective diameter of 44.2 mm.

Cylinders with a surface roughness of 0.094 were produced by coating wooden cylinders (diameter 38.85 mm) with gravel sieved to between 3.35 mm and 4.75 mm. By adding the grain size to the diameter of the wooden cylinder, an effective cylinder diameter of 42.9 mm was calculated.

All cylinders were 890 mm in length. The three different cylinder roughnesses are shown in Figure 9.12.

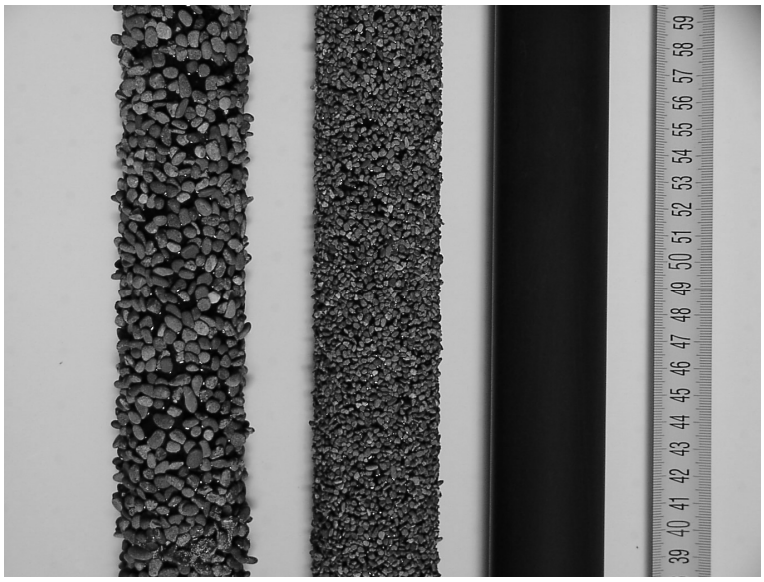

Figure 9.12 Test cylinders used in PTV experiments. From left to right k_s/D= 0.094, 0.045, and painted PVC. The scale (right) is in cm.

Test specimens were screwed to the underside of a rectangular Perspex boat attached to the trolley. The purpose of the boat was to provide a clear view into the tank avoiding refraction and reflection of light by surface waves. The boat was partly submerged with the underside of the boat 10-15 mm below the water surface. Different sized boats were used depending on the experimental configuration. Perspex boat dimensions for the single cylinder experiments and arrays across the tank were 600 mm x 1400 mm (long-dimension across the tank), and 950 mm x 1200 mm for arrays angled to the flow.

9.3.3 Particle Seeding

To enable Particle Tracking Velocimetry, the water in the tank was seeded with Pliolite VTEC resin, with a specific gravity of 1.03, ground to a sieve size between 180 and 250 μm. A particle seeding density of 40 g m^{-3} was found to give suitable particle density for the PTV process. The particles were added in batches by mixing ~ 40 g of particles in a 1 litre bottle with a small amount of surfactant. The contents of the bottle were injected beneath the water surface at various locations in the tank to obtain an even particle distribution.

Due to the slight negative buoyancy of the particles, over time the particles would settle to the bottom of the tank, requiring periodic re-suspension. A broom was found to be an effective implement to sweep the

particles from the tank floor, and to agitate particles into suspension. After re-suspension, the tank was left to sit for 30 minutes to allow motions generated by stirring to decay. Likewise, 10 minutes was allowed between runs for fluid motions generated during the experiment to decay. Repeated runs at intervals from 2 to 30 minutes showed that no significant difference could be detected in data provided runs were spaced more than 5 minutes apart.

9.3.4 White Light Source

To illuminate the particles in the flow, a white light sheet was generated using light boxes. The light boxes had dimensions of width 600 mm, length 560 mm, and height 200 mm; each containing a 2 kW halogen bulb approximately 300 mm long, and 10 mm in diameter. Due to the considerable heat generated by the bulbs, the boxes were vented, using two fans to drive air over the bulb. The bulb was positioned towards the rear of the box, with light passing through 2 horizontal slits. The first slit measured 12 mm wide by 400 mm long, and was located 200 mm from the bulb. The second slit, at the front of the box, measured 6 mm wide by 400 mm long. A sketch showing the light box dimensions is given in Figure 9.13, and a photograph in Figure 9.14.

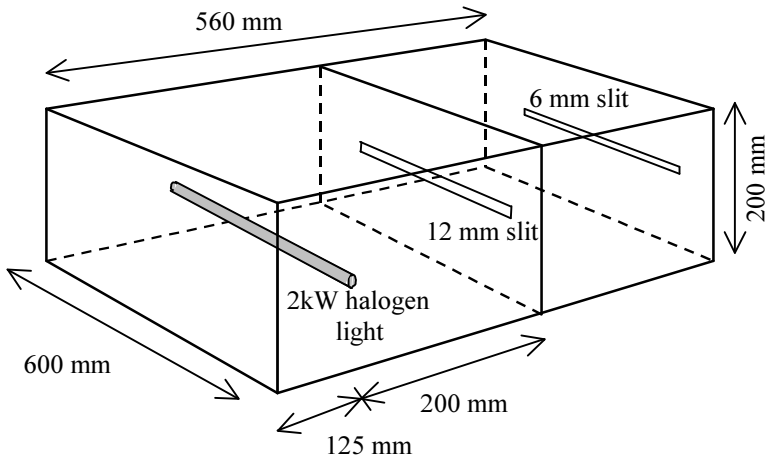

Figure 9.13 Diagram of light box used to generate white light sheet.

Six light boxes were used, three along each side of the tank (Figure 9.14). The light boxes were positioned so that the overlapping sheets illuminated a length of 3 m within the tank. The light sheets diverged after passing through the slits, and at the centre of the tank, the light sheet thickness measured approximately 20 mm.

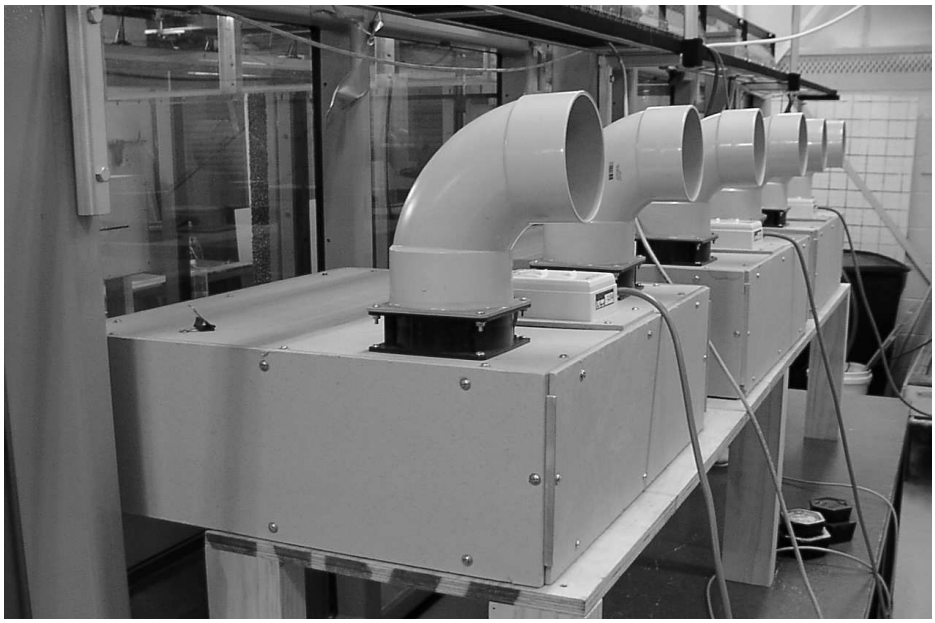

Figure 9.14 Photograph of light boxes. The white PVC tubes are vents, and the black objects between the tubes and the boxes are fans.

9.3.5 Camera and Image Capture

Images were captured using a digital video camera mounted on the trolley, positioned to view the flow through the clear Perspex boat. Images were captured on computer using a program developed in LabView. Three different cameras were tested to find the optimal balance between resolution, frame capture rate, and light sensitivity (Table 9.1).

Camera	Frame Rate (Hz)	Resolution (pix)
Pulnix 1010	15	1008x1008
Pulnix 6710	60 or 120	640x480
JAI CV-M7+	24 or 43.55	1292x1028/512

Table 9.1 Digital camera capture rates and resolution.

The Pulnix 1010 had the highest light sensitivity with high resolution, enabling a high number of particles to be detected. However the low frame capture rate meant that this camera was only suitable for low towing speeds, as at higher speeds particle displacements between frames hindered the particle matching process.

The Pulnix 6710 allowed much higher frame capture rates, however it had poor light sensitivity, resulting in low particle intensities. This camera was found to be unsuitable due to its poor light sensitivity.

The JAI CV-M7+ camera could operate at different frame capture rates by capturing either full frame images at 24 Hz, or half frame images at 43.55 Hz. The camera could also be operated in quarter or eighth

frame mode at higher frequencies; however, these images were too slender to be of practical use. This camera had a moderate light sensitivity, between that of the Pulnix 1010 and 6710 cameras. The JAI camera was a Bayer filter colour camera. The raw images could not be used directly due to the higher light sensitivity of the green pixels. Software was required to convert the raw images to true colour images.

The experimental configuration used for the PTV experiments is summarised in Figure 9.15.

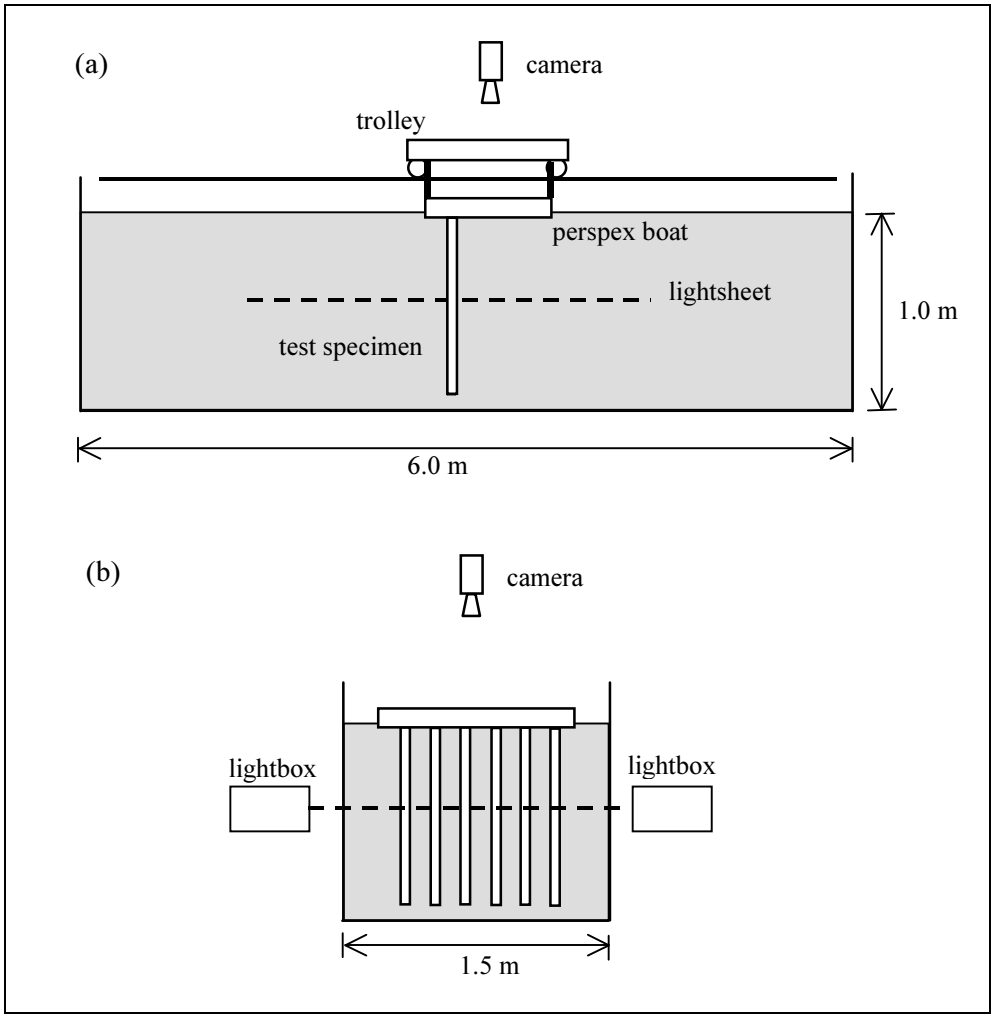

Figure 9.15 Experimental configuration (a) from side, (b) from end.

9.4 Methodology for Drag Measurement

9.4.1 Load Cell Apparatus

Drag experiments were performed in the same towing tank used for flow visualisation. Two different load cell apparatus were used to measure the drag on cylinders or arrays of cylinders.

A two-component load-cell was used to obtain drag and cross-stream force components for cylinder arrays. Two load-cells were attached at right angles, with the upper load-cell attached to the underside of the trolley, and the lower load-cell attached to the test specimen. The load-cells were obtained from electronic scales, and had a ±15 kg maximum load rating. This was far greater than the maximum loads applied during testing, but the stiffness of the load-cells reduced vibration and flex. Load-cell output was amplified then digitised at sampling frequencies of either 8 Hz (before 14 March 2002) or 200 Hz (after 14 March 2002). Where only drag forces were required, the cross-stream load-cell was removed to improve the rigidity of the fixture. The single load-cell configuration is shown in Figure 9.16.

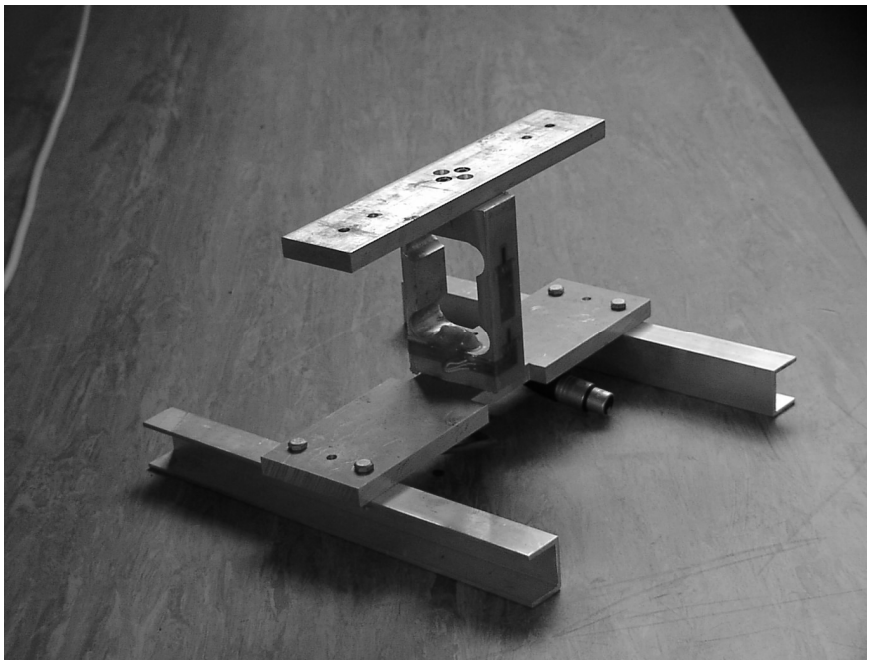

Figure 9.16 Load-cell apparatus 1 in single load-cell configuration.

A more sensitive load measuring apparatus was fabricated for measuring drag on single or low numbers of cylinders. This apparatus consisted of a ± 2 kg load-cell measuring horizontal forces; while out of plane (vertical or cross-stream) forces and rotations were resisted by a parallelogram shaped hinged support. A schematic diagram of this system is shown in Figure 9.17, and a photograph in Figure 9.18.

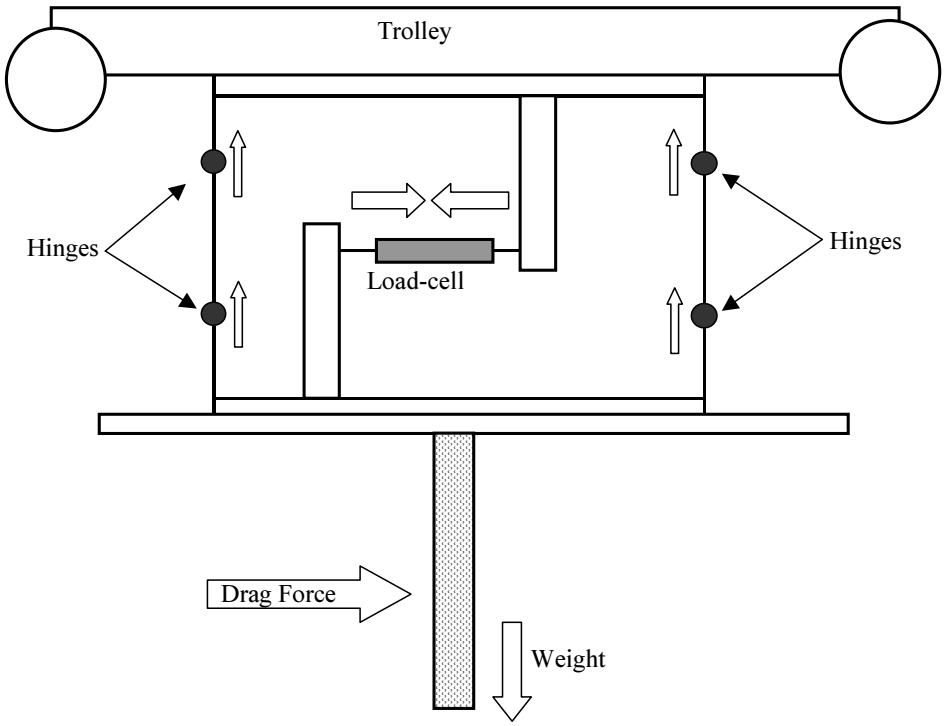

Figure 9.17 Schematic of load cell apparatus 2 with 2 kg load-cell. Horizontal forces are measured by the load-cell, while the hinges support vertical forces.

Figure 9.18 Photograph of load-cell apparatus 2, with 2kg load-cell.

9.4.2 Load-cell Calibration

Load-cells were calibrated by measuring the load-cell output in response to the application of known loads. The 15 kg load-cells (apparatus 1) were calibrated with weights from 0 to 5 kg. The calibration

procedure also allowed the two load-cells to be adjusted to so that they were oriented at 90°. Both load-cells responded only to single-axis force components (out of plane forces had no effect on load-cell output). After signal digitisation, load-cell output sensitivity was ± 0.03 N.

Load-cell apparatus 2 was calibrated using weights from 0 to 1 kg. The calibration procedure also demonstrated that cross-stream forces and vertical forces had no effect on load-cell output. The sensitivity of this load-cell apparatus was ± 0.008 N.

9.4.3 Test Specimens

Cylinders were constructed from 20 mm nominal diameter (actual diameter 20.2 mm) wooden dowel, as well as 40 mm (actual diameter 39.65 mm) wooden dowel and 42.2 mm PVC. The cylinders were painted, and additional roughness added by coating with 2 mm or 4 mm gravel as described in section 9.3.2 (see also section 10.2.1). The wooden cylinders used for the 40 mm nominal diameter specimens were obtained from a different source to those used for the flow visualisation, hence the slightly larger diameter.

9.4.4 Data Analysis

Raw data was processed by filtering and re-sampling at a lower frequency (with averaging) using the Matlab "decimate" function (Figure 9.19). Prior to re-sampling, the decimate function filtered the data with an eighth order Chebyshev Type I low-pass filter with cut-off frequency 0.8*(Fs/2)/R, where Fs is the original sampling frequency, and the data is re-sampled at 1/R times the original sampling rate. The re-sampling rate used was $1/10^{th}$ of the raw sampling frequency.

The average drag force for each run was calculated from the processed data set after correcting for zero offset and discarding the data recorded during the trolley acceleration and deceleration periods.

The high frequency fluctuations in the raw data signal (Figure 9.19(a)) were due to transmission of vibration from the trolley drive and rails.

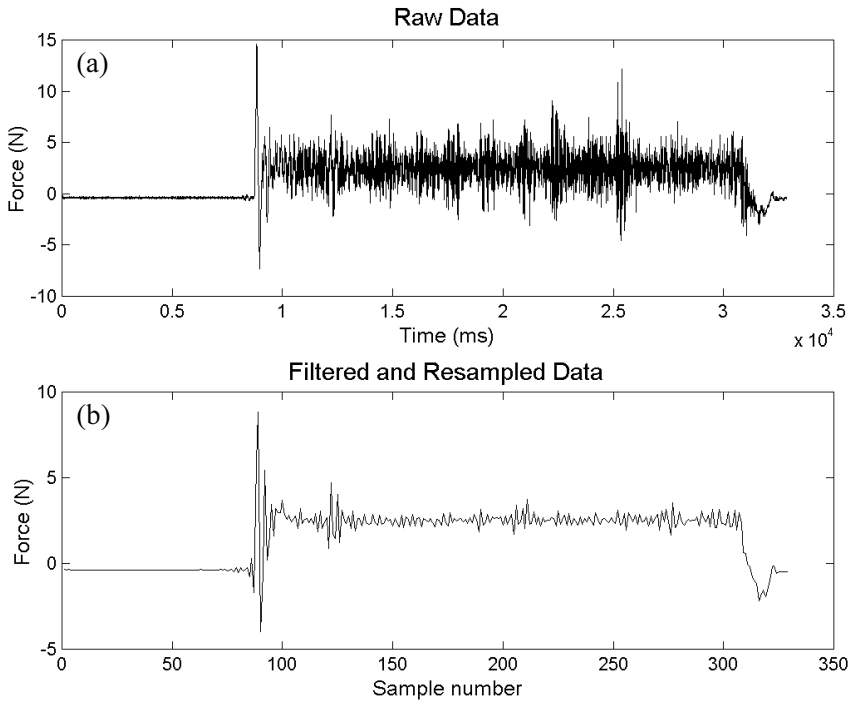

Figure 9.19 Example of (a) raw and (b) filtered drag data time series.

Drag coefficients for each cylinder configuration were calculated in two ways. Firstly, to compare drag coefficients at different Reynolds numbers, the drag coefficients C_D were calculated for each run from the averaged drag force F and measured velocity U using equation 9.6, where A is the projected area of the cylinder or cylinder array (cylinder diameter x length), and ρ the water density.

$$C_D = \frac{1}{\frac{1}{2}\rho A} F / U^2 \tag{9.6}$$

Alternatively, if drag coefficients were sufficiently uniform over the velocity range used in the experiments, an averaged drag coefficient was obtained by plotting the drag force against velocity squared for all runs. The slope F/U^2 was calculated from a linear regression forced through zero force at zero velocity. Drag coefficients were then calculated using the regression slope for F/U^2 in equation 9.6.

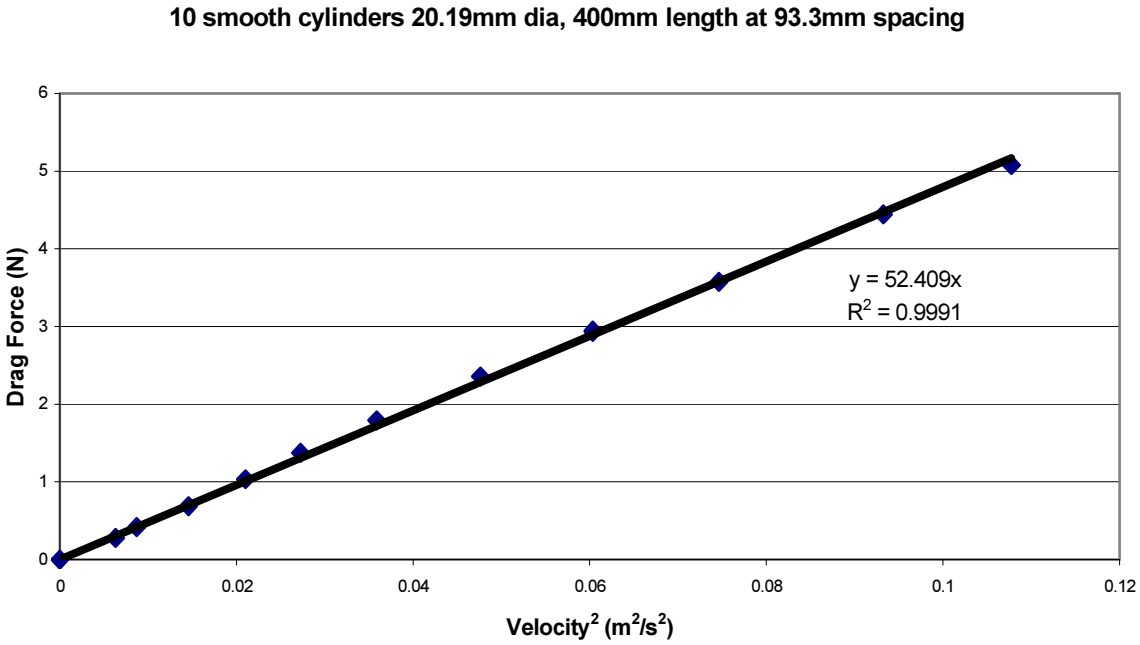

Figure 9.20 Drag force plotted against Velocity^2.

Estimates of the error for the drag coefficient were obtained from the confidence interval for a linear regression not forced through zero. In all measurements the difference in the regression slopes of F versus U^2 forced and not forced through zero were small. For example, a standard linear regression for the data presented in Figure 9.20 gives a slope of 47.492 and a y-intercept of 0.0327. The difference in slope is 1%. The zero-intercept regression was used for calculating the drag coefficient as more consistent comparisons were found between tests. Details of the estimate of error are given in Appendix G.

CHAPTER 10 EFFECT OF EXTREME SURFACE ROUGHNESS ON THE FLOW AROUND SINGLE CYLINDERS

10.1 Introduction

In this thesis, a mussel long-line has been described as an array of cylinders, with each vertical mussel dropper represented by a cylinder. To determine if this is an accurate model of a mussel long-line, it is first necessary to compare the flow around an irregular, rough mussel dropper with that of a cylinder. The mussel droppers resemble extremely rough cylinders. The purpose of this chapter is to assess the effect of the extreme surface roughness for the flow around a cylinder. In this chapter, only single cylinders are studied. Experiments with multiple cylinders are presented in Chapters 11 and 12.

The influence of surface roughness on single cylinders has received much attention, dating back to the early studies of Fage and Warsap (1929). It has been demonstrated that only a very small surface roughness is required to trigger the onset of boundary layer turbulence, leading to a drop in cylinder drag coefficient at reduced Reynolds numbers. Surface roughness is expressed as the ratio k_s/D where k_s is the surface roughness size (equivalent sand grain diameter), and D the cylinder diameter. Experimental evidence shows that increasing the surface roughness ratio causes the drag coefficient reduction to occur at a lower Reynolds number. At Reynolds numbers below this transition, the surface roughness appears to have no effect on drag coefficient. However, the decrease in drag coefficient is smaller as the roughness is increased. At Reynolds numbers higher than this transition, the drag coefficient approaches a near constant value that is determined by the cylinder roughness. It appears that as roughness is increased, the drag coefficients for rough cylinders at high Reynolds numbers begin to collapse to a value of about 1. Generally most experiments with rough cylinders have been limited to $k_s/D < 0.02$. In environmental situations such as the flow around mussel-incrusted ropes in aquaculture long-lines, the roughness can be much higher. For example, densely seeded mature mussels with a shell length of 80 mm growing on a 25 mm diameter rope form a very rough cylinder, with the roughness ratio approaching 0.5 (section 8.2.6).

A wide range of behaviours have been described in the literature for the flow around smooth cylinders. These different flow regimes are a function of Reynolds number. In this chapter, experiments are used to investigate the modifications to flow caused by extreme surface roughness. However, the experiments will be confined to a relatively narrow range of Reynolds numbers, partly due to time and equipment constraints, but mostly as only Reynolds numbers applicable to typical mussel farm situations are relevant for the purpose of this thesis. With typical velocities at mussel farm sites of the order 0.01-0.2 m/s, and dropper diameters of 0.10-0.15 m, relevant Reynolds numbers are from 10^3 to $3\text{x}10^4$. Experiments presented here were conducted towards the lower end of this range. The practical limit using the PTV

system was $Re \sim 5000$ for a cylinder of 40 mm diameter, with a camera frame capture rate of 43.55 Hz. This was a trolley speed of $U_0 \sim 125$ mm/s. Above this speed, the particle displacements between frames were too large to allow a high rate of particle matches.

The general process followed in this chapter is to make comparison between smooth and rough cylinders. We are particularly interested in factors that will be useful for understanding mussel farms. Drag is a fundamental parameter, as the drag on the mussel droppers will determine the structural loads, and the effect on the flow. The generation and dissipation of turbulence is intrinsically linked to energy loss, which has implications for the flow through the farm. Turbulence also plays an important role in the transport of nutrients and waste.

An understanding of the effect of extreme surface roughness on cylinders may have other applications beyond mussel farming. With this in mind, cylinders with a range of surface roughness were used in the experiments presented here.

10.2 Methodology

10.2.1 Drag Tests

Drag tests were performed to measure the effect of surface roughness on single cylinders. Three cylinders were tested, each made from 39.65 mm diameter wood with different surface roughness:

- $D = 39.65$ mm, surface smoothed using fine sand-paper, then painted,
- effective diameter $D = 41.65$ mm, 2 mm surface roughness, $k_s/D = 0.048$,
- effective diameter $D = 43.65$ mm, 4 mm surface roughness, $k_s/D = 0.092$.

Cylinders were towed at speeds of between 20 and 320 mm/s (Re 700 to 12,000). All cylinders had a length of 447 mm, but were submerged to a depth of 428 mm, giving length/diameter ratios of 10.8, 10.3, and 9.8 for the smooth, 2 mm rough, and 4 mm rough cylinders respectively. The cylinders protruded through the free surface, and the top of the cylinders were attached to the underside of the load-cell apparatus. The water depth was 980 mm.

Drag was also measured for two short lengths of a mussel dropper. Only short lengths could be tested due to the depth of the tank. One of the samples cut from the mussel dropper was re-tested after gutting, cleaning, and reattaching the shells to the dropper rope (using glue). This enabled further testing without the unpleasant consequences of decomposing mussel tissue.

10.2.2 PTV Visualisation

Experiments were conducted on cylinders with 3 different surface roughnesses. Smooth cylinders were fabricated from PVC pipe with a nominal diameter of 40 mm (actual diameter 42.2 mm). Cylinders were painted black to reduce light reflection. The actual roughness of these cylinders could not be measured, however PVC pipe is generally considered to be hydraulically smooth, particularly at Reynolds numbers relevant to this study. A cylinder with a surface roughness ratio k_s/D = 0.045 was produced by coating a PVC cylinder (nominal diameter of 40 mm) with coarse sand sieved to a uniform diameter of 2 mm. The sand coating increased the effective diameter of the cylinder to 44.2 mm, giving a roughness ratio of 0.045. Very rough cylinders were produced by coating a wooden cylinder with fine gravel sieved to a size range 3.35 mm to 4.73 mm (average 4.05 mm). The effective diameter of this cylinder was 42.9 mm, giving a surface roughness ratio of k_s/D = 0.094. The wooden cylinders used for the flow visualisation experiments were of a slightly smaller diameter than those used in the drag tests, explaining the difference in effective diameters and surface roughness ratios. All cylinders were 890 mm in length, giving length to diameter ratios of $L/D \sim 21$. Reynolds numbers for the PTV experiments presented here are in the range 1300 to 5000.

Data were analysed using the PTV system described in the previous chapter. For the experiments presented here, data from a minimum of 4 repeated runs were combined to obtain time-averaged velocity fields.

10.3 Results and Discussion

10.3.1 Cylinder Drag

The experiments presented here cover a Reynolds number range of 700 to 12,000, which would be classified as TrSL2 (Zdravkovich, 1997) for the smooth cylinder. This flow state is defined by the formation of eddies in the shear layer. Drag coefficients measured from the tow-tests are plotted in Figure 10.1. At Reynolds numbers below approximately 4000, the drag on the individual cylinders was too low for accurate measurement, giving a large variation in drag coefficients. At Reynolds numbers below 4000 (velocity of ~ 100 mm/s), the mean drag force was ~ 0.08 N, which is close to the sensitivity of the load-cell apparatus (± 0.008 N, see section 9.4.2). Also, the force fluctuations due to vibration were larger than the mean drag force at these low speeds. Therefore, the drag measurements for single cylinders at Reynolds numbers less than 4000 (velocity ~ 100 mm/s) have been discarded. At Reynolds numbers above ~ 5000, drag coefficients for all cylinders were within the range 0.9 to 1.2. The drag coefficients for the smooth and k_s/D = 0.092 cylinders were similar, with slightly lower values measured for the cylinder with k_s/D = 0.048.

An average of the drag-coefficients from Re = 5,000 to 12,000 in Figure 10.1 can be used as a representative value for each of the three cylinders. This provides drag coefficients for the smooth cylinder of 1.07 ± 0.11 (90% confidence interval), 0.98 ± 0.06 for k_s/D = 0.048, and 1.10 ± 0.06 for k_s/D = 0.092.

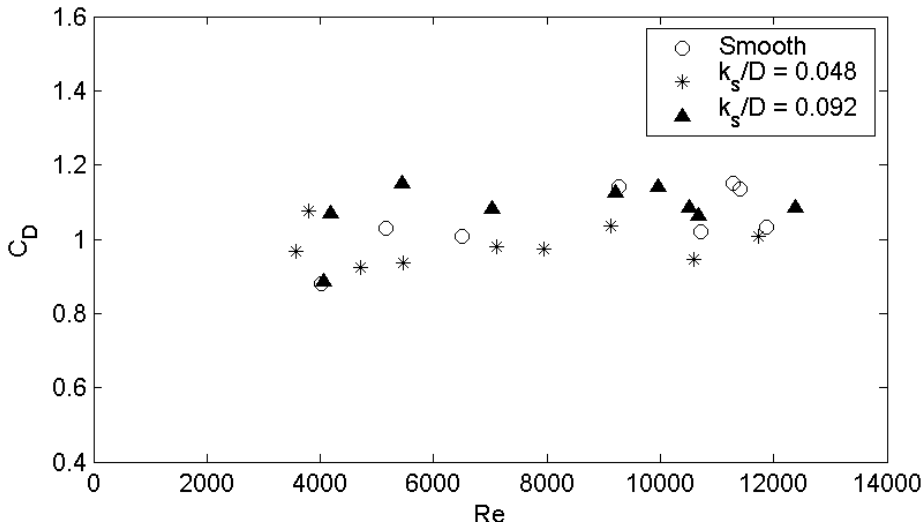

Figure 10.1 Drag coefficients versus Reynolds number from experimental drag tests.

A second estimate of drag-coefficient was obtained by plotting the drag force against U^2, and using the regression slope to calculate C_D (see equation 9.6). For example, drag force is plotted against U^2 for the smooth cylinder in Figure 10.2. The slope for a least squares regression fit to the data (forced through the origin) is 9.22 ± 0.35 N s^2 m^{-2} (90% confidence interval). The drag coefficient for the smooth cylinder is calculated as 1.09 ± 0.04. The drag coefficients for the rough cylinder with k_s/D = 0.048 was C_D = 0.99 ± 0.02, and for k_s/D = 0.092, C_D = 1.08 ± 0.03. These are in agreement with the previous estimates.

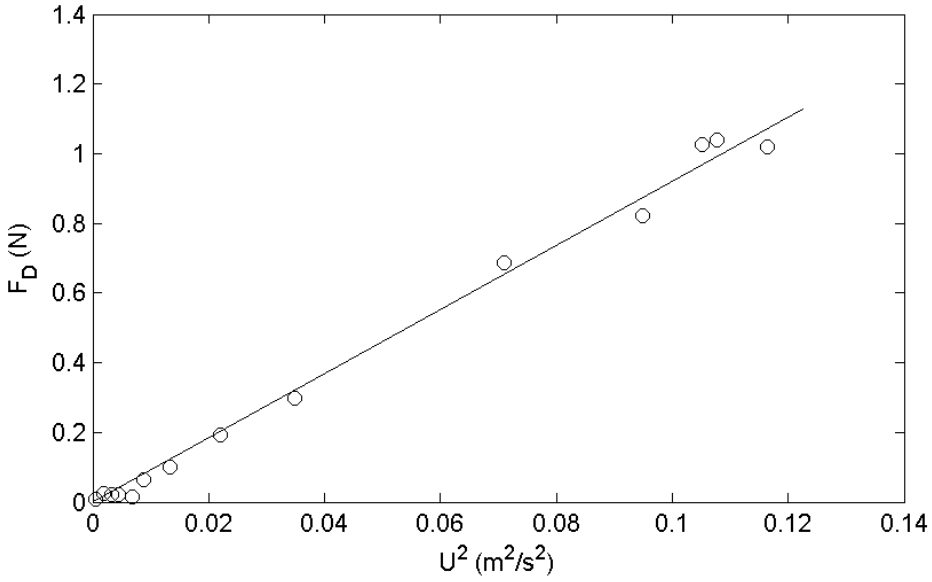

Figure 10.2 Drag force plotted against velocity squared for smooth cylinder, *L/D* = 10.8. Open circles are measured data, and the solid line is a least squares regression fit through the origin.

As the cylinders used for the drag experiments were relatively short, a correction is required to account for the free end at the base of the cylinder. For a cylinder attached to a flat surface, the effective aspect ratio is doubled as the surface provides a plane of symmetry. Assuming that the free-surface also acts as a plane of symmetry, the effective aspect ratios of the cylinders were approximately $L/D \sim 20$. Published values for the drag coefficient of a smooth cylinder, summarised by Figure 21.78 in Zdravkovich (2003), at $L/D \sim 20$ are $C_D \sim 0.94 - 1.0$ ($Re \sim 10{,}000$). For truly two-dimensional cylinders, the accepted values for drag coefficients in the TrSL2 region are between 1.0 and 1.2, increasing with Reynolds number (see Chapter 8; Figure 8.4). This implies that a correction factor accounting for the cylinder aspect ratio is approximately $C_D/C_{D0} \sim 0.88$, where C_D and C_{D0} are raw and corrected drag coefficients respectively. Raw and corrected values of C_D for the three cylinders are given in Table 10.1. Wave drag has not been accounted for in the calculation of drag coefficient. Some energy will be lost to free-surface waves. As the Froude numbers were low (maximum of $F_r = U/\sqrt{gH} \sim 0.03$), wave drag is not considered to be significant.

Cylinder Roughness	Aspect Ratio Actual (effective)	Raw Drag Coefficient	Drag Coefficient corrected for Aspect Ratio
Smooth	10.8 (21.6)	1.09 ± 0.04	1.24 ± 0.05
$k_s/D = 0.048$	10.3 (20.6)	0.99 ± 0.02	1.13 ± 0.02
$k_s/D = 0.092$	9.8 (19.6)	1.08 ± 0.03	1.23 ± 0.03

Table 10.1 Measured drag coefficients for single smooth and rough cylinders.

10.3.2 Drag on a Length of Mussel Dropper

Drag measurements were also made for two sections of a mussel dropper (referred to as samples 1 and 2 below). Mussels from the first sample were stripped from the line, cleaned, removed of mussel tissue, and re-attached to the crop rope to form a third sample (sample 3). The lengths of the samples were 0.63 m for samples 1 and 3, and 0.47 m for sample 2.

The relationship between drag coefficient and drag force for bluff bodies is normally based on the projected area. For a cylinder, this area is the diameter multiplied by the length. For an irregularly shaped object such as a mussel dropper, the area is more difficult to determine. The projected area for sample 3 was measured using a planimeter to trace the shadow cast from a distant light source. A representative projected area of 77,165 mm^2 (for a 0.63 m length) was obtained by averaging the projected area from three orientations of the mussel dropper. This area was also used for sample 1. The projected area for sample 2 was estimated by multiplying the length of the sample by an average diameter, determined from a 50 cm long section of the projected area of sample 3 (avoiding the ends of the mussel dropper). The

average diameter based on projected area was 0.137 m. Drag coefficients were calculated from the regression of drag force versus velocity squared, as in Figure 10.2.

Length to diameter ratios were low due to the space limitations imposed by the depth of the available towing tank. Length to diameter ratios for samples 1 and 3 were L/D = 4.6, and for sample 2, L/D = 3.43. As in the cylinder tests, the free surface provided a plane of symmetry effectively doubling the aspect ratio. Correction factors for the drag coefficients (Zdravkovich, 2003) are C_D/C_{D0} ~ 0.78 for samples 1 and 3, and C_D/C_{D0} ~ 0.74 for sample 2. The drag coefficients for samples 1 and 3 are in agreement, however the drag coefficient for sample 2 is 10% higher (Table 10.2). The values for samples 1 and 3 are considered more reliable due to the greater length of dropper tested.

Mussel Line	Length (m)	F/U^2 ($N.s^2.m^{-2}$)	Drag Coefficient C_D	Corrected Drag Coefficient
Sample 1	0.63	39.67	1.03 ± 0.06	1.32 ± 0.08
Sample 2	0.47	36.73	1.14 ± 0.04	1.46 ± 0.05
Sample 3 – shells only	0.63	41.80	1.08 ± 0.07	1.38 ± 0.09

Table 10.2 Drag coefficients for mussel dropper (with 90% confidence interval) based on projected area, Reynolds number range $1.1x10^4$ to $3.4x10^4$.

As the mussel dropper is a highly irregular and 3-dimensional object, the projected area is a rather inconvenient and difficult quantity to measure. Noting that drag force is the product of drag coefficient and projected area, other length-scales may be used to estimate the effective area of the dropper provided that the drag coefficient is modified appropriately. The length of the dropper can be determined easily, and is one obvious length scale. The second length scale for a cylinder is the diameter, which is more difficult to estimate. Using projected area, the diameter was estimated as 0.137 m. An alternative diameter scale is to calculate an equivalent cylinder diameter based on the volume of the mussel dropper. By submerging a length of dropper (sample 3) to obtain the displaced volume, an equivalent cylinder diameter of 0.084 m was estimated. Drag coefficients based on this diameter were ~ 2.1 (corrected for aspect ratio).

A more convenient length scale that also approximates closely the visual, or apparent, diameter of the dropper is to assume the dropper diameter is twice the average mussel shell length. The average length of the mussel shells for samples 1 and 3 was 83.4 mm, giving a diameter scale of 0.167 m, and a drag coefficient of 1.10 ± 0.07 (corrected for aspect ratio). For industry application, a representative diameter, and associated drag coefficient, based on the mussel shell size is likely to be the most convenient scale. However, there is the possibility that drag coefficient varies as the mussels grow in size. The drag coefficient has only been measured here for a particular mussel size, which is representative of the size at

which mussels are commonly harvested. This is perhaps the most important drag coefficient as this is when the mussels are largest and likely to have the greatest effect on the flow.

10.3.3 Centreline Velocity Profiles behind Smooth Cylinder

The following notation is used in interpreting the PTV data. Instantaneous velocities consist of a mean (time-averaged) component U or V, and a turbulent fluctuation of u or v. Triangular brackets around a quantity (< >) signify that the variable is time-averaged, e.g. $\langle uu \rangle$ is the average of the squared streamwise velocity fluctuation. By definition, $\langle u \rangle = \langle v \rangle = 0$. The normal convention of $-\langle uv \rangle$ is used for the turbulent shear stresses.

PTV measurements of time-averaged centreline velocity close behind a smooth cylinder are plotted in Figure 10.3. Profiles are taken along a line in the downstream (x) direction passing through the cylinder centreline ($y = 0$). As described in section 9.2.5.4, centreline profiles were calculated using 15 mm limits on the velocity field interpolation triangles with 5 mm bin limits imposed if the triangle limits were exceeded. Velocities were calculated at 2 mm increments along the centreline. Mean values were averaged from a minimum of 4 runs, each of between 600 and 1000 frames.

Immediately downstream of the cylinder, a region of negative velocities occurs with flow recirculating back towards the cylinder. The length of this region, or near wake, x_0 is defined as the point where $U = 0$. As indicated in Figure 10.3, the length of this zone behind a smooth cylinder is a function of Reynolds number (Re), with the length decreasing with increasing Re.

For comparison, data published by Norberg (1998) is also plotted in Figure 10.3. Norberg measured centreline velocity profiles with a commercial (Dantec) Laser Doppler Velocimetry system behind a cylinder of diameter 6 mm, length 390 mm with end plates in a wind tunnel. The blockage ratio (the proportion of the wind tunnel cross-section filled by the cylinder) was 1.5%.

There are considerable differences in both the length of the recirculating zone and the maximum negative velocity when comparing the present PTV data with Norberg's LDV data at similar Reynolds numbers. The PTV data (these experiments) showed a greater variation in wake length, with x_0/D decreasing from 2.8 at Re 1330, to $x_0/D = 1.5$ at Re 4950. Norberg recorded a change from $x_0/D = 2.3$ at $Re = 1500$ to $x_0/D = 1.9$ at $Re = 5000$. Also, the maximum negative velocity in the near wake region measured by PTV was ~ -0.24, while Norberg recorded $U/U_0 \sim -0.45$. The differences between the present PTV data and Norberg's results were even greater for the stream-wise velocity fluctuations (Figure 10.4). In particular the locations of peak u_{rms} were further downstream in the PTV data, and the velocities in the peak were also smaller. The double peak recorded by Norberg was not detected with the PTV system.

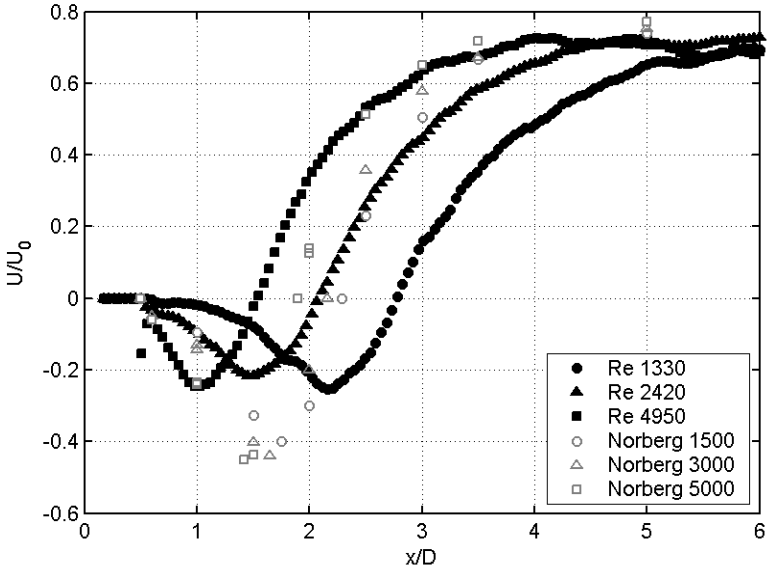

Figure 10.3 Centreline velocities behind a smooth cylinder from PTV and Norberg (1998).

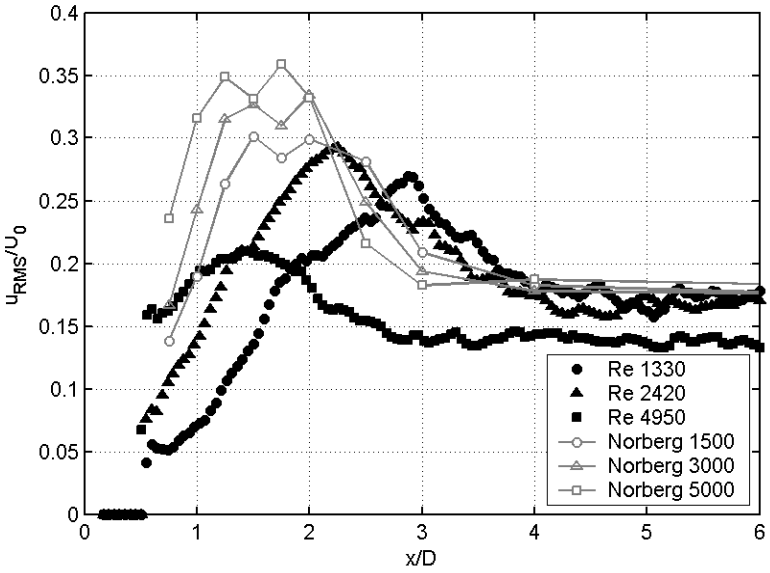

Figure 10.4 Centreline u_{rms} behind a smooth cylinder from PTV and Norberg (1998).

The downstream u_{rms} values at *Re* of 4950 (Figure 10.4) were lower than those at *Re* = 1330 and 2420. There was also a greater difference between the present data at *Re* = 4950 and Norberg's results at a similar Reynolds number (*Re* = 5000) than between the two data sets at lower Reynolds numbers. The PTV results for u_{rms} at high Reynolds numbers are less reliable due to a lower success rate in matching particles between frames. Two of the factors responsible are that particle displacements are larger at the higher velocities, and the particle images also smear slightly as shutter speeds were limited by camera light sensitivity. The smearing made it more difficult to locate particles, and the large particle displacements hampered the matching process between frames. As a consequence, it is expected that u_{rms}

values are underestimated, although mean velocities should be accurate. At the lower Reynolds numbers, the particle displacements were small, and image smearing was not significant.

Two possible reasons for the difference between the current PTV data and the LDV data of Norberg are that the difference may be due to either errors generated in the PTV process, or differences in the experimental configuration (it is also possible that there are errors in Norberg's LDV data). The most likely source of error in the PTV system is in the interpolation of velocities onto grid points. The spatial averaging as a result of using interpolation triangles may reduce the peak return flow within the near wake. However the near constant rate of recovery of velocities downstream would indicate that the location of the point where $U/U_0 = 0$ should be measured with sufficient accuracy. Also, using a binning process (with a 3 mm bin size) instead of interpolation triangles gave the same position of $U/U_0 = 0$. Indeed, the locations of the point of wake closure ($U = 0$) in Figure 10.3 are consistent with the observed particle paths (see Figure 10.5 and Figure 10.6, which show the traces of particles detected by the PTV system). The velocity profiles from the PTV analysis are consistent with the observed flow, providing confidence in the PTV results. It is more likely that the difference in near wake length between the current data and Norberg's data are due to experimental configuration rather than errors in the PTV process.

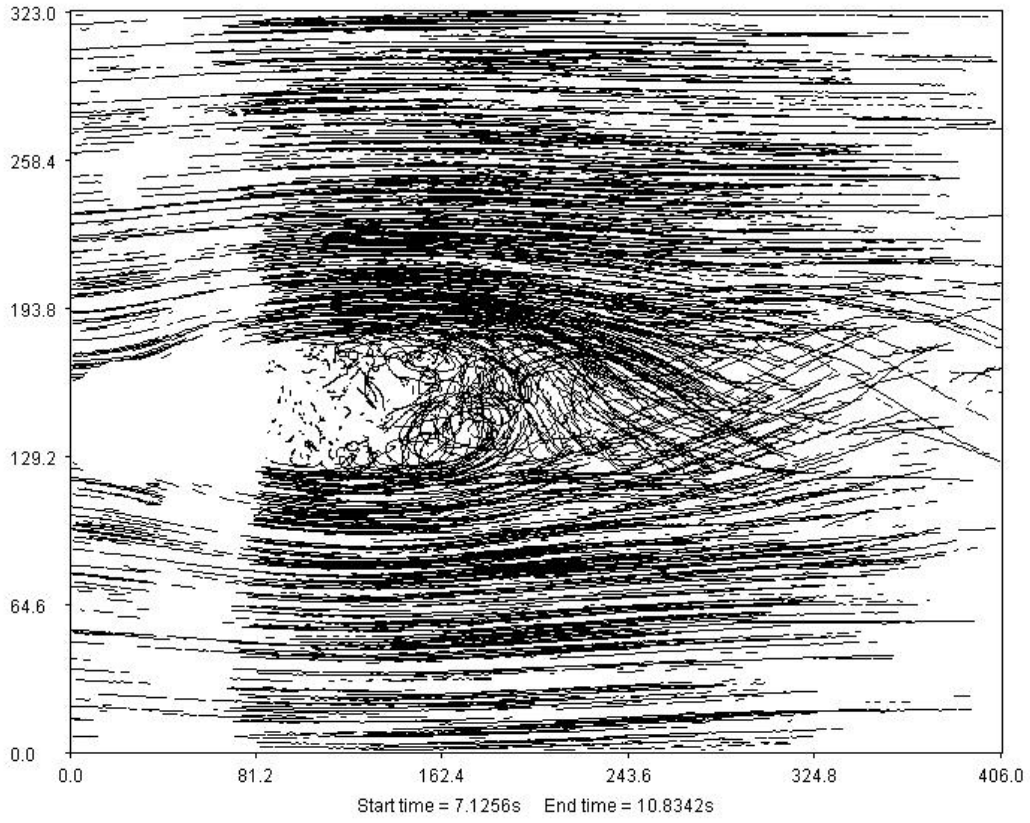

Figure 10.5 Particle paths for the flow past a smooth cylinder at Re 1330. Horizontal and vertical scales are in mm. The cylinder centre is at x = 63.8 mm, y = 150.3 mm, D = 42.2 mm.

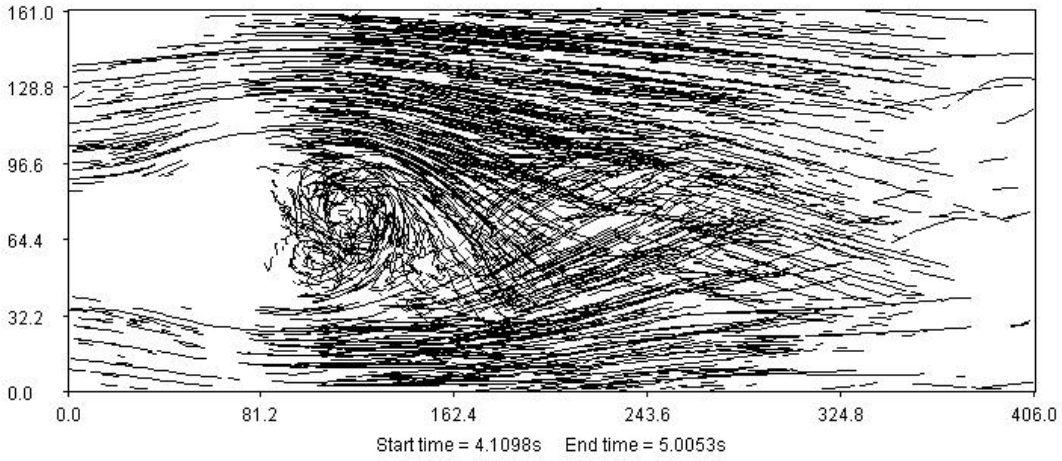

Figure 10.6 Particle paths for the flow past a smooth cylinder at Re 4950. Horizontal and vertical scales are in mm. The cylinder centre is at x = 65.4 mm, y = 72.0 mm, D = 42.2 mm.

The most significant differences in experimental configuration between the current and Norberg's data are in the aspect ratio (Norberg: 65; present: 21) and end conditions (Norberg: circular end plates 5 times the diameter of the cylinder; present: one free end and the other attached to a moving Perspex sheet). Also, the blockage ratio was higher in the PTV tests (Norberg 1.5%; present 2.5%). While differences in free-stream turbulence can have a strong effect on eddies formed along the free-shear layers in the TrSL2 regime (see section 8.2.4), turbulence intensities were low in both studies. Norberg reported a free-stream turbulence of 0.1%, and the fluid was essentially motionless in the present study. There was, however, a small amount of vibration of the cylinders in the current study due to flex in the cylinders and the Perspex boat to which the cylinders were fixed.

Norberg reports that their data at Re = 10,000 did not agree with the LDV-results of McKillop and Durst (1984) at Re 14,000. McKillop and Durst's data showed a wake closure length of x_0/D = 1.65, 9% higher than Norberg's results at Re 10,000. McKillop and Durst also found a smaller return velocity of ~ U/U_0 = -0.32, whereas Norberg reports -0.38 at Re = 10,000. Norberg attributes the differences to the lower free stream turbulence (0.1% as compared to 2.3%), lower blockage ratios (1.5% compared to 10%), and higher aspect ratios (65 compared to 10.5) of his experimental configuration. Norberg also reports that the three-dimensional numerical simulations of Beaudan and Moin (1994) at Re = 3900 gave similar wake closure lengths, but lower return velocities of U/U_0 = -0.30 to -0.33, compared to Norberg's value of –0.45. It appears that the near wake region is particularly sensitive to experimental configuration.

10.3.4 Centreline Velocity and TKE behind Rough Cylinders

Surface roughness caused changes to time-averaged stream-wise velocity (U) and Turbulent Kinetic Energy (TKE) profiles downstream of the cylinder. Centreline streamwise velocity (U) and TKE for a smooth and rough (k_s/D = 0.045) cylinder are compared in Figure 10.7. The time-averaged TKE is

calculated from the velocity fluctuations in the x and y directions (u and v) only, as vertical motions could not be measured with the PTV system,

$$TKE = \frac{1}{2}\left\langle u^2 + v^2 \right\rangle \tag{10.1}$$

TKE for the smooth cylinder shows a variation with Re similar to that detected in streamwise velocity, Figure 10.7(b). The peak value of TKE increases from Re = 1330 to Re = 3780, but does not increase further at Re = 4950. The peak TKE occurs slightly downstream of the end of the recirculation zone (between 0.1D and 0.4D downstream of the point where U = 0).

The length of the recirculating zone behind the rough cylinder (k_s/D = 0.045, Figure 10.7) varies with Reynolds number in a similar fashion to the smooth cylinder, with the length decreasing with increasing Re. The length of this zone appears to be independent of Reynolds number at Re > 3700 for both the smooth and rough cylinder.

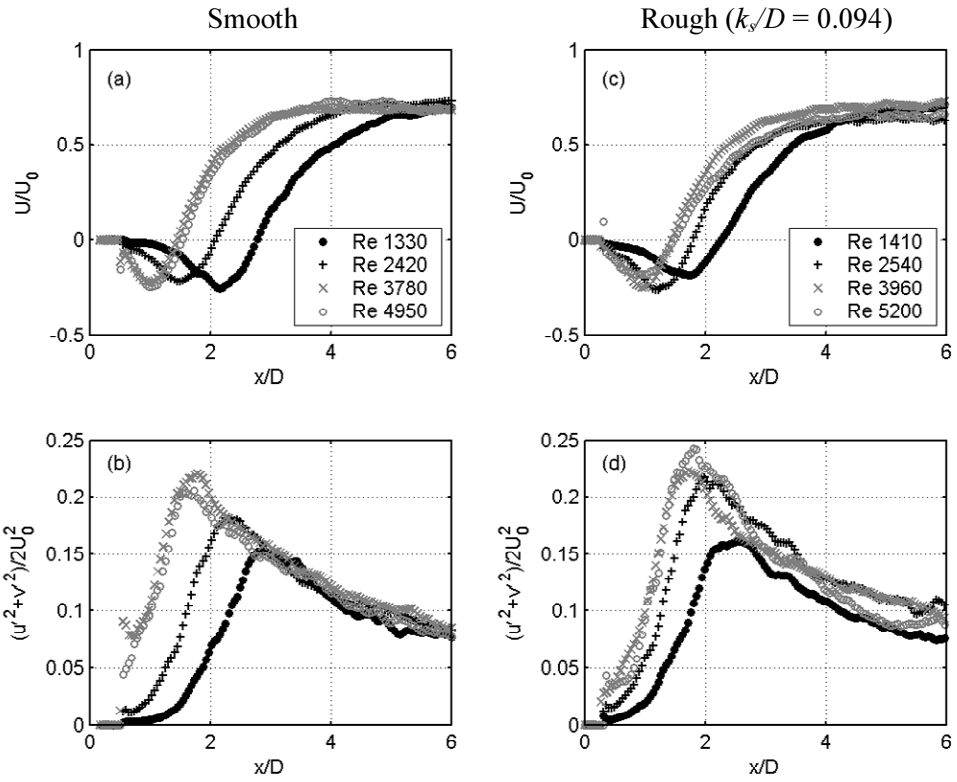

Figure 10.7 (a) centreline U velocity behind smooth cylinder, (b) TKE (horizontal velocity components only) behind a smooth cylinder, (c) U velocity behind a rough cylinder with k_s/D = 0.045, and (d) TKE behind a rough cylinder with k_s/D = 0.045.

There are noticeable differences in the profiles of U and TKE behind the smooth and rough cylinders, as can be seen more clearly in Figure 10.8 where data for the three cylinders are plotted by Reynolds number. The length of the near-wake region is reduced behind the rough cylinders, particularly at the lower Reynolds numbers of 1400 and 2500. The maximum negative velocity within the near wake is also

reduced, particularly at *Re* ~ 1400. As Reynolds numbers increase to ~ 5100, the velocity profiles behind the smooth and rough cylinders appear to collapse onto a single curve. The velocity profiles for the two rough cylinders, k_s/D = 0.045 and k_s/D = 0.094, are nearly identical, except at *Re* ~ 3900 where the recovery of velocity beyond the near-wake occurs more gradually with distance behind the roughest cylinder (k_s/D = 0.094). At the lower *Re* of 1400, the length of the near-wake is reduced from 2.8*D* for the smooth cylinder to 2.3*D* for the rough cylinders. At *Re* ~ 2500, the roughness reduces the near wake length from 2.1*D* to 1.8*D*. At the higher Reynolds numbers of 3800-4000 and 5000-5200, the length of the near wake region is the same behind all three cylinders (~1.45 *D*).

Values of TKE are higher behind the rough cylinders than behind the smooth cylinder at all Reynolds numbers; however the difference is small at *Re* ~ 3900. The TKE profiles for the two rough cylinders do not collapse as well as the *U* profiles. This may be due to either differences in the turbulence characteristics, such as changes to vortex shedding, or to experimental error. Errors in measuring TKE will be higher than for velocities as the calculation for TKE requires squared velocity values.

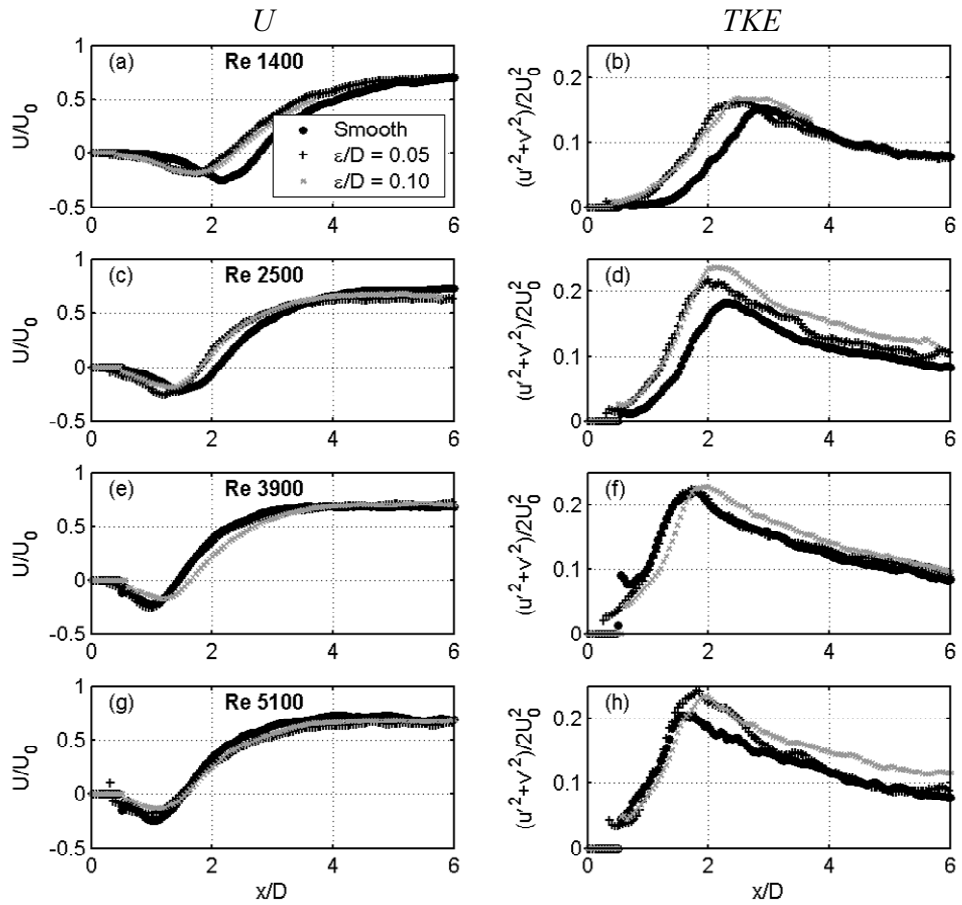

Figure 10.8 (a) *U* and (b) TKE at Re ~ 1400, (c) *U* and (d) TKE at Re ~ 2500, (e) *U* and (f) TKE at Re ~ 3900, (g) *U* and (h) TKE at Re ~ 5100 for smooth cylinders, k_s/D=0.045, and k_s/D =0.094.

10.3.5 Single Cylinder Velocity Spectra

Velocity time series measured with the PTV system have been used to calculate velocity spectra at selected points within the flow. Velocities were calculated with no limits on the size of the interpolation triangles in order to obtain a continuous time series. As most experiments were conducted with multiple runs (usually 4), spectra were calculated separately for each run, then averaged. Velocity spectra were calculated for both longitudinal (u) and lateral (v) velocity components. Power spectral densities E have been non-dimensionalised by U_0D where U_0 is the speed at which the cylinder was towed, and D the cylinder diameter. Frequencies were non-dimensionalised by the frequency of vortex shedding for a smooth cylinder in a free stream, $f_0=S_t\ U_0/D$. The accepted value of the smooth cylinder Strouhal number at a Reynolds number of 1350 is $S_t = 0.21$.

Spectra were calculated at 2 diameters upstream of the cylinder to provide a measure of the ambient turbulence and noise level, and at various distances downstream. Spectra for the rough cylinder (k_s/D = 0.094) are plotted in Figure 10.9. The noise threshold appears to be about $E/U_0D \sim 10^{-4}$ (Figure 10.9(a)). Inside the recirculating region (x/D = 1), spectral energies were low, and similar in magnitude for both u and v components. At x/D = 2 and x/D = 4, the vortex shedding can be seen by the peak in the v component. This peak, representing the large eddies shed from the cylinder, persists downstream but decays after x/D = 6 (Figure 10.9(e)).

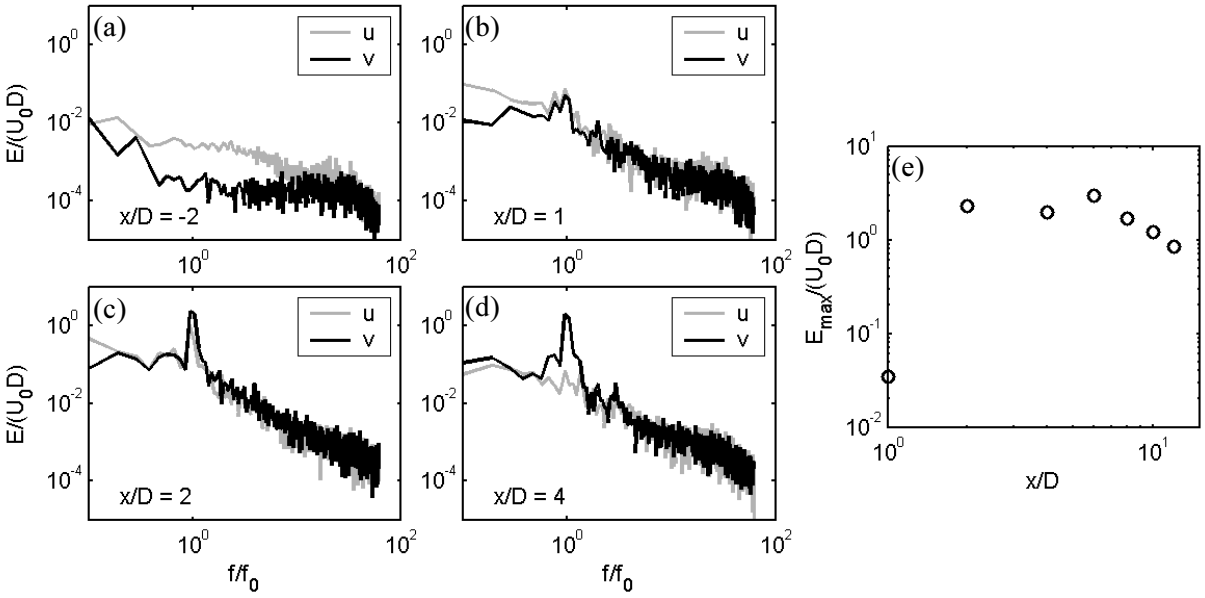

Figure 10.9 Velocity spectra along centreline for single rough cylinder at Re 1350 at (a) x/D = -2, (b) x/D = 1, (c) x/D = 2, (d) x/D = 4, and (e) peak power spectral density as function of distance downstream.

Velocity spectra over the Reynolds number range of 1300 to 5000 show a constant Strouhal number for both smooth and rough cylinders, although the Strouhal number is lower for the rough cylinders. The spectra for the smooth cylinder at 4 different Reynolds numbers are plotted in Figure 10.10.

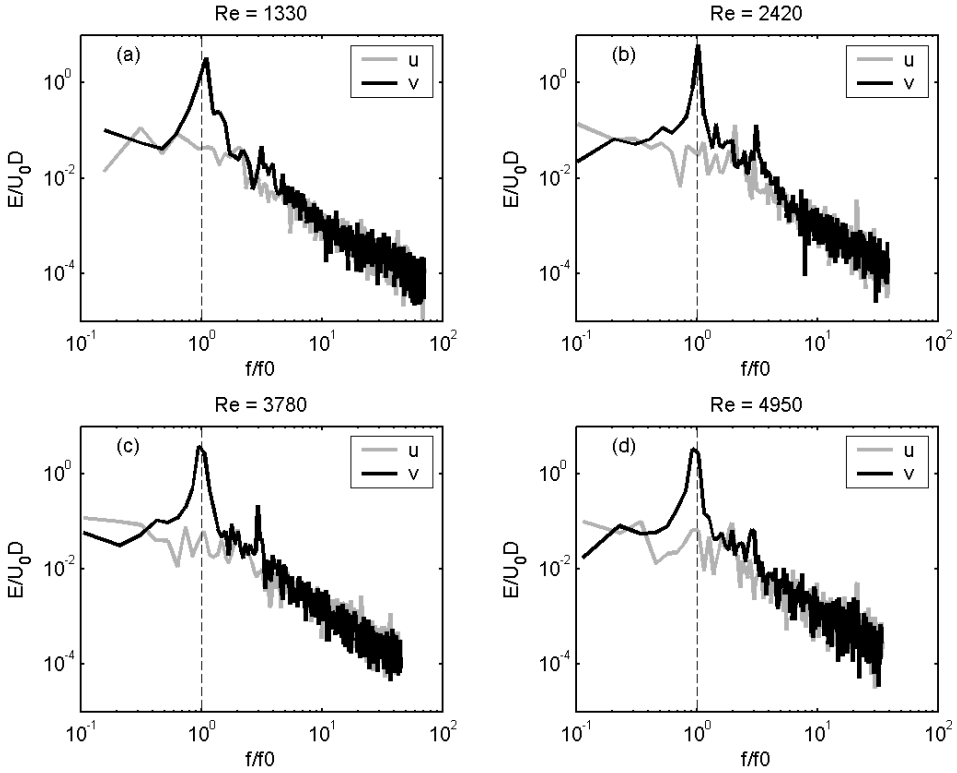

Figure 10.10 Velocity spectra for smooth cylinder for *Re* = (a) 1330, (b) 2420, (c) 3780 and (d) 4950 at *x/D* = 4.

The reduction in Strouhal number for the rough cylinders can be seen in Figure 10.11. At k_s/D = 0.048, the peak energy occurs at f/f_0 = 0.93, or S_t = 0.19. At k_s/D = 0.094, the peak is at a lower frequency of f/f_0 = 0.80, giving a Strouhal number of 0.17.

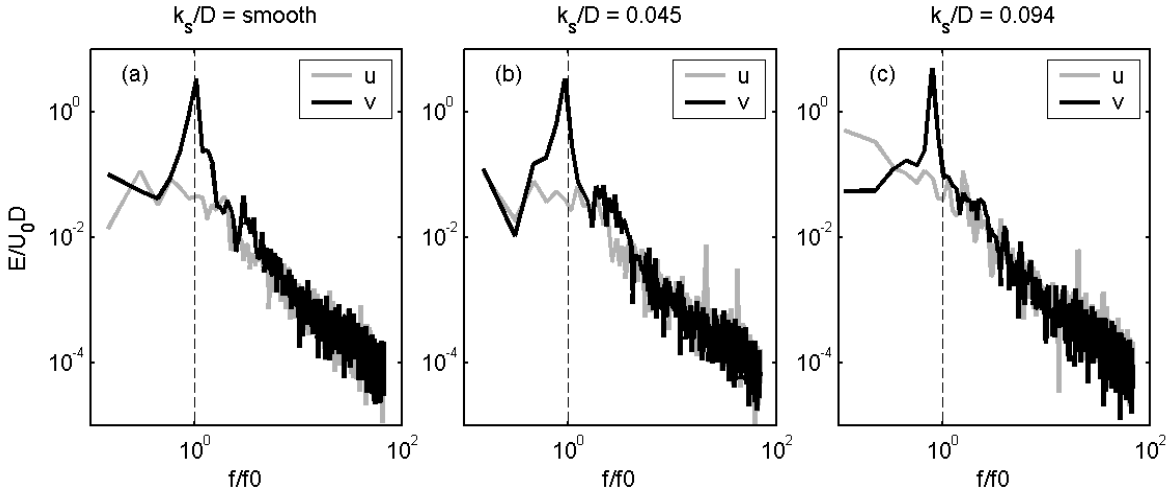

Figure 10.11 Velocity spectra at *x/D* = 4 for (a) smooth cylinder, (b) k_s/D = 0.045 and (c) k_s/D = 0.094, at *Re* ~ 1330 to 1410.

10.3.6 Two-dimensional Flow Fields behind Single Cylinders

The greatest attraction of the PTV system is the ability to measure both instantaneous and time-averaged two-dimensional fields of velocity from which other quantities, such as TKE and turbulent stresses, may be calculated. Time-averaged velocity fields for the smooth and rough cylinder (k_s/D = 0.094) at Re ~ 1340 are plotted in Figure 10.12. The smaller recirculation zone behind the rough cylinder can be clearly seen.

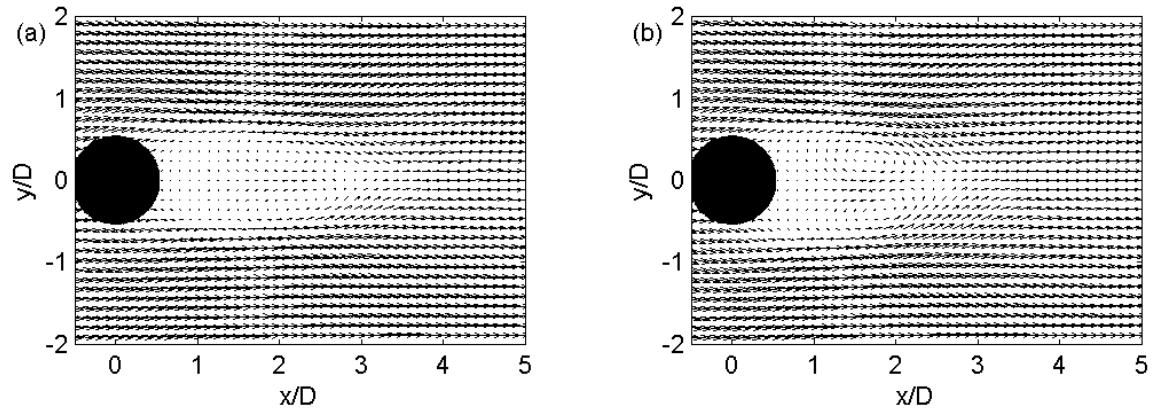

Figure 10.12 Time-averaged velocity fields behind (a) smooth cylinder, and (b) rough cylinder (k_s/D = 0.094) at Re = 1340.

A magnified view of the near wake region shows more clearly the double circulation of the mean flow.

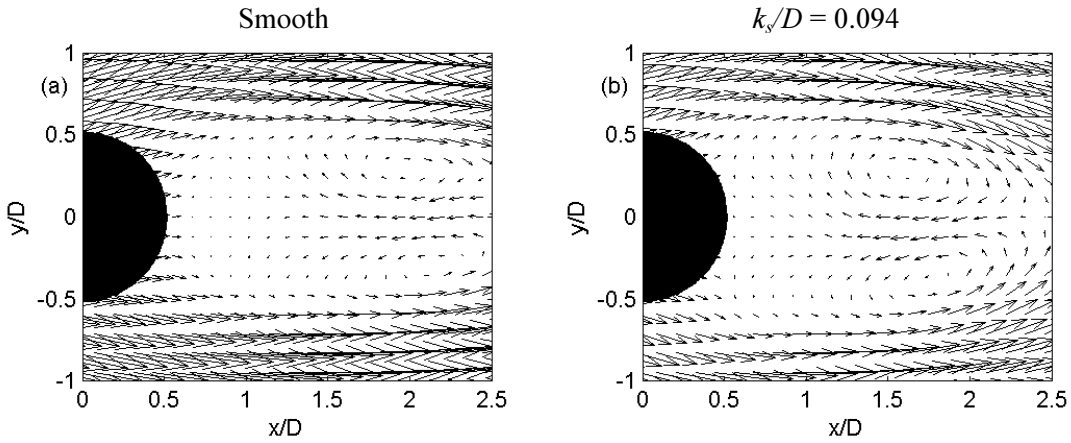

Figure 10.13 Magnified view of time-averaged velocity vectors behind (a) smooth, and (b) rough k_s/D = 0.094 cylinders at Re = 1340.

The time-averaged velocity fields show a stagnation point downstream of the cylinder, with two symmetrical eddies within the near wake region. These features are produced by the averaging process, and are not a feature of the instantaneous flow. Time-series of velocity vectors behind a smooth and

rough (k_s/D = 0.094) cylinder at a Reynolds number ~ 1340 are plotted in Figure 10.14. The time step between each plot is 0.2 $D/(S_tU_0)$, where the Strouhal numbers for the smooth and rough cylinders are S_t = 0.21 and 0.17 respectively (see Section 10.3.4). The graphs therefore show an entire shedding cycle for the smooth cylinder in Figure 10.14 (a) to (e), and for the rough cylinder in Figure 10.14 (f) to (j). There are no stagnation points within the flow downstream of the cylinder.

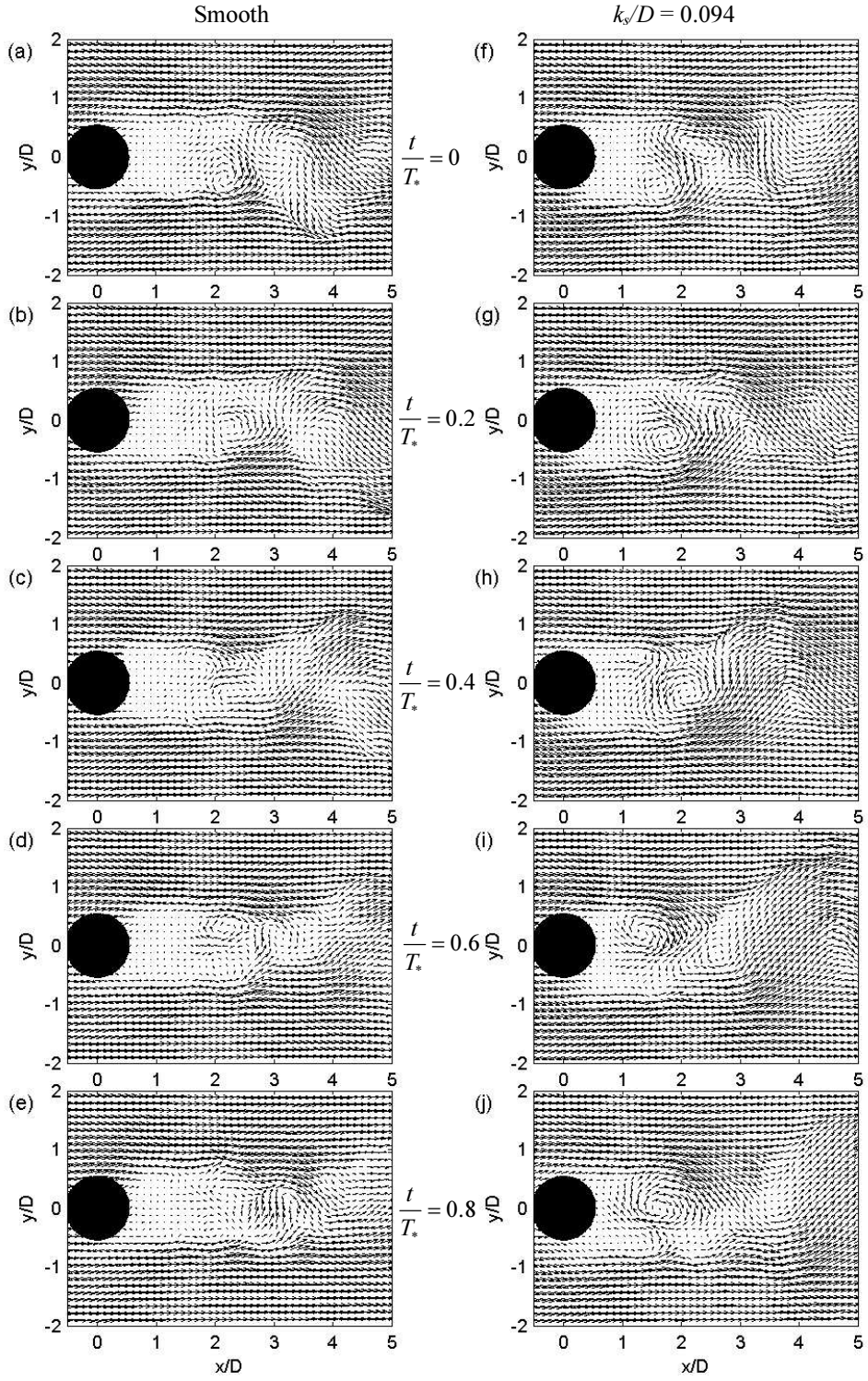

Figure 10.14 Time-series of instantaneous velocity vectors behind (a) - (e) smooth cylinder; and (f) - (h) rough cylinder k_s/D = 0.095 at time steps of dt = 0.2 T_* where T_* = $D/(S_tU_0)$, at Re = 1340.

More detail of the flow structure in the near-wake region can be seen in Figure 10.15. The formation of vortices occurs at the edge of the near-wake region. The vortices are larger, more coherent, and form further upstream behind the rough cylinder than behind the smooth. This may be due to small scale turbulence in the free-shear layer generated by the surface roughness.

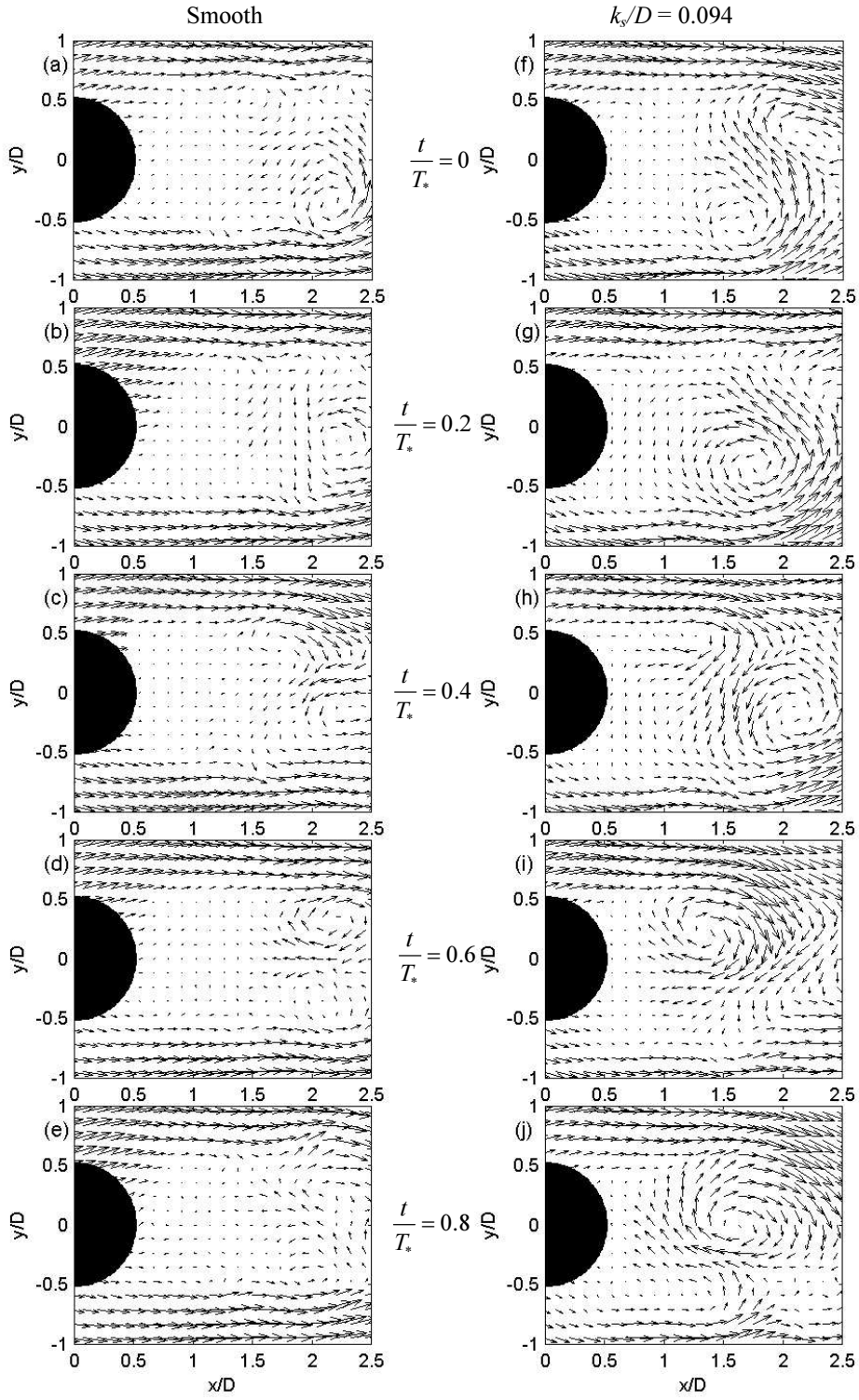

Figure 10.15 Time-series of instantaneous velocity vectors in near-wake region behind smooth and rough cylinders, *Re* = 1340.

Mean turbulence statistics, calculated from the PTV analysis, behind the smooth and rough (k_s/D = 0.094) cylinders are plotted in Figure 10.16 and Figure 10.17. As the profiles of U and TKE behind the cylinders with k_s/D = 0.045 and k_s/D = 0.094 collapse over most of the range of Reynolds numbers used (see Figure 10.8), only flow fields for the roughest cylinder are considered further. For both the smooth and rough cylinders, TKE is dominated by fluctuations in the cross-stream (v) velocity component.

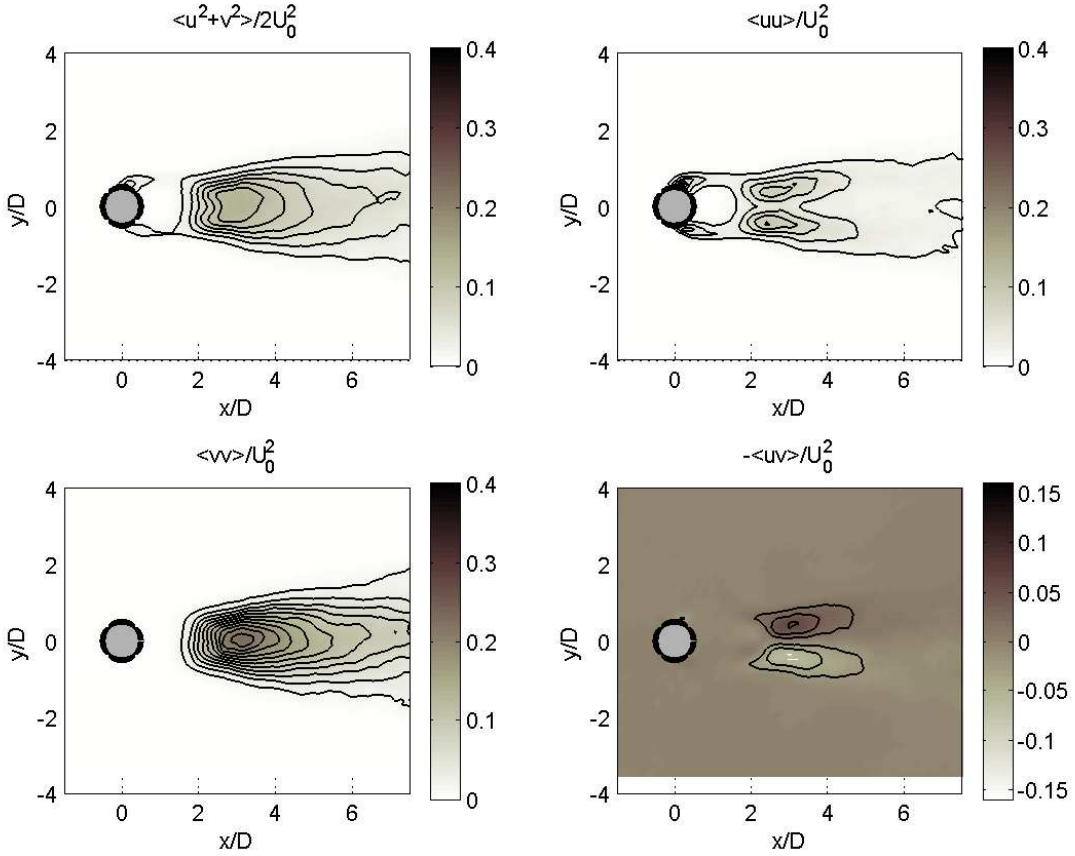

Figure 10.16 Turbulent stress components behind a single smooth cylinder, *Re* = 1330, contours are at 0.02 intervals.

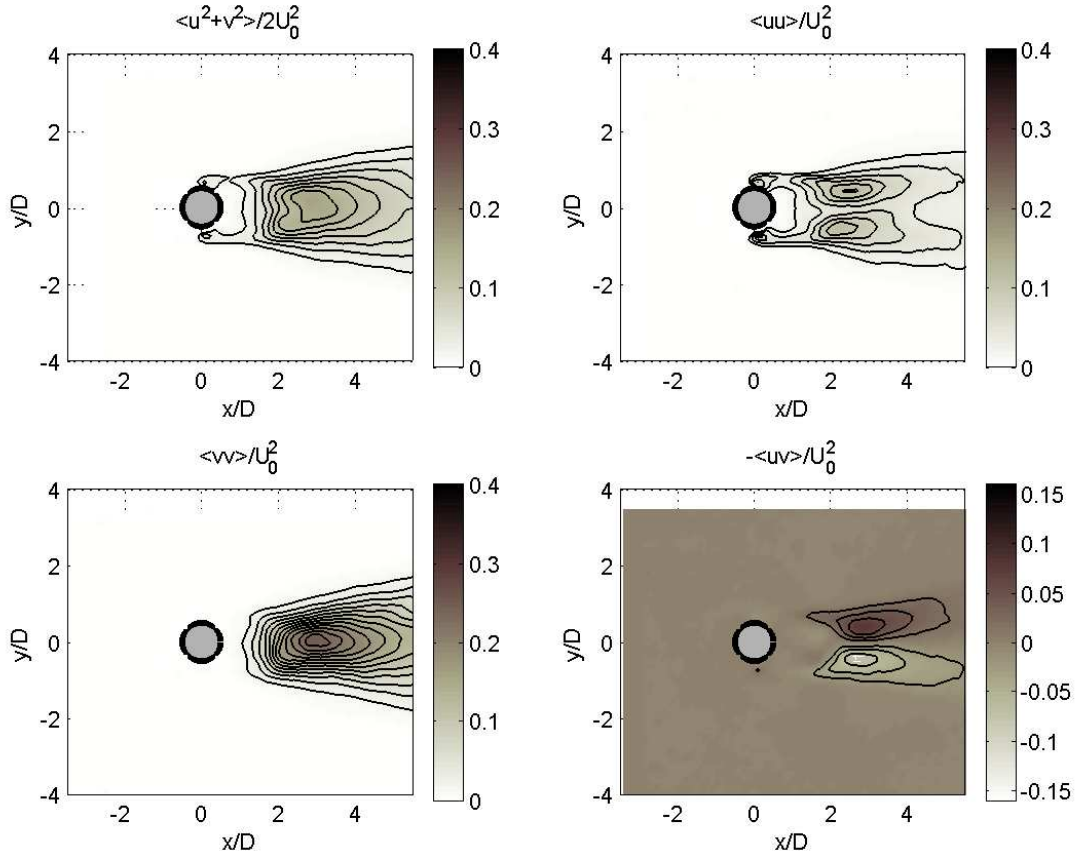

Figure 10.17 Turbulent stress components behind a single rough cylinder (k_s/D = 0.094), Re = 1350, contours are at 0.02 intervals.

The TKE contours give the appearance of a greater lateral spread of the wake behind the rough cylinder. This is confirmed by cross-sections of velocity and TKE taken through the wakes downstream of the cylinders, see Figure 10.18.

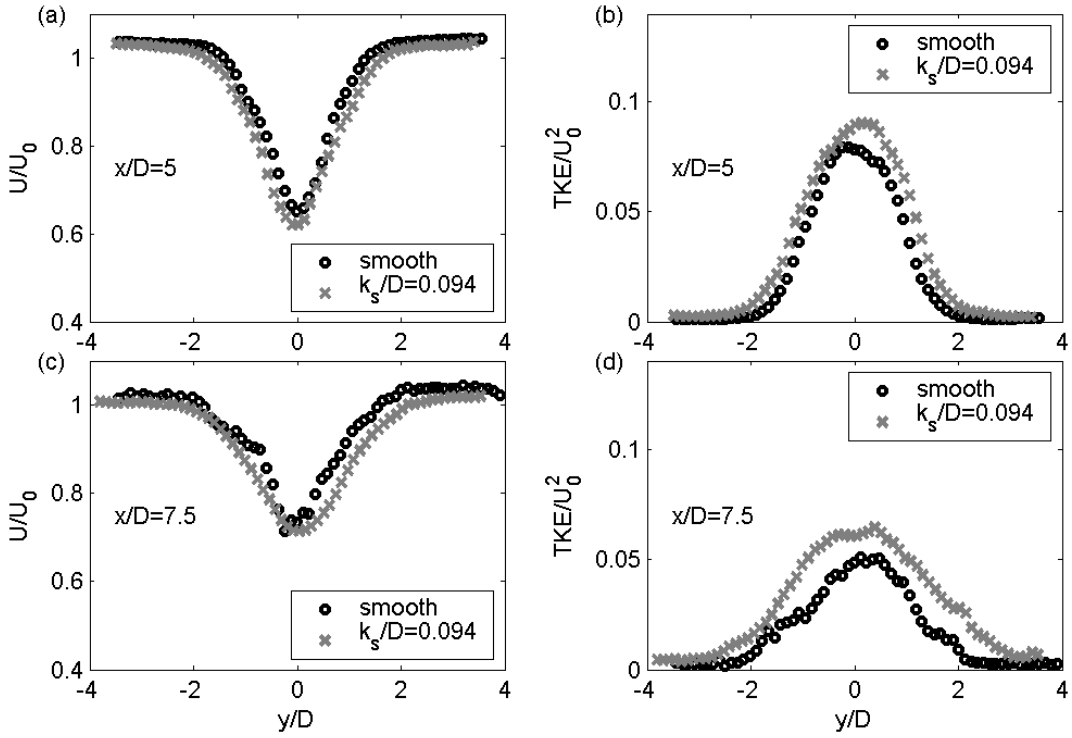

Figure 10.18 Cross-sections of velocity and TKE at *x/D* = 5 and *x/D* = 7.5 through the wake of a smooth and rough cylinder, *Re* = 1340.

Using subscript notation, turbulent production is calculated from

$$P = -\left\langle u_i u_j \right\rangle S_{ij}, \tag{10.2}$$

where the mean strain rate S_{ij} is calculated from

$$S_{ij} = \frac{1}{2}\left(\frac{\partial U_i}{\partial x_j} + \frac{\partial U_j}{\partial x_i} \right). \tag{10.3}$$

The PTV data provides two-dimensional velocity fields, so the production term, when expanded, contains contributions from both the turbulent shear and normal stresses,

$$P = -\left\langle uv \right\rangle \left(\frac{\partial U}{\partial y} + \frac{\partial V}{\partial x} \right) - \left\langle uu \right\rangle \frac{\partial U}{\partial x} - \left\langle vv \right\rangle \frac{\partial V}{\partial y}. \tag{10.4}$$

These three contributions and their total for the flow around the smooth cylinder are plotted in Figure 10.19. The contribution from the streamwise velocity <*uu*> is negligible due to the low gradients of $\partial U/\partial x$; however, the contribution from the normal stresses in the cross-stream direction <*vv*>$\partial V/\partial y$ are of similar magnitude to the contribution from the turbulent shear <*uv*>($\partial U/\partial y + \partial V/\partial x$).

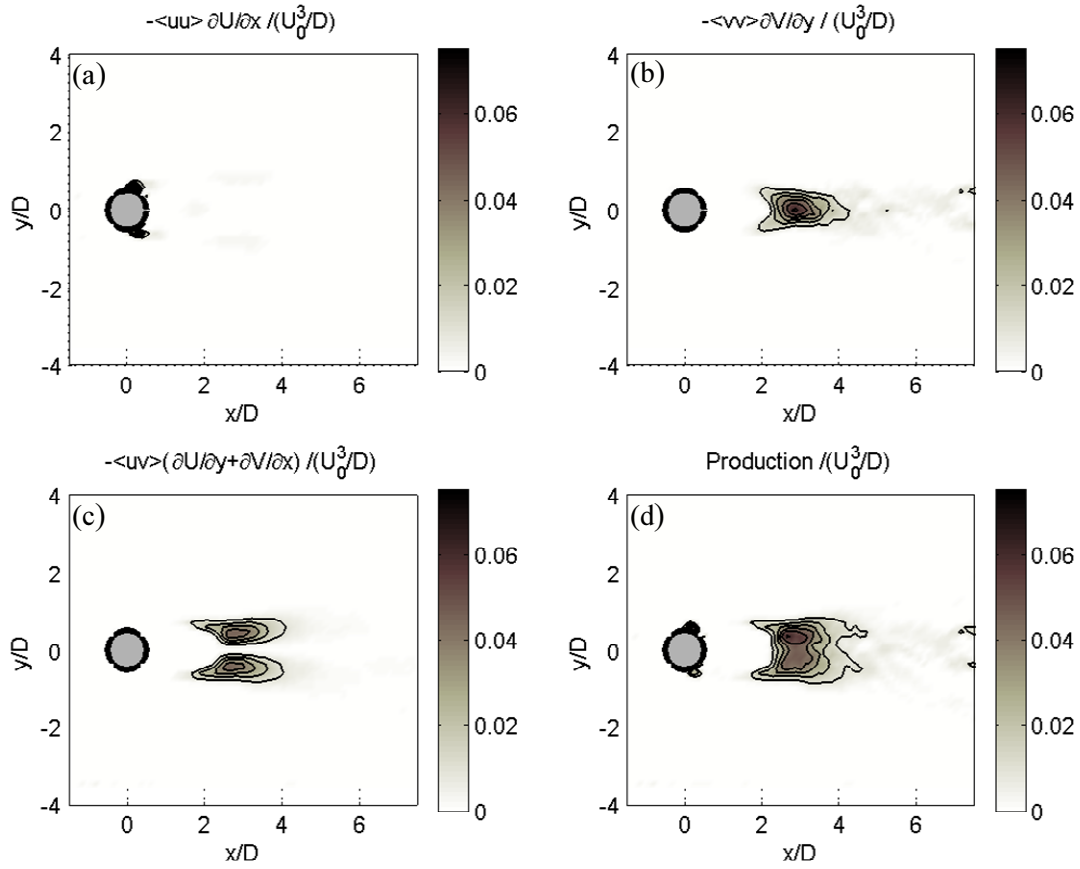

Figure 10.19 Individual terms for turbulent production behind a smooth cylinder at *Re* 1330. Production in (d) is the sum of the terms in (a), (b), and (c). Contours are at 0.01 intervals.

The concentration of peak production is consistent with the peak TKE (Figure 10.16), however high levels of TKE persist downstream whereas production decreases rapidly, indicating a transport of turbulent kinetic energy downstream.

In the Reynolds equations, dissipation ε is related to the fluctuating rate of strain s_{ij} and viscosity ν,

$$\varepsilon = 2\nu\left\langle s_{ij}s_{ij}\right\rangle \tag{10.5}$$

where

$$s_{ij} = \tfrac{1}{2}\left(\frac{\partial u_i}{\partial x_j} + \frac{\partial u_j}{\partial x_i}\right). \tag{10.6}$$

The fluctuating strain rates are dominated by small-scale fluctuations at or near the Kolmogorov scale. As typical pixel resolution in the experiments was 0.3 mm/pixel, the Kolmogorov scale could not be resolved. Instead, dissipation is estimated using an eddy viscosity relationship derived from the flow field, as follows.

In k-ε models, dissipation is modelled by a turbulent eddy viscosity (Rodi, 1980),

$$\nu_t = C_u k^2/\varepsilon, \tag{10.7}$$

where the constant $C_u = 0.09$, and k is the turbulent kinetic energy (TKE).

In the turbulent-viscosity hypothesis, the deviatoric Reynolds stress is proportional to the mean rate of strain (Pope, 2000),

$$-\left\langle u_i u_j \right\rangle = \nu_T \left(\frac{\partial U_i}{\partial x_j} + \frac{\partial U_j}{\partial x_i} \right) - \tfrac{2}{3} k \delta_{ij} \qquad (10.8)$$
$$= 2\nu_T S_{ij} - \tfrac{2}{3} k \delta_{ij}$$

where ν_T is the turbulent viscosity (or eddy viscosity), and δ_{ij} has the value 1 if $i = j$, or 0 if $i \neq j$. In the turbulent-viscosity hypothesis, the eddy viscosity is assumed to be a scalar, and therefore isotropic. However, the turbulence is clearly anisotropic, as indicated by the normal stresses <*uu*> and <*vv*> in Figure 10.16. Nevertheless, reasonable estimates of dissipation can be obtained using a scalar ν_T in simple shear flows where the mean shear gradients are strong compared to the normal velocity gradients. The dominant mean velocity gradient behind a smooth cylinder is $\partial U/\partial y$, with the other velocity gradients an order of magnitude smaller (Figure 10.20). The flow is generally a shear flow, so a simple approximation for the turbulent-viscosity may give reasonable estimates of dissipation, despite the non-isotropy of the turbulence.

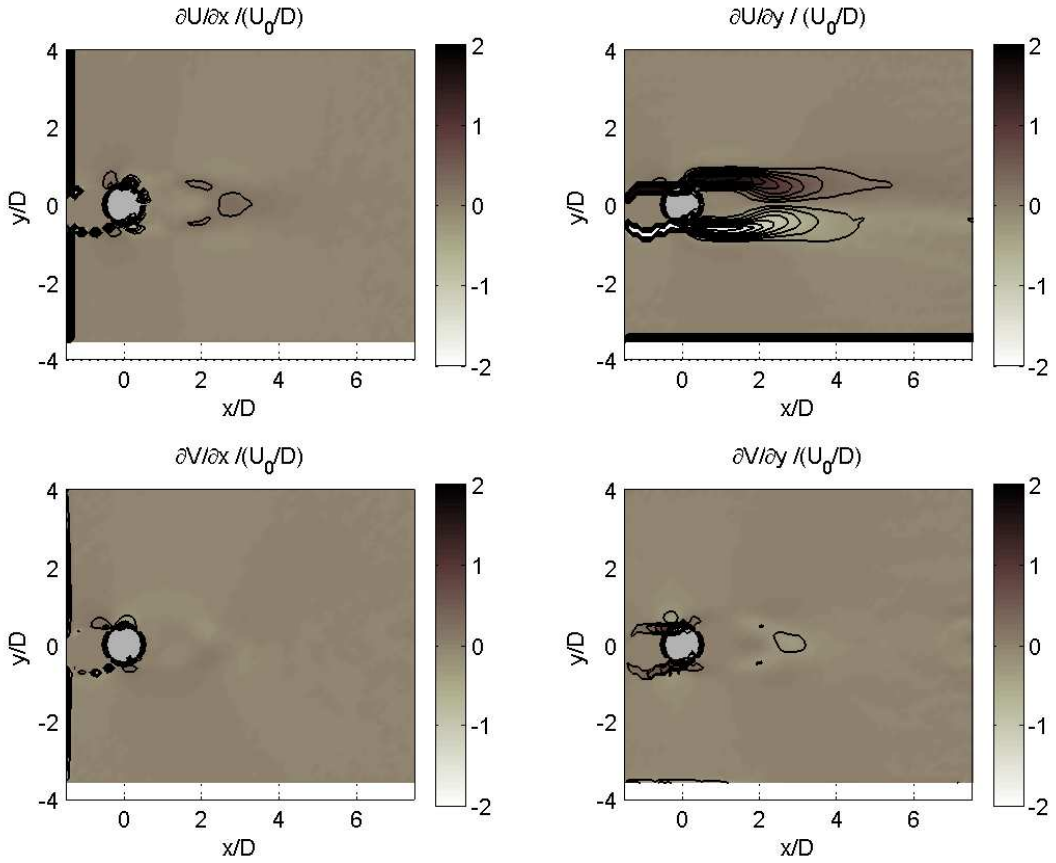

Figure 10.20 Mean velocity gradients for a smooth cylinder at Re 1330. Contours are at 0.2 intervals.

As the dominant velocity gradient is $\partial U/\partial y$, the parts of equation (10.8) that contain this velocity gradient will be used to estimate the turbulent viscosity. In two dimensional flow, equation (10.8) becomes

$$\begin{bmatrix} -\langle uu \rangle & -\langle uv \rangle \\ -\langle vu \rangle & -\langle vv \rangle \end{bmatrix} = \begin{bmatrix} 2\nu_T \dfrac{\partial U}{\partial x} - \frac{2}{3}k & \nu_T \left(\dfrac{\partial U}{\partial y} + \dfrac{\partial V}{\partial x} \right) \\ \nu_T \left(\dfrac{\partial V}{\partial x} + \dfrac{\partial U}{\partial y} \right) & 2\nu_T \dfrac{\partial U}{\partial x} - \frac{2}{3}k \end{bmatrix} \tag{10.9}$$

The model for the eddy viscosity will therefore be

$$-\langle uv \rangle = \nu_T \left(\frac{\partial U}{\partial y} + \frac{\partial V}{\partial x} \right) \tag{10.10}$$

Substituting into equation (10.7) gives

$$\varepsilon = -\frac{C_u k^2}{\langle uv \rangle} \left(\frac{\partial U}{\partial y} + \frac{\partial V}{\partial x} \right) \tag{10.11}$$

As $\partial V/\partial x$ is small (Figure 10.20), the dissipation can be estimated from

$$\varepsilon = -\frac{C_u k^2}{\langle uv \rangle} \left(\frac{\partial U}{\partial y} \right). \tag{10.12}$$

One difficulty in using equation (10.12) is that dissipation is undefined where $\langle uv \rangle$ is zero, for example along the centreline behind the cylinder. Similarly, if $\langle uv \rangle$ is small, then small errors in $\langle uv \rangle$ will result in large errors in dissipation. For this reason, a simple filter has been applied to the calculated dissipation, so that the dissipation is set to zero if $|\langle uv \rangle / U_o^2| < 0.005$. The estimated production and filtered dissipation for the smooth and rough cylinders are shown in Figure 10.21. Production is slightly higher behind the rough cylinder, consistent with the increased TKE.

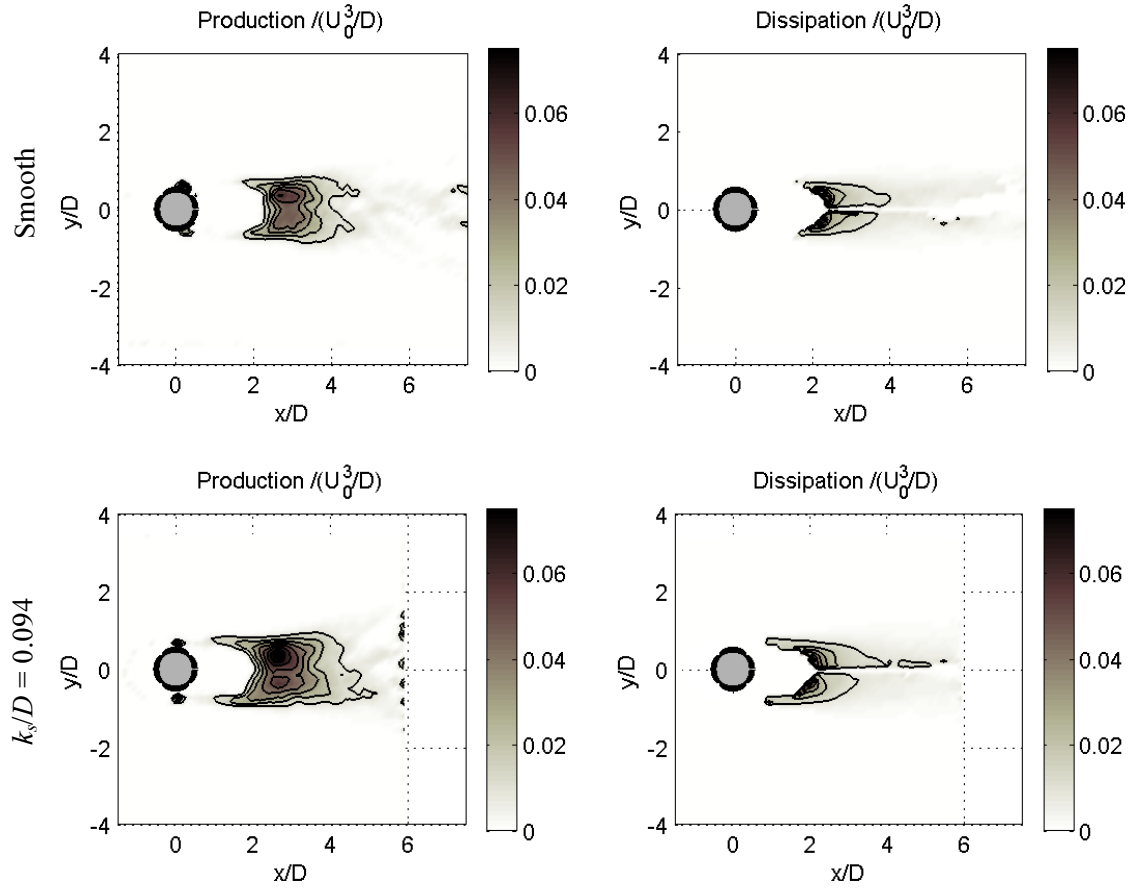

Figure 10.21 Production and filtered dissipation behind a smooth and rough cylinder at Re ~ 1340. Contours are at 0.01 intervals.

The estimated production and dissipation can be compared by integrating over the domain plotted in Figure 10.21. Integrated production and dissipation for the smooth and rough cylinder are given in Table 10.3. The integrated production and dissipation are higher behind the rough cylinder, which is consistent with the observed higher TKE. Dissipation for both cylinders is less than production by 46% for the smooth, and 55% for the rough. While some of this difference may be due to the method of calculating dissipation, it is clear from the persistence of the large vortices downstream (the large vortices are included in the calculation of TKE) that TKE is advected downstream from the cylinder rather than being completely dissipated locally. As a further comparison, the rate that work is done moving the cylinder through the flow can be calculated by multiplying the drag force by the velocity. For the smooth cylinder, this gives a rate of work done of 1.08 x 10^{-3} W/m, indicating that approximately 25% of the energy input from towing the cylinder goes into producing turbulence.

	Integrated Production	Integrated Dissipation
Smooth	2.66 x 10^{-4} W/m	1.43 x 10^{-4} W /m
k_s/D = 0.094	3.52 x 10^{-4} W/m	1.57 x 10^{-4} W/m

Table 10.3 Net production and dissipation (per unit length of cylinder) behind smooth and rough cylinders at Re 1340.

10.3.7 Wake Exchange Rates

A fundamental issue with assessing the effects of aquaculture is the potential for depletion of phytoplankton. The ability of mussels to take up phytoplankton is likely to be limited by the supply. Time-averaged velocity fields showed that a recirculating region forms behind cylinders. For a mussel dropper, the food supply to mussels located on the downstream side of the dropper will depend on the exchange between this near-wake region and the surrounding flow. With no exchange, all the available phytoplankton would eventually be consumed, potentially restricting the growth of the mussels on the downstream side of the cylinder. The exchange is due to turbulence, and as there are differences in the turbulence behind the smooth and rough cylinders, surface roughness may result in changes in the exchange between the recirculation region and the surrounding flow. This is a further factor that should be considered if attempting to model mussel droppers as cylinders.

The instantaneous two-dimensional velocity fields can be used to estimate how long particles are retained within the cylinder wake. This can be used as an indication of the exchange between the cylinder wake and the surrounding flow. Only losses of particles from the wake due to the flow are considered here. This is a separate process from the loss of particles behind a mussel dropper due to the mussels feeding. Low rates of exchange behind a mussel dropper are likely to result in greater reduction of phytoplankton in the near wake due to uptake. To calculate particle loss rates (from exchange between the near-wake and the flow), the instantaneous velocity fields obtained from a PTV analysis were used to simulate the motion of particles within the flow. This is almost the reverse of the PTV analysis where particles were tracked to determine the velocity fields. Particles in the experimental flow were subject to 3-dimensional turbulent motion, and therefore may move vertically out of the light sheet. Particle matches may also have been missed in the PTV analysis. By using the velocity fields to simulate particle movements, only two-dimensional motions result, and the particles cannot be lost unless they move out of the flow domain. It seems reasonable to assume that vertical losses or gains offset each other, so three-dimensional motions may be neglected. The particle loss rates are calculated by initially seeding the flow domain with an even distribution of particles. At each time-step, velocities from a PTV analysis are used to calculate the displacement of each particle. By counting the particles within a defined counting region (representing the cylinder near-wake) at each time step, a particle loss rate can be calculated. The size of the counting region was related to the length of the recirculating region in the averaged-velocity fields (see Figure 10.8 and Figure 10.12), and the cylinder diameter. Thus for the smooth cylinder at Re 1340, the counting region in which particles were counted was $0 < x/D < 2.8$, and $-1 < y/D < 1$. For the rough cylinder (k_s/D) at Re 1340, the counting region was of the same width, but from $0 < x/D < 2.3$. The size of the region selected had minimal effect on the retention rates as once particles moved outside of this region, they were rapidly swept downstream. It did, however, allow for a more accurate estimate of changes in particle

concentration (or density) within the region. Particle positions simulated in this manner are plotted in Figure 10.22.

As each experiment was repeated 4 times, four velocity field time-series were used for the particle simulation analysis. Each time-series was analysed three times by starting partway through the velocity field time series, providing 12 particle simulations from which an average particle loss rate could be obtained.

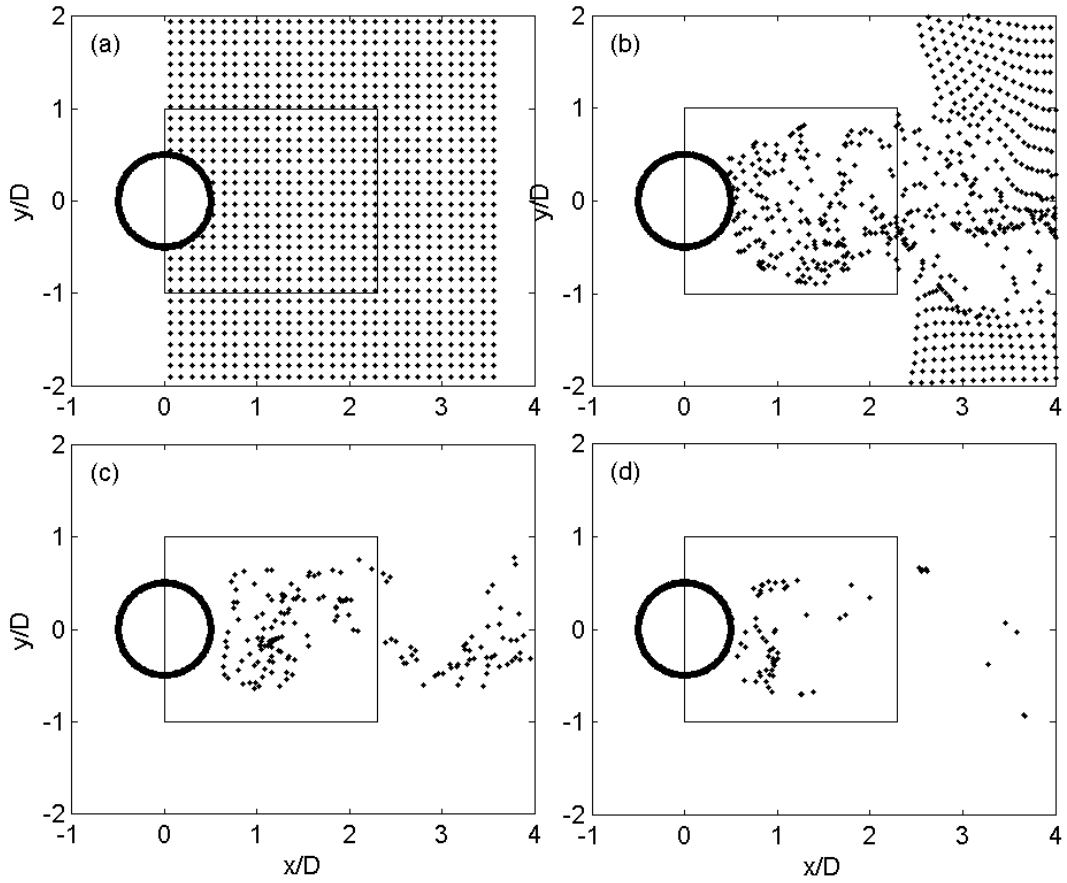

Figure 10.22 Simulated particle positions at (a) t = 0, (b) t = 2.5 D/U_0, (c) t = 10 D/U_0, and (d) t = 20 D/U_0 behind a rough (k_s/D = 0.094) cylinder at Re ~ 1340. The rectangle indicates the region in which particles are counted.

The number of particles within the counting region n_p were non-dimensionalised by the number of particles at $t/(D/U_0)$ = 2.5 (n_{p0}) to ensure that only particles inside the region were counted (the rectangular regions would include some particles outside the recirculation zone at t = 0). Elapsed time was non-dimensionalised by the time-scale D/U_0. Average particle numbers within the cylinder near-wake are plotted over time for the smooth and rough (k_s/D = 0.094) cylinders at Re ~ 1340 in Figure 10.23.

By fitting a regression to the later part of the n versus t curves (where they are linear with a logarithmic y axis), an exponential loss coefficient k_p can be obtained of the form

$$\frac{n_p}{n_{p0}} = \exp\left[-k_p \frac{tU_0}{D}\right]. \tag{10.13}$$

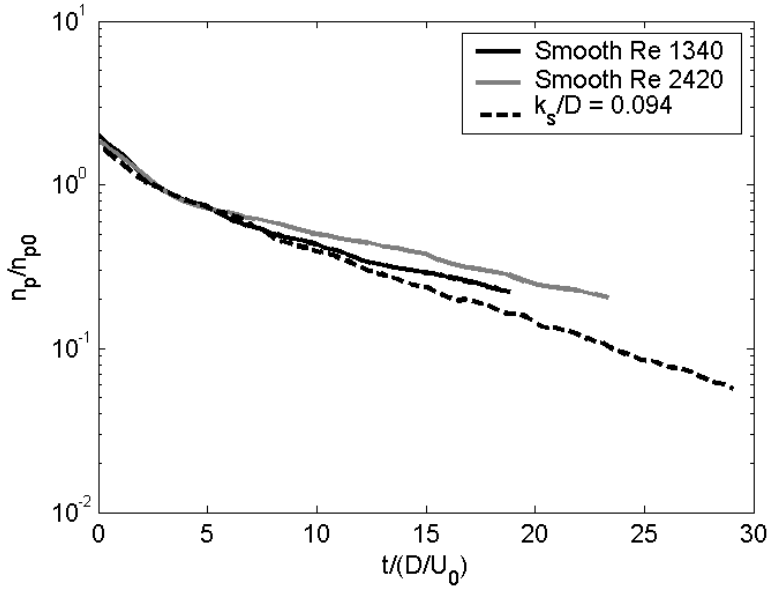

Figure 10.23 Particles retained in cylinder wake for a smooth and rough cylinder.

As Figure 10.23 shows, particles are lost more rapidly from behind the rough cylinder. Loss-rate coefficients for the smooth cylinder were 0.072 at $Re \sim 1340$, and 0.070 at $Re \sim 2420$, indicating an independence from Reynolds number. The loss-rate coefficient for the rough cylinder was 0.103. The higher retention of particles behind the smooth cylinder is consistent with the lower turbulent kinetic energy. In terms of transport, roughness increases the rate at which substances in the cylinder wake are replaced.

10.3.8 Mussel Dropper Flow Fields

The PTV system was used to analyse the flow field behind a simulated mussel dropper. The mussel dropper was manufactured by gluing mussel shells onto a 22 mm diameter steel tube, at the same density (mussels per metre length) as the original dropper. The mussels were attached with the foot of the mussel to the tube or other shells, but otherwise in a random fashion. Visually, the manufactured dropper closely resembled the original. The diameter of the mussel dropper (using the definition of twice the mussel shell length) was $D \sim 170$ mm. The instantaneous velocity vectors show a complex pattern of turbulent eddies within the near-wake region (Figure 10.24). These small scale eddies are formed from individual mussel shells, with larger and more coherent eddies forming along the free-shear layer at the edge of the wake.

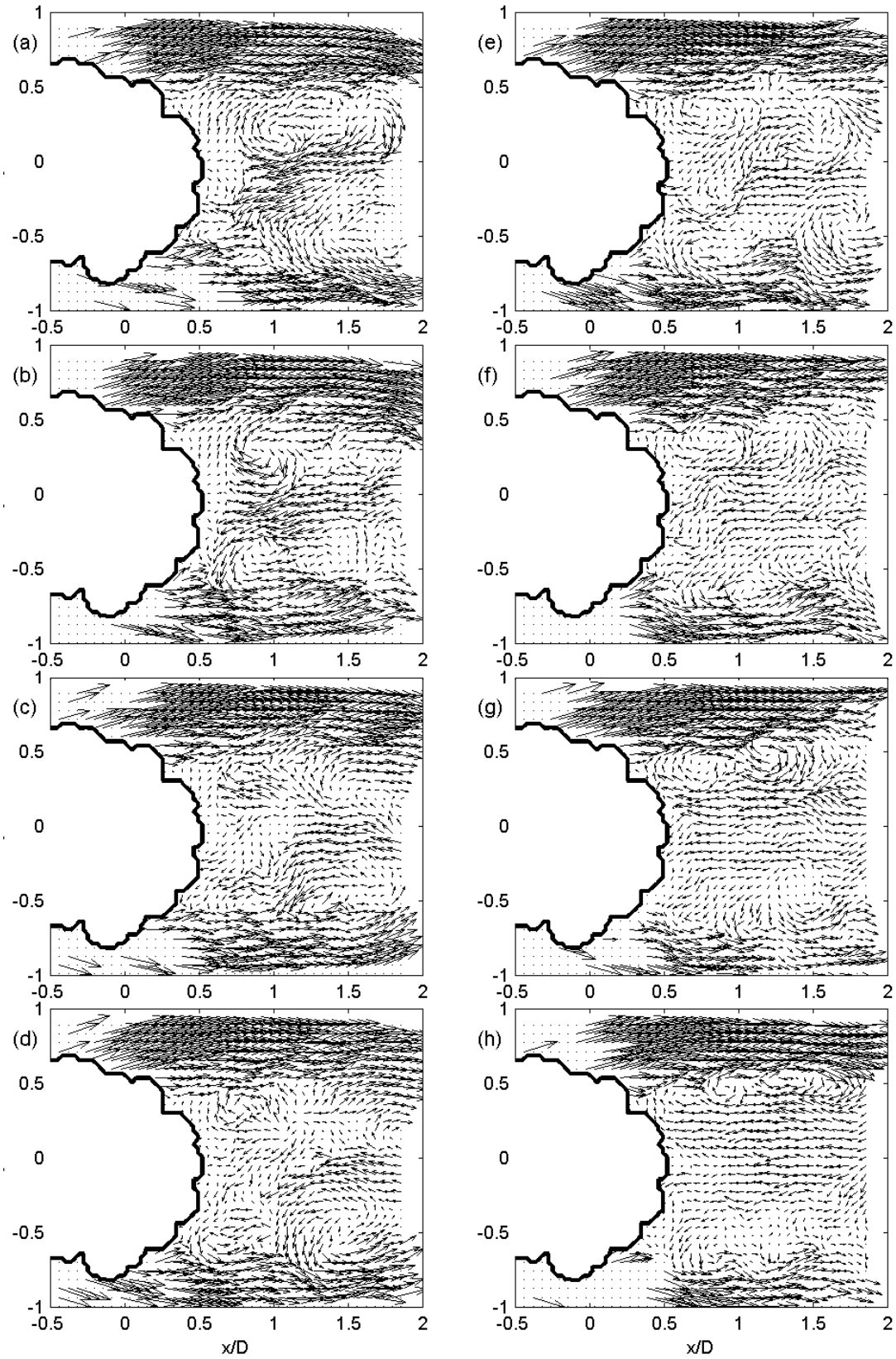

Figure 10.24 Time-series of instantaneous velocity vectors behind mussel dropper at *Re* = 9780, D ~ 170 mm, at intervals of dt = 0.125*D*/(S_tU_0).

As a result of the turbulence generated by the individual shells, turbulent kinetic energy was higher within the near-wake region of the mussel dropper than that of a smooth cylinder. The turbulence within the near-wake region is nearly isotropic, with <*uu*> and <*vv*> of similar size. The turbulent stresses, averaged over 6 runs, are plotted in Figure 10.25, and slightly further downstream (average of 4 runs) in Figure 10.26 at *Re* = 9780. The higher levels of turbulence in the near wake region are likely to increase the transport of nutrients to mussels on the downstream side of the cylinder.

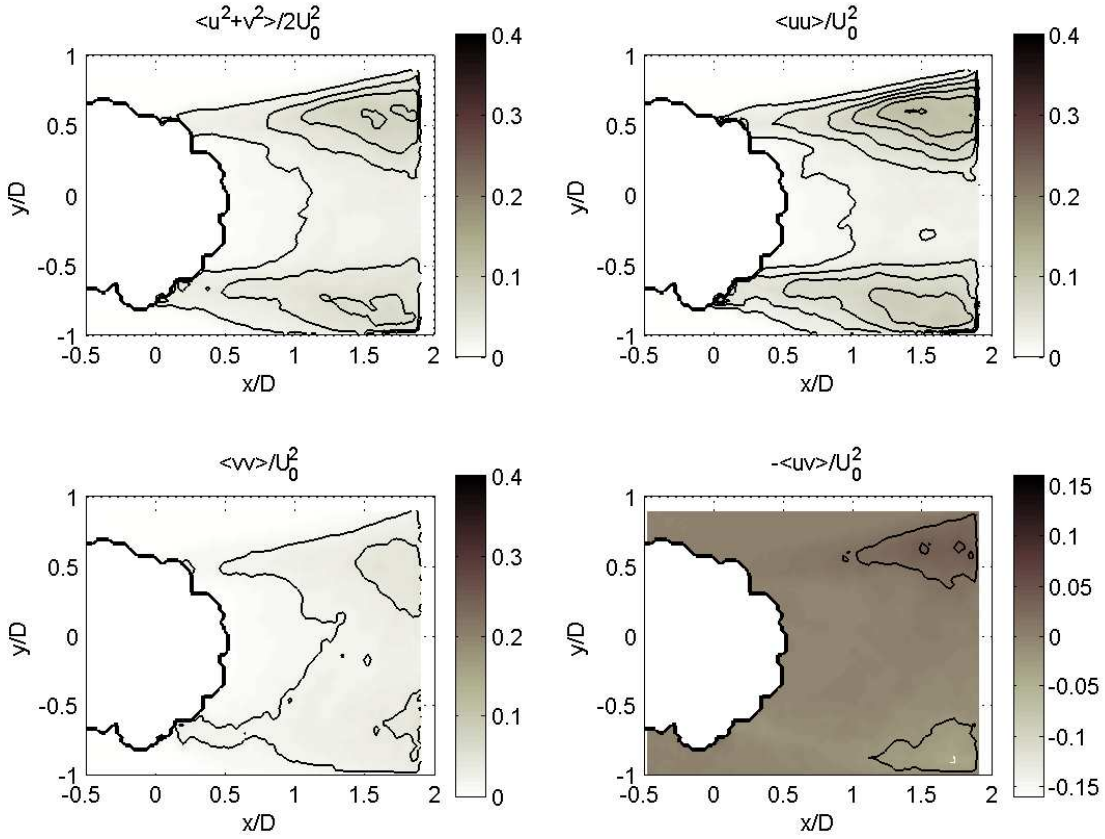

Figure 10.25 Turbulent stress components behind a mussel dropper at Re 9780.

Turbulent kinetic energy production is concentrated along the free-shear layers, with very little production within the near wake region due to the low time-averaged velocity gradients $\partial U_i/\partial x_j$. With the exception of along the free-shear layers immediately downstream of the separation points where streamwise fluctuations contribute, turbulent production is dominated by the turbulent shear stresses, Figure 10.27. Dissipation, calculated using equation (10.12) occurs in the same region as production, but is lower in magnitude (Figure 10.28).

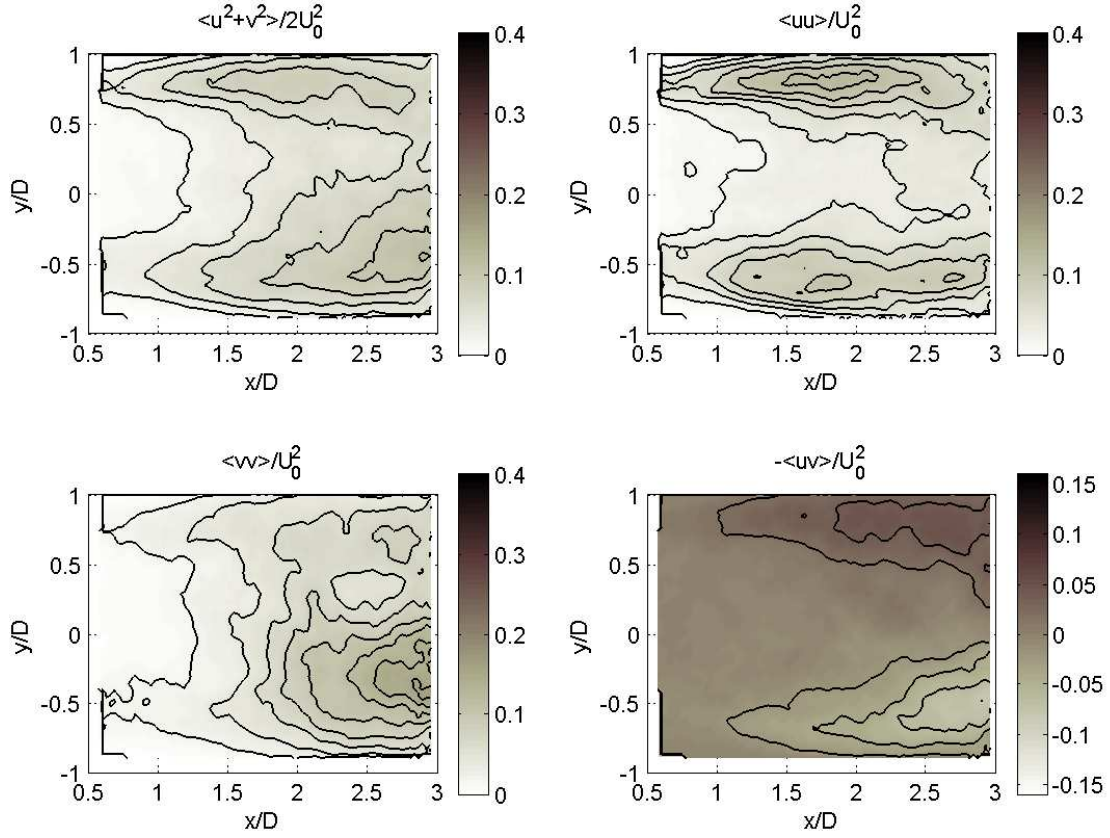

Figure 10.26 Turbulent stress components downstream of mussel dropper at *Re* = 9780. Contours are at 0.02 intervals.

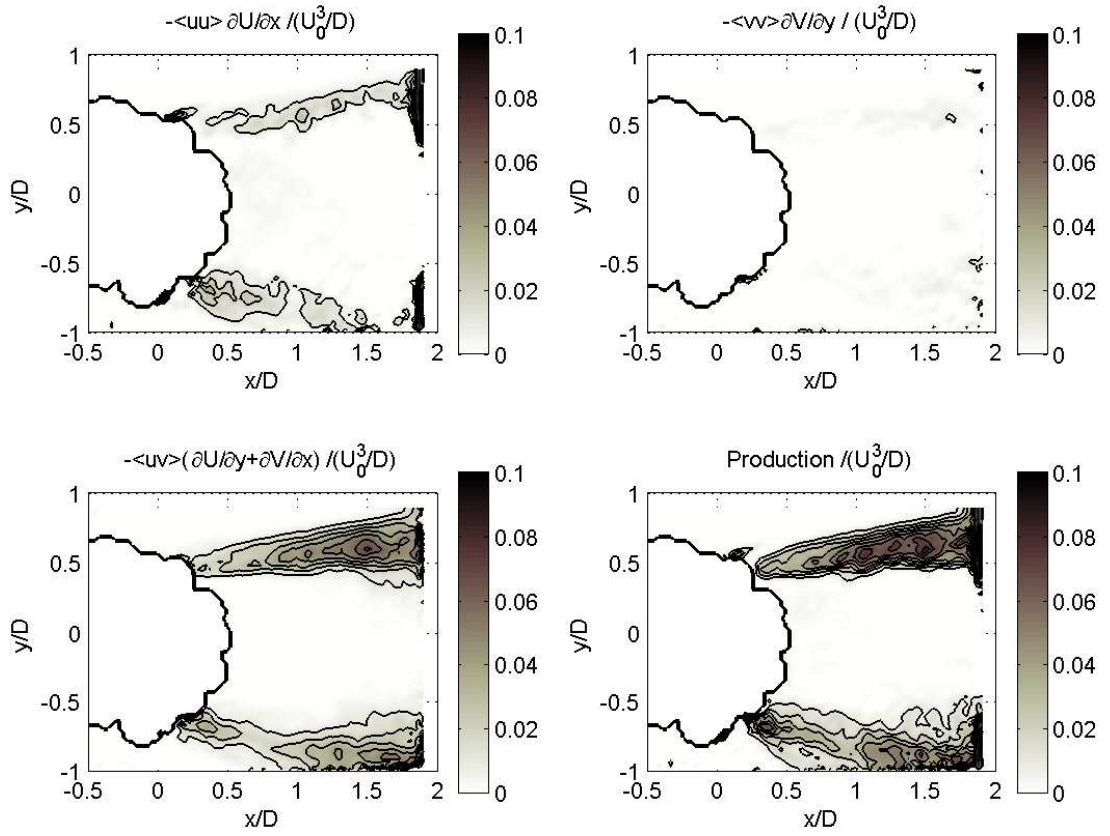

Figure 10.27 Turbulent production terms calculated from flow fields for a mussel dropper, *Re* = 9780. Contours are at 0.01 intervals.

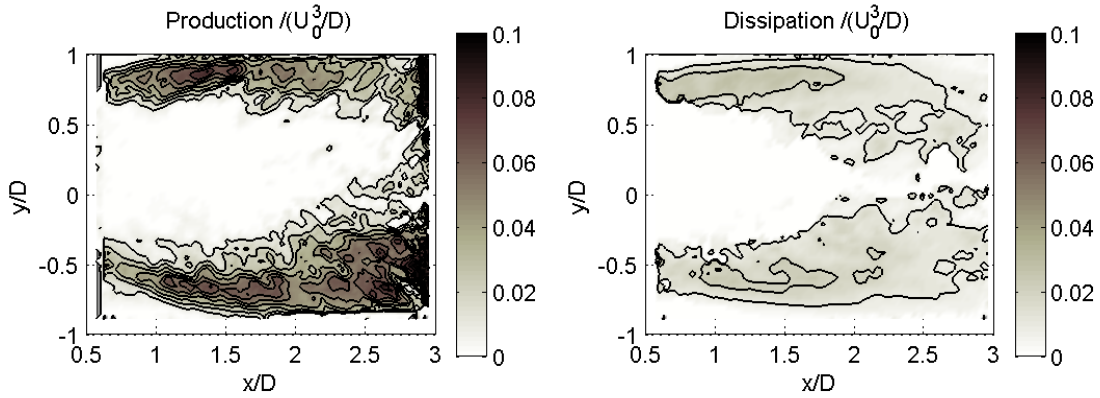

Figure 10.28 Production and dissipation calculated from flow fields for a mussel dropper, *Re* = 9780. Contours are at 0.01 intervals.

The flow around the mussel dropper is insensitive to Reynolds number over the range tested. Time-average velocity vectors, TKE, and calculated production at *Re* = 5350 and 9780, each averaged from 6 runs, are plotted in Figure 10.29 and show little variation.

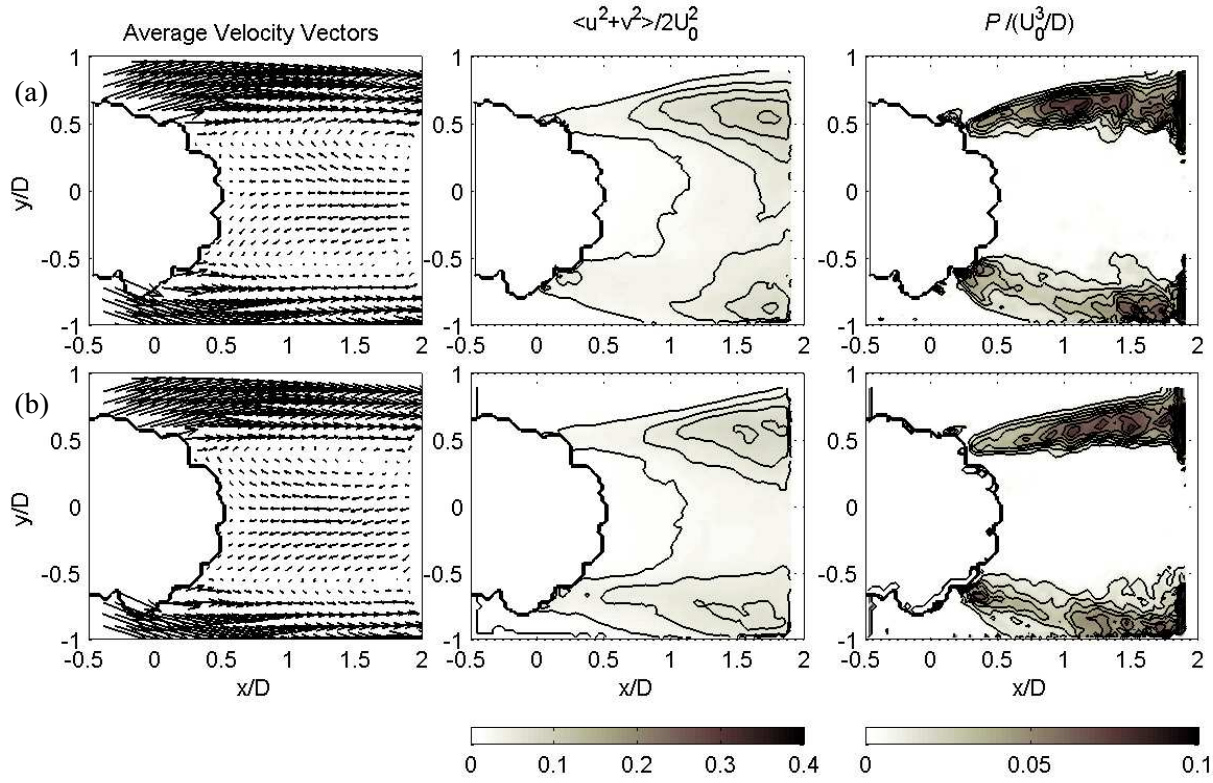

Figure 10.29 Time-averaged velocity vectors, turbulent kinetic energy (contours at 0.02 intervals), and production (contours at 0.01 intervals) behind a mussel dropper at (a) Re 5350, and (b) Re 9780.

Velocity spectra at *x/D* = 2.5, *y/D* = 0, averaged from 4 runs at Re 9780 are plotted in Figure 10.30. The peak in the velocity spectra occurs at a Strouhal number of 0.17 ± 0.04, consistent with the lower Strouhal number detected for the rough cylinders. The precision of the Strouhal number estimate for the mussel

dropper is poor as the low eddy shedding frequency and the short length of tank (useable tow length of 4 m) meant that no more than 2.5 shedding cycles could be recorded in each run.

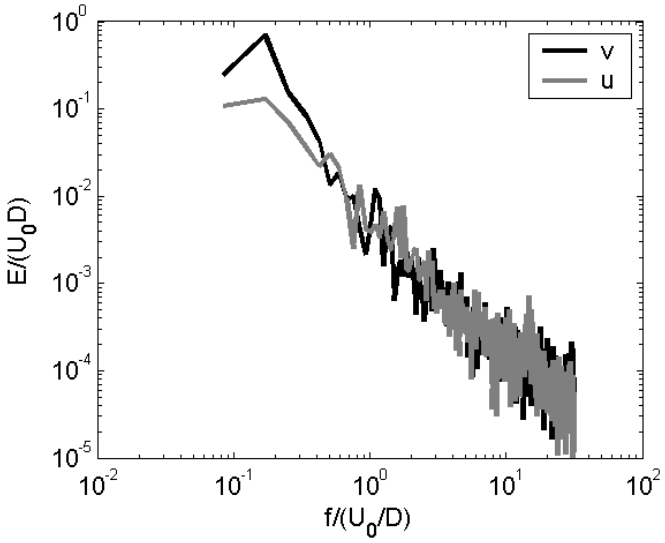

Figure 10.30 Velocity spectra behind a mussel dropper at *x/D* = 2.75, *Re* = 9780.

With the current experimental configuration, PTV flow visualisation further downstream ($x/D > 3$) of the mussel dropper could not be obtained. However, visual observation revealed regular large eddies similar to that for the circular cylinders. The mussel dropper therefore behaves similarly to a rough cylinder, but with low intensity turbulence within the near wake presumably from eddies shed from individual mussel droppers. As Figure 10.28 indicates, turbulent production near the dropper is highest along the edges of the free-shear layers, similar to the pattern seen for the rough cylinder (e.g. Figure 10.21). It is likely that TKE behind the mussel dropper will peak at the back of the near-wake region as it did for the smooth and rough cylinders.

10.4 Summary

Measurements of drag on smooth and rough cylinders indicate that roughness has a minor effect on drag coefficient at Reynolds numbers in the range 4,000 to 12,000. The drag coefficient (corrected for aspect ratio) for the smooth cylinder was 1.24 ± 0.05, and for the rough cylinders, C_D = 1.13 ± 0.02 (k_s/D = 0.048) and 1.23 ± 0.03 (k_s/D = 0.092). An allowance was made for the increase in diameter caused by the roughness coating on the cylinder surfaces (by adding the size of the surface roughness to the diameter, as described in section 8.2.3).

The diameter of a mussel dropper is difficult to define clearly due to the highly irregular profile and slight porosity. For design purposes, the product of drag coefficient and diameter may be used to calculate the drag on a mussel dropper. The mussels on the length of dropper used for these experiments were of

typical harvest size (average length 83.4 mm), and so provide a useful estimate of the maximum drag on a mussel dropper. The product of diameter and drag-coefficient for the mussel dropper was 0.18 m ± 0.01 m. A convenient estimate of the mussel dropper diameter that both resembles the visual diameter, and provides a drag coefficient comparable to that of a rough cylinder, is to double the average mussel shell length. Using this diameter of 0.167 m, the mussel dropper had a drag coefficient of 1.10 ± 0.07.

The PTV system described in Chapter 9 was used to obtain centreline profiles of time-averaged velocity U, and turbulent kinetic energy (TKE) behind smooth and rough (k_s/D = 0.048 and 0.094) cylinders. Time-averaged stream-wise velocity fields showed a region of return flow (negative velocities) behind the cylinders. The length of this region was shorter for rough cylinders than for the smooth. In a similar fashion, a peak in TKE occurred closer to the cylinder for the rough cylinders than for the smooth. This peak was located a short distance downstream from the end of the region of return flow. Peak TKE was higher for the rough cylinders, but little difference was seen between the two different roughnesses. Both centreline velocity and TKE profiles showed a Reynolds number dependence, with the return flow region decreasing in size, and TKE increasing as the Reynolds number increased from ~ 1400 to ~ 5100. The rough cylinders were less sensitive than the smooth, with smaller variations in TKE and centreline velocity from Re = 2500 to 5200.

A reduction in Strouhal number was detected behind the rough cylinders. While the smooth cylinder gave a value of St = 0.21 at Re between 1300 and 5000, values for the rough cylinders were S_t = 0.19 and 0.17 for k_s/D = 0.048 and 0.094 respectively. The Strouhal number for a mussel dropper based on spectra at x/D = 2.75 was estimated at 0.17 ± 0.04, consistent with the reduction in S_t recorded for the rough cylinders.

Flow fields behind the mussel dropper showed the presence of small scale eddies, presumably shed from individual shells. As a result, turbulent kinetic energy was higher in the recirculating region behind the mussel dropper than the cylinders. Further downstream, larger eddies developed, generated from the free-shear layers as seen for the cylinder flows.

Calculations of turbulent kinetic energy production terms indicate that turbulent energy behind the smooth and rough cylinders was due to both the $\langle vv \rangle \partial V/\partial y$ and $\langle uv \rangle (\partial U/\partial y + \partial V/\partial x)$ terms. Production in the shear layers in the region near the mussel droppers was dominated by the turbulent shear stresses $\langle uv \rangle (\partial U/\partial y + \partial V/\partial x)$.

CHAPTER 11 EFFECTS OF SPACING AND ROUGHNESS ON THE FLOW THROUGH SINGLE ROWS OF CYLINDERS

11.1 Introduction

Mussel long-lines consist of either individual dropper ropes which hang vertically, or a continuous crop rope which hangs in loops along the length of the mussel long-line (see Figures 1.1 and 1.2). The vertical lengths of mussel-encrusted rope of either configuration resemble a row of rough cylinders. The spacing of the vertical ropes will have an important effect on the drag on and flow around the long-line. A close spacing permits more mussels to be grown on a long-line. There is no clear industry standard for the spacing of the vertical dropper ropes, which therefore varies from site to site. As diameters of the dropper ropes change with the growth of the mussels, the possible spacing to diameter ratio (S/D) covers a broad range. With mature mussels ($D \sim 0.25$ m) and closely spaced droppers ($S \sim 0.4$ m), the spacing ratio could be as low as $S/D = 1.6$. This is probably the lowest practical spacing, as if the droppers are too close, wave motion would make them likely to collide, damaging the crop. At the other end of the range, mussel droppers may be spaced as widely as $S = 1$ m, and with an immature crop, mussel dropper diameters may be as low as $D = 0.05$ m, giving $S/D \sim 20$.

In this chapter, the effects of cylinder spacing and high surface roughness on a row of cylinders are investigated. Both drag measurement and flow visualisation (PTV) are used. The focus is on single rows of cylinders orientated across the flow. Other configurations, such as double rows and arrays at an angle to the flow, are investigated in Chapter 12. This chapter builds on the work in Chapter 10, where the effect of surface roughness on single cylinders was investigated.

In the literature review (Chapter 8), it was established that the flow behind single rows of cylinders aligned normal to the flow could be divided into two categories based on cylinder spacing and the resulting flow fields. At wide spacing, the wakes behind adjacent cylinders are similar to each other and there is little interaction between the cylinders, except far downstream where the wakes merge. At close spacings, the jets that form between the cylinders tend to pair, forming quasi-steady wake patterns where wakes differ behind adjacent cylinders. The accepted cylinder spacing below which the non-uniform flow patterns occur is $S/D \sim 2.0$ to 2.2. The experimental configurations used in this chapter are either side of this threshold spacing.

11.2 Methodology

The experimental methodology has been described in detail in Chapter 9. Briefly, drag tests were made of smooth cylinders, $D = 20.2$ mm; rough cylinders, $D = 22.2$ mm, $k_s/D = 0.090$; and very rough cylinders,

D = 24.0 mm, k_s/D = 0.167. All cylinders were of length 420 mm. Cylinder spacings were varied in increments of 23.3 mm.

PTV flow visualisation was used for arrays of smooth cylinders made from PVC, diameter 42.2 mm, length 890 mm; and rough cylinders with k_s/D = 0.094, diameter 42.9 mm, and length 890 mm. Cylinders were spaced across the tank at intervals of 80 mm, 120 mm, and 160 mm.

11.3 Results and Discussion

11.3.1 Drag on Cylinder Arrays

To investigate the effect of spacing on drag, an array of 7 smooth cylinders was towed at Reynolds numbers (based on cylinder diameter) between 1800 and 6300. The spacing was varied between S/D = 1.15 and 6.93. Drag coefficients, based on the total projected area of the submerged cylinders, are plotted in Figure 11.1(a). Drag was also measured for arrays of cylinders at a fixed spacing, but with variable cylinder numbers. The results from varying the number of cylinders are plotted in Figure 11.1(b).

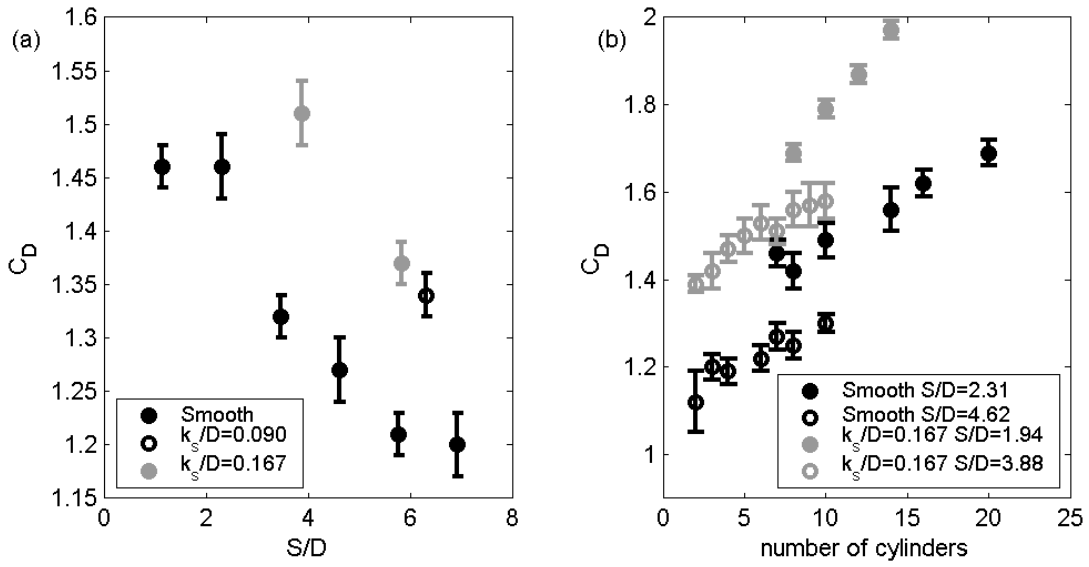

Figure 11.1 Drag on single rows of cylinder as a function of (a) cylinder spacing for 7 cylinders, (b) number of cylinders. The error bars indicate a 90% confidence interval for the drag coefficients.

Drag coefficients were a function of both the cylinder spacing, and the number of cylinders within the array. The increase in drag as the spacing decreases is expected, as the flow suffers greater acceleration in order to pass between the cylinders. The reason for the increase in drag coefficient for larger number of cylinders is the greater tank blockage caused by the cylinder array. A simple correction for the blockage ratio is to multiply the drag coefficients by $(1-\alpha)^2$ to account for the increase in velocity through the array, where α is the solid fraction of the tank cross-sectional area that the cylinders occupy ($\alpha = nDL/WH$, where n is the number of cylinders, D the cylinder diameter, L the cylinder length, W and H the tank

width and depth). After applying this correction, see Figure 11.2, the drag coefficients at the selected cylinder spacing show a greater degree of independence from the number of cylinders used, with the exception of the closely-spaced array of rough cylinders (solid grey circles in Figure 11.2(b)).

From Figure 11.2, it is clear that the drag coefficients for the rough arrays are greater than for smooth arrays (by 10 to 15%). In Chapter 10, it was found that there was little difference between drag coefficients for single smooth and rough cylinders. This data suggests that the surface roughness on cylinder arrays produces some form of wake interaction that increases the drag.

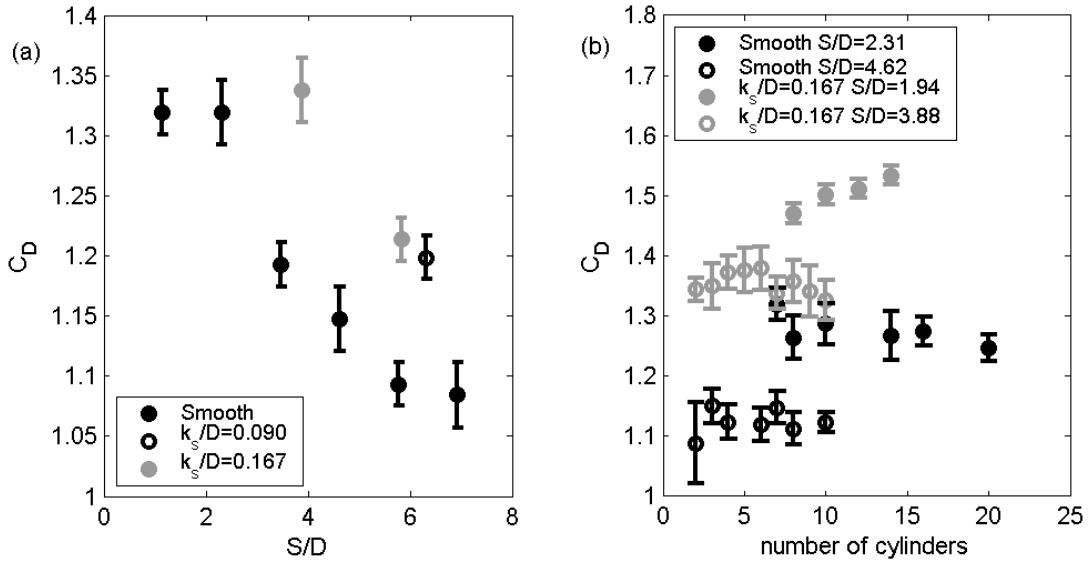

Figure 11.2 Drag coefficients for cylinder arrays corrected for blockage ratio, (a) 7 cylinders, (b) variable number of cylinders.

11.3.2 Wide Cylinder Spacing - Flow Fields

Experiments on single rows of cylinders show that at wide cylinder spacings ($S/D > 2.2$), cylinder wakes resembled that of a single cylinder, Figure 11.3(a). Cylinder wakes were essentially identical across the array, Figure 11.3(b) and (c). The cylinder wakes behind adjacent cylinders remained similar until the spacing was reduced below the threshold for spatial instability of S/D = 2.0-2.2, Figure 11.3(d). In this section, cylinder spacings greater than S/D = 2.2 (wide spacing) will be considered, with further analysis of close cylinder spacings ($S/D < 2.2$) presented in section 11.3.4.

Time-averaged turbulent kinetic energy and turbulent shear stresses (Reynolds stresses) are also plotted in Figure 11.3. As the cylinder spacing decreases, the magnitudes of TKE and Reynolds stresses increase. The peak TKE and $\langle uv \rangle$ move closer to the cylinder, consistent with a reduction in the size of the recirculating region. The distributions behind cylinders within the same array are essentially identical. As the spacing is decreased to S/D = 2.84, the plot of TKE shows the wakes merging from $x/D > 2.5$.

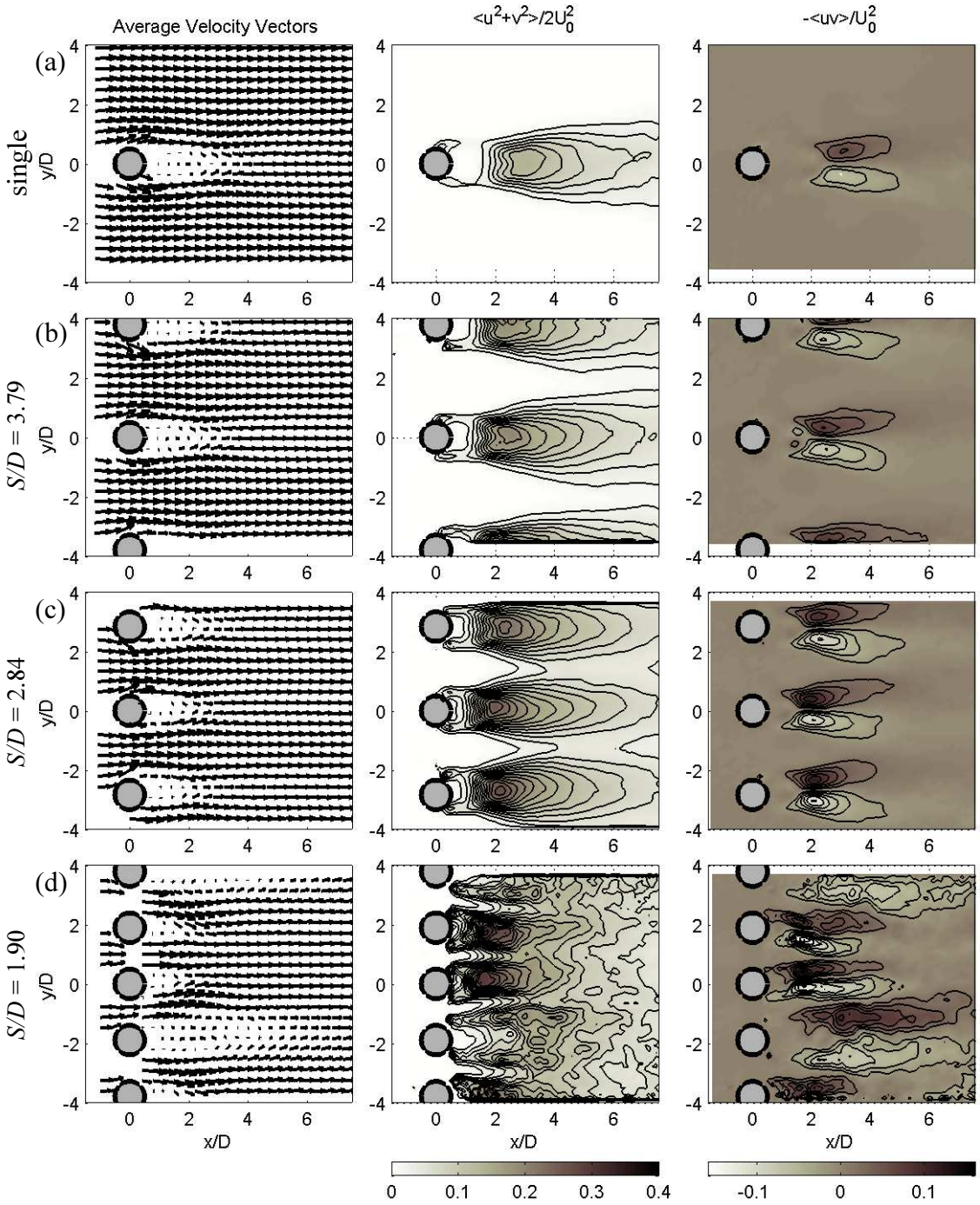

Figure 11.3 Time-averaged velocity vectors, turbulent kinetic energy and turbulent shear stresses behind (a) single smooth cylinder, and smooth cylinders at (b) *S/D* = 3.79, (c) *S/D* = 2.84, and (d) *S/D* = 1.90, *Re* = 1300. Contours are at 0.02 intervals.

Cross-sections of stream-wise velocity and turbulent kinetic energy at x/D = 4 for the widely spaced cylinders are plotted in Figure 11.4. These cross-sections clearly show the acceleration of the fluid through the gaps between the cylinders. The wakes of the cylinders at S/D = 2.84 are merging by this point, explaining the overlapping TKE profiles.

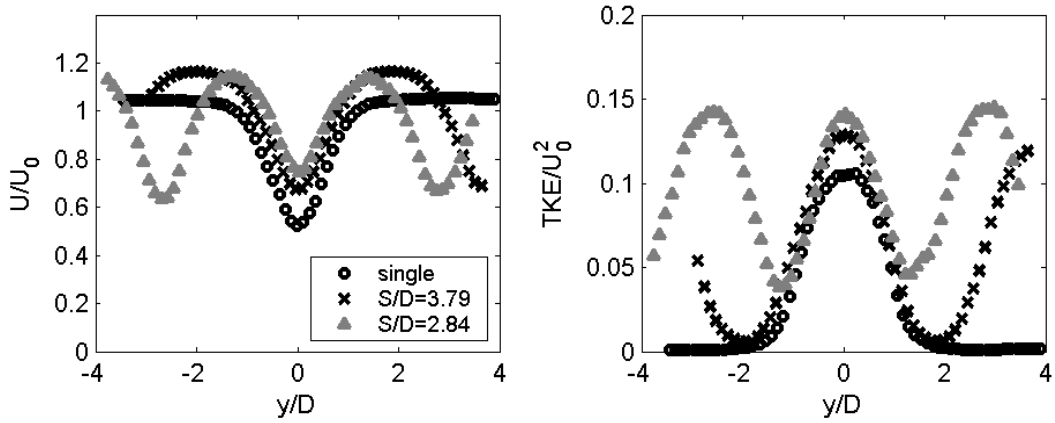

Figure 11.4 Cross-sections of stream-wise velocity and TKE at *x/D* = 4 behind arrays of widely spaced smooth cylinders at *Re* ~ 1300.

Profiles of U, the stream-wise (x-direction) velocity component and TKE along a line passing downstream through the centre of the cylinder are plotted in Figure 11.5. They show a decrease in the length of the near wake, and a reduction in the distances from the cylinder to the point of maximum negative velocity and maximum TKE as the cylinder spacing is reduced.

Some of the change in wake size may be due to the increase of velocities between the cylinders. As the cylinders present a blockage to the flow, the fluid must accelerate to pass through the cylinder array. The faster velocities result in a higher effective Reynolds number for the flow past the cylinders. The effective Reynolds number can be estimated from the geometry of the array. If the cylinder array spans the full width and depth of the tank, then the velocity in the gaps between the cylinders can be calculated from continuity. Given an upstream velocity of U_0, the average gap velocity will be:

$$\frac{U_g}{U_0} = \frac{S/D}{S/D - 1} \tag{11.1}$$

Predicted gap velocities for the cylinder spacings used in these experiments are calculated in Table 11.1.

Spacing S (mm)	160	120	80
Diameter D (mm)	42.2	42.2	42.2
S/D	3.79	2.84	1.90
U_g/U_0	1.36	1.54	2.12

Table 11.1 Predicted gap velocities at typical cylinder spacings used in experiments.

The increased effective Reynolds numbers, based on the gap flow velocities, do not completely account for the reduction in the near wake length. At a cylinder spacing of *S/D* = 2.84, the effective Reynolds number is increased from 1300 to 2000. The near-wake length is *x/D* ~ 1.8, while that of a single cylinder

at *Re* = 2400, an even higher Reynolds number, is *x/D* ~ 2.1. The effect of Reynolds number on the near-wake length for single cylinders was illustrated in section 10.3.4, particularly Figure 10.7.

Another factor that may contribute to the decreased wake size is that the shear gradients ($\partial U/\partial y$) between the cylinders will be stronger at closer cylinder spacings. The stronger shear gradients may promote a more rapid eddy roll-up along the free-shear layers behind the cylinder, reducing the near wake size.

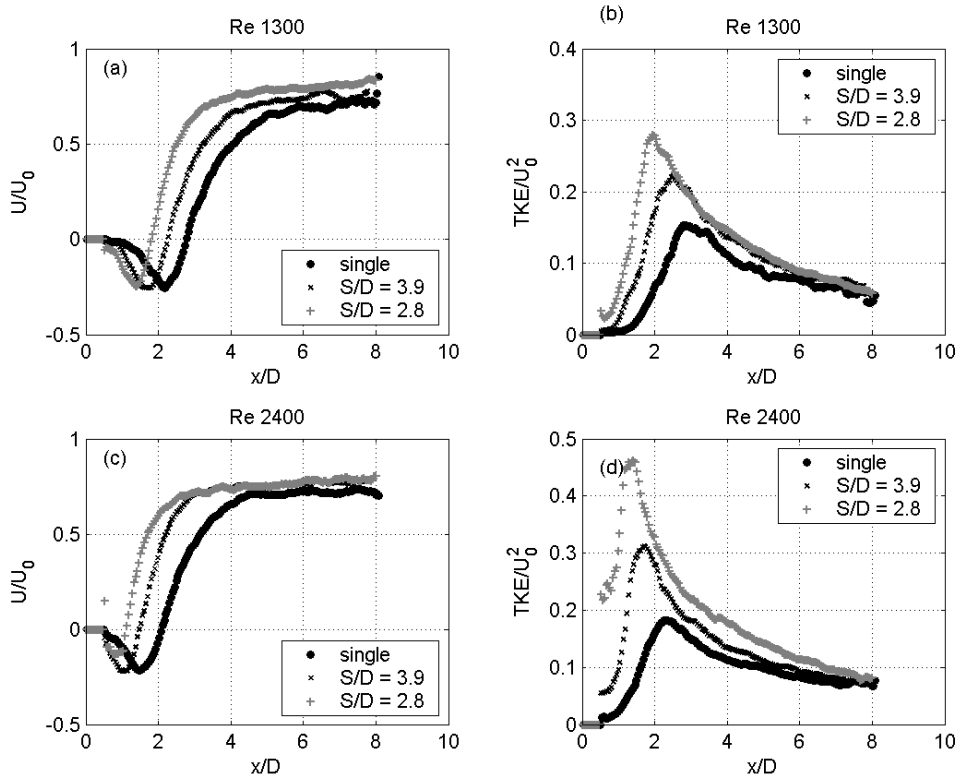

Figure 11.5 (a) Centreline velocities, and (b) TKE at *Re* ~ 1300, (c) centreline velocities, and (d) TKE at *Re* ~ 2400 behind PVC single cylinders, and PVC cylinders in arrays spaced at *S/D* = 3.89 and 2.84.

The cylinder wake sizes and TKE are not independent of Reynolds number over the range used in these experiments. This was shown for single cylinders in the preceding chapter (Figure 10.7), and the data plotted in Figure 11.5 show a similar behaviour occurs for the multi cylinder array. The Reynolds number effects are most evident in the TKE profiles behind the cylinders, with peak TKE increasing by nearly 70% behind the cylinders at *S/D* = 2.84 as *Re* increased from 1300 to 2400 (see Figure 11.5).

In many studies, the gap velocity rather than the free stream velocity is used as the characteristic flow parameter. This to account for the higher velocities as the fluid accelerates to pass between the cylinders. Centreline profiles of stream-wise velocity and TKE normalised using the calculated gap velocity are plotted in Figure 11.6. Using the gap-velocity decreases the variations between peak normalised TKE, but increases the difference between the minimum normalised velocity within the near wake region. The

understanding of the flow is not improved greatly by using gap velocities as opposed to the free-stream velocity.

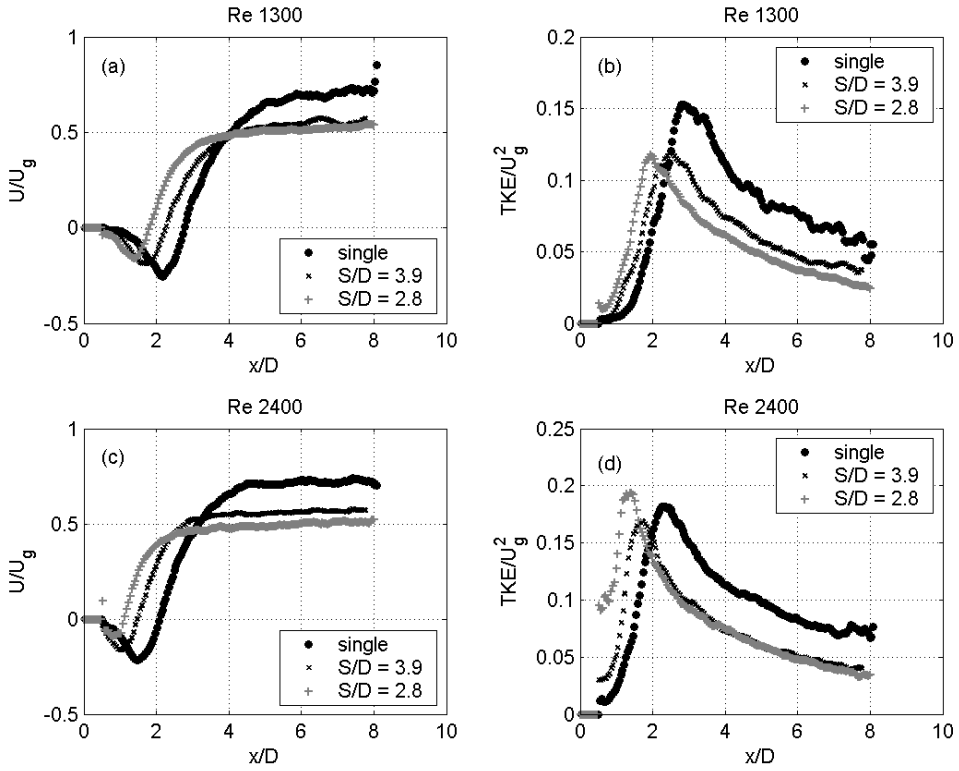

Figure 11.6 (a) Centreline velocities and (b) TKE at *Re* ~ 1300, (c) centreline velocities and (d) TKE at *Re* ~ 2400 behind PVC single cylinders and PVC cylinders in arrays spaced at *S/D* = 3.9 and 2.8 normalised by the gap velocity.

Flow fields behind an array of rough cylinders show significantly higher turbulent kinetic energy, as well as a higher turbulent production (Figure 11.7). The method of calculating production was described in section 10.3.5. The contours give the appearance of TKE spreading across the flow at a more rapid rate behind the array of rough cylinders. However, cross-sections through the wake at x/D = 4 (Figure 11.8) suggest that the spread is similar, and that the contours appear to cover a greater region due to the higher intensity of TKE behind the rough cylinders.

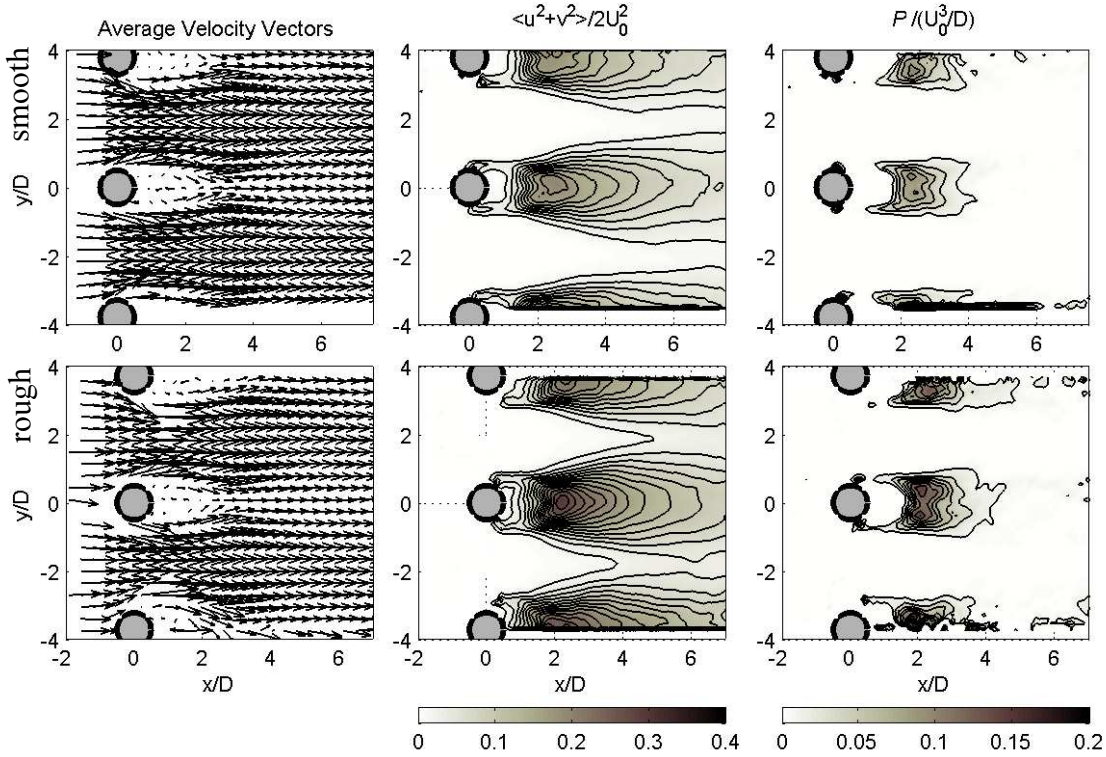

Figure 11.7 Average velocity vectors, turbulent kinetic energy, and turbulent production behind arrays of smooth cylinders at *S/D* = 3.79, and rough cylinders (k_s/D = 0.094) at *S/D* = 3.73, *Re* ~ 1350. Contour lines are at 0.02 intervals.

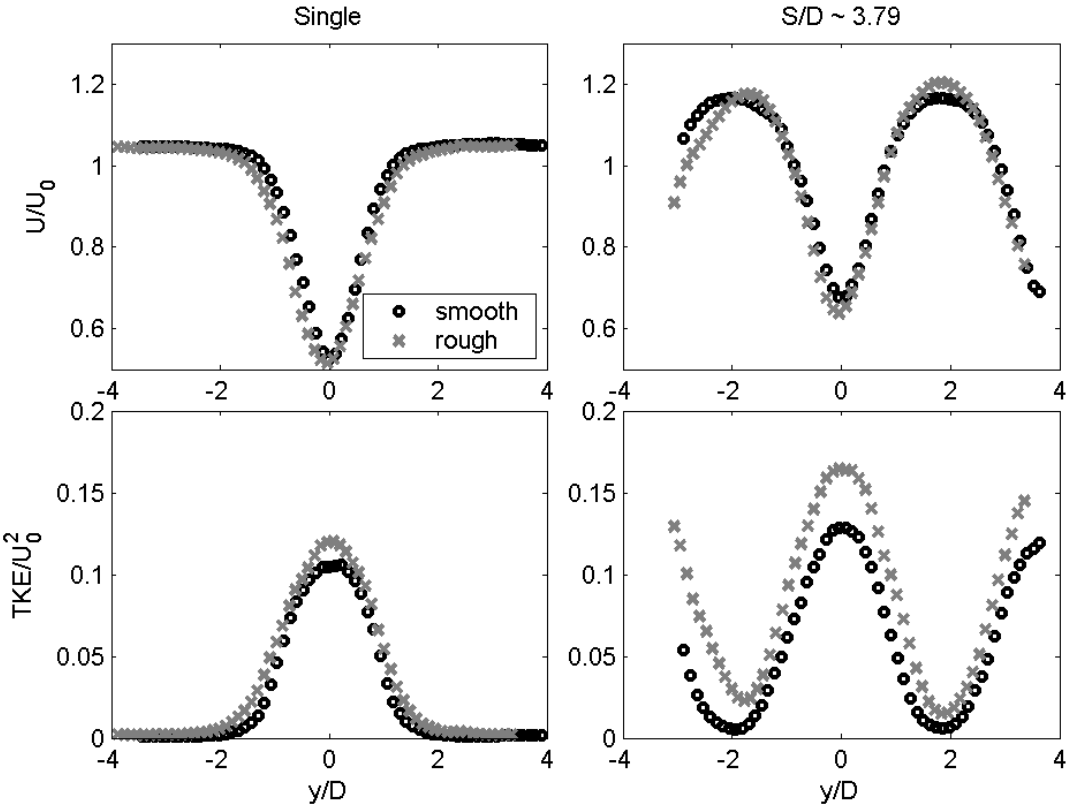

Figure 11.8 Stream-wise velocity and TKE behind single smooth and rough cylinders, and arrays of smooth and rough cylinders at x/D ~ 4.0, *S/D* ~ 3.79, *Re* ~ 1350.

Profiles of time-averaged stream-wise velocity and TKE along $y = 0$ are plotted in Figure 11.9. While the profiles of U for the rough and smooth cylinders collapse well at each Reynolds number, the peak TKE behind the rough cylinder is 49% higher at Re = 1350, 27% higher at Re = 2450, and 29% higher at Re = 3820 (not shown). In comparison, the TKE behind a single rough cylinder was increased by 5 to 24% above that of a single smooth cylinder, depending on Reynolds number (see Figure 10.8). The TKE increase for the cylinder array is more consistent than for the single cylinders.

There is a small difference in cylinder spacing between the rough and smooth array (1.6%), but this is insufficient to account for such a large increase in TKE. The peak production behind the rough array in Figure 11.7 is approximately 50% higher than behind the smooth array, indicating the cylinder roughness enhances the production of turbulent kinetic energy.

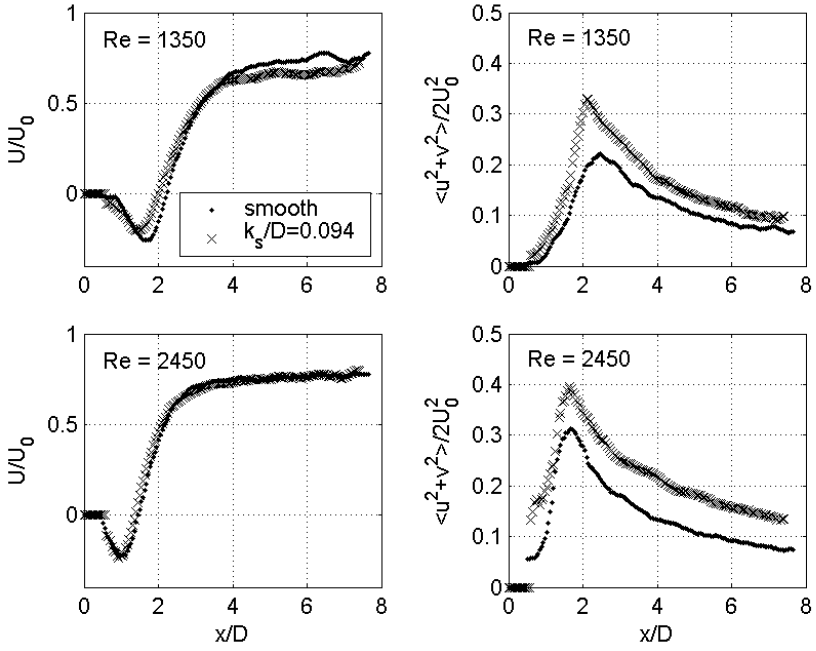

Figure 11.9 Profiles of time-averaged stream-wise velocity and turbulent kinetic energy behind arrays of smooth cylinders (dots) at *S/D* = 3.79, and rough cylinders (crosses, k_s/D = 0.094) at *S/D* = 3.73.

11.3.3 Wide Cylinder Spacing - Velocity Spectra

The Strouhal number increases as the spacing decreases if the tow or free-stream velocity is used to calculate the Strouhal number, see Figure 11.10(a). Estimated Strouhal numbers at Re 1350 were 0.250 at S/D = 3.79, and 0.29 at S/D = 2.84. By using the gap velocity, as in Figure 11.10(b), the Strouhal numbers for the smooth cylinders in the arrays collapse at ~ 0.185, 15% lower than the value for the single cylinder (measured at 0.22, accepted value 0.21).

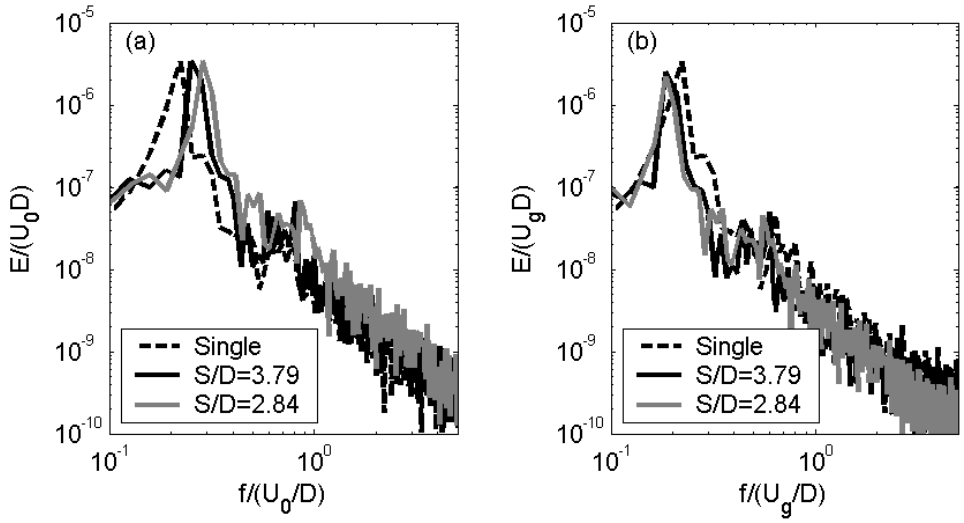

Figure 11.10 Velocity spectra (*v* component) at *x/D* = 4 behind smooth cylinders at different spacings, normalised by (a) tow velocity, and (b) gap velocity, *Re* ~ 1350 (based on tow velocity).

The Strouhal number also increases behind an array of rough cylinders, Figure 11.11. The Strouhal number behind the array of rough cylinders (k_s/D = 0.094) at S/D = 3.73 was 0.23, compared to 0.17 for the single rough cylinder. If the Strouhal number is calculated using the gap velocity, then the value for the array of rough cylinders is unchanged from that of the single cylinder. The result using U_g suggests that the eddy shedding frequency for the array of rough cylinders is primarily determined by the surface roughness. The Strouhal numbers for the rough cylinder array is lower than that for the smooth, irrespective of which velocity is used to non-dimensionalise the eddy shedding frequency.

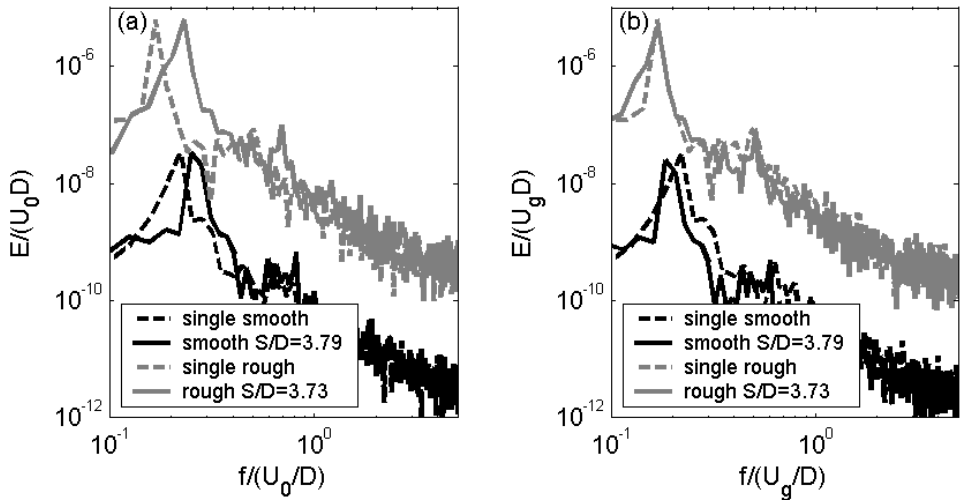

Figure 11.11 Velocity spectra at *x/D* = 4 behind smooth cylinders at *S/D* = 3.79, and rough cylinders (k_s/D) at *S/D* = 3.73, normalised by (a) tow velocity, and (b) gap velocity. Single cylinder values shown as dashed lines. Spectra energies for the smooth cylinders have been offset by 10^{-2}. *Re* ~ 1350 (based on tow velocity).

11.3.4 Close Cylinder Spacing - Flow Fields

When the cylinder spacing is reduced to S/D = 1.90, below the threshold for spatial instability, there are discernable irregularities in the time-averaged turbulence statistics behind adjacent cylinders, as illustrated in Figure 11.3(d). In particular, the size of the near-wake or recirculating region behind the cylinders varies considerably. In the data plotted in Figure 11.3(d), the near-wake regions behind the cylinders at y/D = 0 and 1.9 are very short in comparison with that behind the cylinder at y/D = -1.9. Similarly, the distributions of TKE and turbulent shear stresses vary considerably behind the cylinders.

For the single cylinder and widely spaced cylinder experiments, data were averaged over a number (typically 4) of repeated experimental runs as flow patterns were the same each time. However, at close cylinder spacings with a full-width array (the array spanning the full width of the tank), the wake patterns differed between each run, although they were stable within each run. The flow fields from four consecutive experiments with an array of 17 smooth cylinders at S/D = 1.90, Re = 1440, are plotted in Figure 11.12. Runs 1 and 4 show similar stable states with short near wakes behind the cylinders at y/D = 0 and 1.9, and a long wake behind the cylinder at y/D = -1.9. The general distribution of turbulent kinetic energy and turbulent shear stresses also show similarity. The cylinder wakes in runs 2 and 3 both demonstrate different stable states. While the lengths of the near wake regions behind adjacent cylinders differ in runs 2 and 3, the variations in length between cylinder wakes are less than the extremes seen in runs 1 and 4.

In the experiments presented here, a particular wake configuration, once formed, would persist for the duration of the run (approximately 50 seconds at Re = 1440, and 25 seconds at Re = 2650). Others have found that the flow would periodically transition from one stable state to another (Moretti and Cheng, 1987).

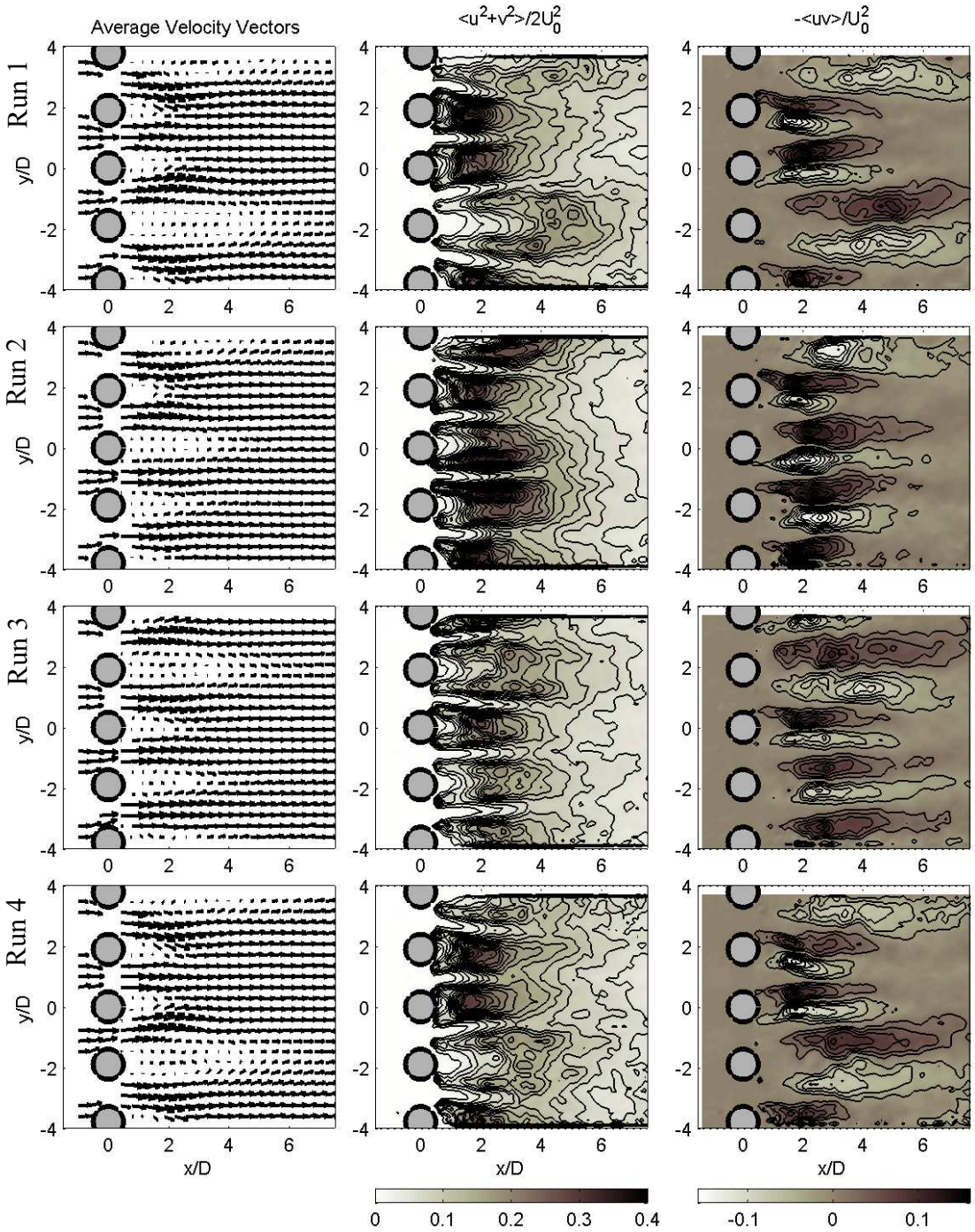

Figure 11.12 Smooth cylinders: time-averaged velocity vectors, turbulent kinetic energy and turbulent shear stresses from four repeated experiments (runs 1 to 4 from top to bottom), *S/D* = 1.90, *Re* = 1440. Contour lines are at intervals of 0.02.

While different wake patterns were produced in each run using smooth cylinders, the wake configurations were nearly identical in every run when using rough cylinders. In Figure 11.13, time-averaged velocity vectors, turbulent kinetic energy, and turbulent shear stresses are shown for four consecutive runs using an array of 17 cylinders, k_s/D = 0.094, at *Re* = 1360. A large wake can be seen behind the central cylinder

in all four runs, although there is some variation both in the length of this recirculating region, and in the associated distributions of TKE and <*uv*>. This variation is much less than seen for the smooth array.

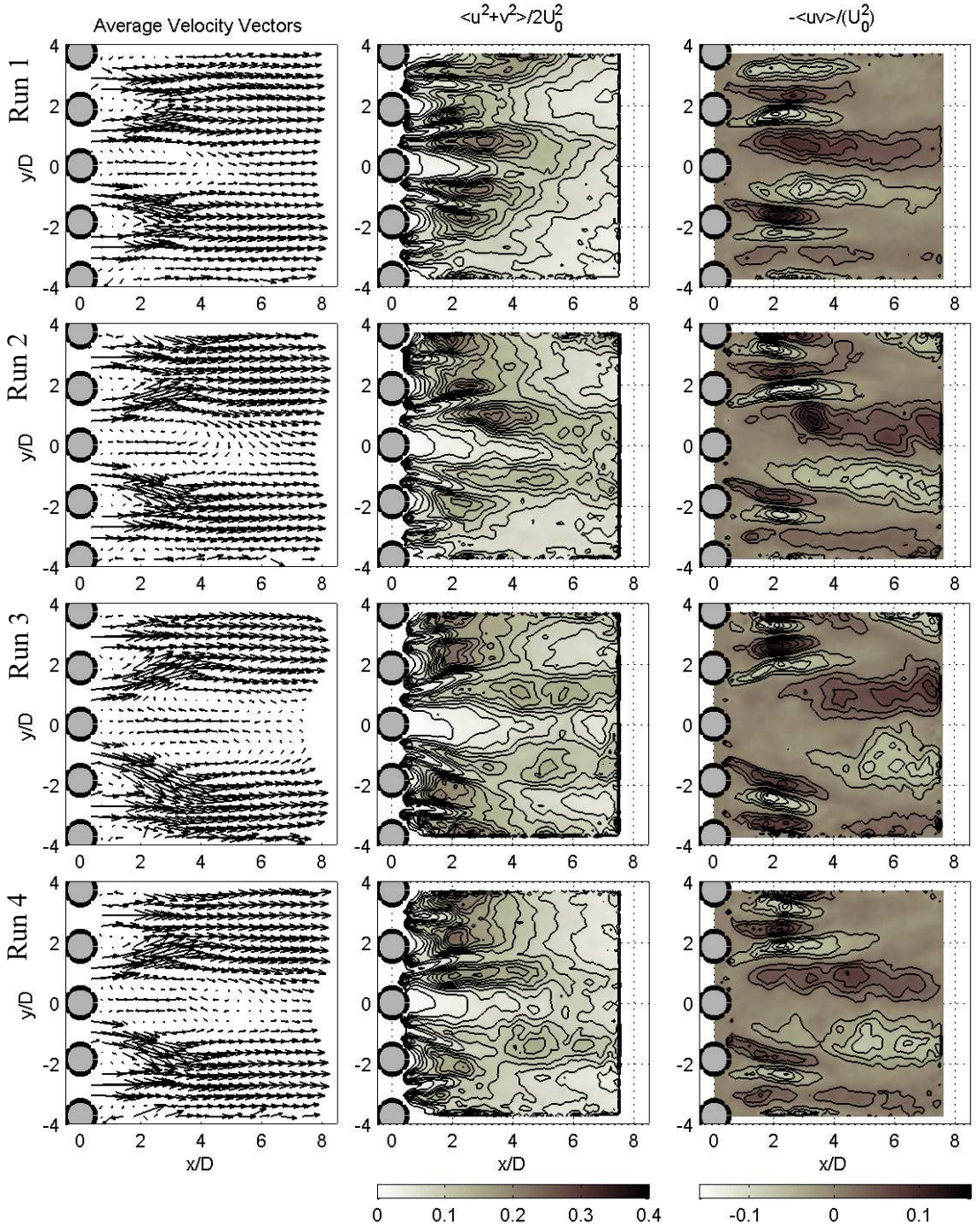

Figure 11.13 Rough cylinders: time-averaged velocity vectors, turbulent kinetic energy and turbulent shear stresses from four repeated experiments (runs 1 to 4 from top to bottom), k_s/D = 0.094, S/D = 1.86, Re = 1360. Contour lines are at intervals of 0.02.

The high surface roughness apparently acts to stabilise the wake structure by favouring a particular wake formation. This is likely to be due to slight variations between the cylinders. Each cylinder has a unique surface roughness distribution due to the procedure of coating the cylinder surface with gravel. If the

meta-stable wake patterns result from a pairing of shed vortices, then it is likely that the uniqueness of each cylinder results in a similar vortex shedding each run, thereby favouring a particular vortex pairing and associated meta-stable flow regime. This could have been checked by swapping the cylinders. Unfortunately this idea did not occur at the time of the experiments. Mussel droppers also have unique surface roughness patterns, as the mussels attach in an essentially random fashion. The wake patterns forming behind closely spaced mussel droppers are also likely to form in a particular wake configuration based on the unique characteristics of the droppers in the array (dropper spacings may be as low as S/D = 1.6 as described in section 11.1).

The mussel droppers are flexible, and able to move in response to applied forces. With the irregular wake patterns forming behind arrays of closely spaced cylinders, it is highly likely that each cylinder is subject to a cross-stream "lift" force due to the asymmetry of the flow. Depending on the strength of these forces, some mussel droppers may move closer together. Data from side-by-side cylinders show that as the spacing between cylinders is decreased, the lift force that acts to push the cylinders together increases (Zdravkovich, 2003). In strong currents, this lift force may either force mussel droppers to touch, or, if the mass of the dropper is sufficient so that gravity provides a balancing force, create unequal spacing between droppers. An unequal spacing is likely to further promote uneven wake distribution patterns behind neighbouring droppers.

The difference in flow structure between runs behind the closely spaced array of smooth cylinders was not seen when the array consisted of only 8 cylinders; the flow patterns behind the half-width array was the same for each run. Using a smaller number of cylinders may have favoured one particular wake pattern due to a proportionally greater influence from flow around the cylinders at the end of the array. With fewer cylinders, a certain amount of flow is diverted around the sides of the array, much as some of the flow was diverted around the mussel farm. This leads to lower velocities through the gaps between the cylinders, which also results in lower TKE and turbulent stresses behind the array (see Figure 11.14).

Interestingly, the array of 8 smooth cylinders (Figure 11.14(b)) showed a similar stable wake pattern to that of an array of 8 rough cylinders (Figure 11.14(c)), except that the length of the wake of the cylinder at y/D = 0 (the 4th cylinder from the left end of the array when facing upstream) was considerably longer behind the rough array.

The distribution of wake sizes behind the rough array of 8 cylinders was very similar to that behind the same cylinders in the array of 17 rough cylinders. The magnitudes of turbulent kinetic energy and turbulent shear stress were lower behind the array of 8 cylinders, which is expected as the velocities between the cylinders were reduced due to the flow around the outside of the array. The cylinders shown

in Figure 11.14(c) are the same cylinders shown in Figure 11.13, (with the outer cylinders removed). This reinforces the view that the unique roughness distributions control the wake sizes.

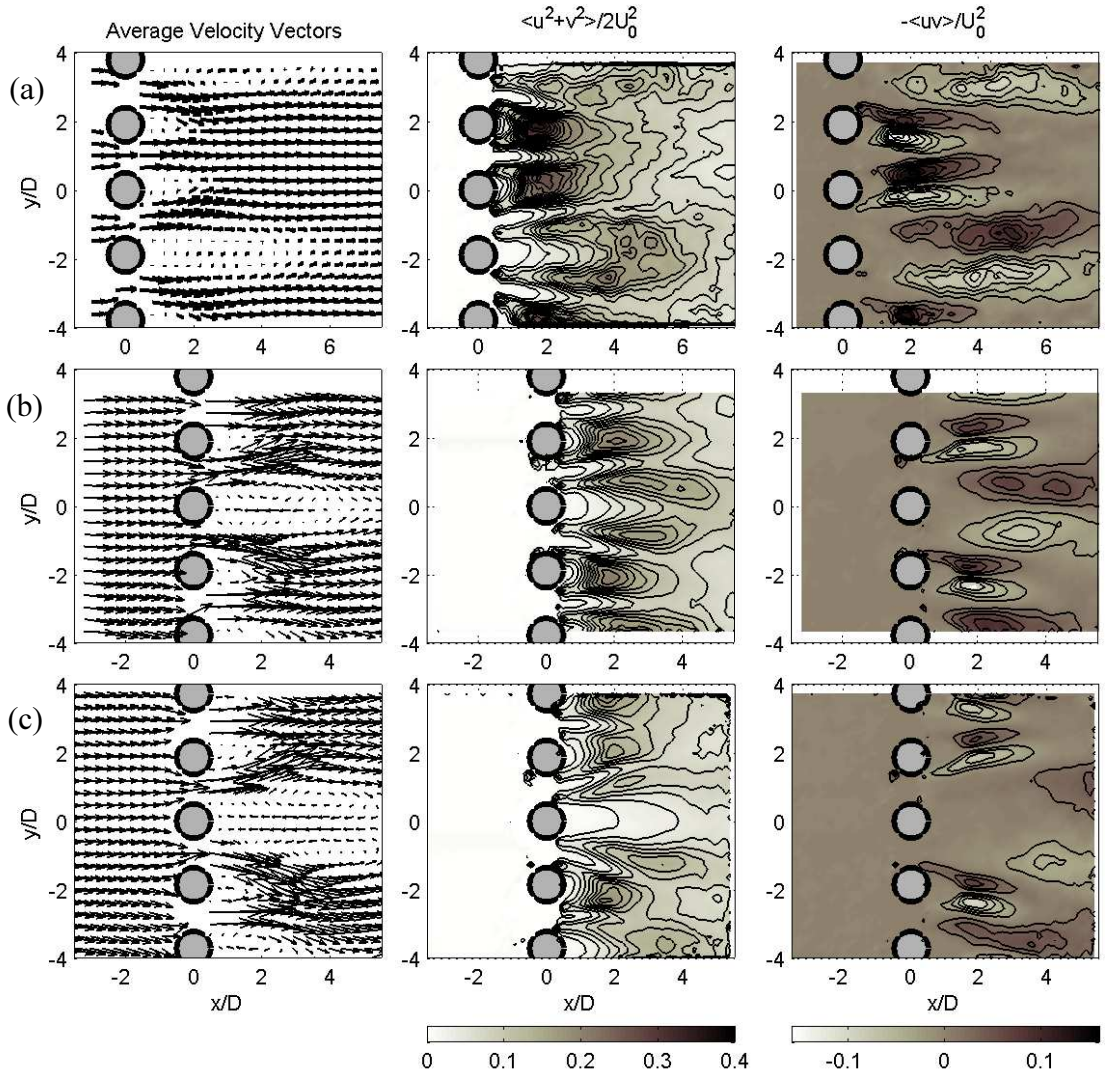

Figure 11.14 (a) example of 17 smooth cylinders at *S/D* = 1.90, (b) 8 smooth cylinders at *S/D* = 1.90, and (c) 8 rough (k_s/D = 0.094) at *S/D* = 1.86, *Re* ~ 1400.

The cylinder at the end of the array has higher velocities around the outer side, which generates a wake bias away from the array. This can be seen in the PTV analysis of flow around the end cylinder of an array at *S/D* = 1.90, Figure 11.15. The wake-bias of the end cylinder is the likely mechanism controlling the wake pattern behind a closely spaced array containing a small number of cylinders. This array end-effect is likely to have a stronger influence over a narrow array, whereas for an array with more cylinders, the central flow region will be less affected by the end conditions.

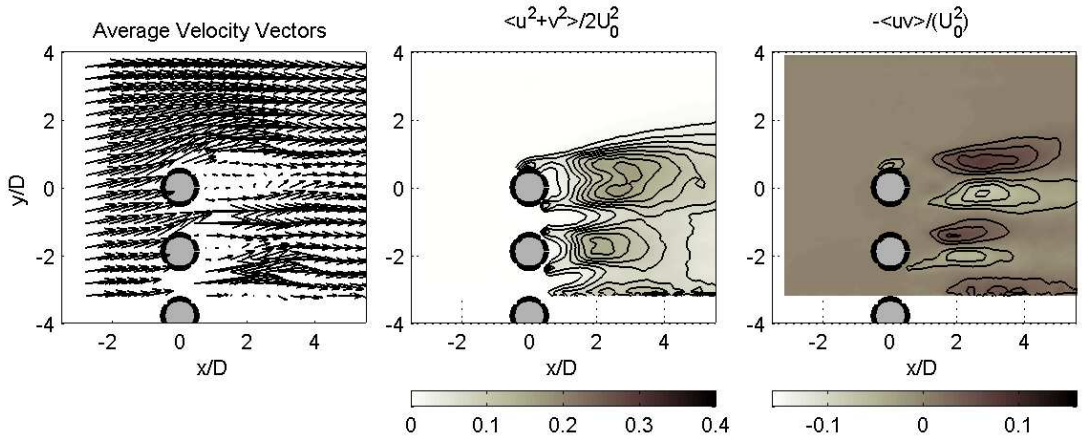

Figure 11.15 Flow around end of array of 8 smooth cylinders at *S/D* = 1.90, *Re* = 1440.

With regard to the anisotropy of the turbulence behind the closely spaced cylinders, the turbulent normal stresses <*uu*> and <*vv*> dominated in different regions of the flow. The relative contributions of each component to the turbulent kinetic energy can be compared by plotting the turbulent stresses (Figure 11.16). In the previous chapter, it was demonstrated that for single cylinders, TKE was highest along the cylinder centreline ($y = 0$), and was dominated by cross-stream velocity fluctuations <*vv*>. There were, however, two lobes of turbulent kinetic energy attached to the cylinder at the wake separation points along which the stream-wise <*uu*> components dominated, particularly for the rough cylinder (see Figure 10.17). Similar distributions occurred behind cylinders in the widely spaced arrays ($S/D > 2.2$, not shown). Behind the closely spaced array ($S/D = 1.9$), the turbulent kinetic energy in the attached lobes was often comparable in magnitude to the peaks forming along the cylinder centreline.

It must be emphasised that flow visualisations for the cylinder arrays were only made at one height, which was at approximately the mid-height of the cylinders. This position was selected based on single cylinder experiments where it was found that over much of the cylinder length, the average velocity fields were nearly identical. There were differences in flow fields towards the upper and lower ends of the cylinder, where the free-end (bottom) and Perspex boat (top) appeared to interfere with the flow structure. It is possible that different flow patterns were formed at different locations along the length of the cylinders for the closely spaced arrays. No attempt was made to determine if this occurred. This would be difficult to do for the smooth cylinder arrays with the current experimental configuration. As the flow patterns must be measured in a horizontal plane to determine the wake pattern, the experiment would need to be repeated with the light sheet moved vertically. With the full-width array of smooth cylinders, different flow patterns formed each run, so the data would not be comparable unless it were possible to measure simultaneously at different heights. By forcing a particular wake configuration by using the half-width array, it is likely that the effects of the end cylinders will control the flow structure similarly at all

depths. The possible three-dimensionality of the wake patterns behind arrays of cylinders is an issue that requires further research.

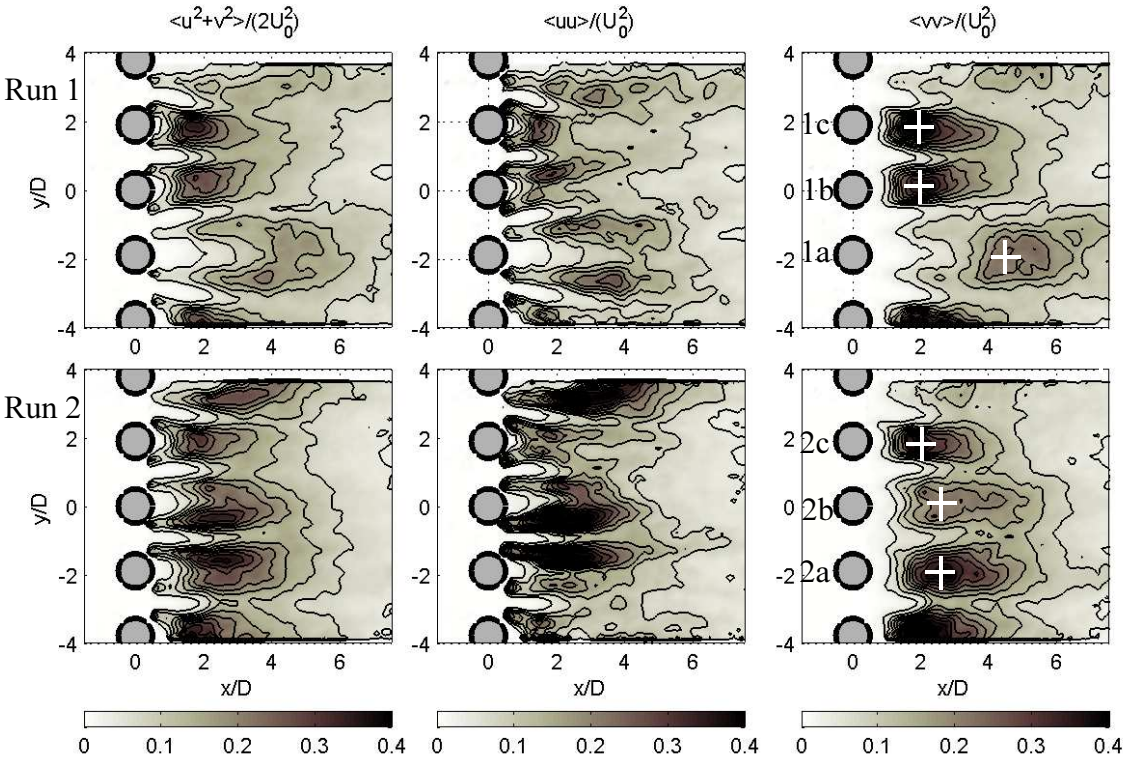

Figure 11.16 TKE, <*uu*>, and <*vv*> behind closely spaced array of smooth cylinders at *Re* = 1440, for two runs. The contours are at 0.04 intervals. White crosses in the <*vv*> plot indicate points where velocity spectra were calculated.

11.3.5 Close Cylinder Spacing - Velocity Spectra

It is clear from the frequency of the peaks in the velocity spectra (Figure 11.17) that eddy-shedding frequencies (and therefore Strouhal numbers) vary considerably between cylinders, and between runs for the same cylinder. The Strouhal number, calculated using the tow or free-stream velocity $S_t = fD/U_0$, is strongly related to the length of the recirculating region, which is also associated with the distance downstream of the cylinder to the peak in <*vv*>. Lower Strouhal numbers occur where the length of the recirculating region is long. Velocity spectra, calculated from the *v* components for 3 cylinders in the array of smooth cylinders, *S/D* = 1.9, *Re* = 1440, are shown in Figure 11.17. The white crosses in Figure 11.16 indicate the points where velocity spectra were measured.

In run 1, the wake behind cylinder 1a was extended, and the Strouhal number low (S_t = 0.156). The wake regions behind cylinders 1b and 1c were short and of similar length. The Strouhal numbers behind these cylinders were higher, with S_t = 0.51 and 0.53 for cylinders 1b and 1c respectively. The spectral peaks were less clearly defined in run 2. However, as the peaks occurred at higher frequencies, it was possible to window the time-series (break into shorter, overlapping time segments), and average the resulting

spectra. While losing some low frequency information, the spectra at higher frequencies were smoothed, and the peaks more clearly defined. Strouhal numbers for the 3 cylinders in run 2 were $S_t \sim 0.38$, 0.38, and 0.63 for cylinders 2a, 2b, and 2c respectively.

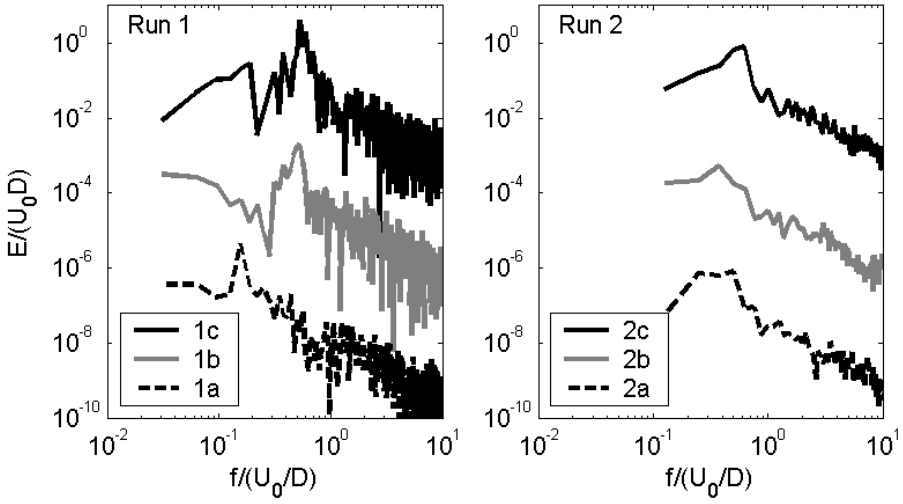

Figure 11.17 Velocity spectra behind array of smooth cylinders, *S/D* = 1.90, *Re* = 1440. Locations are indicated in Figure 11.16. Note that spectra 1b and 2b spectra have been offset by 10^{-3}, and spectra for 1a and 2a by 10^{-6}. The spectra for Run 2 have been smoothed by windowing the velocity time-series.

Moretti and Cheng (1987) suggested that for cylinders at a spacing between $1.5 < S/D < 2.2$, the jets between the cylinders will join in pairs, and that there would be two eddy shedding frequencies due to the formation of two different wake sizes. This is not supported by the current data, which indicates that the joining of the gap flow jets is more complicated than a simple pairing. Due to the limited field of view during the experiments, the wake behind only 3 cylinders could be clearly seen during any experiment. However, wake patterns varied from being all of similar size (e.g. run 3, Figure 11.12), to having some cylinders with large wakes, while neighbouring cylinder wakes were small (e.g. runs 1 and 4, Figure 11.12). There were not always two clearly different wake sizes; in some runs there appeared to be only one distinct wake size, while in others runs there were several wake sizes. It should therefore be expected that several different eddy-shedding frequencies may occur simultaneously behind the closely spaced cylinder array.

Further downstream of the array, eddies shed from the different cylinders interact. At $x/D = 5$, the strongest peak in the velocity spectra occurred at $fD/U_0 = 0.545$, with a smaller peak at a lower frequency of around 0.35 (Figure 11.18). At $x/D = 10$, the higher frequency peak can no longer be seen, indicating that the higher frequency eddies break down quickly as they interact. The lower frequency eddies, associated with the large wake regions, take longer to decay, as indicated by the higher spectral energies in the range $fD/U_0 = 0.25$ to 0.35.

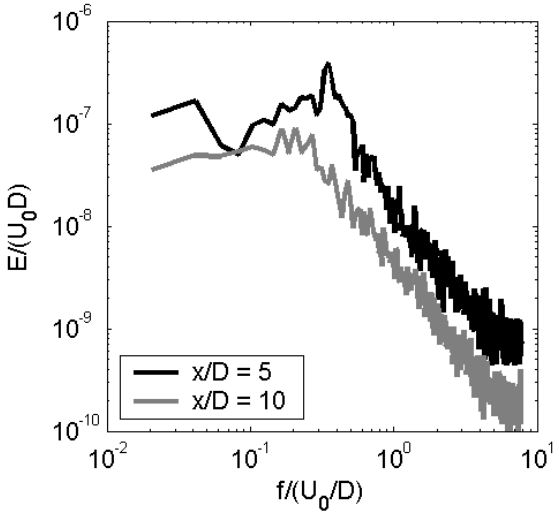

Figure 11.18 Velocity spectra behind array of smooth cylinders, *S/D* = 1.90, *Re* = 2430.

11.3.6 On the Origin of the Wake Bias

The non-uniformity of the cylinder wakes for the closely spaced cylinders is a peculiar phenomenon. It is clearly not caused by slight differences in cylinder spacing, as different wake patterns formed behind the exact same array of smooth cylinders during different experiments (Figure 11.12). PTV analysis of the flow near the cylinders at the start of motion show identical initial flow patterns. This also confirms that variations in geometry are not the cause. No satisfactory explanation of why the bias wake patterns form behind a cylinder array has been presented in the literature. Zdravkovich and Stonebanks (1990) suggest that the metastable flow patterns form as a result of an irregular coalescence of the gap flow jets, but propose no mechanism for how this occurs.

Some insight may be gained from recent advances in the understanding of wake bias behind a pair of cylinders. Zdravkovich (1995) observed the flow behind a side-by-side cylinder pair and noted that the wakes are initially identical. The initial interference takes place in the gap between the shear layers of adjacent cylinders. Zdravkovich suggests that as the shear layers have opposing vorticity, they mutually inhibit the roll-up into eddies. A small deflection of the gap flow to either side disturbs the balance, causing one of the shear layers to roll up. This triggers a further deflection of the gap flow so that a short, narrow wake forms behind the cylinder where the shear-layer roll up first occurs.

For an array of cylinders normal to the flow, such as used in these experiments, the situation is far more complex. The mechanism may be similar, in that the first roll-up of the free-shear layer behind a cylinder triggers the formation of a short, narrow wake. However, the early roll-up may occur behind different cylinders throughout the array. The disturbances to the gap flows around these cylinders will trigger further wake bias behind neighbouring cylinders. At some point, the disturbances propagating across the

array will interact, which may either reinforce or counteract the bias in the gap flows. The final wake pattern would therefore depend on which cylinders first experience an early free-shear layer roll up, and the resulting interaction as the disturbances propagate across the array. This would explain why different patterns are formed behind the same configuration of smooth cylinders in different runs, as the initial eddy roll-up is a random occurrence. For the array of rough cylinders, it might be expected that slight variations in the surface roughness of the cylinders would promote the early roll-up behind a particular cylinder through increased turbulence caused by the surface roughness interfering with the free-shear layer.

There is insufficient evidence from the present data to validate this theory. Part of the difficulty in verifying this theory is that a wide portion of the array must be seen at a high resolution to determine where the shear layer roll-up first occurs. With the current configuration, only a small number of cylinders (typically 3 to 5) could be seen at any one time. If the camera was moved further away, or a wide angle lens used, then the light reflection from the particles within the flow was insufficient for good performance of the particle detection process. This is an area suggested for further research.

11.4 Summary

Drag tests showed that the drag coefficient of a cylinder in an array normal to the flow is a function of the cylinder spacing, with drag increasing as the spacing is decreased. The drag coefficient of an array of cylinders with high surface roughness increases at a greater rate than an array of smooth cylinders. This suggests that there is a different and stronger interaction of the wakes behind the array of rough cylinders.

The peak turbulent kinetic energy behind an array of widely spaced (S/D ~ 3.73) rough cylinders was 49% higher than that behind similar spaced smooth cylinders at Re = 1350, and ~ 28 % higher at Re = 2450 and 3820. This is greater than the increase in TKE seen behind single rough cylinders of between 5% and 24% (varying with Reynolds number). This is further evidence of a stronger interaction of wakes behind the rough cylinders.

The Strouhal number for smooth cylinders in arrays at S/D = 3.79 and 2.84 was 0.185 (using the gap velocity). This is lower than the single cylinder value of 0.21. In contrast, the Strouhal number behind an array of rough cylinders (k_s/D = 0.094, S/D = 3.73), non-dimensionalised by the gap velocity, was the same as that for the single rough cylinder (S_t = 0.17). This indicates that high surface roughness exerts more control over eddy shedding than cylinder spacing, at least when the spacing is large.

As in previous studies, at close cylinder spacings (S/D = 1.90 in these experiments) the wake pattern behind cylinders becomes non-uniform, with the size of the recirculating region behind each cylinder varying across the array. With arrays of smooth cylinders, a different, but stable, wake pattern developed during each experimental run. A transition between different stable wake patterns, as reported by others (Moretti and Cheng, 1987; Zdravkovich and Stonebanks, 1990), was not seen in these experiments. This may be due to the short duration of each experiment, which was limited by the available tank length.

It is suggested that the wake pattern that forms behind the array is determined by which cylinders first experience the roll-up into eddies along the free-shear layers. As the first occurrence of shear-layer roll up is a random process, the wake patterns behind the array will differ each run.

A closely spaced array of rough cylinders (k_s/D = 0.094, S/D = 1.86) generated very similar wake patterns during each run. The effect of the surface roughness was to favour one particular wake configuration. A suggested mechanism is the uniqueness of each cylinder, due to the method of roughening the cylinders by coating with fine gravel. The distribution of the surface roughness elements is likely to create greater turbulence, which will in turn promote instability of the free-shear layers. A cylinder that generates greater turbulence from the surface roughness is likely to produce an early roll-up of the free-shear layer, triggering the formation of a particular wake pattern.

By reducing the number of cylinders in the array of smooth cylinders (S/D = 1.90) from 17 to 8, a repeatable wake pattern was generated. With only 8 cylinders, the array spanned less than half of the tank width. Flow could then be diverted around the array. A biased wake formed behind the cylinders on the end of the array, which in turn influenced the wakes behind the adjacent cylinders. It is thought that with only 8 cylinders, the end effects were able to control the flow further along the array, favouring a particular wake pattern. With more cylinders in the array, the flow at the ends of the array will have substantially less influence on the wake patterns in the middle of the array.

It was not determined if the spatial variations behind closely spaced cylinders are the same along the cylinder length, or if different patterns develop at different heights. This is a topic for further research.

With regard to the implications for mussel farming, these experiments show that the effect of large values of surface roughness is important in terms of drag, and turbulence production. This effect should therefore be considered in any attempt to model the flow around mussel droppers. An additional factor that may need to be considered is that the mussel droppers are flexible, and able to move in response to applied forces. With the irregular wake patterns forming behind arrays of closely spaced cylinders, it is highly likely that each cylinder is subject to a cross-stream “lift” force due to the asymmetry of the flow.

Depending on the strength of these forces, some mussel droppers may move closer together. Gravity acting on the mass of the dropper provides a balancing force. As the spacing between cylinders is decreased, the lift force that acts to push the cylinders together increases. An unequal spacing is likely to enhance the uneven wake distribution patterns behind neighbouring droppers.

CHAPTER 12 OTHER CYLINDER CONFIGURATIONS

12.1 Introduction

In previous chapters, data were presented showing the effect of large surface roughness on single cylinders and single rows of cylinders oriented normal to the flow. The effect of cylinder spacing was also investigated. In this chapter, other configurations of cylinders are examined in a less detailed fashion. The main areas of interest in this chapter are the effect on drag and flow of a second row of cylinders placed behind the first, and of the effect of array angle. These factors are relevant to the study of New Zealand mussel long-lines as the arrangement of the droppers resembles a double row of cylinders, and the long-line may be orientated at any direction relative to the approaching flow. As described in the previous chapter, the spacing of droppers along a long-line may range between S/D = 1.6 and 20. The rows of droppers are generally at a fixed spacing of ~ 1 m, which is the length of a mussel buoy (the two back-bone ropes attach to either end of the buoys, see Figure 1.1). As the diameter of a mussel dropper may vary between 0.05 m and 0.25 m, the row spacing will be in the range R/D = 4 and 20. The intention here is not to develop a deep understanding of the effect of double rows or angled arrays. The goal is instead to provide guidance as to what influence these factors have on drag and flow, to highlight key behaviours, and to identify areas where more detailed investigation is required.

In this chapter, a brief description of the experimental methodology is given in section 12.2, and results from drag measurement of double rows of cylinders, and rows angled to the flow are presented in section 12.3. Flow fields from PTV analysis for the double row, and angled row configurations are presented and discussed in section 12.4.

12.2 Methodology

A detailed description of the methodology for the drag tests and PTV visualisation and analysis can be found in Chapter 9. Key aspects of the experimental configurations are described here.

Drag tests were performed to quantify the effect of a second row of cylinders on array drag. Tests were performed at a cylinder spacing of S/D = 4.62, and row spacings of R/D = 2.1 and R/D = 4.2. In comparison, mussel long-lines have dropper spacings of $1.6 < S/D < 20$ and row spacings of $4 < R/D < 20$. The experiments with R/D = 4.2 represent a mature crop. The closer spacing of R/D = 2.1 is smaller than that currently employed in the field, but is used here to provide comparative data, and to investigate the effect of placing downstream cylinders in the near wake region of those upstream. Reynolds numbers for the drag tests were in the range $1800 < Re < 6300$. Smooth cylinders of diameter 20.19 mm,

submerged length 420 mm were used, with 7 cylinders in each row. Rows are orientated perpendicular to the flow. The second row was positioned with the cylinders directly behind those in the first row.

Experiments to determine the effect on drag of the angle of a row of cylinders to the flow were conducted using arrays of small aluminium cylinders configured as an approximate 1:100 scale model of a typical long-line. Long-line models consisted of either single or double rows of aluminium cylinders, 3.22 mm in diameter, 120 mm submerged length, spaced at S/D = 2.17. This spacing is slightly larger than that required to generate metastable wake patterns (Section 8.2.7). Each row consisted of 158 cylinders, and a second row of cylinders was located at R/D = 3.73. Reynolds numbers, based on cylinder diameter, were in the range 280 to 1000. Force was measured in both the stream-wise and transverse directions using a double load-cell configuration. Measurements were made with arrays at angles between 0^o and 90^o to the flow in 15^o increments, where 0^o is in-line to the flow, and 90^o is perpendicular (across) the flow.

PTV data for double row and angled array configurations were obtained using smooth cylinders of diameter 42.2 mm, and length 890 mm. In the double row experiments, cylinders were spaced at S/D = 3.79 within each row, 9 cylinders per row, with a spacing between the rows of R/D = 5.0. The experiment was repeated with the second cylinder row staggered relative to the front row. Single row cylinder arrays were tested at three angles, 0^o, 30^o, and 60^o, and at 3 cylinder spacings, S/D = 3.79, 2.84, and 1.90. All of the PTV data presented in this chapter were recorded at a Reynolds number of 1340.

12.3 Drag Results

12.3.1 Double Rows of Cylinders

Drag coefficients for the double row configuration are based on the projected area of a single row of cylinders. This allows for a clear assessment of the change in drag resulting from the addition of the second row. Results are given in Table 12.1. The used notation for cylinder spacing is S for the spacing normal to the flow (along a row), and R for the spacing in the direction of the flow (between rows). Adding a second row of cylinders at R/D = 2.1 had no significant effect on the total array drag, but placing the second row at R/D = 4.2 increased the total drag on the array by 54% (± 7%).

Configuration	Drag coefficient
Single Row	1.20 ± 0.05
R/D = 2.1	1.20 ± 0.07
R/D = 4.2	1.85 ± 0.05

Table 12.1 Effect of second cylinder row on drag coefficient (corrected for blockage ratio) at Re = 1800 to 6300, S/D = 4.62.

The results obtained with the double cylinder rows at R/D = 4.2 are consistent with published data for 2 in-line cylinders, a compilation of which is found in Zdravkovich (2003), Fig. 26.18. The nature of the flow past in-line cylinders depends greatly on the spacing between them. At large spacings (R/D > ~ 3.7), the second cylinder sits in an area of reduced velocities, therefore the fluid drag is understandably less. As the mean velocity behind a cylinder recovers with distance downstream, the closer the downstream cylinder, the less the drag on that cylinder. At close spacings the behaviour is more complicated. From R/D = 1.2 to ~ 3.7, the free shear layers from the upstream cylinder attach permanently, intermittently, or alternatively (with decreasing spacing) to the downstream cylinder. At very close spacings (R/D < 1.2), the free-shear layers that separate from the upstream cylinder do not attach to the downstream cylinder, which sits within the recirculation region seen in the flow fields for a single cylinder. The drag force on the second cylinder is upstream, and the drag on the first cylinder is also reduced as the pair forms a more streamlined obstacle than a single cylinder.

The drag coefficient of the second cylinder of a pair in-line to the flow is negative, or upstream, at stream-wise spacings of R/D < 2 - 2.5, and increases towards the single cylinder value as the spacing is increased. At a stream-wise spacing of ~ 2.1, the drag coefficient for the second cylinder is nearly zero, while the upstream cylinder drag coefficient is approximately the same as that of a single cylinder. Thus the total drag on the cylinder pair at R/D = 2.1 will be close to that of a single cylinder. The experimental data, which showed no increase in drag for a double row of cylinders at R/D = 2.1, is in agreement with the published values for a cylinder pair at the same stream-wise spacing.

At a stream-wise spacing of 4.2 and Reynolds number 3400, Zdravkovich gives drag coefficients of 0.92 and 0.55 for the upstream and downstream cylinders, giving a combined drag coefficient of ~ 1.47. This is a 47% increase over the drag coefficient of a single cylinder at a similar Reynolds number (see Figure 8.4). This is slightly lower than the increase in drag obtained from the current experiments (54% ± 7%). Some of the increased drag in the current experiment may have been due to a slight misalignment of some of the cylinders in the second row.

The current experiments with 2 rows of 7 cylinders indicate that the increase in drag from a second row of cylinders at wide cylinder spacings can be accurately estimated from published data for 2 in-line cylinders. The drag on a double row of cylinders where the cylinders in each row are closely spaced (S/D < 2.2) was not measured.

12.3.2 Rows of Cylinders at an Angle to the Flow

Experiments to determine the effect of the angle of a row of cylinders to the flow were conducted using a 1:100 scale model of a typical long-line. Reynolds numbers, based on cylinder diameter (3.22 mm), were

in the range 280 to 1000. Due to the small diameter of the cylinders, these Reynolds numbers are lower than in experiments presented elsewhere in this thesis. While the drag values may not be directly comparable, the effect of angle on the drag should be similar at higher Reynolds numbers. Drag coefficients have been calculated based on the solid area of a single row of cylinders (number of cylinders multiplied by cylinder length and cylinder diameter).

The drag coefficient varied with angle following a sine relationship as is indicated by the curve plotted in Figure 12.1(a). The sine relationship is consistent with the reduction of the projected bulk area, where the bulk area is the array length multiplied by the array height. A bulk drag coefficient can be calculated based on the porosity of the array (the projected area of the cylinders divided by the bulk area). For the single row of cylinders, the porosity was 46%; therefore the bulk drag coefficient at 90^o was 0.71 ± 0.04. There is some deviation from a sine curve at very low angles to the flow. The drag force for the single row was too low to be accurately measured at 0^o. The drag coefficient for cylinder arrays aligned with the flow (at 0^o) will be a function of the cylinder spacing. The minimum drag is likely to occur when the cylinders are touching, at which point the array resembles a rough, flat plate. As the cylinder spacing is increased, the drag will increase as the interference between the cylinders decreases. For example, Igarashi and Suzuki (1984) present drag measurements for an in-line array of 3 cylinders, showing the drag coefficient increasing with spacing, and Aiba *et al* (1981) present similar results for an in-line array of 4 cylinders. Both studies show that the drag coefficient of the array shows a sudden increase at a cylinder spacing of $S/D = 3.5$ to 4. This occurs as the large spacing allows the eddy shedding process to occur behind all the cylinders in the array.

The drag force on the double row of cylinders was on average 35% higher than that on a single row at angles above 30^o. The cylinders in the second row are somewhat sheltered, sitting in the wakes formed by the front row cylinders; therefore the drag on the second row is reduced relative the first. The double cylinder row gave a slightly higher drag at 75^o than at 90^o, although this increase was not significant relative to the uncertainty in the drag measurement (the error bars in Figure 12.1 indicate a 90% confidence interval). A slight increase may have arisen as rotating the array slightly would move the second row of cylinders away from their sheltered position directly behind cylinders in the front row. A transverse or “lift” force was also measured for the array, and is plotted in Figure 12.1(b). The transverse force was highest at an angle of $\sim 15^o$. There was no significant difference in the transverse force between the single and double row of cylinders.

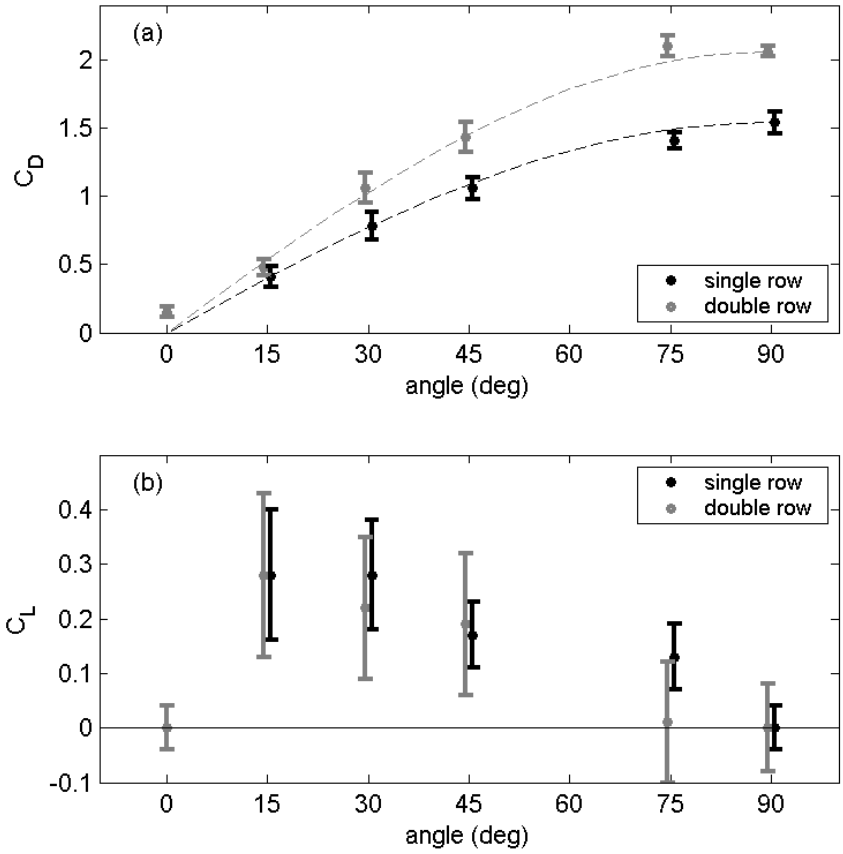

Figure 12.1 (a) Drag and (b) lift (transverse) coefficients for arrays of cylinders as function of angle to the flow (0^o is inline with the flow, 90^o normal to the flow). The dashed line in (a) is a sine curve. Note data points have been offset slightly to assist in comparing the results for the single and double row. The error bars indicate a 90% confidence interval for the drag and lift coefficients.

12.4 Flow Visualisation

12.4.1 Difficulties Encountered in Obtaining the PTV Data

Flow visualisation using PTV was attempted for angled arrays and double cylinder rows with limited success. The primary difficulty was in providing adequate illumination to the area of interest so that sufficient particles could be detected. Due to the divergence of light from the light boxes and consequential drop in light intensity, the light boxes could only be positioned either side of the tank, and not at the ends. The experimental configuration was optimised for studying the flow behind arrays of cylinders normal to the direction of motion. With arrays of cylinders at an angle, considerable shadows were cast by the cylinders, leaving regions of low light intensity where few particles were illuminated. Considerable variation is seen in the measured flow fields behind adjacent cylinders due to insufficient averaging and a low coverage factor, particularly at close cylinder spacings. As a result, the data presented for the angled arrays is sufficient for general observations regarding the trends and distributions of time-averaged flow properties, but the actual values may not be accurate. Derived quantities such as

turbulent production have therefore not been calculated. Also, due to the sparsity of the data, velocity spectra could not be resolved accurately.

Similar problems hampered the tracking of particles between the rows of cylinders for the double row configuration. Due to these difficulties, experiments were only performed at a single Reynolds number (~1340) where the low towing speed allowed a slower camera shutter speed to be used without causing smearing of particles in the captured images. Experiments with a double cylinder row were only conducted with wide cylinder spaces, although staggered and non-staggered configurations were tested. Particle illumination was sufficient to allow spectra to be calculated downstream of the second row of cylinders.

All data shown in this section is averaged from between 4 and 6 repeated runs, except where otherwise stated.

12.4.2 Flow Fields for Double Cylinder Rows

Flow fields were measured using PTV for a double row of smooth cylinders with the cylinders in each row spaced at S/D = 3.79, and rows spaced at R/D = 5, with 9 cylinders in each row. Time-averaged velocity vectors, turbulent kinetic energy, and turbulent shear stresses are shown for a non-staggered arrangement in Figure 12.2, and for a staggered arrangement in Figure 12.3. In the staggered configuration, cylinders in the second row were positioned in the middle of the gap between cylinders in the front row.

For the non-staggered or in-line configuration, cylinders in the second row were clearly within the wake of the upstream cylinders. Although they were beyond the (time-averaged) recirculation region, cylinders in the second row were still within an area of low velocity. The peak turbulent kinetic energy behind cylinders in the second row was 67% of the peak behind the first row. This is in good agreement with the decreased velocity measured behind a single row of cylinders with S/D = 3.79 at x/D = 5 of U/U_0 = 0.72, indicating that the reduced velocity is responsible for the reduction in TKE. This reduction is also similar to the difference in drag coefficients for the front (C_D ~ 0.9) and rear (C_D ~ 0.6) cylinders of a two cylinder in-line arrangement, see Fig. 26.18 in Zdravkovich (2003). Similarly, the turbulent shear stresses (which are strongly linked to regions of turbulent production) were lower behind the second row of cylinders. Interestingly, the symmetrical lobes of $\langle uv \rangle$ were also elongated behind the second row of cylinders. This may be caused by the interaction between the vortices shed from the upstream and downstream cylinders.

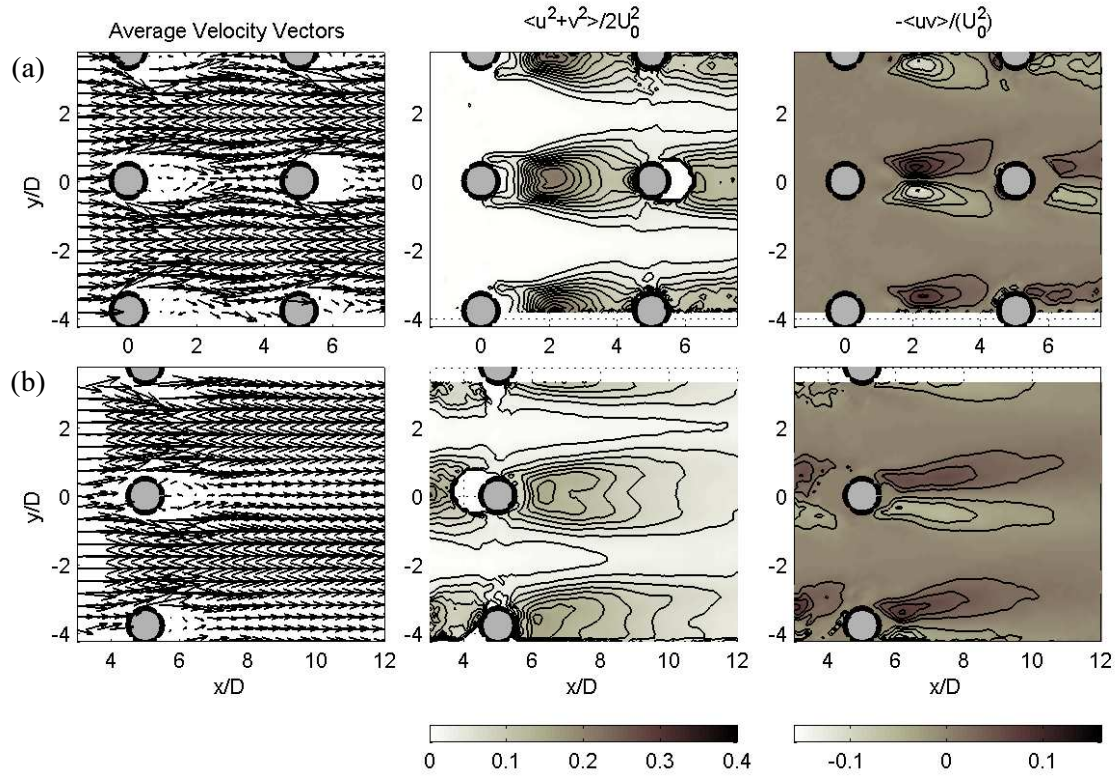

Figure 12.2 Time-averaged velocity vectors, turbulent kinetic energy, and turbulent shear stress behind (a) front row, (b) second row for a double row of smooth cylinders, *S/D* = 3.79, *R/D* = 5.0, *Re* = 1340, in a non-staggered configuration. Contours are at 0.02 intervals (zero contour not shown for turbulent shear stresses).

Flow patterns were considerably different when cylinders in the second row were staggered in relation to the front row. Instead of being in an area of lower velocities, such as in the non-staggered configuration, the downstream cylinders were in an area of slightly faster flow as they were outside the wakes of the upstream cylinders. Consequently, peak turbulent kinetic energy was slightly higher (~ 9%) behind the downstream cylinders than behind cylinders in the front row. The peak turbulent shear stresses -<*uv*> were similar behind front and rear cylinders. However, an elongation of the symmetrical lobes of <*uv*> occurred behind the rear cylinders, similar to that seen behind rear cylinders in the non-staggered configuration. Although drag was not measured, the flow visualisation data indicate that the drag on the staggered cylinder array will be higher than on the non-staggered array.

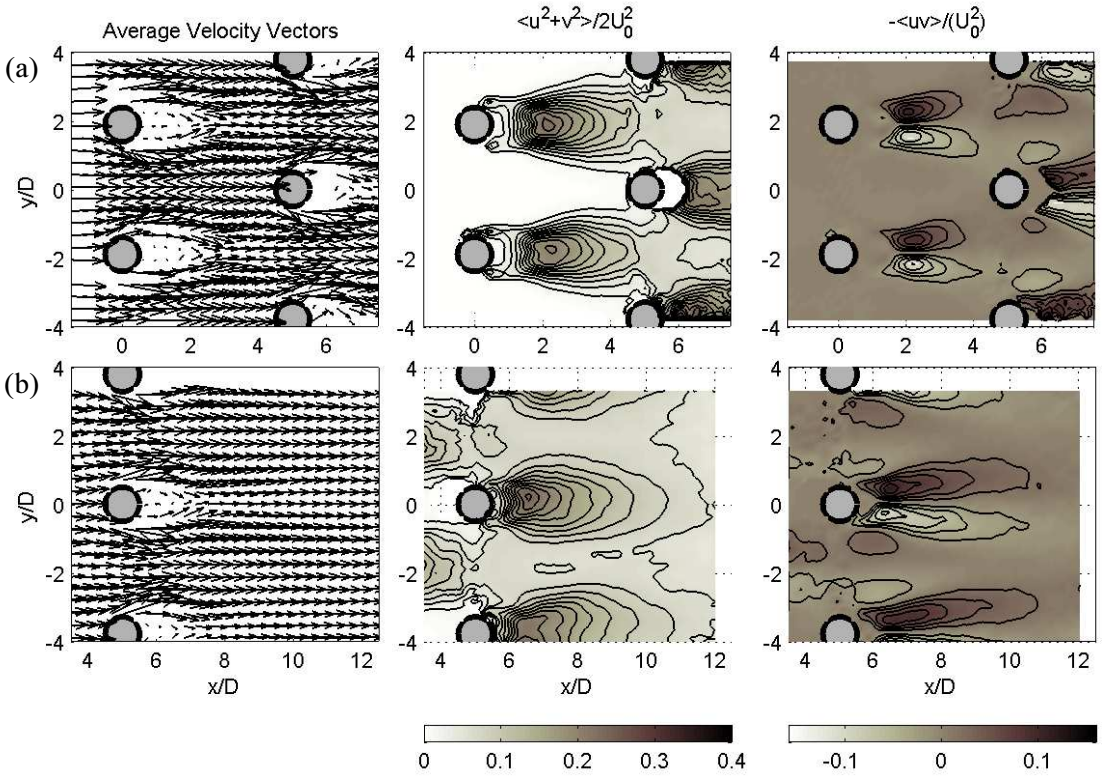

Figure 12.3 Time-averaged velocity vectors, turbulent kinetic energy, and turbulent shear stress behind (a) front row, (b) second row for a double row of smooth cylinders, *S/D* = 3.79, *R/D* = 5.0, *Re* = 1340, in a staggered configuration. Contours are at 0.02 intervals (zero contour not shown for turbulent shear stresses).

The regions of turbulent kinetic energy production for the two double-row configurations are shown in Figure 12.4. The turbulent production behind the upstream cylinder was similar in both the staggered and non-staggered configurations, except for where the production region separated around the downstream cylinder in the non-staggered configuration (Figure 12.4(a)). Production behind the downstream cylinder in the non-staggered arrangement was approximately 60% of that behind the upstream cylinder, while production behind the downstream, staggered, cylinder was similar to that of the upstream cylinder. This is similar to the relative levels of TKE behind the front and rear cylinders in each arrangement. The level of TKE behind the downstream cylinder was related to the velocity at the cylinder location, and a similar connection can be made between production and velocity.

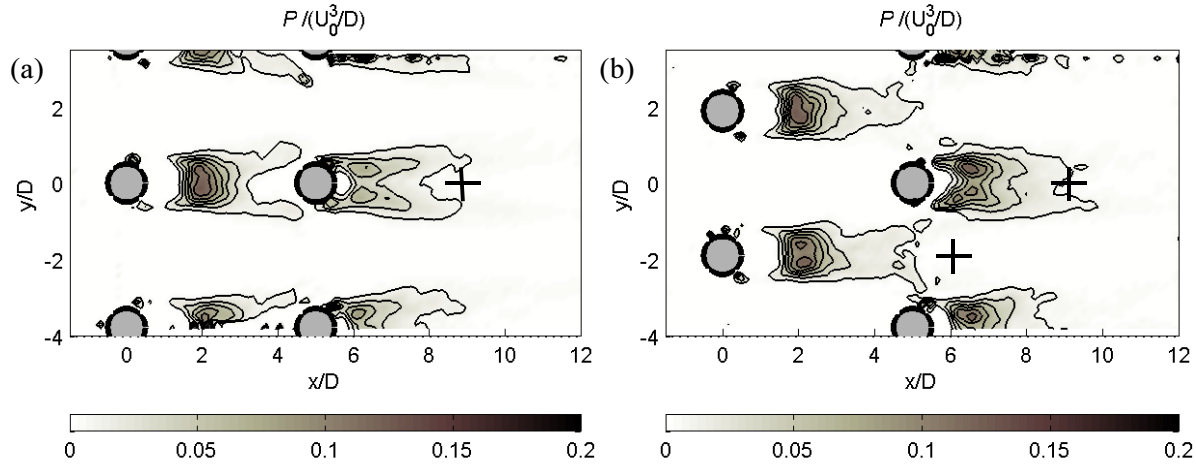

Figure 12.4 Calculated production behind (a) front and rear cylinders in a non-staggered configuration, (b) front and rear cylinders in a staggered configuration, *S/D* = 3.79, *R/D* = 5.0, *Re* = 1340. Contours are at 0.02 intervals. The crosses indicate positions where velocity spectra were recorded, see Figure 12.5.

Continuous velocity time-series of sufficient length to obtain spectra between the cylinder rows could not be obtained due to the gaps in the data resulting from shadowing. However, eddy shedding frequencies for cylinders in the front row could be estimated from direct inspection of velocity time-series. These indicate that the Strouhal number for cylinders in the front row of both the staggered and non-staggered configurations were the same as that for a single row at the same spacing. Spectra could be calculated for the flow behind the second row of cylinders (Figure 12.5). These indicate the presence of two eddy shedding frequencies for the inline cylinder configuration (indicated by the arrows in Figure 12.5(a)). The highest frequency peaks behind the double (in-line) row configuration match the frequency of the peak in the spectra for the single row of cylinders (see dashed vertical line in Figure 12.5(a)). This peak is most likely the eddy shed from the upstream cylinder. A lower frequency peak is expected in the spectra for the inline configuration as the second cylinder is in the wake of the first where velocities are lower. With a velocity at x/D = 5 of U/U_0 = 0.72, the eddy shedding frequency for the second row of cylinders, assuming the same Strouhal number (S_t = 0.25 ± 0.015 based on free-stream velocity), would be f = 0.18 U_0/D. This is close to the lower frequency peak estimated as 0.20 ± 0.01 U_0/D.

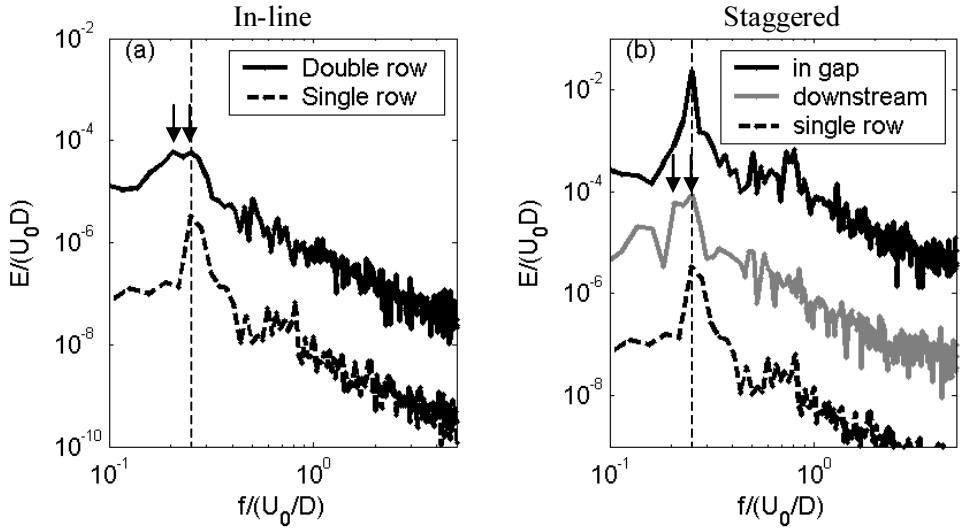

Figure 12.5 Velocity spectra at (a) *x/D* = 4 behind single row and double row of in-line cylinders, (b) *x/D* = 5 behind downstream cylinder in staggered array, compared with spectra in gap between downstream cylinders and single row of cylinders, *S/D* = 3.79, *R/D* = 5.0, *Re* = 1340. Locations where spectra were recorded are indicated in Figure 12.4. Note that spectra have been offset vertically by 10^{-2} or 10^{-4} for clarity. The arrows identify peaks in the frequency spectra.

Velocity spectra taken in the gaps between the downstream cylinders in a staggered array show strong similarity to those taken downstream of a single row, as expected. However, spectra at *x/D* = 4 directly behind a cylinder in the second row of the staggered array are similar to those behind the non-staggered array, with what appears to be either a broad frequency peak, or a double peak, see Figure 12.5(b). The PTV system could not resolve spectra at sufficient resolution at low frequencies to provide convincing evidence of a lower frequency peak as opposed to a broad peak as the length of the tank limited the length of the time-series. A lower frequency peak cannot be explained by a reduction of the velocity at the downstream cylinders as for the non-staggered cylinder. Instead, the velocity near the downstream cylinder will be slightly higher than the free-stream velocity, suggesting that the eddy shedding from the downstream staggered cylinder should be at a higher frequency. The spectra behind the downstream cylinder suggest that the wake from upstream cylinders interferes with the eddy shedding of the downstream cylinders. A closer inspection of the flow fields indicate that the free-shear layers of the upstream cylinders impinge on the staggered cylinders. Mean shear gradients, plotted in Figure 12.6, show that the shear layers from the upstream cylinders are also intensified as the flow converges between the second row of cylinders. Where the shear layers from the upstream cylinders impinge on the shear layer from the downstream cylinders, they generate eddies of opposing vorticity. The eddies from the upstream cylinder may therefore disrupt the formation of eddies in the wake of the downstream cylinders, or weaken them through the opposing vorticity.

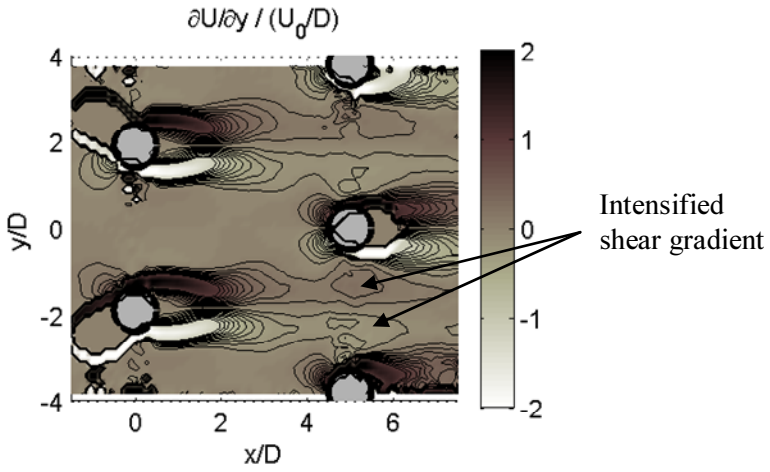

Figure 12.6 Mean shear gradients for flow through staggered array, *S/D* = 3.79, *x/D* = 5.0, *Re* = 1340.

12.4.3 Flow Fields for Single Rows at 60°

Mean velocity vectors, turbulent kinetic energy, and turbulent shear stresses for single row arrays of smooth cylinders oriented at 60° to the flow are shown for cylinder spacings of *S/D* = 3.79, 2.84, and 1.90 in Figure 12.7 (*S* is the cylinder spacing along the row, ignoring the orientation of the row with respect to the flow). Generally the wake behind the lower cylinder in each plot is irregular in shape, which is due to low particle densities, and consequently poor PTV performance, in this region of the flow. However, a number of trends may be deduced from Figure 12.7. Even at the wide cylinder spacing of *S/D* = 3.79, the gap flows and cylinder wakes were inclined relative to the stream-wise direction. The angle of inclination was ~ 9° at *S/D* = 3.79, increasing as the spacing decreases to 13° at *S/D* = 2.84, and 24° at *S/D* = 1.90. Downstream of the cylinders, the wake realigned in the stream-wise (*x*) direction. This is particularly evident in the plot of the turbulent shear stresses for the cylinders at *S/D* = 2.84, see Figure 12.7(b).

Turbulent kinetic energy increased as the cylinder spacing was decreased from *S/D* = 3.79 to 2.84. A similar increase was seen for the arrays normal to the flow in Chapter 11. The data plotted in Figure 12.7 indicate an increase in peak TKE of ~ 60%, although this value should be treated with caution. In comparison, the increase behind cylinders at the same spacing normal to the flow was ~ 27% (see Figure 11.3(b)). Other similarities to the results for the normal array are a shift of peak TKE towards the cylinder, and a reduction in the size of the recirculation zone as the spacing is decreased.

An important feature of the flow behind cylinder arrays at close spacing (*S/D* < 2.2) normal to the flow was the variation between cylinder wakes due to the pairing of the gap-flow jets. A variation of wake size also occurred behind the closely spaced cylinders (*S/D* = 1.90) at an angle of 60°. A wake pattern from a single run is shown in Figure 12.7(c). The wake pattern also varied between runs, as was seen for the closely spaced arrays normal to the flow.

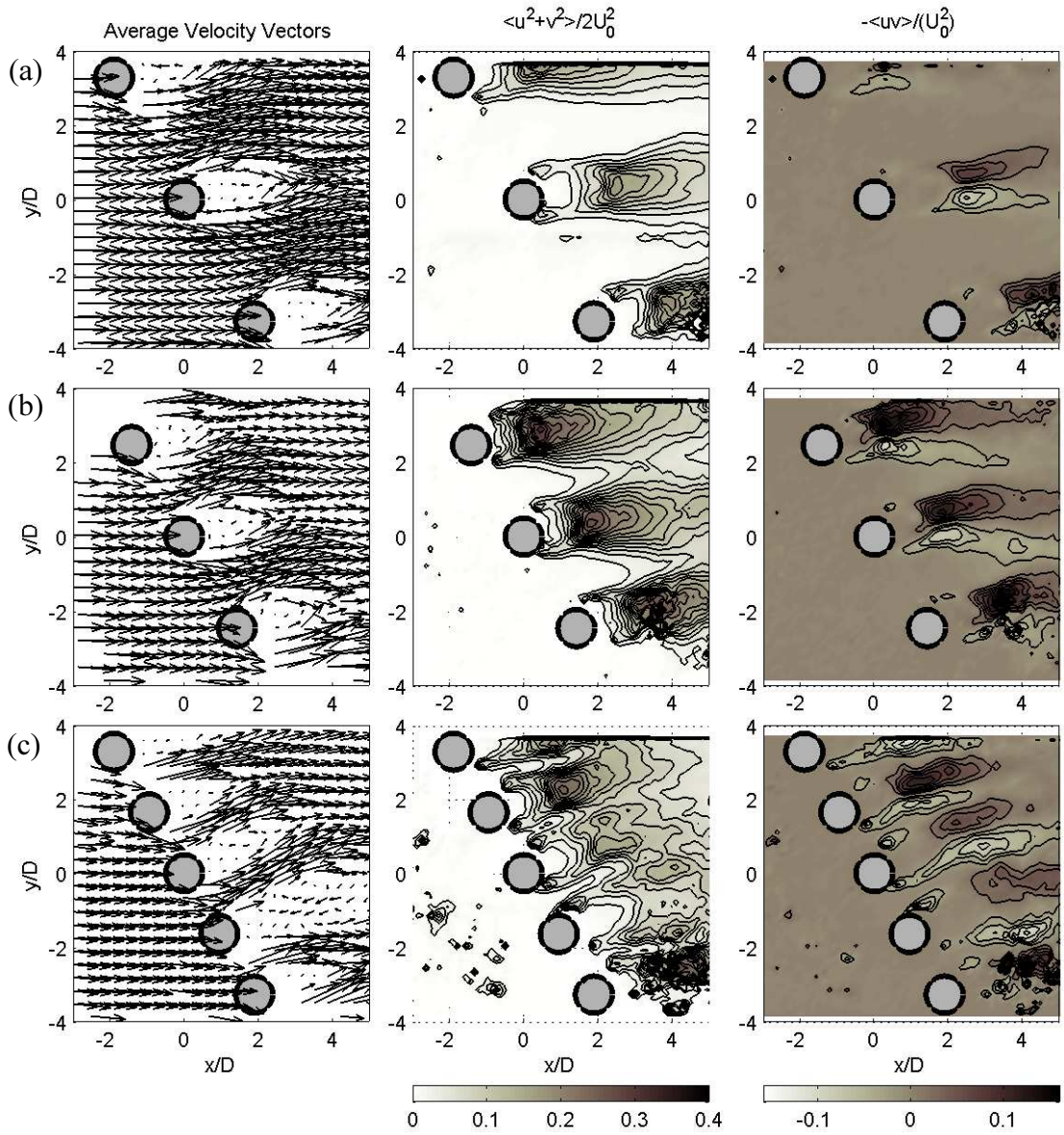

Figure 12.7 Single row of cylinders at 60° to approaching flow at cylinder spacings of *S/D* = (a) 3.79, (b) 2.84, and (c) 1.90, *Re* = 1340. Data in (a) and (b) have been averaged from multiple runs, while (c) represents a single run. Contours are at 0.02 intervals.

12.4.4 Flow Fields for Single Rows at 30°

Mean velocity vectors, turbulent kinetic energy, and turbulent shear stresses for single row arrays of smooth cylinders oriented at 30° to the flow are shown for cylinder spacings of *S/D* = 3.79, 2.84, and 1.90 in Figure 12.8. Turbulent kinetic energy behind the arrays at 30° was lower than that at 60°, consistent with the lower drag coefficients for arrays at low angles to the flow. Another note-worthy feature was the uniformity of wake sizes behind the closely spaced array (*S/D* = 1.90). The characteristic variation in wake sizes seen for closely spaced cylinders in arrays normal to flow, caused by pairing of the gap flow jets from between the cylinders, was not seen behind the 30° array at the same cylinder spacing. The mechanism producing the instability is evidently suppressed as the angle between the array and the flow

is reduced. As the experiments were only conducted at four array angles (0°, 30°, 60°, and 90°) the angle where the instability disappears is not known.

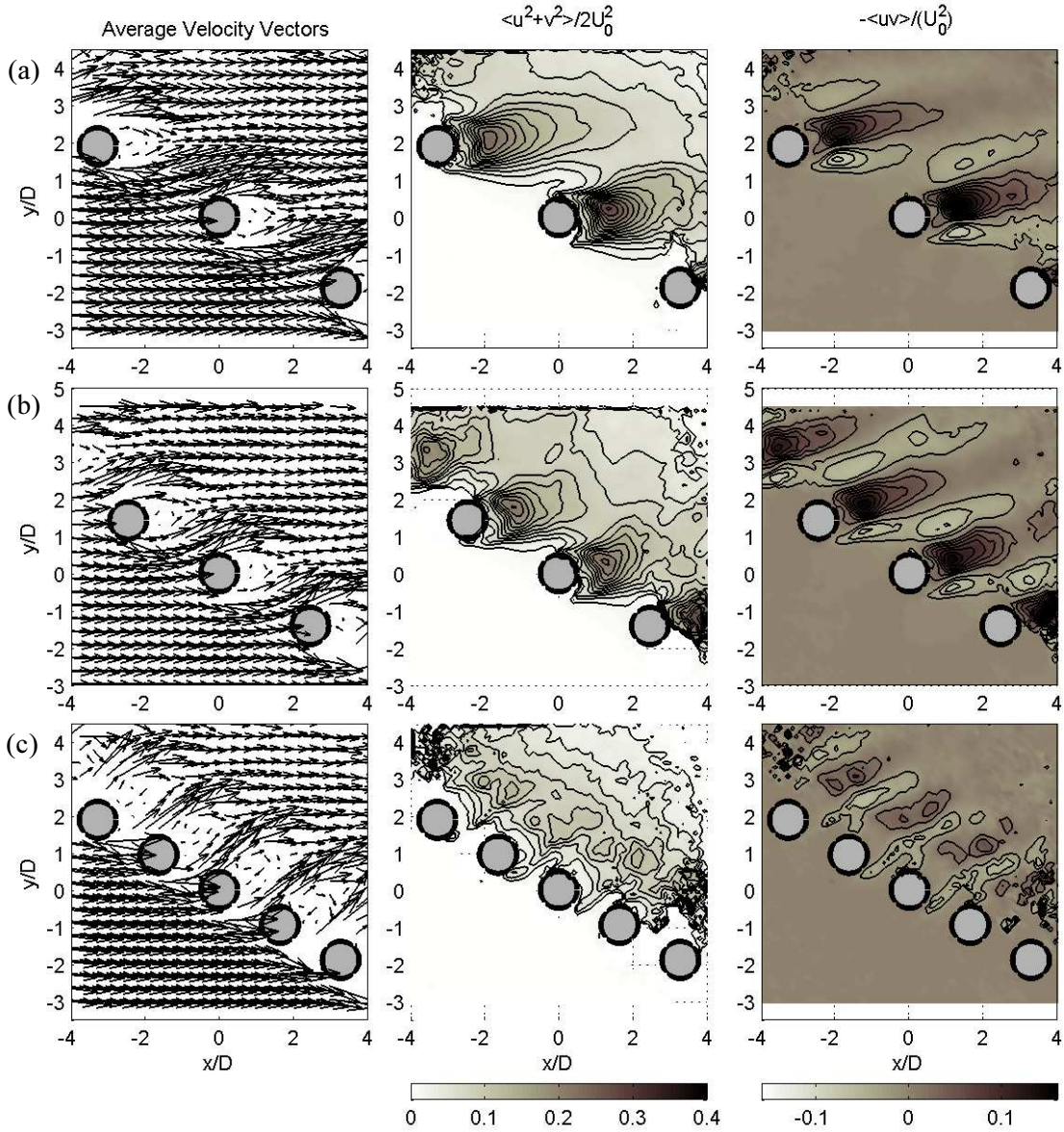

Figure 12.8 Single row of cylinders at 30° to approaching flow at cylinder spacings of *S/D* = (a) 3.79, (b) 2.84, and (c) 1.90, Re = 1340. Contours are at 0.02 intervals.

The drag tests of angled arrays showed that appreciable transverse or "lift" forces could be measured on cylinder arrays at spacings of *S/D* = 2.17. It is highly likely that the array lift coefficient is a function of cylinder spacing, decreasing as cylinders are moved further apart, although experiments were not done to confirm this. Certainly if cylinders are very widely spaced, the transverse force (force in the *y* direction) is expected to be zero. The lift force on an aerofoil or a flat plate inclined to the flow is due to a pressure difference caused by higher velocities along one side of the object. With an array of cylinders that are not touching, the transverse force on the array results from the sum of the forces on the individual cylinders. However, the velocity vectors plotted in Figure 12.8 and the streamlines, plotted in Figure 12.9, do not

provide convincing evidence of higher velocities along the upper (positive *y* direction) surface of each cylinder to provide a lift force. Rather, the streamlines suggest that at least part of the transverse force on the cylinder array is due to an anti-clockwise rotation of the drag-force vector on each cylinder. The streamlines between the cylinders show that the flow is rotated counter-clockwise (left with respect to the *x* axis), which is in the direction of the transverse force. The cylinder wakes are also rotated in the same direction, indicating that a component of the drag will be in the *y* direction.

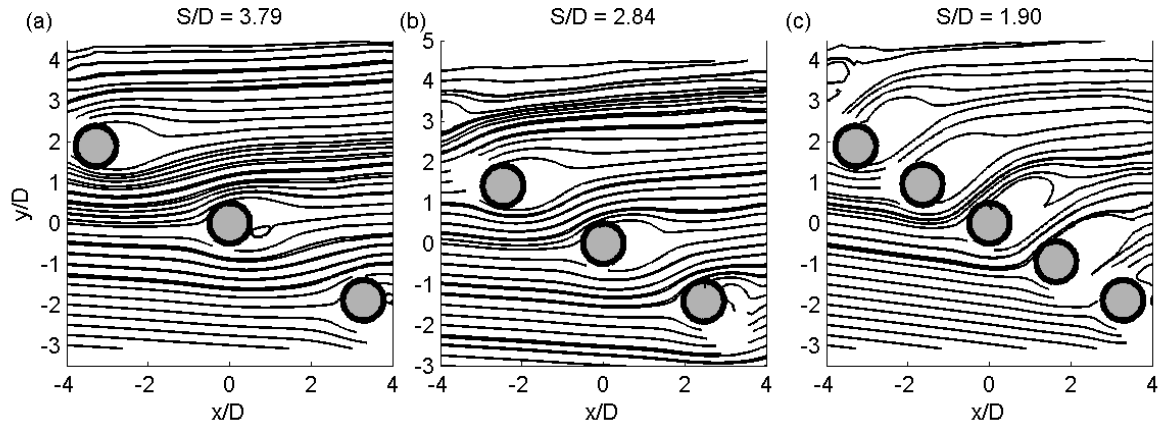

Figure 12.9 Selected streamlines for flow around arrays of smooth cylinders orientated at 30^o spaced at (a) *S/D* = 3.79, (b) *S/D* = 2.84, and (c) *S/D* = 1.90, at Re = 1340.

At first glance, the net shift of streamlines in the positive *y* direction would suggest that there should be a force on the fluid in the positive *y* direction to cause the change in momentum. The opposing reaction on the cylinders would be the negative *y* direction, opposite to that measured. However, only a small part of the flow affected by the pressure fields from the cylinders can be seen in Figure 12.9. Each cylinder generates a pressure field, with higher pressures in front, and lower pressures immediately behind. With an array of cylinders, the pressure fields combine. If pressure contours were plotted for the angled array, they would show contour lines upstream of the cylinders that lie nearly parallel to the array. Thus, upstream of the cylinders, flow would be diverted in the negative *y* direction by the pressure field that increases as the cylinders are approached. This effect would extend some distance upstream. Evidence of this is that the streamlines at the extreme left of all the plots in Figure 12.9 are already rotated clockwise with respect to the *x*-axis.

Similar parallel contours of lower pressure would lie downstream of the array. However, downstream of the cylinders, after an initial minimum close to the cylinders, the pressure recovers. The pressure recovery provides the force to realign the flow in the *x*-direction.

While there is a net pressure differential across the array consistent with a lift force, it appears that the rotation of the drag force on each cylinder provides a force component transverse to the free-stream flow.

As the rotation of the cylinder wakes increases as the spacing decreases, the transverse force will also increase.

An unusual feature occurring downstream of the cylinders oriented at 30^o was the formation of what appears to be a 3rd lobe in the turbulent shear stresses, which can be seen most clearly at S/D = 3.79, Figure 12.8(a). The two lobes of turbulent shear stress behind a cylinder in all other data presented in this thesis show a negative region below (in the minus y-direction) and a positive region above a line through the centre of the cylinder (see Figure 12.2 as an example). For the array angled at 30^o, there were two negative regions behind each cylinder, but only one region of positive turbulent stress. The turbulent stress was stronger in the positive region, which was also more centred behind the cylinder than the two negative stress regions. The negative turbulent stress was greater in the region below the cylinder centreline than in the region above. As the spacing between the cylinders was decreased to S/D = 2.84, the upper lobe of negative turbulent stress joined with the region generated by the cylinder upstream. The third lobe is in fact an extension and enhancement of the region of negative turbulent shear from the upstream cylinder.

It is not clear what mechanism is responsible for increasing the turbulent shear stress in this region. There are some aspects of the flow that may be related, although the mechanism linking these is not certain. One of the potential related factors is the distortion of the shear gradients around the cylinder wake by a downstream cylinder. In nearly all regions of the flow, the dominant mean velocity gradient is $\partial U/\partial y$. There is generally a strong similarity between areas of strong mean shear and turbulent stress, indicating that turbulent stress results from the mean shear of the fluid. Indeed, this relationship was the basis of the eddy viscosity model used to estimate dissipation in Chapter 10.

Turbulent shear stress and $\partial U/\partial y$ for the array with S/D = 3.79 are plotted in Figure 12.10(a) and (b), and contours of velocity gradient have been plotted over a colour map of $-\langle uv \rangle$ in Figure 12.10(c). The colour maps for the $-\langle uv \rangle$ plots have been scaled to highlight the difference between the positive and negative regions. The diagram shows that the regions of turbulent shear stress and mean velocity shear are closely related, particularly close to the cylinders. The mean velocity gradients are produced in two ways. Firstly, flow is accelerated around the cylinder, producing velocity gradients with higher velocities near the cylinder. Downstream of the cylinders, the velocity gradient is due to the low velocities within the wake. Velocities outside the wake are slightly higher than the free-stream velocity, as continuity must be maintained. With the staggered arrangement, with cylinders numbered as shown in Figure 12.10, the region of negative mean shear forms downstream of cylinder 1 because of the low velocities in the wake behind the cylinder. However, as the flow encounters cylinder 2, it is accelerated around the cylinder, resulting in increased velocities between cylinders 1 and 2. The increased velocities enhance the velocity

gradient across the wake of cylinder 1. This accounts for the lengthening of the region of negative $\partial U/\partial y$ downstream of cylinder 1 in comparison to the length of the region of positive mean shear. The lengthening of the region of negative mean shear would consequently extend the region of negative turbulent stress. However, this is insufficient to explain why the turbulent stresses increase, as there is no associated increase in $\partial U/\partial y$ at this location in the flow.

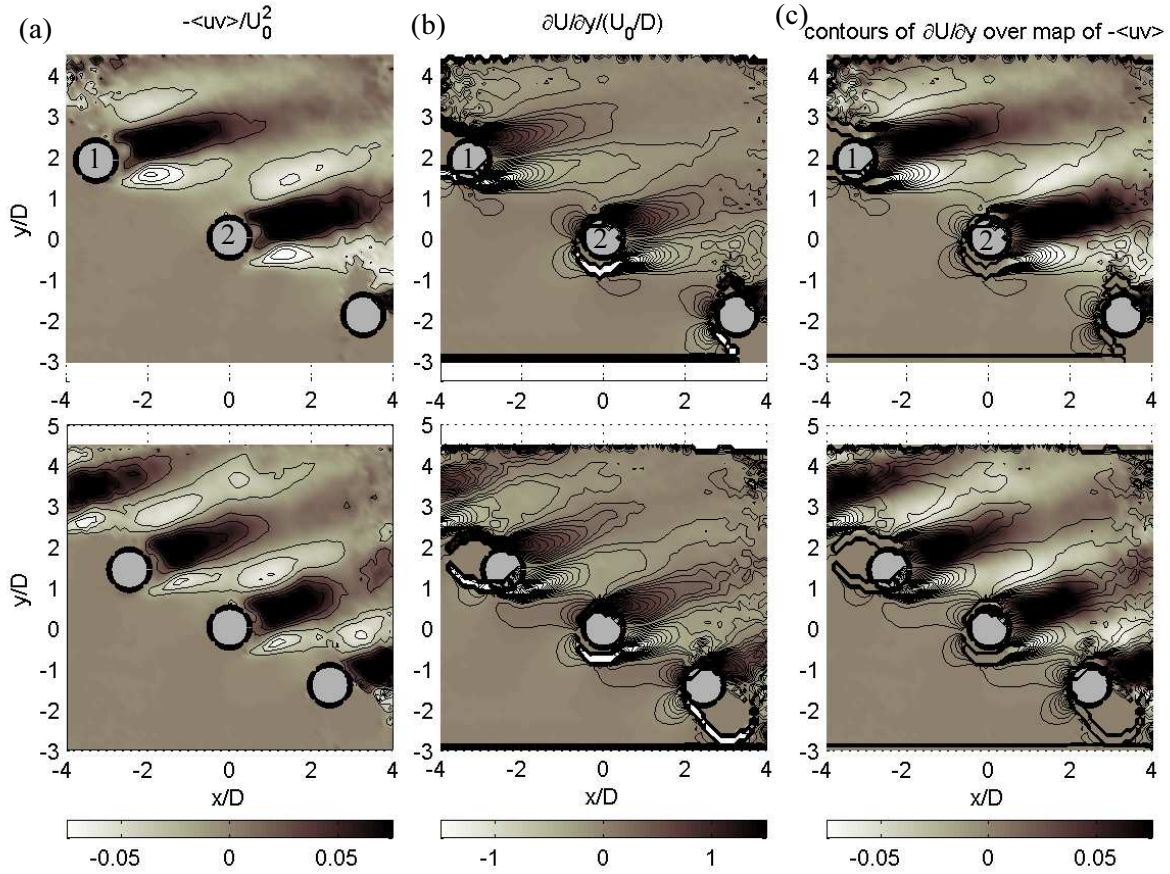

Figure 12.10 (a) Turbulent stresses, (b) mean velocity shear, and (c) contours of $\partial U/\partial y$ plotted over colour map of turbulent stresses for array of cylinders at 30°, S/D = 3.79, Re = 1340.

Another possibility is in the interaction of eddies shed from the upstream cylinder with those produced by the second cylinder. Noting that the sign of the turbulent shear stresses and the mean velocity gradient agree where turbulence is produced (production is negative if they are opposite), there is a connection between the sign of the turbulent stresses and the direction of rotation for the eddies generated by the mean velocity gradients. Where the mean velocity gradient $\partial U/\partial y$ is positive, the shear will produce clockwise rotating eddies. For cylinder 1, eddies developing along the lower (with respect to the y axis) edge of the wake will rotate anti-clockwise, while eddies generated along the upper edge of the wake of cylinder 2 will rotate clockwise. If the clockwise eddies from cylinder 1 are carried downstream close to the wake of cylinder 2, as the streamlines suggest, then they may be accelerated by clockwise rotating eddies of cylinder 2. This may provide a feed-back mechanism that enhances the turbulent shear stresses.

12.4.5 Flow fields for Single Rows at 0°

In Figure 12.11, time-averaged velocity vectors, turbulent kinetic energy, and turbulent shear stresses are plotted for an array of cylinders in-line (0°) with the flow at two spacings, S/D = 3.79 and 1.90. As the camera was positioned directly above the cylinders, the top of the cylinders blocked the view of the flow immediately around the cylinder. While this occurred to some degree with all the flow visualisation presented in this thesis, for most configurations the camera could be positioned behind or to the side of the cylinder of interest so that the region of interest next to the cylinder could be clearly seen. The top of the cylinders can be identified by the white circular region in the turbulent kinetic energy plots. Five cylinders were used in the array at S/D = 3.79; the cylinder at x = 0 was the third cylinder in the array. Eight cylinders were used in the array where S/D = 1.90, and the cylinder at x = 0 was the fifth cylinder from the upstream end. Due to the cylinders obscuring the view, TKE and turbulent shear stresses cannot be compared within the closely spaced, in-line array. However it is clear that at the close cylinder spacing, the flow around each cylinder is strongly affected by the upstream cylinders. While the mean velocities were low between the closely spaced cylinders, there was a strongly fluctuating flow, alternating in the y direction. This is indicated to a degree by the high values of TKE between the cylinders in Figure 12.11(b), and more clearly in velocity time-series taken downstream of cylinders 2 and 3 plotted in Figure 12.12.

The TKE behind cylinder 3 in Figure 12.11(a) is higher than that behind cylinder 2. As the coverage factor (indicating the proportion of frames where particle matches were made) is high in this region, the relative magnitudes of the TKE are considered to be reliable.

It is also clear from the turbulent kinetic energy distribution, and to a lesser extent the velocity vectors, that the wake region spreads laterally further downstream. Using a flat plate as an analogy, a boundary layer will form along the array. The spreading wake indicates that this boundary layer is still developing.

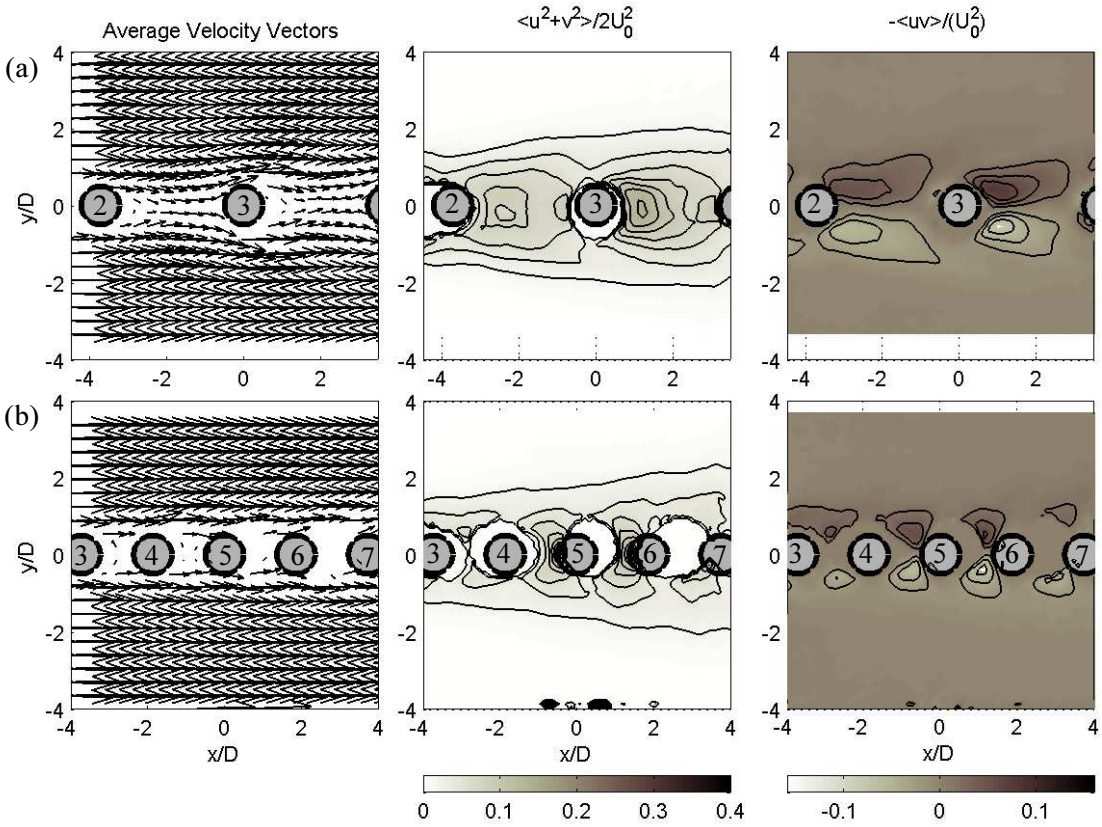

Figure 12.11 Single row of cylinders at 0° to the flow at cylinder spacings of *S/D* = (a) 3.79, and (b) 1.90, *Re* = 1340. Contours are at 0.02 intervals. The numbers indicate the position of the cylinder in the array.

There was no consistent synchronisation or phase locking of the velocity fluctuations behind adjacent cylinders. As Figure 12.12 illustrates, the velocities fluctuations behind cylinder 2 and 3 varied in magnitude and frequency. The velocity fluctuations between the cylinders occurred at a frequency considerably lower than the eddy shedding frequency for a single cylinder. The frequency of oscillation was approximately $f = 0.11U_0/D$ for the third cylinder in the array at $S/D = 3.79$, while there was greater variability in frequency for the second cylinder, with f varying from 0.11 to 0.14 (Figure 12.13).

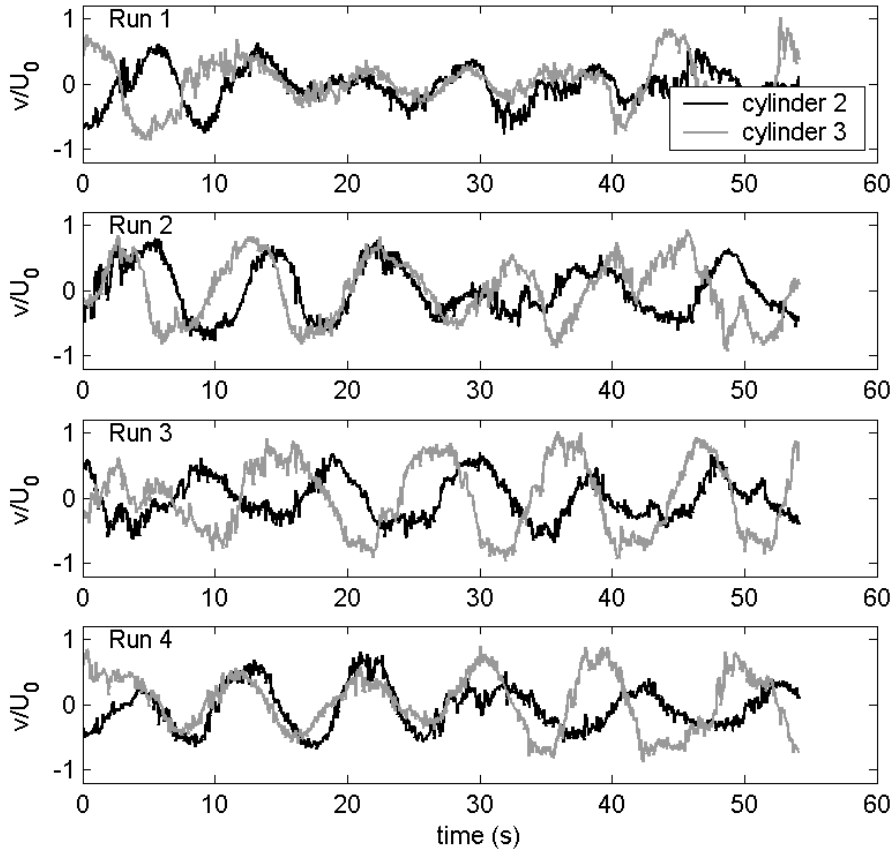

Figure 12.12 Cross-stream velocities at *x/D* = 1.25 behind cylinder 2 and 3 of an in-line array at *S/D* = 3.79, *Re* = 1340.

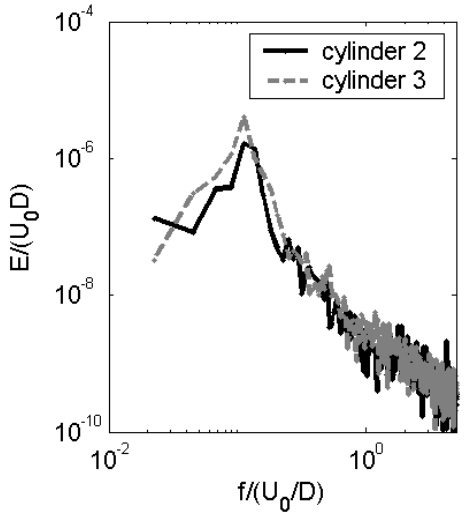

Figure 12.13 Velocity spectra (averaged over 4 runs) at *x/D* = 1.25 behind second and third cylinders of in-line array at S/D = 3.79, *Re* = 1340.

12.5 Summary

Drag measurements indicate that the increase in drag resulting from a second row of cylinders, where the cylinders in the second row are directly behind cylinders in the first, may be accurately estimated from previously published data for a pair of cylinders. It is not known what effect a second row of cylinders will have if the cylinder spacing is less than $S/D = 2.2$. The non-uniform wake patterns and pairing of the gap flow jets may alter the drag versus spacing relationship from that of the two cylinder configuration. PTV analysis shows that cylinders in the second row are within the wake of upstream cylinders, accounting for the reduced drag. PTV analysis of a double row configuration (normal to the flow) where the second row was staggered in relation to the first showed that the intensity of the turbulence produced by cylinders in the second row was similar to that produced by cylinders in the first row. In the configuration tested ($S/D = 3.79$, $R/D = 5.0$), the staggered cylinders were in a region of slightly faster flow, due to the divergence of flow around the upstream cylinders and cylinder wakes. The PTV data suggest that the drag on the staggered array will be higher than on the non-staggered array.

For arrays at an angle to the flow, the relationship between drag and angle can be approximated with a sine function, except at low angles. A cross-stream lift force was also measured, which for cylinders at a spacing of $S/D = 2.17$, was highest at ~ 15^o. The addition of a second row of cylinders (non-staggered) at $R/D = 3.73$ resulted in an average increase in the drag coefficient of approximately 35%, but had no significant effect on the cross-stream force.

PTV analysis showed that there was a reduction in the turbulent kinetic energy behind the array as the angle to the flow was decreased. This was consistent with the measured reduction in array drag. The cross-stream force measured at low array angles was linked with the rotation of streamlines, and presumably a corresponding rotation of the drag force, as the flow is diverted through the array.

At both 30^o and 60^o, the cylinder wakes were angled with respect to the stream-wise direction (and away from the array). The angle of the wake increased as cylinder spacing decreased.

The distributions of TKE and turbulent shear stresses behind the arrays at 60^o showed a considerable resemblance to that behind arrays at 90^o. A different distribution of turbulent shear stress was detected for the array at 30^o. While two lobes of turbulent shear stress occur behind widely spaced ($S/D > 2.2$) cylinders in arrays normal, or at a large angle, to the flow, a third region of high turbulent shear stress was detected at an angle of 30^o. This third region was located to the side of the cylinder wake, and behind the cylinder upstream. With the occurrence of this third region, the turbulent shear stress distributions were no longer symmetrical about the cylinder centreline. The third region of turbulent shear stress was connected to the region of turbulent stress of the same sign generated behind the next cylinder upstream.

It is not entirely clear what causes the enhancement of the turbulent shear stresses. It appears to be related to the acceleration of the fluid around the downstream cylinder. This acceleration increases the mean shear gradient, which may in turn enhance the production of turbulence. Another possibility is that the increased turbulent shear stress results from an interaction of eddies generated from the upstream cylinder with those produced by the shear layer in the wake of the second cylinder.

PTV analysis of the flow around closely spaced (S/D = 1.90 in these experiments) single row arrays angled to the flow show that at some angle between 30^o and 60^o, the non-uniformity in the wake sizes disappears. Offsetting the cylinders in a downstream direction disrupted the mechanism responsible for generating the non-uniformity.

Implications for the mussel long-line application are that a double row of droppers will have a higher drag than that of a single row. The drag on the long-line will also vary with the angle to the approaching flow. Modifying the drag by using a sine function, as was used in Chapter 3, will give suitable values for most long-line angles. The drag on a long-line at 0^o to the flow will not be zero, as a sine-function suggests, but will be a function of the dropper spacing, with the drag increasing with spacing. The drag at 0^o will be small in comparison with that of a long-line normal to the flow. The drag coefficient for a long-line may be estimated by first modifying the drag of a mussel dropper to account for the dropper spacing, applying a second modification if the long-line is configured as a double row, and then adjusting for the angle of the long-line relative to the flow. A cross-stream force will occur where long-lines are at low angles to the flow. This may need to be considered for numerical models, as there will be an opposing reaction on the fluid.

The issue of long-line orientation in relation to the flow has been the subject of much discussion amongst both researchers and industry. There are opposing views as to whether long-lines should be oriented in-line with (0^o) or normal to (90^o) the dominant currents.

For a single long-line, the optimal configuration with regard to an even nutrient supply along the length of the long-line is to orient the long-line at 90^o to the flow. This configuration minimises the flow interference between the droppers, and minimises the extent to which droppers are within the wakes of other droppers. For a long-line orientated at a low angle to the flow, the wakes of upstream droppers will affect the flow to droppers located downstream. The reduced velocities in the wake of the upstream droppers, combined with any phytoplankton consumption will reduce the phytoplankton supplied to those droppers downstream. This reduced nutrient supply is likely to be greater if droppers are spaced more closely.

Orienting mussel long-lines at 90^{o} produces the greatest drag, and therefore the greatest attenuation of currents. For a large farm with many long-lines, orienting the long-lines at 90^{o} to the flow will result in the greatest attenuation of currents, and therefore the greatest reduction of phytoplankton supply to the farm as a whole. Thus, there is a trade-off between reducing the long-line drag to minimise the farm-scale reduction in velocities, and orienting the mussel droppers so that an even supply of phytoplankton is provided along the length of the long-line. Generally currents at mussel farm sites are tidal, and reverse every 6 hours. Also, currents are seldom uni-directional. It is therefore unlikely that a long-line would be permanently aligned with the flow. The natural variability of flow direction is likely to be sufficient to ensure an adequate supply to all droppers along a long-line, even at low angles to the flow. In conclusion, for a large mussel farm, the advantages of aligning the mussel long-lines at low angles to the dominant currents, reducing the interference between long-lines, should outweigh any sheltering effects between individual droppers along a long-line.

CHAPTER 13 CONCLUSIONS AND RECOMMENDATIONS FOR FURTHER WORK

13.1 Introduction

The study of the hydrodynamic aspects of aquaculture is a new field, but one that requires urgent attention due to the rapid growth of the industry. Consequently, a wide range of topics have been covered in this thesis in order to address some of the most pressing concerns, particularly the effects of mussel farms on currents and waves. Two approaches have been used. Firstly, field measurements were taken to look at the large-scale effects. Measurements of water velocities, interaction with stratification, and dissipation of wave energy are presented in Chapters 3 to 5. These chapters provide a number of tools by which the potential effects of a long-line mussel farm can be assessed. Other field data presented include a brief consideration of anchor rope loadings (Chapter 6), and seston depletion (Chapter 7). The second approach used in this thesis was to look at small-scale flow features through laboratory experiments. The large-scale effects of the farm on currents, stratification, and waves result from the combined interactions of the flow around thousands of mussel droppers. The laboratory experiments provide a number of insights as to the effect of extreme cylinder surface roughness and of the spacing and orientation of cylinder arrays. While these findings are of interest in their own right, it is hoped that the laboratory study also provides data that will guide further research where numerical models are used to study the flow around long-lines and groups of long-lines.

In this final chapter, the key results from each of the areas investigated are summarised, and the two approaches connected. Obviously there are still large gaps in the knowledge and understanding of the hydrodynamic effects of mussel farms and aquaculture in general. A number of these areas are identified in section 13.5, with some suggestions on how to approach these problems.

13.2 Hydrodynamic Effects of Mussel Farms

Field-based measurements presented in Chapters 3, 4 and 5 show that significant effects on currents, stratification, and, to a lesser extent, on waves can be associated with a large long-line mussel farm. The fieldwork was mainly based on one study site (Collingwood, Golden Bay), but the results are not completely site specific. The understanding of the physical hydrodynamics of the Collingwood farm developed in this thesis can be used to evaluate the effect of other farms in different locales.

The local effects on currents at the study site were significant. Drag on the submerged mussel farm structures reduced water velocities within the farm by between 47% and 67%. This reduction in velocities

has important implications for the supply of phytoplankton to the farm, and for the likely depletion of phytoplankton within the farm. Assessment of potential sites for future mussel farms must include a drag-induced velocity reduction to avoid overestimating the available phytoplankton supply.

The farm presents a porous obstacle to the flow. The flow that does not pass through the farm must be diverted around or beneath the farm. At the study site, the field measurements indicated that most of the flow was diverted around the farm despite the large horizontal dimensions of the farm. Velocities were higher beneath the farm than within, generating a shear layer below. However, the undercurrent was not significantly greater than velocities recorded upstream of the farm. The droppers at this site extended over most of the water column (average dropper length ~ 8 m, average water depth ~ 11 m), providing a restriction to the flow beneath the farm. A second restriction was the strength of the density stratification, favouring a horizontal diversion in most cases. The bulk Richardson number is a useful indicator of whether the stratification is likely to be sufficient to restrict a diversion of flow beneath the farm.

Many other mussel farms in New Zealand are located in deeper water (20 to 40 m). As the present practice is to use the greatest dropper length possible, the flow around such farms will therefore be mostly two-dimensional. For farms with short dropper lengths relative to the water depth, the strength of the stratification will determine whether flow is diverted under or around the farm. This will depend on the location of the density interface if there are sharp changes in stratification. An interface sufficiently far below the farm may have little effect, while an interface close to the bottom of the mussels would exert a greater influence.

Apart from the current beneath the farm, the flow around the farm was essentially two-dimensional. This suggests that two-dimensional numerical models should be sufficient to obtain reasonable predictions of the velocity drop within, and diversion around, mussel farms. A simple pipe-network model gave reasonable estimates of the velocity through the farm, demonstrating that an increased bed friction in the area of the farm may adequately parameterise the drag on the mussel droppers. For more complex three-dimensional models, local friction coefficients could be employed to similar effect.

The issue of how much vertical mixing can be produced by the flow through a mussel farm remains unresolved. Two mechanisms for vertical mixing were considered in Chapter 4, the shear layer beneath the farm generated by the undercurrent, and the turbulence from the flow past the mussel droppers. The gradient Richardson number at the study site indicated that the strength of the density stratification was likely to be sufficient to prevent instabilities from the shear layer causing much mixing. While this was a site-specific observation, the shear layers generated beneath mussel farms are likely to be weak unless

ambient currents are strong. Weak stratification would be required for this mechanism to generate significant mixing.

The second mixing mechanism considered was the turbulence generated by the mussel droppers. An analogy can be made to grid-generated turbulence, as the rows of mussel droppers are a form of grid. While grid mixing efficiencies are generally low (< 6%), considerable energy loss occurs due to the drag on the farm. This energy loss occurs largely through the generation of turbulence. Despite the low mixing efficiencies, the combined action of the turbulence from the thousands of mussel droppers is likely to have some effect on vertical mixing. The laboratory studies showed that the turbulence generated by the flow past a cylinder was increased by extreme surface roughness, and that turbulent kinetic energy was also increased by close cylinder spacings. As the mussel long-lines resemble arrays of closely spaced, very rough cylinders, there is a strong potential for mixing.

The Collingwood mussel farm was shown to have a small effect on wave energy. Frequency dependent wave attenuation was measured, and predicted with some success by an analytical model. The measurements and the model both predict that wave dissipation increases as the wave period decreases. The field measurements were restricted to shallow water and transitional waves as bottom-mounted pressure sensors were used to measure the wave field. Wave energy dissipation at the Collingwood site averaged approximately 10%, however a peculiarly low dissipation was seen at wave frequencies of around 0.2 Hz, suggesting the farm is more porous to waves of particular frequencies. Again, these observations were site specific, relating to a particular farm configuration with long-lines orientated normal to the direction of wave propagation. As wave heights were small during the two deployments, no assessment can be made of the effect on moderate or large waves.

The analytical wave model indicates the importance of dropper density as well as farm size on the dissipation of wave energy. An attempt was made to include the inertial forces in the dissipation calculations. The model results indicate that the drag force dominates except at very high frequencies, and the accelerative forces need not be considered in most situations.

Measurements of anchor rope tension indicated the loadings are induced by the tide, currents, and waves. Generally the load consisted of a quasi-static (slowly varying) component determined by the tide, with the effects of currents and waves superimposed. Dynamic wave loadings were sometimes significant, with force fluctuations of 8 kN recorded for an estimated significant wave height of 1.9 m at the Pigeon Bay site. At the Pigeon Bay site, the long-lines were oriented inline with the waves, and the highest loadings were recorded on the offshore anchor rope.

The issue of seston or phytoplankton depletion was considered briefly in Chapter 7 through the examination of fluorescence, turbidity, and acoustic backscatter data. Although the results were consistent with a reduction of seston within the farm, differences between the inside and outside of the farm were not statistically significant. An assessment of feeding rates indicated that the farm is likely to consume around 13% of the supplied nutrients, although the level of depletion may be cumulative as the same patch of water is carried repeatedly through the farm on successive tidal cycles. A mixing layer analogy presented in Chapter 3 suggests that horizontal diffusion would be small, therefore the accumulated depletion would depend mostly on the residual tidal currents (averaged over many tidal cycles), and the rate of phytoplankton regrowth.

13.3 The Effect of Extreme Surface Roughness and Spacing on Cylinders

The laboratory experiments conducted with smooth and rough cylinders showed that over the Reynolds number range of 4,000 to 12,000, high surface roughness ($k_s/D \sim 0.092$) had little effect on the drag coefficient of single cylinders, yet the drag coefficient for an array of cylinders normal to the flow was increased. This suggests that there is a greater interaction between the wakes of the rough cylinders, resulting in greater energy dissipation and drag.

For single cylinders, the effect of high surface roughness was to shorten the length of the near wake region, defined here as the point downstream of the cylinder where the time-averaged velocity is zero. Peak turbulent kinetic energy was also higher behind the rough cylinders, and this peak occurred closer to the cylinder. It is proposed that the decreased near-wake length is due to turbulence generated by the surface roughness elements disturbing the free-shear layers, causing them to roll up into eddies closer to the cylinder. A reduction in the eddy shedding frequency was also measured behind the rough cylinders, with $S_t = 0.19$ and 0.17 for cylinders with surface roughness ratios of $k_s/D = 0.048$ and 0.094 respectively. In comparison, the Strouhal number for a smooth cylinder is $S_t = 0.21$.

Due to the irregularity of the outline of a mussel dropper, the projected area is an inconvenient quantity to use in determining drag. A more convenient measure proposed in this thesis was to use a dropper diameter defined as twice the average shell size. Using this definition, a mussel dropper with shells of average length 83.4 mm had a diameter of 167 mm, with a corresponding drag coefficient of 1.10 ± 0.07. This was similar to the drag coefficients of the smooth and rough cylinders tested in the experiments. The wake of the mussel dropper consisted of small eddies, presumably shed from individual mussel shells, with larger eddies generated further downstream by the free-shear layers, as seen for the cylinders. The dominant eddy shedding frequency was similar to that of the roughest cylinder tested, with $S_t = 0.17$.

Arrays of rough cylinders normal to the flow demonstrated similar characteristics to those of smooth cylinders. At cylinder spacings of $S/D < 2.2$, non-uniform but stable wake patterns formed behind arrays of smooth and rough cylinders. The effect of the surface roughness was to favour the formation of a particular distribution of wake structures behind the array, whereas different patterns were seen in each run behind arrays of smooth cylinders. It is proposed that the non-uniform wake patterns result from the biasing of the gap flows as the shear layer behind a cylinder first rolls up to form an eddy. As all of the rough cylinders were unique, the turbulence shed from the cylinder surface would act to cause shear layer roll-up behind particular cylinders sooner than other cylinders, resulting in the same distribution of wake sizes each run.

Experiments with arrays of cylinders at angles to the flow confirm that the drag on an array varies with the sine of the angle to the flow, except where the array is inline with (or at very low angles to) the flow. Drag is also related to spacing, with drag increasing as cylinder spacing is decreased. The opposite is likely to occur with cylinder arrays inline with the flow, where the array drag will be lower when the cylinders are closer together as more effective sheltering can occur.

13.4 Linkages between the Field Work and Laboratory Experiments

While the fieldwork and laboratory experiments approach the study of mussel farm hydrodynamics from completely different scales, there are a number of linkages between them. Some of these have been identified above, including the effect of long-line orientation and dropper spacing on drag and turbulence. As reduction of velocities within the mussel farm is ultimately due to the drag on the droppers (directly via friction and indirectly via flow diversion), the interaction between the mussel droppers is of great importance.

Based on typically long-line design at the time of writing, dropper spacings in the field are in the range of $1.6 < S/D < 20$, and the spacing between the two rows of droppers on a long-line is in the range $4 < R/D < 20$. The higher end of the range for both dropper and row spacing represents an immature crop. The low dropper and row spacings are of more importance as these represent mature mussels (forming large dropper diameters of 0.15 m to 0.25 m) which will generate more drag and energy dissipation. Consequently the laboratory experiments focused on dropper and row spacing typical of more mature mussels. The laboratory experiments show that at long-line back-bone spacings and dropper spacings typical of a mature crop, the double dropper row configuration will have a higher drag than a single row. The drag on the long-line will be a function of the angle of the long-line to the flow, with lowest the drag when the long-line is inline with, or at a low angle to, the flow. Thus, to minimise the reduction of

velocities within the farm, and thereby increase the flux of seston through the farm (and minimise depletion), long-lines should be oriented along the direction of the dominant currents.

The PTV analysis has shown that, at low angles to the flow, cylinders would be within the wake of upstream cylinders. This would reduce the available seston supply to mussel droppers in a long-line oriented in-line with the flow. However, the natural variability in flow direction, turbulent exchange, coupled with the higher velocities within a large farm resulting from aligning long-lines with the flow are more likely to ensure an adequate food supply to all mussel droppers within the farm than if long-lines were oriented across the flow.

The laboratory comparison of smooth and rough cylinders indicates that models (physical or computational) developed to study the flow on small to moderate scales (from flow around a long-line to flow within a larger farm) should incorporate the effect of high surface roughness due to the increase in drag and turbulence.

13.5 Implications

The results of this research have a number of implications for the design of mussel farms and for the assessment of their effects. The field data showed that there is a significant reduction of water velocities within the farm. Consideration of nutrient depletion or bio-deposition should therefore account for the fact that water velocities will be lower within the farm. As a consequence of the lower velocities, nutrient flux through the farm will be reduced and detritus may not be transported as far from the site. This may result in a greater nutrient depletion and build up of detritus beneath the farm than would be predicted using ambient velocities measured in the absence of the farm.

The reduction in velocities within a farm may be minimised by aligning long-lines with the mean currents at the site. Laboratory tests confirmed that long-lines in this orientation had the lowest drag. Consequently, the effect on flow will also be minimised. The advantage of higher velocities is a greater nutrient flux through the farm, and consequently a reduced potential of nutrient depletion and a greater dispersal of detritus.

The effect of large mussel farms on currents may be estimated in 2-dimensional numerical models by invoking a higher friction in the area occupied by the farm. This form of approximation is likely to give reasonable bulk estimates of velocity drop within the farm (and accompanying acceleration of fluid around the perimeter). However, there are likely to be local variances in velocity caused by wakes from

and diversion around individual long-lines. A more detailed model incorporating each individual long-line will be required if a detailed prediction of velocity distribution within a mussel farm is required.

Dissipation of wave energy was minor for the large mussel farm (Collingwood) investigated in this research. Field measurements were taken only during relatively calm conditions, but both field measurements and an analytical model show that wave dissipation is a function of frequency, with the low frequency ocean waves being relatively unaffected. While they may provide some dissipation of high frequency waves, mussel farms can not be considered as an effective form of wave protection due to their high permeability to the mid to long period waves (5 to 20 seconds) that are likely to be of concern for shore protection. Similarly, there is unlikely to be a significant effect on surf down-wave of a long-line mussel farm.

The long-line mooring loads are dominated by tidal pretension and waves. The buoyancy of the floats means that mooring loads correspond to changes in the free-surface. For long-lines oriented in-line with waves, higher dynamic loads were measured at the offshore mooring. The field data from Pigeon Bay indicated that the offshore anchor loadings respond strongly to high frequency waves (see Figure 6.20(b) and Figure 6.21(c)), which is thought to be due to the inertia of the buoys and mussel droppers near the offshore anchor rope. It may be possible to reduce the wave loadings by designing the buoys so that their buoyancy changes less for the same amount of submergence. For example, tall vertical cylinders would experience less buoyancy change for a moderate change in submergence than the squat horizontal cylindrical floats currently used.

13.6 Suggestions for Further Research

This thesis forms an exploratory investigation of the hydrodynamic effects of aquaculture structures, and there are many areas where further research is required.

This study has focused on large scale (the size of the farm) and small scale (of individual droppers) hydrodynamics. The mid-scale, not investigated here, includes the flow features of the size of mussel long-lines, such as flow interactions between long-lines, and flow patterns within mussel farms. This project indicates the difficulty in obtaining good quality field data, particularly at high resolution, over areas the size of typical mussel farms. The ability to measure mid-scale flow features will be hampered by the variability caused by tides and water conditions. While physical modelling is a possibility, such models would need to be of a large scale in order to achieve Reynolds number similarity. Numerical modelling is a second possibility, but again the effects of the dropper roughness will need to be incorporated in some manner.

Among the farm-scale flow effects not well understood is the farm wake. It is proposed here that the size of the wake will be limited by the tidal excursion, and a mixing layer analogy suggests that the wake will spread slowly. More research is required to confirm these hypotheses. On a larger scale, mention was made in Chapter 7 of the possible effect of the farm on residual currents (the net displacement of bodies of water averaged over several tidal cycles), and how this may affect depletion of phytoplankton within the farm. Related to this is whether mussel farms would have any effect on coastal drift or circulation within an embayment. Changes to these large-scale features may have implications for phytoplankton distributions over areas much larger than the farm. Similarly, there may also be implications for coastal sediment transport. These are areas that may be best addressed through numerical modelling. The findings in this thesis suggest that the farm drag in a large scale numerical model may be parameterised by increased friction.

The interaction of the farm with a density stratified fluid and quantifying the degree of mixing induced by the farm are other areas worthy of further consideration. These two factors are closely related as strong stratification exerts control over the degree of vertical mixing that may occur.

Waves were considered somewhat briefly in this thesis. It was shown that mussel farms are able to cause a dissipation of wave energy. The orientation of long-lines to the wave field has not been addressed in terms of energy dissipation. This is an important topic as the optimal design orientation of long-lines at exposed, offshore sites may be determined more by the wave field than currents. The response of long-lines to waves, and the implications for the survival of long-lines, requires a far more in-depth consideration than given here.

On the small (dropper) scale, a number of issues have been identified from the laboratory experiments where further research is required. It was proposed that the stability of the metastable wakes behind an array of closely spaced rough cylinders was determined by the unique surface characteristics of each cylinder. This could be verified easily by swapping the position of rough cylinders within an array.

The flow patterns behind the closely spaced arrays were assumed to be two-dimensional. It is possible that different metastable flow patterns form at different heights along the cylinders simultaneously, forming longitudinal cells. The ability to determine this would be hampered by the random nature of the patterns for smooth cylinders. While the same metastable pattern was repeated for a rough array, variations in the surface texture along the cylinders might also trigger different wake patterns at different heights.

No measurement was made of vertical (out of plane, or along the cylinder axis) velocities or vertical velocity fluctuations. While the mean flow is expected to be two-dimensional, the vertical component of turbulence will play a role in energy dissipation. This could be studied using vertical light sheets. A vertical light sheet may also aid in determining whether the metastable wake patterns behind closely spaced arrays are two-dimensional.

A third lobe, or rather an extension and increase of a lobe from an upstream cylinder, was seen in the turbulent shear stress distributions behind cylinders in a single row array at 30^{o} to the flow. The conditions and mechanism responsible for the generation of this area of increased turbulent shear stress are not currently understood. Research could begin by determining the range of angles and cylinder spacings required for this lobe of turbulent shear stress to be generated.

APPENDIX A COMPASS CORRECTION FOR MOORED ADP

Data from both Sontek ADP instruments deployed during the Collingwood 2003 experiment (ADP 1 and ADP 2) required a directional correction for a compass error. Each instrument had a large battery placed directly under the instrument. ADP 2 (C283) also had a second battery below and to the side of the instrument which powered an Acoustic Doppler Velocimeter (ADV) (see Figure A.1).

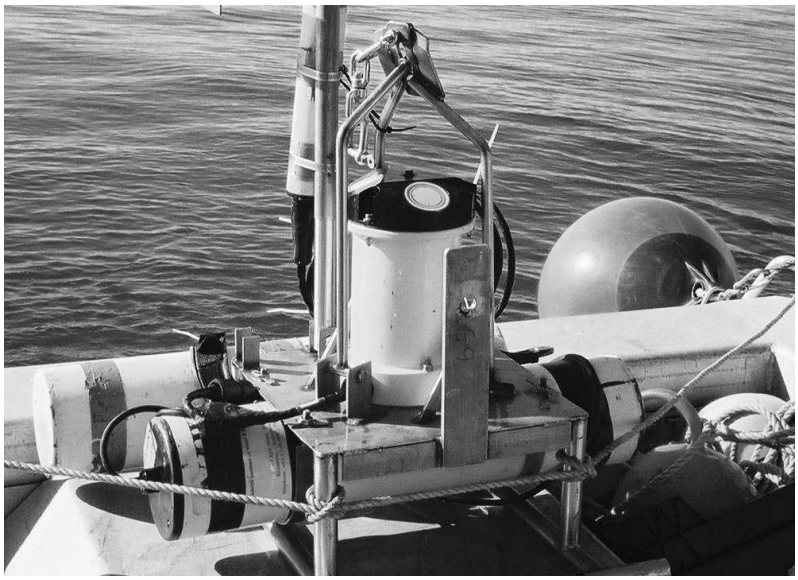

Figure A.1 ADP 2 (C283) with an ADV attached. Battery for the ADP is located underneath instrument (horizontal cylinder). The second battery (behind) is for the ADV.

When orientated to magnetic north, the internal compasses in ADP 1 and ADP 2 gave headings of 331^{o} and 251^{o} respectively. However, the internal compass error changes with the orientation with the instrument. Figure A.2 and Figure A.3 show the ADP compass reading against the instrument orientation (with respect to magnetic north).

The internal compass reading for both instruments was recorded during the deployment, and is indicated by a horizontal line in Figure A.2 and Figure A.3. As can be seen, there are two possible orientations for each instrument based on the internal compass readings. ADP 1 could have been orientated at either 174^{o} or 252^{o} (with respect to magnetic north), and ADP 2 at either 2^{o} or 324^{o}. The correct orientation cannot be determined without comparison with other measurements. By comparing both orientations for each instrument with the ADCP-wave measurements and ADCP transects, the correct orientation appears to be ADP 1 at 174^{o} and ADP 2 at 324^{o}. The compass correction factor is obtained by subtracting the ADP internal compass deployment heading from the actual instrument heading (magnetic). For ADP 1 the correction is 174^{o} - 300.7^{o} = -126.7^{o}. The correction for ADP 2 is 324^{o} – 249.9^{o} = +74.1^{o}.

The velocity vector directions are obtained from the raw ADP velocity directions by adding the compass correction + magnetic deviation. The magnetic deviation is estimate at 21.15^{o} based on Hydrographic Chart NZ61 Golden Bay (1999).

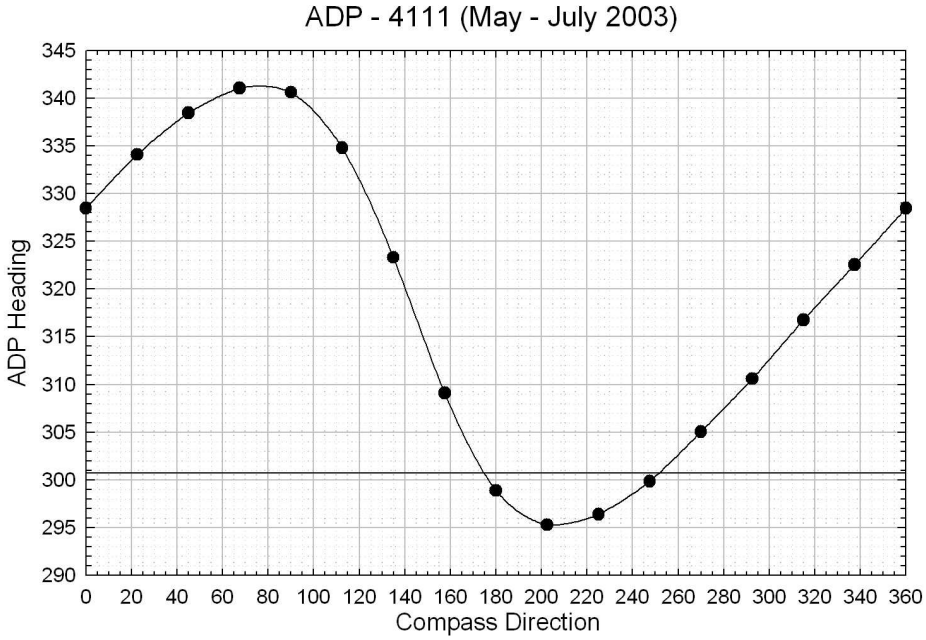

Figure A.2 ADP 1 (4111) internal compass versus instrument orientation. The horizontal line indicates ADP heading during deployment.

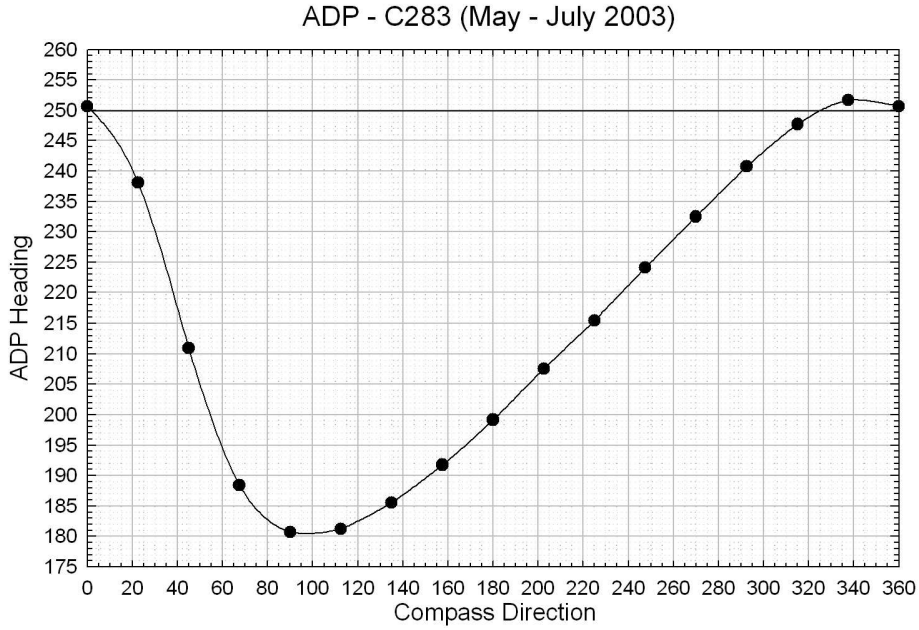

Figure A.3 ADP 2 (C283) internal compass versus instrument orientation. The horizontal line indicates ADP heading during deployment.

APPENDIX B TIDAL CORRECTION OF VELOCITY TRANSECTS

Due to the size of the Collingwood mussel farm and the strong tides, the time required to record velocity transects meant that tidal variations in water velocity obscured farm-induced velocity reductions. To reduce this effect, velocity transects were adjusted based on velocities recorded at ADP moorings over the duration of the transects. This correction procedure is demonstrated here for two transects, plotted as Figures 3.10 and 3.12 in chapter 3.

B.1 Transect A

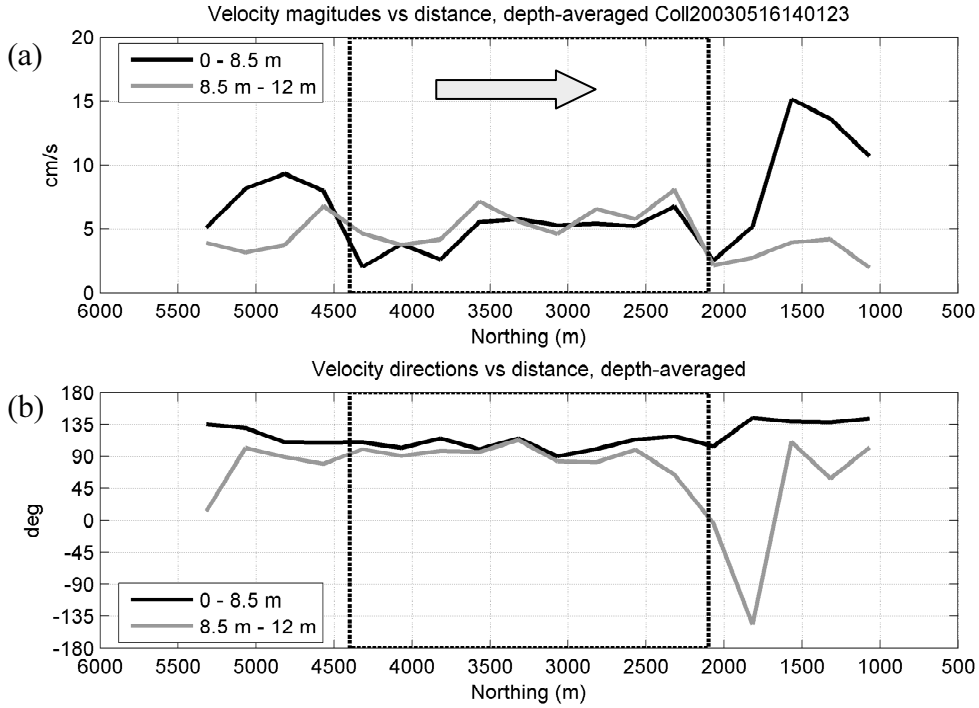

Figure B.1 (a) velocity magnitude and (b) direction averaged within farm (upper 8.5 m) and beneath farm (below 8.5 m) from transect 3, 16 May 2002. The arrow indicates the direction of flow.

As this transect was recorded towards the end of the falling tide, tidal variations in water velocity are expected. This transect was measured from south to north, so velocities to the north may appear lower due to the tide. Depth-averaged velocity magnitudes recorded at ADP 1 and ADP 2 over this time period are plotted in Figure B.2. A 30 minute moving average has been used to filter the time series (grey line). The open circles show the start and end time of the transect plotted above. Over the transect duration, velocities at ADP 1 decreased from 8.65 cm/s to 6.76 cm/s (22% decrease), while at ADP 2, velocities decreased from 4.31 cm/s to 1.24 cm/s (72% decrease).

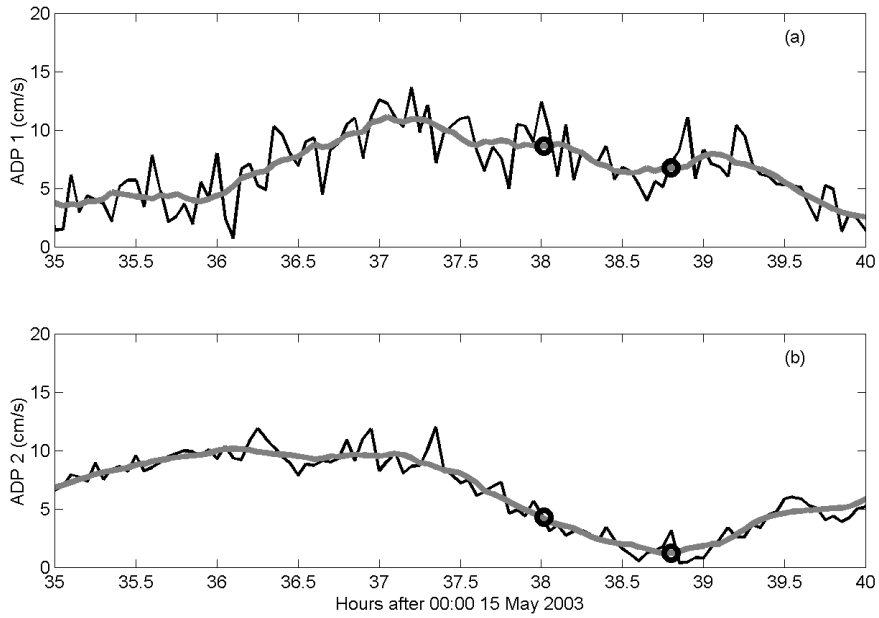

Figure B.2 Depth-averaged velocity magnitudes (grey line 30min moving average) at (a) ADP 1, and (b) ADP 2. Open circles indicate start and end time of ADCP transect 3, 16 May 2003.

To account for the variation in water velocity due to the tide, a tidal velocity correction has been applied based on the depth-averaged velocities recorded at ADP 1. The velocity values plotted in Figure B.1 were calculated by averaging data over 250 m intervals. These measurements were not at regular time intervals as this transect was interrupted periodically to take CTD measurements (refer Chapter 4 for these results). However, for the purpose of deriving a tidal velocity correction factor, it was assumed that time intervals between the spatially averaged profiles were equal so that a distance-based correction factor could be applied. As a further simplification, the correction factor was assumed to be linear with time (and therefore distance).

The correction factor was derived such that velocities at the end of this transect are scaled by the ratio of the depth-averaged velocities recorded at ADP 1 corresponding to the start and end time of the transect. Expressed as a function of distance x along the transect of length L, the tidally corrected velocity U_m was calculated from the recorded velocity U as

$$U_m = \frac{1}{\left(1 + \frac{U_f - U_0}{U_f}\frac{x}{L}\right)} U \qquad \text{(B.1)}$$

where U_0 and U_f are the depth-averaged velocities at ADP 1 at the time of the start and end of the transect. Tidally corrected velocities through the farm are plotted in Figure B.3.

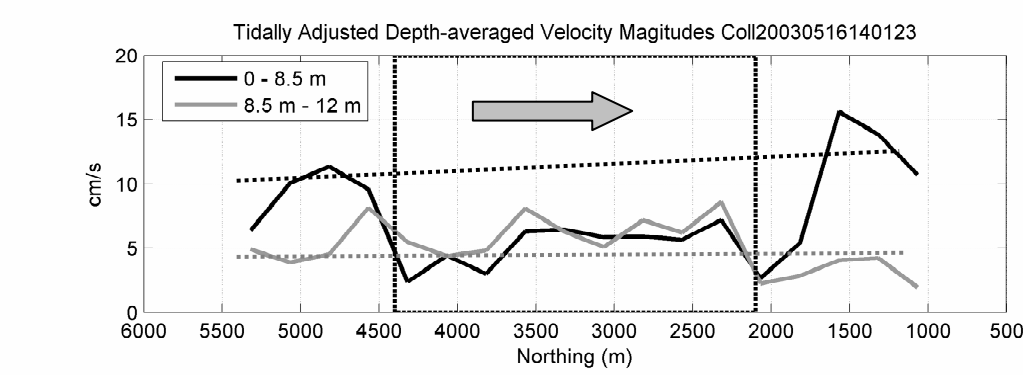

Figure B.3 Velocity magnitudes from transect 3, 16 May 2003, with tidal correction applied. Dotted line indicates likely velocity in absence of farm.

B.2 Transect B

The second transect was recorded on the rising tide, and is plotted in Figure 3.11. Velocity magnitudes are plotted in Figure B.4.

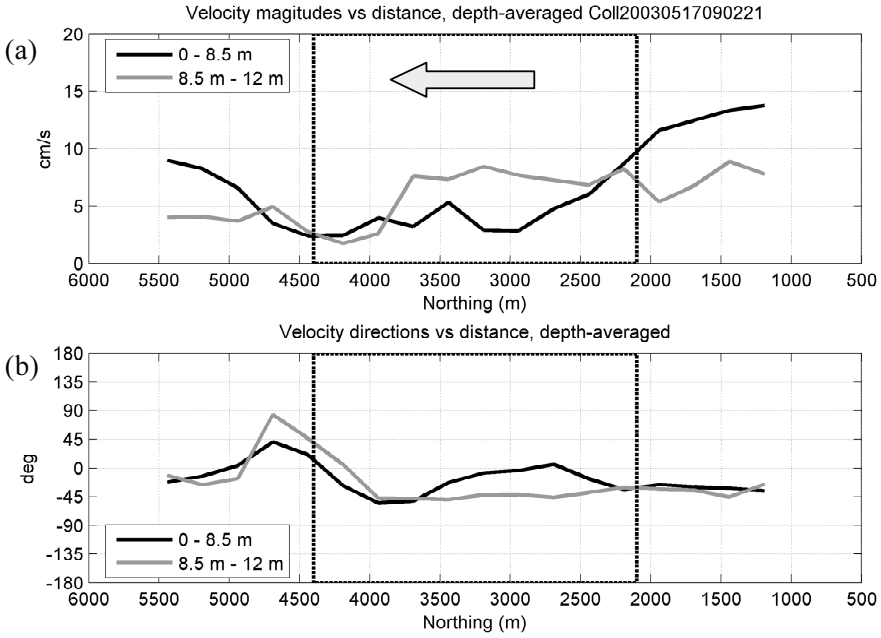

Figure B.4 (a) Velocity magnitude in upper 8.5 m (approximate depth of farm), and below 8.5 m (below farm), (b) direction of water currents in upper 8.5 m and below 8.5 m for transect through farm, 17 May 2002

Depth-averaged velocity magnitudes recorded at ADP 1 and ADP 2 over the period this transect was recorded are shown in Figure B.5. At both instruments, the velocity magnitude decreased by similar amounts. Depth-averaged velocity magnitudes at ADP 1 corresponding to the time of the start and end of the transect were 8.64 cm/s and 5.17 cm/s. At ADP 2, the start and end velocity magnitudes were 6.57 cm/s and 3.96 cm/s respectively. The ratio of the start and end are 1.67 at ADP 1, and 1.66 at ADP 2. As the ratio is nearly identical, 1.67 is used to calculate the tidal correction factor for this transect.

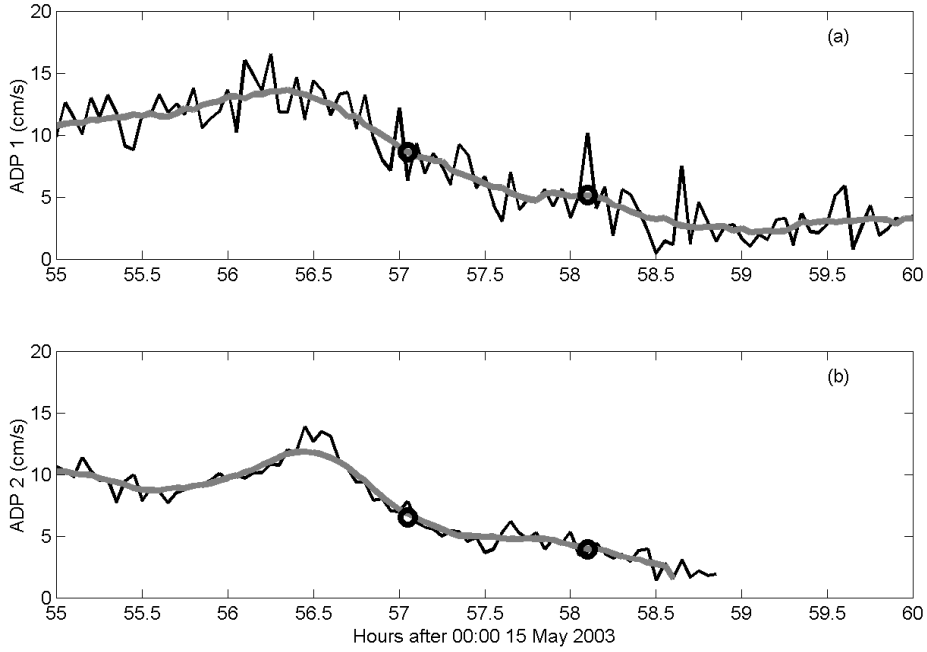

Figure B.5 (a) Depth-averaged velocity magnitudes (grey line 30min moving average) at ADP 1, and (b) ADP 2. Open circles indicate start and end time of ADCP transect, 17 May 2002.

The tidally corrected velocity transect is plotted in Figure B.6.

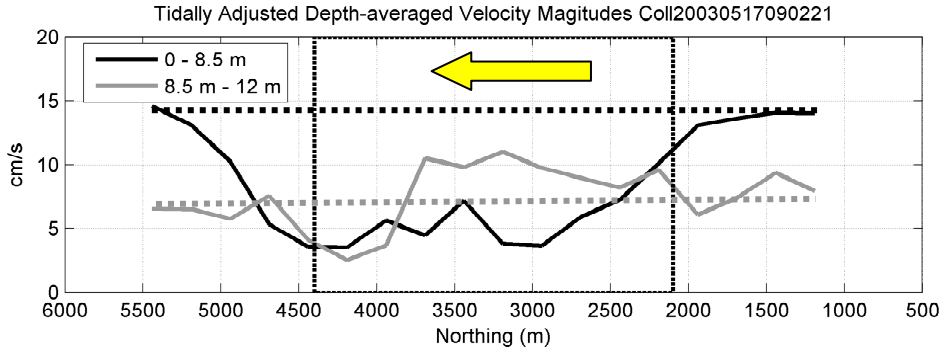

Figure B.6 Velocity magnitudes from transect through farm, 17 May 2002 with tidal correction applied. Dotted lines indicate likely velocity in absence of farm.

APPENDIX C PIPE NETWORK MODEL DEVELOPMENT

The pipe-network model developed here is a simple, quasi two-dimensional pressure driven model that can be used to gain insight into the diversion of flow around the farm. The model is not strictly two-dimensional as the momentum equations are reduced to one-dimensional form. Pipe nodes are regularly spaced to form a rectangular grid. Each node is connected to the nearest neighbouring nodes by pipes. Frictional losses through each pipe are a function of the pipe length L, diameter D, and friction factor f. The pipe length (L) is determined by the node spacing. The energy or pressure change through a pipe is a function of the velocity,

$$\Delta H = -f \frac{L}{D} \frac{U|U|}{2g} . \tag{C.1}$$

The negative sign in (3.4) indicates a loss of energy in the direction of fluid flow. At each node in the pipe network, there will be inflows and outflows from the attached pipes. The flow through each pipe is determined by the pressure drop along the pipe. Pipe flow is simply the velocity multiplied by the cross-sectional area

$$Q_p = \frac{\pi D^2}{4} U . \tag{C.2}$$

At each node, continuity must be maintained. Therefore an iterative scheme is used to calculate pressure at the nodes so that the inflows and outflows balance at each node. The equations for the pipe-network model are modified slightly to use a friction coefficient of the form used in open channel flow. The bed friction is parameterised by a coefficient C_f, such that the shear stress on the bed is

$$\tau = \frac{1}{2} \rho C_f U|U| . \tag{C.3}$$

Energy slope S in uniform flow is related to bed shear stress and hydraulic radius R by

$$S = \frac{\tau}{\rho g R} . \tag{C.4}$$

The energy slope can then be calculated by

$$S = \frac{C_f}{R} \frac{U|U|}{2g} . \tag{C.5}$$

The energy slope can be approximated by the pressure gradient $S = -dH/dx$, giving an expression for the pressure change along the pipe (positive indicating an increase in pressure) as

$$\Delta H = -\frac{C_f L}{R} \frac{U|U|}{2g} . \tag{C.6}$$

The drag from the farm is represented by increased frictional losses; therefore pipes in the area representing the farm have a higher friction coefficient C_f than outside the farm. The friction coefficient within the farm represents both the bottom friction and the farm drag.

In the adapted pipe-network model, the cross-sectional area for each pipe is the product of the water depth (or hydraulic radius, R) and the pipe width w. The pipe width must be specified if the grid spacings vary in the x and y directions. Otherwise, if widths are assumed to be the same, the capacity of the network to transport fluid will be reduced in one direction (less total area of pipes in one direction) resulting in higher velocities (and therefore higher frictional losses) in that direction to maintain continuity. To account for differences in grid spacing, the pipe width is specified as the spacing between the grid points such that pipes oriented in the y direction have a width $w = dx$, and pipes in the x direction have a width $w = dy$. As velocities are of more interest than pipe flows, the actual values of pipe width are less important than their ratio. If equal grid spacing is used in both directions, the widths cancel. As the pressure variations over the site are likely to be small (a few mm) compared to the water depth (~10 m), variations in water depth between pipes can be assumed to be due only to the shape of the bed and variations in the free-surface. For simplicity, a flat bed is assumed. In terms of the pipe-network analogy, this is equivalent to specifying that all pipes have equal diameter (or equal hydraulic radius in this model).

The flow rate in each pipe j is therefore

$$\begin{aligned} Q_j &= RwU \\ &= \left(-\frac{\Delta H}{|\Delta H|} \right) Rw \sqrt{\frac{2gR|\Delta H|}{C_f L}} \,. \end{aligned} \tag{C.7}$$

The term in brackets on the right of equation (C.7) accounts for the direction of flow, so that Q is positive in the direction of decreasing pressure.

The pressure at each node point in the grid is calculated iteratively so that continuity at each node is satisfied,

$$\sum_{j=1}^{N} Q_j = 0 \,. \tag{C.8}$$

However this is complicated by the non-linear relationship between flow and pressure drop through a pipe. Pipe flows are functions of $\sqrt{|h_0 - h_j|}$ where h_0 is the pressure at the node of interest, and h_j is the pressure at the opposite end of the pipe. In order to solve for the pressure at the node, it is convenient to linearise the relationship between Q and the pressure differential $h_0 - h_j$ as

$$Q_j = f_j \left(h_0 - h_j \right). \tag{C.9}$$

The resistance f_j for each pipe is also a function of the pressure differential, however the changes in resistance are assumed small for small changes in pressure differential.

$$f_j = Rw\sqrt{\frac{2gR}{C_f L\left|h_0 - h_j\right|}}\,. \tag{C.10}$$

At a node, continuity gives

$$\sum_{j=1}^{N} f_j\left(h_0 - h_j\right) = 0\,. \tag{C.11}$$

This can be rearranged to solve for the node pressure h_0 giving a Gauss-Seidel type iterative procedure

$$h_0 = \frac{\sum_{j=1}^{N} f_j h_j}{\sum_{j=1}^{N} f_j}\,. \tag{C.12}$$

The pipe-network model is implemented as follows.

- A regularly spaced rectangular grid is laid out with pipes (pathways) connecting neighbouring nodes (Figure 3.18). Friction factors C_f and hydraulic radius R are specified for each pathway, with higher values of C_f for pipes within the area of the farm.
- Known pressures are specified for inlet nodes along one edge of the grid, and lower pressures along outlet nodes at the opposite end of the grid. This creates a pressure gradient across the pipe-network to drive the flow.
- Stepping through each node in turn (except for nodes where the pressure is specified), equation (C.12) is used to calculate the pressure at the node from the pressure at surrounding nodes.
- The last step is repeated until the changes in pressure at node points are acceptable small. The flow within each conduit can then be determined from the calculated pressures.
- Velocities components (in the x and y directions) at each grid point are calculated by dividing the sum of the flows in each direction by the pipe areas.

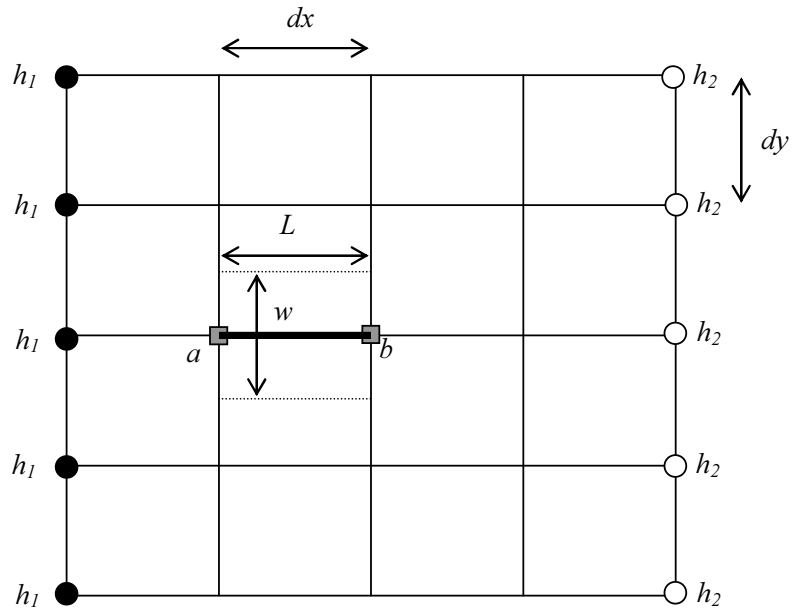

Figure C.1 Example of grid for pipe-network model. Nodes are spaced at dx and dy in the x and y directions. Pressures are specified at inlet nodes (h1) and outlet nodes (h2). The pipe connecting nodes a and b (marked by the thick line) has a length L = dx, and width w = dy.

The choice of friction factor is important as it is the key factor determining the pressure losses. The choice of pressure at the inlet and outlet nodes will determine the velocities within the grid. However, as pressure scales with the square of velocity, the velocities at the grid points can be non-dimensionalised (by an upstream velocity) so that inlet and outlet node pressures are arbitrary. Similarly, in terms of assessing the likely diversion of flow around the farm, the absolute values of friction factor are less important than the ratio of bed-friction to farm friction. Further issues are the size and resolution of the grid. The grid needs to extend sufficiently far from the farm that velocities along the grid boundaries are not affected by the farm. An overly coarse grid will not simulate the farm well, while a very fine grid will be computationally intensive to solve. These issues are best addressed by trial and error, starting with a coarse grid and refining the resolution until the solution is suitably independent, and altering the size until velocities near the edges are satisfactorily uniform.

The pipe-network model only calculates a pressure driven flow, and does not account for turbulent momentum diffusion. This is particularly important in the wake region downstream of the farm. Also, the pipe-network model only provides a steady-state solution, and can not in this form be used to simulate time-varying flows over a tidal cycle. As a quasi two-dimensional model, the farm is assumed to extend to the bed, and influence of density stratification on flow is not resolved.

To parameterise the farm drag in the pipe-network model, the friction coefficient in the area of the farm is increased. The force per unit area (stress) from drag on the droppers can be expressed as a function of the dropper diameter ϕ, length L_d, density n and drag coefficient C_d

$$\tau_{farm} = \rho n C_d \phi L_d \frac{U|U|}{2}. \quad \text{(C.13)}$$

When compared with equation C.3, a friction coefficient for the pipes within the farm can be derived as

$$C_{farm} = n C_d \phi L_d. \quad \text{(C.14)}$$

The friction inside the farm is the sum of both the dropper drag and the bed friction. For pipes within the farm, the friction coefficient is $C_{bed} + C_{farm}$. Using the unmodified value of $C_D\phi = 0.18$, dropper density 0.06, and dropper length 8.5 m, the farm friction factor is $C_{farm} = 0.0918$.

The bed-friction coefficient C_{bed} will be a function of the roughness of the bed. The lower limit for C_{bed} is that for a smooth bottom. By assuming a logarithmic velocity profile, the bed-friction coefficient may be derived as a function of Reynolds number. Using the formulation of Uijttewaal and Booij (2000) with a modification for the factor of 2 due to their different formulation of bed shear (see equation C.3), the smooth bed friction can be derived as

$$\frac{1}{\sqrt{2C_f}} = \frac{1}{\kappa}\left(\ln\left(\mathrm{Re}\sqrt{2C_f}\right) + 1.0\right). \quad \text{(C.15)}$$

For a smooth bed, C_f decreases with increasing Re. However the difference is small. For typical mussel farm scales of $U \sim 0.05$ to 0.15 m s^{-1}, $h \sim 8$ to 15 m, Reynolds numbers are in the range 4 x 10^5 to 2 x 10^6. From equation (C.15), smooth bottom friction coefficients will be in the range 0.0022 to 0.0028.

An estimate of friction coefficient for the rough bed can obtained from pipe friction data. Comparing equations C.1 and C.5, the bed friction coefficient for a channel C_f can be related to the pipe friction factor f by

$$C_f = f\frac{R}{D}. \quad \text{(C.16)}$$

The ratio of hydraulic radius to diameter for a pipe is $R = D/4$. Bed friction can then be calculated from the Moody diagram, or from the following approximation (Swamee and Jain, 1976)

$$f = \frac{1.325}{\left[\ln\left(\frac{\varepsilon}{3.75D} + \frac{5.74}{\mathrm{Re}^{0.9}}\right)\right]^2}. \quad \text{(C.17)}$$

The Reynolds number in equation C.17 is calculated from the pipe diameter, $Re = UD/v$. The sea bed at the Collingwood farm is mostly sand, although detritus from the farm (shells) may present

additional roughness. A roughness element size of ε = 2 mm is assumed. Based on an assumed depth of 10 m, and average velocities of 0.10 m s^{-1}, the bed friction coefficient is estimated from C.16 and C.17 as C_f = 0.0028. The friction coefficient within the area of the farm is therefore C_f = 0.0918 + 0.0027 = 0.0945.

An example of the model results with the flow along the long-axis of the farm is shown in Figure C.2. By symmetry, only ½ of the farm width needs to be modelled if a no-flow boundary is placed along the farm centreline. The modelled farm dimensions are therefore 2400 m in length, with a half-width of 300 m.

Test runs with the model with the driving pressure gradient oriented along the farm axis showed that pressures across the grid at the mid-point of the farm are equal. Over the upstream part of the farm, the pressure within the farm is higher, driving flow out of the farm. However over the downstream half of the farm, the pressure losses are greater than outside the farm resulting in flows back into the farm (Figure C.2). This second symmetry means that only the upstream half of the farm needs to be modelled if pressures are specified equal at the mid-length.

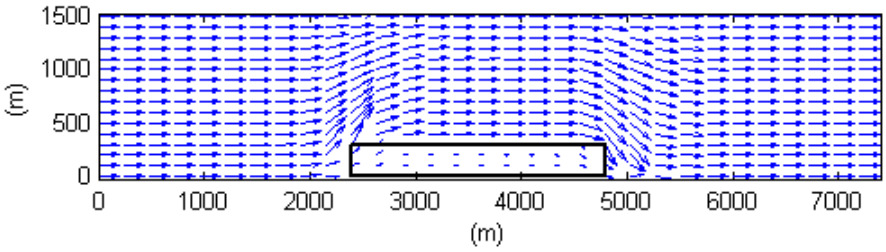

Figure C.2 Example of velocities calculated using pipe flow model, with grid spacing of n_x=31, dx = 240 m, n_y = 16, dy = 100 m. The position of the farm is indicated by the black rectangle.

The deviation of velocities around the farm begins a small distance upstream, and little deviation is seen at > L/2 from the farm. However velocities are affected over several farm widths to the side of the farm.

The influence of grid spacing is demonstrated in Figure C.3, where the flows through the upstream part of the farm are modelled with progressively finer square grids in (a) to (c), and rectangular grids in (d). Changing the grid resolution has little effect on the calculated velocity fields. Streamlines are essentially identical for the 4 grids in Figure C.3.

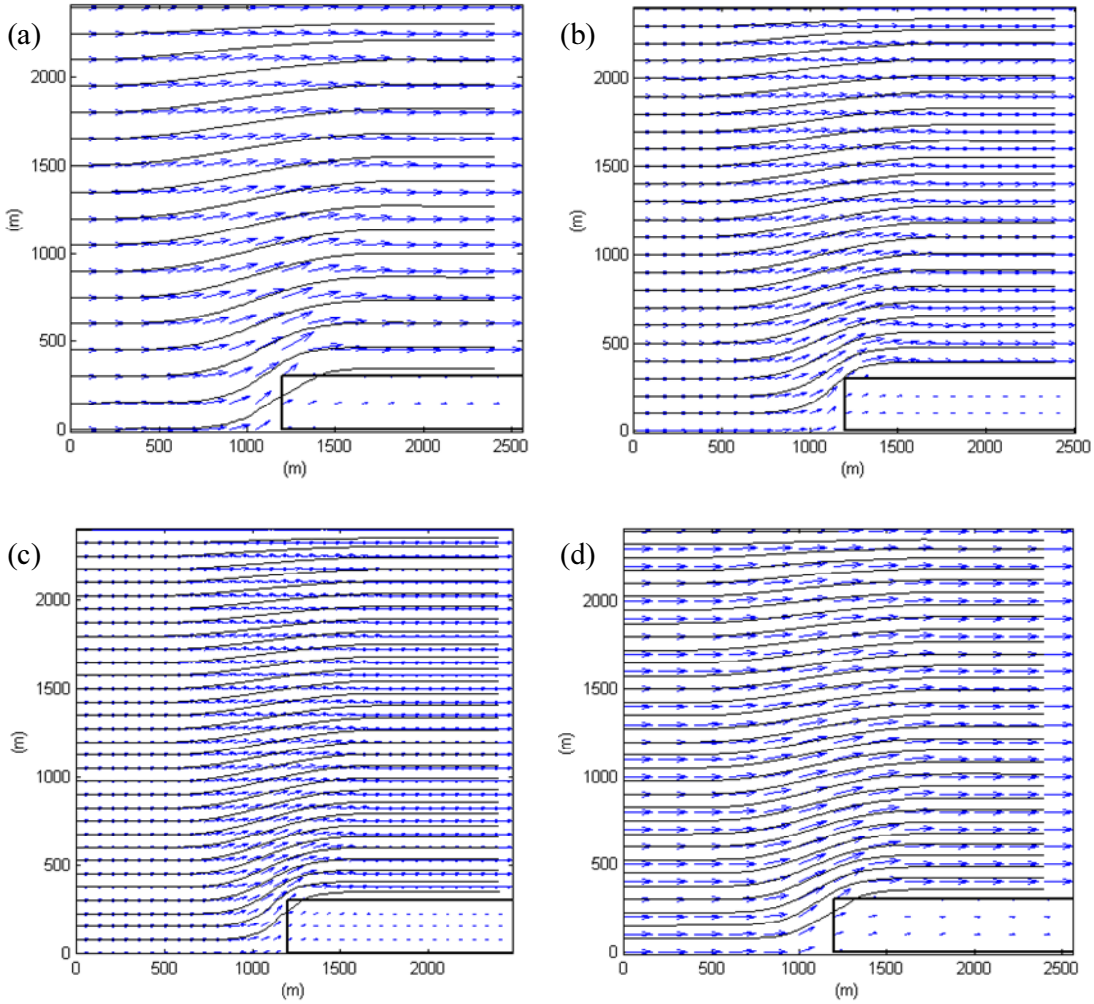

Figure C.3 Pipe-network model for flow around upstream half of farm (rectangle), with grid spacing of (a) 150 m x 150 m, (b) 100 m x 100 m (c) 75 m x 75 m (d) 200 m x 100 m; H = 1.0 along left boundary, H = 0.5 along right boundary, C_{bed} = 0.003, $C_f(farm)$ = 0.095.

The higher drag in the region of the farm induces a velocity reduction that can be detected upstream of the farm (Figure C.4(a)).

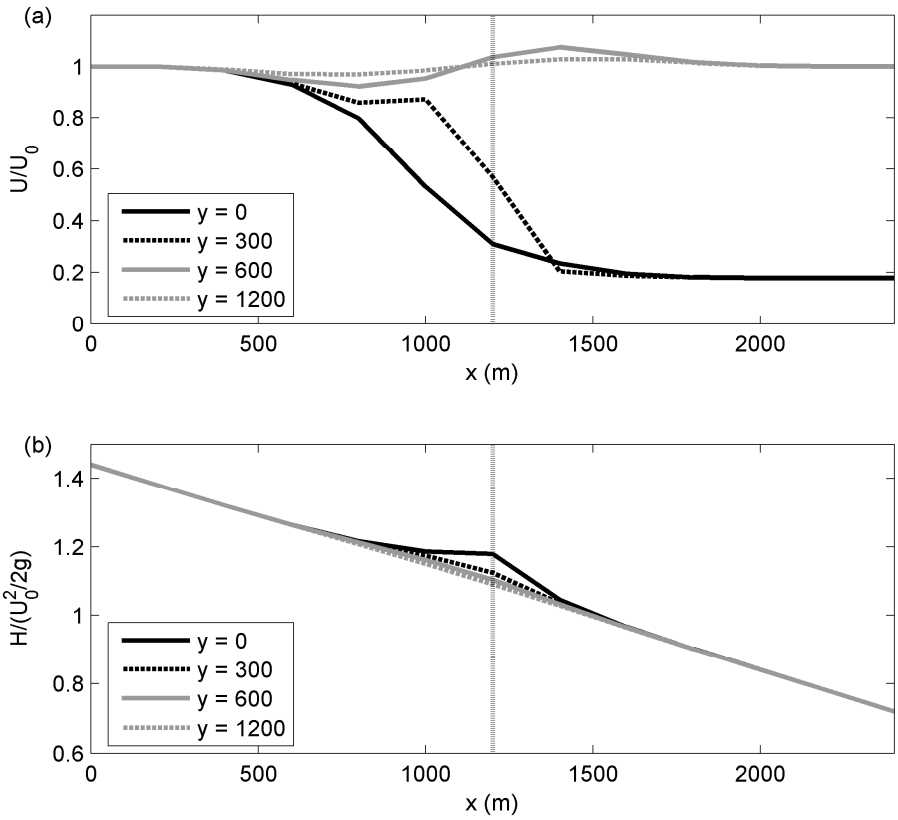

Figure C.4 (a) velocity and (b) pressure calculated from a 200 m x 100 m grid, with H = 1.0 along left boundary, H = 0.5 along right boundary, C_{bed} = 0.003, $C_f(farm)$ = 0.095. Velocity and pressure are calculated along the farm centreline (y = 0), the farm edge (y = 300), 300 m from the edge of the farm (y = 600), and 900 m from the edge of the farm (y = 1200). The upstream farm boundary is indicated by the vertical dotted line.

APPENDIX D CTD TRANSECTS THROUGH COLLINGWOOD MUSSEL FARM

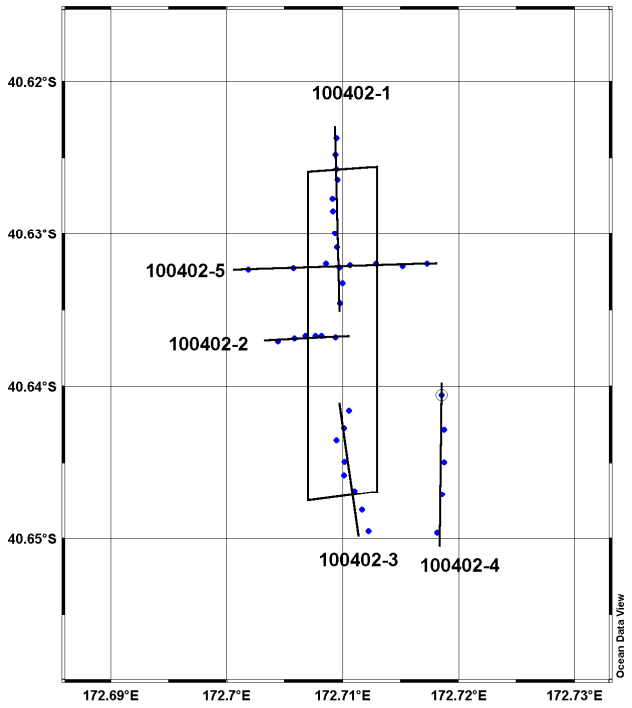

Figure D.1 Location of CTD profiles and transects, 10 April 2002.

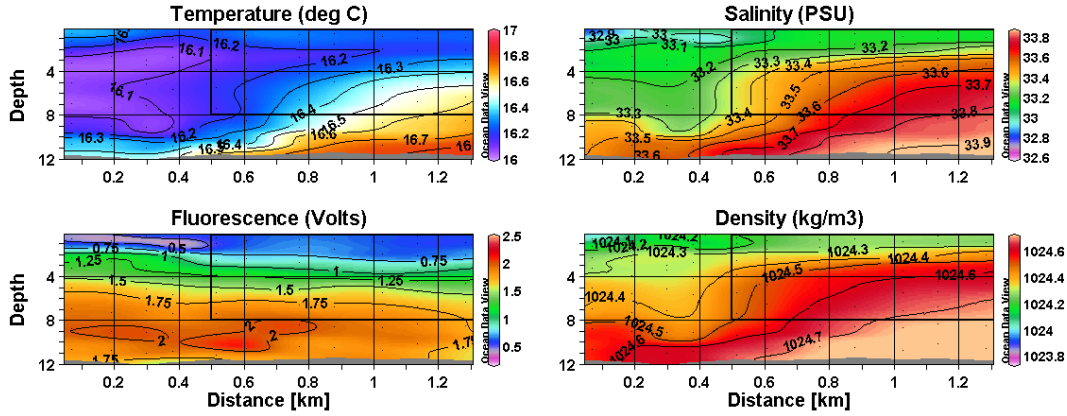

Figure D.2 Transect 100402-1

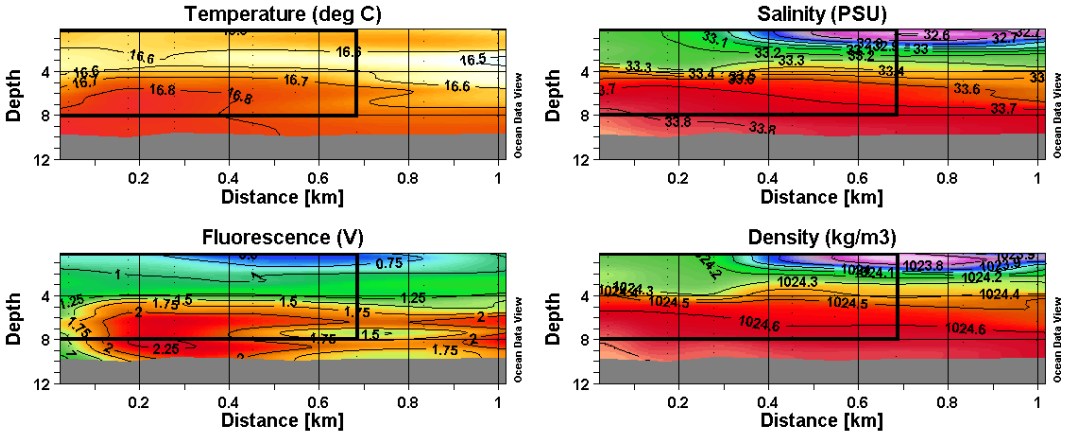

Figure D.3 Transect 100402-3

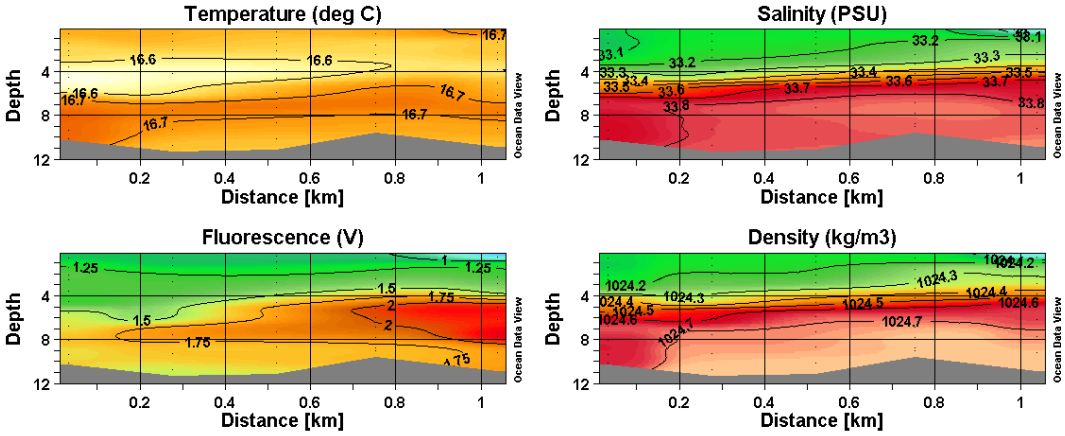

Figure D.4 Transect 100402-4

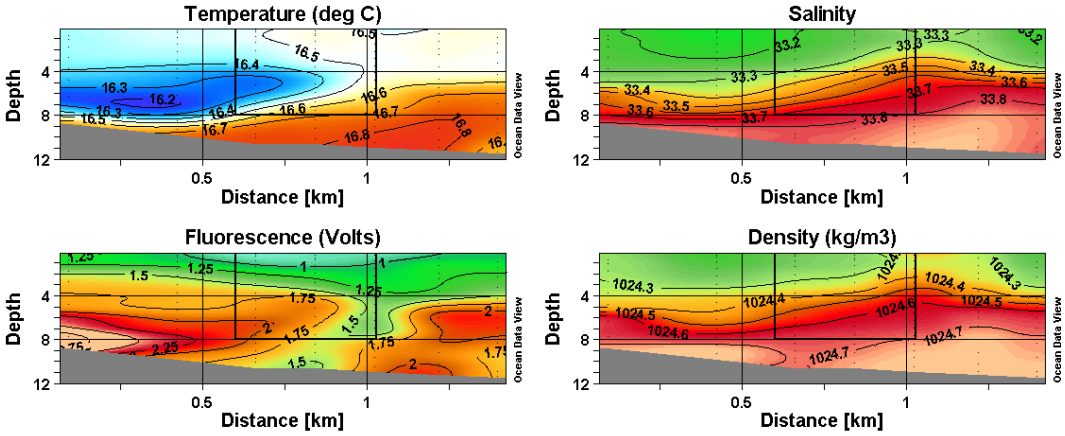

Figure D.5 Transect 100402-5,

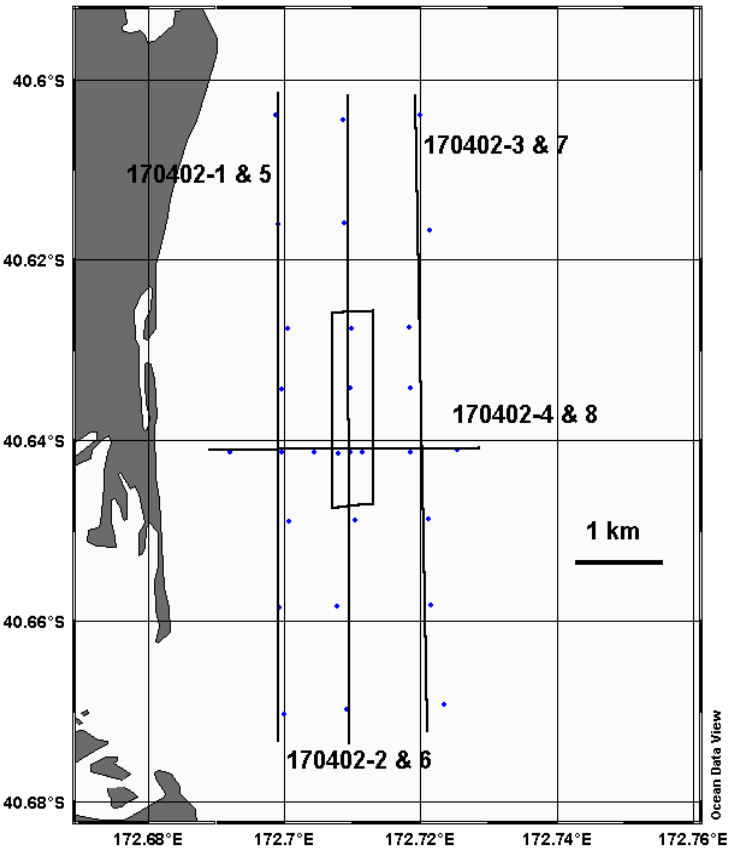

Figure D.6 Location of CTD transects 17 April 2002

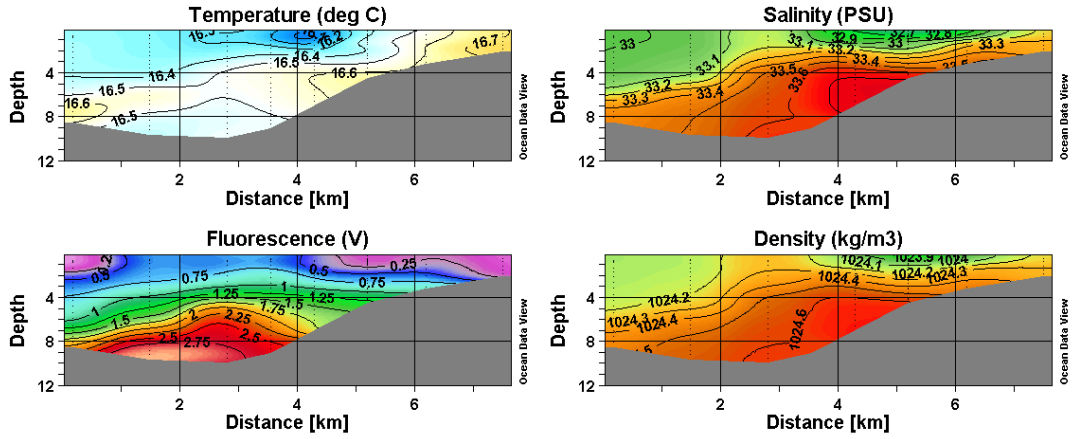

Figure D.7 Transect 170402-1.

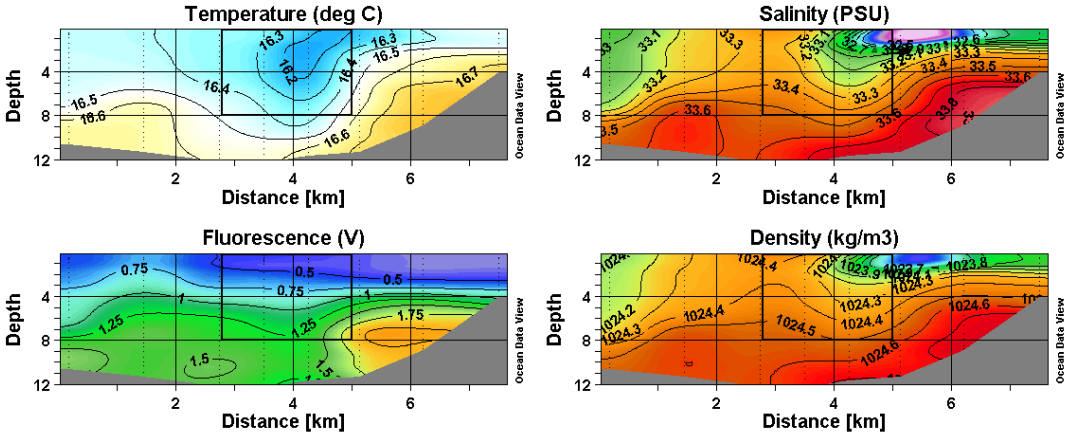

Figure D.8 Transect 170402-2.

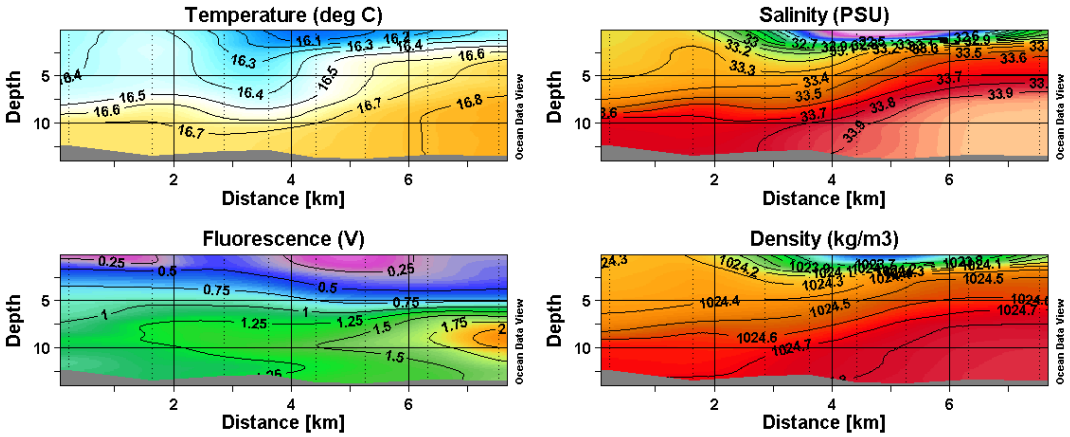

Figure D.9 Transect 170402-3.

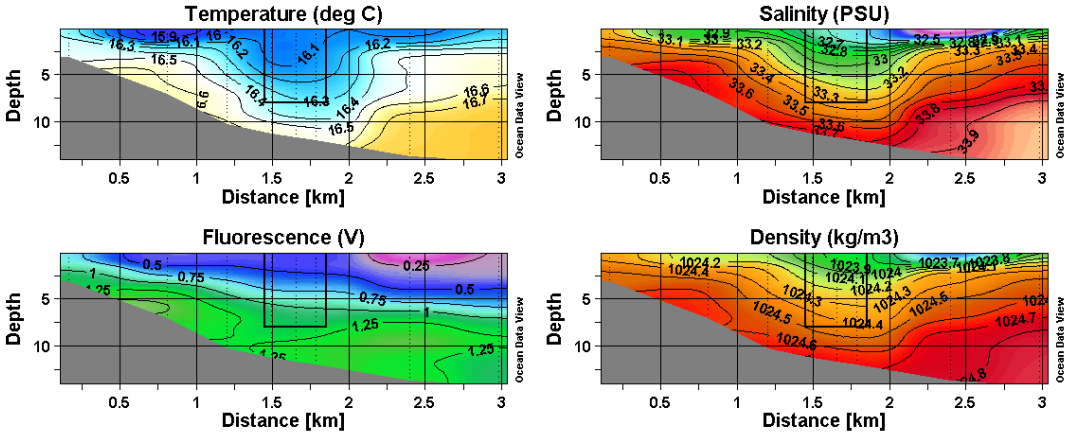

Figure D.10 Transect 170402-4.

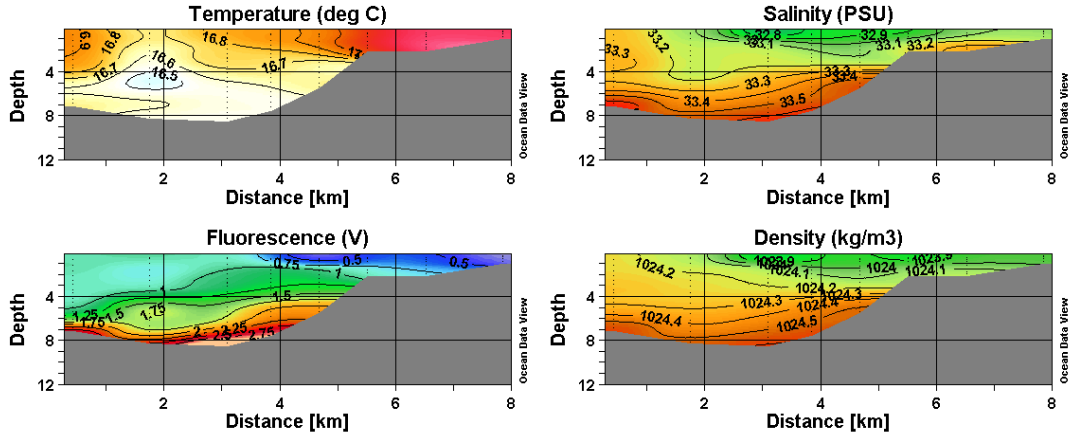

Figure D.11 Transect 170402-5.

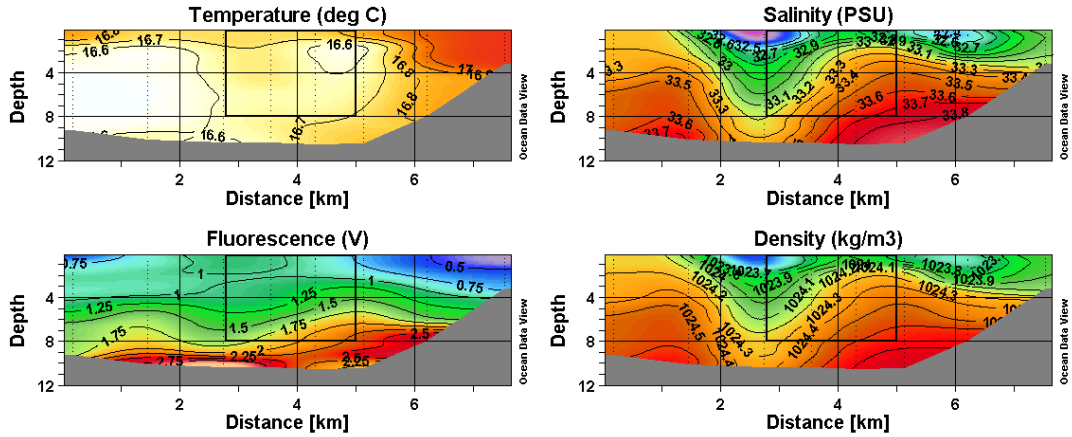

Figure D.12 Transect 170402-6.

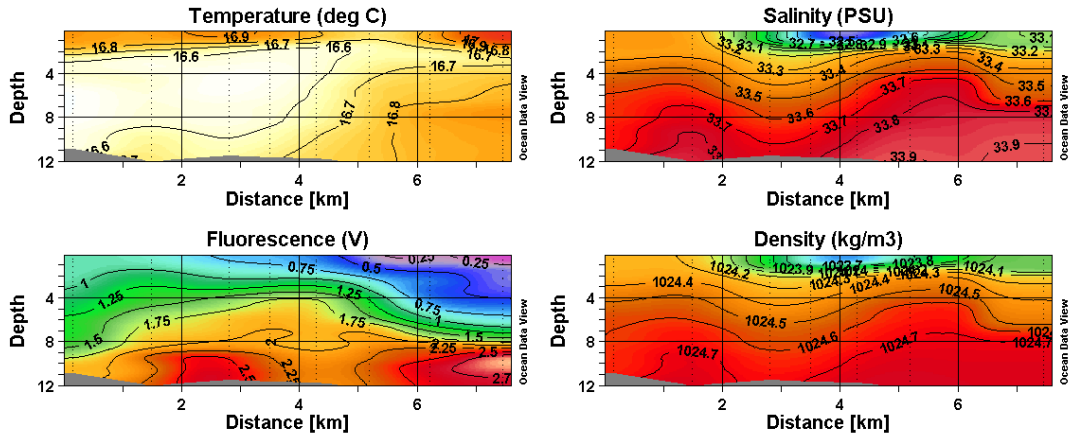

Figure D.13 Transect 170402-7.

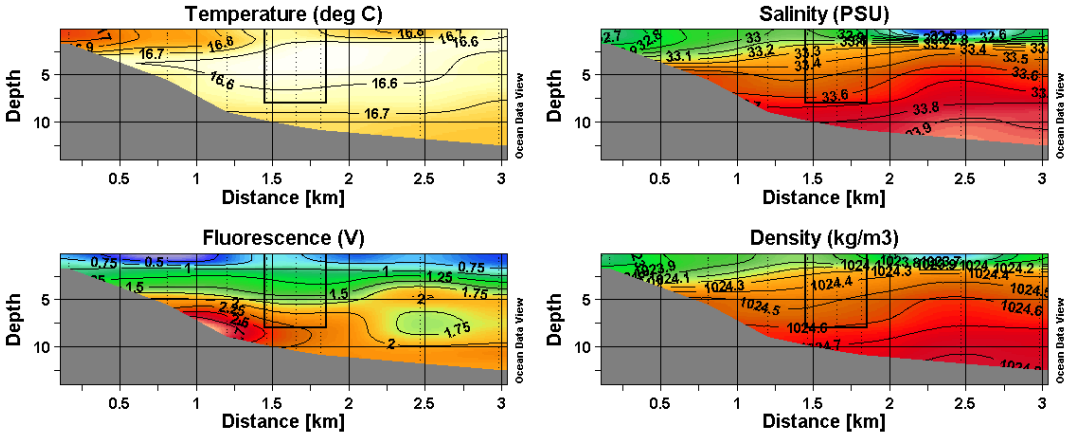

Figure D.14 Transect 170402-8.

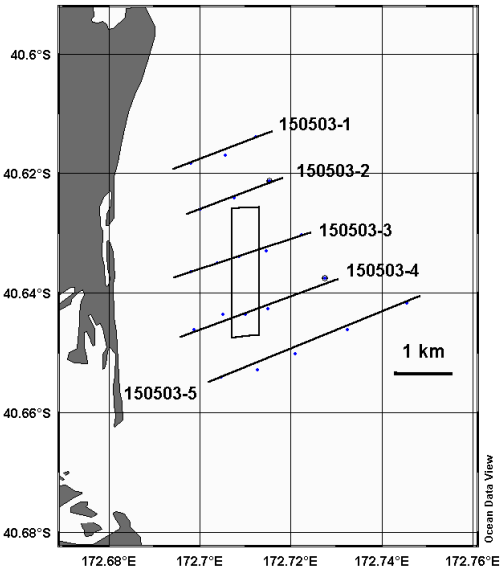

Figure D.15 Location of transects 15 May 2003

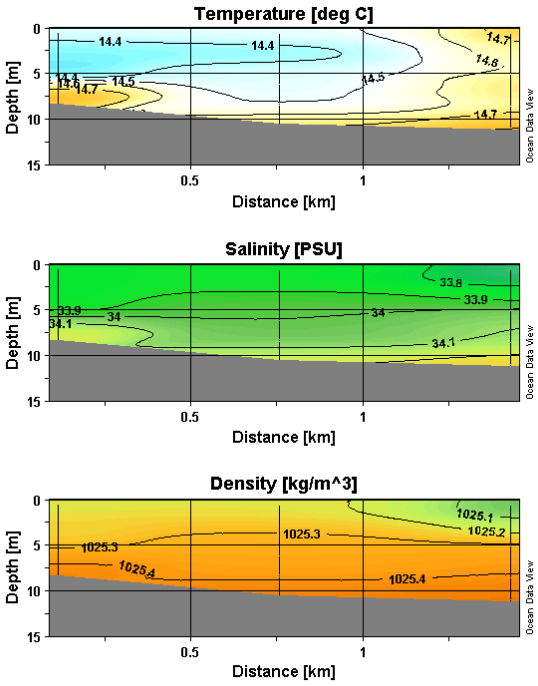

Figure D.16 Transect 150503-1

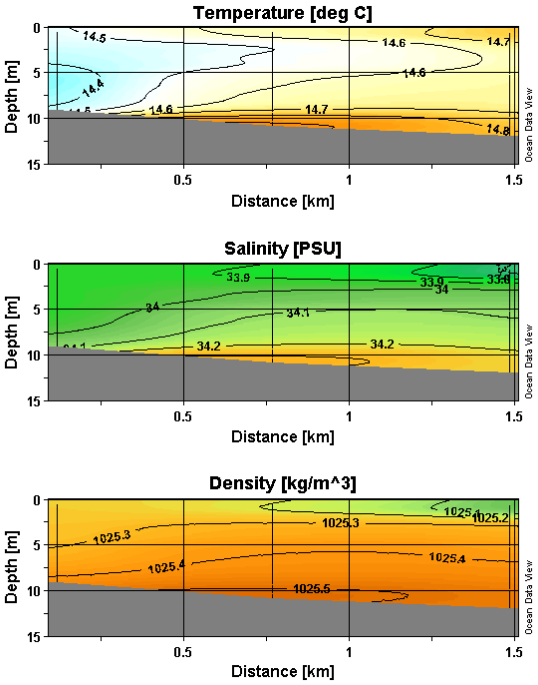

Figure D.17 Transect 150503-2

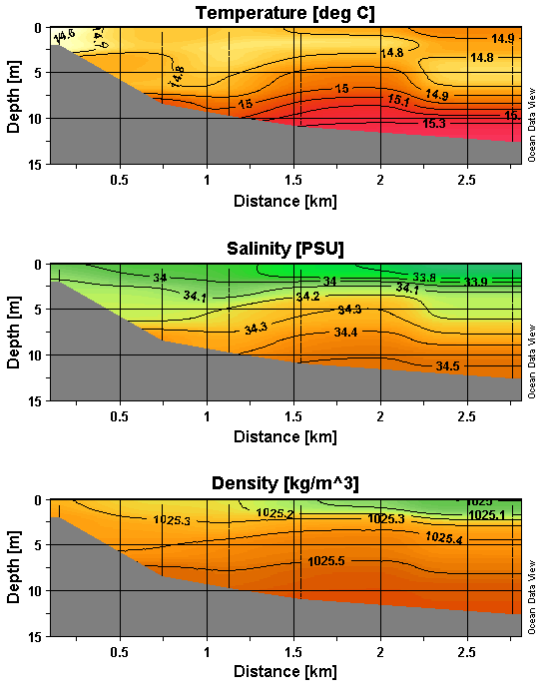

Figure D.19 Transect 150503-4

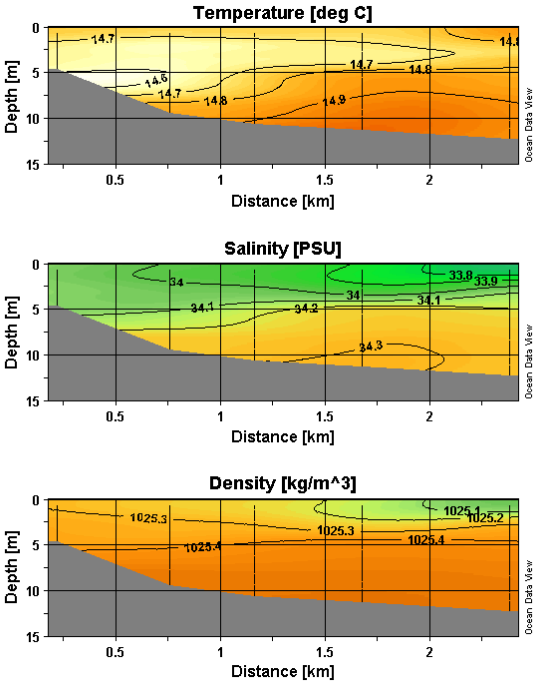

Figure D.18 Transect 150503-3

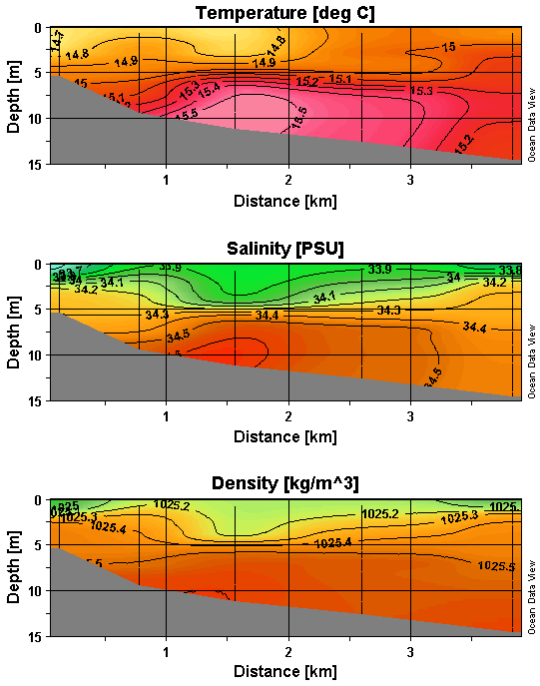

Figure D.20 Transect 150503-5

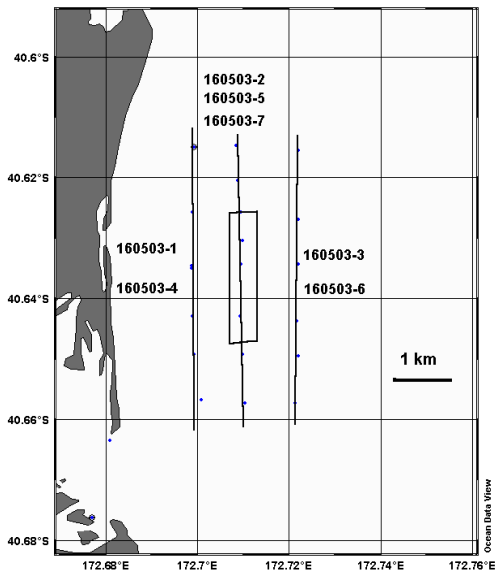

Figure D.21 Location of transects 16 May 2003.

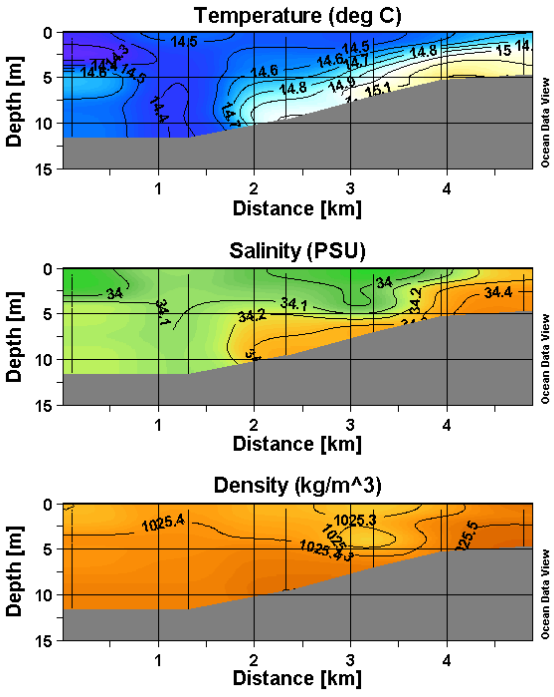

Figure D.22 Transect 160503-1

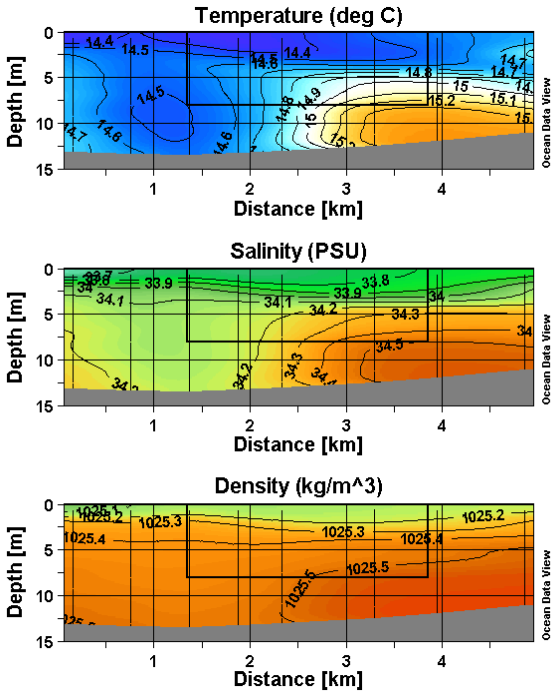

Figure D.23 Transect 160503-2

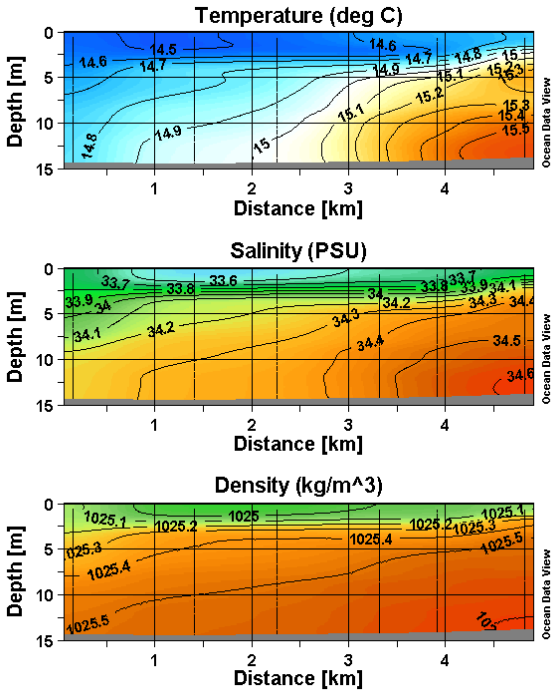

Figure D.24 Transect 160503-3

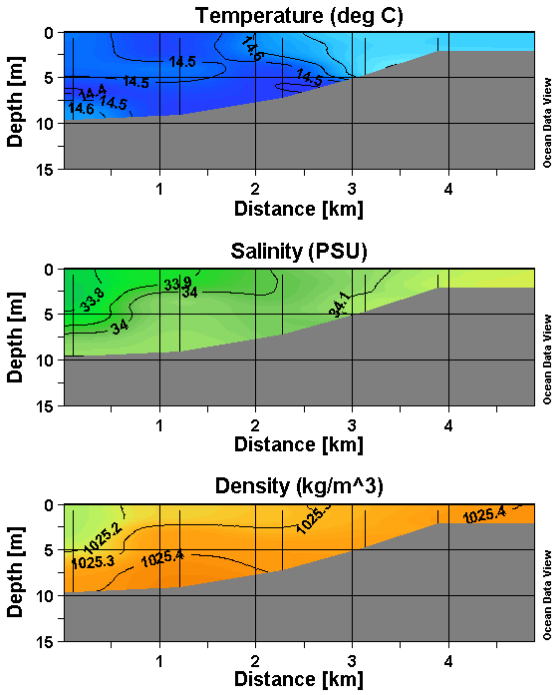

Figure D.25 Transect 160503-4.

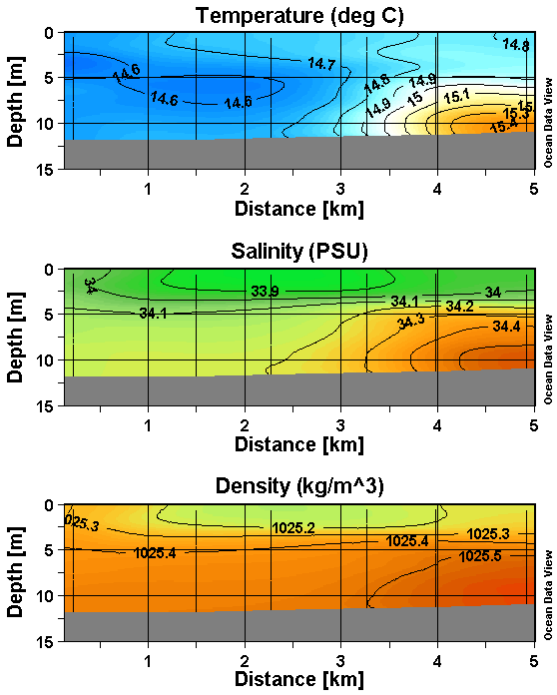

Figure D.27 Transect 160503-6.

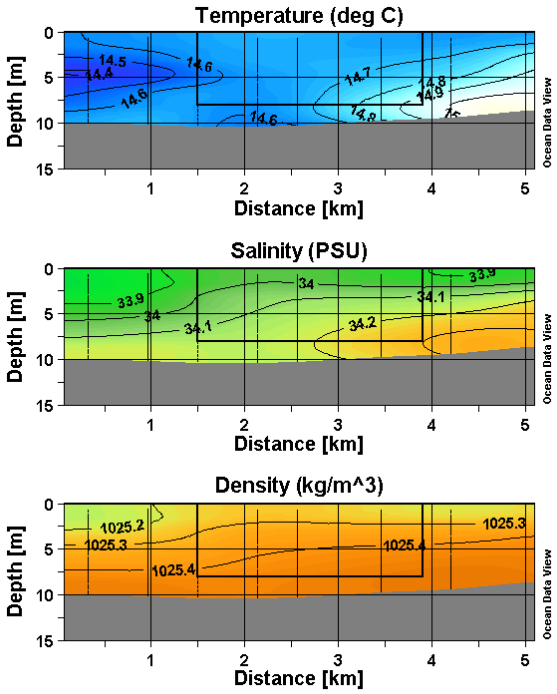

Figure D.26 Transect 160503-5.

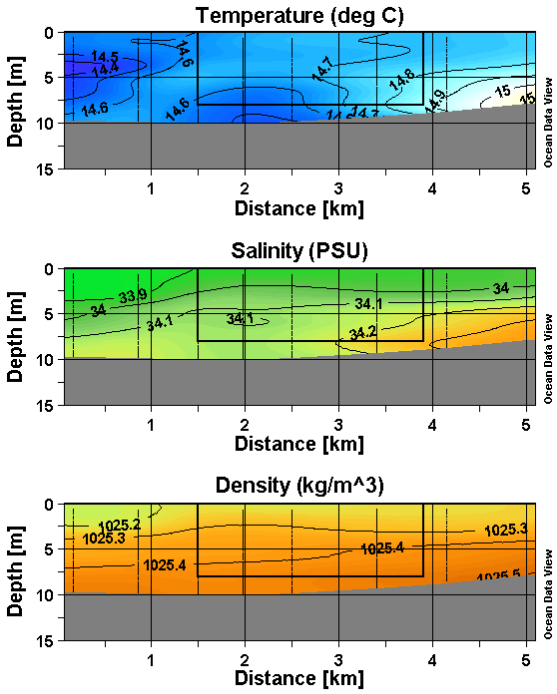

Figure D.28 Transect 160503-7.

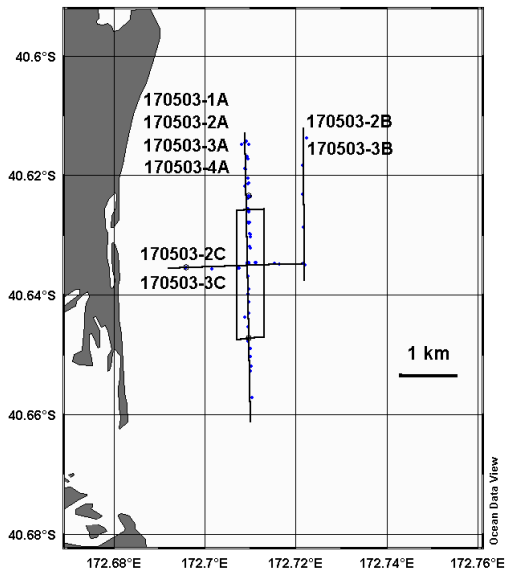

Figure D.29 Location of CTD transects 17 May 2003.

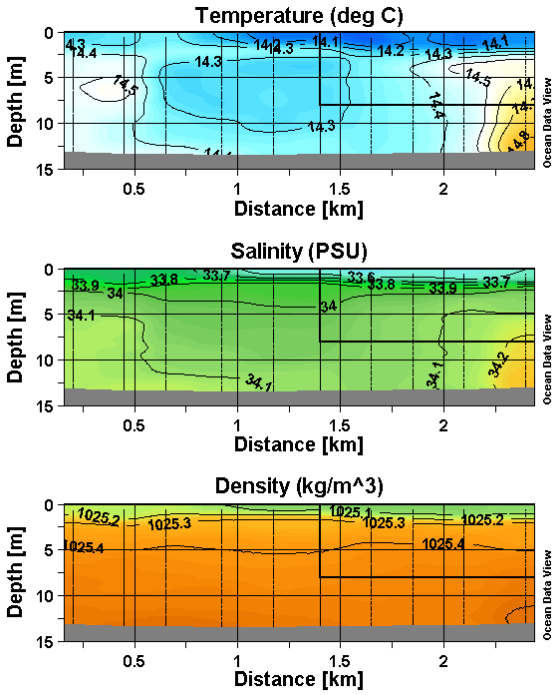

Figure D.31 Transect 170503-2A

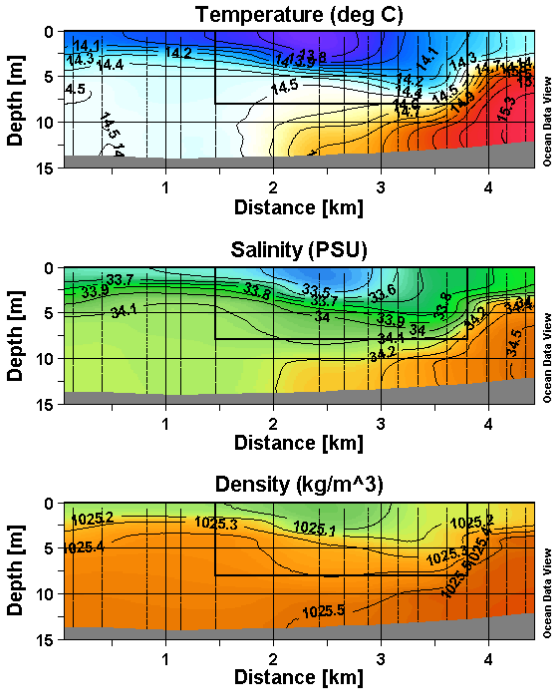

Figure D.30 Transect 170503-1A

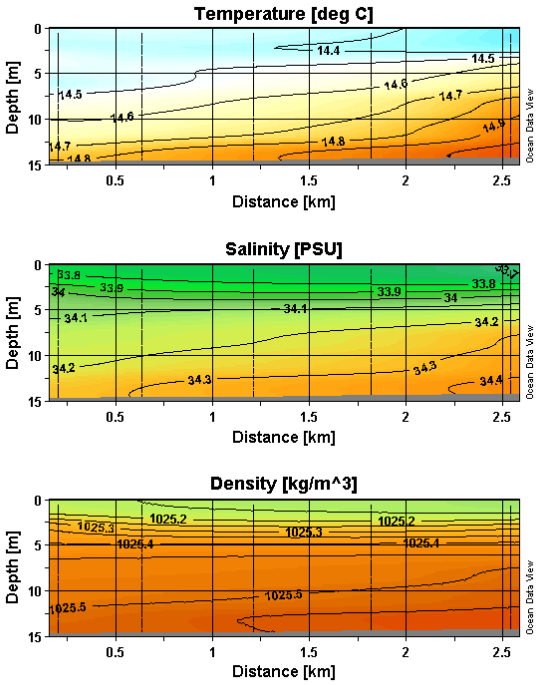

Figure D.32 Transect 170503-2B

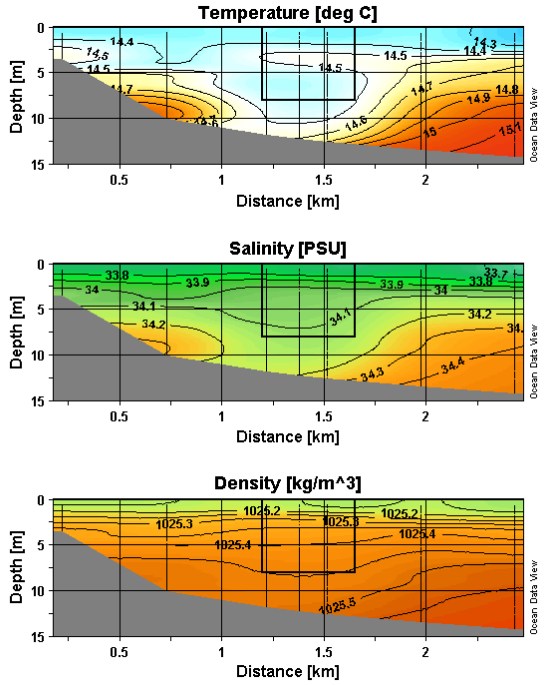

Figure D.33 Transect 170503-2C

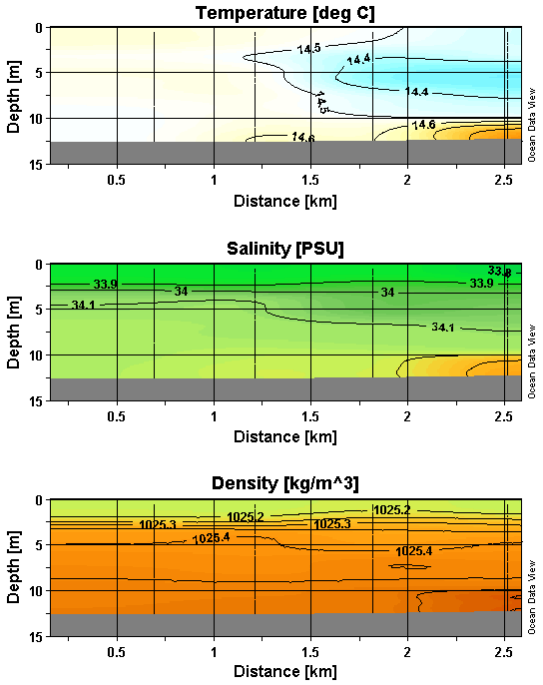

Figure D.35 Transect 170503-3B

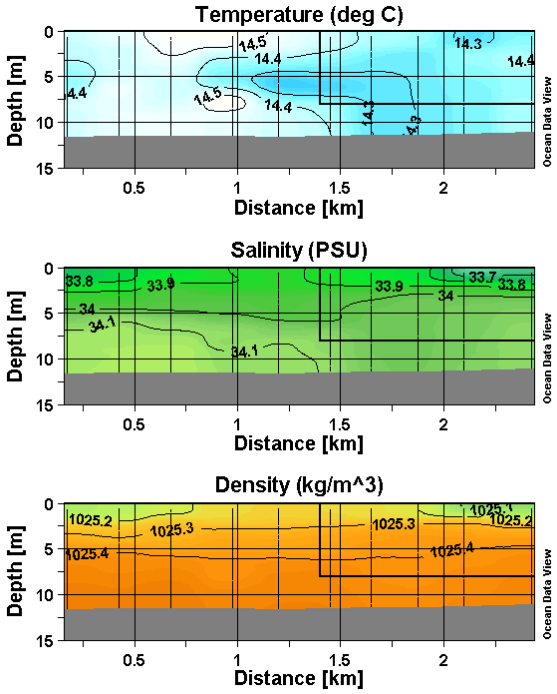

Figure D.34 Transect 170503-3A

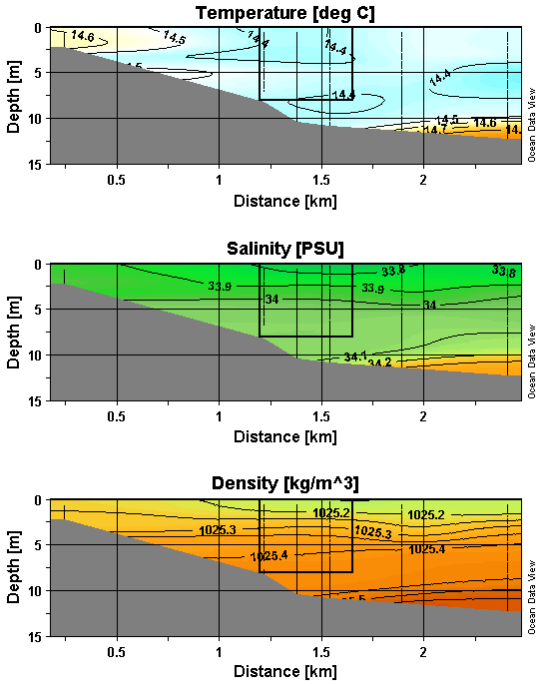

Figure D.36 Transect 170503-3C

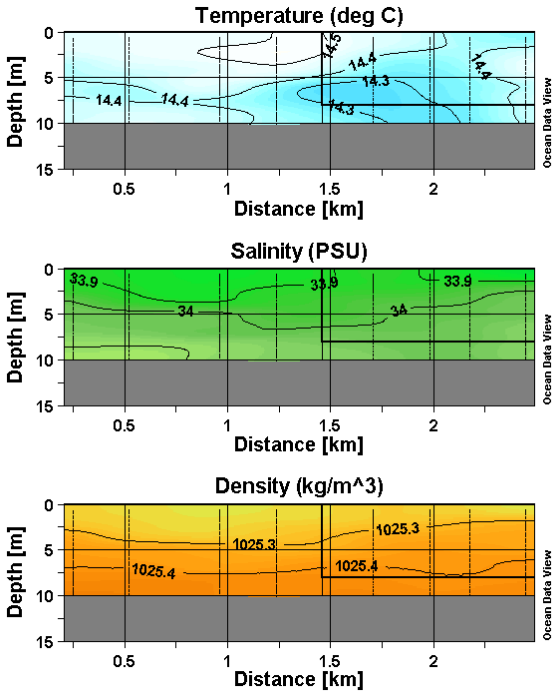

Figure D.37 Transect 170503-4A (closeup).

Plot settings:

10 & 17 April 2002

Temperature range 15.5-17.5 deg C

Salinity Range 32 – 24 PSU

Density Range 1023 - 1025 kg/m3

Fluorescence 0 – 3 V

15 - 17 May 2003

Temperature range 14-16 deg C

Salinity Range 33 – 35 PSU

Density Range 1024 - 1026 kg/m3

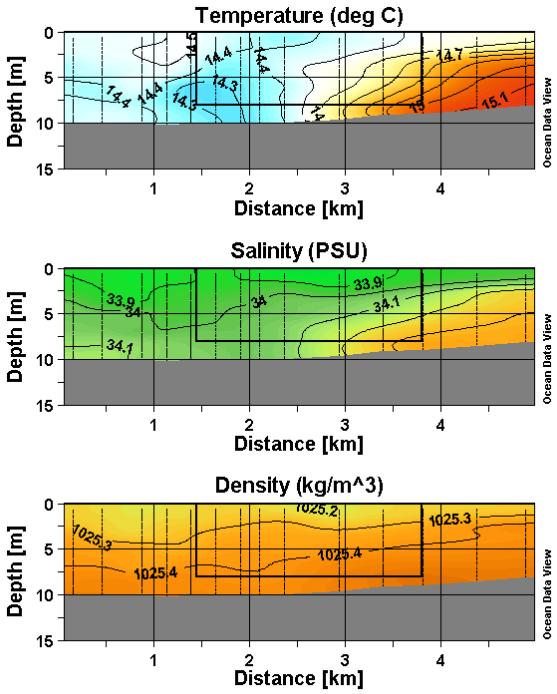

Figure D.38 Transect 170503-4A

APPENDIX E CONTROL VOLUME METHOD FOR CALCULATING DIAPYCNAL MIXING RATES

E.1 Background

Quantifying the degree of mixing caused by the farm is difficult due to the large spatial scale of the farm, the variability of water velocities and properties (particularly density), over the farm area, and the large changes in water level and velocities caused by the tide. Of particular interest here is the non-reversible mixing of different density fluids. In a closed system, non-reversible mixing of a fluid with a vertically stable stratification can be detected by an increase in potential energy. Stable, in this context, refers to a vertical distribution with density increasing with depth. However to determine mixing from changing potential energy, it is first necessary to separate potential energy changes into reversible and non-reversible components (Winters *et al* 1995).

Potential energy is calculated by integrating the density multiplied by the height above a datum over the volume of the fluid,

$$PE = \int_V \rho g z dV \,. \qquad \text{(E.1)}$$

For a closed body of fluid at rest and with stable stratification, vertical mixing results in raising the centre of mass and increasing the total potential energy. This is illustrated in Figure E.1 where a fluid of two layers with different density (with the higher density fluid at the bottom) is mixed, with a resulting increase of potential energy.

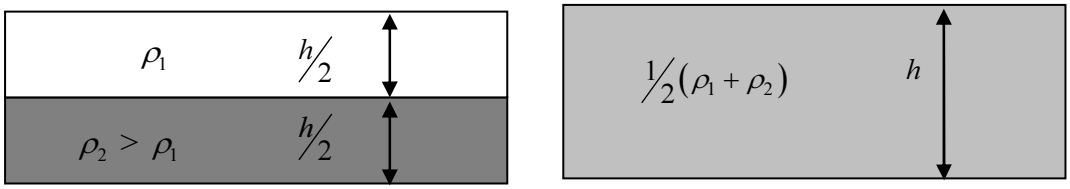

$$PE = (3\rho_1 + \rho_2)\frac{gAh^2}{8} \qquad PE = 2(\rho_1 + \rho_2)\frac{gAh^2}{8}$$

$$\Delta PE = (\rho_2 - \rho_1)\frac{gAh^2}{8}$$
$$\rho_2 > \rho_1 \rightarrow \Delta PE > 0$$

Figure E.1 Example of increasing potential energy caused by vertically mixing a stably stratified fluid in a box with depth *h* and cross-sectional area *A*.

The increase in potential energy caused by mixing is irreversible in that the fluid can not be returned to the original state by simple rearrangement. Reversible increases in potential energy occur if the isopycnals are inclined, such as through internal waves. For example, assuming a two layer fluid, the presence of a sloping interface gives an increase in potential energy above that of the fluid when the interface is horizontal. As Figure E.2 illustrates, the potential energy is increased when the interface of a two layer fluid is tilted.

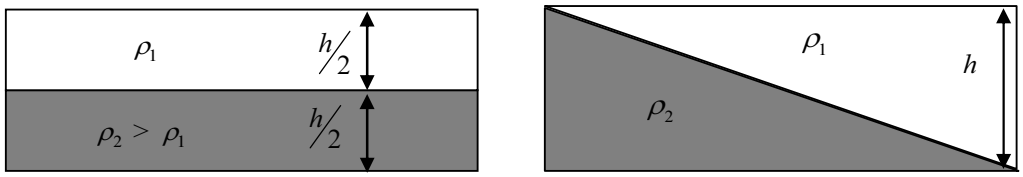

$$PE = \left(3\rho_1 + \rho_2\right)\frac{gAh^2}{8} \qquad PE = \left(2\rho_1 + \rho_2\right)\frac{gAh^2}{6}$$

$$\Delta PE = \left(\rho_2 - \rho_1\right)\frac{gAh^2}{24}$$
$$\rho_2 > \rho_1 \rightarrow \Delta PE > 0$$

Figure E.2 Example of increase in potential energy due to sloping isopycnals in box with depth *h* and cross-sectional area *A*.

There is a configuration for the distribution of fluid within a volume where the potential energy will be a minimum. This will occur when isopycnals are horizontal with the densest fluid at the greatest depth, and the least dense at the surface. This concept of a minimum or background potential energy provides a method of determining whether changes in density distributions are reversible (e.g. from sloping isopycnals) or irreversible (from diapycnal mixing). The minimum potential energy can be considered to be the background potential energy, with internal waves or horizontal gradients providing additional, reversible potential energy. For any body of fluid where the density distribution is known, the background (minimum possible) potential energy can be determined by rearranging the fluid so that isopycnals are horizontal and density increases with depth. Increases of background potential energy indicate that non reversible diapycnal (across isopycnals, or essentially vertical) mixing is occurring.

By redistributing the density distribution to give the minimum potential energy, a vertical density profile will be obtained (isopycnals will be horizontal) such that

$$\rho = \rho\left(z_*\right) \tag{E.2}$$

where z_* is the reference height at which a fluid element of density ρ will occur in the minimum potential energy density profile. Once this profile is found, the background or minimum potential energy can be calculated from

$$E_B = \int_V \rho g z_* dV \tag{E.3}$$

E.2 Control Volume Equations

In an open system, the fluxes of fluid through the boundaries may also result in an increase or decrease of the background potential energy in addition to any mixing. For such a system it is necessary to use a control volume approach to account for fluxes of background energy through the boundaries, as well as internal storage and mixing. This control volume approach was used with field data to attempt to quantify the degree of diapycnal mixing induced by the farm. A control volume was constructed by measuring velocities (with ADCP) and density distributions (with BIOFISH) around the perimeter of the Collingwood mussel farm, forming a rectangular control volume. Before presenting the field data, the equations for the control volume are developed below. These equations are an expansion of the methodology of Winters *et al.* (1995), who presented a method of calculating background potential energy changes in a closed system and applied it to the results of a direct numerical simulation.

The control volume equation for continuity of background potential energy (Winters *et al.*, 1995) is

$$\frac{d}{dt} E_b = \frac{d}{dt} \int_V g z_*(\mathbf{x},t) \rho(\mathbf{x},t) dV \tag{E.4}$$

Winters *et al*. give an expression for calculating the reference height z_* for a fluid element of density ρ in a control volume of uniform depth and constant plan-form area A. However for a non-uniform depth and variable area, it is first necessary to obtain the dependence of volume V with depth z

$$V(z) = \int_{z_0}^{z} A(z) dz \tag{E.5}$$

$A(z)$ is the area inside the depth contour with elevation z. The cumulative volume distribution with decreasing density is then calculated by integrating

$$V_*(\rho) = \int_{V'} H\big(\rho(\mathbf{x}',t) - \rho(\mathbf{x},t)\big) dV' \tag{E.6}$$

where H is the Heaviside step function

$$H\big(\rho(\mathbf{x},t) - \rho(\mathbf{x}_0,t)\big) = \begin{cases} 0, & \rho(\mathbf{x},t) < \rho(\mathbf{x}_0,t) \\ \frac{1}{2}, & \rho(\mathbf{x},t) = \rho(\mathbf{x}_0,t) \\ 1, & \rho(\mathbf{x},t) > \rho(\mathbf{x}_0,t) \end{cases} \tag{E.7}$$

Equation (E.6) calculates the volume of fluid with density greater than ρ. The reference height z_* is a function of density, so may be obtained by first inverting (E.5) to find $z(V)$, the depth at which the volume beneath is V, and then using the cumulative density distribution from (E.6) to obtain

$$z_*(\rho) = z(V_*) \tag{E.8}$$

Using Leibnitz's formulation for differentiating a volume integral (e.g. Bird *et al*. (1960)), the control volume equation can be expressed as a volume integral and a surface integral

$$\frac{d}{dt}E_b = \int_V g\left[z_* \frac{\partial \rho}{\partial t} + \rho \frac{\partial z_*}{\partial t}\right] dV + g \oint \rho z_* \mathbf{u}_\mathbf{s} \cdot \hat{n} dS \,. \tag{E.9}$$

The last term on the right of equation (E.9) is a surface flux arising from the changing size of the control volume. This term is not included by Winters *et al.* as they assume a constant control volume size. The velocity $\mathbf{u}_\mathbf{s}$ in this term is the velocity of the control volume surface in the direction of the outward-pointing normal vector $\hat{n}$ (i.e. the rate that the control volume is expanding or contracting). This term may also be neglected if the control volume is defined in such a manner that there is no control volume boundary movement. For the field experiments, control volumes are defined as rectangular boxes with vertical sides, bounded by the sea floor at the bottom, and extending above the free-surface as shown in Figure E.3. There are therefore no fluxes through the top or bottom of the control volume.

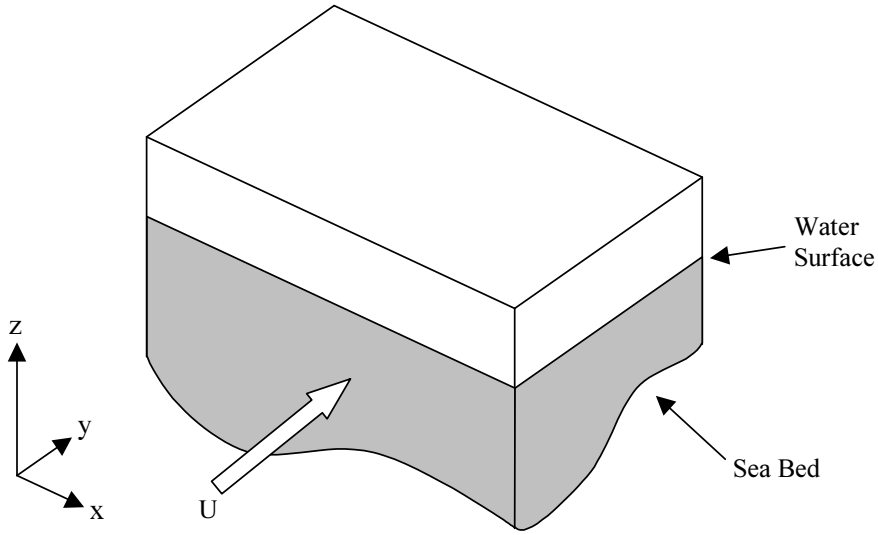

Figure E.3 Control Volume

For a fixed control volume in which the total mass is conserved (e.g. Winters *et al.*), it can be deduced that

$$g \int_V \rho \frac{\partial z_*}{\partial t} dV = 0 \,. \tag{E.10}$$

However, if the mass inside is permitted to change (through mass flux), this integral is non-zero and must be evaluated. It is therefore retained in the equations presented here.

For a Boussinesq fluid, conservation of mass gives,

$$\frac{\partial}{\partial t}\rho + \mathbf{u}\cdot\nabla\rho = \kappa\nabla^2\rho\,, \tag{E.11}$$

where κ is the molecular diffusivity. The rate of change of background energy can now be expressed as

$$\frac{d}{dt}E_b = \int_V g z_* \left\{-\mathbf{u}\cdot\nabla\rho + \kappa\nabla^2\rho\right\} dV + g\int_V \rho\frac{\partial z_*}{\partial t}dV \tag{E.12}$$

Following Winters *et al.*, as the spatial dependence of z_* is determined through the density distribution $\rho(\mathrm{x},t)$, it is possible to write

$$z_*\nabla\rho = \nabla\psi \quad \text{where } \psi = \int^{\rho} z_*(\hat{\rho})d\hat{\rho}\,. \tag{E.13}$$

It then follows that the rate of change of E_b can be written in terms of volume and surface integrals in the following form

$$\frac{d}{dt}E_b = -g\oint\psi\mathbf{u}\cdot\hat{n}dS + \kappa g\int_V z_*\nabla^2\rho dV + g\int_V \rho\frac{\partial z_*}{\partial t}dV\,. \tag{E.14}$$

The final step, using $\nabla z_* = \left(dz_*/d\rho\right)\nabla\rho$ gives

$$\frac{d}{dt}E_b = \underbrace{-g\oint\psi\mathbf{u}\cdot\hat{n}dS}_{advection} + \underbrace{\kappa g\oint z_*\nabla\rho\cdot\hat{n}dS}_{diffusion} + \underbrace{\kappa g\int_V -\frac{dz_*}{d\rho}\left|\nabla\rho\right|^2 dV}_{\Phi_d} + \underbrace{g\int_V \rho\frac{\partial z_*}{\partial t}dV}_{changing\ mass} \tag{E.15}$$

The first term on the right gives a rate of flux of E_b through the control volume sides. The second term is the diffusion of background potential energy through the control volume sides. For closed systems, the first, second and fourth terms are all zero. The third term gives the rate of change of E_b within the control volume due to diapycnal mixing. As $\left(dz_*/d\rho\right) < 0$ for a stable system, the mixing always leads to an increase in E_b. The rate of mixing within the control volume can be calculated from

$$\Phi_d = \frac{d}{dt}E_b \underbrace{+g\oint\psi\mathbf{u}\cdot\hat{n}dS}_{advection} \underbrace{-\kappa g\oint z_*\nabla\rho\cdot\hat{n}dS}_{diffusion} \underbrace{-g\int_V \rho\frac{\partial z_*}{\partial t}dV}_{changing\ mass}\,. \tag{E.16}$$

E.3 Practicalities of calculating the energy budget terms

The rate of mixing from equation (E.16) requires instantaneous velocity distributions, and also the molecular diffusion through the control volume boundaries. Winters *et al.* apply these equations to a direct numerical simulation, so are able to use instantaneous velocities in the advection term. With field based measurements, it was not feasible to measure instantaneous (turbulent) velocities due to both the time required to circle the farm, and the inherent spatial averaging of velocities from using an ADCP (due to the sampling volume). Instead, mean velocities will be used for the surface flux terms in equation (E.16), and it is assumed that the spatial averaging from the ADCP combined with the averaging caused by integrating velocities over the surface of the control volume is sufficient to approximate the mean advection.

In addition, a continuous record of density inside the control volume was not obtained during the field measurements. Instead, density profiles were measured at the start and end of the control volume survey. Therefore, the volume integral in equation (E.16) accounting for changes in mass within the control volume was estimated by averaging the integral evaluated at the start and end of the survey. This term contains the time-derivative of the reference depth z_*. An estimate of this derivative was obtained from comparison of the reference depth profiles calculated at the start and end of the survey.

$$\frac{\partial z_*}{\partial t} \approx \frac{z_*(\rho(t_2)) - z_*(\rho(t_1))}{t_2 - t_1} \tag{E.17}$$

Although this derivative represents the rate of change at the mid-point of the survey, it was used as an estimate of the rate of change at t_1 and t_2.

$$\underbrace{g\int_V \rho \frac{\partial z_*}{\partial t} dV}_{changing\ mass} \approx \frac{g}{2}\left[\int_{V_1} \rho(t_1)\frac{\partial z_*}{\partial t} dV + \int_{V_2} \rho(t_2)\frac{\partial z_*}{\partial t} dV\right] \tag{E.18}$$

The diffusion term requires calculating density gradients normal to the surface of the control volume. Only horizontal density gradients are important as diffusion occurs through the sides of the control volume, but not through the bottom (the sea bed) or the top (the free surface). As the small scale density gradients responsible for molecular diffusion are not measured, diffusion must be parameterised using a turbulent diffusivity and mean density gradients.

$$\underbrace{\kappa g \iint z_* \nabla\rho \cdot \hat{n} dS}_{diffusion} = \kappa g \iint z_* \left(\frac{\partial \rho}{\partial x}\hat{i} + \frac{\partial \rho}{\partial y}\hat{j} + \frac{\partial \rho}{\partial z}\hat{k}\right) \cdot \hat{n} dS\,. \tag{E.19}$$

There is still a problem in that density profiles were measured along the control volume surface, allowing calculation of density gradients parallel to the control volume surface, but not normal to the surface.

Density gradients in the horizontal were small however, and are likely to be similar both normal and parallel to the control volume surface. Mean density gradients were typically much less than ~ 0.1 kg m^3 per 10 m, or 0.01 kg m^{-3} per m. The turbulent eddy diffusivity could also only be obtained by estimation. From Fischer *et al.* (1979), eddy diffusivity in open channels can be estimated as

$$\kappa_t = 0.15 H \sqrt{\frac{C_f}{2}} U \,, \tag{E.20}$$

where H is the water depth, U the mean velocity, and C_f the bed friction coefficient. With typical scales for the depth of ~ 10 m, and velocity ~ 0.1 m s^{-1}, and using the bed friction coefficient calculated in the previous chapter of 0.003, the eddy diffusivity was estimated as approximately $\kappa_t \sim 0.0058$. Even with these estimates, the diffusion term could not be accurately calculated for the control volume. The relative order of magnitude of the diffusion term in comparison to the advection term may be estimated using scales for the density and velocity.

Assuming density gradients of order 0.01 kg.m^{-3} per m, and a control volume with sides 2.5 km long and 10 m deep, densities ~ 1025 kg.m^{-3}, and approximating z_* with z, the diffusion term along one face of the control volume will be

$$\begin{aligned} \underbrace{\kappa g \iint z_* \nabla \rho \cdot \hat{n} dS}_{diffusion} &\approx 0.0058 \times 2500 \times g \times \int_0^{10} 0.01 z dz \\ &\approx 71 \text{ J s}^{-1} \end{aligned} \,. \tag{E.21}$$

In comparison, the advection term, with typical velocities of order 0.1 m s^{-1}, is significantly larger. The term ψ in equation (E.13) can be estimated as being of magnitude $\sim \rho h_s$ where h_s is the free surface elevation. Therefore, the flux of background potential energy through one side of the control volume will be of order

$$\begin{aligned} \underbrace{g \iint \psi \mathbf{u} \cdot \hat{n} dS}_{advection} &\approx 2500 \times g \times \int_0^{10} 1025 \times 10 \times 0.1 dz \\ &\approx 1.3 \times 10^9 \text{ J s}^{-1} \end{aligned} \,. \tag{E.22}$$

The diffusion is integrated around the control volume surface so that a net diffusion is calculated. Therefore the diffusion term may be assumed negligible in comparison to the mean flux of background potential energy through the control volume.

The rate of change of background potential energy within the control volume was calculated from density profiles within the farm before (t_0) and after (t_1) the survey of velocities around the perimeter.

$$\frac{d}{dt}E_b = \frac{\int_V \rho(t_2)gz_*(t_2)dV(t_2) - \int_V \rho(t_1)gz_*(t_1)dV(t_1)}{t_2 - t_1}. \qquad \text{(E.23)}$$

E.4 Field Methodology

Water velocities were measured along the perimeter of a rectangular control volume, or flux box, containing the farm with a boat-mounted ADCP. At the same time, water column properties (temperature and salinity) where measured using a BIOFISH CTD profiler. This provided a record of velocity and water density profiles around the farm perimeter. A total of twelve circuits were made of the farm during the period 2-9 August 2002. An example of water velocities recorded around the farm is shown in Figure E.4.

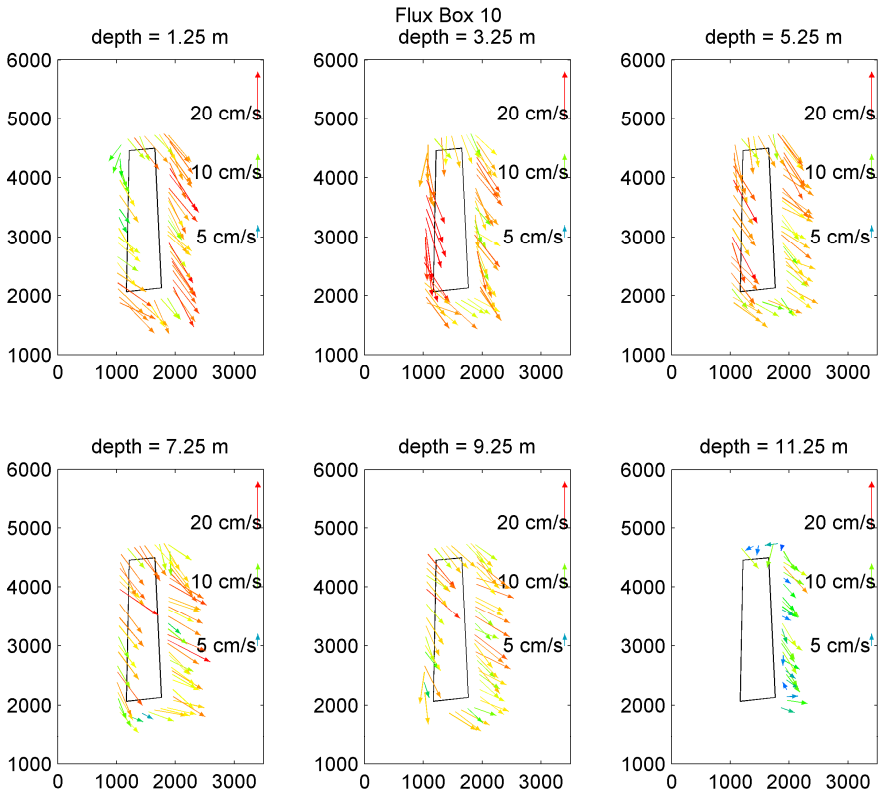

Figure E.4 Velocities recorded for flux box 10.

Velocity data from the ADCP were averaged over 30 second intervals, with each 30 second average providing a profile of velocity with a vertical resolution of 0.5 m. Water column properties (salinity, temperature and density) obtained from the BIOFISH were also collated into 0.5 m vertical bins, and averaged horizontally to obtain values at the locations of the ADCP profiles. The horizontal distance between profiles depended on the speed of the boat, but averaged 70 m.

At the start and end of the flux box survey, water column properties were recorded at 9 stations to allow calculation of the volume integral terms and the change in background potential within the flux box. One of stations was sited in the middle of the flux box, and the other 8 around the perimeter. The locations of the fixed stations in relation to the farm boundaries and one of the flux boxes are shown in Figure E.5.

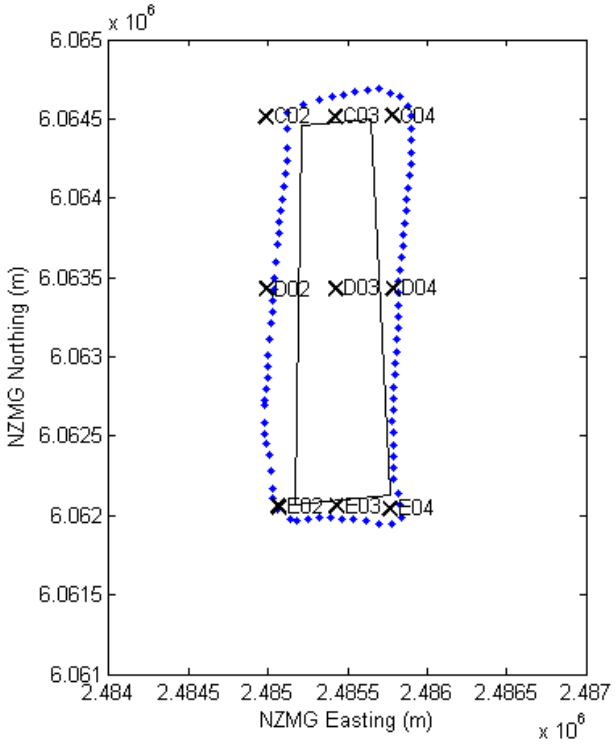

Figure E.5 Location of velocity and water column profiles for flux box 1, and the position of the fixed stations where profiles were recorded before and after the flux box survey.

The rectangular flux boxes were divided into 9 areas, with divisions midway between each station. Each station represented water properties for part of the flux box (Figure E.6). The contributions of each station to the total surface area of the flux box were:

- C02, C04, E02 and E04 = area/16,
- C03, D02, D04 and E03 = area/8
- D03 = area/4.

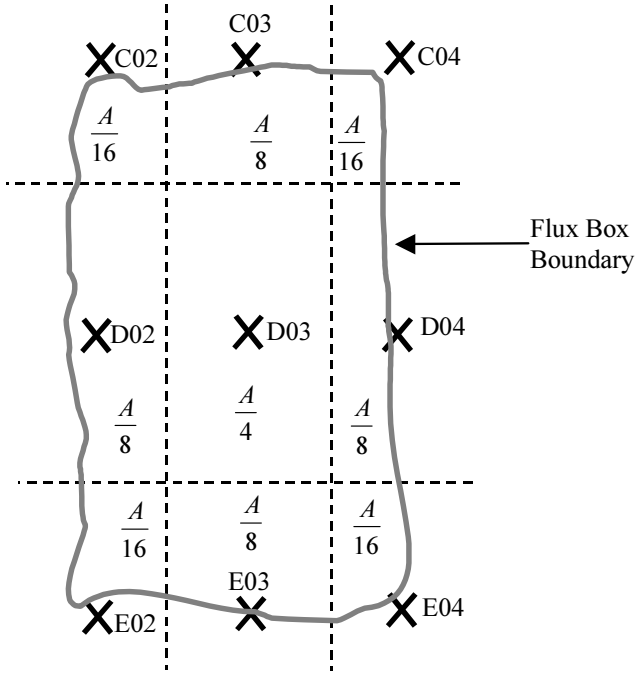

Figure E.6 Division of flux box surface area by stations.

Density profiles were calculated at each station from salinity and temperature for the initial and final casts, e.g. Figure E.7(a). To allow potential energy to be calculated, casts taken before the flux box circuit were referenced to a water surface elevation of 15 m above an arbitrary datum. The tidal increase or decrease in water depth between measuring the initial and final casts was recorded by a DOBIE wave gauge. Casts taken after the flux box circuit were adjusted so that the height of the water surface was increased or decreased by the tidal variation with respect to the chosen datum. As casts before and after may have been measured in slightly different locations, there was typically a small variation in the recorded sea-bed height above datum at a station. As this would result in a volume error, the height of the sea-bed at each station was specified by the measured water depth of the initial (before) casts, and the profiles from the final casts (at the end of the circuit) extrapolated or truncated accordingly.

The vertical profiles were divided into 0.5 m vertical segments. Each segment had a representative density, and the vertical thickness of the segment multiplied by the appropriate surface area for that cast gave the volume of fluid with that density (sub-volume) within the control volume. The accumulated volume with depth, Figure E.7(b), accounts for the sea-bed slope across the site.

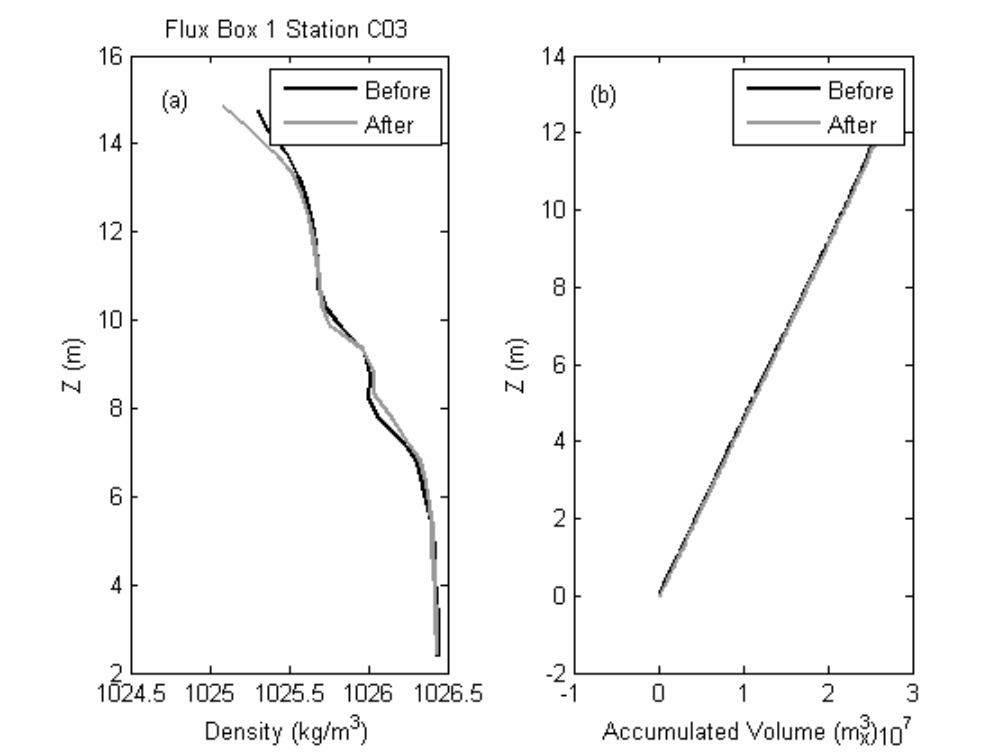

Figure E.7 (a) an example density distribution at a fixed station, and (b) accumulated flux box volume with height above bed (flux box 1).

To obtain the minimum potential energy distribution, sub-volumes were reordered by decreasing density to obtain a distribution of accumulated volume versus density, e.g. Figure E.8(a). Using the reordered volume/density profiles, the flux box volume was organised so that the densest fluid was at the bottom, and the least dense at the surface. This density distribution (with horizontal isopycnals) satisfied the conditions for minimum potential energy. Reference depths for the minimum potential energy density distribution, $z_*(\rho)$, were obtained by matching the distributions of volume and density, Figure E.7(b), with volume and depth, Figure E.8(a).

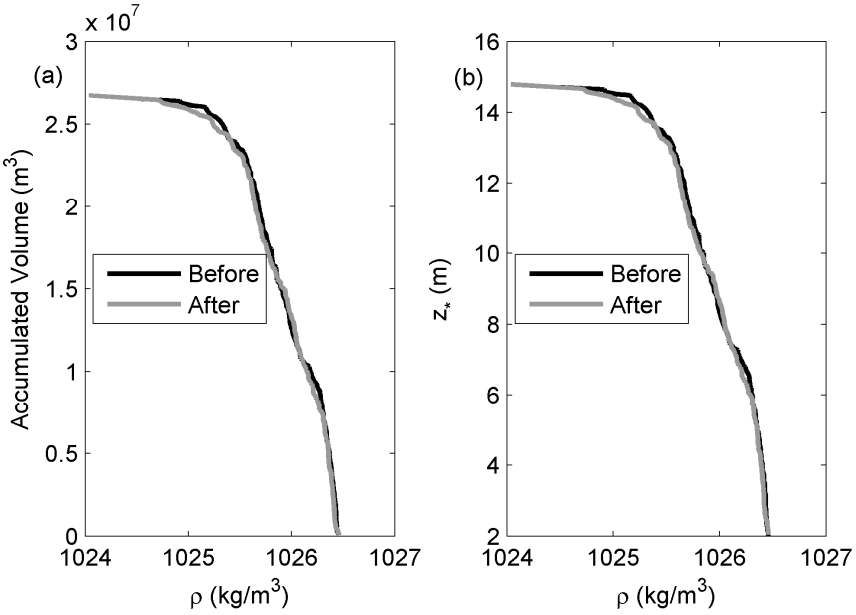

Figure E.8 (a) accumulated volume with increasing density, and (b) minimum potential energy profiles for Flux box 1.

The changes in background potential energy within the flux boxes were calculated by equation (E.23). The term accounting for changes in mass was evaluated using equation (E.18). The variable ψ in the advection term was estimated by averaging the results of equation (E.13) using the profiles of z_* from both before and after each control volume survey.

E.5 Results

When using the field data to construct control volumes, a first check of the data was to apply continuity. In strict terms, mass should be conserved in the control volume. However, continuity of fluid volume was preferred as a data check for the following reasons. Firstly the fluid is essentially incompressible. Secondly, calculating the flux of mass through the control volume surface introduces an additional error source, as density must be first calculated from temperature and salinity (both of which may contain error), and multiplying by velocity (again containing error). Thirdly, with only 9 profiles within the flux box, with a surface area of ~2.4 x 10^6 m^2, the change in mass within the control volume could not be accurately calculated. The change of volume could be estimated with less error by simply multiplying the rate of change in free-surface elevation dh_s/dt by the surface area A_s.

The volumetric flux through the sides of the control volume is obtained by a surface integration. Continuity of volume is satisfied when

$$\oint U \cdot \hat{n} dS + A_s \frac{dh_s}{dt} = 0 \qquad \text{(E.24)}$$

The continuity equation is evaluated for each control volume survey in Table E.1.

Flux Box	dh_s/dt (m/hr)	surface area (m^2)	dVdt (m3/s)	Net Flux (m3/s)	Balance Flux+dVdt (m3/s)
1	0.0555	2101300	32.395	-166.8	-134.4
2	0.447	2064900	256.39	-66.1	190.3
3	-0.612	2878900	-489.41	339.6	-149.8
4	-0.669	2333100	-433.57	572.4	138.8
5	-0.3828	2383500	-253.44	104.0	-149.5
6	-0.786	2418100	-527.96	474.0	-54.0
7	-0.72	2368000	-473.6	617.7	144.1
8	0.315	2383500	208.56	-80.1	128.4
9	-0.42	2360500	-275.39	-34.2	-309.6
10	-0.858	2419100	-576.55	580.3	3.7
11	-0.8235	2454000	-561.36	595.6	34.2
12	-0.2892	2489000	-199.95	-124.6	-324.5

Table E.1 Continuity of volume applied to control volumes.

As Table E.1 shows, the continuity equation was not satisfied for the control volumes, and in some cases the error was large. There are a number of reasons why the continuity equation was not satisfied. The most important is that velocity data were not instantaneous, which is a requirement of control volume theory. The average circuit time for a flux box was 44 minutes. The velocity record was therefore subject to both turbulent and tidal velocity variations. By integrating the volume flux around the flux box, the velocity data is spatially averaged, which reduces the influence of turbulence (although time-averaging rather than spatial-averaging is required to obtain true mean velocities). The variation of velocity due to tide is more of a concern, and this is also accompanied by changes in water surface height over the time taken to complete a circuit.

To adjust the velocity data for tidal variation, a time-based correction method was applied so that continuity was conserved. The error in continuity of volume was assumed to be caused by velocities changing over time because of tidal action. A time-linear correction for velocities was calculated,

$$\oint\left(1+s\frac{t}{\Delta t}\right)U\cdot\hat{n}dS+A_s\frac{dh_s}{dt}=0 \quad , \tag{E.25}$$

Where t s the time when the velocity U was recorded, Δt the duration of the survey, and s the correction factor (constant). The correction factor was found by trial and error. In practice, the scale factor s could be quickly found, as the error in (E.25) is linear with s. The values of s satisfying continuity for the twelve flux boxes are given in Table E.2.

flux box	s	dQ (m^3/s)	dV/dt (m^3/s)	balance (m^3/s)
1	-0.52825	-32.397	32.395	0.0
2	0.42961	-256.39	256.39	0.0
3	0.161078	489.41	-489.41	0.0
4	1.232188	433.57	-433.57	0.0
5	-0.57462	253.44	-253.44	0.0
6	0.058613	527.95	-527.96	0.0
7	1.698059	473.59	-473.6	0.0
8	0.749111	-208.56	208.56	0.0
9	-0.53381	275.39	-275.39	0.0
10	-0.00403	576.55	-576.55	0.0
11	0.187077	561.36	-561.36	0.0
12	6.118641	199.93	-199.95	0.0

Table E.2 Volume fluxes with velocities scaled with time-based correction.

The effect of this correction factor can be applied to a mass balance of salinity. As salinity is conservative (there no appreciable sources or sinks within the control volume), continuity of salt mass should be satisfied. The control volume equation for continuity of salt mass is simpler than that for background potential energy, containing fewer terms. Continuity of salt mass is satisfied by

$$\frac{dS}{dt} = -\underbrace{\iint s\left(\mathbf{u}\cdot\hat{n}\right)dS}_{advection} + \underbrace{\kappa\iint \nabla s\cdot\hat{n}dS}_{diffusion} + \underbrace{\iint s\left(\mathbf{u}_s\cdot\hat{n}\right)dS}_{expansion}. \qquad \text{(E.26)}$$

Neglecting the diffusion term, the change of salt within the control volume should be balanced by the advection and control volume expansion. By defining the control volume such that the top is above the free-surface, the expansion term is removed, and there are no salt fluxes through the top surface.

$$\frac{dS}{dt} + \underbrace{\iint s\left(\mathbf{u}\cdot\hat{n}\right)dS}_{advection} = 0. \qquad \text{(E.27)}$$

The two terms in equation (E.27) are evaluated for each flux box using the raw velocity data in Table E.3, and using the corrected velocity data in Table E.4. The velocity correction improved the error in salinity conservation from an average of -1062 kg/s to 302 kg/s.

Flux Box	salt in (kg/s)	salt out (kg/s)	Net Salt Flux (kg/s)	$\frac{dSalt}{dt}$ (kg/s)	balance kg/s
1	-28068	22423	-5644.6	814.04	-4831
2	-34242	31892	-2349.7	8825.9	6476
3	-58262	70156	11894	-17708	-5814
4	-47005	65990	18985	-15169	3816
5	-43175	46578	3403	-5943.1	-2540
6	-75792	91638	15845	-17313	-1468
7	-53166	74156	20990	-15605	5385
8	-59854	57039	-2815.5	7566.6	4751
9	-65803	64978	-825.3	-8280.7	-9106
10	-100400	120150	19749	-19326	423
11	-62577	82926	20349	-19311	1038

Table E.3 Salt balance using raw velocity data.

Flux Box	Sal in (kg/s)	Sal out (kg/s)	net Sal (kg/s)	$\frac{dSalt}{dt}$ (kg/s)	Balance (kg/s)
1	-19544	18398	-1146.2	814.04	-332.16
2	-44484	35745	-8739	8825.9	86.9
3	-60558	77494	16936	-17708	-772
4	-83995	98189	14194	-15169	-975
5	-28519	36998	8479.5	-5943.1	2536.4
6	-77354	95022	17667	-17313	354
7	-106590	122810	16217	-15605	612
8	-84503	77397	-7105.4	7566.6	461.2
9	-44539	54021	9482.4	-8280.7	1201.7
10	-100250	119870	19623	-24473	297
11	-69141	88383	19242	-14631	-69
12	-130700	137750	7054.9	-4954.7	218.1

Table E.4 Salt balance using corrected velocity data.

The rate of mixing calculated using the method developed above is calculated for the twelve flux boxes in Table E.5

Flux Box	Net ψ flux (1) (J/s)	$\frac{d}{dt}E_b$ (2) (J/s)	mass change (3) (J/s)	Mixing (1)+(2)-(3) Φ_d (J/s)	Flux Box Volume (m^3)	Mixing Rate Φ_d/V (W/m^3)
1	3.049×10^5	7.202×10^4	-8.146×10^6	8.522×10^6	2.655×10^7	0.32
2	-1.690×10^7	-8.729×10^4	2.327×10^7	-4.025×10^7	2.364×10^7	-1.70
3	1.905×10^7	-2.344×10^6	-8.132×10^7	9.803×10^7	2.613×10^7	3.75
4	3.132×10^7	-4.324×10^6	-8.106×10^7	1.081×10^8	3.388×10^7	3.19
5	4.232×10^7	-9.390×10^5	-9.497×10^6	5.087×10^7	3.071×10^7	1.66
6	1.024×10^8	-4.312×10^6	-4.494×10^7	1.430×10^8	3.000×10^7	4.77
7	6.795×10^6	-3.712×10^6	-8.754×10^7	9.063×10^7	2.736×10^7	3.31
8	-1.154×10^7	-2.916×10^4	8.450×10^7	-9.607×10^7	3.077×10^7	-3.12
9	1.844×10^7	-1.299×10^6	-3.377×10^6	2.052×10^7	3.212×10^7	0.64
10	5.514×10^7	-4.498×10^6	-1.008×10^8	1.514×10^8	3.032×10^7	4.99
11	3.638×10^7	-4.944×10^6	-8.780×10^7	1.192×10^8	2.774×10^7	4.30
12	-3.699×10^5	-9.101×10^5	-7.360×10^6	9.681×10^6	2.549×10^7	0.38
			average	**3.857×10^7**		**1.34**

Table E.5 Mixing calculated from background potential energy.

The calculated value of mixing for two of the flux boxes is negative (flux boxes 2 and 8). However inspection of the field data shows that these two surveys were recorded during strong winds, and the velocity records show strong surface currents (Figure E.9 and Figure E.10). As wind gusts may have resulted in higher surface velocities over part of the survey, the data from these two flux boxes are considered unreliable. Excluding surveys 2 and 8, the average rate of mixing was 2.73 W/m^3 with a standard deviation of 1.85 W/m^3. This is an unrealistically high mixing rate in comparison with the energy dissipation from the drag on the mussel droppers. As a rough estimate, the drag force per unit area on the mussel droppers can be obtained from equation 3.17. The rate of work done can be calculated by multiplying the force by the velocity. Assuming a velocity within the farm of ~ 0.075 m/s and a friction coefficient of 0.095, the rate of work within the farm is of order

$$\begin{aligned}\frac{dE}{dt} &= \tfrac{1}{2}\rho C_f U^3 \\ &= \tfrac{1}{2} \times 1025 \times 0.095 \times 0.075^3 \\ &= 0.02 \text{ W/m}^2\end{aligned}$$

With an average depth inside the farm of ~ 12 m, this equates to ~ 0.002 W/m^3. The estimated mixing rate based on potential energy of ~ 2.7 W/m^3 is over 1000 times greater than the dissipation of energy through drag. This large discrepancy indicates that the data were of insufficient quality for the control volume method to be accurate. In particular, the two volume integrals, (2) and (3) in Table E.5 were calculated from only 9 stations within an area of 1.6×10^6 m^2. This resolution was insufficient to represent the variations of density distribution within the control volume. The changing water depth due to the tide also hinders the estimate of mixing rates, as the increases or decreases in potential energy due to the changing

water depth (changes of up to 1.2 m with a total water depth of 12 m) were much larger than any changes expected from mixing.

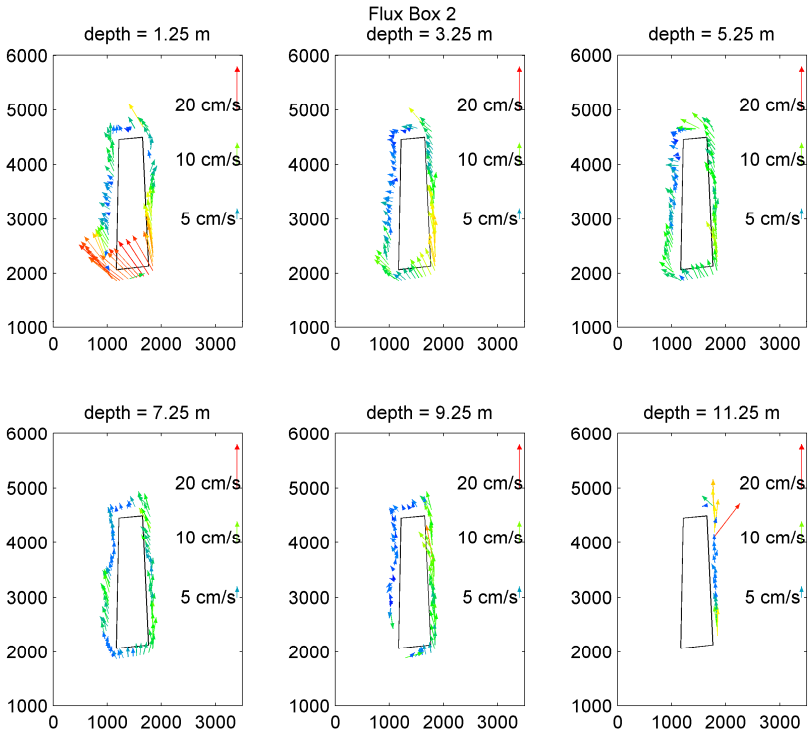

Figure E.9 Velocities for flux box 2. Note strong surface currents near south end of farm.

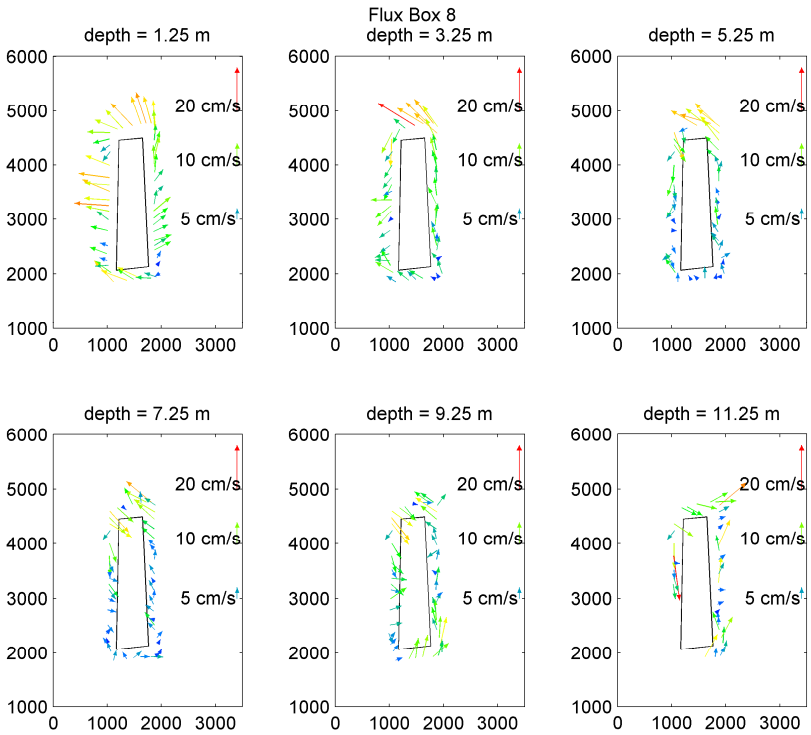

Figure E.10 Velocities for flux box 8. Note strong surface currents along west and north edges of farm.

APPENDIX F CALCULATION OF SIGNIFICANT WAVE HEIGHT FROM PRESSURE SERIES DATA

The following is a reproduction of NIWA Instrument Systems Technical Note No. 98/5 –Task 4/0. This note is available on the internet at:
http://www.niwa.co.nz/rc/instrumentsystems/dobie-tnote5

NIWA Instrument Systems
Technical Note No. 98/5 - Task 4/0 (Wave Statistics) Explained; Plus an Explanation of "Reality Checks"

All wave statistics are calculated from burst time series of "hydrostatic water depth", h(t), which are related to raw pressure time series, p(t), by:

$$h(t) = \frac{p(t)F}{\rho g} + z_p - 10\text{m} \qquad \text{(F.1)}$$

where g is acceleration due to gravity (9.81 m/s^2), ρ is water density and F is a factor (6895 kg/[s^{2}m]/psi) used to convert pressure in pounds per square inch to pressure in kg/(s^{2}m). For this calculation, DOBIE assumes the water density to be 1025 kg/m^3 (which is a typical seawater density). The subtraction of 10 m is a correction that removes a depth of water equal to a nominal atmospheric pressure. z_p is elevation of DOBIE above the bed.

Mean Water Depth

Mean (i.e. burst-averaged) water depth $\overline{h}$ is calculated by DOBIE directly from $h(t)$. The mean water depth calculated in this way is true water depth because the act of averaging the pressure removes the fluctuating pressure component due to the waves (see Technical Notes 98/3 and 98/4). You can use the PEDP to recompute water depth and the consequent changes in wave statistics using a different value for the water density and/or atmospheric pressure and/or sensor elevation.

Standard Deviation

The standard deviation h_{SD} is calculated from $h(t)$ as:

$$h_{SD} = SD[h(t)] - N \qquad \text{(F.2)}$$

where N is the sensor noise level (units of metres). See Technical Note 98/2 for how to check the sensor noise level.

Mean Spectral Period

The mean spectral period is calculated by DOBIE as:

$$\overline{T} = 2\pi m_0 / m_1 \tag{F.3}$$

where m_n is the nth moment of the spectrum of $h(t)$:

$$m_n = \int_{1/T_2}^{1/T_1} f^n S_h(f)\mathrm{d}f \tag{F.4}$$

f is frequency (1/period), T_1 is the minimum wave period specifed during pre-deployment instrument setup and T_2 is the maximum period. Changing the choices for water density, atmospheric pressure, sensor elevation and sensor noise in the PEDP has no effect on mean spectral period. If the mean spectral period does not fall in the range defined by the user (maximum allowable wave period to minimum allowable wave period) then the quality check fails and the error flag is set to 6. DOBIE uses this check to help it distinguish between sensor noise and "real" signal. Use the PEDP to redefine the period range and bypass this quality check if desired.

Spectral Width

The dimensionless width is calculated by DOBIE as:

$$v = \mu / \varpi^2 m_0 \tag{F.5}$$

where $\varpi = 2\pi/\overline{T}$ and $\mu_2 = (m_2 m_0 - m_1^2)/m_0$. Changing the choices for water density, atmospheric pressure, sensor elevation and sensor noise in the PEDP has no effect on spectral width. The spectral width signifies "sea state": 0.1 corresponds to clean swell, and >0.4 corresponds to choppy, confused sea.

Significant Wave Height

The significant wave height is calculated by DOBIE as:

$$H_s = 4h_{SD}\frac{\cosh(\overline{kh})}{\cosh[\overline{k}(z^* + \overline{h})]} \tag{F.6}$$

where z^* is depth of DOBIE below mean water level and $\overline{k}$ is wavenumber corresponding to the mean spectral period, which is calculated using the linear-wave dispersion relationship. The significant wave height is the average height of the highest one-third waves, which has been shown to be equal to what the casual observer would call "wave height". The significant wave height is commonly used to characterise wave height in engineering applications. In order to estimate H_s the raw pressure signal must be amplified to correct for attenuation of pressure fluctuations with depth. The correction used above is robust, but can still cause problems when there simply is not enough information in the raw pressure data to work with in the first place. See below for the use of "reality checks" to detect such problems, and see Technical Note 98/1 for a full discussion of the problem. Changing the choice for noise level in the PEDP will change the significant wave height.

Significant Orbital Speed at the Bed

The significant orbital speed at the bed is:

$$U_s = \frac{4\pi h_{SD} \cosh(\bar{k}\bar{h})}{\bar{T} \cosh[\bar{k}(z^* + \bar{h})] \sinh(\bar{k}\bar{h})} \tag{F.7}$$

The significant orbital speed is the maximum (i.e., maximum in the wave cycle) orbital speed at the bed corresponding to the mean spectral period and the significant wave height. Note that even if DOBIE is unable to estimate significant wave height, this parameter is still valid. This is because even though significant orbital speed is defined in terms of significant wave height, it is calculated directly from the raw pressure data. If DOBIE is deployed on the bed then U_s will be very accurate, but even if DOBIE is deployed above the bed U_s should still be reasonable because in that case the pressure signal is attenuated to estimate U_s, not amplified as it is in the estimation of H_s. See Technical Note 98/1 for a full discussion. Changing the choice for noise level in the PEDP will change the significant orbital speed.

Penetration

The penetration is calculated by DOBIE as:

$$\frac{\cosh[\bar{k}(z^* + \bar{h})]}{\cosh(\bar{k}\bar{h})} \tag{F.8}$$

Penetration is an indicator of how much the pressure signal has been attenuated between the surface and the level of the DOBIE. For instance, if the penetration is 0.15, then only 15% of the surface pressure-fluctuation signal has penetrated to the level of the DOBIE. In effect, the pressure signal is multiplied by the reciprocal of the penetration to "transform the pressure data back up to surface". If penetration is very small (say, less than 0.05) then chances are most of the signal is really just sensor noise. When the noise is multiplied by 1/0.05 then huge (and erroneous!) wave heights result, which is why DOBIE applies "reality checks" to the wave statistics. If the reality checks are not failed but the penetration is still very low, then use the wave statistics only with caution.

Reality Check #1

The maximum wave steepness is set at:

$$(\bar{k}H_s)_{\max} = \frac{2\pi}{7 \tanh(\bar{k}\bar{h})} \tag{F.9}$$

This is the first of the "real-world" checks on the estimated wave height. If the wave steepness exceeds the theoretical maximum wave steepness then the wave is deemed by DOBIE to be physically unrealistic and the error flag is set 13. Use the PEDP to bypass this reality check if desired.

Reality Check #2

The maximum ratio of wave height to water depth is:

$$H_s / \overline{h} = 1 \qquad \text{(F.10)}$$

This is the second "real-world" check on the estimated wave height. If the wave height is larger than the water depth theoretically allows, then the wave is deemed by DOBIE to be physically unrealistic and the error flag is set to 14. This check is rather conservative: values of the wave height to water depth ratio at the breakpoint as high as 2.5 have been observed. Use the PEDP to bypass this reality check if desired.

APPENDIX G LINEAR REGRESSIONS AND CONFIDENCE INTERVALS

At a number of points in this thesis, a least squares regression was used to find a relationship between two variables. For example, linear regressions were used to calculate wave energy transmission ratios (section 5.4.4), frequency response functions for anchor rope wave loadings (sections 6.3.3 and 6.4.3), and drag coefficients from tow tests (see sections 9.4.4 and 10.3.1). The standard linear regression is described in many texts on mathematics and statistics (for example Kreyszig, 2003; particularly section 24.12). However, a modified linear regression has been used at various places where the regression line is forced through the origin. This has been used where the physics suggest that there must be zero output if the input is zero. The derivation of the linear regression and the modified linear regression are given below. It is also desirable to calculate a confidence interval for the regression coefficients, and the means of doing this is also given below.

G.1 Linear Regression

In a linear regression, a straight line is fit through the data with a slope k_1 and intercept k_0 (Figure G.1) such that the sum of the squared-errors between the dependent variable y_i and the predicted values y_p are minimised. The predicted values are calculated from the value of the independent variable x for each data point by

$$y_p = k_1 x_i + k_0 \,. \tag{G.1}$$

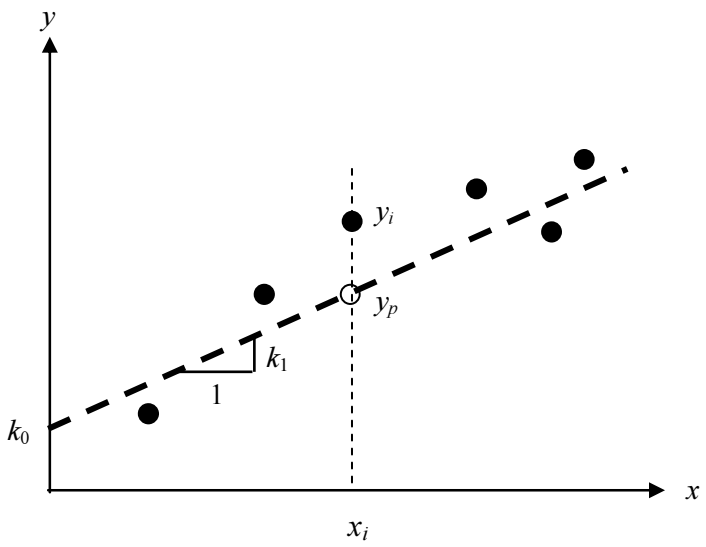

Figure G.1 Least-mean-squared linear regression.

The squared-errors for each data point are summed to give the total error (quotient) q

$$q = \sum_{j=1}^{n} \left(y_i - y_p \right)^2 = \sum_{j=1}^{n} \left(y_i - k_0 - k_1 x_j \right)^2 . \tag{G.2}$$

where n is the number of data points.

The total error is minimised by changing the regression coefficients k_1 and k_0, so that

$$\frac{\partial q}{\partial k_1} = 0 \text{ and } \frac{\partial q}{\partial k_0} = 0 \tag{G.3}$$

The solutions are

$$k_1 = \frac{\sum_{j=1}^{n} x_j y_j - \frac{1}{n} \sum_{j=1}^{n} x_j \sum_{j=1}^{n} y_j}{\sum_{j=1}^{n} x_j^{\,2} - \frac{1}{n} \left(\sum_{j=1}^{n} x_j \right)^2}, \tag{G.4}$$

$$k_0 = \frac{1}{n} \sum_{j=1}^{n} y_j - k_1 \frac{1}{n} \sum_{j=1}^{n} x_j . \tag{G.5}$$

These can be re-written using the mean values $\overline{x} = \frac{1}{n} \sum_{j=1}^{n} x_j$ and $\overline{y} = \frac{1}{n} \sum_{j=1}^{n} y_j$, giving

$$k_1 = \frac{\sum_{j=1}^{n} x_j y_j - \overline{y} \sum_{j=1}^{n} x_j}{\sum_{j=1}^{n} x_j^{\,2} - \overline{x} \sum_{j=1}^{n} x_j}, \tag{G.6}$$

$$k_0 = \overline{y} - k_1 \overline{x} . \tag{G.7}$$

G.2 Linear Regression with Zero Intercept

The same method can be used to derive a linear regression in with a zero intercept (Figure G.2). There is only one regression coefficient to solve for, as $k_0 = 0$. The predicted values are calculated from the x value for each data point by

$$y_p = k_1 x_i . \tag{G.8}$$

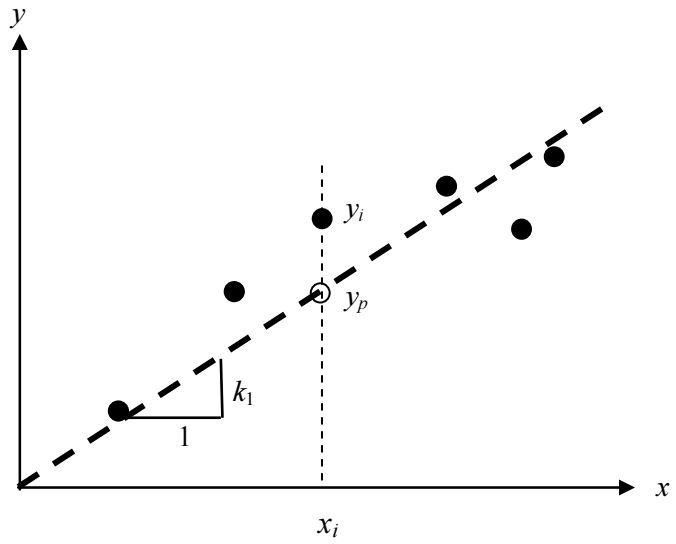

Figure G.2 Least-mean-squared linear regression with zero intercept.

The total squared-error is

$$q = \sum_{j=1}^{n} \left(y_i - y_p \right)^2 = \sum_{j=1}^{n} \left(y_i - k_1 x_j \right)^2 . \tag{G.9}$$

The total error is minimised by changing the regression coefficient k_1 so that

$$\frac{\partial q}{\partial k_1} = 0 . \tag{G.10}$$

The solution is

$$k_1 = \frac{\sum_{j=1}^{n} x_j y_j}{\sum_{j=1}^{n} x_j^{\,2}} , \tag{G.11}$$

G.3 Confidence Interval for a Regression Coefficient

A confidence for the slope of a linear regression can be calculated as follows.

The estimated values for each value of x can be calculated from

$$y_p = k_1 x_i + k_0 . \tag{G.12}$$

A zero value for the intercept k_0 may be used if the regression is force through the origin. The standard error of the estimate s_{yx} is calculated from

$$s_{yx} = \sqrt{\frac{\sum_{j=1}^{n}\left(y_j - y_p\right)^2}{n-2}}\,. \tag{G.13}$$

The standard error of the slope s_k is calculated from

$$s_k = \frac{s_{yx}}{\sqrt{\sum_{j=1}^{n}\left(x_j - \bar{x}\right)^2}}\,. \tag{G.14}$$

The confidence interval for the slope is then determined by

$$conf = \pm t \cdot s_k\,. \tag{G.15}$$

where t is determined from the Student's t distribution. The t value is calculated by first choosing a confidence interval, e.g. c = 95%. This gives an exceedance probability P = 1- c/100 (0.05 in this example). From a two-tailed Student's t distribution, the t value is determined which has an exceedance probability of P with n-2 degrees of freedom.

G.4 R^2 value for a Regression

The square of the Pearson product moment correlation coefficient (R^2) value indicates the proportion of the variance in the variable z_2 attributable to the variance in z_1. The R^2 can be calculated for a regression by comparing the actual values y with those predicted by the regression y_p. A value of R^2 of 1 indicates a perfect fit between the regression and the data.

$$R^2 = 1 - \frac{\sum_{j=1}^{n}\left(y_j - y_p\right)^2}{\sum_{j=1}^{n} y_j{}^2 - \left(\sum_{j=1}^{n} y_j\right)^2}, \tag{G.16}$$

REFERENCES

Achenbach, E. (1971). "Influence of surface roughness on the cross-flow around a circular cylinder." Journal of Fluid Mechanics **46**: 321-335.

Achenbach, E. and E. Heinecke (1981). "On vortex shedding from smooth and rough cylinders in the range of Reynolds numbers 6 x 10^3 to 5 x 10^6." Journal of Fluid Mechanics **109**: 239-251.

Aiba, S., H. Tsuchida and T. Ota (1981). "Heat transfer around a tube in a bank." Bulletin of Japan Society of Mechanical Engineers **25**: 919-926.

Alridge, T. R., B. S. Piper and J. C. R. Hunt (1978). "The drag coefficient of finite-aspect-ratio perforated circular cylinders." Journal of Industrial Aerodynamics **3**: 251-257.

Asano, T., S. Tsutsui and T. Sakai (1988). Wave damping characteristics due to seaweed. 35th Coastal Engineering Conference in Japan, Japan Society of Civil Engineers.

Bearman, P. W. (1969). "On vortex shedding from a circular cylinder in the critical Reynolds number region." Journal of Fluid Mechanics **37**: 577-587.

Bearman, P. W. and Morel, T. (1983). "Effect of free stream turbulence on the flow around bluff bodies." Progress in Aerospace Sciences, **20**: 97-123.

Beaudan, P. and P. Moin (1994). Numerical experiments on the flow past a circular cylinder at sub-critical Reynolds number, Report TF-62, M.E. Dept, Stanford University.

Bird, R. B., W. E. Stewart and E. N. Lightfoot (1960). Transport phenomena.New York, Wiley.

Blanco, J., M. Zapata and Á. Moroño (1996). "Some aspects of the water flow through mussel rafts." Scientia Marina **60**(2-3): 275-282.

Boyd, A. J. and K. G. Heasman (1998). "Shellfish mariculture in the Benguela system: water flow patterns within a mussel farm in Saldanha Bay, South Africa." Journal of Shellfish Research **17**(1): 25-32.

Bradford, J. M., F. H. Chang, R. Baldwin, B. Chapman, M. Downes and P. Woods (1987). "Hydrology, plankton, and nutrients in Pelorus Sound, New Zealand, July 1981 and May 1982." New Zealand Journal of Marine and Freshwater Research **21**: 223-233.

Bradshaw, P. (1965). "The effect of wind-tunnel screens on nominally two-dimensional boundary layers." Journal of Fluid Mechanics **22**(4): 679-687.

Buresti, G. (1981). "The effect of surface roughness on the flow regime around circular cylinders." Journal of Wind Engineering and Industrial Aerodynamics **8**: 115-122.

Chen, D. and G. H. Jirka (1995). "Experimental study of plane turbulent wakes in a shallow water layer." Fluid Dynamics Research **16**: 11-41.

Chen, D. and G. H. Jirka (1997). "Absolute and convective instabilities of plane turbulent wakes in a shallow water layer." Journal of Fluid Mechanics **338**: 157-172.

Chu, V. H. and S. Babarutis (1988). "Confinement and bed-friction effects in shallow turbulent mixing layers." Journal of Hydraulic Engineering **114**(10): 1257-1274.

Chu, V. H., J. H. Wu and R. E. Kayat (1983). Stability in turbulent shear flow in shallow channel. Proceedings of the 20th I.A.H.R. Congress, Moscow.

Chu, V. H., J. H. Wu and R. E. Kayat (1991). "Stability in turbulent shear flow in shallow channel." Journal of Hydraulic Engineering **117**(10): 1370-1389.

Cionco, R. M. (1965). "A mathematical model for air flow in a vegetative canopy." Journal of Applied Meteorology **4**: 517-522.

Cline, A. K. and R. L. Renka (1984). "A storage-efficient method for construction of a Thiessen triangulation." Rocky Mountain Journal of Mathematics **14**(1): 119-139.

Cook, N. J. (1985). The designer's guide to the wind loading of building structures, Part 2 Static Structures, Butterworths.

Coutanceau, M. and J. R. Defaye (1991). "Circular cylinder configurations: a flow visualization survey." Applied Mechanics Review **44**(6): 255-305.

Cowdrey, C. F. (1968). Some observations of the flow of air through a single row of closely spaced cylinders. NPL Aerodynamics Note 1064, British National Physics Laboratory.

Cowen, E. A. and S. G. Monismith (1997). "A hybrid digital particle tracking velocimetry technique." Experiments in Fluids **22**: 199-211.

Cullen, J. J. (1982). "The deep chlorophyll maximum: comparing vertical profiles of chlorophyll *a*." Canadian Journal of Fisheries and Aquatic Sciences **39**: 791-803.

Dahlback, N. and L. A. H. Gunnarsson (1981). "Sedimentation and sulphate reduction under a mussel culture." Marine Biology **63**: 269-275.

Dalrymple, R. A., J. T. Kirby and P. A. Hwang (1984). "Wave diffraction due to areas of energy dissipation." Journal of Waterway, Port, Coastal, and Ocean Engineering **110**(1): 67-79.

Dark, A. (2003). Double Diffusive Jets, Research Report, Department of Civil Engineering, University of Canterbury, Christchurch, New Zealand.

Dean, R. G. and R. A. Dalrymple (1991). Water wave mechanics for engineers and scientists, World Scientific.

Elwany, M. J. S., W. C. O'Reilly, R. T. Guza and R. E. Flick (1995). "Effects of southern california kelp bends on waves." Journal of Waterway, Port, Coastal, and Ocean Engineering **121**(2): 143-150.

Fage, A. and J. H. Warsap (1929). The effects of turbulence and surface roughness on the drag of a circular cylinder, British Aeronautical Research Council (A.R.C.) Reports and Memoranda No. 1283.

Falnes, J. (2002). Ocean waves and oscillating systems, Cambridge University Press.

FAOSTAT (2004). Food and Agriculture Organisation of the United Nations. Available: http://apps.fao.org.

Finnigan, J. J. (2000). "Turbulence in plant canopies." Annual Review of Fluid Mechanics **32**: 519-571.

Fisher, H. B., E. J. List, R. C. Y. Koh, J. Imberger and N. H. Brooks (1979). Mixing in inland and coastal waters.New York, Academic Press.

Flagg, C. N. and S. L. Smith (1989). "On the use of the Acoustic Doppler Current Profiler to measure zooplankton abundance." Deep-Sea Research **36**: 455-474.

Gerrard, J. H. (1965). "A disturbance-sensitive Reynolds number range of the flow past a circular cylinder." Journal of Fluid Mechanics **22**: 187-196.

Ghisalberti, M. and H. M. Nepf (2002). "Mixing layers and coherent structures in vegetated aquatic flows." Journal of Geophysical Research **107**(0).

Gibbs, M. M., M. R. James, S. E. Pickmere, P. H. Woods, B. S. Shakespeare, R. W. Hickman and J. Illingworth (1991). "Hydrodynamic and water column properties at six stations associated with mussel farming in Pelorus Sound, 1984-85." New Zealand Journal of Marine and Freshwater Research **25**: 239-254.

Gibbs, M. M., S. E. Pickmere, P. H. Woods, G. W. Payne, M. R. James and J. Illingworth (1992). "Nutrient and chlorophyll-a variability at six stations associated with mussel farming in Pelorus Sound, 1984-85." New Zealand Journal of Marine and Freshwater Research **26**(197-211).

Gibbs, M. M. and W. N. Vant (1997). "Seasonal changes in factors controlling phytoplankton growth in Beatrix Bay, New Zealand." New Zealand Journal of Marine and Freshwater Research **32**: 237-248.

Grant, J. and C. Bacher (2001). "A numerical model of flow modification induced by suspended aquaculture in a Chinese bay." Canadian Journal of Fisheries and Aquatic Sciences **58**: 1003-1011.

Grant, J., A. Hatcher, D. B. Scott, P. Pocklington, C. T. Schafer and G. V. Winters (1995). "A multidisciplinary approach to evaluating impacts of shellfish aquaculture on benthic communities." Estuaries **63**: 269-275.

Gray, J. S. and M. B. Farrukh (1979). "A possible method for the detection of pollution-induced disturbance on marine benthic communities." Marine Pollution Bulletin **10**: 142-146.

Grosenbaugh, M., S. Anderson, R. Trask, J. Gobat, W. Paul, B. Butman and R. Weller (2002). "Design and performance of a horizontal mooring for upper-ocean research." Journal of Atmospheric and Oceanic Technology **19**: 1376-1389.

Güven, O., C. Farell and V. C. Patel (1980). "Surface-roughness effects on the mean flow past circular cylinders." Journal of Fluid Mechanics **98**(4): 673-701.

Haamer, J. (1996). "Improving water quality in a eutrophied system with mussel farming." Ambio **25**(6): 356-362.

Hatcher, A., J. Grant and Schofield (1994). "Effects of suspended mussel culture (Mytilus spp.) on sedimentation, benthic respiration and sediment nutrient dynamics in a coastal bay." Marine Ecology Progress Series **115**: 219-235.

Hawkins, A. J. S., M. R. James, R. W. Hickman, S. Hatton and M. Weatherhead (1999). "Modelling of suspension-feeding and growth in the green-lipped mussel *Perna canaliculus* exposed to natural and experimental variations of seston availability in the Marlborough Sounds, New Zealand." Marine Ecology Progress Series **191**: 217-232.

Hayden, B. J. (1995). Factors affecting recruitment of farmed greenshell mussels, *Perna canliculus*, (Gmelin) 1791, in Marlborough Sounds: a thesis submitted for the degree of Doctor of Philosophy. Dunedin, New Zealand, University of Otago**:** 274.

Hickman, R. W. (1989). "Farming the green mussel in New Zealand, current practice and potential." World Aquaculture **20**(4): 20-28.

Hickman, R. W. (1991). *Perna canaliculus* (Gmelin) in New Zealand. Estuarine and Marine Bivalve Mollusk Culture. W. Menzel. Boca Raton, CRC Press**:** 325-334.

Igarashi, T. (1986). "Characteristics of the flow around four circular cylinders arranged in-line." Bulletin of Japan Society of Mechanical Engineers **29**: 751-757.

Igarashi, T. and K. Suzuki (1984). "Characteristics of the flow around three circular cylinders." Bulletin of Japan Society of Mechanical Engineers **27**: 2397-2404.

Jackson, G. A. (1998). "Currents in the high drag environment of a coastal kelp stand off California." Continental Shelf Research **17**(15): 1913-1928.

Jackson, G. A. and C. D. Winant (1983). "Effect of a kelp forest on coastal currents." Continental Shelf Research **2**(1): 75-80.

Kamphuis, J. W. (1975). "Friction factor under oscillatory waves." Journal of the Waterway, Harbour and Coastal Engineering Division **101**: 135-145.

Kaspar, H. F., P. A. Gillespie, I. C. Boyer and A. L. Mackenzie (1985). "Effects of mussel aquaculture on the nitrogen cycle and benthic communities in Kenepuru Sound, Marlborough Sounds, New Zealand." Marine Biology **85**: 127-136.

Kobayashi, N., A. W. Raichle and T. Asano (1993). "Wave attenuation by vegetation." Journal of Waterway, Port, Coastal, and Ocean Engineering **119**(1): 30-48.

Kreyszig, E. (2003), Advanced Engineering Mathematics, Wiley.

Lindsey, W. F. (1938). Drag of cylinders of simple shapes. Report No. 619, National Advisory Committee for Aeronautics**:** 169-176.

Lorenzen, C. J. (1966). "A method for the continous measurement of *in vivo* chlorophyll concentration." Deep-Sea Research **13**: 223-227.

Mani, J. S. and S. Jayakumar (1995). "Wave transmission by suspended pipe breakwater." Journal of Waterway, Port, Coastal, and Ocean Engineering **121**(6): 335-338.

Massa, D. E. and K. F. Bosma (2000). Hydroacoustic measurement of detritus from the Delaware estuary. Oceans 2000 MTS/IEEE Conference and Exhibition, 11-14 Sept. 2000.

Massel, S. R. (1976). "Interaction of water waves with cylindrical barrier." Journal of Waterway, Port, Coastal, and Ocean Engineering **102**(WW2): 165-187.

Mauti, B., W. Faber and G. P. Romano (2000). The effect of a cylinder on the velocity field at the outlet of a circular jet measured by PIV and PTV. 10th International Symposium on Applications of Laser Techniques to Fluid Mechanics, 10-13 July 2000, Lisboa, Portugal.

McKillop, A. and F. Durst (1984). A laser anemometry study of separated flow behind a circular cylinder. Laser Anemometry in Fluid Mechanics, Ladoan Lisboa, Portugal.

Michell, J. H. (1893). "On the highest wave in water." Philosophical Magazine **36**: 430-435.

Miles, J. W. (1961). "On the stability of heterogeneous shear flows." Journal of Fluid Mechanics **10**: 496-508.

Miller, G. S., J. H. Saylor and M. J. McCormick (1999). Detecting storm-generated suspended materials in Lake Michigan using ADCP echo intensities. IEEE Sixth Working Conference on Current Measurement.

Mirto, S., T. La Rosa, R. Danovaro and A. Mazzola (2000). "Microbial and meiofaunal response to intensive mussel-farm biodeposition in coastal sediments of the western Mediterranean." Marine Pollution Bulletin **40**: 244-252.

Moretti, P. M. and M. Cheng (1987). "Instability of flow through tube rows." Journal of Fluids Engineering **109**: 197-198.

Morgan, P. G. (1960). "The stability of flow through porous screens." Journal of the Royal Aeronautical Society **64**: 359-362.

Morison, J. R., M. P. O'Brien, J. W. Johnson and S. A. Schaaf (1950). "The forces exerted by surface waves on piles." Petroleum Transactions, AIME **189**: 149-157.

Moser, R. D. and M. M. Rogers (1993). "The three-dimensional evolution of a plane mixing layer: pairing and transition to turbulence." Journal of Fluid Mechanics **247**: 257.

Murali, K. and J. S. Mani (1997). "Performance of cage floating breakwater." Journal of Waterway, Port, Coastal, and Ocean Engineering **123**(4): 172-179.

Nath, J. H. (1987). "On wave force coefficient variability." Journal of Offshore Mechanics and Arctic Engineering **109**: 295-306.

Niemann, H. J. and N. Hölscher (1990). A review of recent experiments on the flow past circular cylinders. Bluff Body Aerodynamics and its Applications. M. e. a. Ito. Amsterdam, Elsevier**:** 179-210.

NIWA (1998). Technical note no. 98/5 - task 4/0 (wave statistics) explained, NIWA Instrument Systems, available online at http://www.niwa.co.nz/rc/instrumentsystems/dobie-tnote5.

Nokes, R. I. (2004a). Streamline 5.0. Christchurch**:** Particle Tracking Velocimetry Software.

Nokes, R. I. (2004b). Streamline operation manual. Christchurch, New Zealand, University of Canterbury Department of Civil Engineering.

Nokes, R. I., S. A. Blackett and M. J. Davidson (submitted). "Design, performance and application of a generalised, optimisation-based particle tracking velocimetry system." submitted to Experiments in Fluids.

Norberg, C. (1986). "Interaction between free stream turbulence and vortex shedding for a single tube in a cross flow." Journal of Wind Engineering and Industrial Aerodynamics **23**: 501-514.

Norberg, C. (1998). LDV-measurements in the near wake of a circular cylinder. Advances in Understanding of Bluff Body Wakes and Vortex-Induced Vibration, Washington DC, June 1998.

Ogilvie, S. C. (2000). Phytoplankton depletion in cultures of the mussel Perna canaliculus. Zoology. Christchurch, University of Canterbury**:** 129.

Ogilvie, S. C., A. H. Ross and D. R. Schiel (2000). "Phytoplankton biomass associated with mussel farms in Beatrix Bay, New Zealand." Aquaculture **181**: 71-80.

Panchang, V., G. Cheng and C. Newell (1997). "Modeling hydrodynamics and aquaculture waste transport in coastal maine." Estuaries **20**(1): 14-41.

Papanicolaou, P. N. and E. J. List (1988). "Investigations of round vertical turbulent buoyant jets." Journal of Fluid Mechanics **195**: 341-391.

Paul, W. and G. Grosenbaugh (2000). Submerged coastal and offshore mussel aquaculture system (SCOMAS) a multidisciplinary approach. Cambridge, Massachusetts, Woods Hole Oceanographic Institute.

Philips, R., B. Bradley and T. International (2003). New Zealand from space 2.Auckland, New Zealand, Penguin Books.

Pilditch, C. A., J. Grant and K. R. Bryan (2001). "Seston supply to scallops in suspended culture." Canadian Journal of Fisheries and Aquatic Sciences **58**(2): 241-253.

Plew, D., C. Stevens, R. Spigel and N. Hartstein (2005). "Hydrodynamic implications of large offshore mussel farms." IEEE Journal of Oceanic Engineering **30**(1).

Pope, S. B. (2000). Turbulent Flows.Cambridge, University Press, Cambridge.

Prandtl, L. (1961). Collected Works (*in German*).Berlin, Springer.

Price, S. J., M. P. Païdoussis and B. Mark (1995). "Flow visualisation of the interstitual cross-flow through parallel triangular and rotated square arrays of cylinders." Journal of Sound and Vibration **181**(1): 85-98.

Raman-Nair, W. and B. Colbourne (2003). "Dynamics of a mussel longline system." Aquacultural Engineering **27**: 191-212.

Rehmann, C. R. and J. R. Koseff (2004). "Mean potential energy change in stratified grid turbulence." Dynamics of Atmospheres and Oceans **37**: 271-294.

Rodi, W. (1980). Turbulent models and their application in hydraulics: a state of the art review, Delft: International Association for Hydraulic Research.

Roe, H. S. J., G. Griffiths, M. Hartman and N. Crisp (1996). "Variability in biological distributions and hydrography from concurrent Acoustic Doppler Current Profiler and SeaSoar surveys." ICES Journal of Marine Science **53**: 131-138.

Rosenberg, R. and L.-O. Loo (1983). "Energy-flow in a Mytilus edulis culture in western Sweden." Aquaculture **35**: 151-161.

Roshko, A. (1961). "Experiments on the flow past a circular cylinder at very high Reynolds numbers." Journal of Fluid Mechanics **10**: 345-56.

Roshko, A. and W. Fiszdon (1969). On the persistance of transition in the nearwake. Problems of Hydrodynamics and Continuum Mechanics, Society for Industrial and Applied Mathematics, Philadelphia.

Ross, A. and S. Hooker (2001). "Marine models aid mussel production." Aniwaniwa (NIWA resource management newsletter) **16**.

Ross, A. H., M. M. Gibbs, M. James and T. Osborne (1998). "Changes in nutrients affecting phytoplankton abundance in Pelorus Sound 1994-1998." Seafood New Zealand **6**(9): 32-37.

Sarpkaya, T. (1987). "Oscillating flow about smooth and rough cylinders." Journal of Offshore Mechanics and Arctic Engineering **109**: 307-313.

Sarpkaya, T. (1990). "On the effect of roughness on cylinders." Journal of Offshore Mechanics and Arctic Engineering **112**: 334-340.

Schlitzer, R. (2004). Ocean Data View, http://www.awi-bremerhaven.de/GEO/ODV.

Seymour, R. J. (1996). "Discussion of Effects of southern California kelp beds on Waves." Journal of Waterway, Port, Coastal, and Ocean Engineering **122**(4): 207-208.

Seymour, R. J. and D. M. Hanes (1979). "Performance analysis of tethered float breakwaters." Journal of Waterway, Port, Coastal, and Ocean Engineering **105**: 265-280.

Stanton, T. K., D. Chu and P. H. Wiebe (1996). "Acoustic scattering characteristics of several zooplankton groups." ICES Journal of Marine Science **53**: 289-295.

Stevens, C. L. (2003). "Turbulence in an estuarine embayment: Observations from Beatrix Bay, New Zealand." Journal of Geophysical Research **108**(C2): 12-1 to 12-15.

Stevens, C. L., C. L. Hurd and P. E. Isachsen (2003). "Modelling of diffusion boundary-layers in subtidal macroalgal canopies: The response to waves and currents." Aquatic Sciences **65**: 81-91.

Stevens, C. L., C. L. Hurd and M. J. Smith (2001). "Water motion relative to subtidal kelp fronds." Limnology and Oceanography **46**(3): 668-678.

Surry, D. (1972). "Some effects of intense turbulence on the aerodynamics of a circular cylinder at subcritical Reynolds number." Journal of Fluid Mechanics **52**: 543-563.

Swamee, P. K. and A. K. Jain (1976). "Explicit equations for pipe-flow problems." Journal of the Hydraulics Division, Proceedings of the American Society of Civil Engineers: 657-664.

Trump, C. L., N. Allan and G. O. Marmorino (2000). "Side-looking ADCP and Doppler radar measurements across a coastal front." IEEE Journal of Oceanic Engineering **25**(4): 423-429.

Turner, J. S. (1973). Buoyancy effects in fluids.London, Cambridge University Press.

Uijttewaal, W. S. J. and R. Booij (2000). "Effects of shallowness on the development of the free-surface mixing layers." Physics of Fluids **12**(2): 392-402.

Umeda, S. and W.-J. Yang (1999). "Interaction of von Kármán vortices and intersecting main streams in staggered tube bundles." Experiments in Fluids **26**: 389-396.

USACE (2003). Meteorology and Wave Climate. Coastal Hydrodynamics. D. T. Resio, S. Bratos and E. F. Thompson. **Chapter 2**.

Vincent, W. G. (1979). "Mechanisms of rapid photosynthetic adaptation in natural phytoplankton communities. I. Redistribution of excitation energy between photosystems I and II." Journal of Phycology **15**: 429-434.

Waite, R. P. (1989). The nutritional biology of Pena canaliculus with special reference to intensive mariculture systems. Zoology. Christchurch, University of Canterbury**:** 136.

Wieselsberger, C. (1921). "New data on the laws of fluid resistance." Physikalische Zeitschrift **22**: 321-328.

Williams, A. N. and W. G. McDougal (1996). "A dynamic submerged breakwater." Journal of Waterway, Port, Coastal, and Ocean Engineering **122**(6): 288-296.

Winters, K. B., P. N. Lombard, J. J. Riley and E. D'Asaro (1995). "Available potential energy and mixing in density stratified fluids." Journal of Fluid Mechanics **289**: 115-128.

Wolfram, J. and M. Naghipour (1999). "On the estimation of Morison force coefficients and their predictive accuracy for very rough circular cylinders." Applied Ocean Research **21**: 311-328.

Young, I. R. (1999). Wind generated ocean waves, Elsevier.

Yu, X. (1995). "Diffraction of water waves by porous breakwaters." Journal of Waterway, Port, Coastal, and Ocean Engineering **121**(6): 275-282.

Zdravkovich, M. M. (1990). "Conceptual overview of laminar and turbulent flows past smooth and rough circular cylinders." Journal of Wind Engineering and Industrial Aerodynamics **33**: 53-62.

Zdravkovich, M. M. (1993). "On suppressing metastable interstitial flow behind a tube array." Journal of Fluids and Structures **7**: 245-252.

Zdravkovich, M. M. (1995). Interaction of bistable/metastable flows and stabilizing devices. 6th International Conference on Flow-Induced Vibration, Balkema, Rotterdam.

Zdravkovich, M. M. (1997). Flow around circular cylinders : a comprehensive guide through flow phenomena, experiments, applications, mathematical models, and computer simulations. 1: Fundamentals, Oxford University Press.

Zdravkovich, M. M. (2003). Flow around circular cylinders : a comprehensive guide through flow phenomena, experiments, applications, mathematical models, and computer simulations. 2: Applications, Oxford University Press.

Zdravkovich, M. M. and K. L. Stonebanks (1990). "Intrinsically nonuniform and metastable flow in and behind tube arrays." Journal of Fluids and Structures **4**: 305-319.